

# Ultrafast Optical Physics II

Franz X. Kaertner

SoSe 2017



# Contents

<b>1</b>	<b>Introduction</b>	<b>1</b>
1.1	Course Mission . . . . .	1
1.2	Pulse Characteristics . . . . .	1
1.3	Applications . . . . .	4
1.4	Review of Laser Essentials	
	10	
1.5	History . . . . .	15
1.6	Laser Materials . . . . .	17
<b>2</b>	<b>Linear Pulse Propagation</b>	<b>25</b>
2.1	Maxwell's Equations of Homogeneous Media . . . . .	25
2.1.1	Helmholtz Equation for Linear Media . . . . .	27
2.1.2	Plane-Wave Solutions (TEM-Waves) and Complex No- tation . . . . .	28
2.1.3	Poynting Vectors, Energy Density and Intensity . . . .	30
2.2	Classical Permittivity . . . . .	31
2.3	Optical Pulses . . . . .	35
2.4	Pulse Propagation . . . . .	39
2.4.1	Dispersion . . . . .	41
2.4.2	Loss and Gain . . . . .	49
2.5	Sellmeier Equation and Kramers-Kronig Relations . . . . .	51
2.6	Summary . . . . .	55
<b>3</b>	<b>Nonlinear Pulse Propagation</b>	<b>59</b>
3.1	The Optical Kerr-effect . . . . .	59
3.2	Self-Phase Modulation (SPM) . . . . .	60
3.3	The Nonlinear Schrödinger Equation . . . . .	63
3.3.1	The Solitons of the NLSE . . . . .	63

3.3.2	The Fundamental Soliton . . . . .	64
3.3.3	Higher Order Solitons . . . . .	66
3.3.4	Inverse Scattering Theory . . . . .	69
3.4	Universality of the NLSE . . . . .	73
3.5	Soliton Perturbation Theory . . . . .	73
3.6	Soliton Instabilities by Periodic Perturbations . . . . .	80
3.7	Pulse Compression . . . . .	85
3.7.1	General Pulse Compression Scheme . . . . .	85
3.7.2	Spectral Broadening with Guided Modes . . . . .	87
3.7.3	Dispersion Compensation Techniques . . . . .	88
3.7.4	Dispersion Compensating Mirrors . . . . .	93
3.7.5	Hollow Fiber Compression Technique . . . . .	109
3.8	Summary . . . . .	110
3.9	Appendix: Sech-Algebra . . . . .	110
<b>4</b>	<b>Laser Dynamics</b>	<b>123</b>
4.1	Two-Level Atoms and Bloch Equations . . . . .	123
4.1.1	The Two-Level Model . . . . .	124
4.1.2	The Atom-Field Interaction In Dipole Approximation . . . . .	126
4.1.3	Rabi-Oscillations . . . . .	127
4.1.4	Energy- and Phase-Relaxation . . . . .	131
4.1.5	The Bloch Equations . . . . .	134
4.1.6	Dielectric Susceptibility and Saturation . . . . .	135
4.1.7	Rate Equations and Cross Sections . . . . .	138
4.2	Laser Rate Equations . . . . .	140
4.3	Built-up of Laser Oscillation and Continuous Wave Operation . . . . .	145
4.4	Stability and Relaxation Oscillations . . . . .	147
4.5	Laser Efficiency . . . . .	151
4.6	Q-Switching . . . . .	152
4.6.1	Single-Frequency Q-Switched Pulses . . . . .	156
4.6.2	Active Q-Switching . . . . .	158
4.6.3	Passive Q-Switching . . . . .	162
4.7	Example: Single Mode CW-Q-Switched Microchip Lasers . . . . .	171
4.7.1	Set-up of the Passively Q-Switched Microchip Laser . . . . .	171
4.7.2	Dynamics of a Q-Switched Microchip Laser . . . . .	173
4.8	Q-Switched Mode Locking . . . . .	179
4.9	Summary . . . . .	183



<b>5</b>	<b>Active Mode Locking</b>	<b>189</b>
5.1	The Master Equation of Mode Locking . . . . .	190
5.2	Active Mode Locking by Loss Modulation . . . . .	193
5.3	Active Mode-Locking by Phase Modulation . . . . .	198
5.4	Active Mode Locking with Additional SPM . . . . .	199
5.5	Active Mode Locking with Soliton Formation . . . . .	202
5.5.1	Stability Condition . . . . .	204
5.5.2	Numerical simulations . . . . .	212
5.5.3	Experimental Verification . . . . .	217
5.6	Active Modelocking with Detuning . . . . .	219
5.6.1	Dynamics of the Detuned Actively Mode-locked Laser .	224
5.6.2	Nonnormal Systems and Transient Gain . . . . .	227
5.6.3	The Nonnormal Behavior of the Detuned Laser . . . . .	229
5.7	Summary . . . . .	233
<b>6</b>	<b>Passive Modelocking</b>	<b>237</b>
6.1	Slow Saturable Absorber Mode Locking . . . . .	239
6.2	Fast Saturable Absorber Mode Locking . . . . .	244
6.2.1	Without GDD and SPM . . . . .	245
6.2.2	With GDD and SPM . . . . .	249
6.3	Soliton Mode Locking . . . . .	253
6.4	Dispersion Managed Soliton Formation . . . . .	258
<b>7</b>	<b>Kerr-Lens and Additive Pulse Mode Locking</b>	<b>271</b>
7.1	Kerr-Lens Mode Locking (KLM) . . . . .	271
7.1.1	Review of Paraxial Optics and Laser Resonator Design	272
7.1.2	Two-Mirror Resonators . . . . .	275
7.1.3	Four-Mirror Resonators . . . . .	284
7.1.4	The Kerr Lensing Effects . . . . .	289
7.2	Additive Pulse Mode Locking . . . . .	294
<b>8</b>	<b>Semiconductor Saturable Absorbers</b>	<b>303</b>
8.1	Carrier Dynamics and Saturation Properties . . . . .	305
8.2	High Fluence Effects . . . . .	309
8.3	Break-up into Multiple Pulses . . . . .	313
8.4	Summary . . . . .	320

<b>9</b>	<b>Pulse Characterization</b>	<b>323</b>
9.1	Intensity Autocorrelation . . . . .	323
9.2	Interferometric Autocorrelation (IAC) . . . . .	326
9.2.1	Interferometric Autocorrelation of an Unchirped Sech- Pulse . . . . .	331
9.2.2	Interferometric Autocorrelation of a Chirped Gaussian Pulse . . . . .	332
9.2.3	Second Order Dispersion . . . . .	332
9.2.4	Third Order Dispersion . . . . .	333
9.2.5	Self-Phase Modulation . . . . .	335
9.3	Frequency Resolved Optical Gating (FROG) . . . . .	336
9.3.1	Polarization Gate FROG . . . . .	339
9.3.2	FROG Inversion Algorithm . . . . .	341
9.3.3	Second Harmonic FROG . . . . .	343
9.3.4	FROG Geometries . . . . .	345
9.4	Spectral Interferometry and SPIDER . . . . .	346
9.4.1	Spectral Interferometry . . . . .	346
9.4.2	SPIDER . . . . .	348
9.4.3	Characterization of Sub-Two-Cycle Ti:sapphire Laser Pulses . . . . .	354
9.4.4	Pros and Cons of SPIDER . . . . .	356
9.5	Two-Dimensional Spectral Shearing Interferometry . . . . .	356
<b>10</b>	<b>Femtosecond Laser Frequency Combs</b>	<b>361</b>
10.1	The Mode Comb . . . . .	362
10.2	Group- and Phase Velocity of Solitons . . . . .	366
10.3	Femtosecond Laser Frequency Combs . . . . .	368
10.4	Noise in Mode-Locked Lasers . . . . .	372
10.4.1	The Optical Spectrum . . . . .	376
10.4.2	The Microwave Spectrum . . . . .	380
10.4.3	Example: Er-fiber laser: . . . . .	381
<b>11</b>	<b>Ultrafast Measurement Techniques</b>	<b>387</b>
11.1	Pump Probe Measurements . . . . .	387
11.1.1	Non-Colinear Degenerate Pump-Probe Measurement: . . . . .	388
11.1.2	Colinear Pump-Probe Measurement: . . . . .	390
11.1.3	Heterodyne Pump Probe . . . . .	392
11.2	Four-Wave Mixing . . . . .	393

11.3 Electro-Optic Sampling: . . . . .	395
11.4 THz Spectroscopy and Imaging . . . . .	397
<b>12 Short Pulse Amplification</b>	<b>403</b>
12.1 Cavity Dumping . . . . .	404
12.2 Laser Amplifiers . . . . .	405
12.2.1 Frantz-Nodvick Equation . . . . .	406
12.2.2 Regenerative Amplifiers . . . . .	411
12.2.3 Multipass Amplifier . . . . .	412
12.3 Chirped Pulse Amplification . . . . .	413
12.4 Stretchers and Compressors . . . . .	414
12.5 Gain Narrowing . . . . .	417
12.6 Pulse Contrast . . . . .	418
12.7 Scaling to Large Average Power by Cryogenic cooling . . . . .	420
12.8 Optical Parametric Amplifiers and Oscillators . . . . .	422
12.8.1 Optical Parametric Generation (OPG) . . . . .	422
12.8.2 Nonlinear Optical Suszeptibilities . . . . .	425
12.8.3 Continuous Wave OPA . . . . .	426
12.8.4 Theory of Optical Parametric Amplification . . . . .	428
12.8.5 Phase Matching . . . . .	432
12.8.6 Quasi-Phase Matching . . . . .	435
12.8.7 Ultrashort Pulse Optical Parametric Amplification . . . . .	435
12.8.8 Optical Parametric Amplifier Designs . . . . .	442
12.8.9 Noncollinear Optical Parametric Amplifier (NOPA) . . . . .	445
12.8.10 Optical Parametric Chirped Pulse Amplifiers OPCPA . . . . .	451
<b>13 High Harmonic Generation</b>	<b>455</b>
13.1 Atomic units . . . . .	456
13.2 The three step model . . . . .	457
13.2.1 Ionization . . . . .	459
13.2.2 Propagation . . . . .	462
13.2.3 Recombination . . . . .	464
13.3 Attosecond pulses . . . . .	469
13.3.1 The intensity challenge . . . . .	471
13.3.2 The necessity of short drive pulses . . . . .	471
13.3.3 Quantum diffusion . . . . .	473
13.3.4 Propagation effects – phase matching . . . . .	474

# Chapter 1

## Introduction

### 1.1 Course Mission

- Generation of ultrashort pulses: Nano-, Pico-, Femto-, Attosecond Pulses
- Propagation of ultrashort pulses, linear and nonlinear effects
- Pulse Characterization
- Pulse Amplification
- Applications in high precision measurements, nonlinear optics, optical signal processing, optical communications, ultrafast EUV/XUV pulse generation via high harmonics,....

### 1.2 Pulse Characteristics

Most often, there is not an isolated pulse, but rather a pulse train.

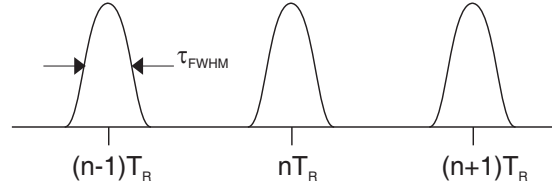


Figure 1.1: Periodic pulse train

$T_R$ : pulse repetition time

$W$  : pulse energy

$P_{ave} = W/T_R$  : average power

$\tau_{FWHM}$  is the Full Width at Half Maximum of the intensity envelope of the pulse in the time domain.

The peak power is roughly given by

$$P_p = \frac{W}{\tau_{FWHM}} = P_{ave} \frac{T_R}{\tau_{FWHM}}, \quad (1.1)$$

and the peak electric field is given by

$$E_p = \sqrt{2Z_{F_0} \frac{P_p}{A_{eff}}}. \quad (1.2)$$

$A_{eff}$  is the beam cross-section and  $Z_{F_0} = 377 \Omega$  is the free space impedance.

Time scales:

1 ns	$\sim$	30 cm	(high-speed electronics, GHz)
1 ps	$\sim$	300 $\mu$ m	
1 fs	$\sim$	300 nm	
1 as = $10^{-18}$ s	$\sim$	0.3 nm = 3 Å	(typ-lattice constant in metal)

The shortest optical pulses generated to date are about 3 – 5 fs at 800 nm ( $\lambda/c = 2.7$  fs), less than two optical cycles, and 80 as in the EUV at 10 nm. For few-cycle pulses, the electric field becomes important, not only the intensity!

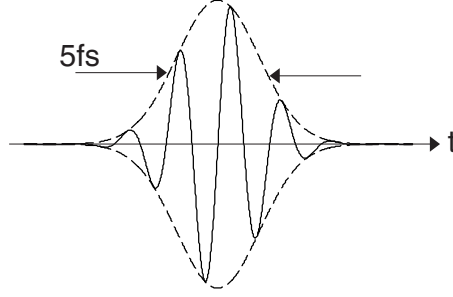


Figure 1.2: Electric field waveform of a 5 fs pulse at a center wavelength of 800 nm. The electric field depends on the carrier-envelope phase.

average power:

$$P_{ave} \sim 1W - 1kW$$

repetition rates:

$$T_R^{-1} = f_R = \text{mHz} - 100 \text{ GHz}$$

pulse energy:

$$W = 1\text{pJ} - 1\text{kJ}$$

pulse width:

$$\tau_{\text{FWHM}} = \begin{array}{ll} 5 \text{ fs} - 50 \text{ ps}, & \text{modelocked} \\ 30 \text{ ps} - 100 \text{ ns}, & \text{Q-switched} \end{array}$$

peak power:

$$P_p = \frac{1 \text{ kJ}}{1 \text{ ps}} = \frac{1 \text{ J}}{1 \text{ fs}} \sim 1 \text{ PW},$$

obtained with Nd:glass (LLNL - USA, [1][2][4]) and Ti:sapphire lasers [3].

For a typical laboratory pulse, the peak power is

$$P_p = \frac{10 \text{ nJ}}{10 \text{ fs}} \sim 1 \text{ MW}$$

peak field of typical laboratory pulse:

$$E_p = \sqrt{2 \times 377 \times \frac{10^6 \times 10^{12}}{\pi \times (1.5)^2} \frac{\text{V}}{\text{m}}} \approx 10^{10} \frac{\text{V}}{\text{m}} = \frac{10 \text{ V}}{\text{nm}},$$

which is a field strength at the onset of plasma generation in a solid.

### 1.3 Applications

- High time resolution: Ultrafast Spectroscopy, tracing of ultrafast physical processes in condensed matter (see Fig. 1.3), chemical reactions, physical and biological processes, influence chemical reactions with femtosecond pulses: Femto-Chemistry (Noble Prize, 2000 to A. Zewail).

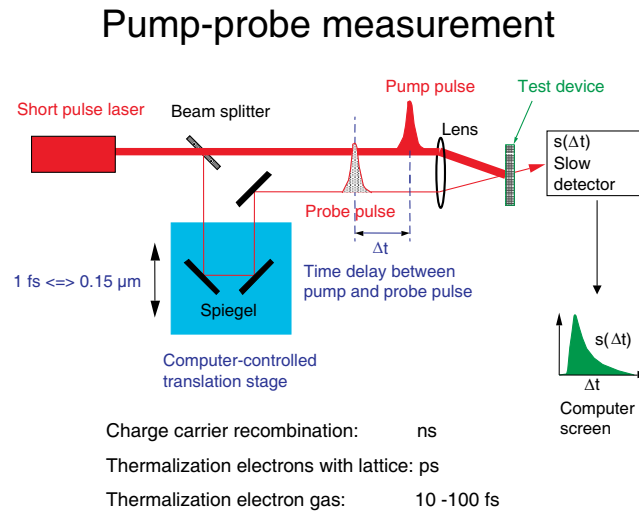
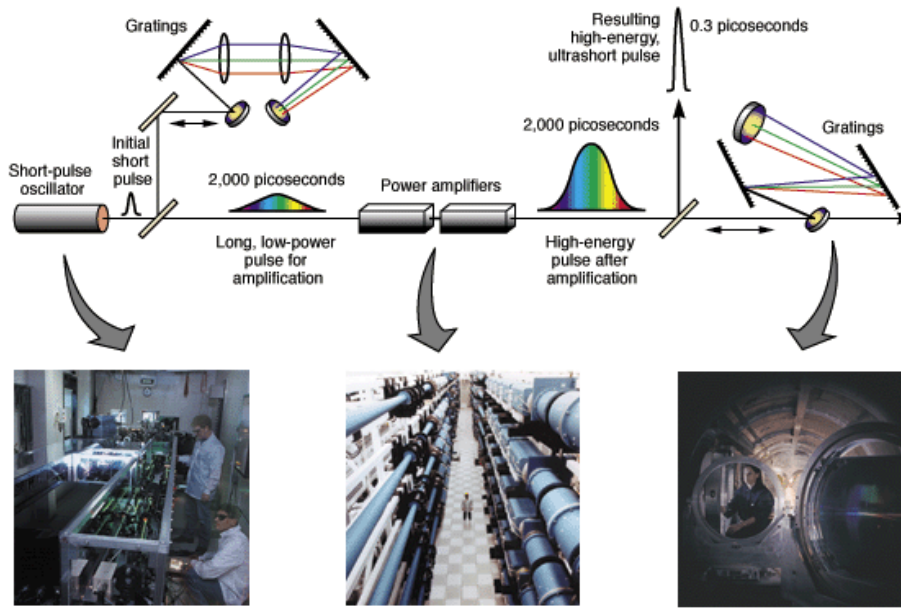


Figure 1.3: Pump-probe setup to extract time constants relevant for the carrier dynamics in semiconductors.

- High power lasers with average powers of tens of kilowatts can cut many centimeter thick steel plates at high speed using thermal melting.
- Short pulses enable high peak power at low average power: Nonthermal laser material processing, surgery.
- Nonlinear frequency conversion
- Ultra high intensity physics: x-ray generation, particle acceleration, Extreme Nonlinear Optics. Laser systems reaching petawatts ( $10^{15}$  Watt) of peak power were built at Lawrence Livermore Laboratory for the

first time in 1996, (see Fig. 1.4) and much more compact versions are under construction at several laboratories around the world reaching peak intensities approaching  $10^{23} \text{ Watt/cm}^2$ . The enormous peak power (the average power consumption of the earth is on the order of a few Terawatt ( $10^{12} \text{ Watt}$ )), even though only available over a fraction of a picosecond, enables the investigation of new physics and fundamental interactions at extreme intensities, such as the scattering of photons with each other invoking vacuum nonlinearities (the Quantum Electrodynamic Vacuum), see Figure 1.5.



The chirped-pulse amplification technique makes it possible for the Petawatt laser's high-power pulses to pass through laser optics without damaging them. Before amplification, low-energy laser pulses are passed through diffraction gratings to stretch their duration by as much as 25,000 times. After amplification, the pulses are recompressed back to near their original duration. Because the pulses pass through the laser optics when they are long, they cause no damage.

Figure 1.4: First petawatt laser system installed at LLNL using chirped pulse amplification and the NOVA amplifier chain, see <http://www.llnl.gov/str/MPerry.html>.



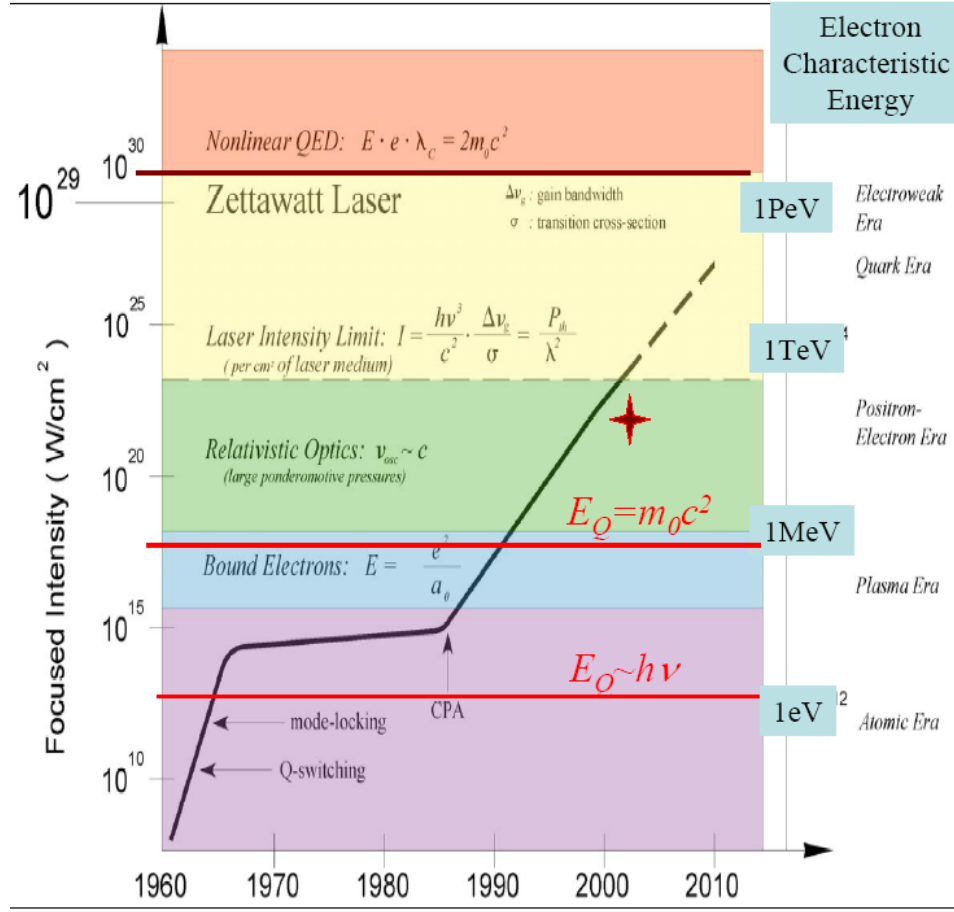


Figure 1.5: Progress in peak intensity generation from lasers over the last 45 years. Courtesy Gerard Mourou.

- High speed sampling of fast electrical signals with low jitter, see Fig. 1.6.  
As we will see, femtosecond lasers have the potential to generate pulse trains with equal spacing to the level of 100 attoseconds and below over time periods stretching over a millisecond.

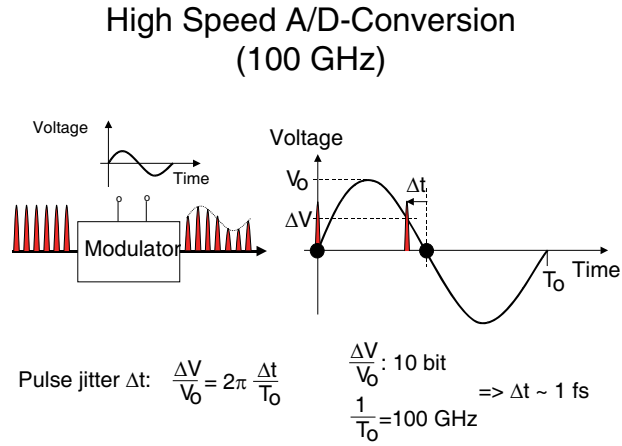


Figure 1.6: High speed A/D conversion with a high repetition rate pico- or femtosecond laser.

- High spatial resolution:  $c\tau_{\text{FWHM}}$ ; optical imaging, e.g. optical coherence tomography, see Figs. 1.7-1.9).

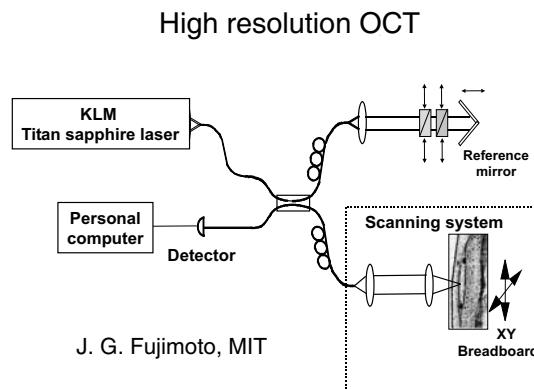


Figure 1.7: Setup for optical coherence tomography.

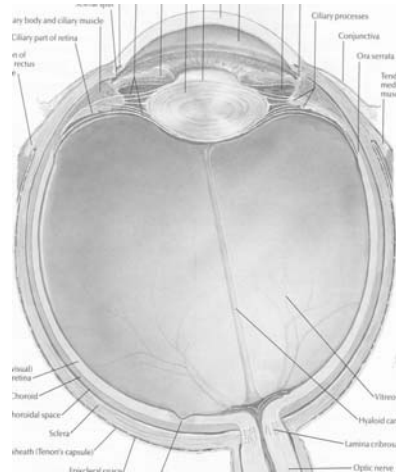


Figure 1.8: Cross section through the human eye.

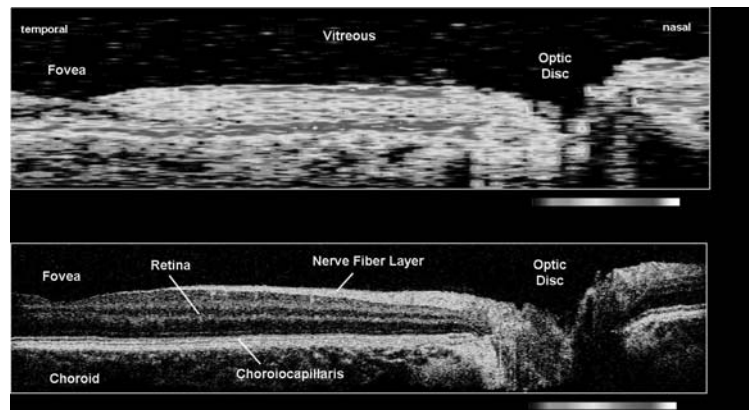


Figure 1.9: Comparison of retinal images taken with a superluminescence diode (top) versus a broadband Ti:sapphire laser (below).

- **Optical Frequency Metrology:** Optical spectrum of periodic pulse train is a set of discrete equally spaced lines. Can be used as ruler in the frequency domain. Enables direct measurement of optical frequencies with sub-Hz level precision and the construction of optical clocks, see Figure 1.10

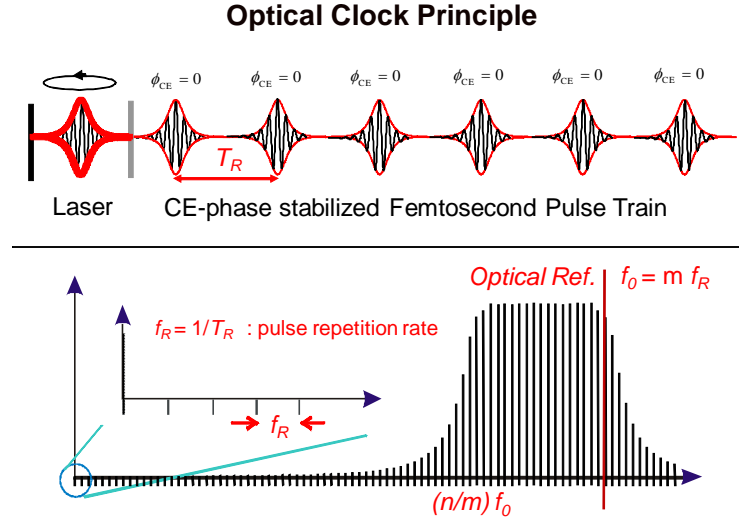


Figure 1.10: Principle of femtosecond laser frequency combs and optical clocks

- High Order Harmonic Generation in the EUV/XUV range and Attosecond Pulse Generation

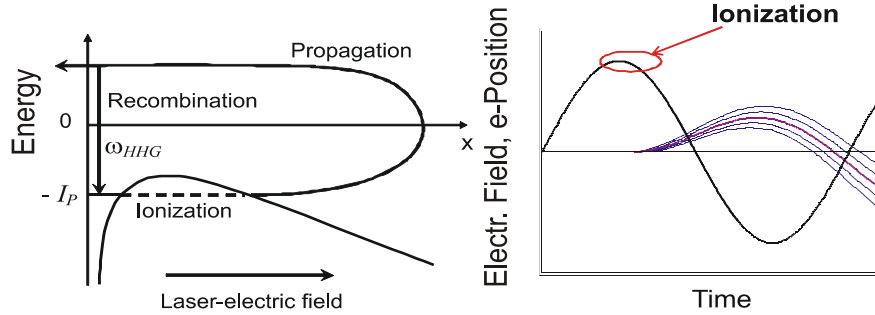


Figure 1.11: Three step model of high order harmonic generation: (a) Energy scale of electron ionized by strong field tunneling from an atom, acceleration within a laser cycle, and recollision with the parent ion.(b) Electric field waveform and electron trajectories depending on the time of ionization.

## 1.4 Review of Laser Essentials

Linear and ring cavities:

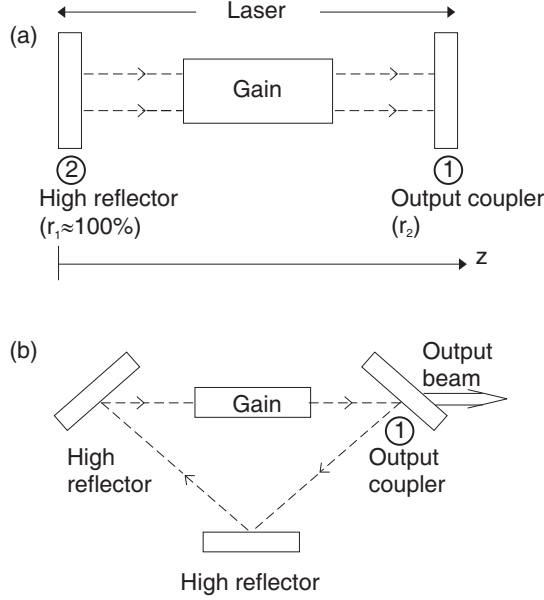


Figure 1.12: Possible cavity configurations. (a) Schematic of a linear cavity laser. (b) Schematic of a ring laser. [1]

Steady-state operation: Electric field must repeat itself after one roundtrip. Consider a monochromatic, linearly polarized field

$$E(z, t) = \Re \{ E_0 e^{j(\omega t - kz)} \}, \quad (1.3)$$

where

$$k = \frac{\omega}{c} n \quad (1.4)$$

is the propagation constant in a medium with refractive index  $n$ .

Consider linear resonator in Fig. 1.12a. Propagation from (1) to (2) is determined by  $n = n' + jn''$  (complex refractive index), with the electric field given by

$$E = \Re \left\{ E_0 e^{\frac{\omega}{c} n'' \ell_g} e^{j\omega t} e^{-j\frac{\omega}{c} (n' \ell_g + \ell_a)} \right\}, \quad (1.5)$$

where  $n_g$  is the complex refractive index of the gain medium (outside the gain medium  $n = 1$  is assumed),  $\ell_g$  is the length of the gain medium,  $\ell_a$  is the outside gain medium, and  $\ell = n_g \ell_g + \ell_a$  is the optical path length in the resonator.

Propagation back to (1), i.e. one full roundtrip results in

$$E = \Re \left\{ r_1 r_2 e^{2\frac{\omega}{c} n_g'' \ell_g} E_0 e^{j\omega t - j2\frac{\omega}{c} \ell} \right\} \Rightarrow r_1 r_2 e^{2\frac{\omega}{c} n_g'' \ell_g} = 1, \quad (1.6)$$

i.e. the gain equals the loss, and furthermore, we obtain the phase condition

$$\frac{2\omega\ell}{c} = 2m\pi. \quad (1.7)$$

The phase condition determines the resonance frequencies, i.e.

$$\omega_m = \frac{m\pi c}{\ell} \quad (1.8)$$

and

$$f_m = \frac{mc}{2\ell}. \quad (1.9)$$

The mode spacing of the longitudinal modes is

$$\Delta f = f_m - f_{m-1} = \frac{c}{2\ell} \quad (1.10)$$

(only true if there is no dispersion, i.e.  $n \neq n(\omega)$ ). Assume frequency independent cavity loss and bell shaped gain (see Fig. 1.13).

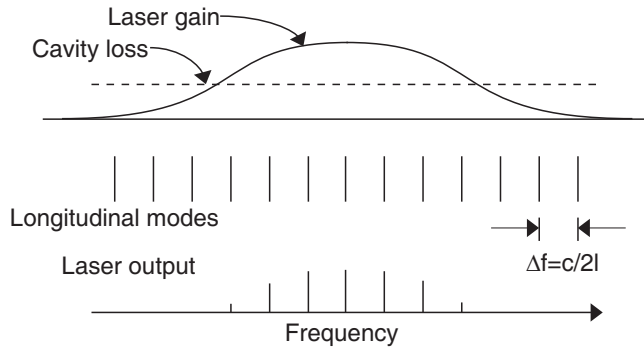


Figure 1.13: Laser gain and cavity loss spectra, longitudinal mode location, and laser output for multimode laser operation.

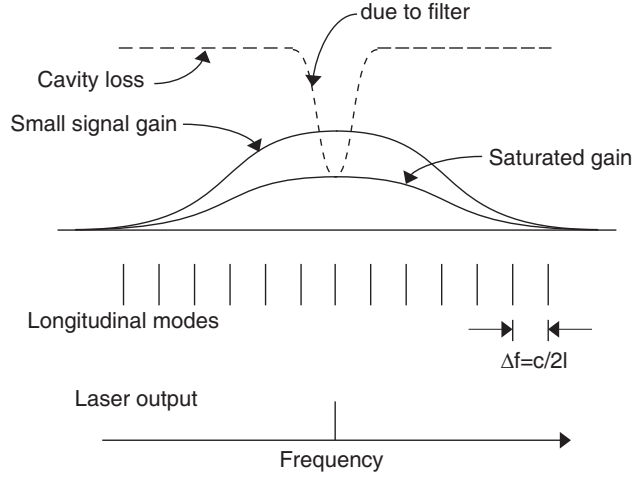


Figure 1.14: Gain and loss spectra, longitudinal mode locations, and laser output for single mode laser operation.

To assure single frequency operation use filter (etalon); distinguish between homogeneously and inhomogeneously broadened gain media, effects of spectral hole burning! Distinguish between small signal gain  $g_0$  per roundtrip, i.e. gain for laser intensity  $I \rightarrow 0$ , and large signal gain, most often given by

$$g = \frac{g_0}{1 + \frac{I}{I_{\text{sat}}}}, \quad (1.11)$$

where  $I_{\text{sat}}$  is the saturation intensity. Gain saturation is responsible for the steady state gain (see Fig. 1.14), and homogeneously broadened gain is assumed.

To generate short pulses, i.e. shorter than the cavity roundtrip time, we wish to have many longitudinal modes running in steady state. For a multimode laser the laser field is given by

$$E(z, t) = \Re \left[ \sum_m \tilde{E}_m e^{j(\omega_m t - k_m z + \phi_m)} \right], \quad (1.12a)$$

$$\omega_m = \omega_0 + m\Delta\omega = \omega_0 + \frac{m\pi c}{\ell}, \quad (1.12b)$$

$$k_m = \frac{\omega_m}{c}, \quad (1.12c)$$

where the symbol  $\hat{\phantom{x}}$  denotes a frequency domain quantity. Equation (1.12a) can be rewritten as

$$E(z, t) = \Re \left\{ e^{j\omega_0(t-z/c)} \sum_m \tilde{E}_m e^{j(m\Delta\omega(t-z/c) + \phi_m)} \right\} \quad (1.13a)$$

$$= \Re [A(t - z/c) e^{j\omega_0(t-z/c)}] \quad (1.13b)$$

with the complex envelope

$$A\left(t - \frac{z}{c}\right) = \sum_m \tilde{E}_m e^{j(m\Delta\omega(t-z/c) + \phi_m)} = \text{complex envelope (slowly varying)}. \quad (1.14)$$

$e^{j\omega_0(t-z/c)}$  is the carrier wave (fast oscillation). Both carrier and envelope travel with the same speed (no dispersion assumed). The envelope function is periodic with period

$$T = \frac{2\pi}{\Delta\omega} = \frac{2\ell}{c} = \frac{L}{c}. \quad (1.15)$$

$L$  is the roundtrip length (optical)!

Examples:

We assume  $N$  modes with equal amplitudes  $\tilde{E}_m = E_0$  and equal phases  $\phi_m = 0$ , and thus the envelope is given by

$$A(z, t) = E_0 \sum_{m=-(N-1)/2}^{(N-1)/2} e^{j(m\Delta\omega(t-z/c))}. \quad (1.16)$$

With

$$\sum_{m=0}^{q-1} a^m = \frac{1 - a^q}{1 - a}, \quad (1.17)$$

we obtain

$$A(z, t) = E_0 \frac{\sin \left[ \frac{N\Delta\omega}{2} \left( t - \frac{z}{c} \right) \right]}{\sin \left[ \frac{\Delta\omega}{2} \left( t - \frac{z}{c} \right) \right]}. \quad (1.18)$$

The laser intensity  $I$  is proportional to  $E(z, t)^2$ , averaged over one optical cycle:  $I \sim |A(z, t)|^2$ . At  $z = 0$ , we obtain

$$I(t) \sim |E_0|^2 \frac{\sin^2 \left( \frac{N\Delta\omega t}{2} \right)}{\sin^2 \left( \frac{\Delta\omega t}{2} \right)}. \quad (1.19)$$



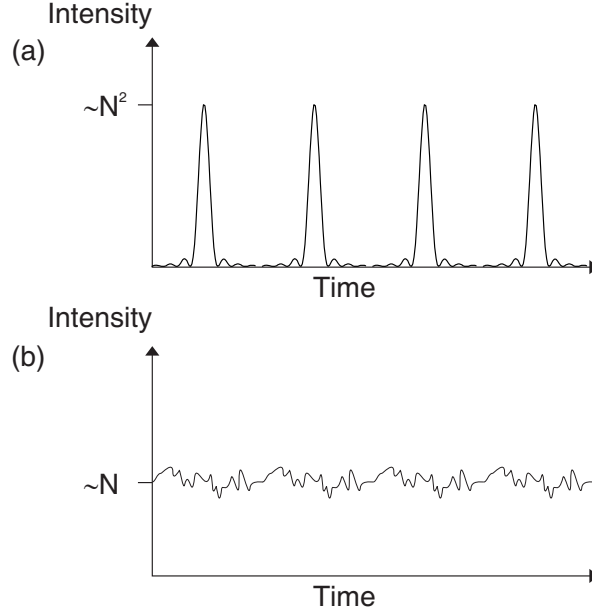


Figure 1.15: (a) mode-locked laser output with constant mode phase. (b) Laser output with randomly phased modes.

(a) Periodic pulses given by Eq. (1.19), period  $T = 1/\Delta f = L/c$

- pulse duration

$$\Delta t = \frac{2\pi}{N\Delta\omega} = \frac{1}{N\Delta f} \quad (1.20)$$

- peak intensity  $\sim N^2|E_0|^2$
- average intensity  $\sim N|E_0|^2 \Rightarrow$  peak intensity is enhanced by a factor  $N$ .

(b) If phases of modes are not locked, i.e.  $\phi_m$  random sequence

- Intensity fluctuates randomly about average value ( $\sim N|E_0|^2$ ), same as modelocked case
- correlation time is  $\Delta t_c \approx \frac{1}{N\Delta f}$
- Fluctuations are still periodic with period  $T = 1/\Delta f$ .

In a usual multimode laser,  $\phi_m$  varies over  $t$ .

## 1.5 History

1960: First laser, ruby, Maiman [5].

1961: Proposal for  $Q$ -switching, Hellwarth [6].

1963: First indications of mode locking in ruby lasers, Guers and Mueller [7],[8], Statz and Tang [9]. on He-Ne lasers.

1964: Activemodelocking (HeNe, Ar, etc.), DiDomenico [10], [11] and Yariv [12].

1966: Passive modelocking with saturable dye absorber in ruby by A. J. DeMaria, Mocker and Collins [13].

1966: Dye laser, F. P. Schäfer, et al. [14].

1968: mode-locking (Q-Switching) of dye-lasers, Schmidt, Schäfer [15].

1972: cw-passive modelocking of dye laser, Ippen, Shank, Dienes [16].

1972: Analytic theories on active modelocking [22, 23].

1974: Sub-ps-pulses, Shank, Ippen [17].

1975: Theories for passive modelocking with slow [1], [25] and fast saturable absorbers [26] predicted hyperbolic secant pulse.

1981: Colliding-pulse mode-locked laser (CPM), [18].

1982: Pulse compression [21].

1984: Soliton Laser, Mollenauer, [27].

1985: Chirped pulse amplification, Strickland and Morou, [2].

1986: Ti:sapphire (solid-state laser), P. F. Moulton [29].

1987: 6 fs at 600 nm, external compression, Fork et al. [19, 20].

1988: Additive Pulse Modelocking (APM),[30, 31, 32].

1991: Kerr-lens modelocking, Spence et al. [33, 34, 35, 36, 37].

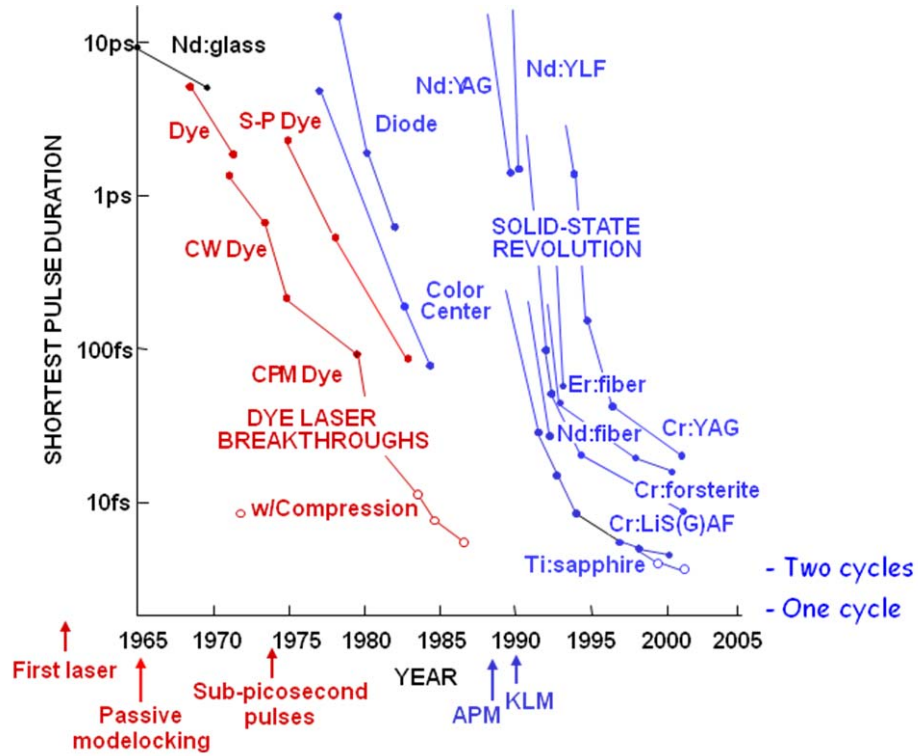


Figure 1.16: Development of short pulse laser systems based on different laser materials.

1993: Stretched pulse laser, Tamura et al [38].

1994: Chirped mirrors, Szipoecs et al. [39, 40]

1997: Double-chirped mirrors, Kaertner et al.[41]

2001: 5 fs, sub-two cycle pulses, octave spanning, Ell et al.[43]

2001: 250 as by High-Harmonic Generation,Hentschel et al.[7]

2008: 80 as, Goulielmakis et al.[45]

2010: Single-cycle pulse synthesis for Erbium doped fiber lasers, Krauss et al.[46]

## 1.6 Laser Materials

Laser Materials	Absorption Wavelength	Average Emission $\lambda$	Band Width	Pulse Width
Nd:YAG	808 nm	1064 nm	0.45 nm	$\sim 6$ ps
Nd:YLF	797 nm	1047 nm	1.3 nm	$\sim 3$ ps
Nd:LSB	808 nm	1062 nm	4 nm	$\sim 1.6$ ps
Nd:YVO <sub>4</sub>	808 nm	1064 nm	2 nm	$\sim 4.6$ ps
Nd:fiber	804 nm	1053 nm	22-28 nm	$\sim 33$ fs
Nd:glass	804 nm	1053 nm	22-28 nm	$\sim 60$ fs
Yb:YAG	940, 968 nm	1030 nm	6 nm	$\sim 300$ fs
Yb:glass	975 nm	1030 nm	30 nm	$\sim 90$ fs
Ti:Al <sub>2</sub> O <sub>3</sub>	480-540 nm	796 nm	200 nm	$\sim 5$ fs
Cr <sup>4+</sup> :Mg <sub>2</sub> SiO <sub>4</sub> :	900-1100 nm	1260 nm	200 nm	$\sim 14$ fs
Cr <sup>4+</sup> :YAG	900-1100 nm	1430 nm	180 nm	$\sim 19$ fs

Transition metals: (Cr<sup>3+</sup>, Ti<sup>3+</sup>, Ni<sup>2+</sup>, CO<sup>2+</sup>, etc.) (outer  $3d$ -electrons)  
 $\rightarrow$  broadband

Rare earth: (Nd<sup>3+</sup>, Tm<sup>3+</sup>, Ho<sup>3+</sup>, Er<sup>3+</sup>, etc.) (shielded  $4f$ -electrons)  
 $\rightarrow$  narrow band.



# Bibliography

- [1] M. D. Perry and G. Mourou, "Terawatt to Petawatt Subpicosecond Lasers," Science, Vol. 264 (1994), p. 917.
- [2] M. D. Perry et al., "Petawatt Laser Pulses," Optics Letters, Vol. 24 (1999), p. 160.
- [3] E. W. Gaul, M. Martinez, J. Blakeney, A. Jochmann, M. Ringuette, D. Hammond, T. Borger, R. Escamilla, S. Douglas, W. Henderson, G. Dyer, A. Erlandson, R. Cross, J. Caird, Ch. Ebberts, and T. Ditmire, "Demonstration of a 1.1 petawatt laser based on a hybrid optical parametric chirped pulse amplification/mixed Nd:glass amplifier, Applied Optics, Vol. 49, Issue 9, pp. 1676-1681 (2010) doi:10.1364/AO.49.001676.
- [4] T. Tajima and G. Mourou, Phys. Rev. Spec. Topics-Accelerators and Beams 5(031301) 1 (2002). See also [www.wapr.apr.jaeri.go.jp/aprc/e/index\\_e.html](http://www.wapr.apr.jaeri.go.jp/aprc/e/index_e.html), [www.eecs.umich.edu/CUOS/HERCULES/index](http://www.eecs.umich.edu/CUOS/HERCULES/index), [www.clf.rl.ac.uk](http://www.clf.rl.ac.uk)
- [5] T. H. Maimann, "Stimulated optical radiation in ruby", Nature **187**, 493-494, (1960).
- [6] R. W. Hellwarth, Ed., *Advances in Quantum Electronics*, Columbia Press, NY (1961).
- [7] K. Gürs, R. Müller: "Breitband-Modulation durch Steuerung der Emission eines Optischen Masers (Auskoppel-modulation)", Phys. Lett. **5**, 179-181 (1963).
- [8] K. Gürs (Ed.): "Beats and modulation in optical ruby laser," in *Quantum Electronics III* (Columbia University Press, New York 1964).

- [9] H. Statez, C.L. Tang (Eds.): "Zeeman effect and nonlinear interactions between oscillating laser modes", in *Quantum Electronics III* (Columbia University Press, New York 1964).
- [10] M. DiDomenico: "Small-signal analysis of internal (coupling type) modulation of lasers," J. Appl. Phys. **35**, 2870-2876 (1964).
- [11] L.E. Hargrove, R.L. Fork, M.A. Pollack: "Locking of He-Ne laser modes induced by synchronous intracavity modulation," Appl. Phys. Lett. **5**, 4-5 (1964).
- [12] A. Yariv: "Internal modulation in multimode laser oscillators," J. Appl. Phys. **36**, 388-391 (1965).
- [13] H.W. Mocker, R.J. Collins: "Mode competition and self-locking effects in a Q-switched ruby laser," Appl. Phys. Lett. **7**, 270-273 (1965).
- [14] F. P. Schäfer, F. P. W. Schmidt, J. Volze: "Organic Dye Solution Laser," Appl. Phys. Lett. **9**, 306 – 308 (1966).
- [15] F. P. W. Schmidt, F. P. Schäfer: "Self-mode-locking of dye-lasers with saturable absorbers," Phys. Lett. **26A**, 258-259 (1968).
- [16] E.P. Ippen, C.V. Shank, A. Dienes: "Passive mode locking of the cw dye laser," Appl. Phys. Lett. **21**, 348-350 (1972).
- [17] C.V. Shank, E.P. Ippen: "Sub-picosecond kilowatt pulses from a mode-locked cw dye laser," Appl. Phys. Lett. **24**, 373-375 (1974).
- [18] R.L. Fork, B.I. Greene, C.V. Shank: "Generation of optical pulses shorter than 0.1 psec by colliding pulse mode-locking," Appl. Phys. Lett. **38**, 617-619 (1981).
- [19] W.H. Knox, R.L. Fork, M.C. Downer, R.H. Stolen, C.V. Shank, J.A. Valdmanis: "Optical pulse compression to 8 fs at a 5-kHz repetition rate," Appl. Phys. Lett. **46**, 1120-1122 (1985).
- [20] R.L. Fork, C.H.B. Cruz, P.C. Becker, C.V. Shank: "Compression of optical pulses to six femtoseconds by using cubic phase compensation," Opt. Lett. **12**, 483-485 (1987).
- [21] D. Grischowsky, A. C. Balant: TITLE, Appl. Phys. Lett. **41**, pp. (1982).

- [22] J. Kuizenga, A. E. Siegman: "FM und AM mode locking of the homogeneous laser - Part I: Theory, IEEE J. Quantum Electron. **6**, 694-708 (1970).
- [23] J. Kuizenga, A. E. Siegman: "FM und AM mode locking of the homogeneous laser - Part II: Experimental results, IEEE J. Quantum Electron. **6**, 709-715 (1970).
- [24] G.H.C. New: Pulse evolution in mode-locked quasicontinuous lasers, IEEE J. Quantum Electron. **10**, 115-124 (1974).
- [25] H.A. Haus: Theory of mode locking with a slow saturable absorber, IEEE J. Quantum Electron. **QE 11**, 736-746 (1975).
- [26] H.A. Haus, C.V. Shank, E.P. Ippen: Shape of passively mode-locked laser pulses, Opt. Commun. **15**, 29-31 (1975).
- [27] L.F. Mollenauer, R.H. Stolen: The soliton laser, Opt. Lett. **9**, 13-15 (1984).
- [28] D. Strickland and G. Morou: "Compression of amplified chirped optical pulses," Opt. Comm. **56**, 219-221, (1985).
- [29] P. F. Moulton: "Spectroscopic and laser characteristics of Ti:Al<sub>2</sub>O<sub>3</sub>", JOSA B **3**, 125-132 (1986).
- [30] K. J. Blow and D. Wood: "Modelocked Lasers with nonlinear external cavity," J. Opt. Soc. Am. B **5**, 629-632 (1988).
- [31] J. Mark, L.Y. Liu, K.L. Hall, H.A. Haus, E.P. Ippen: Femtosecond pulse generation in a laser with a nonlinear external resonator, Opt. Lett. **14**, 48-50 (1989).
- [32] E.P. Ippen, H.A. Haus, L.Y. Liu: Additive pulse modelocking, J. Opt. Soc. Am. B **6**, 1736-1745 (1989).
- [33] D.E. Spence, P.N. Kean, W. Sibbett: 60-fsec pulse generation from a self-mode-locked Ti:Sapphire laser, Opt. Lett. **16**, 42-44 (1991).
- [34] D.K. Negus, L. Spinelli, N. Goldblatt, G. Feugnet: TITLE, in *Advanced Solid-State Lasers* G. Dubé, L. Chase (Eds.) (Optical Society of America, Washington, D.C., 1991) pp. 120-124.



- [35] F. Salin, J. Squier, M. Piché: Mode locking of Ti:Al<sub>2</sub>O<sub>3</sub> lasers and self-focusing: A Gaussian approximation, *Opt. Lett.* **16**, 1674-1676 (1991).
- [36] M. Piché: Beam reshaping and self-mode-locking in nonlinear laser resonators, *Opt. Commun.* **86**, 156-160 (1991)
- [37] U. Keller, G.W. 'tHooft, W.H. Knox, J.E. Cunningham: TITLE, *Opt. Lett.* **16**, 1022-1024 (1991).
- [38] K. Tamura, E.P. Ippen, H.A. Haus, L.E. Nelson: 77-fs pulse generation from a stretched-pulse mode-locked all-fiber ring laser, *Opt. Lett.* **18**, 1080-1082 (1993)
- [39] A. Stingl, C. Spielmann, F. Krausz: "Generation of 11-fs pulses from a Ti:sapphire laser without the use of prism," *Opt. Lett.* **19**, 204-206 (1994)
- [40] R. Szipöcs, K. Ferencz, C. Spielmann, F. Krausz: Chirped multilayer coatings for broadband dispersion control in femtosecond lasers, *Opt. Lett.* **19**, 201-203 (1994)
- [41] F.X. Kärtner, N. Matuschek, T. Schibli, U. Keller, H.A. Haus, C. Heine, R. Morf, V. Scheuer, M. Tilsch, T. Tschudi: Design and fabrication of double-chirped mirrors, *Opt. Lett.* **22**, 831-833 (1997)
- [42] Y. Chen, F.X. Kärtner, U. Morgner, S.H. Cho, H.A. Haus, J.G. Fujimoto, E.P. Ippen: Dispersion-managed mode locking, *J. Opt. Soc. Am. B* **16**, 1999-2004 (1999)
- [43] R. Ell, U. Morgner, F.X. Kärtner, J.G. Fujimoto, E.P. Ippen, V. Scheuer, G. Angelow, T. Tschudi: Generation of 5-fs pulses and octave-spanning spectra directly from a Ti:Sapphire laser, *Opt. Lett.* **26**, 373-375 (2001)
- [44] H. Hentschel, R. Kienberger, Ch. Spielmann, G. A. Reider, N. Milošević, T. Brabec, P. Corkum, U. Heinzmann, M. Drescher, F. Krausz: "Attosecond Metrology," *Nature* **414**, 509-513 (2001).
- [45] E. Goulielmakis, M. Schultze, M. Hofstetter, V. S. Yakovlev, J. Gagnon, M. Uiberacker, A. L. Aquila, E. M. Gullikson, D. T. Attwood, R. Kienberger, F. Krausz, and U. Kleineberg, "Single-Cycle Nonlinear Optics," *Science*, vol. 320, pp. 1614 (2008).

- [46] G. Krauss, S. Lohss, T. Hanke, A. Sell, S. Eggert, R. Huber and A. Leitenstorfer, "Synthesis of a single cycle of light with compact erbium-doped fibre technology," *Nat. Photonics* 4, pp.33-36 (2009).



## Chapter 2

# Linear Pulse Propagation

Classical electromagnetic phenomena are completely described by Maxwell's Equations. The simplest case we may consider is that of electrodynamics of isotropic media

### 2.1 Maxwell's Equations of Homogeneous Media

Maxwell's Equations are

$$\vec{\nabla} \times \vec{H} = \frac{\partial \vec{D}}{\partial t} + \vec{J}, \quad (2.1a)$$

$$\vec{\nabla} \times \vec{E} = -\frac{\partial \vec{B}}{\partial t}, \quad (2.1b)$$

$$\vec{\nabla} \cdot \vec{D} = \rho, \quad (2.1c)$$

$$\vec{\nabla} \cdot \vec{B} = 0. \quad (2.1d)$$

The material equations accompanying Maxwell's equations are:

$$\vec{D} = \epsilon_0 \vec{E} + \vec{P}, \quad (2.2a)$$

$$\vec{B} = \mu_0 \vec{H} + \vec{M}. \quad (2.2b)$$

Here,  $\vec{E}$  and  $\vec{H}$  are the electric and magnetic field strength,  $\vec{D}$  the electric flux density,  $\vec{B}$  the magnetic flux density,  $\vec{J}$  the current density of free charges,  $\rho$  is the free charge density,  $\vec{P}$  is the polarization, and  $\vec{M}$  the magnetization.

Note, it is Eqs.(2.2a) and (2.2b) which make electromagnetism an interesting and always a hot topic with never ending possibilities. All advances in engineering of artificial materials or finding of new material properties, such as superconductivity, bring new life, meaning and possibilities into this field.

By taking the curl of Eq. (2.1b) and considering

$$\vec{\nabla} \times (\vec{\nabla} \times \vec{E}) = \vec{\nabla} (\vec{\nabla} \cdot \vec{E}) - \Delta \vec{E},$$

where  $\vec{\nabla}$  is the Nabla operator and  $\Delta = \vec{\nabla}^2$  the Laplace operator, we obtain

$$\Delta \vec{E} - \mu_0 \frac{\partial}{\partial t} \left( \vec{j} + \epsilon_0 \frac{\partial \vec{E}}{\partial t} + \frac{\partial \vec{P}}{\partial t} \right) = \frac{\partial}{\partial t} \vec{\nabla} \times \vec{M} + \vec{\nabla} (\vec{\nabla} \cdot \vec{E}) \quad (2.3)$$

and hence

$$\left( \Delta - \frac{1}{c_0^2} \frac{\partial^2}{\partial t^2} \right) \vec{E} = \mu_0 \left( \frac{\partial \vec{j}}{\partial t} + \frac{\partial^2}{\partial t^2} \vec{P} \right) + \frac{\partial}{\partial t} \vec{\nabla} \times \vec{M} + \vec{\nabla} (\vec{\nabla} \cdot \vec{E}). \quad (2.4)$$

with the vacuum velocity of light

$$c_0 = \sqrt{\frac{1}{\mu_0 \epsilon_0}}. \quad (2.5)$$

For dielectric non magnetic media, which we often encounter in optics, with no free charges and currents due to free charges, there is  $\vec{M} = \vec{0}$ ,  $\vec{j} = \vec{0}$ ,  $\rho = 0$ . One can also show that the electric field can be decomposed into a longitudinal and transverse component  $\vec{E}_L$  and  $\vec{E}_T$ , which are characterized by [2]

$$\vec{\nabla} \times \vec{E}_L = 0 \text{ and } \vec{\nabla} \cdot \vec{E}_T = 0 \quad (2.6)$$

If there are no free charges, the longitudinal component is zero and only a transverse component is left over. Therefore, for the purpose of this class (and most of optics) the wave equation greatly simplifies to

$$\left( \Delta - \frac{1}{c_0^2} \frac{\partial^2}{\partial t^2} \right) \vec{E} = \mu_0 \frac{\partial^2}{\partial t^2} \vec{P}. \quad (2.7)$$

This is the wave equation driven by the polarization of the medium.

### 2.1.1 Helmholtz Equation for Linear Media

In general, the polarization in dielectric media may have a nonlinear dependence on the field. For linear, isotropic and local media the polarizability of the medium at each point is described by the dielectric susceptibility function  $\chi(t)$  and the dielectric constant in vacuum  $\epsilon_0$

$$\vec{P}(\vec{r}, t) = \epsilon_0 \int dt' \chi(t - t') \vec{E}(\vec{r}, t'). \quad (2.8)$$

which leads to a total dielectric response function or permittivity

$$\epsilon(t) = \epsilon_0(\delta(t) + \chi(t)) \quad (2.9)$$

with which the electric displacement field,  $\vec{D}(\vec{r}, t)$ , in medium can be written as

$$\vec{D}(\vec{r}, t) = \epsilon_0 \vec{E}(\vec{r}, t) + \vec{P}(\vec{r}, t) = \int dt' \epsilon(t - t') \vec{E}(\vec{r}, t'). \quad (2.10)$$

If the medium is linear and has only an induced polarization, completely described in the time domain  $\chi(t)$  or in the frequency domain by its Fourier transform, the complex susceptibility  $\tilde{\chi}(\omega) = \tilde{\epsilon}_r(\omega) - 1$  with the relative permittivity  $\tilde{\epsilon}_r(\omega) = \tilde{\epsilon}(\omega)/\epsilon_0$ , we obtain in the frequency domain with the Fourier transform relationship

$$\tilde{\vec{E}}(\vec{r}, \omega) = \int_{-\infty}^{+\infty} \vec{E}(\vec{r}, t) e^{-j\omega t} dt, \quad (2.11)$$

$$\tilde{\vec{P}}(\vec{r}, \omega) = \epsilon_0 \tilde{\chi}(\omega) \tilde{\vec{E}}(\vec{r}, \omega), \quad (2.12)$$

where, the tildes denote the Fourier transforms in the following. Substituted into (2.7)

$$\left( \Delta + \frac{\omega^2}{c_0^2} \right) \tilde{\vec{E}}(\omega) = -\omega^2 \mu_0 \epsilon_0 \tilde{\chi}(\omega) \tilde{\vec{E}}(\omega), \quad (2.13)$$

we obtain

$$\left( \Delta + \frac{\omega^2}{c_0^2} (1 + \tilde{\chi}(\omega)) \right) \tilde{\vec{E}}(\omega) = 0, \quad (2.14)$$

with the refractive index  $n(\omega)$  and  $1 + \tilde{\chi}(\omega) = n^2(\omega)$  results in the Helmholtz equation

$$\left(\Delta + \frac{\omega^2}{c^2}\right) \tilde{\vec{E}}(\omega) = 0, \quad (2.15)$$

where  $c(\omega) = c_0/n(\omega)$  is the velocity of light in the medium. This equation is the starting point for finding monochromatic wave solutions to Maxwell's equations in linear media, as we will study for different cases in the following. Also, so far we have treated the susceptibility  $\tilde{\chi}(\omega)$  as a real quantity, which may not always be the case as we will see later in detail.

### 2.1.2 Plane-Wave Solutions (TEM-Waves) and Complex Notation

The wave equation (2.7) for the real electric field in a linear medium has real monochromatic plane wave solutions  $\vec{E}_{\vec{k}}(\vec{r}, t)$ , which can be written most efficiently in terms of the complex plane-wave solutions  $\underline{\vec{E}}_{\vec{k}}(\vec{r}, t)$  according to

$$\vec{E}_{\vec{k}}(\vec{r}, t) = \frac{1}{2} \left[ \underline{\vec{E}}_{\vec{k}}(\vec{r}, t) + \underline{\vec{E}}_{\vec{k}}(\vec{r}, t)^* \right] = \Re \left\{ \underline{\vec{E}}_{\vec{k}}(\vec{r}, t) \right\}, \quad (2.16)$$

with

$$\underline{\vec{E}}_{\vec{k}}(\vec{r}, t) = \underline{E}_{\vec{k}} e^{i(\omega t - \vec{k} \cdot \vec{r})} \vec{e}(\vec{k}). \quad (2.17)$$

Note, we explicitly underlined the complex wave to indicate that this is a complex quantity. Here,  $\vec{e}(\vec{k})$  is a unit vector indicating the direction of the electric field which is also called the polarization of the wave, and  $\underline{E}_{\vec{k}}$  is the complex field amplitude of the wave with wave vector  $\vec{k}$ . Substitution of eq.(2.16) into the wave equation results in the dispersion relation, i.e. a relationship between wave vector and frequency necessary to satisfy the wave equation

$$|\vec{k}|^2 = \frac{\omega^2}{c(\omega)^2} = k(\omega)^2. \quad (2.18)$$

Thus, the dispersion relation is given by

$$k(\omega) = \pm \frac{\omega}{c_0} n(\omega). \quad (2.19)$$

with the wavenumber

$$k = 2\pi/\lambda, \quad (2.20)$$

where  $\lambda$  is the wavelength of the wave in the medium with refractive index  $n$ ,  $\omega$  the angular frequency,  $\vec{k}$  the wave vector. Note, the natural frequency  $f = \omega/2\pi$ . From  $\nabla \cdot \vec{E} = 0$ , for all time, we see that  $\vec{k} \perp \vec{e}$ . Substitution of the electric field 2.16 into Maxwell's Eqs. (2.1b) results in the magnetic field

$$\vec{H}_{\vec{k}}(\vec{r}, t) = \frac{1}{2} \left[ \underline{\vec{H}}_{\vec{k}}(\vec{r}, t) + \underline{\vec{H}}_{\vec{k}}(\vec{r}, t)^* \right] \quad (2.21)$$

with

$$\underline{\vec{H}}_{\vec{k}}(\vec{r}, t) = \underline{H}_{\vec{k}} e^{j(\omega t - \vec{k} \cdot \vec{r})} \vec{h}(\vec{k}). \quad (2.22)$$

This complex component of the magnetic field can be determined from the corresponding complex electric field component using Faraday's law

$$-j\vec{k} \times \left( \underline{E}_{\vec{k}} e^{j(\omega t - \vec{k} \cdot \vec{r})} \vec{e}(\vec{k}) \right) = -j\mu_0\omega \underline{\vec{H}}_{\vec{k}}(\vec{r}, t), \quad (2.23)$$

or

$$\underline{\vec{H}}_{\vec{k}}(\vec{r}, t) = \frac{\underline{E}_{\vec{k}}}{\mu_0\omega} e^{j(\omega t - \vec{k} \cdot \vec{r})} \vec{k} \times \vec{e} = \underline{H}_{\vec{k}} e^{j(\omega t - \vec{k} \cdot \vec{r})} \vec{h} \quad (2.24)$$

with

$$\vec{h}(\vec{k}) = \frac{\vec{k}}{|\vec{k}|} \times \vec{e}(\vec{k}) \quad (2.25)$$

and

$$\underline{H}_{\vec{k}} = \frac{|\vec{k}|}{\mu_0\omega} \underline{E}_{\vec{k}} = \frac{1}{Z_F} \underline{E}_{\vec{k}}. \quad (2.26)$$

The characteristic impedance of the TEM-wave is the ratio between electric and magnetic field strength

$$Z_F = \mu_0 c = \sqrt{\frac{\mu_0}{\epsilon_0 \epsilon_r}} = \frac{1}{n} Z_{F_0} \quad (2.27)$$

with the refractive index  $n = \sqrt{\epsilon_r}$  and the free space impedance

$$Z_{F_0} = \sqrt{\frac{\mu_0}{\epsilon_0}} \approx 377 \, \Omega. \quad (2.28)$$

Note that the vectors  $\vec{e}$ ,  $\vec{h}$  and  $\vec{k}$  form an orthogonal trihedral,

$$\vec{e} \perp \vec{h}, \quad \vec{k} \perp \vec{e}, \quad \vec{k} \perp \vec{h}. \quad (2.29)$$



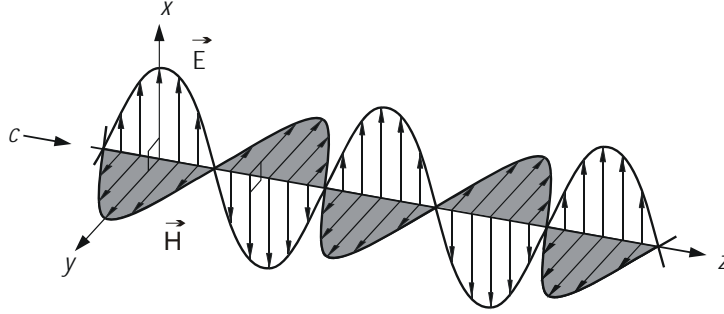


Figure 2.1: Transverse electromagnetic wave (TEM) [1]

That is why we call these waves transverse electromagnetic (TEM) waves. We consider the electric field of a monochromatic electromagnetic wave with frequency  $\omega$  and electric field amplitude  $E_0$ , which propagates in vacuum along the  $z$ -axis, and is polarized along the  $x$ -axis, (Fig. 2.1), i.e.  $\frac{\vec{k}}{|\vec{k}|} = \vec{e}_z$ , and  $\vec{e}(\vec{k}) = \vec{e}_x$ . Then we obtain from Eqs.(2.16) and (2.17)

$$\vec{E}(\vec{r}, t) = E_0 \cos(\omega t - kz) \vec{e}_x, \quad (2.30)$$

and similar for the magnetic field

$$\vec{H}(\vec{r}, t) = \frac{E_0}{Z_{F0}} \cos(\omega t - kz) \vec{e}_y, \quad (2.31)$$

see Figure 2.1. Note, that for a backward propagating wave with  $\vec{E}(\vec{r}, t) = \underline{E} e^{j\omega t + j\vec{k} \cdot \vec{r}} \vec{e}_x$ , and  $\vec{H}(\vec{r}, t) = \underline{H} e^{j(\omega t + \vec{k} \cdot \vec{r})} \vec{e}_y$ , there is a sign change for the magnetic field

$$\underline{H} = -\frac{|\vec{k}|}{\mu_0 \omega} \underline{E}, \quad (2.32)$$

so that the  $(\vec{k}, \vec{E}, \vec{H})$  always form a right handed orthogonal system.

### 2.1.3 Poynting Vectors, Energy Density and Intensity

The table below summarizes the instantaneous electric and magnetic energy densities, the Poynting vector, Poynting theorem and intensity for an arbitrary electric field and the corresponding time averaged quantities for a time harmonic field

Quantity	Real fields	Complex fields
Electric and magnetic energy density	$w_e = \frac{1}{2} \vec{E} \cdot \vec{D} = \frac{1}{2} \epsilon_0 \epsilon_r \vec{E}^2$ $w_m = \frac{1}{2} \vec{H} \cdot \vec{B} = \frac{1}{2} \mu_0 \mu_r \vec{H}^2$ $w = w_e + w_m$	$\langle w_e \rangle = \frac{1}{4} \epsilon_0 \epsilon_r  \underline{\vec{E}} ^2$ $\langle w_m \rangle = \frac{1}{4} \mu_0 \mu_r  \underline{\vec{H}} ^2$ $\langle w \rangle = \langle w_e \rangle + \langle w_m \rangle$
Poynting vector	$\vec{S} = \vec{E} \times \vec{H}$	$\underline{\vec{T}} = \frac{1}{2} \underline{\vec{E}} \times \underline{\vec{H}}^*$
Poynting theorem	$\text{div} \vec{S} + \vec{E} \cdot \vec{j} + \frac{\partial w}{\partial t} = 0$	$\text{div} \underline{\vec{T}} + \frac{1}{2} \underline{\vec{E}} \cdot \underline{\vec{j}}^* +$ $+ 2j\omega(\langle w_m \rangle - \langle w_e \rangle) = 0$
Intensity	$I =  \vec{S}  = cw$	$I = \text{Re}\{\underline{\vec{T}}\} = c \langle w \rangle$

Table 2.1: Poynting vector and energy density in EM-fields

For a plane wave with a complex electric field  $\underline{\vec{E}}(\vec{r}, t) = \underline{E} e^{j(\omega t - kz)} \vec{e}_x$  we obtain for the energy density in units of [J/m<sup>3</sup>]

$$w = \frac{1}{2} \epsilon_r \epsilon_0 |\underline{E}|^2, \quad (2.33)$$

the complex Poynting vector

$$\underline{\vec{T}} = \frac{1}{2 Z_F} |\underline{E}|^2 \vec{e}_z, \quad (2.34)$$

and the intensity in units of [W/m<sup>2</sup>]

$$I = \frac{1}{2 Z_F} |\underline{E}|^2 = \frac{1}{2} Z_F |\underline{H}|^2. \quad (2.35)$$

## 2.2 Classical Permittivity

In this section we want to get insight into propagation of an electromagnetic wavepacket in an isotropic and homogeneous medium, such as a glass optical fiber due to the interaction of radiation with the medium. The electromagnetic properties of a dielectric medium is largely determined by the electric polarization  $\vec{P}(t)$  induced by an electric field in the medium. The polarization is defined as the total induced dipole moment per unit volume. If  $\vec{p}$  is the dipole moment of the elementary unit (atom, molecule, ...) constituting the medium and  $N$  is density of elementary units, then the polirization is

$$\vec{P}(t) = \frac{\text{dipole moment}}{\text{volume}} = N \cdot \vec{p}(t), \quad (2.36)$$

In the frequency domain, i.e. after Fourier transformation we obtain

$$\tilde{\underline{P}}(\omega) = \frac{\text{dipole moment}}{\text{volume}} = N \cdot \tilde{\underline{p}}(\omega) = \epsilon_0 \tilde{\underline{\chi}}(\omega) \tilde{\underline{E}}(\omega), \quad (2.37)$$

assuming again a linear polarizability proportional to the electric field. Or expressed in a different way the dielectric susceptibility is the frequency response function of the polarization in a medium to an applied field

$$\tilde{\underline{\chi}}(\omega) = \frac{N \cdot \tilde{\underline{p}}(\omega)}{\epsilon_0 \tilde{\underline{E}}(\omega)}. \quad (2.38)$$

Atoms and Molecules are composed of charge particles, such as a positively charged nucleus and electrons bound to the nucleus by the Coulomb force. As a first approximation towards the interaction of light and matter we consider a simple model for matter, where the elementary units, the atoms or molecules are modelled by a positively charge nucleus and an electron bound to it by a force increasing linear with distance between nucleus and electron, see Figure 2.2.

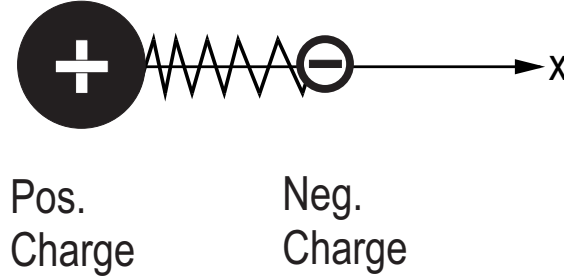


Figure 2.2: Classical harmonic oscillator model for radiation matter interaction

As it turns out (justification later) this simple model correctly describes many aspects of the interaction of light with matter at very low electric field strength, i.e. the fields do not change the electron distribution in the atom considerably or even ionize the atom. This model is called Lorentz model after the famous physicist A. H. Lorentz (Dutchman) studying electromagnetic phenomena at the turn of the 19th century. He also found the Lorentz

Transformation and Invariance of Maxwell's Equations with respect to these transformation, which showed the path to Special Relativity.

The equation of motion for such a unit is the damped harmonic oscillator driven by an electric field in one dimension,  $x$ . At optical frequencies, the distance of elongation,  $x$ , is much smaller than an optical wavelength (atoms have dimensions on the order of a tenth of a nanometer, whereas optical fields have wavelength on the order of microns) and, therefore, we can neglect the spatial variation of the electric field during the motion of the charges within an atom (dipole approximation, i.e.  $\vec{E}(\vec{r}, t) = \vec{E}(\vec{r}_A, t) = E(t)\vec{e}_x$ . The equation of motion is then.

$$m \frac{d^2 x}{dt^2} + 2 \frac{\Omega_0}{Q} m \frac{dx}{dt} + m \Omega_0^2 x = -e_0 E(t), \quad (2.39)$$

where  $\underline{E}(t) = \underline{\tilde{E}} e^{j\omega t}$ . Here,  $m$  is the mass of the electron assuming the that the rest atom has infinite mass,  $e_0$  the charge of the electron,  $\Omega_0$  is the resonance frequency of the undamped oscillator and  $Q$  the quality factor of the resonance, which determines the damping of the oscillator. By using the trial solution  $\underline{x}(t) = \underline{\tilde{x}} e^{j\omega t}$ , we obtain for the complex amplitude of the dipole moment  $\underline{\tilde{p}}$  with the time dependent response  $\underline{p}(t) = -e_0 \underline{x}(t) = \underline{\tilde{p}} e^{j\omega t}$

$$\underline{\tilde{p}} = \frac{\frac{e_0^2}{m}}{(\Omega_0^2 - \omega^2) + 2j\frac{\Omega_0}{Q}\omega} \underline{\tilde{E}}. \quad (2.40)$$

Note, that we included ad hoc a damping term in the harmonic oscillator equation. At this point it is not clear what the physical origin of this damping term is and we will discuss this at length later in chapter 4. For the moment, we can view this term simply as a consequence of irreversible interactions of the atom with its environment. The simplest damping mechanism is that an accelerated electron radiates, i.e. radiation damping. We then obtain from (2.37) for the susceptibility

$$\underline{\tilde{\chi}}(\omega) = \frac{N \frac{e_0^2}{m} \frac{1}{\epsilon_0}}{(\Omega_0^2 - \omega^2) + 2j\omega \frac{\Omega_0}{Q}} \quad (2.41)$$

or

$$\underline{\tilde{\chi}}(\omega) = \frac{\omega_p^2}{(\Omega_0^2 - \omega^2) + 2j\omega \frac{\Omega_0}{Q}}, \quad (2.42)$$

where  $\omega_p$  is called the plasma frequency defined as  $\omega_p^2 = Ne_0^2/m\epsilon_0$ . The meaning of the plasma frequency will be further elucidated in recitations and on problem sets. Figure 2.3 shows the real and imaginary part of the resulting classical dielectric susceptibility,  $\tilde{\chi}(\omega) = \tilde{\chi}_r(\omega) + j\tilde{\chi}_i(\omega)$ , (2.42), normalized to the absolute value of the imaginary part at  $\omega = \Omega_0$ , which is  $\omega_p^2 Q / (2\Omega_0^2)$ .

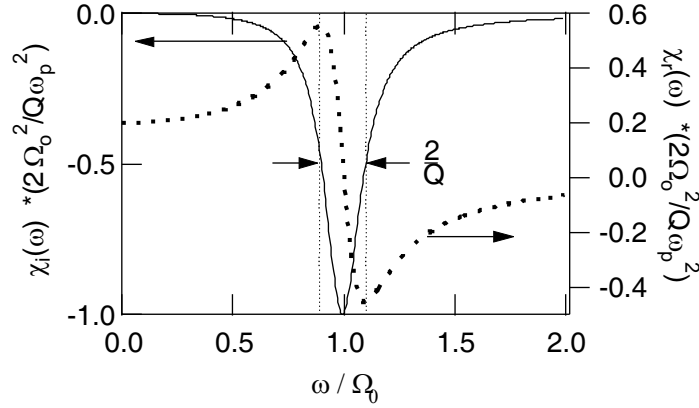


Figure 2.3: Real part (dashed line) and imaginary part (solid line) of the susceptibility of the classical oscillator model for the dielectric polarizability.

Note, that there is a small resonance shift (almost invisible) due to the loss. Off resonance, the imaginary part approaches zero very quickly. Not so the real part, which approaches a constant value  $\omega_p^2/\Omega_0^2$  below resonance for  $\omega \rightarrow 0$ , and approaches zero far above resonance, but much slower than the imaginary part. As we will see later, this is the reason why there are low loss, i.e. transparent, media with refractive index very much different from 1, because as discussed above the real part of the dielectric susceptibility contributes to the refractive index in a material. The negative imaginary part describes absorption of the electromagnetic wave in the medium made up of damped harmonic oscillators driven by the electric field of the electromagnetic wave. Strong absorption occurs when the driving frequency is on resonance with the damped harmonic oscillator, i.e. the absorption resonance of the medium.

After having a model for the dielectric susceptibility of a medium, we can study how optical signals may propagate in such a medium, most importantly optical pulses, such as those used in optical communications.

## 2.3 Optical Pulses

Optical pulses are wave packets constructed by a continuous superposition of monochromatic plane waves. Consider a TEM-wavepacket, i.e. a superposition of waves with different frequencies, polarized along the x-axis and propagating along the z-axis

$$\underline{\vec{E}}(\vec{r}, t) = \int_0^\infty \frac{d\Omega}{2\pi} \underline{\vec{E}}(\Omega) e^{j(\Omega t - K(\Omega)z)} \vec{e}_x. \quad (2.43)$$

Correspondingly, the magnetic field is given by

$$\underline{\vec{H}}(\vec{r}, t) = \int_0^\infty \frac{d\Omega}{2\pi Z_F(\Omega)} \underline{\vec{E}}(\Omega) e^{j(\Omega t - K(\Omega)z)} \vec{e}_y \quad (2.44)$$

Again, the physical electric and magnetic fields are real and related to the complex fields by

$$\vec{E}(\vec{r}, t) = \frac{1}{2} \left( \underline{\vec{E}}(\vec{r}, t) + \underline{\vec{E}}(\vec{r}, t)^* \right) \quad (2.45)$$

$$\vec{H}(\vec{r}, t) = \frac{1}{2} \left( \underline{\vec{H}}(\vec{r}, t) + \underline{\vec{H}}(\vec{r}, t)^* \right). \quad (2.46)$$

Here,  $|\underline{\vec{E}}(\Omega)|e^{j\varphi(\Omega)}$  is the complex wave amplitude of the electromagnetic wave at frequency  $\Omega$  and  $K(\Omega) = \Omega/c(\Omega) = n(\Omega)\Omega/c_0$  the wavenumber, where,  $\tilde{n}(\Omega)$  is again the refractive index of the medium

$$\tilde{n}^2(\Omega) = 1 + \tilde{\chi}(\Omega), \quad (2.47)$$

$c$  and  $c_0$  are the velocity of light in the medium and in vacuum, respectively. The planes of constant phase propagate with the phase velocity  $c$  of the wave.

The wavepacket consists of a superposition of many frequencies with the spectrum shown in Fig. 2.4. At a given point in space, for simplicity  $z = 0$ , the complex field of a pulse is given by (Fig. 2.4)

$$\underline{E}(z = 0, t) = \frac{1}{2\pi} \int_0^\infty \underline{\vec{E}}(\Omega) e^{j\Omega t} d\Omega. \quad (2.48)$$

Optical pulses often have relatively small spectral width compared to the center frequency of the pulse  $\omega_0$ , as it is illustrated in the upper part of Figure 2.4. For example typical pulses used in optical communication systems for 10Gb/s transmission speed are 20 ps in length and have a center wavelength

of  $\lambda = 1550$  nm. Thus the spectral width is only on the order of 50 GHz, whereas the center frequency of the pulse is 200 THz, i.e. the bandwidth is 4000 smaller than the center frequency. In such cases it is useful to separate the complex electric field in Eq. (2.48) into a carrier frequency  $\omega_0$  and an envelope  $\underline{A}(t)$  and represent the absolute frequency as  $\Omega = \omega_0 + \omega$ .

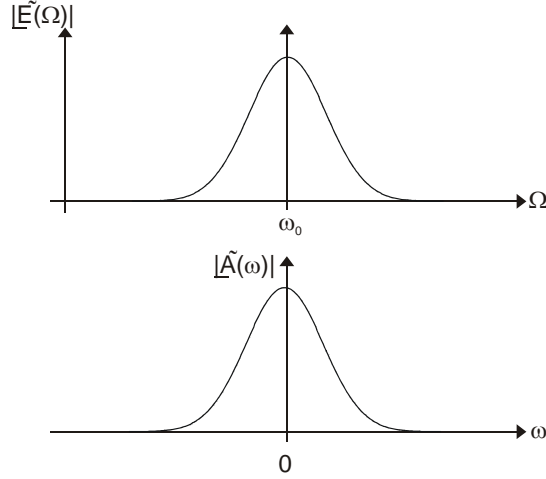


Figure 2.4: Spectrum of an optical wave packet described in absolute and relative frequencies

We can then rewrite Eq.(2.48) as

$$\underline{E}(z = 0, t) = \frac{1}{2\pi} \int_{-\omega_0}^{\infty} \underline{\tilde{E}}(\omega_0 + \omega) e^{j(\omega_0 + \omega)t} d\omega \quad (2.49)$$

$$\begin{aligned} &= \frac{1}{2\pi} e^{j\omega_0 t} \int_{-\omega_0}^{\infty} \underline{\tilde{E}}(\omega_0 + \omega) e^{j\omega t} d\omega \\ &= \underline{A}(t) e^{j\omega_0 t}. \end{aligned} \quad (2.50)$$

The envelope, see Figure 2.8, is given by

$$\underline{A}(t) = \frac{1}{2\pi} \int_{-\omega_0 \rightarrow -\infty}^{\infty} \underline{\tilde{A}}(\omega) e^{j\omega t} d\omega \quad (2.51)$$

$$= \frac{1}{2\pi} \int_{-\infty}^{\infty} \underline{\tilde{A}}(\omega) e^{j\omega t} d\omega, \quad (2.52)$$

where  $\tilde{A}(\omega) = \tilde{E}(\omega_0 + \omega)$  is the spectrum of the envelope with,  $\tilde{A}(\omega) = 0$  for  $\omega \leq -\omega_0$ . To be physically meaningful, the spectral amplitude  $\tilde{A}(\omega)$  must be zero for negative frequencies less than or equal to the carrier frequency, see Figure 2.8. Note, that waves with zero frequency can not propagate, since the corresponding wave vector is zero. The pulse and its envelope are shown in Figure 2.5.

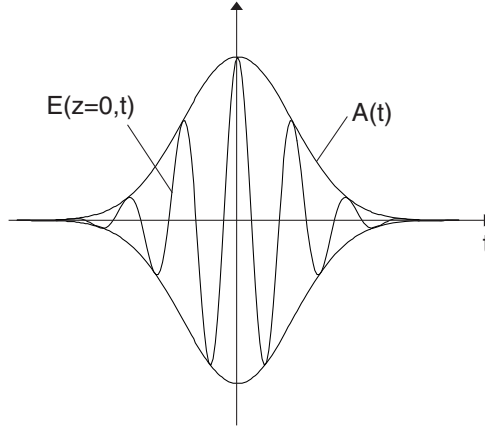


Figure 2.5: Electric field and envelope of an optical pulse.

Table 2.2 shows pulse shape and spectra of some often used pulses as well as the pulse width and time bandwidth products. The pulse width and bandwidth are usually specified as the Full Width at Half Maximum (FWHM) of the intensity in the time domain,  $|A(t)|^2$ , and the spectral density  $|\tilde{A}(\omega)|^2$  in the frequency domain, respectively. Pulse shapes and corresponding spectra to the pulses listed in Table 2.2 are shown in Figs 2.6 and 2.7.



Pulse Shape	Fourier Transform	Pulse Width	Time-Bandwidth Product
$\underline{A}(t)$	$\underline{\tilde{A}}(\omega) = \int_{-\infty}^{\infty} a(t)e^{-j\omega t} dt$	$\Delta t$	$\Delta t \cdot \Delta f$
Gaussian: $e^{-\frac{t^2}{2\tau^2}}$	$\sqrt{2\pi}\tau e^{-\frac{1}{2}\tau^2\omega^2}$	$2\sqrt{\ln 2}\tau$	0.441
Hyperbolic Secant: $\text{sech}(\frac{t}{\tau})$	$\frac{\tau}{2} \text{sech}(\frac{\pi}{2}\tau\omega)$	$1.7627 \tau$	0.315
Rect-function: $\begin{cases} 1, &  t  \leq \tau/2 \\ 0, &  t  > \tau/2 \end{cases}$	$\tau \frac{\sin(\tau\omega/2)}{\tau\omega/2}$	$\tau$	0.886
Lorentzian: $\frac{1}{1+(t/\tau)^2}$	$2\pi\tau e^{- \tau\omega }$	$1.287 \tau$	0.142
Double-Exp.: $e^{- \frac{t}{\tau} }$	$\frac{\tau}{1+(\omega\tau)^2}$	$\ln 2 \tau$	0.142

Table 2.2: Pulse shapes, corresponding spectra and time bandwidth products.

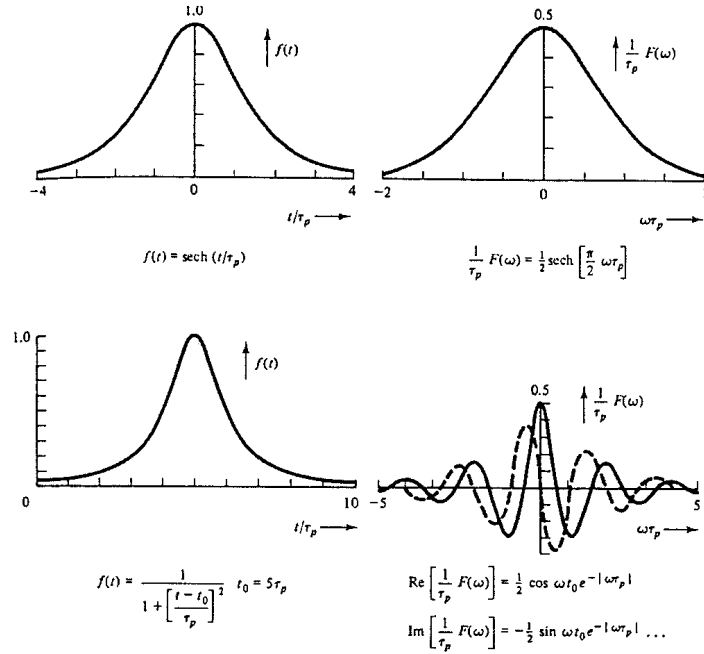


Figure 2.6: Fourier transforms to pulse shapes listed in table 2.2 [14].

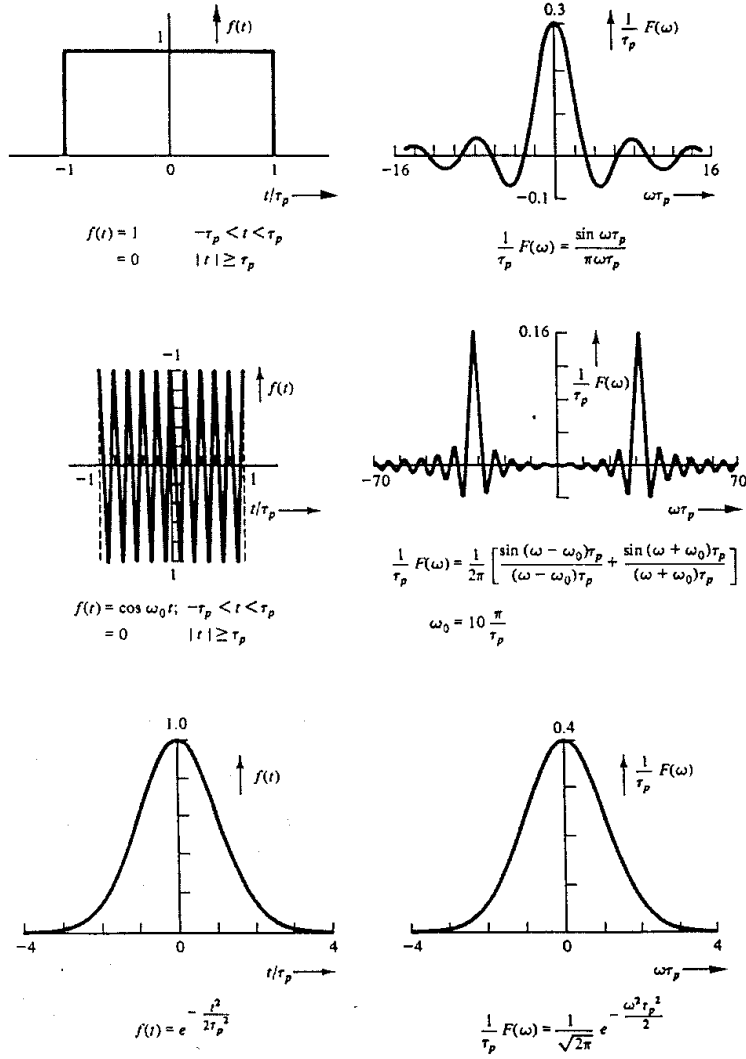


Figure 2.7: Fourier transforms to pulse shapes listed in table 2.2 continued [14].

## 2.4 Pulse Propagation

In many cases, mode locking of lasers can be most easily studied in the time domain. Then mode locking becomes a nonlinear, dissipative wave

propagation problem. In this chapter, we discuss the basic elements of pulse propagation in linear media.

Having a basic model for the interaction of light and matter at hand, via section 2.2, we can investigate what happens if an electromagnetic wave packet, i.e. an optical pulse propagates through such a medium. We start from Eqs.(2.43) to evaluate the wave packet propagation for an arbitrary propagation distance  $z$

$$\underline{E}(z, t) = \frac{1}{2\pi} \int_0^\infty \tilde{\underline{E}}(\Omega) e^{j(\Omega t - K(\Omega)z)} d\Omega. \quad (2.53)$$

Analogous to Eq. (2.49) for a pulse at a given position, we can separate an optical pulse into a carrier wave at frequency  $\omega_0$  and a complex envelope  $A(z, t)$ ,

$$\underline{E}(z, t) = \underline{A}(z, t) e^{j(\omega_0 t - K(\omega_0)z)}. \quad (2.54)$$

By introducing the offset frequency  $\omega$ , the offset wavenumber  $k(\omega)$  and spectrum of the envelope  $\tilde{\underline{A}}(\omega)$

$$\omega = \Omega - \omega_0, \quad (2.55)$$

$$k(\omega) = K(\omega_0 + \omega) - K(\omega_0), \quad (2.56)$$

$$\tilde{\underline{A}}(\omega) = \tilde{\underline{E}}(\Omega = \omega_0 + \omega). \quad (2.57)$$

we can rewrite Eq.(2.53) as

$$\underline{E}(z, t) = \frac{1}{2\pi} \int_{-\infty}^\infty \tilde{\underline{A}}(\omega) e^{j(\omega t - k(\omega)z)} d\omega e^{j(\omega_0 t - K(\omega_0)z)}. \quad (2.58)$$

Thus the envelope at propagation distance  $z$ , see Fig.2.8, is expressed as

$$\underline{A}(z, t) = \frac{1}{2\pi} \int_{-\infty}^\infty \tilde{\underline{A}}(\omega) e^{j(\omega t - k(\omega)z)} d\omega, \quad (2.59)$$

with the same constraints on the spectrum of the envelope as before, i.e. the spectrum of the envelope must be zero for negative frequencies beyond the carrier frequency. In the frequency domain Eq.(2.59) corresponds to

$$\tilde{\underline{A}}(z, \omega) = \tilde{\underline{A}}(z = 0, \omega) e^{-jk(\omega)z}. \quad (2.60)$$

Depending on the dispersion relation  $k(\omega)$ , (see Fig. 2.9), the pulse will be reshaped during propagation as discussed in the following section.

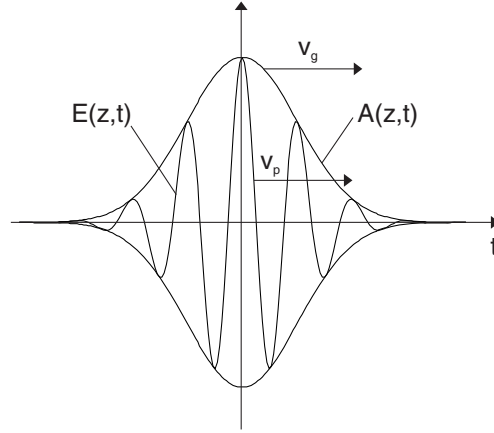


Figure 2.8: Electric field and pulse envelope in time domain.

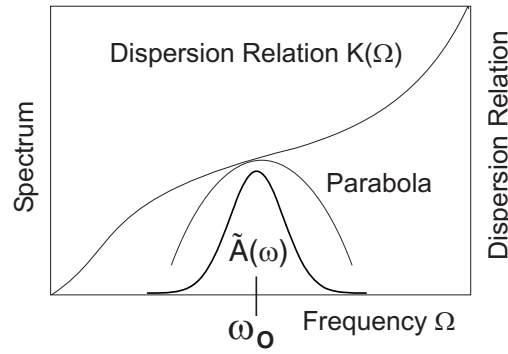


Figure 2.9: Taylor expansion of dispersion relation at the center frequency of the wave packet.

### 2.4.1 Dispersion

The dispersion relation  $K(\Omega)$  or differential propagation constant,  $k(\omega)$ , indicates how much phase shift each frequency component experiences during propagation. These phase shifts, if not linear with respect to frequency, will lead to distortions of the pulse. If the dispersion relation  $K(\Omega)$  is only slowly varying over the pulse spectrum, it is useful to represent it or by its Taylor

expansion, see Fig. 2.9,

$$k(\omega) = k'\omega + \frac{k''}{2}\omega^2 + \frac{k^{(3)}}{6}\omega^3 + O(\omega^4). \quad (2.61)$$

If the refractive index depends on frequency, the dispersion relation is no longer linear with respect to frequency, see Fig. 2.9 and the pulse propagation according to (2.59) can be understood most easily in the frequency domain

$$\frac{\partial \tilde{\underline{A}}(z, \omega)}{\partial z} = -jk(\omega)\tilde{\underline{A}}(z, \omega). \quad (2.62)$$

Transformation of Eq.(2.62) into the time domain gives

$$\frac{\partial \underline{A}(z, t)}{\partial z} = -j \sum_{n=1}^{\infty} \frac{k^{(n)}}{n!} \left( -j \frac{\partial}{\partial t} \right)^n \underline{A}(z, t). \quad (2.63)$$

If we keep only the first term, the linear term, in Eq.(2.60), then we obtain for the pulse envelope from (2.59)

$$\tilde{\underline{A}}(z, \omega) = \tilde{\underline{A}}(z=0, \omega)e^{-jk'\omega z}. \quad (2.64)$$

According to the shift theorem for Fourier Transforms, a linear phase over the spectrum corresponds to a shift in the time domain,

$$\underline{A}(z, t) = \underline{A}(0, t - z/v_{g0}), \quad (2.65)$$

where we introduced the group velocity at frequency  $\omega_0$

$$v_{g0} = 1/k' = \left( \frac{dk(\omega)}{d\omega} \Big|_{\omega=\omega_0} \right)^{-1} = \left( \frac{dK(\Omega)}{d\Omega} \Big|_{\Omega=\omega_0} \right)^{-1} \quad (2.66)$$

Thus the derivative of the dispersion relation at the carrier frequency determines the propagation velocity of the envelope of the wave packet or group velocity, whereas the ratio between propagation constant and frequency determines the phase velocity of the carrier

$$v_{p0} = \omega_0/K(\omega_0) = \left( \frac{K(\omega_0)}{\omega_0} \right)^{-1}. \quad (2.67)$$

To get rid of the trivial motion of the pulse envelope with the group velocity, we introduce the retarded time  $t' = t - z/v_{g0}$ . With respect to this retarded

time the pulse shape is invariant during propagation, if we approximate the dispersion relation by the slope at the carrier frequency

$$\underline{A}(z, t) = \underline{A}(0, t'). \quad (2.68)$$

Note, if we approximate the dispersion relation by its slope at the carrier frequency, i.e. we retain only the first term in Eq.(2.63), we obtain

$$\frac{\partial \underline{A}(z, t)}{\partial z} + \frac{1}{v_{g0}} \frac{\partial \underline{A}(z, t)}{\partial t} = 0, \quad (2.69)$$

and (2.68) is its solution. If, we transform this equation to the new coordinate system

$$z' = z, \quad (2.70)$$

$$t' = t - z/v_{g0}, \quad (2.71)$$

with

$$\frac{\partial}{\partial z} = \frac{\partial}{\partial z'} - \frac{1}{v_{g0}} \frac{\partial}{\partial t'}, \quad (2.72)$$

$$\frac{\partial}{\partial t} = \frac{\partial}{\partial t'} \quad (2.73)$$

the transformed equation is

$$\frac{\partial \underline{A}(z', t')}{\partial z'} = 0. \quad (2.74)$$

Thus we see that the pulse shape doesn't change during propagation. The propagation can be simply accounted for by introducing a retarded time  $t' = t - z/v_{g0}$ . Since  $z$  is equal to  $z'$  we keep  $z$  in the following.

If the spectrum of the pulse is broad enough or the propagation distance long enough, so that the second order term in (2.61) becomes important, the pulse will no longer keep its shape. When keeping in the dispersion relation terms up to second order it follows from (2.63) and (2.70,2.71)

$$\frac{\partial \underline{A}(z, t')}{\partial z} = j \frac{k''}{2} \frac{\partial^2 \underline{A}(z, t')}{\partial t'^2}. \quad (2.75)$$

This is the first non trivial term in the wave equation for the envelope. Because of the superposition principle, the pulse can be thought of to be

decomposed into wavepackets (sub-pulses) with different center frequencies. Now, the group velocity depends on the spectral component of the pulse, see Figure 2.10, which will lead to broadening or dispersion of the pulse.

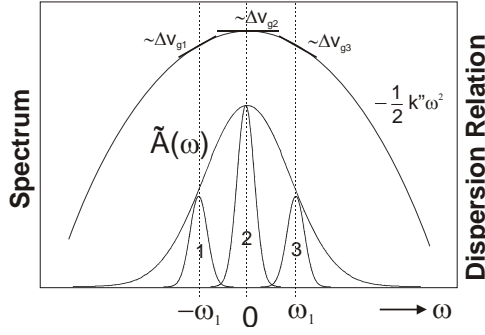


Figure 2.10: Decomposition of a pulse into wave packets with different center frequency. In a medium with dispersion the wavepackets move at different relative group velocity.

Fortunately, for a Gaussian pulse, the pulse propagation equation 2.75 can be solved analytically. The initial pulse is then of the form

$$\underline{E}(z = 0, t) = \underline{A}(z = 0, t)e^{j\omega_0 t} \quad (2.76)$$

$$\underline{A}(z = 0, t = t') = \underline{A}_0 \exp \left[ -\frac{1}{2} \frac{t'^2}{\tau^2} \right] \quad (2.77)$$

Eq.(2.75) is most easily solved in the frequency domain since it transforms to

$$\frac{\partial \tilde{\underline{A}}(z, \omega)}{\partial z} = -j \frac{k'' \omega^2}{2} \tilde{\underline{A}}(z, \omega), \quad (2.78)$$

with the solution

$$\tilde{\underline{A}}(z, \omega) = \tilde{\underline{A}}(z = 0, \omega) \exp \left[ -j \frac{k'' \omega^2}{2} z \right]. \quad (2.79)$$

The pulse spectrum acquires a parabolic phase. Note, that here  $\omega$  is the Fourier Transform variable conjugate to  $t'$  rather than  $t$ . The Gaussian pulse has the advantage that its Fourier transform is also a Gaussian

$$\tilde{\underline{A}}(z = 0, \omega) = A_0 \sqrt{2\pi\tau} \exp \left[ -\frac{1}{2} \tau^2 \omega^2 \right]. \quad (2.80)$$

Note, in the following we will often use the Gaussian Integral

$$\frac{1}{\sqrt{2\pi\sigma}} \int_{-\infty}^{\infty} e^{-\frac{x^2}{2\sigma}} e^{-jx\varsigma} dx = e^{-\frac{\varsigma^2}{2\sigma}} \text{ for } \text{Re}\{\sigma\} \geq 0 \quad (2.81)$$

In the spectral domain the solution at an arbitray propagation distance  $z$  is

$$\underline{\tilde{A}}(z, \omega) = A_0 \sqrt{2\pi\tau} \exp \left[ -\frac{1}{2} (\tau^2 + jk''z) \omega^2 \right]. \quad (2.82)$$

With the Gaussian integral (2.81) the inverse Fourier transform is

$$\underline{A}(z, t') = A_0 \left( \frac{\tau^2}{(\tau^2 + jk''z)} \right)^{1/2} \exp \left[ -\frac{1}{2} \frac{t'^2}{(\tau^2 + jk''z)} \right] \quad (2.83)$$

The exponent can be written as real and imaginary part and we finally obtain

$$\underline{A}(z, t') = A_0 \left( \frac{\tau^2}{(\tau^2 + jk''z)} \right)^{1/2} \exp \left[ -\frac{1}{2} \frac{\tau^2 t'^2}{(\tau^4 + (k''z)^2)} + j \frac{1}{2} k''z \frac{t'^2}{(\tau^4 + (k''z)^2)} \right] \quad (2.84)$$

As we see from Eq.(2.84) during propagation the FWHM of the Gaussian determined by

$$\exp \left[ -\frac{\tau^2 (\tau'_{FWHM}/2)^2}{(\tau^4 + (k''z)^2)} \right] = 0.5 \quad (2.85)$$

changes from

$$\tau_{FWHM} = 2\sqrt{\ln 2} \tau \quad (2.86)$$

at the start to

$$\begin{aligned} \tau'_{FWHM} &= 2\sqrt{\ln 2} \tau \sqrt{1 + \left( \frac{k''L}{\tau^2} \right)^2} \\ &= \tau_{FWHM} \sqrt{1 + \left( \frac{k''L}{\tau^2} \right)^2} \end{aligned} \quad (2.87)$$

at  $z = L$ . For large stretching this result simplifies to

$$\tau'_{FWHM} = 2\sqrt{\ln 2} \left| \frac{k''L}{\tau} \right| \text{ for } \left| \frac{k''L}{\tau^2} \right| \gg 1. \quad (2.88)$$



The strongly dispersed pulse has a width equal to the difference in group delay over the spectral width of the pulse.

Figure 2.11 shows the evolution of the magnitude of the Gaussian wave packet during propagation in a medium which has no higher order dispersion in normalized units, i.e. ( $[z] = m, [t] = s, [k] = s^2/m, k_j = 2$ ). The pulse spreads continuously..

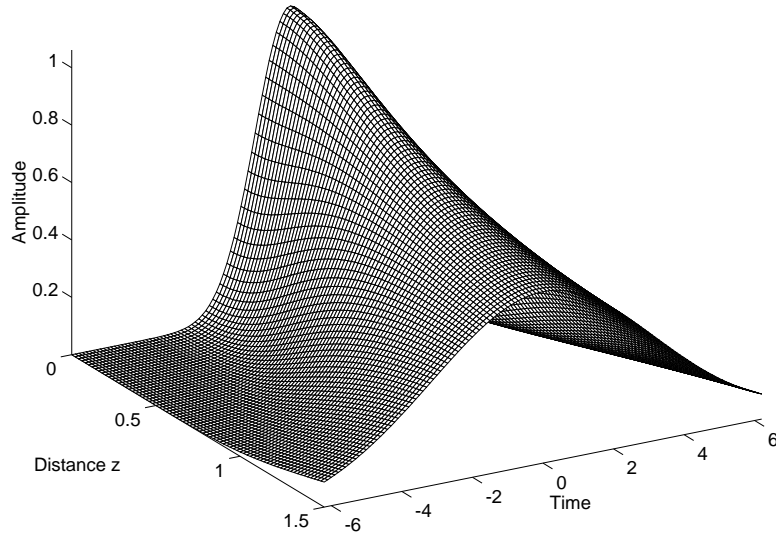


Figure 2.11: Magnitude of the complex envelope of a Gaussian pulse,  $|A(z, t')|$ , in a dispersive medium.

As discussed before, the origin of this spreading is the group velocity dispersion (GVD),  $k'' \neq 0$ . The group velocity varies over the pulse spectrum significantly leading to a group delay dispersion (GDD) after a propagation distance  $z = L$  of  $k''L \neq 0$ , for the different frequency components. This leads to the build-up of chirp in the pulse during propagation. We can understand this chirp by looking at the parabolic phase that develops over the pulse in time at a fixed propagation distance. The phase is, see Eq.(2.84)

$$\phi(z = L, t') = -\frac{1}{2} \arctan \left[ \frac{k''L}{\tau^2} \right] + \frac{1}{2} k''L \frac{t'^2}{(\tau^4 + (k''L)^2)}. \quad (2.89)$$

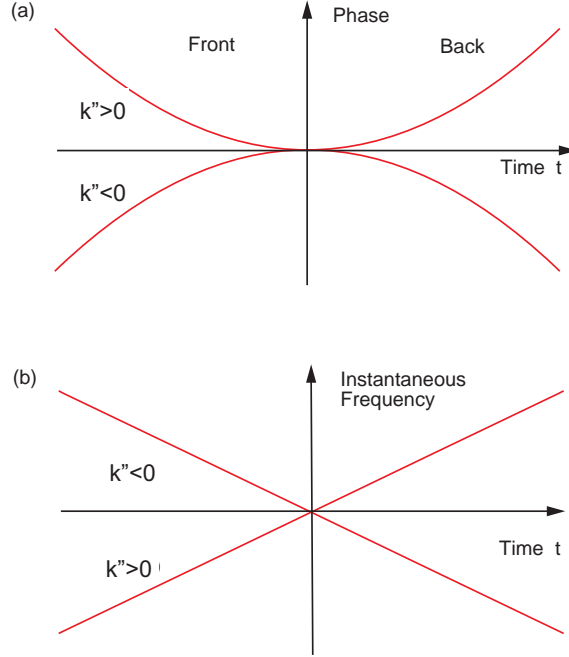


Figure 2.12: (a) Phase and (b) instantaneous frequency of a Gaussian pulse during propagation through a medium with positive or negative dispersion.

This parabolic phase, see Fig. 2.12 (a), can be understood as a locally varying frequency in the pulse, i.e. the derivative of the phase gives the instantaneous frequency shift in the pulse with respect to the center frequency

$$\omega(z = L, t') = \frac{\partial}{\partial t'} \phi(L, t') = \frac{k'' L}{(\tau^4 + (k'' L)^2)} t' \quad (2.90)$$

see Fig. 2.12 (b). The instantaneous frequency indicates that for a medium with positive GVD, i.e.  $k'' > 0$ , the low frequencies are in the front of the pulse, whereas the high frequencies are in the back of the pulse, since the sub-pulses with lower frequencies travel faster than sub-pulses with higher frequencies. The opposite is the case for negative dispersive materials.

It is instructive for later purposes, that this behaviour can be completely understood from the center of mass motion of the sub-pulses, see Figure 2.10.

Note, we can choose a set of sub-pulses, with such narrow bandwidth, that dispersion does not matter. In the time domain, these pulses are of course very long, because of the time bandwidth relationship. Nevertheless, since they all have different carrier frequencies, they interfere with each other in such a way that the superposition is a very narrow pulse. This interference, becomes destroyed during propagation, since the sub-pulses propagate at different speed, i.e. their center of mass propagates at different speed.

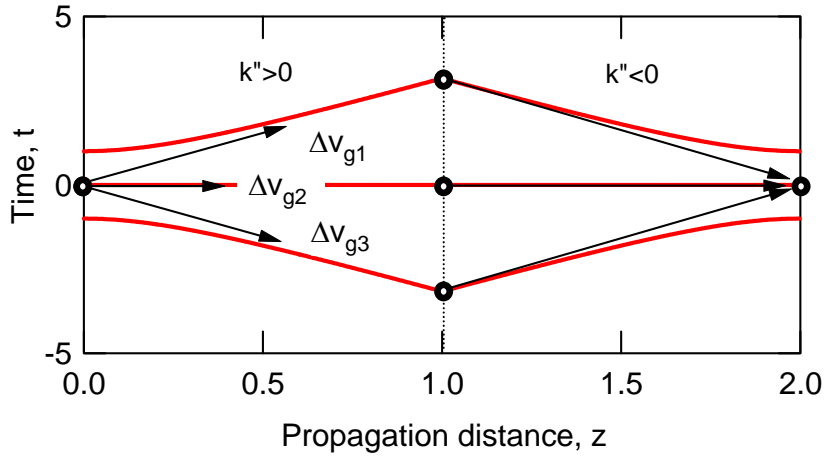


Figure 2.13: Pulse spreading by following the center of mass of sub-pulses according to Fig. 2.10. For  $z < 1$ , the pulses propagate in a medium with positive dispersion and for  $z > 1$  in a medium with negative dispersion.

The differential group delay  $\Delta T_g(\omega) = k'' L \omega$  of a sub-pulse with its center frequency  $\omega$  different from 0, is due to its differential group velocity  $\Delta v_g(\omega) = -v_{g0} \Delta T_g(\omega) / T_{g0} = -v_{g0}^2 k'' \omega$ . Note, that  $T_{g0} = L / v_{g0}$ . This is illustrated in Figure 2.13 by plotting the trajectory of the relative motion of the center of mass of each sub-pulse as a function of propagation distance, which asymptotically approaches the formula for the pulse width of the highly dispersed pulse Eq.(2.88). If we assume that the pulse propagates through a negative dispersive medium following the positive dispersive medium, the group velocity of each sub-pulse is reversed. The sub-pulses propagate towards each other until they all meet at one point (focus) to produce again a short and unchirped initial pulse, see Figure 2.13. This is a very powerful

technique to understand dispersive wave motion and is also the connection between ray optics and physical optics.

### 2.4.2 Loss and Gain

If the medium considered has loss, described by the imaginary part of the dielectric susceptibility, see (2.42) and Fig. 2.3, we can incorporate this loss into a complex refractive index

$$\tilde{n}(\Omega) = n_r(\Omega) + jn_i(\Omega) \quad (2.91)$$

via

$$\tilde{n}(\Omega) = \sqrt{1 + \tilde{\chi}(\Omega)}. \quad (2.92)$$

For an optically thin medium (weakly absorbing gases), i.e.  $\tilde{\chi} \ll 1$  the following approximation is very useful

$$\tilde{n}(\Omega) \approx 1 + \frac{\tilde{\chi}(\Omega)}{2}. \quad (2.93)$$

As one can show, the complex susceptibility (2.42) can be approximated close to resonance, i.e.  $\Omega \approx \Omega_0$ , by the complex Lorentzian lineshape

$$\tilde{\chi}(\Omega) = \frac{-j\chi_0}{1 + jQ\frac{\Omega - \Omega_0}{\Omega_0}}, \quad (2.94)$$

where  $\chi_0 = Q\frac{\omega_p^2}{2\Omega_0^2}$  will turn out to be related to the peak absorption of the resonance, which is proportional to the density of atoms.  $\Omega_0$  is the center frequency and  $\Delta\Omega = \frac{\Omega_0}{Q}$  is the half width half maximum (HWHM) linewidth of the transition. The real and imaginary part of the complex Lorentzian are

$$\tilde{\chi}_r(\Omega) = \frac{-\chi_0 \frac{(\Omega - \Omega_0)}{\Delta\Omega}}{1 + \left(\frac{\Omega - \Omega_0}{\Delta\Omega}\right)^2}, \quad (2.95)$$

$$\tilde{\chi}_i(\Omega) = \frac{-\chi_0}{1 + \left(\frac{\Omega - \Omega_0}{\Delta\Omega}\right)^2}. \quad (2.96)$$

In the derivation of the wave equation for the pulse envelope (2.63) in section 2.4.1, there was no restriction to a real refractive index. Therefore, the wave equation (2.63) also treats the case of a complex refractive index.

If we assume a medium with the complex refractive index (2.93), then the wavenumber is given by

$$\underline{\tilde{K}}(\Omega) = \frac{\Omega}{c_0} \left( 1 + \frac{1}{2} (\tilde{\chi}_r(\Omega) + j\tilde{\chi}_i(\Omega)) \right). \quad (2.97)$$

Since we introduced a complex wavenumber, we have to redefine the group velocity as the inverse derivative of the real part of the wavenumber with respect to frequency. At line center, we obtain

$$v_g^{-1} = \left. \frac{\partial K_r(\Omega)}{\partial \Omega} \right|_{\Omega_0} = \frac{1}{c_0} \left( 1 - \frac{\chi_0}{2} \frac{\Omega_0}{\Delta\Omega} \right). \quad (2.98)$$

Thus, for a narrow absorption line,  $\chi_0 > 0$  and  $\frac{\Omega_0}{\Delta\Omega} \gg 1$ , the absolute value of the group velocity can become much larger than the velocity of light in vacuum. The opposite is true for an amplifying medium,  $\chi_0 < 0$ . There is nothing wrong with this finding, since the group velocity only describes the motion of the peak of a Gaussian wave packet, which is not a causal wave packet. A causal wave packet is identical to zero for some earlier time  $t < t_0$ , in some region of space. A Gaussian wave packet fills the whole space at any time and can be reconstructed by a Taylor expansion at any time. Therefore, the motion of the peak of such a signal with a speed greater than the speed of light does not contradict special relativity.

The imaginary part in the wave vector (2.97) leads with  $K = \frac{\Omega}{c_0}$  to absorption

$$\alpha(\Omega) = -\frac{K}{2} \tilde{\chi}_i(\Omega). \quad (2.99)$$

In the envelope equation (2.62) for a wavepacket with carrier frequency  $\omega_0 = \Omega_0$  and wave number  $K_0 = \frac{\Omega_0}{c_0}$  the loss leads to a term of the form

$$\left. \frac{\partial \tilde{A}(z, \omega)}{\partial z} \right|_{(loss)} = -\alpha(\Omega_0 + \omega) \tilde{A}(z, \omega) = \frac{-\chi_0 K_0 / 2}{1 + \left(\frac{\omega}{\Delta\Omega}\right)^2} \tilde{A}(z, \omega). \quad (2.100)$$

In the time domain, we obtain up to second order in the inverse linewidth for  $\frac{\omega}{\Delta\Omega} \ll 1$

$$\left. \frac{\partial \underline{A}(z, t')}{\partial z} \right|_{(loss)} = -\frac{\chi_0 K_0}{2} \left( 1 + \frac{1}{\Delta\Omega^2} \frac{\partial^2}{\partial t'^2} \right) \underline{A}(z, t'), \quad (2.101)$$

which corresponds to a parabolic approximation of the line shape at line center, (Fig. 2.3). As we will see later, for an amplifying optical transition we obtain a similar equation. We only have to replace the loss by gain

$$\left. \frac{\partial \underline{A}(z, t')}{\partial z} \right|_{(gain)} = g \left( 1 + \frac{1}{\Omega_g^2} \frac{\partial^2}{\partial t^2} \right) \underline{A}(z, t'), \quad (2.102)$$

where  $g = -\frac{\chi_0 K_0}{2}$  is the peak gain at line center per unit length and  $\Omega_g$  is the HWHM linewidth of a transition providing gain.

## 2.5 Sellmeier Equation and Kramers-Kroenig Relations

The linear susceptibility is the frequency response or impulse response of a linear system to an applied electric field, see Eq.(2.40). For a real physical system this response is causal, and therefore real and imaginary parts obey Kramers-Kroenig Relations

$$\chi_r(\Omega) = \frac{2}{\pi} \int_0^{\infty} \frac{\omega \chi_i(\omega)}{\omega^2 - \Omega^2} d\omega = n^2(\Omega) - 1, \quad (2.103)$$

$$\chi_i(\Omega) = -\frac{2}{\pi} \int_0^{\infty} \frac{\Omega \chi_r(\omega)}{\omega^2 - \Omega^2} d\omega. \quad (2.104)$$

For optical media these relations have the consequence that the refractive index and absorption of a medium are not independent, which can often be exploited to compute the index from absorption data or the other way around. The Kramers-Kroenig Relations also give us a good understanding of the index variations in transparent media, which means the media are used in a frequency range far away from resonances. Then the imaginary part of the susceptibility related to absorption can be approximated by

$$\chi_i(\Omega) = \sum_i A_i \delta(\omega - \omega_i), \quad (2.105)$$

i.e. the absorption lines are approximated by delta-functions, and the Kramers-Kroenig relation results in the following Sellmeier Equation for the refractive

index

$$n^2(\Omega) = 1 + \sum_i A_i \frac{\omega_i}{\omega_i^2 - \Omega^2} = 1 + \sum_i a_i \frac{\lambda}{\lambda^2 - \lambda_i^2}. \quad (2.106)$$

This formula is very useful in fitting the refractive index of various media over a large frequency range with relatively few coefficients. For example Table 2.3 shows the Sellmeier coefficients for fused quartz and sapphire.

	Fused Quartz	Sapphire
$a_1$	0.6961663	1.023798
$a_2$	0.4079426	1.058364
$a_3$	0.8974794	5.280792
$\lambda_1^2$	$4.679148 \cdot 10^{-3}$	$3.77588 \cdot 10^{-3}$
$\lambda_2^2$	$1.3512063 \cdot 10^{-2}$	$1.22544 \cdot 10^{-2}$
$\lambda_3^2$	$0.9793400 \cdot 10^2$	$3.213616 \cdot 10^2$

Table 2.3: Table with Sellmeier coefficients for fused quartz and sapphire.

In general, each absorption line contributes a corresponding index change to the overall optical characteristics of a material, see Fig. 2.14.

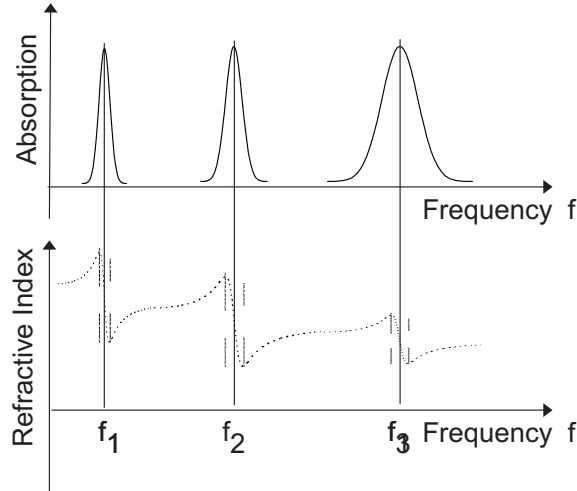


Figure 2.14: Each absorption line must contribute to an index change via the Kramers-Kronig relations.

## 2.5. SELLMEIER EQUATION AND KRAMERS-KROENIG RELATIONS 53

A typical situation for a material having resonances in the UV and IR, such as glass, is shown in Fig. 2.15. As Fig. 2.15 shows, due to the Lorentzian line shape, outside of an absorption line the refractive index is always decreasing as a function of wavelength. In the classical optics terminology, where transparent materials are used for refraction of light, for example in prisms, this behavior is called normal dispersion. The opposite behaviour, i.e. an increase of refractive index with wavelength that occurs within the absorption lines is called anomalous dispersion.

$$\text{Classical Optics} \quad \left\{ \begin{array}{l} \frac{dn}{d\lambda} < 0 : \text{normal dispersion (blue refracts more than red)} \\ \frac{dn}{d\lambda} > 0 : \text{anomalous dispersion} \end{array} \right.$$

As we have seen in the previous section, in ultrafast optics we are more concerned with the group velocity dispersion of the material  $k''$ , which is related to the second order derivative of the index,  $k'' \sim \frac{d^2n}{d\lambda^2}$ , as summarized in table 2.4

$$\text{Ultrafast Optics} \quad \left\{ \begin{array}{l} \frac{d^2n}{d\lambda^2} > 0 : \text{normal dispersion} \\ \text{short wavelengths slower than long wavelengths} \\ \frac{d^2n}{d\lambda^2} < 0 : \text{anomalous dispersion} \\ \text{short wavelengths faster than long wavelengths} \end{array} \right.$$

This behavior is also responsible for the mostly positive group delay dispersion, i.e. normal dispersion, over the transparency range of a material at the longwavelength side of an absorption line, and the mostly negative group delay dispersion, i.e. anomalous dispersion, when approaching a resonance from the short wavelength side. typical absorption and refractive index as a function of wavelength for media that are transparent in the visible, like glasses. Therefore, glasses with their typical absorption lines in the UV and IR show positive dispersion in the visible and change to negative dispersion in the IR with a zero dispersion wavelength somewhere between 1 and 2 micron wavelength.



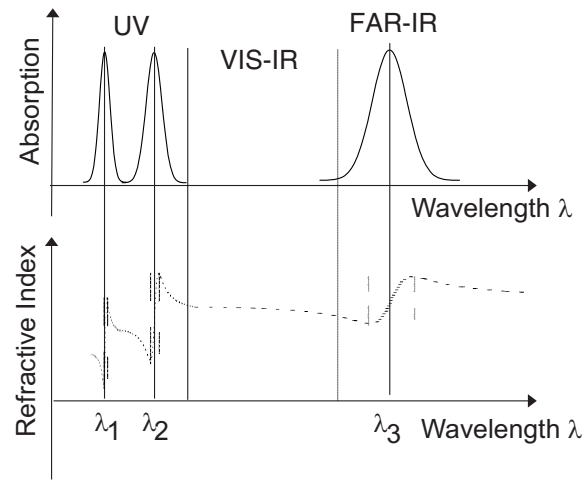


Figure 2.15: Typical distribution of absorption lines in a medium transparent in the visible.

Fig.2.16 shows the transparency range of some often used media.

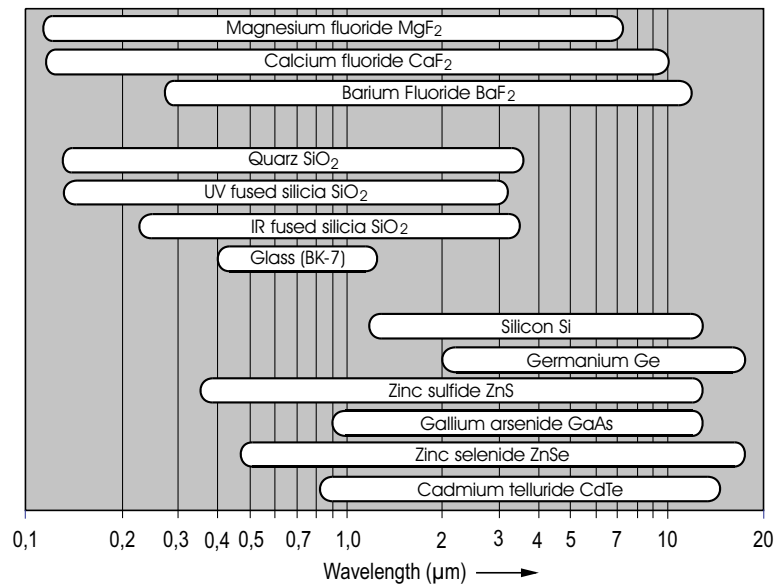


Figure 2.16: Transparency range of some materials according to Saleh and Teich, Photonics p. 175.

GVD and GDD are defined as the variation of the inverse group velocity or group delay as a function of frequency, see Eqs.(2.66) , i.e.

$$GVD = \left. \frac{d^2 k(\omega)}{d\omega^2} \right|_{\omega=0} = \left. \frac{d}{d\omega} \frac{1}{v_g(\omega)} \right|_{\omega=0} = \left. \frac{-1}{v_g^2(\omega)} \frac{dv_g(\omega)}{d\omega} \right|_{\omega=0} \quad (2.107)$$

$$GDD = \left. \frac{d^2 k(\omega)}{d\omega^2} \right|_{\omega=0} L = \left. \frac{d}{d\omega} \frac{L}{v_g(\omega)} \right|_{\omega=0} = \left. \frac{d}{d\omega} T_g(\omega) \right|_{\omega=0} \quad (2.108)$$

where  $T_g(\omega) = L/v_g(\omega)$  is the group delay of a wave packet with relative center frequency  $\omega$ . Often theses quantities need to be calculated from the refractive index given by the Sellmeier equation, i.e.  $n(\lambda)$ . The corresponding quantities are listed in Table 2.4. The computations are done by substituting the frequency with the wavelength.

Dispersion Characteristic	Definition	Comp. from $n(\lambda)$
medium wavelength: $\lambda_n$	$\frac{\lambda}{n}$	$\frac{\lambda}{n(\lambda)}$
medium wavenumber: $k_n$	$\frac{2\pi}{\lambda_n}$	$\frac{2\pi}{\lambda} n(\lambda)$
phase velocity: $v_p$	$\frac{\omega}{k}$	$\frac{c_0}{n(\lambda)}$
group velocity: $v_g$	$\frac{d\omega}{dk}; d\lambda = \frac{-\lambda^2}{2\pi c_0} d\omega$	$\frac{c_0}{n} \left(1 - \frac{\lambda}{n} \frac{dn}{d\lambda}\right)^{-1}$
group velocity dispersion: $GVD$	$\frac{d^2 k}{d\omega^2}$	$\frac{\lambda^3}{2\pi c_0^2} \frac{d^2 n}{d\lambda^2}$
group delay: $T_g = \frac{L}{v_g} = \frac{d\phi}{d\omega}$	$\frac{d\phi}{d\omega} = \frac{d(kL)}{d\omega}$	$\frac{n}{c_0} \left(1 - \frac{\lambda}{n} \frac{dn}{d\lambda}\right) L$
group delay dispersion: $GDD$	$\frac{dT_g}{d\omega} = \frac{d^2(kL)}{d\omega^2}$	$\frac{\lambda^3}{2\pi c_0^2} \frac{d^2 n}{d\lambda^2} L$

Table 2.4: Table with important dispersion characteristics and how to compute them from the wavelength dependent refractive index  $n(\lambda)$  using  $|d\omega| = 2\pi c_0/\lambda^2 d|\lambda|$ .

## 2.6 Summary

Starting from Maxwell's Equations in an isotropic linear medium, we found that there exist TEM-plane wave solutions, where the electric, magnetic and propagation vector of the wave build a right handed system. The magnitude of the electric and magnetic field vector are connected via the characteristic impedance of the medium or the refractive index. An often encountered expression for the refractive index in a medium or the dielectric susceptibility can be derived from the harmonic oscillator model for an electronic

transition in a medium. Lossy media can be treated by a complex refractive index. Causality of the response of the medium to an external field requires that the real part and imaginary part of the dielectric susceptibility fully fill Kramers-Kroenig relations. Optical pulses are electromagnetic wavepackets. The dynamics of optical pulses propagating through a linear medium is most easily treated in the frequency domain and are completely described by the complex wave vector or complex refractive index. Besides the group delay, the pulse may suffer dispersion and loss or gain which may depend on frequency.

# Bibliography

- [1] B.E.A. Saleh and M.C. Teich, "Fundamentals of Photonics," John Wiley and Sons, Inc., 1991.
- [2] H. A. Haus, "Fields and Waves in Optoelectronics", Prentice Hall 1984.



## Chapter 3

# Nonlinear Pulse Propagation

There are many nonlinear pulse propagation problems worthwhile of being considered in detail. A comprehensive discussion of various nonlinear pulse propagation phenomena can be found in [1]. In this chapter we discuss the nonlinear pulse dynamics due to the Kerr-effect which is most important for understanding pulse propagation problems in optical communications, short pulse generation and pulse compression.

### 3.1 The Optical Kerr-effect

In a homogeneous medium, which has an inversion symmertry at the molecular level, or in an isotropic medium, to lowest order, the refractive index of such a medium can only depend quadratically on the field, i.e. on the intensity [26]

$$n = n(\omega, |A|^2) \approx n_0(\omega) + n_{2,L}|A|^2. \quad (3.1)$$

Here, we assume, that the pulse envelope  $A$  is normalized such that  $|A|^2$  is the intensity of the pulse. This is the optical Kerr effect and  $n_{2,L}$  is called the intensity dependent refractive index coefficient. Note, the nonlinear index depends on the polarization of the field and without going further into details, we assume that we treat a linearly polarized electric field. For most transparent materials the intensity dependent refractive index is positive.

Material	Refractive index $n$	$n_{2,L}[cm^2/W]$
Sapphire ( $Al_2O_3$ )	1.76 @ 850 nm	$3 \cdot 10^{-16}$
Fused Quartz	1.45 @ 1064 nm	$2.46 \cdot 10^{-16}$
Glass (LG-760)	1.5 @ 1064 nm	$2.9 \cdot 10^{-16}$
YAG ( $Y_3Al_5O_{12}$ )	1.82 @ 1064 nm	$6.2 \cdot 10^{-16}$
YLF ( $LiYF_4$ ), $n_e$	1.47 @ 1047 nm	$1.72 \cdot 10^{-16}$
Si	3.3 @ 1550 nm	$4 \cdot 10^{-14}$

Table 3.1: Nonlinear refractive index coefficients for different materials. In the literature most often the electro-statitic unit system is in use. The conversion is  $n_{2,L}[cm^2/W] = 4.19 \cdot 10^{-3} n_{2,L}[esu]/n_0$

## 3.2 Self-Phase Modulation (SPM)

In a purely one dimensional propagation problem, the intensity dependent refractive index imposes an additional self-phase shift on the pulse envelope during propagation, which is proportional to the instantaneous intensity of the pulse

$$\frac{\partial A(z, t)}{\partial z} = -jk_0 n_{2,L} |A(z, t)|^2 A(z, t) = -j\delta |A(z, t)|^2 A(z, t). \quad (3.2)$$

where  $\delta = k_0 n_{2,L}$  is the self-phase modulation coefficient. Self-phase modulation (SPM) leads only to a phase shift in the time domain. Therefore, the intensity profile of the pulse does not change only the spectrum of the pulse changes, as discussed in the class on nonlinear optics. Figure (3.1) shows the spectrum of a Gaussian pulse subject to SPM during propagation (for  $\delta = 2$  and normalized units). New frequency components are generated by the nonlinear process via four wave mixing (FWM). If we look at the phase of the pulse during propagation due to self-phase modulation, see Fig. 3.2 (a), we find, that the pulse redistributes its energy, such that the low frequency contributions are in the front of the pulse and the high frequencies in the back of the pulse, similar to the case of normal dispersion.

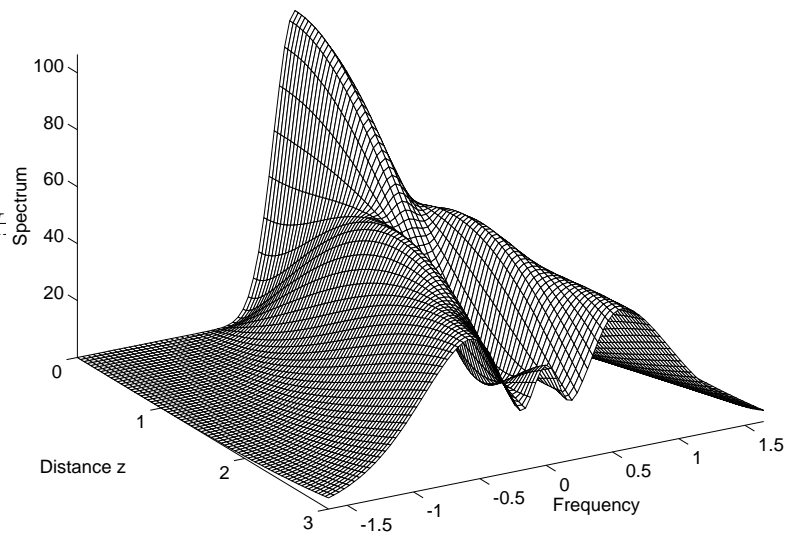


Figure 3.1: Spectrum  $|\hat{A}(z, \omega = 2\pi f)|^2$  of a Gaussian pulse subject to self-phase modulation.



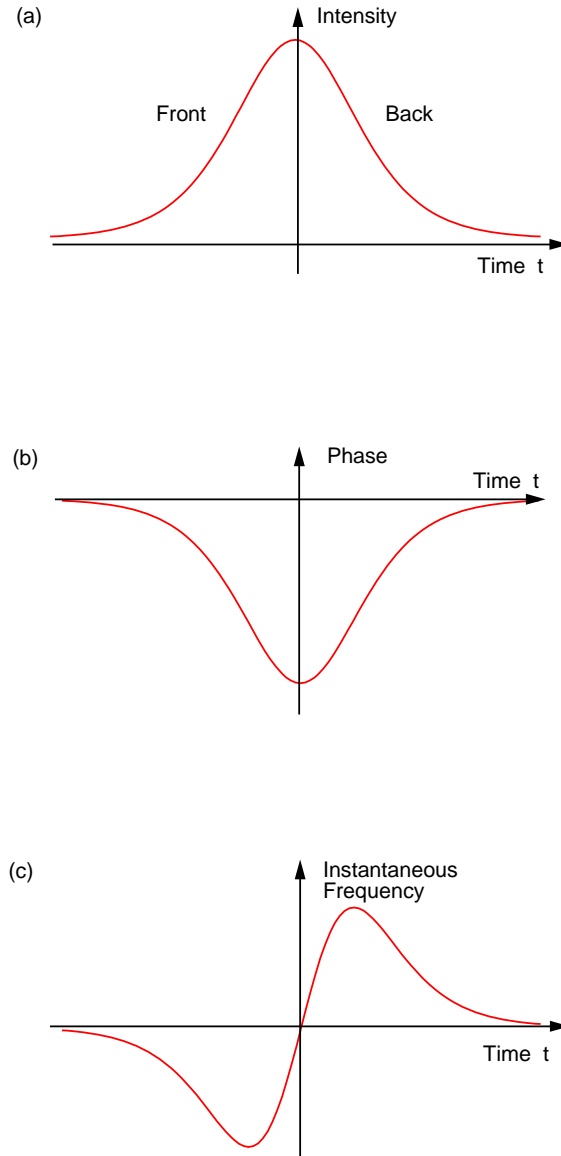


Figure 3.2: (a) Intensity, (b) phase and (c) instantaneous frequency of a Gaussian pulse during propagation through a medium with positive self-phase modulation.

### 3.3 The Nonlinear Schrödinger Equation

If both effects, dispersion and self-phase modulation, act simultaneously on the pulse, the field envelope obeys the equation

$$j\frac{\partial A(z,t)}{\partial z} = -D_2\frac{\partial^2 A}{\partial t^2} + \delta|A|^2A, \quad (3.3)$$

This equation is called the Nonlinear Schrödinger Equation (NLSE) - if we put the imaginary unit on the left hand side -, since it has the form of a Schrödinger Equation. Its called nonlinear, because the potential energy is derived from the square of the wave function itself. As we have seen from the discussion in the last sections, positive dispersion and positive self-phase modulation lead to a similar redistribution of the spectral components. This enhances the pulse spreading in time. However, if we have negative dispersion, i.e. a wave packet with high carrier frequency travels faster than a wave packet with a low carrier frequency, then, the high frequency wave packets generated by self-phase modulation in the front of the pulse have a chance to catch up with the pulse itself due to the negative dispersion. The opposite is the case for the low frequencies. This arrangement results in pulses that do not disperse any more, i.e. solitary waves. That negative dispersion is necessary to compensate the positive Kerr effect is also obvious from the NLSE (3.3). Because, for a positive Kerr effect, the potential energy in the NLSE is always negative. There are only bound solutions, i.e. bright solitary waves, if the kinetic energy term, i.e. the dispersion, has a negative sign,  $D_2 < 0$ .

#### 3.3.1 The Solitons of the NLSE

In the following, we study different solutions of the NLSE for the case of negative dispersion and positive self-phase modulation. We do not intend to give a full overview over the solution manifold of the NLSE in its full mathematical depth here, because it is not necessary for the following. This can be found in detail elsewhere [4, 10, 1, 11].

Without loss of generality, by normalization of the field amplitude  $A = \frac{A'}{\tau}\sqrt{\frac{2D_2}{\delta}}$ , the propagation distance  $z = z' \cdot \tau^2/D_2$ , and the time  $t = t' \cdot \tau$ , the NLSE (3.3) with negative dispersion can always be transformed into the

normalized form

$$j \frac{\partial A(z, t)}{\partial z} = \frac{\partial^2 A}{\partial t^2} + 2|A|^2 A \quad (3.4)$$

This is equivalent to set  $D_2 = -1$  and  $\delta = 2$ . For the numerical simulations, which are shown in the next chapters, we simulate the normalized eq.(3.4) and the axes are in normalized units of position and time.

### 3.3.2 The Fundamental Soliton

We look for a stationary wave function of the NLSE (3.3), such that its absolute square is a self-consistent potential. A potential of that kind is well known from Quantum Mechanics, the  $\text{sech}^2$ -Potential [3], and therefore the shape of the solitary pulse is a  $\text{sech}$

$$A_s(z, t) = A_0 \text{sech} \left( \frac{t}{\tau} \right) e^{-j\theta}, \quad (3.5)$$

where  $\theta$  is the nonlinear phase shift of the soliton

$$\theta = \frac{1}{2} \delta A_0^2 z. \quad (3.6)$$

The soliton phase shift is constant over the pulse with respect to time in contrast to the case of self-phase modulation only, where the phase shift is proportional to the instantaneous power. The balance between the nonlinear effects and the linear effects requires that the nonlinear phase shift is equal to the dispersive spreading of the pulse

$$\theta = \frac{|D_2|}{\tau^2} z. \quad (3.7)$$

Since the field amplitude  $A(z, t)$  is normalized, such that the absolute square is the intensity, the soliton energy fluence is given by

$$w = \int_{-\infty}^{\infty} |A_s(z, t)|^2 dt = 2A_0^2 \tau. \quad (3.8)$$

From eqs.(3.6) to (3.8), we obtain for constant pulse energy fluence, that the width of the soliton is proportional to the amount of negative dispersion

$$\tau = \frac{4|D_2|}{\delta w}. \quad (3.9)$$

Note, the pulse area for a fundamental soliton is only determined by the dispersion and the self-phase modulation coefficient

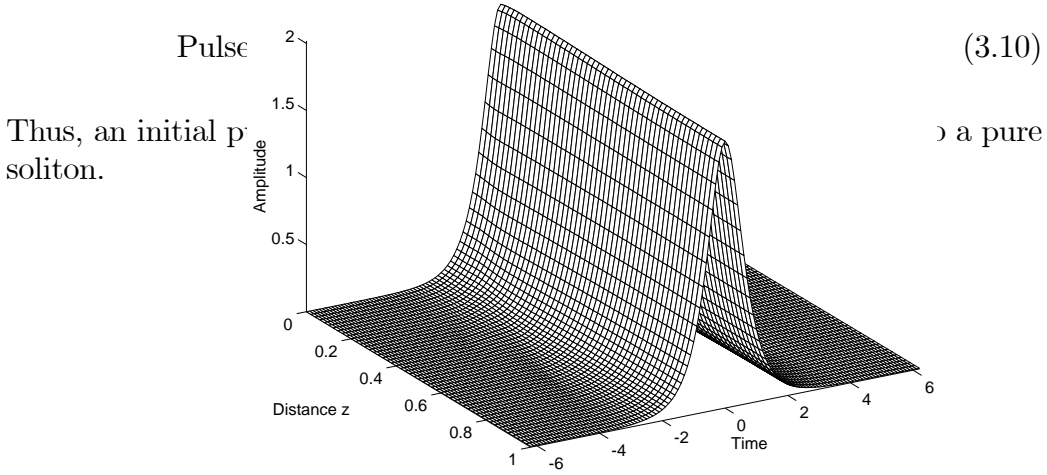


Figure 3.3: Propagation of a fundamental soliton.

Figure 3.3 shows the numerical solution of the NLSE for the fundamental soliton pulse. The distance, after which the soliton acquires a phase shift of  $\pi/4$ , is called the soliton period, for reasons, which will become clear in the next section.

Since the dispersion is constant over the frequency, i.e. the NLSE has no higher order dispersion, the center frequency of the soliton can be chosen arbitrarily. However, due to the dispersion, the group velocities of the solitons with different carrier frequencies will be different. One easily finds by a Gallilei tranformation to a moving frame, that the NLSE possesses the following general fundamental soliton solution

$$A_s(z, t) = A_0 \text{sech}(x(z, t)) e^{-j\theta(z, t)}, \quad (3.11)$$

with

$$x = \frac{1}{\tau}(t - 2|D_2|p_0z - t_0), \quad (3.12)$$

and a nonlinear phase shift

$$\theta = p_0(t - t_0) + |D_2| \left( \frac{1}{\tau^2} - p_0^2 \right) z + \theta_0. \quad (3.13)$$

Thus, the energy fluence  $w$  or amplitude  $A_0$ , the carrier frequency  $p_0$ , the phase  $\theta_0$  and the origin  $t_0$ , i.e. the timing of the fundamental soliton are not yet determined. Only the soliton area is fixed. The energy fluence and width are determined if one of them is specified, given a certain dispersion and SPM-coefficient.

### 3.3.3 Higher Order Solitons

The NLSE has constant dispersion, in our case anomalous (or negative) dispersion. That means the group velocity depends linearly on frequency. We assume, that two fundamental solitons are far apart from each other, so that they do not interact. Then this linear superposition is for all practical purposes another solution of the NSE. If we choose the carrier frequency of the soliton, starting at a later time, higher than the one of the soliton in front, the later soliton will catch up with the leading soliton due to the negative dispersion and the pulses will collide.

Figure 3.4 shows this situation. Obviously, the two pulses recover completely from the collision, i.e. the NSE has true soliton solutions. The solitons have particle like properties. A solution, composed of several fundamental solitons, is called a higher order soliton. If we look closer to Figure 3.4, we recognize, that the soliton at rest in the local time frame, and which follows the  $t = 0$  line without the collision, is somewhat pushed forward due to the collision. A detailed analysis of the collision would also show, that the phases of the solitons have changed [4]. The phase changes due to soliton collisions are used to built all optical switches [5], using backfolded Mach-Zehnder interferometers, which can be realized in a self-stabilized way by Sagnac fiber loops.

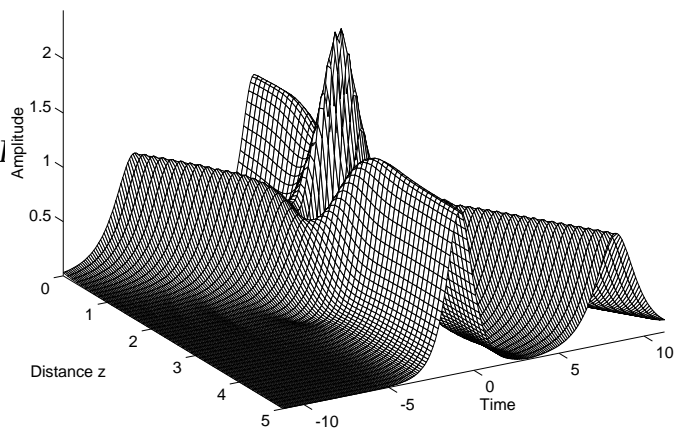


Figure 3.4: A soliton with high carrier frequency collides with a soliton of lower carrier frequency. After the collision both pulses recover completely.

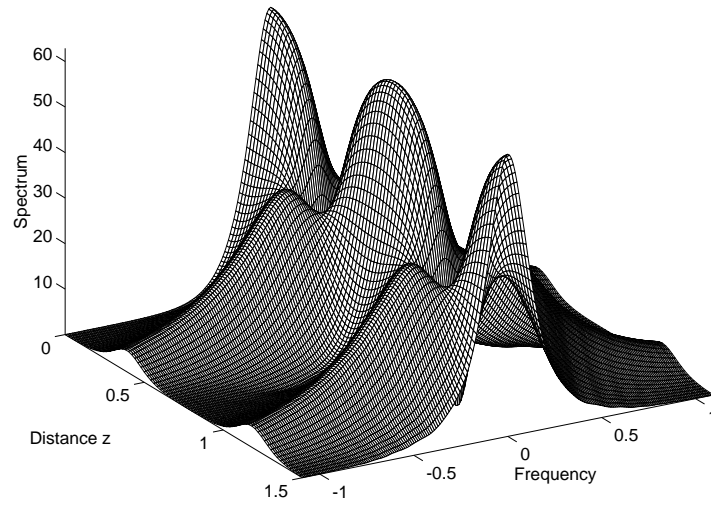
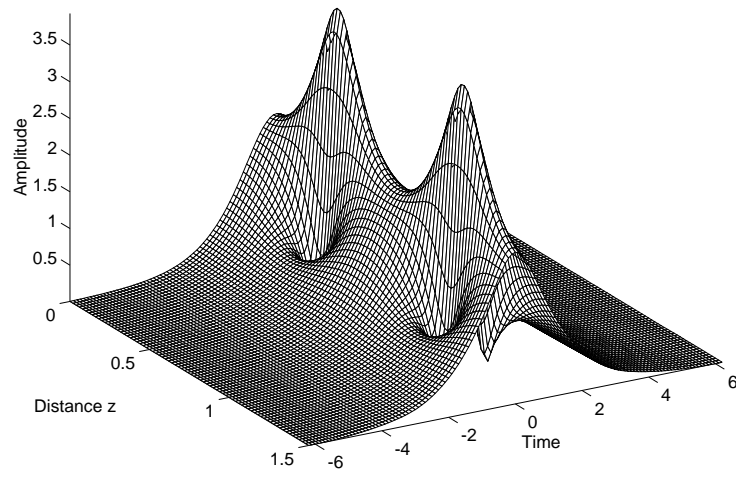


Figure 3.5: (a) Amplitude and, (b) Spectrum of a higher order soliton composed of two fundamental solitons with the same carrier frequency

The NLSE also shows higher order soliton solutions, that travel at the same speed, i.e. they possess the same carrier frequency, the so called breather solutions. Figures 3.5(a) and (b) show the amplitude and spectrum of such a higher order soliton solution, which has twice the area of the fundamental soliton. The simulation starts with a sech-pulse, that has twice the area of the fundamental soliton, shown in Fig. 3.3. Due to the interaction of the two solitons, the temporal shape and the spectrum exhibits a complicated but periodic behaviour. This period is the soliton period  $z = \pi/4$ , as mentioned above. As can be seen from Figures 3.5(a) and 3.5(b), the higher order soliton dynamics leads to an enormous pulse shortening after half of the soliton period. This process has been used by Mollenauer, to build the soliton laser [9]. In the soliton laser, the pulse compression, that occurs for a higher order soliton as shown in Fig. 3.5(a), is exploited for modelocking. Mollenauer pioneered soliton propagation in optical fibers [9], as proposed by Hasegawa and Tappert [8], with the soliton laser, which produced the first picosecond pulses at  $1.55 \mu\text{m}$ . A detailed account on the soliton laser is given by Haus [7].

So far, we have discussed the pure soliton solutions of the NLSE. But, what happens if one starts propagation with an input pulse that does not correspond to a fundamental or higher order soliton?

### 3.3.4 Inverse Scattering Theory

Obviously, the NLSE has solutions, which are composed of fundamental solitons. Thus, the solutions obey a certain superposition principle which is absolutely surprising for a nonlinear system. Of course, not arbitrary superpositions are possible as in a linear system. The deeper reason for the solution manifold of the NLSE can be found by studying its physical and mathematical properties. The mathematical basis for an analytic formulation of the solutions to the NLSE is the inverse scattering theory [12, 13, 4, 14]. It is a spectral transform method for solving integrable, nonlinear wave equations, similar to the Fourier transform for the solution of linear wave equations [15].



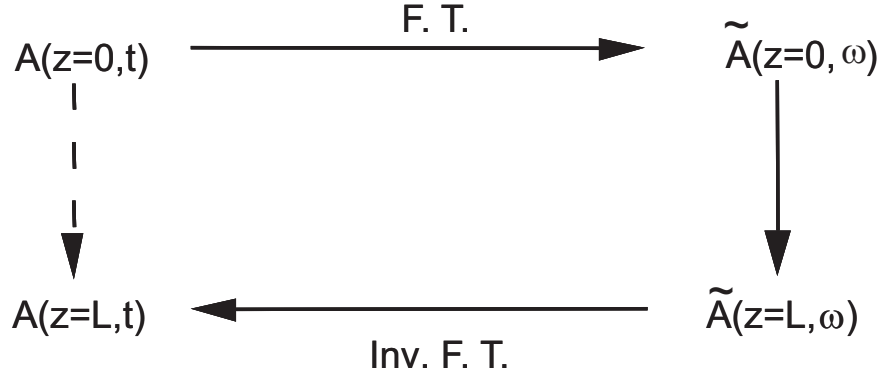


Figure 3.6: Fourier transform method for the solution of linear, time invariant partial differential equations.

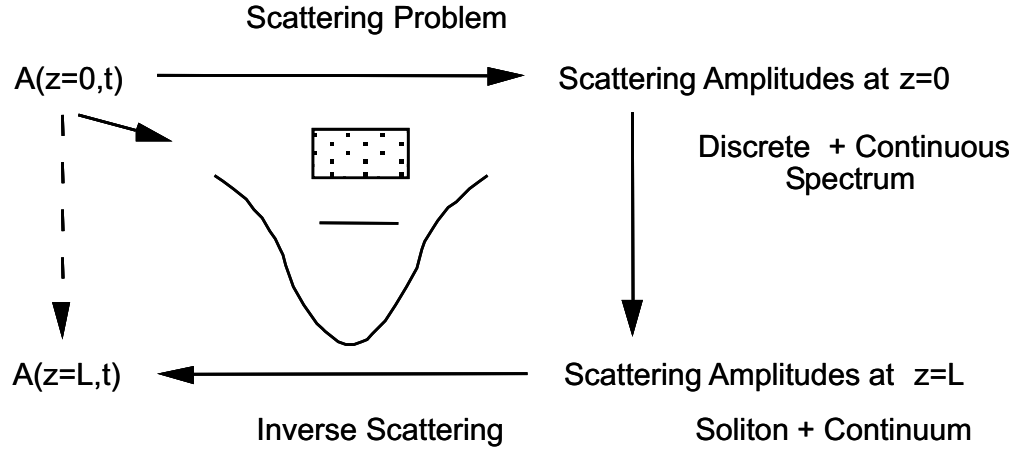


Figure 3.7: Schematic representation of the inverse scattering theory for the solution of integrable nonlinear partial differential equations.

Let's remember briefly, how to solve an initial value problem for a linear partial differential equation (p.d.e.), like eq.(2.63), that treats the case of a purely dispersive pulse propagation. The method is sketched in Fig. 3.6. We Fourier transform the initial pulse into the spectral domain, because, the exponential functions are eigensolutions of the differential operators with

constant coefficients. The right side of (2.63) is only composed of powers of the differential operator, therefore the exponentials are eigenfunctions of the complete right side. Thus, after Fourier transformation, the p.d.e. becomes a set of ordinary differential equations (o.d.e.), one for each partial wave. The excitation of each wave is given by the spectrum of the initial wave. The eigenvalues of the differential operator, that constitutes the right side of (2.63), is given by the dispersion relation,  $k(\omega)$ , up to the imaginary unit. The solution of the remaining o.d.e is then a simple exponential of the dispersion relation. Now, we have the spectrum of the propagated wave and by inverse Fourier transformation, i.e. we sum over all partial waves, we find the new temporal shape of the propagated pulse.

As in the case of the Fourier transform method for the solution of linear wave equations, the inverse scattering theory is again based on a spectral transform, (Fig.3.7). However, this transform depends now on the details of the wave equation and the initial conditions. This dependence leads to a modified superposition principle. As is shown in [11], one can formulate for many integrable nonlinear wave equations a related scattering problem like one does in Quantum Theory for the scattering of a particle at a potential well. However, the potential well is now determined by the solution of the wave equation. Thus, the initial potential is already given by the initial conditions. The stationary states of the scattering problem, which are the eigensolutions of the corresponding Hamiltonian, are the analog to the monochromatic complex oscillations, which are the eigenfunctions of the differential operator. The eigenvalues are the analog to the dispersion relation, and as in the case of the linear p.d.e's, the eigensolutions obey simple linear o.d.e's.

A given potential will have a certain number of bound states, that correspond to the discrete spectrum and a continuum of scattering states. The characteristic of the continuous eigenvalue spectrum is the reflection coefficient for waves scattered upon reflection at the potential. Thus, a certain potential, i.e. a certain initial condition, has a certain discrete spectrum and continuum with a corresponding reflection coefficient. From inverse scattering theory for quantum mechanical and electromagnetic scattering problems, we know, that the potential can be reconstructed from the scattering data, i.e. the reflection coefficient and the data for the discrete spectrum [14]. This is true for a very general class of scattering potentials. As one can almost guess now, the discrete eigenstates of the initial conditions will lead to soliton solutions. We have already studied the dynamics of some of these

soliton solutions above. The continuous spectrum will lead to a dispersive wave which is called the continuum. Thus, the most general solution of the NLSE, for given arbitrary initial conditions, is a superposition of a soliton, maybe a higher order soliton, and a continuum contribution.

The continuum will disperse during propagation, so that only the soliton is recognized after a while. Thus, the continuum becomes an asymptotically small contribution. The continuum contribution to the NLSE can be solved by the linear wave equation.

The basic idea is as simple as in solving a linear problem: the solution of the linear problem is a superposition of plane waves.

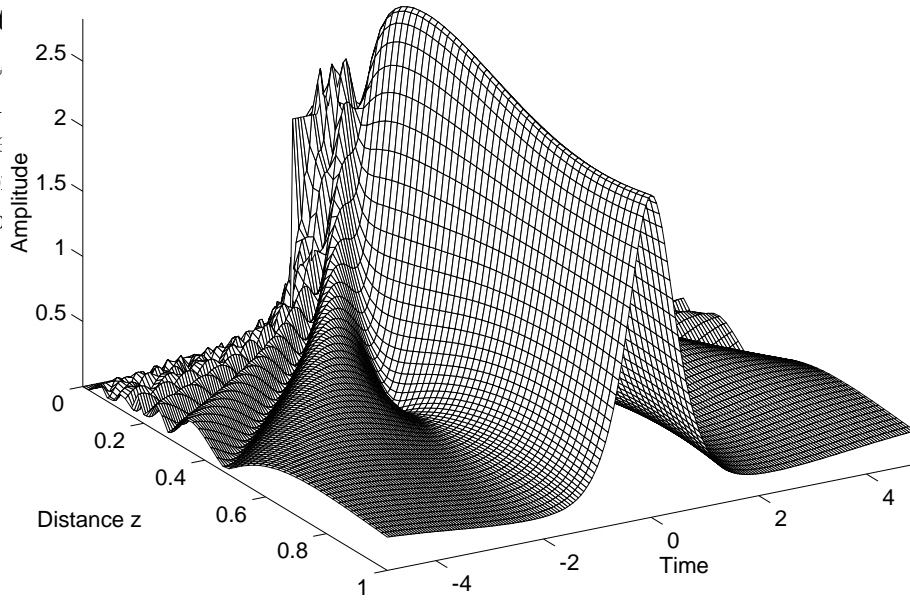


Figure 3.8: Solution of the NSE for an unchirped and rectangular shaped initial pulse.

To appreciate these properties of the solutions of the NLSE, we solve the NLSE for a rectangular shaped initial pulse. The result is shown in Fig. 3.8.

The scattering problem, that has to be solved for this initial condition, is the same as for a nonrelativistic particle in a rectangular potential box [31]. The depth of the potential is chosen small enough, so that it has only one bound state. Thus, we start with a wave composed of a fundamental soliton and continuum. It is easy to recognize the continuum contribution, i.e. the dispersive wave, that separates from the soliton during propagation. This solution illustrates, that soliton pulse shaping due to the presence of dispersion and self-phase modulation may have a strong impact on pulse generation [17]. When the dispersion and self-phase modulation are properly adjusted, soliton formation can lead to very clean, stable, and extremely short pulses in a modelocked laser.

### 3.4 Universality of the NLSE

Above, we derived the NSE in detail for the case of disperison and self-phase modulation. The input for the NLSE is surprisingly low, we only have to admitt the first nontrivial dispersive effect and the lowest order nonlinear effect that is possible in an isotropic and homogeneous medium like glass, gas or plasmas. Therefore, the NLSE and its properties are important for many other effects like self-focusing [18], Langmuir waves in plasma physics, and waves in proteine molecules [19]. Self-focusing will be treated in more detail later, because it is the basis for Kerr-Lens Mode Locking.

### 3.5 Soliton Perturbation Theory

From the previous discussion, we have full knowledge about the possible solutions of the NLSE that describes a special Hamiltonian system. However, the NLSE hardly describes a real physical system such as, for example, a real optical fiber in all its aspects [20, 21]. Indeed the NLSE itself, as we have seen during the derivation in the previous sections, is only an approximation to the complete wave equation. We approximated the dispersion relation by a parabola at the assumed carrier frequency of the soliton. Also the instantaneous Kerr effect described by an intensity dependent refractive index is only an approximation to the real  $\chi^{(3)}$ -nonlinearity of a Kerr-medium [22,

23]. Therefore, it is most important to study what happens to a soliton solution of the NLSE due to perturbing effects like higher order dispersion, finite response times of the nonlinearities, gain and the finite gain bandwidth of amplifiers, that compensate for the inevitable loss in a real system.

The investigation of solitons under perturbations is as old as the solitons itself. Many authors treat the perturbing effects in the scattering domain [24, 25]. Only recently, a perturbation theory on the basis of the linearized NLSE has been developed, which is much more illustrative than a formulation in the scattering amplitudes. This was first used by Haus [26] and rigorously formulated by Kaup [27]. In this section, we will present this approach as far as it is indispensable for the following.

A system, where the most important physical processes are dispersion and self-phase modulation, is described by the NLSE complimented with some perturbation term  $F$

$$\frac{\partial A(z, t)}{\partial z} = -j \left[ |D_2| \frac{\partial^2 A}{\partial t^2} + \delta |A|^2 A \right] + F(A, A^*, z). \quad (3.14)$$

In the following, we are interested what happens to a solution of the full equation (3.14) which is very close to a fundamental soliton, i.e.

$$A(z, t) = \left[ a\left(\frac{t}{\tau}\right) + \Delta A(z, t) \right] e^{-jk_s z}. \quad (3.15)$$

Here,  $a(x)$  is the fundamental soliton according to eq.(3.5)

$$a\left(\frac{t}{\tau}\right) = A_0 \operatorname{sech}\left(\frac{t}{\tau}\right), \quad (3.16)$$

and

$$k_s = \frac{1}{2} \delta A_0^2 \quad (3.17)$$

is the phase shift of the soliton per unit length, i.e. the soliton wave vector.

A deviation from the ideal soliton can arise either due to the additional driving term  $F$  on the right side or due to a deviation already present in the initial condition. We use the form (3.15) as an ansatz to solve the NSE to first order in the perturbation  $\Delta A$ , i.e. we linearize the NSE around the fundamental soliton and obtain for the perturbation

$$\begin{aligned} \frac{\partial \Delta A}{\partial z} = & -jk_s \left[ \left( \frac{\partial^2}{\partial x^2} - 1 \right) \Delta A + 2 \operatorname{sech}^2(x) (2\Delta A + \Delta A^*) \right] \\ & + F(A, A^*, z) e^{jk_s z}, \end{aligned} \quad (3.18)$$

where  $x = t/\tau$ . Due to the nonlinearity, the field is coupled to its complex conjugate. Thus, eq.(3.18) corresponds actually to two equations, one for the complex field amplitude and one for its complex conjugate. Note, we could also use the real and imaginary part of the complex field amplitude. Therefore, we introduce the vector notation

$$\Delta \mathbf{A} = \begin{pmatrix} \Delta A \\ \Delta A^* \end{pmatrix}. \quad (3.19)$$

We further introduce the normalized propagation distance  $z' = k_s z$  and the normalized time  $x = t/\tau$ . The linearized perturbed NLSE is then given by

$$\frac{\partial}{\partial z'} \Delta \mathbf{A} = \mathbf{L} \Delta \mathbf{A} + \frac{1}{k_s} \mathbf{F}(A, A^*, z) e^{jz'} \quad (3.20)$$

Here,  $\mathbf{L}$  is the operator which arises from the linearization of the NLSE

$$\mathbf{L} = -j\sigma_3 \left[ \left( \frac{\partial^2}{\partial x^2} - 1 \right) + 2 \operatorname{sech}^2(x)(2 + \sigma_1) \right], \quad (3.21)$$

where  $\sigma_i, i = 1, 2, 3$  are the Pauli matrices

$$\sigma_1 = \begin{pmatrix} 0 & 1 \\ 1 & 0 \end{pmatrix}, \sigma_2 = \begin{pmatrix} 0 & -j \\ j & 0 \end{pmatrix}, \sigma_3 = \begin{pmatrix} 1 & 0 \\ 0 & -1 \end{pmatrix}. \quad (3.22)$$

For a solution of the inhomogeneous equation (3.20), we need the eigenfunctions and the spectrum of the differential operator  $\mathbf{L}$ . We found in section 3.3.2, that the fundamental soliton has four degrees of freedom, four free parameters. This gives already four known eigensolutions and mainsolutions of the linearized NSE, respectively. They are determined by the derivatives of the general fundamental soliton solutions according to eqs.(3.11) to (3.13) with respect to free parameters. These eigenfunctions are

$$\mathbf{f}_w(x) = \frac{1}{w}(1 - x \tanh x) a(x) \begin{pmatrix} 1 \\ 1 \end{pmatrix}, \quad (3.23)$$

$$\mathbf{f}_\theta(x) = -j a(x) \begin{pmatrix} 1 \\ -1 \end{pmatrix}, \quad (3.24)$$

$$\mathbf{f}_p(x) = -j x \tau a(x) \begin{pmatrix} 1 \\ -1 \end{pmatrix}, \quad (3.25)$$

$$\mathbf{f}_t(x) = \frac{1}{\tau} \tanh(x) a(x) \begin{pmatrix} 1 \\ 1 \end{pmatrix}, \quad (3.26)$$

and they describe perturbations of the soliton energy, phase, carrier frequency and timing. One component of each of these vector functions is shown in Fig. 3.9.

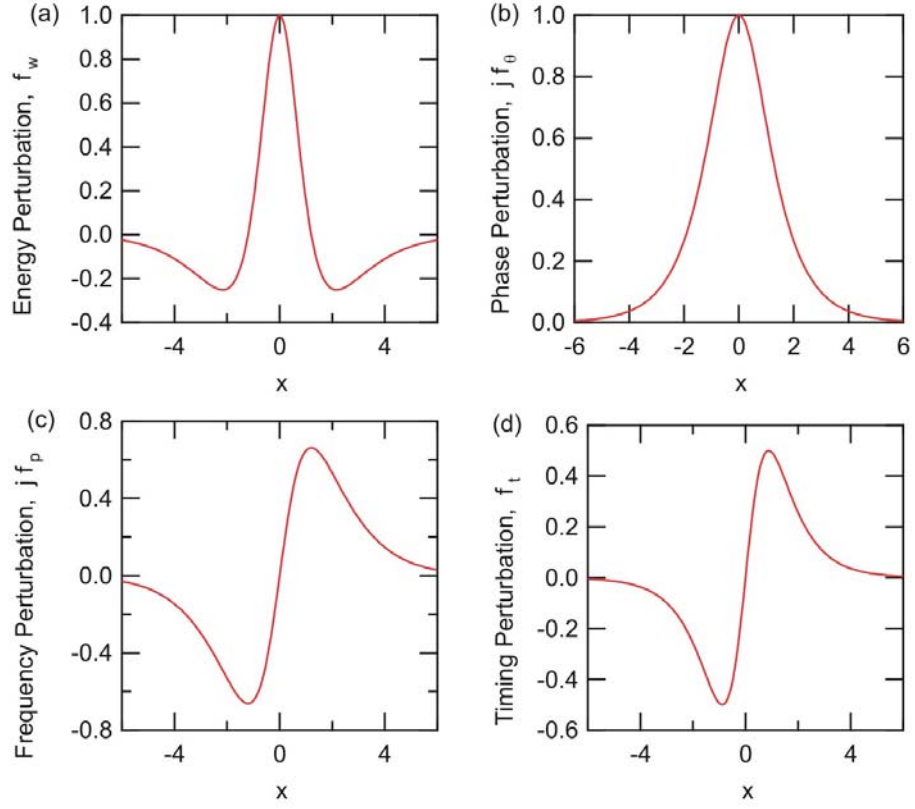


Figure 3.9: Perturbations in soliton amplitude (a), phase (b), frequency (c), and timing (d).

The action of the evolution operator of the linearized NSE on these soliton perturbations is

$$\mathbf{L}f_w = \frac{1}{w}f_\theta, \quad (3.27)$$

$$\mathbf{L}f_\theta = 0, \quad (3.28)$$

$$\mathbf{L}f_p = -2\tau^2 f_t, \quad (3.29)$$

$$\mathbf{L}f_t = 0. \quad (3.30)$$

Equations (3.27) and (3.29) indicate, that perturbations in energy and carrier frequency are converted to additional phase and timing fluctuations of the pulse due to SPM and GVD. This is the base for soliton squeezing in optical fibers [26]. The timing and phase perturbations can increase without bounds, because the system is autonomous, the origin for the Gordon-Haus effect, [28] and there is no phase reference in the system. The full continuous spectrum of the linearized NSE has been studied by Kaup [27] and is given by

$$\mathbf{L}\mathbf{f}_k = \lambda_k \mathbf{f}_k, \quad (3.31)$$

$$\lambda_k = j(k^2 + 1), \quad (3.32)$$

$$\mathbf{f}_k(x) = e^{-jkx} \begin{pmatrix} (k - j \tanh x)^2 \\ \text{sech}^2 x \end{pmatrix}, \quad (3.33)$$

and

$$\mathbf{L}\bar{\mathbf{f}}_k = \bar{\lambda}_k \bar{\mathbf{f}}_k, \quad (3.34)$$

$$\bar{\lambda}_k = -j(k^2 + 1), \quad (3.35)$$

$$\bar{\mathbf{f}}_k = \sigma_1 \mathbf{f}_k. \quad (3.36)$$

Our definition of the eigenfunctions is slightly different from Kaup [27], because we also define the inner product in the complex space as

$$\langle \mathbf{u} | \mathbf{v} \rangle = \frac{1}{2} \int_{-\infty}^{+\infty} \mathbf{u}^+(x) \mathbf{v}(x) dx. \quad (3.37)$$

Adopting this definition, the inner product of a vector with itself in the subspace where the second component is the complex conjugate of the first component is the energy of the signal, a physical quantity.

The operator  $\mathbf{L}$  is not self-adjoint with respect to this inner product. The physical origin for this mathematical property is, that the linearized system does not conserve energy due to the parametric pumping by the soliton. However, from (3.21) and (3.37), we can easily see that the adjoint operator is given by

$$\mathbf{L}^+ = -\sigma_3 \mathbf{L} \sigma_3, \quad (3.38)$$

and therefore, we obtain for the spectrum of the adjoint operator

$$\mathbf{L}^+ \mathbf{f}_k^{(+)} = \lambda_k^{(+)} \mathbf{f}_k^{(+)}, \quad (3.39)$$

$$\lambda_k^{(+)} = -j(k^2 + 1), \quad (3.40)$$

$$\mathbf{f}_k^{(+)} = \frac{1}{\pi(k^2 + 1)^2} \sigma_3 \mathbf{f}_k, \quad (3.41)$$



and

$$\mathbf{L}^+ \bar{\mathbf{f}}_k^{(+)} = \bar{\lambda}_k^{(+)} \bar{\mathbf{f}}_k^{(+)}, \quad (3.42)$$

$$\bar{\lambda}_k^{(+)} = j(k^2 + 1), \quad (3.43)$$

$$\bar{\mathbf{f}}_k^{(+)} = \frac{1}{\pi(k^2 + 1)^2} \sigma_3 \bar{\mathbf{f}}_k. \quad (3.44)$$

The eigenfunctions to  $\mathbf{L}$  and its adjoint are mutually orthogonal to each other, and they are already properly normalized

$$\begin{aligned} \langle \mathbf{f}_k^{(+)} | \mathbf{f}_{k'} \rangle &= \delta(k - k'), & \langle \bar{\mathbf{f}}_k^{(+)} | \bar{\mathbf{f}}_{k'} \rangle &= \delta(k - k') \\ \langle \bar{\mathbf{f}}_k^{(+)} | \mathbf{f}_{k'} \rangle &= \langle \mathbf{f}_k^{(+)} | \bar{\mathbf{f}}_{k'} \rangle = 0. \end{aligned}$$

This system, which describes the continuum excitations, is made complete by taking also into account the perturbations of the four degrees of freedom of the soliton (3.23) - (3.26) and their adjoints

$$\mathbf{f}_w^{(+)}(x) = j2\tau\sigma_3 \mathbf{f}_\theta(x) = 2\tau a(x) \begin{pmatrix} 1 \\ 1 \end{pmatrix}, \quad (3.45)$$

$$\begin{aligned} \mathbf{f}_\theta^{(+)}(x) &= -2j\tau\sigma_3 \mathbf{f}_w(x) \\ &= \frac{-2j\tau}{w} (1 - x \tanh x) a(x) \begin{pmatrix} 1 \\ -1 \end{pmatrix}, \end{aligned} \quad (3.46)$$

$$\mathbf{f}_p^{(+)}(x) = -\frac{2j\tau}{w} \sigma_3 \mathbf{f}_t(x) = \frac{2i}{w} \tanh x a(x) \begin{pmatrix} 1 \\ -1 \end{pmatrix}, \quad (3.47)$$

$$\mathbf{f}_t^{(+)}(x) = \frac{2j\tau}{w} \sigma_3 \mathbf{f}_p(x) = \frac{2\tau^2}{w} x a(x) \begin{pmatrix} 1 \\ 1 \end{pmatrix}. \quad (3.48)$$

Now, the unity can be decomposed into two projections, one onto the continuum and one onto the perturbation of the soliton variables [27]

$$\begin{aligned} \delta(x - x') &= \int_{-\infty}^{\infty} dk \left[ |\mathbf{f}_k \rangle \langle \mathbf{f}_k^{(+)}| + |\bar{\mathbf{f}}_k \rangle \langle \bar{\mathbf{f}}_k^{(+)}| \right] \\ &+ |\mathbf{f}_w \rangle \langle \mathbf{f}_w^{(+)}| + |\mathbf{f}_\theta \rangle \langle \mathbf{f}_\theta^{(+)}| \\ &+ |\mathbf{f}_p \rangle \langle \mathbf{f}_p^{(+)}| + |\mathbf{f}_t \rangle \langle \mathbf{f}_t^{(+)}|. \end{aligned} \quad (3.49)$$

Any deviation  $\Delta A$  can be decomposed into a contribution that leads to a soliton with a shift in the four soliton parameters and a continuum contribution  $a_c$

$$\Delta \mathbf{A}(z') = \Delta w(z') \mathbf{f}_w + \Delta \theta(z') \mathbf{f}_\theta + \Delta p(z') \mathbf{f}_p + \Delta t(z') \mathbf{f}_t + \mathbf{a}_c(z'). \quad (3.50)$$

Further, the continuum can be written as

$$\mathbf{a}_c = \int_{-\infty}^{\infty} dk [g(k)\mathbf{f}_k(x) + \bar{g}(k)\bar{\mathbf{f}}_k(x)]. \quad (3.51)$$

If we put the decomposition (3.50) into (3.20) we obtain

$$\begin{aligned} \frac{\partial \Delta w}{\partial z'} \mathbf{f}_w + \frac{\partial \Delta \theta}{\partial z'} \mathbf{f}_\theta + \frac{\partial \Delta p}{\partial z'} \mathbf{f}_p + \frac{\partial \Delta t}{\partial z'} \mathbf{f}_t + \frac{\partial}{\partial z'} \mathbf{a}_c = \\ \mathbf{L}(\Delta w(z')\mathbf{f}_w + \Delta p(z')\mathbf{f}_p + \mathbf{a}(z')_c) + \frac{1}{k_s} \mathbf{F}(A, A^*, z') e^{-iz'}. \end{aligned} \quad (3.52)$$

By building the scalar products (3.37) of this equation with the eigensolutions of the adjoint evolution operator (3.39) to (3.44) and using the eigenvalues (3.27) to (3.36), we find

$$\frac{\partial}{\partial z'} \Delta w = \frac{1}{k_s} \langle \mathbf{f}_w^{(+)} | \mathbf{F} e^{jz'} \rangle, \quad (3.53)$$

$$\frac{\partial}{\partial z'} \Delta \theta = \frac{\Delta w}{w} + \frac{1}{k_s} \langle \mathbf{f}_\theta^{(+)} | \mathbf{F} e^{jz'} \rangle, \quad (3.54)$$

$$\frac{\partial}{\partial z'} \Delta p = \frac{1}{k_s} \langle \mathbf{f}_p^{(+)} | \mathbf{F} e^{jz'} \rangle, \quad (3.55)$$

$$\frac{\partial}{\partial z'} \Delta t = 2\tau \Delta p + \frac{1}{k_s} \langle \mathbf{f}_t^{(+)} | \mathbf{F} e^{jz'} \rangle, \quad (3.56)$$

$$\frac{\partial}{\partial z'} g(k) = j(1 + k^2)g(k) + \frac{1}{k_s} \langle \mathbf{f}_k^{(+)} | \mathbf{F}(A, A^*, z') e^{jz'} \rangle. \quad (3.57)$$

Note, that the continuum  $\mathbf{a}_c$  has to be in the subspace defined by

$$\sigma_1 \mathbf{a}_c = \mathbf{a}_c^*. \quad (3.58)$$

The spectra of the continuum  $g(k)$  and  $\bar{g}(k)$  are related by

$$\bar{g}(k) = g(-k)^*. \quad (3.59)$$

Then, we can directly compute the continuum from its spectrum using (3.33), (3.51) and (3.58)

$$a_c = -\frac{\partial^2 G(x)}{\partial x^2} + 2 \tanh(x) \frac{\partial G(x)}{\partial x} - \tanh^2(x) G(x) + G^*(x) \operatorname{sech}^2(x), \quad (3.60)$$

where  $G(x)$  is, up to the phase factor  $e^{iz'}$ , Gordon's associated function [32]. It is the inverse Fourier transform of the spectrum

$$G(x) = \int_{-\infty}^{\infty} g(k) e^{ikx} dk. \quad (3.61)$$

Since  $g(k)$  obeys eq.(3.57), Gordon's associated function obeys a pure dispersive equation in the absence of a driving term  $F$

$$\frac{\partial G(z', x)}{\partial z'} = -j \left( 1 + \frac{\partial^2}{\partial x^2} \right) G(z', x). \quad (3.62)$$

It is instructive to look at the spectrum of the continuum when only one continuum mode with normalized frequency  $k_0$  is present, i.e.  $g(k) = \delta(k - k_0)$ . Then according to eqs. (3.60) and (3.61) we have

$$a_{c,k}(x) = [k_0^2 - 2jk_0 \tanh(x) - 1] e^{-jk_0 x} + 2\text{sech}^2(x) \cos(x). \quad (3.63)$$

The spectrum of this continuum contribution is

$$\begin{aligned} \tilde{a}_{c,k}(\omega) = & 2\pi(k_0^2 - 1)\delta(\omega - k_0) + 2k_0 P.V. \left( \frac{2}{\omega - k_0} + \frac{\pi}{\sinh\left(\frac{\pi}{2}(\omega - k_0)\right)} \right) \\ & + \pi \frac{\omega - k_0}{\sinh\left(\frac{\pi}{2}(\omega - k_0)\right)} + \pi \frac{\omega + k_0}{\sinh\left(\frac{\pi}{2}(\omega + k_0)\right)}. \end{aligned} \quad (3.64)$$

### 3.6 Soliton Instabilities by Periodic Perturbations

Periodic perturbations of solitons are important for understanding ultrashort pulse lasers as well as long distance optical communication systems [29, 30]. Along a long distance transmission system, the pulses have to be periodically amplified. In a mode-locked laser system, most often the nonlinearity, dispersion and gain occur in a lumped manner. The solitons propagating in these systems are only average solitons, which propagate through discrete components in a periodic fashion, as we will see later.

The effect of this periodic perturbations can be modelled by an additional term  $F$  in the perturbed NLSE according to Eq.(3.14)

$$F(A, A^*, z) = \xi \sum_{n=-\infty}^{\infty} \delta(z - nz_A) A(z, t). \quad (3.65)$$

The periodic kicking of the soliton leads to shedding of energy into continuum modes according to Eq.(3.57)

$$\frac{\partial}{\partial z}g(k) = jk_s(1+k^2)g(k) + \langle \mathbf{f}_k^{(+)} | \mathbf{F}(A, A^*, z) e^{jk_s z} \rangle. \quad (3.66)$$

$$\langle \mathbf{f}_k^{(+)} | \mathbf{F}(A, A^*, z) e^{jk_s z} \rangle = \xi \sum_{n=-\infty}^{\infty} \delta(z - nz_A) \frac{1}{2}. \quad (3.67)$$

$$\begin{aligned} & \int_{-\infty}^{+\infty} \frac{1}{\pi(k^2+1)^2} e^{jkx} \begin{pmatrix} (k + j \tanh x)^2 \\ -\text{sech}^2 x \end{pmatrix} \cdot \begin{pmatrix} 1 \\ 1 \end{pmatrix} A_0 \text{sech} x \, dx \\ &= \xi \sum_{n=-\infty}^{\infty} \delta(z - nz_A) \cdot \\ & \int_{-\infty}^{+\infty} \frac{A_0}{2\pi(k^2+1)^2} e^{jkx} (k^2 + 2jk \tanh x - 1) \cdot \text{sech} x \, dx \end{aligned} \quad (3.68)$$

Note,  $\frac{d}{dx} \text{sech} x = -\text{sech} x \tanh x$ , and therefore after partial integration we obtain

$$\begin{aligned} & \langle \mathbf{f}_k^{(+)} | \mathbf{F}(A, A^*, z) e^{jk_s z} \rangle = -\xi \sum_{n=-\infty}^{\infty} \delta(z - nz_A) \cdot \\ & \int_{-\infty}^{+\infty} \frac{A_0}{2\pi(k^2+1)} e^{jkx} \cdot \text{sech} x \, dx \\ &= -\xi \sum_{n=-\infty}^{\infty} \delta(z - nz_A) \frac{A_0}{4(k^2+1)} \text{sech} \left( \frac{\pi k}{2} \right). \end{aligned} \quad (3.69)$$

Using  $\sum_{n=-\infty}^{\infty} \delta(z - nz_A) = \frac{1}{z_A} \sum_{m=-\infty}^{\infty} e^{jm \frac{2\pi}{z_A} z}$  we obtain

$$\frac{\partial}{\partial z}g(k) = jk_s(1+k^2)g(k) - \frac{\xi}{z_A} \sum_{m=-\infty}^{\infty} e^{jm \frac{2\pi}{z_A} z} \frac{A_0}{4(k^2+1)} \text{sech} \left( \frac{\pi k}{2} \right). \quad (3.70)$$

Eq.(3.70) is a linear differential equation with constant coefficients for the continuum amplitudes  $g(k)$ , which can be solved by variation of constants with the ansatz

$$g(k, z) = C(k, z) e^{jk_s(1+k^2)z}, \quad (3.71)$$

and initial conditions  $C(z = 0) = 0$ , we obtain

$$\frac{\partial}{\partial z} C(k, z) = -\frac{\xi}{z_A} \sum_{m=-\infty}^{\infty} \frac{A_0}{4(k^2 + 1)} \operatorname{sech}\left(\frac{\pi k}{2}\right) e^{-j\left(k_s(1+k^2) - m\frac{2\pi}{z_A}z\right)}, \quad (3.72)$$

or

$$\begin{aligned} C(k, z) &= -\frac{\xi}{z_A} \frac{A_0}{4(k^2 + 1)} \operatorname{sech}\left(\frac{\pi k}{2}\right) \cdot \sum_{m=-\infty}^{\infty} \int_0^z e^{j(-k_s(1+k^2) + m\frac{2\pi}{z_A})z} dz \\ C(k, z) &= -\frac{\xi}{z_A} \frac{A_0}{4(k^2 + 1)} \operatorname{sech}\left(\frac{\pi k}{2}\right) \cdot \\ &\quad \sum_{m=-\infty}^{\infty} \frac{e^{j(-k_s(1+k^2) + m\frac{2\pi}{z_A})z} - 1}{m\frac{2\pi}{z_A} - k_s(1 + k^2)}. \end{aligned} \quad (3.73)$$

There is a resonant denominator, which blows up at certain normalized frequencies  $k_m$  for  $z \rightarrow \infty$ . Those frequencies are given by

$$m\frac{2\pi}{z_A} - k_s(1 + k_m^2) = 0 \quad (3.74)$$

$$\text{or} \quad k_m = \pm \sqrt{\frac{m\frac{2\pi}{z_A}}{k_s} - 1}. \quad (3.75)$$

Removing the normalization by setting  $k = \omega\tau$ ,  $k_s = |D_2|/\tau^2$  and introducing the nonlinear phase shift of the soliton acquired over one periode of the perturbation  $\phi_0 = k_s z_A$ , we obtain a handy formula for the location of the resonant sidebands

$$\omega_m = \pm \frac{1}{\tau} \sqrt{\frac{2m\pi}{\phi_0} - 1}, \quad (3.76)$$

and the coefficients

$$\begin{aligned} C(\omega, z) &= -j \frac{\xi}{z_A} \frac{A_0}{4((\omega\tau)^2 + 1)} \operatorname{sech}\left(\frac{\pi\omega\tau}{2}\right) \\ &\quad \cdot \sum_{m=-\infty}^{\infty} \frac{e^{j(-k_s(1+(\omega\tau)^2) + m\frac{2\pi}{z_A})z} - 1}{2\pi m - \phi_0(1 + (\omega\tau)^2)}. \end{aligned} \quad (3.77)$$

The coefficients stay bounded for frequencies not equal to the resonant condition and they grow linearly with propagation distance  $z$  at resonance, which

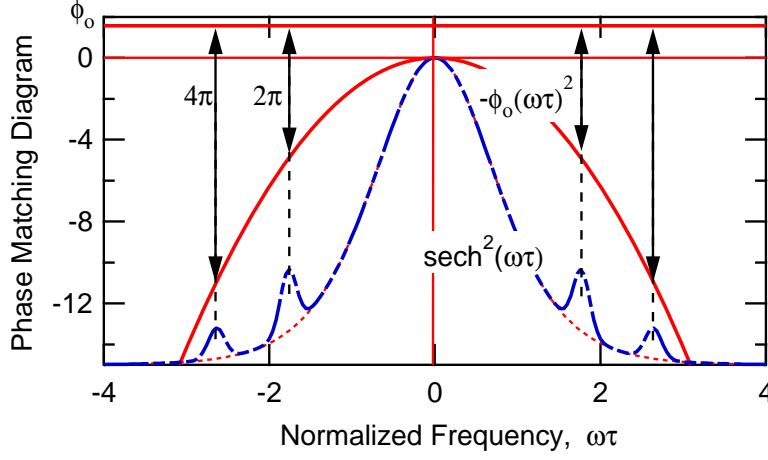


Figure 3.10: Phasematching between soliton and continuum due to periodic perturbations leads to resonant sideband generation. The case shown is for  $\phi_0 = \pi/2$ .

leads to a destruction of the pulse. To stabilize the soliton against this growth of resonant sidebands, the resonant frequencies have to stay outside the spectrum of the soliton, see Fig. 3.10, which feeds the continuum, i.e.  $\omega_m \gg \frac{1}{\tau}$ . This condition is only fulfilled if  $\phi_0 \ll \pi/4$ . This condition requires that the soliton period is much longer than the period of the perturbation. As an example Fig. 3.10 shows the resonant sidebands observed in a fiber laser. For optical communication systems this condition requires that the soliton energy has to be kept small enough, so that the soliton period is much longer than the distance between amplifiers, which constitute periodic perturbations to the soliton. These sidebands are often called Kelly-Sidebands, according to the person who first described its origin properly [29].

To illustrate its importance we discuss the spectrum observed from the long cavity Ti:sapphire laser system illustrated in Fig. 3.11 and described in full detail in [36]. Due to the low repetition rate, a rather large pulse energy builds up in the cavity, which leads to a large nonlinear phase shift per roundtrip. Figure 3.12 shows the spectrum of the output from the laser. The Kelly sidebands are clearly visible. It is this kind of instability, which limits further increase in pulse energy from these systems operating in the soliton pulse shaping regime. Energy is drained from the main pulse into

the sidebands, which grow at the expense of the pulse. At some point the pulse shaping becomes unstable because of conditions to be discussed in later chapters.

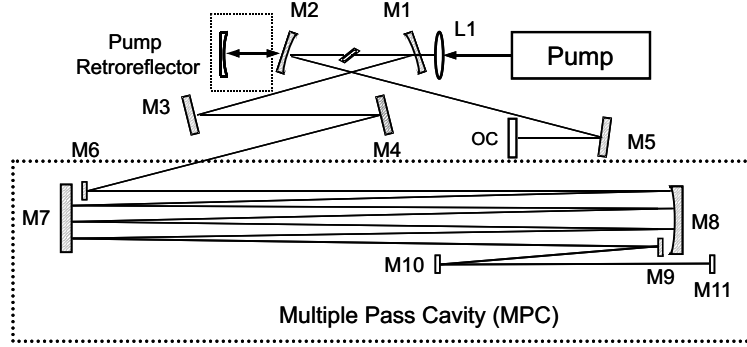


Figure 3.11: Schematic layout of a high pulse energy laser cavity. All shaded mirrors are (Double-chirped mirrors) DCMs. The standard 100 MHz cavity with arms of 45 cm and 95 cm extends from the OC to M6 for the short and long arms respectively. The multiple pass cavity (MPC) is enclosed in the dotted box. The pump source is a frequency doubled Nd:Vanadate that produces up to 10W at 532 nm [36].

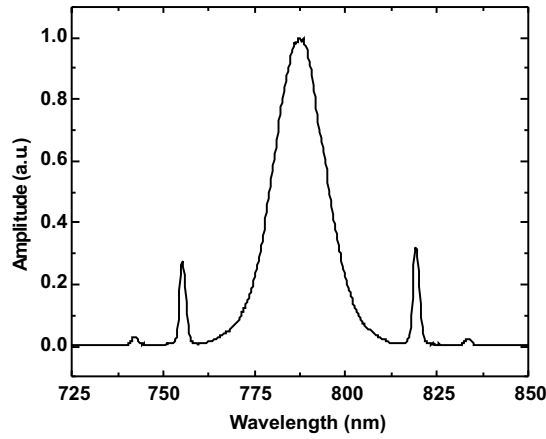


Figure 3.12: Measured modelocked spectrum with a 16.5 nm FWHM centered at 788 nm

## 3.7 Pulse Compression

So far we have discussed propagation of a pulse in negative dispersive media and positive self-phase modulation. Then for large enough pulse energy a soliton can form, because the low and high frequency components generated by SPM in the front and the back of the pulse are slow and fast, and therefore, slow down or catch up to stay together with the generating pulse. What happens if the dispersion is positive? Clearly, the low and high frequency components generated by SPM in the front and back of the pulse are fast and slow and move away from the pulse in a continuous fashion. This leads to highly chirped pulse, but the chirp is mostly linear. Thus the pulse can be compressed after the nonlinear propagation by sending it through a dispersive medium or prism pair or grating pair generating the corresponding negative chirp. In that way, pulses can be compressed by large factors of 3 to 20. This pulse compression process can be formulated in a more general way.

### 3.7.1 General Pulse Compression Scheme

The general scheme for pulse compression of optical pulses was independently proposed by Gires and Tournois in 1964 [37] and Giordmaine *et al.* in 1968 [38]. The input pulse is first spectrally broadened by a phase modulator. The phase over the generated spectrum is hopefully in a form that can be conveniently removed afterwards, i.e. all spectral components can be rephased to generate a short as possible pulse in the time domain. To compress femtosecond pulses an ultrafast phase modulator has to be used, that is the pulse has to modulate its phase itself by self-phase modulation. In 1969 Fisher *et al.* [39] proposed that picosecond pulses can be compressed to femtosecond duration using the large positive chirp produced around the peak of a short pulse by SPM in an optical Kerr liquid. In the same year Laubereau [40] used several cells containing CS<sub>2</sub> and a pair of diffraction gratings to compress, by approximately ten times, 20-ps pulses generated by a mode-locked Nd:glass laser.

As discussed in section 3.2, the optical Kerr effect in a medium gives rise to an intensity dependent change of the refractive index  $\Delta n = n_{2,L}I(t)$ , where  $n_{2,L}$  is the nonlinear-index coefficient and  $I(t)$  is the optical intensity. The self-induced intensity-dependent nonlinear phase shift experienced by an optical field during its propagation in a Kerr medium of length  $\ell$  is given by  $\Delta\phi(t) = -(\omega_0/c)n_2I(t)\ell$  where  $\omega_0$  is the carrier frequency of the



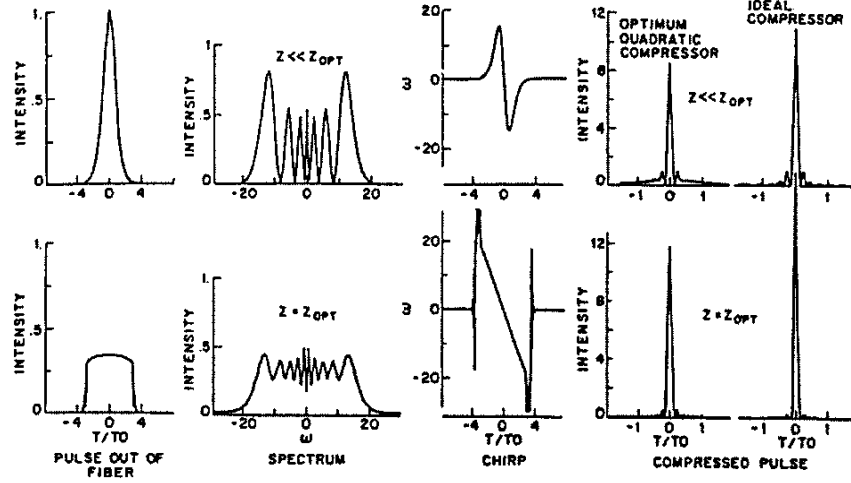


Figure 3.13: Intensity profile, spectrum, instantaneous frequency, optimum quadratic compression and ideal compression for two cases: top row for a short fiber, i.e. high nonlinearity and low dispersion; bottom row optimum nonlinearity and dispersion.[41]

pulse. The induced frequency sweep over the pulse can be calculated from  $\Delta\omega = d\Delta\phi/dt$ , see Fig. 3.13. Around the central part of the pulse, where most of the energy is concentrated, the phase is parabolic, leading to an approximately linear chirp in frequency. The region with linear chirp can be enlarged in the presence of positive dispersion in a Kerr medium of the same sign [41]. To compress the spectrally broadened and chirped pulse, a dispersive delay line can be used, characterized by a nearly linear group delay  $T_g(\omega)$ . Or if the chirp generated over the newly generated spectrum is nonlinear this chirp needs to be removed by a correspondingly nonlinear group delay  $T_g(\omega)$ . Figure 3.13 shows that in the case SPM and positive GDD a smoother spectrum with more linear chirp is created and therefore the final compressed pulse is of higher quality, i.e. a higher percentage of the total pulse energy is really concentrated in the short pulse and not in a large uncompressed pulse pedestal.

For a beam propagating in a homogenous medium, unfortunately the nonlinear refractive index does not only lead to a temporal phase modulation but also to a spatial phase modulation, which leads to self-focusing or defocus-

ing and small-scale instabilities [42]. Therefore, a fundamental requirement for pulse compression is that the Kerr effect is provided by a guiding non-linear medium so that a spatially uniform spectral broadening is obtained. In 1974 Ippen *et al.* reported the first measurement of SPM in the absence of self-trapping and self-focusing by using a guiding multimode optical fiber filled with liquid CS<sub>2</sub> [43]. In 1978 Stolen and Lin reported measurements of SPM in single-mode silica core fibers [44]. The important advantage of the single-mode fiber is that the phase modulation can be imposed over the entire transverse profile of the beam, thus removing the problem of unmodulated light in the wings of the beam [43]. In 1981 Nakatsuka *et al.* [41] performed the first pulse compression experiment using fibers as a Kerr medium in the positive dispersion region.

### 3.7.2 Spectral Broadening with Guided Modes

The electric field of a guided mode can be written as [51]:

$$E(\mathbf{r}, \omega) = A(z, \omega)F(x, y) \exp[i\beta(\omega)z] \quad (3.78)$$

where  $A(z, \omega)$  is the mode-amplitude for a given frequency component,  $F(x, y)$  is the mode-transverse field distribution and  $\beta(\omega)$  is the mode-propagation constant. The propagation equation for the guided field splits into two equations for amplitude  $A(z, \omega)$  and field pattern  $F(x, y)$ . In first order perturbation theory a perturbation  $\Delta n = \bar{n}_2|E|^2$  of the refractive index, which is much smaller than the index step that defines the mode, does not change the modal distribution  $F(x, y)$ , while the mode propagation constant  $\bar{\beta}(\omega)$  can be written as  $\bar{\beta}(\omega) = \beta(\omega) + \Delta\beta$ , where the perturbation  $\Delta\beta$  is given by

$$\Delta\beta = \frac{(\omega_0/c) \int \int \Delta n |F(x, y)|^2 dx dy}{\int \int |F(x, y)|^2 dx dy}. \quad (3.79)$$

As shown by Eq.(3.79), the perturbation  $\Delta\beta$ , which includes the effect due to the fiber nonlinearity, is related to a spatial average on the fiber transverse section of the perturbation  $\Delta n$ . In this way, spatially uniform SPM is realized.

Using regular single mode fibers and prism-grating compressors, pulses as short as 6 fs at 620 nm were obtained in 1987 from 50-fs pulses generated by a colliding-pulse mode-locking dye laser [45] see Figure 3.14. More recently, 13-fs pulses from a cavity-dumped Ti:sapphire laser were compressed to 4.5

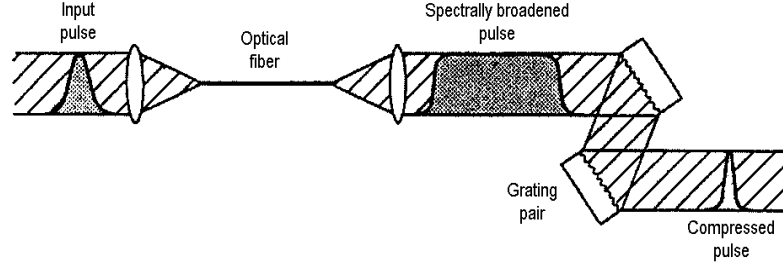


Figure 3.14: Fiber-grating pulse compressor to generate femtosecond pulses [52]

fs with the same technique using a compressor consisting of a quartz  $45^\circ$ -prism pair, broadband chirped mirrors and thin-film Gires-Tournois dielectric interferometers [46, 53]. The use of a single-mode optical fiber limits the pulse energy to a few nanojoule.

In 1996, using a phase modulator consisting of a hollow fiber (leaky waveguide) filled with noble gas, a powerful pulse compression technique has been introduced, which handles high-energy pulses [47]. The implementation of the hollow-fiber compression technique using 20-fs seed pulses from a Ti:sapphire system and chirped-mirrors that form a dispersive delay line has led to the generation of pulses with duration down to 4.5 fs [48] and energy up to 0.55 mJ [49]. This technique presents the advantages of a guiding element with a large-diameter mode and of a fast nonlinear medium with high damage threshold.

The possibility to take advantage of the ultrabroadband spectrum which can be generated by the phase modulation process, is strictly related to the development of dispersive delay lines capable of controlling the frequency-dependent group delay over such bandwidth.

### 3.7.3 Dispersion Compensation Techniques

The pulse frequency sweep (chirp) imposed by the phase modulation is approximately linear near the peak of the pulse, where most of the energy is concentrated. In the presence of dispersion in the phase modulator the chirp becomes linear over almost the whole pulse. Therefore, optimum temporal compression requires a group delay,  $T_{g,comp}(\omega) = \partial\phi/\partial\omega$ , characterized by a

nearly linear dependence on frequency in the dispersive delay line. Since in the case of SPM the nonlinear index  $n_2$  is generally positive far from resonance, a negative group delay dispersion ( $GDD = \partial T_g / \partial \omega$ ) is required in the compressor. In order to generate the shortest pulses, the pulse group delay after the phase modulator and the compressor must be nearly frequency independent.  $T_g(\omega)$  can be expanded into a Taylor series around the central frequency  $\omega_0$ :

$$T_g(\omega) = \phi'(\omega_0) + \phi''(\omega_0)\Delta\omega + \frac{1}{2}\phi'''(\omega_0)\Delta\omega^2 + \frac{1}{3!}\phi''''(\omega_0)\Delta\omega^3 + \dots \quad (3.80)$$

where  $\Delta\omega = \omega - \omega_0$ , and  $\phi''(\omega_0)$ ,  $\phi'''(\omega_0)$ , and  $\phi''''(\omega_0)$  are the second-, the third-, and the fourth-order-dispersion terms, respectively. Critical values of these dispersion terms above which dispersion causes a significant change of the pulse are given by a simple scaling expression:  $\phi^{(n)} = \tau_p^n$ , where  $\phi^{(n)}$  is the  $n$ th-order dispersion term and  $\tau_p$  is the pulse duration. For example, a second order dispersion with  $\phi'' = \tau_p^2$  results in a pulse broadening by more than a factor of two. Therefore dispersion-induced pulse broadening and distortion become increasingly important for decreasing pulse durations. Equation (3.80) shows that to compress a pulse to near the transform limit one should eliminate these high order dispersion terms. For instance, assuming a transform-limited input pulse to the phase modulator, the condition for third-order-dispersion-compensated compression is the following:

$$\phi''(\omega_0) = \phi''_{modulator} + \phi''_{compressor} = 0 \quad (3.81)$$

$$\phi'''(\omega_0) = \phi'''_{modulator} + \phi'''_{compressor} = 0 \quad (3.82)$$

Several compressor schemes have been developed so far that included such components as: diffraction gratings, Brewster-cut prism pairs, combination of gratings and prisms, thin prisms and chirped mirrors, and chirped mirrors only, etc. In the following we will briefly outline the main characteristics of these compressor schemes.

### Grating and Prism Pairs

In 1968 Treacy demonstrated for the first time the use of a pair of diffraction gratings to achieve negative GDD [54]. In 1984 Fork et al. obtained negative GDD with pairs of Brewster-angled prisms [55]. Prism pairs have been widely used for dispersion control inside laser oscillators since they can be very low

loss in contrast to grating pairs. In both optical systems the origin of the adjustable dispersion is the angular dispersion that arises from diffraction and refraction, respectively. The dispersion introduced by these systems can be easily calculated, by calculating the phase accumulated between the input and output reference planes [77]. To understand the main properties of these systems, we will refer to Fig. 3.15. The first element scatters the input beam with wave vector  $\mathbf{k}_{in}$  and input path vector  $\mathbf{l}$  into the direction  $\mathbf{k}_{out}$ . The beam passes between the first and the second element and is scattered back into its original direction.

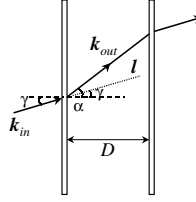


Figure 3.15: Optical path difference in a two-element dispersive delay line [105]

The phase difference by the scattered beam and the reference beam without the grating is:  $\phi(\omega) = \mathbf{k}_{out}(\omega) \cdot \mathbf{l}$ . Considering free-space propagation between the two elements, we have  $|\mathbf{k}_{out}| = \omega/c$ , and the accumulated phase can be written as

$$\phi(\omega) = \frac{\omega}{c} |\mathbf{l}| \cos[\gamma - \alpha(\omega)] = \frac{\omega}{c} \frac{D}{\cos(\gamma)} \cos[\gamma - \alpha(\omega)] \quad (3.83)$$

where:  $\gamma$  is the angle between the incident wave vector and the normal to the first element;  $\alpha$  is the angle of the outgoing wave vector, which is a function of frequency;  $D$  is the spacing between the scattering elements along a direction parallel to their normal. In the case of a grating pair the

frequency dependence of the diffraction angle  $\alpha$  is governed by the grating law, that in the case of m-th-order diffraction is given by:

$$m \frac{2\pi c}{\omega d} = [\sin \alpha(\omega) - \sin \gamma] \quad (3.84)$$

where  $d$  is the groove spacing of the grating. From the grating condition Eq.(3.84), we find

$$\cos \alpha(\omega) \frac{d\alpha}{d\omega} = -\frac{2\pi c}{\omega^2 d} m \quad (3.85)$$

Using Eq.(3.83) and Eqs.(3.84,3.85), it is possible to obtain analytic expressions for the GDD and the higher-order dispersion terms for a single pass through the grating pair:

$$\phi''(\omega) = -\frac{4\pi^2 c D}{\omega^3 d^2 \cos^3 \alpha(\omega)} m^2 \quad (3.86)$$

$$\phi'''(\omega) = \frac{12\pi^2 c D}{\omega^4 d^2 \cos^3 \alpha(\omega)} \left( 1 + \frac{2\pi c \sin \alpha(\omega)}{\omega d \cos^2 \alpha(\omega)} \right) m^3 \quad (3.87)$$

It is evident from Eq.(3.86) that grating pairs give negative dispersion.  $D$  is the distance between the gratings. A disadvantage of the grating pair is the diffraction loss. For a double-pass configuration the loss is typically 75%. Also the bandwidth for efficient diffraction is limited.

In the case of a Brewster-angled prism pair

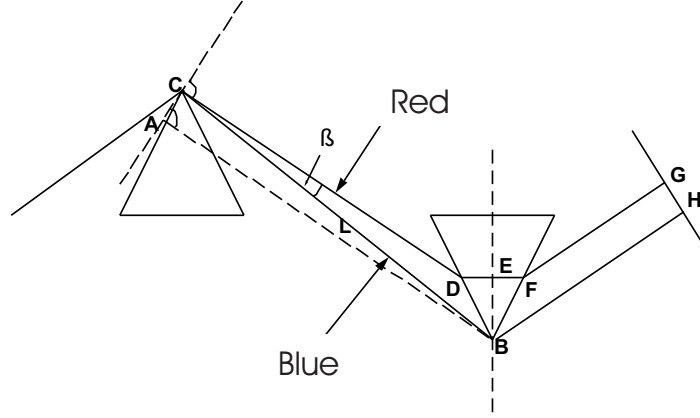


Figure 3.16: Prism pair for dispersion compensation. The blue wavelengths have less material in the light path than the red wavelengths. Therefore, blue wavelengths are less delayed than red wavelength

Eq.(3.83) reduces to the following expression (for single pass) [55]:

$$\phi(\omega) = \frac{\omega}{c} \ell_p \cos \beta(\omega) \quad (3.88)$$

where  $\ell_p$  is the distance between prism apices and  $\beta(\omega)$  is the angle between the refracted ray at frequency  $\omega$  and the line joining the two apices. The second and third order dispersion can be expressed in terms of the optical path  $P(\lambda) = \ell_p \cos \beta(\lambda)$ :

$$\phi''(\omega) = \frac{\lambda^3}{2\pi c^2} \frac{d^2 P}{d\lambda^2} \quad (3.89)$$

$$\phi'''(\omega) = -\frac{\lambda^4}{4\pi^2 c^3} \left( 3 \frac{d^2 P}{d\lambda^2} + \lambda \frac{d^3 P}{d\lambda^3} \right) \quad (3.90)$$

with the following derivatives of the optical path with respect to wavelength evaluated at Brewster's angle:

$$\frac{d^2 P}{d\lambda^2} = 2[n'' + (2n - n^{-3})(n')^2] \ell_p \sin \beta - 4(n')^2 \ell_p \cos \beta \quad (3.91)$$

$$\begin{aligned} \frac{d^3 P}{d\lambda^3} = & [6(n')^3(n^{-6} + n^{-4} - 2n^{-2} + 4n^2) + 12n'n''(2n - n^{-3}) \\ & + 2n''']\ell_p \sin \beta + 12[(n^{-3} - 2n)(n')^3 - n'n'']\ell_p \cos \beta \end{aligned} \quad (3.92)$$

$$(3.93)$$

where  $n$  is the refractive index of the prism material;  $n'$ ,  $n''$  and  $n'''$  are respectively, the first-, second- and third-order derivatives of  $n$ , with respect to wavelength. The prism-compressor has the advantage of reduced losses. Using only fused silica prisms for dispersion compensation, sub-10-fs light pulses have been generated directly from an oscillator in 1994 [78]. In 1996, pulses with tens of microjoules energy, spectrally broadened in a gas-filled hollow fiber were compressed down to 10 fs using a prism compressor [47]. Both in the case of grating and prism pairs, negative GDD is associated with a significant amount of higher-order dispersion, which cannot be lowered or adjusted independently of the desired GDD, thus limiting the bandwidth over which correct dispersion control can be obtained. This drawback has been only partially overcome by combining prism and grating pairs with third-order dispersion of opposite sign. In this way pulses as short as 6 fs have been generated in 1987 [45], and less than 5 fs in 1997 [46], by external compression. This combination cannot be used for few-optical-cycle pulse generation either in laser oscillators, due to the high diffraction losses of the gratings, or in external compressors at high power level, due to the onset of unwanted nonlinearities in the prisms.

### 3.7.4 Dispersion Compensating Mirrors

Chirped mirrors are used for the compression of high energy pulses, because they provide high dispersion with little material in the beam path, thus avoiding nonlinear effects in the compressor.

Grating and prism compressors suffer from higher order dispersion. In 1993 Robert Szipoecs and Ferenc Krausz [79] came up with a new idea, so called chirped mirrors. Laser mirrors are dielectric mirrors composed of alternating high and low index quarter wavelength thick layers resulting in strong Bragg-reflection. In chirped mirrors the Bragg wavelength is chirped so that different wavelength penetrate different depth into the mirror upon reflection giving rise to a wavelength dependent group delay. It turns out that the generation of few-cycle pulses via external compression [94] as well as direct generation from Kerr lens mode-locked lasers [57] relies heavily on the existence of chirped mirrors [56, 82, 58] for dispersion compensation.



There are two reasons to employ chirped mirrors. First the high-reflectivity bandwidth,  $\Delta f$ , of a standard dielectric Bragg-mirror is determined by the Fresnel reflectivity  $r_B$  of the high,  $n_H$ , and low,  $n_L$ , index materials used for the dielectric mirror

$$r_B = \frac{\Delta f}{f_c} = \frac{n_H - n_L}{n_H + n_L} \quad (3.94)$$

where  $f_c$  is again the center frequency of the mirror. Metal mirrors are in general too lossy, especially when used as intracavity laser mirrors. For material systems typically used for broadband optical coatings such as Silicon Dioxide and Titanium Dioxide with  $n_{SiO_2} = 1.48$  and  $n_{TiO_2} = 2.4$ , (these indexes might vary depending on the deposition technique used), a fractional bandwidth  $\Delta f/f_c = 0.23$  can be covered. This fractional bandwidth is only about a third of an octave spanning mirror  $\Delta f/f_c = 2/3$ . Furthermore, the variation in group delay of a Bragg-mirror impacts already pulses that fill half the spectral range  $\Delta f = 0.23f_c$ . A way out of this dilemma was found by introducing chirped mirrors [56], the equivalent of chirped fiber Bragg gratings, which at that time were already well developed components in fiber optics [59]. When the Bragg wavelength of the mirror stack is varied slowly enough and no limitation on the number of layer pairs exists, an arbitrary high reflectivity range of the mirror can be engineered. The second reason for using chirped mirrors is based on their dispersive properties due to the wavelength dependent penetration depth of the light reflected from different positions inside the chirped multilayer structure. Mirrors are filters, and in the design of any filter, the control of group delay and group delay dispersion is difficult. This problem is further increased when the design has to operate over wavelength ranges up to an octave or more.

**The matching problem** Several designs for ultra broadband dispersion compensating mirrors have been developed over the last years. For dispersion compensating mirrors which do not extend the high reflectivity range far beyond what a Bragg-mirror employing the same materials can already achieve, a multi-cavity filter design can be used to approximate the desired phase and amplitude properties [60, 61]. For dispersion compensating mirrors covering a high reflectivity range of up to  $\Delta f/f_c = 0.4$  the concept of double-chirped mirrors (DCMs) has been developed [82][80]. It is based on the following observations. A simple chirped mirror provides high-reflectivity over an arbitrary wavelength range and, within certain limits, a custom designable average group delay via its wavelength dependent penetration depth

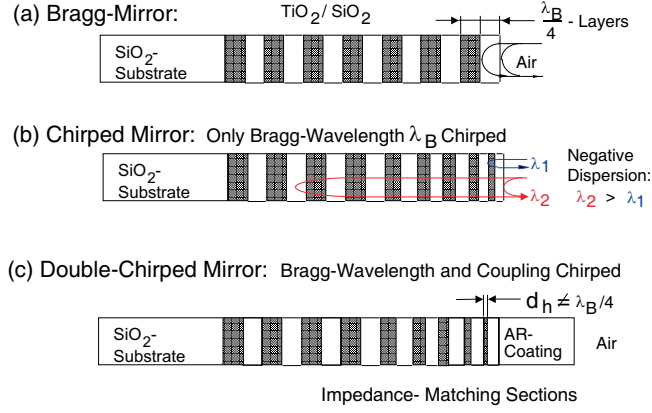


Figure 3.17: a) Standard Bragg mirror; (b) Simple chirped mirror, (c) Double-chirped mirror with matching sections to avoid residual reflections causing undesired oscillations in the GD and GDD of the mirror.

[72] (see Fig. 3.17 (a) and (b) ). However, the group delay as a function of frequency shows periodic variations due to the impedance mismatch between the ambient medium and the mirror stack, as well as within the stack (see Figure 3.17 b and Figure 3.18). A structure that mitigates these mismatches and gives better control of the group delay dispersion (GDD) is the double-chirped mirror (DCM) (Fig. 3.17 c), in a way similar to that of an apodized fiber Bragg grating [63].

Figure 3.18 shows the reflectivity and group delay of several Bragg and chirped mirrors composed of 25 index steps, with  $n_H = 2.5$  and  $n_L = 1.5$ , similar to the refractive indices of  $\text{TiO}_2$  and  $\text{SiO}_2$ , which result in a Fresnel reflectivity of  $r_B = 0.25$ . The Bragg-mirror can be decomposed in symmetric index steps [82]. The Bragg wavenumber is defined as  $k_B = \pi/(n_L d_L + n_H d_H)$ , where  $d_L$  and  $d_H$  are the thicknesses of the low and high index layer, respectively. The Bragg wavenumber describes the center wavenumber of a Bragg mirror composed of equal index steps. In the first case, (Figure 3.18, dash-dotted line) only the Bragg wave number is linearly chirped from  $6.8\mu\text{m}^{-1} < k_B < 11\mu\text{m}^{-1}$  over the first 20 index steps and held constant over the last 5 index steps. The reflectivity of the structure is computed assuming

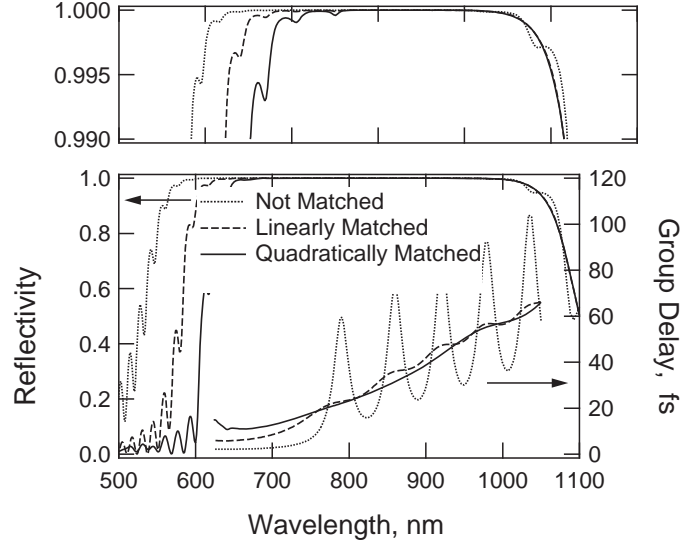


Figure 3.18: Comparison of the reflectivity and group delay of chirped mirrors with 25 layer pairs and refractive indices  $n_H = 2.5$ , and  $n_L = 1.5$ . The upper portion shows the enlarged top one percent of the reflectivity. The dotted curves show the result for a simple chirped mirror. The dashed and solid curves show the result for double-chirped mirrors where in addition to the chirp in the Bragg wave number  $k_B$  the thickness of the high-index layers is also chirped over the first 12 layer pairs from zero to its maximum value for a linear chirp, i.e.  $\alpha = 1$ , (dashed curves) and for a quadratic chirp, i.e.  $\alpha = 2$  (solid curves). [82].

the structure imbedded in the low index medium. The large oscillations in the group delay are caused by the different impedances of the chirped grating and the surrounding low index material causing a strong reflection at the interface of the low index material and the grating stack. By adiabatic matching of the grating impedance to the low index material this reflection can be avoided. This is demonstrated in Fig. 3.18 by the dashed and solid curves, corresponding to an additional chirping of the high index layer over the first 12 steps according to the law  $d_H = (m/12)^\alpha \lambda_{B,12}/(4n_H)$  with  $\alpha = 1$ , and 2, for linear and quadratic adiabatic matching. The argument  $m$  denotes the  $m$ -th index step and  $\lambda_{B,12} = 0.740 \mu m$ . The strong reduction of the oscillations in the group delay by the double-chirp technique is clearly visible.

Quadratic tapering of the high index layer, and therefore, of the grating already eliminates the oscillations in the group delay completely, which can also be shown analytically by coupled mode analysis [80]. Because of the double chirp a high transmission window at the short wavelength end of the mirror opens up which is ideally suited for the pumping of Ti:sapphire lasers. So far, the double-chirped mirror is only matched to the low index material of the mirror. Ideally, the matching can be extended to any other ambient medium by a properly designed AR-coating. However, this AR-coating has to be of very high quality, i.e. very low residual reflectivity ideally a power reflectivity of  $10^{-4}$ , i.e. an amplitude reflectivity of  $r = 10^{-2}$  is required. The quality of the AR-coating can be relaxed, if the residual reflection is directed out of the beam path. This is achieved in so called tilted front-side or back-side coated mirrors [64], [65], (Fig. 3.19 (a) and (b)). In the back-side coated mirror the ideal DCM structure, which is matched to the low index material of the mirror is deposited on the back of a substrate made of the same or at least very similar low index material. The AR-coating is deposited on the front of the slightly wedged substrate, so that the residual reflection is directed out of the beam and does not affect the dispersion properties. Thus the task of the AR-coating is only to reduce the Fresnel losses of the mirror at the air-substrate interface, and therefore, it is good enough for some applications, if the residual reflection at this interface is of the order of 0.5%. However, the substrate has to be very thin in order to keep the overall mirror dispersion negative, typically on the order of 200-500  $\mu\text{m}$ . Laser grade quality optics are hard to make on such thin substrates and the stress induced by the coating leads to undesired deformation of the substrates. The front-side coated mirror overcomes this shortcoming by depositing the ideal DCM-structure matched to the index of the wedge material on a regular laser grade substrate. A 100-200  $\mu\text{m}$  thin wedge is bonded on top of the mirror and the AR-coating is then deposited on this wedge. This results in stable and octave spanning mirrors, which have been successfully used in external compression experiments [68]. Both structures come with limitations. First, they introduce a wedge into the beam, which leads to an undesired angular dispersion of the beam. This can partially be compensated by using these mirrors in pairs with oppositely oriented wedges. The second drawback is that it seems to be impossible to make high quality AR-coatings over one or more than one octave of bandwidth, which have less than 0.5% residual reflectivity [67], i.e. on one reflection such a mirror has at least 1% of loss, and, therefore, such mirrors cause high losses inside a laser.

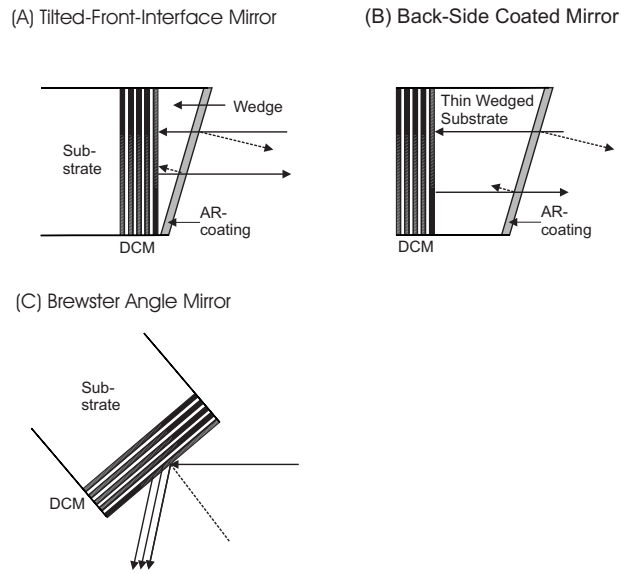


Figure 3.19: Schematic structure of proposed broadband dispersion compensating mirror system avoiding the matching to air: (a) tilted-front-interface mirror; (b) back-side coated mirror and (c) Brewster-angle mirror.

For external compression these losses are acceptable. A third possibility for overcoming the AR-coating problem is given by using the ideal DCM under Brewster-angle incidence, (Fig. 3.19) [66]. In that case, the low index layer is automatically matched to the ambient air. However, under p-polarized incidence the index contrast or Fresnel reflectivity of a layer pair is reduced and more layer pairs are necessary to achieve high reflectivity. Also the penetration depth into the mirror increased, so that scattering and other losses in the layers become more pronounced. On the other hand, such a mirror can generate more dispersion per bounce due to the higher penetration depth. For external compression such mirrors might have advantages because they can cover bandwidths much wider than one octave. This concept is difficult to apply to the fabrication of curved mirrors. There is also a spatial chirp of the reflected beam, which may become sizeable for large penetration depth and has to be removed by back reflection or an additional bounce on another Brewster-angle mirror, that recombines the beam. For intracavity mirrors a way out of this dilemma is found by mirror pairs, which cancel the spurious reflections due to an imperfect AR-coating and matching structure in the chirped mirror [75]. Also this design has its drawbacks and limitations. It requires a high precision in fabrication and depending on the bandwidth of the mirrors it may be only possible to use them for a restricted range of angles of incidence.

### Double-chirped mirror pairs

There have been several proposals to increase the bandwidth of laser mirrors by mutual compensation of GDD oscillations [69, 70, 71] using computer optimization. These early investigations resulted in a rather low reflectivity of less than 95% over almost half of the bandwidth considered. The ideas leading to the DCMs help us to show analytically that a design of DCM-pairs covering one octave of bandwidth, i.e. 600 nm to 1200 nm, with high reflectivity and improved dispersion characteristics is indeed possible [75]. Use of these mirror pairs in a Ti:sapphire laser system resulted in 5 fs pulses with octave spanning spectra directly from the laser [57]. Yet, the potential of these pairs is by no means fully exploited.

A DCM-Pair, see Fig. 3.20, consists of a mirror M1 and M2. Each is composed of an AR-coating and a low-index matched double-chirped back-mirror MB with given wavelength dependent penetration depth. The high reflectivity range of the back-mirror can be easily extended to one octave by

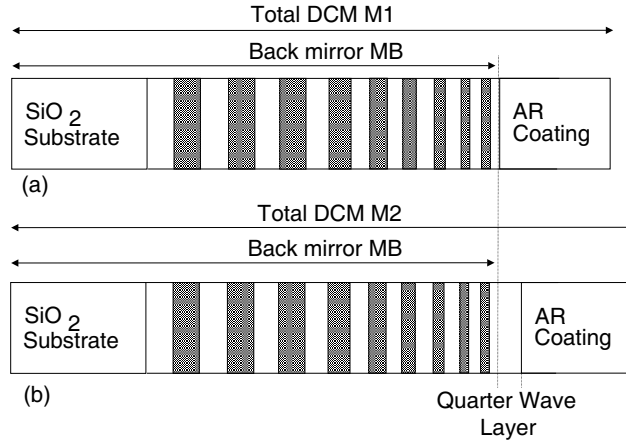


Figure 3.20: DCM-Pair M1 (a) and M2 (b). The DCM M1 can be decomposed in a double-chirped back-mirror MB matched to a medium with the index of the top most layer. In M2 a layer with a quarter wave thickness at the center frequency of the mirror and an index equivalent to the top most layer of the back-mirror MB is inserted between the back-mirror and the AR-coating. The new back-mirror comprising the quarter wave layer can be reoptimized to achieve the same phase as MB with an additional  $\pi$ -phase shift over the whole octave of bandwidth.

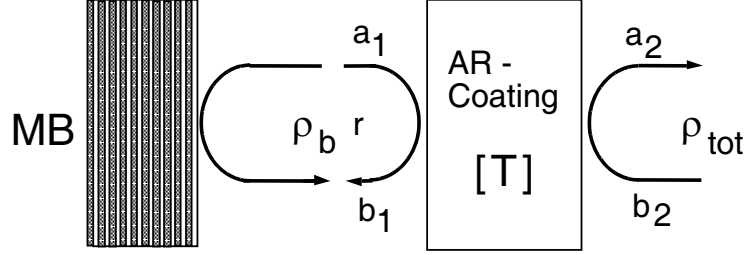


Figure 3.21: Decomposition of a DCM into a double-chirped backmirror MB and an AR-coating.

simply chirping slowly enough and using a sufficient number of layer pairs. However, the smoothness of the resulting GDD strongly depends on the quality of matching provided by the AR-coating and the double-chirped section. Figure 3.21 indicates the influence of the AR-coating on the GDD of the total DCM-structure. The AR-coating is represented as a two - port with two incoming waves  $a_1$ ,  $b_2$  and two outgoing waves  $a_2$ ,  $b_1$ . The connection between the waves at the left port and the right port is described by the transfer matrix

$$\begin{pmatrix} a_1 \\ b_1 \end{pmatrix} = T_{ar} \begin{pmatrix} a_2 \\ b_2 \end{pmatrix} \quad \text{with} \quad T_{ar} = \begin{pmatrix} \frac{1}{t} & \frac{r^*}{t^*} \\ \frac{r}{t} & \frac{1}{t^*} \end{pmatrix} \quad (3.95)$$

where we assumed that the multilayer AR-coating is lossless. Here,  $r$  and  $t$  are the complex coefficients for reflection and transmission at port 1 assuming reflection free termination of port 2. The back-mirror MB, is assumed to be perfectly matched to the first layer in the AR-coating, has full reflection over the total bandwidth under consideration. Thus its complex reflectivity in the range of interest is given by

$$\rho_b = e^{j\phi_b(\omega)} \quad (3.96)$$

The phase  $\phi_b(\omega)$  is determined by the desired group delay dispersion

$$GDD_b = -d^2\phi_b(\omega)/d\omega^2 \quad (3.97)$$

up to an undetermined constant phase and group delay at the center frequency of the mirror,  $\omega_c$ . All higher order derivatives of the phase are determined by the desired dispersion of the mirror. Analytic formulas for the design of DCMs, showing custom designed dispersion properties without



considering the matching problem to the ambient air, can be found in [72]. The resulting total mirror reflectivity including the AR-coating follows from (3.95)

$$\rho_{tot} = \frac{t}{t^*} \rho_b \frac{1 - r^*/\rho_b}{1 - r\rho_b} \quad (3.98)$$

For the special case of a perfectly reflecting back-mirror according to Eq. (3.96) we obtain

$$\rho_{tot} = \frac{t}{t^*} e^{j\phi_b(\omega)} \frac{1 - z^*}{1 - z}, \quad \text{with} \quad z = r e^{j\phi_b(\omega)} \quad (3.99)$$

The new reflectivity is again unity but new contributions in the phase of the resulting reflectivity appear due to the imperfect transmission properties of the AR-coating. With the transmission coefficient of the AR-coating

$$t = |t| e^{j\phi_t}, \quad (3.100)$$

The total phase of the reflection coefficient becomes

$$\phi_{tot} = 2\phi_t + \phi_b(\omega) + \phi_{GTI} \quad (3.101)$$

with

$$\phi_{GTI} = 2 \arctan \left[ \frac{\text{Im}\{z\}}{1 + \text{Re}\{z\}} \right] \quad (3.102)$$

Here,  $\phi_t$  is the phase of the transmission coefficient and  $\phi_{GTI}$  is the phase due to the Gire-Tournois interferometer created by the non-perfect AR-coating, i.e.  $r \neq 0$ , and the back-mirror MB, (Figure 3.21). The phase  $\phi_t$  of a good AR-coating, i.e.  $|r| < 0.1$ , is linear and, therefore, does not introduce undesired oscillations into the GD and GDD. However, the phase  $\phi_{GTI}$  is rapidly varying since  $\phi_b(\omega)$  varies over several  $2\pi$  over the frequency range of interest due to the monotonic group delay of the back-mirror. The size of these oscillations scale with the quality of the AR-coating, i.e. with  $|r|$ . Thus, the GDD oscillations are reduced with smaller residual reflectivity of the AR-coating. Assuming, that the reflectivity  $r$  is real and smaller or equal to 0.1, the oscillations in the group delay and group delay dispersion are easily estimated by

$$T_{g,GTI} = \frac{d\phi_{GTI}}{d\omega} \approx -r T_{gb}(\omega) \cos[\phi_b(\omega)] \quad (3.103)$$

with

$$\begin{aligned}
T_{gb}(\omega) &= -d\phi_b(\omega)/d\omega, \\
GDD_{GTI} &= \frac{d^2\phi_{GTI}}{d\omega^2} \\
&\approx r \left( T_{gb}^2(\omega) \sin[\phi_b(\omega)] - GDD_b \cos[\phi_b(\omega)] \right)
\end{aligned} \tag{3.104}$$

The GTI-reflections add up coherently when multiple reflections on chirped mirrors occur inside the laser over one round-trip, leading to pre- and post pulses if the mode-locking mechanism is not strong enough to suppress them sufficiently. Experimental results indicate that a residual reflection in the AR-coating of  $r < 0.01$  and smaller, depending on the number of reflections per round-trip, is required so that the pre- and post pulses are sufficiently suppressed. This corresponds to an AR-coating with less than  $10^{-4}$  residual power reflectivity, which can only be achieved over a very limited range, as discussed above.

Over a limited wavelength range of 350 nm centered around 800 nm low residual power reflectivities as small as  $10^{-4}$  have been achieved effectively after reoptimization of the AR-coating section and the double-chirped section to form a combined matching section of higher matching quality. For even larger bandwidth, approaching an octave, a residual power reflectivity of  $10^{-4}$  is no longer possible [67]. A way out of this limitation is offered by the observation, that a coherent subtraction of the pre- and post-pulses to first order in  $r$  is possible by reflections on a mirror pair M1 and M2, see Figure 3.20 (a) and (b). A series of two reflections on a mirror with reflectivity (3.99) and on a similar mirror with an additional phase shift of  $\pi$  between the AR-coating and the back-mirror, having a reflectivity (3.99) where  $z$  is replaced by  $-z$ , leads to a coherent subtraction of the first order GTI-effects. The resulting total reflectivity of the two reflections is given by the product of the individual complex reflectivities assuming the same AR-coating

$$\rho_{tot,2} = - \left( \frac{t}{t^*} \right)^2 e^{i2\phi_b(\omega)} \frac{1 - z^{*2}}{1 - z^2} \tag{3.105}$$

Now, the GTI-effects scale like the power reflectivity of the AR-coating  $r^2$  instead of the amplitude reflectivity  $r$ , which constitutes a tremendous improvement, since it is possible to design AR-coatings to the low index material  $\text{SiO}_2$  of the mirror with a residual power reflectivity between 0.001 and 0.01 while covering one octave of bandwidth [67]. However, there does not exist a single physical layer which generates a phase shift of  $\pi/2$  during one passage for all frequency components contained in an octave. Still, a layer with

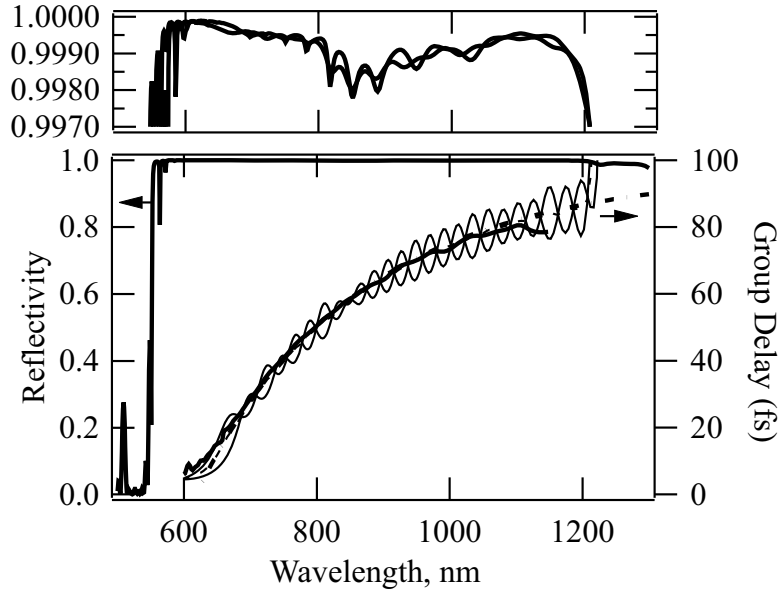


Figure 3.22: Reflectivity of the mirror with pump window shown as thick solid line with scale to the left. The group delay design goal for perfect dispersion compensation of a prismless Ti:sapphire laser is shown as thick dash-dotted line with scale to the right. The individual group delay of the designed mirrors is shown as thin line and its average as a dashed line, which is almost identical with the design goal over the wavelength range from 650-1200 nm. The measured group delay, using white light interferometry, is shown as the thick solid line from 600-1100 nm. Beyond 1100nm the sensitivity of Si-detector used prevented further measurements.

a quarter wave thickness at the center frequency is a good starting design. Then the back-mirror MB in the Mirror M2 can be reoptimized to take care of the deviation from a quarter wave thickness further away from the center frequency, because the back-mirror acts as a highly dispersive medium where the phase or group delay can be designed at will.

Figure 3.23 shows in the top graph the designed reflectivity of both mirrors of the pair in high resolution taking into account the absorption in the layers. The graph below shows the reflectivity of the mirror, which has in addition high transmission between 510-550 nm for pumping of the Ti:sapphire crystal. Each mirror consists of 40 layer pairs of  $\text{SiO}_2$  and  $\text{TiO}_2$  fabricated

using ion-beam sputtering [73, 74]. Both mirror reflectivities cover more than one octave of bandwidth from 580 nm to 1200 nm or 250 to 517 THz, with an average reflectivity of about 99.9% including the absorption in the layers. In addition, the mirror dispersion corrects for the second and higher order dispersion of all intracavity elements such as the Ti:sapphire crystal and the thin, small angle, BaF<sub>2</sub> wedges, for fine adjustment of the dispersion from 650 nm to 1200 nm within the 12 bounces occurring in one roundtrip. The choice for the lower wavelength boundary in dispersion compensation is determined and limited by the pump window of Ti:sapphire. The dispersion measurement was performed using white light interferometry [76], up to about 1100 nm because of the silicon detector roll-off. However, in the average group delay of both mirrors the oscillations are ideally suppressed due to cancellation by more than a factor of ten. Therefore, the effective residual reflectivity of the mirror pair covering one octave,  $r^2$ , is even smaller than that of conventional DCMs.

### Methods for active dispersion compensation

Various schemes for active pulse compression have been developed based on the use of liquid-crystal modulators (LCM), acousto-optic modulators (AOM), and mechanically deformable mirrors.

**Dispersion compensation using liquid crystal modulators** A pulse shaping technique [83] based on the use of a LCM for pulse compression offers the advantage of a large bandwidth (300-1500 nm) and *in situ* adaptive phase control, see Figure 3.23. In 1997 Yelin *et al.* [84] demonstrated an adaptive method for femtosecond pulse compression based on LCM. Strongly chirped 80-fs pulses generated by an oscillator were sent in a 4-*f* pulse shaper composed of a pair of thin holographic transmission gratings. A programmable one-dimensional LCM, placed in the Fourier plane of the shaper, was used as an updatable filter for pulse spectral manipulation. Pulses as short as 11 fs (transform-limited duration: 9 fs) have been obtained, employing an optimization algorithm for adaptive compression based on a search in the two-dimensional space of second- and third-order dispersion coefficients. In 2001, Karasawa *et al.* [85] demonstrated pulse compression, down to 5 fs, of broadband pulses from an argon-filled hollow fiber, using only a LCM for phase compensation. More recently [50], pulses as short as 3.8 fs have been achieved through a closed-loop combination of a liquid-crystal spatial light

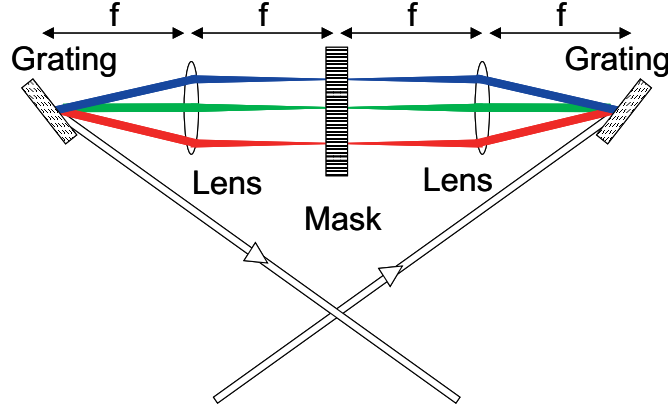


Figure 3.23: Grating Pair and LCM pulse shaper according to Weiner and Heritage [87]. To shape amplitude and phase two pulse shapers with an amplitude and phase mask each are necessary.

modulator for adaptive pulse compression and spectral-phase interferometry for direct electric-field reconstruction (SPIDER) [86] measurements as feedback signal.

One problem of the method is pixelization in the Fourier plane owing to the technology of the liquid-crystal active matrix. Diffraction on pixel edges and absorption by the black matrix introduce parasitic effects. The requirement that the actual spectral modulation should approximate a smooth function despite the fixed, finite size of the individual modulator elements, limits the temporal range over which pulse compression can be achieved [87]. Other problems are related to the optical damage of the LCM, which limits the maximum pulse energy, and to the high losses introduced by the device.

Various nonpixelated devices have been proposed: Dorrer *et al.* have reported on an optically addressed LCM (liquid crystal light valve) [88]. The light valve consists of two continuous transparent electrodes and continuous layers of a nematic twisted liquid crystal and of photoconductive  $\text{Bi}_{12}\text{SiO}_{20}$  (BSO). A local variation of illumination of the BSO layer (in the blue green spectral region) induces a change in conductivity. When a voltage is applied between the two electrodes, the variation of the BSO conductivity results in a change in the voltage drop across the liquid crystal layer. As the birefringence of the liquid crystal is voltage dependent, a local variation of the refractive index is created, which translates into a variation of the optical

phase of the local spectral component. The light valve is addressed by using a display device. Pixelation effects are avoided because the light valve itself is a continuous device. The control of the light valve is more complicated than for the electrically addressed LCM. Moreover, due to its limited spatial frequency response, the spectral resolution is limited.

### Dispersion compensation using acousto-optic modulators

In 1997 Tourniois proposed an acousto-optic programmable dispersive filter (AOPDF), to provide large dispersion-compensation ranges[90]. The device is based on a collinear acousto-optic interaction in a birefringent uniaxial crystal, see Figure 3.24. The acoustic frequency is a variable function of time and provides control over the group delay of the diffracted optical pulse. At the same time, the spectral amplitude of the diffracted pulse is driven by the intensity of the acoustic signal. As demonstrated in Ref. [90], the optical output  $E_{out}(t)$  of the AOPDF is proportional to the convolution of the optical input,  $E_{in}(t)$ , and the scaled acoustic signal:

$$E_{out}(t) \propto E_{in}(t) \otimes S(t/\alpha) \quad (3.106)$$

where the scaling factor  $\alpha = \Delta n(V/c)$  is the ratio of the speed of sound to the speed of light times the index difference between the ordinary and the extraordinary waves. Therefore, by generating the proper function  $S(t)$ , it is possible to generate any arbitrary convolution with a temporal resolution given by the inverse of the filter bandwidth. Such device have been used in kilohertz chirped-pulse amplification laser chains compensating for gain narrowing and residual phase errors with the AOPDF, resulting in the generation of 17-fs transform-limited pulses [91]. The total throughput is 10-50%, depending on the bandwidth of the device. Devices approaching one octave in bandwidth are possible.

### Dispersion compensation using deformable mirrors

Mechanically deformable mirrors can be used for active dispersion control, as proposed by Heritage *et al.* [92]. More recently, pulse compression has been achieved using an electrostatically deformable, gold-coated, silicon nitride membrane mirror, placed in the Fourier plane of a  $4f$  zero-dispersion stretcher [93]. The membrane was suspended over an array of 39 actuator electrodes. The potential applied to each actuator generates an electrostatic

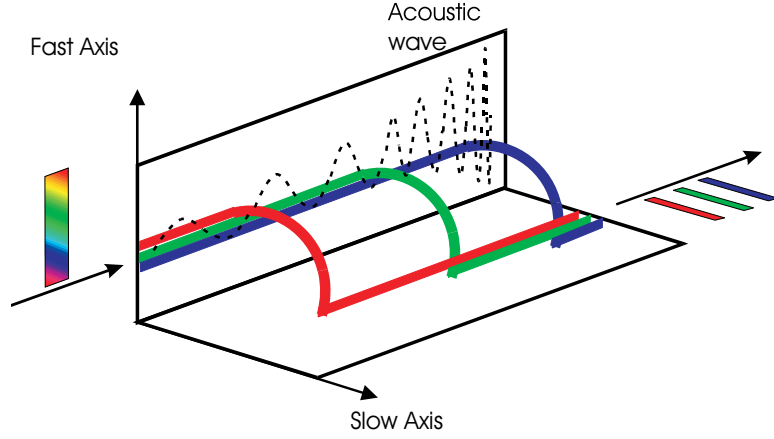


Figure 3.24: Acousto-optic programmable pulse shaper. One element can shape amplitude and phase of the pulse.

attraction between the membrane and the electrode, thus inducing a deformation of the mirror surface, which translates into a modulation of the phase of the spectral components of the input pulse. The total phase difference is  $\phi = 2(2\pi)\Delta z/\lambda$ , where  $\Delta z$  is the deflection of the mirror. The minimum radius of curvature of the mirror membrane is given by  $R = T/P$ , where  $T$  is the membrane tension and  $P$  is the maximum electrostatic pressure. This limitation of the membrane curvature restricts the possibility of the mirror correction of higher-order phases. The main advantages of this method are the following: the phase modulation is smoothly varying; reduced losses due to the high reflectivity (97%) of the mirror; relatively high actuator density. Experiments have been performed with a mode-locked Ti:sapphire laser, where the deformable mirror recompressed a 15 fs pulse, previously stretched to 90 fs by dispersion in glass, back to approximately the bandwidth limit [93].

Recently, dispersion control over a bandwidth of  $\sim 220$  THz has been demonstrated by A. Baltuška et al. [94] using a compressor consisting of a pair of chirped mirrors and a grating dispersion line with a computer-controlled flexible mirror positioned in the focal plane. The total throughput of the pulse shaper was less than 12% because of the low diffraction efficiency of the grating. Using this compressor, the visible-near-IR pulses, generated by optical parametric amplification, were compressed to a 4-fs duration.

### 3.7.5 Hollow Fiber Compression Technique

Single mode fiber only allows compression of low energy pulses. In 1996 the group of DeSilvestri in Milan [47] developed a technique that enables the generation of few-cycle light pulses with energies in the millijoule range. The technique is based on propagation of laser pulses in a hollow fiber filled with noble gases (hollow fiber compression technique), see Fig. 3.25. The modes of the hollow fiber are leaky modes, i.e. they experience radiation loss. However, there is one mode, the  $\text{EH}_{11}$  mode, which has considerably less loss than the higher order modes. This mode is used for pulse compression. The nonlinear index in the fiber can be controlled with the gas pressure. Typical fiber diameters are 100-500  $\mu\text{m}$  and typical gas pressures are in the range of 0.1-3 bar. As in the case of fiber compression it is important to consider the optimization of nonlinear interaction and dispersion. Both the medium and waveguide dispersion has to be taken into account. For more detail see ref. [105].

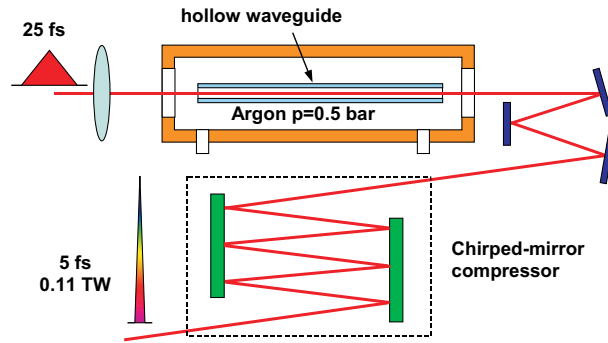


Figure 3.25: Hollow fiber compression technique [47]

For the time being, the hollow fiber compression technique is the only way to generate sub-10fs millijoule pulses. This will change soon with the advent of parametric chirped pulse amplification.



### 3.8 Summary

We found, that the lowest order reversible linear effect, GVD, together with the lowest order reversible nonlinear effect in a homogeneous and isotropic medium, SPM, leads to the Nonlinear Schrödinger Equation for the envelope of the wave. This equation describes a Hamiltonian system. The equation is integrable, i.e., it does possess an infinite number of conserved quantities. The equation has soliton solutions, which show complicated but persistent oscillatory behavior. Especially, the fundamental soliton, a sech-shaped pulse, shows no dispersion which makes them ideal for long distance optical communication. Due to the universality of the NSE, this dynamics is also extremely important for modelocked lasers once the pulses become so short that the spectra experience the dispersion and the peak powers are high enough that nonlinear effects become important. In general, this is the case for sub-picosecond pulses. Further, we found a perturbation theory, which enables us to decompose a solution of the NSE close to a fundamental soliton as a fundamental soliton and continuum radiation. We showed that periodic perturbations of the soliton may lead to side-band generation, if the nonlinear phase shift of the soliton within a period of the perturbation becomes comparable to  $\pi/4$ . Soliton perturbation theory will also give the frame work for studying noise in mode-locked lasers later.

A medium with positive dispersion and self-phase modulation with the same sign can be used for pulse compression. The major problem in pulse compression is to find a compressor that can that exactly inverts the group delay caused by spectral broadening. Depending on bandwidth this can be achieved by gratings, prisms, chirped mirrors, puls shapers, AOPDFs or a combination thereof.

### 3.9 Appendix: Sech-Algebra

The hyperbolic secant is defined as

$$\text{sech}(x) = \frac{1}{\cosh(x)} \quad (3.107)$$

See Figure 3.26

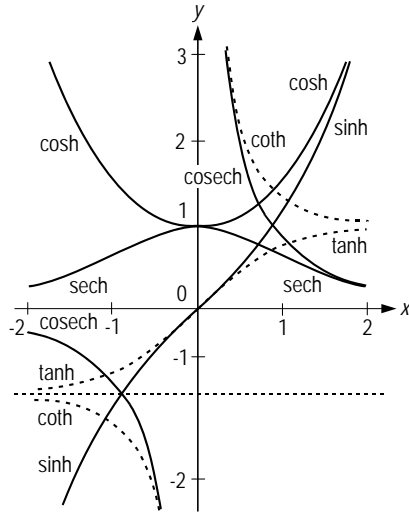


Figure 3.26: Hyperbolic functions

$$\cosh^2(x) - \sinh^2(x) = 1 \quad (3.108)$$

$$\operatorname{sech}^2(x) = 1 - \tanh^2(x) \quad (3.109)$$

$$\frac{d}{dx} \operatorname{sech}(x) = -\tanh(x) \operatorname{sech}(x) \quad (3.110)$$

$$\frac{d^2}{dx^2} \operatorname{sech}(x) = \operatorname{sech}(x) [1 - 2\operatorname{sech}^2(x)] \quad (3.111)$$

$$\int_{-\infty}^{+\infty} \operatorname{sech}(x) dx = \pi \quad (3.112)$$

$$\int_{-\infty}^{+\infty} \operatorname{sech}^2(x) dx = 2 \quad (3.113)$$

$$\int_{-\infty}^{+\infty} x^2 \operatorname{sech}^2(x) dx = \frac{\pi^2}{6} \quad (3.114)$$

function $f(t)$	Fourier-Transform $\tilde{f}(\omega) = \int f(t)e^{-j\omega t}dt$
$\text{sech}(t)$	$\pi \text{sech}(\frac{\pi}{2}\omega)$
$\text{sech}^2(t)$	$\frac{\pi\omega}{\sinh(\frac{\pi}{2}\omega)}$
$\text{sech}^3(t)$	$\frac{1}{2}(1+\omega^2)\pi \text{sech}(\frac{\pi}{2}\omega)$
$\text{sech}^5(t)$	$\frac{1}{24}(\omega^4+10\omega^2+9)\pi \text{sech}(\frac{\pi}{2}\omega)$
$\tanh(t)\text{sech}(t)$	$-j\pi\omega \text{sech}(\frac{\pi}{2}\omega)$
$\tanh^2(t)\text{sech}(t)$	$\frac{1}{2}(1-\omega^2)\pi \text{sech}(\frac{\pi}{2}\omega)$
$\tanh^3(t)\text{sech}(t)$	$-j\frac{\omega}{6}(5-\omega^2)\pi \text{sech}(\frac{\pi}{2}\omega)$
$\tanh(t)\text{sech}^3(t)$	$-j\frac{\omega}{6}(1+\omega^2)\pi \text{sech}(\frac{\pi}{2}\omega)$
$\tanh^2(t)\text{sech}^3(t)$	$\frac{1}{2}(1+\omega^2)\pi \text{sech}(\frac{\pi}{2}\omega) - \frac{1}{24}(\omega^4+10\omega^2+9)\pi \text{sech}(\frac{\pi}{2}\omega)$
$t\tanh(t)\text{sech}(t)$	$\pi \text{sech}(\frac{\pi}{2}\omega) - \frac{\omega\pi^2}{2}\tanh(\frac{\pi}{2}\omega)\text{sech}(\frac{\pi}{2}\omega)$
$t\tanh^2(t)\text{sech}(t)$	$-j\omega\pi \text{sech}(\frac{\pi}{2}\omega) - \frac{\pi^2}{4}(1-\omega^2)\tanh(\frac{\pi}{2}\omega)\text{sech}(\frac{\pi}{2}\omega)$
$t\tanh^3(t)\text{sech}(t)$	$\frac{1}{6}(5-3\omega^2)\pi \text{sech}(\frac{\pi}{2}\omega) - \frac{\omega\pi^2}{12}(5-\omega^2)\tanh(\frac{\pi}{2}\omega)\text{sech}(\frac{\pi}{2}\omega)$
$t\tanh(t)\text{sech}^3(t)$	$\frac{1}{6}(1+3\omega^2)\pi \text{sech}(\frac{\pi}{2}\omega) - \frac{\omega\pi^2}{12}(1+\omega^2)\tanh(\frac{\pi}{2}\omega)\text{sech}(\frac{\pi}{2}\omega)$
$t\text{sech}(t)$	$-j\frac{\pi^2}{6}\tanh(\frac{\pi}{2}\omega)\text{sech}(\frac{\pi}{2}\omega)$
$t\text{sech}^3(t)$	$-j\omega\pi \text{sech}(\frac{\pi}{2}\omega) - j\frac{\pi^2}{4}(1+\omega^2)\tanh(\frac{\pi}{2}\omega)\text{sech}(\frac{\pi}{2}\omega)$

# Bibliography

- [1] G. B. Whitham: "Linear and Nonlinear Waves," John Wiley and Sons, NY (1973).
- [2] A. Yariv, "Quantum Electronics", Wiley Interscience (1975).
- [3] F. Schwabl, "Quantenmechanik," Springer, Berlin (1988).
- [4] V. E. Zakharov and A. B. Shabat, "Exact Theory of Two-Dimensional Self-Focusing and One-Dimensional Self-Modulation of Waves in non-linear Media", Zh. Eksp. Teor. Fiz. **34**, pp. 61 - 68 (1971); [Sov. Phys. - JETP **34**, pp. 62 - 69 (1972).]
- [5] J. D. Moores, K. Bergman, H. A. Haus and E. P. Ippen, "Optical switching using fiber ring reflectors," J. Opt. Soc. Am. B **8**, pp. 594 – 601 (1990).
- [6] L. F. Mollenauer and R. H. Stolen, "The soliton laser" Opt. Lett. **9**, pp. 13 – 15 (1984).
- [7] H. A. Haus and M. N. Islam, "Theory of the soliton laser," IEEE J. Quant. Electron. **QE-21**, pp. 1172 – 88 (1985).
- [8] A. Hasegawa and F. Tapert, "Transmission of stationary nonlinear optical pulses in dispersive dielectric fibers. I. Anomalous dispersion," Appl. Phys. Lett. **23**, pp. 142 - 144 (1973).
- [9] L. F. Mollenauer, R. H. Stolen and J. P. Gordon, "Experimental observation of picosecond pulse narrowing and solitons in optical fibers", Phys. Rev. Lett. **45**, pp. 1095 – 1098 (1980).

- [10] P. G. Drazin, and R. S. Johnson, "Solitons: An Introduction," Cambridge University Press, New York (1990).
- [11] G. L. Lamb, Jr., "Elements of Soliton Theory," New York: Wiley-Interscience (1980).
- [12] N. J. Zabusky and M. D. Kruskal, "Interactions of 'solitons' in a collisionless plasma and the recurrence of initial states," *Phys. Rev. Lett.*, **15**, pp. 240 – 243 (1965).
- [13] C. S. Gardener, J. M. Greene, M. D. Kruskal and R. M. Miura, "Method for solving the Korteweg-de Vries equation," *Phys. Rev. Lett.* **19**, pp. 1095 – 1097 (1967).
- [14] M. J. Ablowitz, D. J. Kaup, A. C. Newell & H. Segur, "The inverse scattering transform - Fourier analysis for nonlinear problems," *Stud. Appl. Math.* **53**, pp. 249 – 315 (1974).
- [15] A. C. Newell, "The Inverse Scattering Transform," In *Topics in current physics. Solitons.* ed. by R. Bulloch & P. Caudrey, Berlin, Springer (1978).
- [16] V. A. Marchenko, "On the reconstruction of the potential energy form phases of the scattered waves," *Dokl. Akad. Nauk SSSR*, **104** 695 – 698 (1955).
- [17] H. A. Haus, "Optical Fiber Solitons, Their Properties and Uses," *Proc. of the IEEE* **81**, pp. 970 – 983 (1993).
- [18] R. Y. Chiao, E. Garmire, and C. H. Townes, "Self-trapping of optical beams," *Phys. Rev. Lett.* **13**, pp. 479 – 482 (1964).
- [19] A. S. Davydov, "Solitons in molecular systems", *Physica Scripta* **20**, pp. 387 – 394 (1979). London: John Murray.
- [20] Y. Kodama, and A. Hasegawa, "Nonlinear Pulse Propagation in a Monomode Dielectric Guide," *IEEE J. Quantum Electron.* **QE-23** pp. 510 – 524 (1987).
- [21] A. Hasegawa, "Optical Solitons in Fibers," Springer Verlag, Berlin (1989).

- [22] G. Placek, Marx Handbuch der Radiologie, ed. by E. Marx (Academische Verlagsgesellschaft, Leipzig, Germany, 1934), 2nd ed., Vol. VI, Part II, p. 209 – 374.
- [23] F. X. Kärtner, D. Dougherty, H. A. Haus, and E. P. Ippen, "Raman Noise and Soliton Squeezing," J. Opt. Soc. Am. B **11**, pp. 1267 – 1276, (1994).
- [24] V. I. Karpman, and E. M. Maslov, "Perturbation Theory for Solitons," Sov. Phys. JETP **46** pp. 281 – 291 (1977); J. P. Keener and D. W. McLaughlin, "Solitons under Perturbations," Phys. Rev. A **16**, pp. 777 – 790 (1977).
- [25] D. J. Kaup, and A. C. Newell, "Solitons as particles, oscillators, and in slowly changing media: a singular perturbation theory," Proc. R. Soc. Lond. A. **361**, pp. 413 – 446 (1978).
- [26] H. A. Haus and Y. Lai, "Quantum theory of soliton squeezing: a linearized approach," Opt. Soc. Am B **7**, 386 – 392 (1990).
- [27] D. J. Kaup, "Perturbation theory for solitons in optical fibers", Phys. Rev. A **42**, pp. 5689 – 5694 (1990).
- [28] J. P. Gordon and H. A. Haus, "Random walk of coherently amplified solitons in optical fiber transmission," Opt. Lett. **11**, 665 – 668.(1986)
- [29] S. M. J. Kelly, "Characteristic sideband instability of periodically amplified average solitons", Electronics Letters, **28**, pp. 806 - 807 (1992).
- [30] J. N. Elgin and S. M. J. Kelly, "Spectral modulation and the growth of resonant modes associated with periodically amplified solitons", Opt. Lett., **21**, pp. 787 - 789 (1993).
- [31] J. Satsuma, and N. Yajima, "Initial Value Problems of One-Dimensional Self-Modulation of Nonlinear Waves in DIspersive Media," Supplement of the Progress in Theoretical Physics, **55**, pp. 284 – 306 (1974).
- [32] J. P. Gordon, "Dispersive perturbations of solitons of the nonlinear Schrödinger equation", J. Opt. Soc. Am. B **9**, pp. 91 – 97 (1992).

- [33] F. M. Mitschke and L. F. Mollenauer, "Discovery of the soliton self-frequency shift", *Opt. Lett.* **11**, pp. 659 – 661 (1986).
- [34] J. P. Gordon, "Theory of the soliton self-frequency shift", *Opt. Lett.* **11**, pp. 662 – 664 (1986).
- [35] A. C. Newell and J. V. Moloney, "Nonlinear Optics," Addison-Wesley Publishing Company, Redwood City, (1993).
- [36] A.M. Kowalewicz, A. T. Zare, F. X. Kärtner, J. G. Fujimoto, S. Dewald, U. Morgner, V. Scheuer, and G. Angelow, "Generation of 150-nJ pulses from a multiple-pass cavity Kerr-lens modelocked Ti:Al<sub>2</sub>O<sub>3</sub> oscillator," *Opt. Lett.*, **28**, 1507-09, 2003.
- [37] F. Gires, P. Tournois, *C.R. Acad. Sci. (Paris)* **258** 6112 (1964)
- [38] J.A. Giordmaine, M.A. Duguay, J.W. Hansen: Compression of optical pulse, *IEEE J. Quantum Electron.* **4** 252-255 (1968)
- [39] R. A. Fisher, P. L. Kelly, T. K. Gustafson: Subpicosecond pulse generation using the optical Kerr effect, *Appl. Phys. Lett.* **14** 140-143 (1969)
- [40] A. Laubereau: External frequency modulation and compression of picosecond pulses, *Phys. Lett.* **29A** 539-540 (1969)
- [41] H. Nakatsuka, D. Grischkowsky, A. C. Balant: Nonlinear picosecond-pulse propagation through optical fibers with positive group velocity dispersion, *Phys. Rev. Lett.* **47** 910-913 (1981)
- [42] A.J. Campillo, S.L. Shapiro, B.R. Suydam: Periodic breakup of optical beams due to self-focusing, *Appl. Phys. Lett.* **23** 628-630 (1973)
- [43] E.P. Ippen, C.V. Shank, T.K. Gustafson: Self-phase modulation of picosecond pulses in optical fibers, *Appl. Phys. Lett.* **24** 190-192 (1974)
- [44] R.H. Stolen, C. Lin: Self-phase-modulation in silica optical fibers, *Phys. Rev. A* **17** 1448-1453 (1978)
- [45] R.L. Fork, C.H.B. Cruz, P.C. Becker, C.V. Shank: Compression of optical pulses to six femtoseconds by using cubic phase compensation, *Opt. Lett.* **12** 483-485 (1987)

- [46] A. Baltuška, Z. Wei, M.S. Pshenichnikov, D.A. Wiersma, R. Szipöcs: Optical pulse compression to 5 fs at a 1-MHz repetition rate, *Opt. Lett.* **22**, 102-104 (1997)
- [47] M. Nisoli, S. De Silvestri, O. Svelto: Generation of high energy 10 fs pulses by a new pulse compression technique, *Appl. Phys. Lett.* **68** 2793-2795 (1996)
- [48] M. Nisoli, S. De Silvestri, O. Svelto, R. Szipöcs, K. Ferencz, Ch. Spielmann, S. Sartania, F. Krausz: Compression of high-energy laser pulses below 5 fs, *Opt. Lett.* **22** 522-524 (1997)
- [49] G. Cerullo, S. De Silvestri, M. Nisoli, S. Sartania, S. Stagira, O. Svelto: Few-optical-cycle laser pulses: from high peak power to frequency tunability, *IEEE J. Selec. Topics in Quantum Electr.* **6** 948-958 (2000)
- [50] B. Schenkel, J. Biegert, U. Keller, C. Vozzi, M. Nisoli, G. Sansone, S. Stagira, S. De Silvestri, O. Svelto: Generation of 3.8-fs pulses from adaptive compression of a cascaded hollow fiber supercontinuum, *Opt. Lett.* **28** 1987-1989 (2003)
- [51] G. P. Agrawal: *Nonlinear Fiber Optics* (Academic Press, San Diego 1995)
- [52] *Ultrashort Laser Pulses*, Ed. W. Kaiser, Springer Verlag, 1988.
- [53] A. Baltuška, Z. Wei, R. Szipöcs, M. S. Pshenichnikov, D. A. Wiersma: All solid-state cavity-dumped sub-5-fs laser, *Appl. Phys. B* **65** 175-188 (1997)
- [54] E.B. Treacy: Compression of picosecond light pulses, *Phys. Lett.* **28A**, 34-35 (1968)
- [55] R.L. Fork, O.E. Martinez, J.P. Gordon: Negative dispersion using pairs of prisms, *Opt. Lett.* **9** 150-152 (1984)
- [56] R. Szipöcs, K. Ferencz, C. Spielmann, and F. Krausz, *Opt. Lett.* **19**, 201-203 (1994).
- [57] R. Ell, U. Morgner, F.X. Kärtner, J.G. Fujimoto, E.P. Ippen, V. Scheuer, G. Angelow, T. Tschudi, *Opt. Lett.* **26**, 373-375 (2001)



- [58] E.J. Mayer, J. Möbius, A. Euteneuer, W.W. Rühle, R. Szipöcs, *Opt. Lett.* **22**, 528 (1997).
- [59] K. O. Hill, F. Bilodeau, B. Malo, T. Kitagawa, S. Theriault, D. C. Johnson, J. Albert, K. Takiguch, *Opt. Lett.* **19**, 1314-1316 (1994).
- [60] A. V. Tikhonravov, M. K. Trubetskov, A. A. Tikhonravov, *OSA Topical Meeting on Optical Interference Coatings*, Tucson Arizona, February 7-12, 1998.
- [61] B. Golubovic, R. R. Austin, M. K. Steiner-Shepard, M. K. Reed, S. A. Diddams, D. J. Jones and A. G. Van Engen, *Opt. Lett.* vol. 25, pp. 175-278, 2000.
- [62] R. Szipöcs, G. DeBell, A. V. Tikhonravov, M. K. Trubetskov, *Ultrafast Optics Conference*, Ascona Switzerland, July 11-16, 1999.
- [63] M. Matsuhara, K. O. Hill, *Applied Optics* **13**, 2886-2888 (1974).
- [64] G. Tempea, V. Yakovlev, B. Bacovic, F. Krausz, and K. Ferencz, *J. Opt. Soc. Am. B* **18**, 1747-50 (2001).
- [65] N. Matuschek, L. Gallmann, D. H. Sutter, G. Steinmeyer, and U. Keller, *Appl. Phys. B* **71**, 509-522 (2000).
- [66] G. Steinmeyer, *Conference on Lasers and Electro-Optics, Cleo 2003*, Baltimore, June 2-6th, 2003.
- [67] J. A. Dobrowolski, A. V. Tikhonravov, M. K. Trubetskov, B. T. Sullivan, and P. G. Verly, *Appl. Opt.* **35**, 644-658, (1996).
- [68] A. Apolonski, A. Poppe, G. Tempea, C. Spielmann, T. Udem, R. Holzwarth, T. Hänsch, and F. Krausz, *Phys.Rev.Lett.* **85**, 740 (2000).
- [69] R. Szipöcs and A. Kohazi-Kis, *Applied Physics B* **65**, 115-135 (1997).
- [70] V. Laude and P. Tournois, paper CTuR4, *Conference on Lasers and Electrooptics*, Baltimore, USA, (1999).
- [71] R. Szipöcs, A. Köházi-Kis, S. Lakó, P. Apai, A. P. Kovács, G. DeBell, L. Mott, A. W. Louderback, A. V. Tikhonravov, M. K. Trubetskov, *Applied Physics B* **70**, S51-557 (2000).

- [72] N. Matuschek, F.X. Kärtner, U. Keller, IEEE Journal of Quantum Electronics ,JQE- **5**, 129-137 (1999).
- [73] V. Scheuer, M. Tilsch, and T. Tschudi, SPIE Conf. Proc.**2253**, 445-454,(1994).
- [74] M. Tilsch, V. Scheuer, and T. Tschudi, SPIE Conf. Proc.**2253**, 414-422 (1994).
- [75] F. X. Kärtner, U. Morgner, T. R. Schibli, E. P. Ippen J. G. Fujimoto, V. Scheuer, G. Angelow and T. Tschudi, J. of the Opt. Soc. of Am. **18**, 882-885 (2001).
- [76] K. Naganuma, K. Mogi, H. Yamada, Opt. Lett. **15**, 393 (1990).
- [77] I. Walmsley, L. Waxer, C. Dorrer: The role of dispersion in ultrafast optics, Rev. Scient. Instrum. **72** 1-29 (2001)
- [78] J. Zhou, G. Taft, C.-P. Huang, M.M. Murnane, H.C. Kapteyn, I.P. Christov: Pulse evolution in a broad-bandwidth Ti:sapphire laser, Opt. Lett. **19** 1149-1151 (1994)
- [79] R. Szipöcs, K. Ferencz, C. Spielmann, and F. Krausz: Chirped multi-layer coatings for broadband dispersion control in femtosecond lasers, Opt. Lett. **19** 201-203 (1994)
- [80] N. Matuschek, F. X. Kärtner, U. Keller: Theory of double-chirped mirrors, IEEE J. Select. Topics Quantum Electron. **4** 197-208 (1998)
- [81] G. Tempea, F. Krausz, Ch. Spielmann, K. Ferencz: Dispersion control over 150 THz with chirped dielectric mirrors, IEEE J. Select. Topics Quantum Electron. **4** 193-196 (1998)
- [82] F.X. Kärtner, N. Matuschek, T. Schibli, U. Keller, H.A. Haus, C. Heine, R. Morf, V. Scheuer, M. Tilsch, T. Tschudi: Design and fabrication of double-chirped mirrors, Opt. Lett. **22** 831-833 (1997)
- [83] A.M. Weiner, D.E. Leaird, J.S. Patel, J.R. Wullert: Programmable femtosecond pulse shaping by use of a multielement liquid-crystal phase modulator, Opt. Lett. **15** 326-328 (1990)

- [84] D. Yelin, D. Meshulach, Y. Silberberg: Adaptive femtosecond pulse compression, *Opt. Lett.* **22** 1793-1795 (1997)
- [85] N. Karasawa, L. Li, A. Suguro, H. Shigekawa, R. Morita, M. Yamashita: Optical pulse compression to 5.0 fs by use of only a spatial light modulator for phase compensation, *J. Opt. Soc. Am. B* **18** 1742-1746 (2001)
- [86] C. Iaconis, I.A. Walmsley: Self-referencing spectral interferometry for measuring ultrashort optical pulses, *IEEE J. Quantum Electron.* **35** 501-509 (1999)
- [87] A.M. Weiner: Femtosecond pulse shaping using spatial light modulators, *Rev. Scient. Instrum.* **71** 1929-1960 (2000)
- [88] C. Dorrer, F. Salin, F. Verluise, J.P. Huignard: Programmable phase control of femtosecond pulses by use of a nonpixelated spatial light modulator, *Opt. Lett.* **23** 709-711 (1998)
- [89] M.A. Dugan, J.X. Tull, W.S. Warren: High-resolution acousto-optic shaping of unamplified and amplified femtosecond laser pulses, *J. Opt. Soc. Am. B* **14** 2348-2358 (1997)
- [90] P. Tournois: Acousto-optic programmable dispersive filter for adaptive compensation of group delay time dispersion in laser systems, *Optics Comm.* **140** 245-249 (1997)
- [91] F. Verluise, V. Laude, Z. Cheng, Ch. Spielmann, P. Tournois: Amplitude and phase control of ultrashort pulses by use of an acousto-optic programmable dispersive filter: pulse compression and shaping, *Opt. Lett.* **25** 575-577 (2000)
- [92] J.P. Heritage, E.W. Chase, R.N. Thurston, M. Stern: A simple femtosecond optical third-order disperser, in *Conference on Lasers and Electro-Optics*, Vol. 10 of 1991 OSA Technical Digest Series (Optical Society of America, Washington, D.C., 1991), paper CTuB3.
- [93] E. Zeek, K. Maginnis, S. Backus, U. Russek, M.M. Murnane, G. Mourou, H. Kapteyn, G. Vdovin: Pulse compression by use of deformable mirrors, *Opt. Lett.* **24** 493-495 (2000)

- [94] A. Baltuška, T. Fuji, T. Kobayashi: Visible pulse compression to 4 fs by optical parametric amplification and programmable dispersion control, *Opt. Lett.* **27** 306-308 (2002)
- [95] E.A.J. Marcatili, R.A. Schmelzter: Hollow metallic and dielectric waveguide for long distance optical transmission and laser, *Bell Syst. Tech. J.* **43** 1783-1809 (1964)
- [96] E.-G. Neumann: *Single-Mode Fibers* (Springer-Verlag, Berlin 1988)
- [97] M. Nisoli, S. Stagira, S. De Silvestri, O. Svelto, S. Sartania, Z. Cheng, M. Lenzner, Ch. Spielmann, F. Krausz: A novel high energy pulse compression system: generation of multigigawatt sub-5-fs pulses, *Appl. Phys. B* **65** 189-196 (1997)
- [98] M. Nisoli, E. Priori, G. Sansone, S. Stagira, G. Cerullo, S. De Silvestri, C. Altucci, R. Bruzzese, C. de Lisio, P. Villoresi, L. Poletto, M. Pascolini, G. Tondello: High-Brightness High-Order Harmonic Generation by Truncated Bessel Beams in the Sub-10-fs Regime, *Phys. Rev. Lett.* **88** 33902-1-4 (2002)
- [99] T. Brabec, F. Krausz: Nonlinear Optical Pulse Propagation in the Single-Cycle Regime, *Phys. Rev. Lett.* **78** 3282-3285 (1997)
- [100] S. Stagira, E. Priori, G. Sansone, M. Nisoli, S. De Silvestri, Ch. Gadermaier: Nonlinear guided propagation of few-optical-cycle laser pulses with arbitrary polarization state, *Phys. Rev. A* (in press) (2002)
- [101] H.J. Lehmeier, W. Leupacher, A. Penzkofer: Nonresonant third order hyperpolarizability of rare gases and N<sub>2</sub> determined by third order harmonic generation, *Opt. Commun.* **56** 67-72 (1985)
- [102] A. Dalgarno, A. E. Kingston: The refractive indices and Verdet constants of the inert gases, *Proc. R. Soc. London Ser. A* **259** 424-429 (1966)
- [103] R. W. Boyd, *Nonlinear Optics*, Academic Press, San Diego (1992)
- [104] G. Tempea, T. Brabec: Theory of self-focusing in a hollow waveguide, *Opt. Lett.* **23**, 762-764 (1998)

- [105] S. De Silvestri, M. Nisoli, G. Sansone, S. Stagira, and O. Svelto, "Few-Cycle Pulses by External Compression" in "Few-Cycle Pulse Generation and Its Applications, Ed. by F. X. Kaertner, Springer Verlag, 2004.
- [106] T. Brabec, F. Krausz: Intense few-cycle laser fields: frontiers of nonlinear optics, *Rev. Mod. Phys.* **72** 545-591 (2000)
- [107] D. E. Spence, P. N. Kean, W. Sibbett: 60-fsec pulse generation from a self-mode-locked Ti:sapphire laser, *Opt. Lett.* **16** 42-44 (1991)
- [108] D. Strickland, G. Mourou: Compression of amplified chirped optical pulses, *Opt. Commun.* **56** 219-221 (1985)

# Chapter 4

## Laser Dynamics

Before starting to look into the dynamics of lasers, we need to better understand the nature of laser gain media. Therefore, we review the most simple model of an atomic system that can provide gain to an optical field, the two-level model. We study first the interaction with a coherent laser field via the Bloch Equations and rederive step by step the classical susceptibility model including possible inversion of the medium. This model will provide a physical basis for the most important parameters of a gain medium. This will prepare us for the study of "single-mode" dynamics of a laser. The term "single-mode" is set in apostrophes, since it doesn't have to be really single-mode. There can be several longitudinal modes running, for example due to spatial holeburning and other effects, but in an incoherent fashion, so that only the average power of the beam matters. For a more detailed account on single-mode laser dynamics and Q-Switching the following references are recommended. [5][7][16][8][9].

### 4.1 Two-Level Atoms and Bloch Equations

The most basic microscopic model for a medium is the two-level model. For an indepth discussion the reader is referred to the book of Allen and Eberly [2].

Atoms in low concentration show line spectra as found in gas-, dye- and some solid-state laser media. Usually, there are infinitely many energy eigenstates in an atomic, molecular or solid-state medium and the spectral lines are associated with allowed transitions between two of these energy eigen-

states. For many physical considerations it is already sufficient to take only two of the possible energy eigenstates into account, for example those which are related to the laser transition. The pumping of the laser can be described by phenomenological relaxation processes into the upper laser level and out of the lower laser level. The resulting simple model is often called a two-level atom, which is mathematically also equivalent to a spin  $1/2$  particle in an external magnetic field, because the spin can only be parallel or anti-parallel to the field, i.e. it has two energy levels and energy eigenstates in the magnetic field. The interaction of the two-level atom or the spin with the electric or magnetic field is described by the Bloch equations.

### 4.1.1 The Two-Level Model

An atom with only two energy eigenvalues is described by a two-dimensional state space spanned by the two energy eigenstates  $|e\rangle$  and  $|g\rangle$ . The two states constitute a complete orthonormal system. The corresponding energy eigenvalues are  $E_e$  and  $E_g$ , see Fig. 4.1.

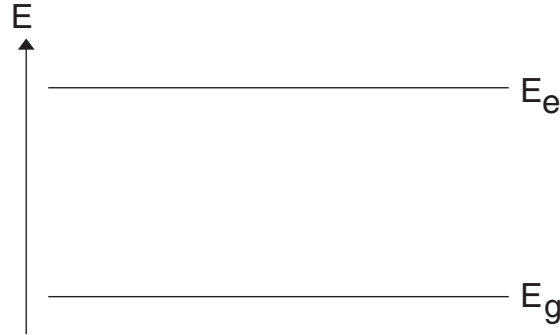


Figure 4.1: Two-level atom

In the position-, i.e.  $x$ -representation, these states correspond to the wave functions

$$\psi_g(x) = \langle x | g \rangle, \quad \text{and} \quad \psi_e(x) = \langle x | e \rangle. \quad (4.1)$$

The Hamiltonian operator of the two-level atom is in the energy representation given by

$$\mathbf{H}_A = E_e |e\rangle \langle e| + E_g |g\rangle \langle g|. \quad (4.2)$$

The states  $|e\rangle$  and  $|g\rangle$  build an orthormal system in this two-dimensional state space

$$\langle e|e\rangle = \langle g|g\rangle = 1 \text{ and } \langle g|e\rangle = \langle e|g\rangle^* = 0 \quad (4.3)$$

and the unity matrix can be expressed as

$$\mathbf{1} = |e\rangle \langle e| + |g\rangle \langle g|, \quad (4.4)$$

An arbitrary state of the two level system is a superposition state

$$|\psi\rangle = c_g |g\rangle + c_e |e\rangle. \quad (4.5)$$

It is convenient to separate off from the Hamiltonian (4.1) the term  $(E_e + E_g)/2 \cdot \mathbf{1}$ , where  $\mathbf{1}$  denotes the unity matrix, we rescale the energy values correspondingly and obtain for the Hamiltonian of the two-level system

$$\mathbf{H}_A = \frac{1}{2} \hbar \omega_{eg} \boldsymbol{\sigma}_z, \quad (4.6)$$

with the transition frequency

$$\omega_{eg} = \frac{1}{\hbar} (E_e - E_g). \quad (4.7)$$

The Shroedinger equation of the free two level system is then given by

$$\mathbf{j} \hbar \frac{d}{dt} |\psi\rangle = \mathbf{H}_A |\psi\rangle. \quad (4.8)$$

or after projecting out with the corresponding bra-vectors we find

$$\frac{d}{dt} c_e = -\mathbf{j} \frac{\omega_{eg}}{2} c_e, \quad (4.9)$$

$$\frac{d}{dt} c_g = +\mathbf{j} \frac{\omega_{eg}}{2} c_g. \quad (4.10)$$

Thus the coefficients of ground and excited state undergo harmonic oscillations in its phases

$$c_e(t) = e^{-\mathbf{j} \frac{\omega_{eg}}{2} t} c_e(0), \quad (4.11)$$

$$c_g(t) = e^{+\mathbf{j} \frac{\omega_{eg}}{2} t} c_g(0), \quad (4.12)$$

however their individual magnitudes don't change, i.e. the probabilities that we find the two-level atom in the excited or ground state stay constant and with it the inversion of the two level systems defined as

$$w = |c_e|^2 - |c_g|^2 = \text{const.} \quad (4.13)$$

stays constant. If we consider an ensemble of  $N$  atoms the total inversion would be  $W = N \langle \psi | \boldsymbol{\sigma}_z | \psi \rangle$ .



### 4.1.2 The Atom-Field Interaction In Dipole Approximation

The dipole moment of an atom  $\vec{\mathbf{d}}$  is determined by the position operator  $\vec{\mathbf{x}}$  via

$$\vec{\mathbf{d}} = -e_0 \vec{\mathbf{x}}. \quad (4.14)$$

Then the expectation value for the dipole moment of an atom in state (4.5) is

$$\begin{aligned} \langle \psi | \vec{\mathbf{d}} | \psi \rangle &= -e_0 (|c_e|^2 \langle e | \vec{\mathbf{x}} | e \rangle + c_e c_g^* \langle g | \vec{\mathbf{x}} | e \rangle \\ &+ c_g c_e^* \langle e | \vec{\mathbf{x}} | g \rangle + |c_g|^2 \langle g | \vec{\mathbf{x}} | g \rangle). \end{aligned} \quad (4.15)$$

For simplicity, we may assume that the medium is an atomic gas. The atoms possess inversion symmetry, therefore, energy eigenstates must be symmetric or anti-symmetric, i.e.  $\langle e | \vec{\mathbf{x}} | e \rangle = \langle g | \vec{\mathbf{x}} | g \rangle = 0$ . We obtain

$$\vec{\mathbf{d}} = \langle \psi | \vec{\mathbf{d}} | \psi \rangle = -e_0 (c_e c_g^* \langle g | \vec{\mathbf{x}} | e \rangle + c_g c_e^* \langle e | \vec{\mathbf{x}} | g \rangle). \quad (4.16)$$

Note, this means there is no permanent dipole moment in an atom, which is in an energy eigenstate. This might not be the case in a solid. The atoms constituting the solid are oriented in a lattice, which may break the symmetry. If so, there are permanent dipole moments and consequently the matrix elements  $\langle e | \vec{\mathbf{x}} | e \rangle$  and  $\langle g | \vec{\mathbf{x}} | g \rangle$  would not vanish.

An atom does only exhibit a dipole moment, if the product  $c_e c_g^* \neq 0$ , i.e. the state of the atom is in a superposition of states  $|e\rangle$  and  $|g\rangle$ . With the dipole matrix elements

$$\vec{\mathbf{M}} = \langle e | \vec{\mathbf{d}} | g \rangle = -e_0 \langle e | \vec{\mathbf{x}} | g \rangle \quad (4.17)$$

the expectation value for the dipole moment can be written as

$$\vec{\mathbf{d}} = \langle \psi | \vec{\mathbf{d}} | \psi \rangle = c_g c_e^* \vec{\mathbf{M}} + c_e c_g^* \vec{\mathbf{M}}^*. \quad (4.18)$$

This is true for an arbitrary superposition state, therefore the dipole operator is represented by the dyadic products

$$\vec{\mathbf{d}} = \vec{\mathbf{M}} |e\rangle \langle g| + \vec{\mathbf{M}}^* |g\rangle \langle e|. \quad (4.19)$$

The energy of a classical electric dipole with dipole moment  $\vec{\mathbf{d}}$  in an electric field is

$$\mathbf{H}_{A-F} = -\vec{\mathbf{d}} \cdot \vec{\mathbf{E}}(\vec{\mathbf{x}}_A, t). \quad (4.20)$$

We assume that the electric field is due to a monochromatic electromagnetic wave. Then the electric field at the position of the atom,  $\vec{x}_A$ , can be written as

$$\vec{E}(\vec{x}_A, t) = \vec{E}(t) = \frac{1}{2} (\underline{E}_0 e^{j\omega t} \vec{e}_p + \underline{E}_0^* e^{-j\omega t} \vec{e}_p^*), \quad (4.21)$$

where  $\underline{E}_0$  denotes the complex electric field amplitude at the position of the atom and  $\vec{e}_p$  is the polarization vector of the wave. The atom-field interaction Hamiltonian operator is then

$$\mathbf{H}_{A-F} = -\vec{\mathbf{d}} \cdot \vec{E}(t) \quad (4.22)$$

The Shroedinger equation of the two level system driven by the classical field is then given by

$$j\hbar \frac{d}{dt} |\psi\rangle = (\mathbf{H}_A + \mathbf{H}_{A-F}) |\psi\rangle.$$

and again after projecting out the equations of motion for the coefficients by multiplying from the right with the bra-vectors we obtain

$$\frac{d}{dt} c_e = -j \frac{\omega_{eg}}{2} c_e + j \frac{\vec{M} \cdot \vec{E}(t)}{\hbar} c_g, \quad (4.23)$$

$$\frac{d}{dt} c_g = +j \frac{\omega_{eg}}{2} c_g + j \frac{\vec{M}^* \cdot \vec{E}(t)}{\hbar} c_e. \quad (4.24)$$

### 4.1.3 Rabi-Oscillations

If the incident light has a constant field amplitude,  $\underline{E}_0$ , and if the light frequency is close to resonance to the atomic transition frequency  $\omega \approx \omega_{eg}$ , Eqs. (4.23) and (4.24) can be solved and we observe an oscillation in the population difference, the Rabi-oscillation [1]. To show this we introduce the detuning between field and atomic resonance

$$\Delta = \frac{\omega_{eg} - \omega}{2} \quad (4.25)$$

and the new probability amplitudes

$$C_e = c_e e^{j\frac{\omega}{2}t}, \quad (4.26)$$

$$C_g = c_g e^{-j\frac{\omega}{2}t}. \quad (4.27)$$

This leads to the new system of equations

$$\frac{d}{dt}C_e = -j\Delta C_e + j\frac{\Omega_r^*}{2}C_g, \quad (4.28)$$

$$\frac{d}{dt}C_g = +j\Delta C_g + j\frac{\Omega_r}{2}C_e. \quad (4.29)$$

with the Rabi-frequency  $\Omega_r$  defined as

$$\Omega_r = \frac{\vec{M}^* \cdot \vec{e}_p}{\hbar} (\underline{E}_0 + \underline{E}_0^* e^{-j2\omega t}). \quad (4.30)$$

If the Rabi-frequency is small  $|\Omega_r| \ll \omega_{eg} \approx \omega$ , the Rotating-Wave Approximation (RWA) [4], can be used, where we only keep the slowly varying components in the interaction, i.e.

$$\Omega_r \approx \frac{\vec{M}_{eg}^* \cdot \vec{e}_p}{\hbar} \underline{E}_0 = \text{const.} \quad (4.31)$$

Note, that Eqs. (4.28) and (4.29) are then identical to coupled mode equations describing the energy exchange between two waveguide modes. But now the coupling is between modes in time, i.e. resonances. The modes are electronic ones instead of photonic modes. But otherwise the dynamics is exactly the same. For the case of vanishing detuning it is especially easy to eliminate one of the variables and we arrive at

$$\frac{d^2}{dt^2}C_e = -\frac{|\Omega_r|^2}{4}C_e \quad (4.32)$$

$$\frac{d^2}{dt^2}C_g = -\frac{|\Omega_r|^2}{4}C_g. \quad (4.33)$$

The solution to this set of equations are population oscillations. If the atom is at time  $t = 0$  in the ground-state, i.e.  $C_g(0) = 1$  and  $C_e(0) = 0$ , respectively, we arrive at

$$C_g(t) = \cos\left(\frac{|\Omega_r|}{2}t\right) \quad (4.34)$$

$$C_e(t) = -j \sin\left(\frac{|\Omega_r|}{2}t\right). \quad (4.35)$$

Then, the probabilities for finding the atom in the ground or excited state are

$$|c_b(t)|^2 = \cos^2\left(\frac{|\Omega_r|}{2}t\right) \quad (4.36)$$

$$|c_a(t)|^2 = \sin^2\left(\frac{|\Omega_r|}{2}t\right), \quad (4.37)$$

as shown in Fig. 4.2. For the expectation value of the dipole operator under the assumption of a real dipole matrix element  $\vec{M} = \vec{M}^*$  we obtain

$$\vec{d} = \langle \psi | \vec{d} | \psi \rangle = \vec{M} c_g c_e^* + c.c. \quad (4.38)$$

$$= -\vec{M} \sin(|\Omega_r|t) \sin(\omega_{eg}t). \quad (4.39)$$

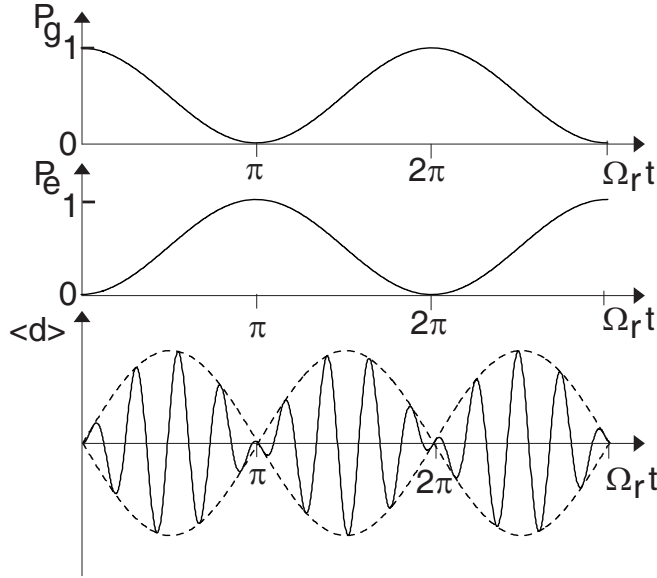


Figure 4.2: Evolution of occupation probabilities of ground and excited state and the average dipole moment of a two-level atom in resonant interaction with a coherent classical field.

The coherent external field drives the population of the atomic system between the two available states with a period  $T_r = 2\pi/\Omega_r$ . Applying the field only over half of this period leads to a complete inversion of the population.

Applying the field only over half of this period leads to a complete inversion of the population. The population inversion is defined as

$$w = P_e - P_g = |c_e|^2 - |c_g|^2 \quad (4.40)$$

These Rabi-oscillations have been observed in various systems ranging from gases to semiconductors. Interestingly, the light emitted from the coherently driven two-level atom is not identical in frequency to the driving field. If we look at the Fourier spectrum of the polarization according to Eq.(4.39), we obtain lines at frequencies  $\omega_{\pm} = \omega_{eg} \pm |\Omega_r|$ . This is clearly a nonlinear output and the sidebands are called Mollow-sidebands [3]. Most important for the existence of these oscillations is the coherence of the atomic system over at least one Rabi-oscillation. If this coherence is destroyed before significant population between the levels is exchanged, the Rabi-oscillations cannot happen and it is then impossible to generate inversion in a two-level system by interaction with light. This is the case for a large class of situations in light-matter interaction and especially for typical laser materials. So we are interested in finding out what happens in the case of loss of coherence in the atomic system due to additional interaction of the atoms with its environment. These non energy preserving processes can not be easily included in the Schroedinger Equation formalism. However, we can treat these processes phenomenologically in the equations of motion for the expectation values of the dipole moment and the population inversion, which are of interest because those quantities feed back into Maxwell's Equations as a driving term.

From the equations of motion for the coefficients of the wave function Eqs. (4.23) and (4.24) we derive equations of motion for the complex slowly varying dipole moment defined as

$$\underline{d} = c_e^* c_g e^{-j\omega t} = C_e^* C_g. \quad (4.41)$$

and by applying the product rule we find

$$\frac{d}{dt} \underline{d} = \left( \frac{d}{dt} C_e^* \right) C_g + C_e^* \left( \frac{d}{dt} C_g \right) \quad (4.42)$$

$$= j\Delta C_e^* C_g - j\frac{\Omega_r}{2} C_g^* C_g + j\Delta C_e^* C_g + j\frac{\Omega_r}{2} C_e^* C_e \quad (4.43)$$

$$= j2\Delta \underline{d} + j\frac{\Omega_r}{2} \cdot w \quad (4.44)$$

and

$$\frac{d}{dt}w = \left(\frac{d}{dt}C_e\right)C_e^* - \left(\frac{d}{dt}C_g\right)C_g^* + c.c. \quad (4.45)$$

$$= \left(-j\Delta C_e C_e^* + j\frac{\Omega_r^*}{2}C_g C_e^* - j\Delta C_g C_g^* - j\frac{\Omega_r}{2}C_e C_g^*\right) + c.c. \quad (4.46)$$

$$= +j\Omega_r^* \underline{d} + c.c \quad (4.47)$$

For the monochromatic wave of Eq.(4.21) and neglecting terms varying at twice the optical frequency, we find

$$\frac{d}{dt}\underline{d} = j(\omega_{eg} - \omega)\underline{d} + j\Omega_r \cdot w \quad (4.48)$$

$$\frac{d}{dt}w = +j\Omega_r^* \underline{d} + c.c \quad (4.49)$$

#### 4.1.4 Energy- and Phase-Relaxation

In reality it is extremely difficult to completely isolate an atom from its environment. Indeed in the case of laser active media, we are interested in radiating atoms, i.e. atoms that have a dipole interaction with the field. These atoms do then not only interact with the driving field, but for example also with all the electromagnetic modes of the environment. The environment can be considered as a large box, the universe, which contains the atom. We are interested in the equations of motion for the expectation value of the dipole moment and the population inversion of an atom that interacts in an uncontrolled fashion with the modes of the universe. Without derivation, the quantum mechanical treatment of interaction of the atom with these free space modes leads to spontaneous emission of photons into these modes, i.e. energy decay in the two-level system. The coupling with the infinitely many modes of the free field leads already to spontaneous emission, an irreversible process. We could treat this process by using the Hamiltonian

$$\mathbf{H} = \mathbf{H}_A + \mathbf{H}_F + \mathbf{H}_{A-F}. \quad (4.50)$$

Here,  $\mathbf{H}_A$  is the Hamiltonian of the atom,  $\mathbf{H}_F$  of the free field in thermal equilibrium at temperature  $T$ , and  $\mathbf{H}_{A-F}$  describes the interaction between them. A complete treatment along these lines would be straight forward using the techniques we learned so far, however it is beyond the scope of this

class. The result of this calculation leads to damping of inversion and with it the polarization. For the case of a two-level atom in thermal equilibrium with its electromagnetic environment there is a change in the excited state population due to induced and spontaneous emission with the rate  $\Gamma_e$  and an increase of excited states by absorption of thermal photons

$$\frac{d}{dt}|c_e(t)|^2 = -\Gamma_e|c_e(t)|^2 + \Gamma_a|c_g(t)|^2 \quad (4.51)$$

with the abbreviations

$$\Gamma_e = \frac{1}{\tau_{sp}}(n_{th} + 1), \quad (4.52)$$

$$\Gamma_a = \frac{1}{\tau_{sp}}n_{th}. \quad (4.53)$$

see Figure 4.3.

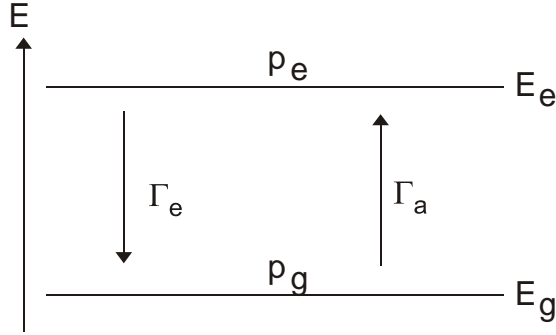


Figure 4.3: Two-level atom with transition rates due to induced and spontaneous emission and absorption.

Here  $n_{th}$  is the number of thermally excited photons in the modes of the free field with frequency  $\omega_{eg}$ ,  $n_{th} = 1/(\exp(\hbar\omega_{eg}/kT) - 1)$ , at temperature  $T$ .

The total probability of being in the excited or the ground state has to be maintained, that is

$$\frac{d}{dt}|c_g(t)|^2 = -\frac{d}{dt}|c_e(t)|^2 = \Gamma_e|c_e(t)|^2 - \Gamma_a|c_g(t)|^2. \quad (4.54)$$

If the populations decay, the polarization does also decay, since  $\underline{d} = c_e^*c_g e^{-j\omega t}$ . It turns out that the polarization dynamics according to Eq.(4.48), besides

the coherent oscillation, also acquires a decay process due to the finite lifetime of the excited state

$$\frac{d}{dt}\underline{d} = j(\omega_{eg} - \omega)\underline{d} - \frac{\Gamma_e + \Gamma_a}{2}\underline{d}. \quad (4.55)$$

Thus the absorption as well as the emission processes are destructive to the phase. Therefore, the corresponding rates add up in the phase decay rate.

In total the equation for the dipole moment  $d = d_r + jd_i$  and the inversion  $w$  can be written as

$$\dot{\underline{d}} = (j(\omega_{eg} - \omega) - \frac{1}{T_2})\underline{d}, \quad (4.56)$$

$$\dot{w} = |c_e(t)|^2 - |c_g(t)|^2 = -\frac{w - w_0}{T_1}, \quad (4.57)$$

with the time constants

$$\frac{1}{T_1} = \frac{2}{T_2} = \Gamma_e + \Gamma_a = \frac{2n_{th} + 1}{\tau_{sp}} \quad (4.58)$$

and the equilibrium inversion  $w_0$ , due to the thermal excitation of the atom by the thermal field

$$w_0 = \frac{\Gamma_a - \Gamma_e}{\Gamma_a + \Gamma_e} = \frac{-1}{1 + 2n_{th}} = -\tanh\left(\frac{\hbar\omega_{eg}}{2kT}\right). \quad (4.59)$$

The time constant  $T_1$  denotes the energy relaxation in the two-level system and  $T_2$  the phase relaxation.  $T_2$  is the correlation time between amplitudes  $c_e$  and  $c_g$ . The coherence between the excited and the ground state described by the dipole moment is destroyed by the interaction of the two-level system with the environment.

In this basic model, the energy relaxation is half the phase relaxation rate or

$$T_2 = 2T_1. \quad (4.60)$$

The atoms in a laser medium do not only interact with the electromagnetic field, but also with phonons, i.e. acoustic vibrations of the host lattice in solid state laser material. Atoms might collide with each other in a gas laser and so on. All these processes must be considered when determining the energy and phase relaxation rates. Thus it might be not only radiative transitions that lead to a finite energy relaxation time  $T_1$ . Some of the processes are elastic,



i.e. there is no energy relaxation but only the phase is influenced during the collision. Therefore, these processes reduce  $T_2$  but have no influence on  $T_1$ . In real systems the phase relaxation time is most often much shorter than twice the energy relaxation time.

$$T_2 \leq 2T_1. \quad (4.61)$$

If the inversion deviates from its equilibrium value,  $w_0$ , it relaxes back into equilibrium with a time constant  $T_1$ . Eq. (4.59) shows that for all temperatures  $T > 0$  the inversion is negative, i.e. the lower level is stronger populated than the upper level. Thus with incoherent thermal light, inversion in a two-level system cannot be achieved. Inversion can only be achieved by pumping with incoherent light, if there are more levels and subsequent relaxation processes into the upper laser level. Due to these relaxation processes the rate  $\Gamma_a$  deviates from the equilibrium expression (4.53), and it has to be replaced by the pump rate  $\Lambda$ . If the pump rate  $\Lambda$  exceeds  $\Gamma_e$ , the inversion corresponding to Eq. (4.59) becomes positive,

$$w_0 = \frac{\Lambda - \Gamma_e}{\Lambda + \Gamma_e}. \quad (4.62)$$

If we allow for artificial negative temperatures, we obtain with  $T < 0$  for the ratio of relaxation rates

$$\frac{\Gamma_e}{\Gamma_a} = \frac{1 + \bar{n}}{\bar{n}} = e^{\frac{\hbar\omega_{eg}}{kT}} < 1. \quad (4.63)$$

Thus the pumping of the two-level system drives the system far away from thermal equilibrium. Now, we have a correct description of an ensemble of atoms in thermal equilibrium with its environment, which is a much more realistic description of media especially of typical laser media.

### 4.1.5 The Bloch Equations

Thus, the total dynamics of the two-level system including the pumping and dephasing processes from Eqs.(4.56) and (4.57) is given by

$$\dot{\underline{d}} = -\left(\frac{1}{T_2} - j(\omega_{eg} - \omega)\right)\underline{d} + j\frac{\Omega_r}{2} w, \quad (4.64)$$

$$\dot{w} = -\frac{w - w_0}{T_1} + j\Omega_r^* \underline{d} - j\Omega_r \underline{d}^*. \quad (4.65)$$

These equations are called the Bloch Equations. They describe the dynamics of a statistical ensemble of two-level atoms interacting with a classical electric field. Together with the Maxwell-Equations, where the polarization of the medium is related to the expectation value of the dipole moment of the atomic ensemble these result in the Maxwell-Bloch Equations.

#### 4.1.6 Dielectric Susceptibility and Saturation

The Bloch Equations are nonlinear. However, for moderate field strength  $\underline{E}_0$ , i.e. the magnitude of the Rabi-frequency is much smaller than the optical frequency,  $|\Omega_r| \ll \omega$ , the inversion does not change much within an optical cycle of the field. We assume that the inversion  $w$  of the atom will only be slowly changing and it adjusts itself to a steady state value  $w_s$ . Similarly the complex slowly varying dipole moment will reach the steady state

$$\underline{d}_s = \frac{j}{2\hbar} \frac{(\vec{M}^* \cdot \vec{e}_p) w_s}{1/T_2 + j(\omega - \omega_{eg})} \underline{E}_0 \quad (4.66)$$

$$w_s = \frac{w_0}{1 + \frac{T_1}{\hbar^2} \frac{1/T_2 |\vec{M}^* \cdot \vec{e}_p|^2}{(1/T_2)^2 + (\omega_{eg} - \omega)^2} |\underline{E}_0|^2}. \quad (4.67)$$

We introduce the normalized lineshape function, which is in this case a Lorentzian,

$$L(\omega) = \frac{(1/T_2)^2}{(1/T_2)^2 + (\omega_{eg} - \omega)^2}, \quad (4.68)$$

and connect the square of the field  $|\underline{E}_0|^2$  to the intensity  $I$  of a propagating plane wave, according to Eq. (2.35),  $I = \frac{1}{2Z_F} |\underline{E}_0|^2$ ,

$$w_s = \frac{w_0}{1 + \frac{I}{I_s} L(\omega)}. \quad (4.69)$$

Thus the stationary inversion depends on the intensity of the incident light. Therefore,  $w_0$  is called the unsaturated inversion,  $w_s$  the saturated inversion and  $I_s$ , with

$$I_s = \left[ \frac{2T_1 T_2 Z_F}{\hbar^2} |\vec{M}^* \cdot \vec{e}_p|^2 \right]^{-1}, \quad (4.70)$$

is the saturation intensity. The expectation value of the dipole operator (4.14) is then given by

$$\langle \tilde{\mathbf{d}} \rangle = \vec{M} \underline{d} e^{j\omega t} + \vec{M}^* \underline{d}^* e^{-j\omega t}. \quad (4.71)$$

Multiplication with the number of atoms per unit volume,  $N$ , relates the dipole moment of the atom to the polarization  $\vec{P}$ . As the electric field, the polarization can be written in terms of complex quantities,  $\underline{\vec{P}}$  of the medium, and therefore to the susceptibility according to

$$\vec{P}(t) = \frac{1}{2} \left( \underline{\vec{P}}_0 e^{j\omega t} + \underline{\vec{P}}_0^* e^{-j\omega t} \right) \quad (4.72)$$

$$= N(\vec{M}\underline{d} e^{j\omega t} + \vec{M}\underline{d}^* e^{-j\omega t}) \quad (4.73)$$

or

$$\underline{\vec{P}}_0 = 2N\vec{M}\underline{d}, \quad (4.74)$$

$$\underline{\vec{P}}_0 = \epsilon_0 \chi(\omega) \vec{e}_p \underline{E}_0. \quad (4.75)$$

From the definitions (4.74), (4.75) and Eq. (4.66) we obtain for the linear susceptibility of the medium

$$\chi(\omega) = \vec{M}\vec{M}^+ \frac{jN}{\hbar\epsilon_0} \frac{w_s}{1/T_2 + j(\omega - \omega_{eg})}, \quad (4.76)$$

which is a tensor. In the following we assume that the direction of the atom is random, i.e. the alignment of the atomic dipole moment,  $\vec{M}$ , and the electric field is random. Therefore, we have to average over the angle enclosed between the electric field of the wave and the atomic dipole moment, which results in

$$\overline{\begin{pmatrix} M_x M_x & M_x M_y & M_x M_z \\ M_y M_x & M_y M_y & M_y M_z \\ M_z M_x & M_z M_y & M_z M_z \end{pmatrix}} = \begin{pmatrix} \overline{M_x^2} & 0 & 0 \\ 0 & \overline{M_y^2} & 0 \\ 0 & 0 & \overline{M_z^2} \end{pmatrix} = \frac{1}{3} |\vec{M}|^2 \mathbf{1}. \quad (4.77)$$

Thus, for homogeneous and isotropic media the susceptibility tensor shrinks to a scalar

$$\chi(\omega) = \frac{1}{3} |\vec{M}|^2 \frac{jN}{\hbar\epsilon_0} \frac{w_s}{1/T_2 + j(\omega - \omega_{eg})}. \quad (4.78)$$

Real and imaginary part of the susceptibility

$$\chi(\omega) = \chi'(\omega) + j\chi''(\omega) \quad (4.79)$$

are then given by

$$\chi'(\omega) = -\frac{|\vec{M}|^2 N w_s T_2^2 (\omega_{eg} - \omega)}{3\hbar\epsilon_0} L(\omega), \quad (4.80)$$

$$\chi''(\omega) = \frac{|\vec{M}|^2 N w_s T_2}{3\hbar\epsilon_0} L(\omega). \quad (4.81)$$

If the incident radiation is weak, i.e.

$$\frac{I}{I_s} L(\omega) \ll 1 \quad (4.82)$$

we obtain  $w_s \approx w_0$ . For optical transitions there is no thermal excitation of the excited state and  $w_0 = -1$ . For an inverted system,  $w_0 > 0$ , the real and imaginary parts of the susceptibility are shown in Fig. 4.4.

The shape of the susceptibility computed quantum mechanically compares well with the classical susceptibility (2.42) derived from the harmonic oscillator model close to the transition frequency  $\omega_{eg}$  for a transition with reasonably high  $Q = T_2\omega_{eg}$ . Note, the quantum mechanical susceptibility is identical to the complex Lorentzian introduced in Eq.(2.94). There is an appreciable deviation, however, far away from resonance. Far off resonance the rotating wave approximation should not be used.

The physical meaning of the real and imaginary part of the susceptibility is of course identical to section 2.4.2. The propagation constant  $k$  of a TEM-wave in such a medium is related to the susceptibility by

$$k = \omega \sqrt{\mu_0 \epsilon_0 (1 + \chi(\omega))} \approx k_0 \left( 1 + \frac{1}{2} \chi(\omega) \right), \quad \text{with} \quad k_0 = \omega \sqrt{\mu_0 \epsilon_0} \quad (4.83)$$

for  $|\chi| \ll 1$ . Under this assumption we obtain

$$k = k_0 \left( 1 + \frac{\chi'}{2} \right) + j k_0 \frac{\chi''}{2}. \quad (4.84)$$

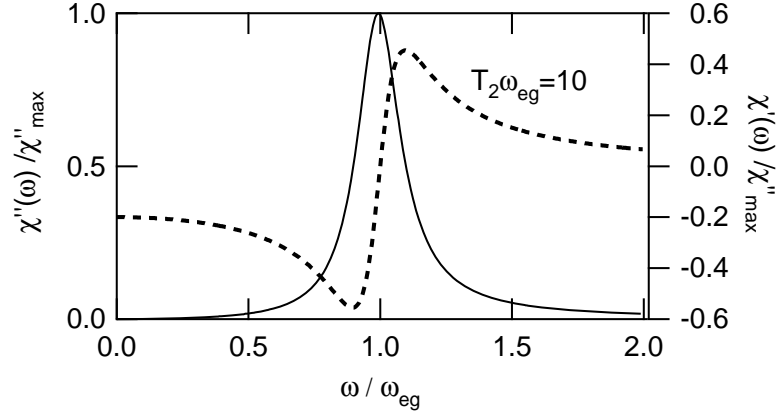


Figure 4.4: Real and imaginary part of the complex susceptibility for an inverted medium  $w_s > 0$ . The positive imaginary susceptibility indicates exponential growth of an electromagnetic wave propagating in the medium.

The real part of the susceptibility contributes to the refractive index  $n = 1 + \chi'/2$ . In the case of  $\chi'' < 0$ , the imaginary part leads to an exponential damping of the wave. For  $\chi'' > 0$  amplification takes place. Amplification of the wave is possible for  $w_0 > 0$ , i.e. an inverted medium.

The phase relaxation rate  $1/T_2$  of the dipole moment determines the width of the absorption line or the bandwidth of the amplifier. The amplification can not occur forever, because the amplifier saturates when the intensity reaches the saturation intensity. This is a strong deviation from the linear susceptibility we derived from the classical oscillator model. The reason for this saturation is two fold. First, the light can not extract more energy from the atoms then there is energy stored in them, i.e. energy conservation holds. Second the induced dipole moment in a two-level atom is limited by the maximum value of the matrix element. In contrast the induced dipole moment in a classical oscillator grows proportionally to the applied field without limits.

#### 4.1.7 Rate Equations and Cross Sections

In many cases the fastest process in the atom-field interaction dynamics is the dephasing of the dipole moment, i. e.  $T_2 \rightarrow 0$ . For example, in semi-conductors  $T_2 < 50fs$ . In those cases the magnitude of the dipole moment

relaxes instantaneously into the steady state and follows the slowly varying field envelope  $E_0(t)$  electromagnetic field, which evolves on a much slower time scale. We obtain with the quasi steady state solution for the dipole moment (4.66), which may now have a slow time dependence due to the slowly varying field envelope  $E_0(t)$ , for the time dependent inversion in the atomic system

$$\dot{w} = -\frac{w(t) - w_0}{T_1} - \frac{w(t)}{T_1 I_s} L(\omega) I(t), \quad (4.85)$$

where  $I(t) = |E_0(t)|^2 / (2Z_F)$  is the intensity of the electromagnetic wave interacting with the two-level atom. In this limit the Bloch Equations became simple rate equations. We only take care of the counting of population differences due to spontaneous and stimulated emissions.

The interaction of an atom with light at a given transition with the stream of photons on resonance, i.e.  $\omega = \omega_{eg}$  is often described by the mass action law. That is, the number of induced transitions from the excited to the ground state, is proportional to the product of the number of atoms in the excited state and the photon flux density  $I_{ph} = I / \hbar \omega_{eg}$

$$\dot{w}|_{induced} = -\sigma w I_{ph} = -\frac{w}{T_1 I_s} I. \quad (4.86)$$

This defines an interaction cross section  $\sigma$  that can be expressed in terms of the saturation intensity as

$$\sigma = \frac{\hbar \omega_{eg}}{T_1 I_s} \quad (4.87)$$

$$= \frac{2\omega_{eg} T_2 Z_F}{\hbar} |\vec{M}^* \cdot \vec{e}_p|^2. \quad (4.88)$$

In this chapter, we have introduced the most important spectroscopic quantities that characterize an atomic transition, which are the lifetime of the excited state or often called upper-state lifetime or longitudinal lifetime  $T_1$ , the phase relaxation time or transverse relaxation time  $T_2$  which is the inverse half-width at half maximum of the line and the interaction cross-section  $\sigma$  that only depends on the dipole matrix element and the linewidth of the transition.

The imaginary part of the susceptibility, which indicates gain or loss is proportional to the inversion in the atomic system, see Eq.(4.76), which also

depends on the field strength or intensity according to the rate equation (4.85)

$$\frac{\partial g(z, t)}{\partial t} = -\frac{g - g_0}{\tau_L} - g \frac{I(z, t)}{E_L}. \quad (4.89)$$

Here,  $E_L = I_s \tau_L$  is called the saturation fluence of the gain medium and  $\tau_L$  the upper state life time of the gain medium.

## 4.2 Laser Rate Equations

After having derived the quantum mechanically correct expression for the gain in an inverted atomic system, we can use the two-level model to study the laser and its dynamics. After discussing the laser concept briefly we will discuss the dynamics of lasers, threshold behavior, steady state behavior, relaxation oscillations and Q-switching.

As we discussed before inversion can not be achieved in a two level system by optical pumping. The coherent regime is typically inaccessible by typical optical pump sources. Inversion by optical pumping can only be achieved when using a three or four-level system, see Figures 4.5 and 4.6

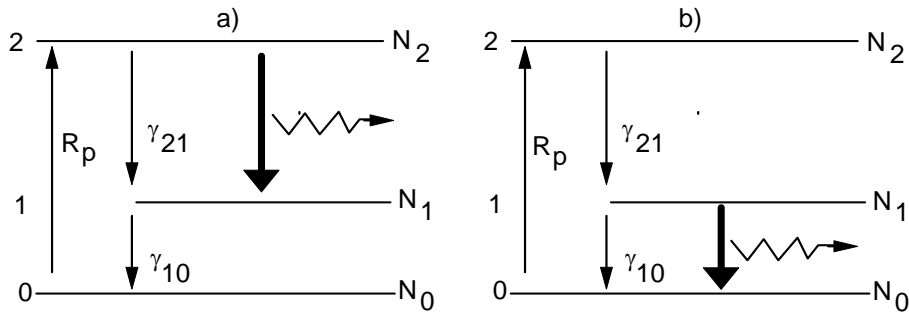


Figure 4.5: Three-level laser medium.

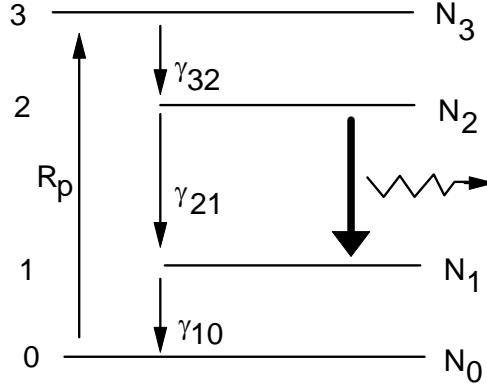


Figure 4.6: Four-level laser medium.

If the medium is in thermal equilibrium, typically only the ground state is occupied. By optical pumping with an intense lamp (flash lamp) or another laser one can pump a significant fraction of the atoms from the ground state with population  $N_0$  into the excited state  $N_3$  both for the three level laser operating according to the scheme shown in figure 140 (a) or  $N_4$  in the case of the four level laser, see Figure 4.6. If the relaxation rate  $\gamma_{10}$  is very fast compared to  $\gamma_{21}$ , where the laser action should occur inversion can be achieved, i.e.  $N_2 > N_1$ . For the four level laser the relaxation rate  $\gamma_{32}$  should also be fast in comparison to  $\gamma_{21}$ . These systems are easy to analyze in the rate equation approximation, where the dipole moments are already adiabatically eliminated. For example, for the three level system in Figure 4.5 a). we obtain the rate equations of the three level system in analogy to the two-level system

$$\frac{d}{dt}N_2 = -\gamma_{21}N_2 - \sigma_{21}(N_2 - N_1)I_{ph} + R_p \quad (4.90)$$

$$\frac{d}{dt}N_1 = -\gamma_{10}N_1 + \gamma_{21}N_2 + \sigma_{21}(N_2 - N_1)I_{ph} \quad (4.91)$$

$$\frac{d}{dt}N_0 = \gamma_{10}N_1 - R_p \quad (4.92)$$

Here,  $\sigma_{21}$  is the cross section for stimulated emission between the levels 2 and 1 and  $I_{ph}$  is the photon flux at the transition frequency  $f_{21}$ . In most cases, there are any atoms available in the ground state such that optical pumping



can never deplete the number of atoms in the ground state  $N_0$ . That is why we can assume a constant pump rate  $R_p$ . If the relaxation rate  $\gamma_{10}$  is much faster than  $\gamma_{21}$  and the number of possible stimulated emission events that can occur  $\sigma_{21} (N_2 - N_1) I_{ph}$ , then we can set  $N_1 = 0$  and obtain only a rate equation for the upper laser level

$$\frac{d}{dt}N_2 = -\gamma_{21} \left( N_2 - \frac{R_p}{\gamma_{21}} \right) - \sigma_{21} N_2 \cdot I_{ph}. \quad (4.93)$$

This equation is identical to the equation for the inversion of the two-level system, see Eq.(4.85). Here,  $\frac{R_p}{\gamma_{21}}$  is the equilibrium upper state population in the absence of photons,  $\gamma_{21} = \frac{1}{\tau_L}$  is the inverse upper state lifetime due to radiative and non radiative processes.

Note, a similar analysis can be done for the three level laser operating according to the scheme shown in Figure 4.5 (b). Then the relaxation rate from level 3 to level 2, which is now the upper laser level has to be fast. But in addition the optical pumping must be so strong that essentially all the ground state levels are depleted. Undepleted groundstate populations will lead to absorption of laser radiation.

For the following, we assume a homogenously broadend laser medium (four level with depeleted lower laser level) and only one cavity mode is able to lase. We want to derive the equations of motion for the population inversion, or population in the upper laser level Eq.(4.93) and the photon number in that mode, see Figure 4.7.

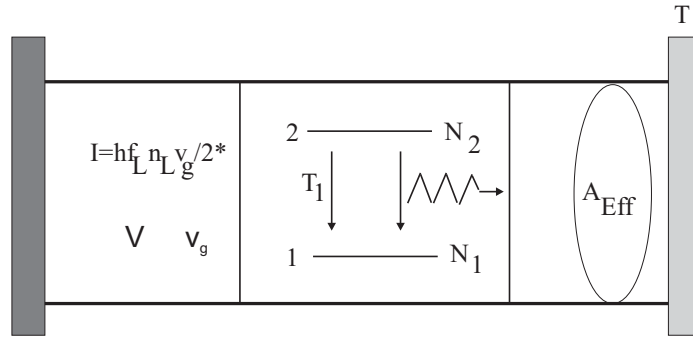


Figure 4.7: Rate equations for a laser with two-level atoms and a linear resonator.

The intensity  $I$  in a mode propagating at group velocity  $v_g$  in one direction with a mode volume  $V$  is related to the number of photons  $N_L$  stored in the mode with volume  $V$  by

$$I = hf_L \frac{N_L}{2^* V} v_g = \frac{1}{2^*} hf_L n_L v_g, \quad (4.94)$$

where  $hf_L$  is the photon energy.  $2^* = 2$  for a linear laser resonator (then only half of the photons are going in one direction), and  $2^* = 1$  for a ring laser. In this first treatment we consider the case of space-independent rate equations, i.e. we assume that the laser is oscillating on a single mode and pumping and mode energy densities are uniform within the laser material. With the interaction cross section  $\sigma$  defined as

$$\sigma = \frac{hf_L}{I_s \tau_L}, \quad (4.95)$$

we rewrite the rate equation Eq. (4.93) for the inversion or upper state population

$$\frac{d}{dt} N_2 = -\frac{N_2}{T_1} - \frac{\sigma v_g}{V} N_2 N_L + R_p \quad (4.96)$$

Note,  $v_g N_L / V$  is the photon flux, thus  $\sigma$  is the stimulated emission cross section between the atoms and the photons.  $R_p$  is the pumping rate into the upper laser level. A similar rate equation can be derived for the photon density

$$\frac{d}{dt} N_L = -\frac{N_L}{\tau_p} + \frac{\sigma v_g}{V} N_2 (N_L + 1) \quad (4.97)$$

Here,  $\tau_p$  is the photon lifetime in the cavity or cavity decay time. The 1 in the term  $(N_L + 1)$  in Eq.(4.97) accounts for spontaneous emission which is equivalent to stimulated emission induced by one photon occupying the mode. For a laser cavity with a semi-transparent mirror with transmission  $T$ , producing a small power loss  $2l = -\ln(1-T) \approx T$  (for small  $T$ ) per round-trip in the cavity, the cavity decay time is  $\tau_p = T_R / 2l$ , if  $T_R = 2^* L / v_g$  is the roundtrip-time in linear cavity with length  $2L$  or a ring cavity with length  $L$ . Internal losses can be treated in a similar way and contribute to the cavity decay time. Note, the decay rate for the inversion in the absence of a field,  $1/T_1$ , is not only due to spontaneous emission, but is also a result of non radiative decay processes. For a laser gain medium we usually denote  $T_1$  as

the upperstate lifetime  $\tau_L$

$$\frac{d}{dt}N_2 = -\frac{N_2}{\tau_L} - \sigma v_g N_2 n_L + R_p \quad (4.98)$$

$$\frac{d}{dt}N_L = -\frac{N_L}{\tau_p} + \frac{\sigma v_g}{V} N_2 (N_L + 1). \quad (4.99)$$

Experimentally, the photon number and the inversion in a laser resonator are not the quantities directly measured. We therefore introduce the circulating intracavity power and the roundtrip gain

$$P = I \cdot A_{eff} = h f_L \frac{N_L}{T_R}, \quad (4.100)$$

$$g = \frac{\sigma v_g}{2V} N_2 T_R. \quad (4.101)$$

The intracavity power is directly proportional to the output power from the laser

$$P_{out} = T \cdot P. \quad (4.102)$$

From Eqs.(4.98) and (4.99) for inversion and photon number, we obtain

$$\frac{d}{dt}g = -\frac{g - g_0}{\tau_L} - \frac{gP}{E_{sat}} \quad (4.103)$$

$$\frac{d}{dt}P = -\frac{1}{\tau_p}P + \frac{2g}{T_R}(P + P_{vac}), \quad (4.104)$$

with

$$E_{sat} = \frac{h f_L V}{\sigma v_g T_R} = \frac{1}{2^*} I_s A_{eff} \tau_L \quad (4.105)$$

$$P_{sat} = E_{sat} / \tau_L \quad (4.106)$$

$$P_{vac} = h f_L / T_R \quad (4.107)$$

$$g_0 = 2^* \frac{R_p}{2 A_{eff}} \sigma \tau_L, \quad (4.108)$$

Note, the factor of two in front of gain and loss is due to the fact, that we defined  $g$  and  $l$  as gain and loss with respect to amplitude. Eq.(4.108) elucidates that the figure of merit that characterizes the small signal gain achievable in a laser connected with the spectroscopic parameters of the laser gain medium is the  $\sigma \cdot \tau_L$ -product. The larger this product the larger is the small signal gain  $g_0$  achievable with a certain laser material. Table 4.1

Laser Medium	Wave-length $\lambda_0$ (nm)	Cross Section $\sigma$ (cm <sup>2</sup> )	Upper-St. Lifetime $\tau_L$ ( $\mu$ s)	Linewidth $\Delta f_{FWHM}$ $\frac{2}{T_2}$ (THz)	Typ	Refr. index $n$
Nd <sup>3+</sup> :YAG	1,064	$4.1 \cdot 10^{-19}$	1,200	0.210	H	1.82
Nd <sup>3+</sup> :LSB	1,062	$1.3 \cdot 10^{-19}$	87	1.2	H	1.47
Nd <sup>3+</sup> :YLF	1,047	$1.8 \cdot 10^{-19}$	450	0.390	H	1.82
Nd <sup>3+</sup> :YVO <sub>4</sub>	1,064	$2.5 \cdot 10^{-19}$	50	0.300	H	2.19
Nd <sup>3+</sup> :glass	1,054	$4 \cdot 10^{-20}$	350	3	H/I	1.5
Er <sup>3+</sup> :glass	1,55	$6 \cdot 10^{-21}$	10,000	4	H/I	1.46
Ruby	694.3	$2 \cdot 10^{-20}$	1,000	0.06	H	1.76
Ti <sup>3+</sup> :Al <sub>2</sub> O <sub>3</sub>	660-1180	$3 \cdot 10^{-19}$	3	100	H	1.76
Cr <sup>3+</sup> :LiSAF	760-960	$4.8 \cdot 10^{-20}$	67	80	H	1.4
Cr <sup>3+</sup> :LiCAF	710-840	$1.3 \cdot 10^{-20}$	170	65	H	1.4
Cr <sup>3+</sup> :LiSGAF	740-930	$3.3 \cdot 10^{-20}$	88	80	H	1.4
He-Ne	632.8	$1 \cdot 10^{-13}$	0.7	0.0015	I	$\sim 1$
Ar <sup>+</sup>	515	$3 \cdot 10^{-12}$	0.07	0.0035	I	$\sim 1$
CO <sub>2</sub>	10,600	$3 \cdot 10^{-18}$	2,900,000	0.000060	H	$\sim 1$
Rhodamin-6G	560-640	$3 \cdot 10^{-16}$	0.0033	5	H	1.33
semiconductors	450-30,000	$\sim 10^{-14}$	$\sim 0.002$	25	H/I	3 - 4

Table 4.1: Wavelength range, cross-section for stimulated emission, upper-state lifetime, linewidth, typ of lineshape (H=homogeneously broadened, I=inhomogeneously broadened) and index for some often used solid-state laser materials, and in comparison with semiconductor and dye lasers.

### 4.3 Built-up of Laser Oscillation and Continuous Wave Operation

In many technical applications, where the dimensions of the laser is large compared to the wavelength and  $P_{vac} \ll P \ll P_{sat} = E_{sat}/\tau_L$ , we can neglect the spontaneous emission, i.e.  $P_{vac}$ . If the laser power is initially small, on the order of  $P_{vac}$ , and the gain is unsaturated,  $g = g_0$ , we obtain from Eq.(4.104),

$$\frac{dP}{P} = 2(g_0 - l) \frac{dt}{T_R} \quad (4.109)$$

or

$$P(t) = P(0)e^{2(g_0 - l)\frac{t}{T_R}}. \quad (4.110)$$

The laser power builds up from vacuum fluctuations, once the small signal gain surpasses the laser losses,  $g_0 > g_{th} = l$ , see Figure ??, until it reaches the saturation power. Saturation sets in within the built-up time

$$T_B = \frac{T_R}{2(g_0 - l)} \ln \frac{P_{sat}}{P_{vac}} = \frac{T_R}{2(g_0 - l)} \ln \frac{A_{eff} T_R}{\sigma \tau_L}. \quad (4.111)$$

Some time after the built-up phase the laser reaches steady state, with the saturated gain and steady state power resulting from Eqs.(4.103-4.104), neglecting in the following the spontaneous emission, and for  $\frac{d}{dt} = 0$  :

$$g_s = \frac{g_0}{1 + \frac{P_s}{P_{sat}}} = l \quad (4.112)$$

$$P_s = P_{sat} \left( \frac{g_0}{l} - 1 \right), \quad (4.113)$$

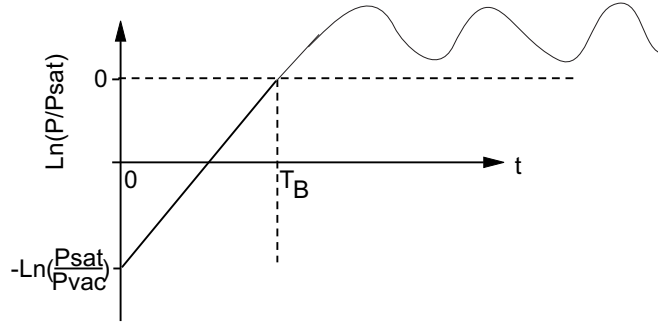


Figure 4.8: Built-up of laser power from spontaneous emission noise.

Figure 4.9 shows output power and gain as a function of small signal gain  $g_0$ , which is proportional to the pump rate  $R_p$ . Below threshold, the output power is zero and the gain increases linearly with increase pumping. After

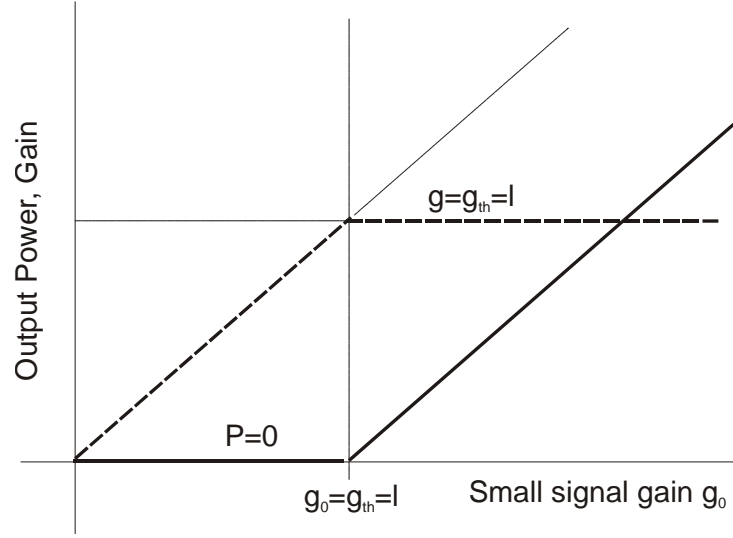


Figure 4.9: Output power and gain of a laser as a function of pump power.

reaching threshold the gain stays clamped at the threshold value determined by gain equal loss and the output power increases linearly. The threshold condition is again

$$g_{th} = l, \quad (4.114)$$

$$R_{p,th} = \frac{2lA_{eff}}{2^*\sigma\tau_L}. \quad (4.115)$$

Thus the pump rate to reach threshold is proportional to the optical loss of the mode per roundtrip, the mode cross section (in the gain medium) and inverse proportional to the  $\sigma \cdot \tau_L$ -product.

## 4.4 Stability and Relaxation Oscillations

How does the laser reach steady state, once a perturbation has occurred?

$$g = g_s + \Delta g \quad (4.116)$$

$$P = P_s + \Delta P \quad (4.117)$$

Substitution into Eqs.(4.103-4.104) and linearization leads to

$$\frac{d\Delta P}{dt} = +2\frac{P_s}{T_R}\Delta g \quad (4.118)$$

$$\frac{d\Delta g}{dt} = -\frac{g_s}{E_{sat}}\Delta P - \frac{1}{\tau_{stim}}\Delta g \quad (4.119)$$

where  $\frac{1}{\tau_{stim}} = \frac{1}{\tau_L} \left(1 + \frac{P_s}{P_{sat}}\right)$  is the stimulated lifetime. The perturbations decay or grow like

$$\begin{pmatrix} \Delta P \\ \Delta g \end{pmatrix} = \begin{pmatrix} \Delta P_0 \\ \Delta g_0 \end{pmatrix} e^{st}. \quad (4.120)$$

which leads to the system of equations (using  $g_s = l$ )

$$A \begin{pmatrix} \Delta P_0 \\ \Delta g_0 \end{pmatrix} = \begin{pmatrix} -s & 2\frac{P_s}{T_R} \\ -\frac{T_R}{E_{sat}2\tau_p} & -\frac{1}{\tau_{stim}} - s \end{pmatrix} \begin{pmatrix} \Delta P_0 \\ \Delta g_0 \end{pmatrix} = 0. \quad (4.121)$$

There is only a solution, if the determinante of the coefficient matrix vanishes, i.e.

$$s \left( \frac{1}{\tau_{stim}} + s \right) + \frac{P_s}{E_{sat}\tau_p} = 0, \quad (4.122)$$

which determines the relaxation rates or eigen frequencies of the linearized system

$$s_{1/2} = -\frac{1}{2\tau_{stim}} \pm \sqrt{\left(\frac{1}{2\tau_{stim}}\right)^2 - \frac{P_s}{E_{sat}\tau_p}}. \quad (4.123)$$

Introducing the pump parameter  $r = 1 + \frac{P_s}{P_{sat}}$ , which tells us how often we pump the laser over threshold, the eigen frequencies can be rewritten as

$$s_{1/2} = -\frac{1}{2\tau_{stim}} \left( 1 \pm j \sqrt{\frac{4(r-1)\tau_{stim}}{r\tau_p} - 1} \right), \quad (4.124)$$

$$= -\frac{r}{2\tau_L} \pm j \sqrt{\frac{(r-1)}{\tau_L\tau_p} - \left(\frac{r}{2\tau_L}\right)^2} \quad (4.125)$$

There are several conclusions to draw:

- (i): The stationary state  $(0, g_0)$  for  $g_0 < l$  and  $(P_s, g_s)$  for  $g_0 > l$  are always stable, i.e.  $\text{Re}\{s_i\} < 0$ .

- (ii): For lasers pumped above threshold,  $r > 1$ , and long upper state lifetimes, i.e.  $\frac{r}{4\tau_L} < \frac{1}{\tau_p}$ , the relaxation rate becomes complex, i.e. there are relaxation oscillations

$$s_{1/2} = -\frac{1}{2\tau_{stim}} \pm j\omega_R. \quad (4.126)$$

with frequency  $\omega_R$  equal to the geometric mean of inverse stimulated lifetime and photon life time

$$\omega_R = \sqrt{\frac{1}{\tau_{stim}\tau_p}}. \quad (4.127)$$

- If the laser can be pumped strong enough, i.e.  $r$  can be made large enough so that the stimulated lifetime becomes as short as the cavity decay time, relaxation oscillations vanish.

The physical reason for relaxation oscillations and later instabilities is, that the gain reacts to slow on the light field, i.e. the stimulated lifetime is long in comparison with the cavity decay time.

#### Example: diode-pumped Nd:YAG-Laser

$$\begin{aligned} \lambda_0 &= 1064 \text{ nm}, \sigma = 4 \cdot 10^{-20} \text{ cm}^2, A_{eff} = \pi (100\mu\text{m} \times 150\mu\text{m}), r = 50 \\ \tau_L &= 1.2 \text{ ms}, l = 1\%, T_R = 10 \text{ ns} \end{aligned}$$

From Eq.(4.95) we obtain:

$$\begin{aligned} I_{sat} &= \frac{hf_L}{\sigma\tau_L} = 3.9 \frac{\text{kW}}{\text{cm}^2}, P_{sat} = I_{sat}A_{eff} = 1.8 \text{ W}, P_s = 91.5 \text{ W} \\ \tau_{stim} &= \frac{\tau_L}{r} = 24\mu\text{s}, \tau_p = 1\mu\text{s}, \omega_R = \sqrt{\frac{1}{\tau_{stim}\tau_p}} = 2 \cdot 10^5 \text{ s}^{-1}. \end{aligned}$$

Figure 4.10 shows the typically observed fluctuations of the output of a solid-state laser with long upperstate life time of several 100  $\mu\text{s}$  in the time and frequency domain.



One can also define a quality factor for the relaxation oscillations by the ratio of imaginary to real part of the complex eigen frequencies 4.125

$$Q = \sqrt{\frac{4\tau_L}{\tau_p} \frac{(r-1)}{r^2}},$$

which can be as large as several thousand for solid-state lasers with long upper-state lifetimes in the millisecond range.

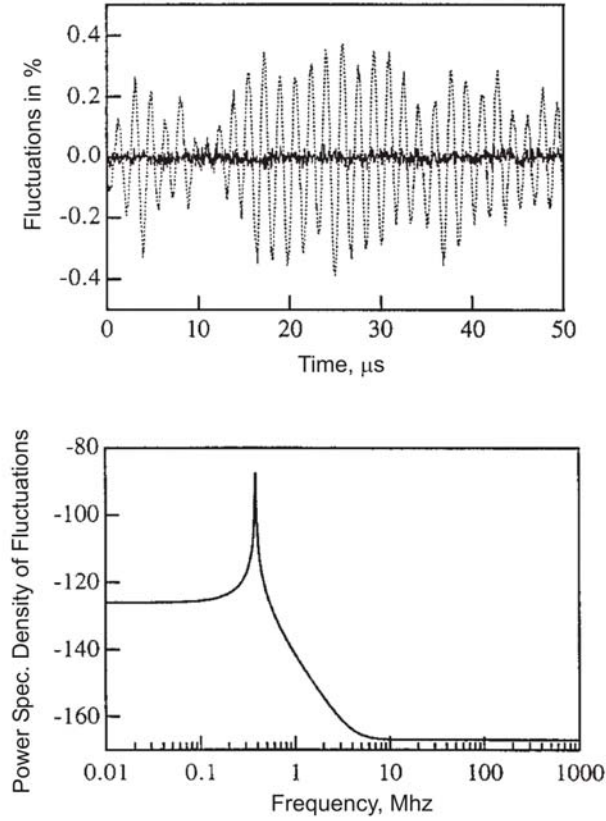


Figure 4.10: Typically observed relaxation oscillations in time and frequency domain.

## 4.5 Laser Efficiency

An important measure for a laser is the efficiency with which pump power is converted into laser output power. To determine the efficiency we must review the important parameters of a laser and the limitations these parameters impose.

From Eq.(4.113) we found that the steady state intracavity power  $P_s$  of a laser is

$$P_s = P_{sat} \left( \frac{2g_0}{2l} - 1 \right), \quad (4.128)$$

where  $2g_0$  is the small signal round-trip power gain,  $P_{sat}$  the gain saturation power and  $2l$  is the power loss per round-trip. Both parameters are expressed in Eqs.(4.105)-(4.108) in terms of the fundamental pump parameter  $R_p$ ,  $\sigma\tau_L$ -product and mode cross section  $A_{eff}$  of the gain medium. For this derivation it was assumed that all pumped atoms are in the laser mode with constant intensity over the beam cross section

$$2g_0 = 2^* \frac{R_p}{A_{eff}} \sigma\tau_L, \quad (4.129)$$

$$P_{sat} = \frac{hf_L}{2^* \sigma\tau_L} A_{eff} \quad (4.130)$$

The power losses of lasers are due to the internal losses  $2l_{int}$  and the transmission  $T$  through the output coupling mirror. The internal losses can be a significant fraction of the total losses. The output power of the laser is

$$P_{out} = T \cdot P_{sat} \left( \frac{2g_0}{2l_{int} + T} - 1 \right) \quad (4.131)$$

The pump power of the laser is given by

$$P_p = R_p hf_P, \quad (4.132)$$

where  $hf_P$  is the energy of the pump photons. In discussing the efficiency of a laser, we consider the overall efficiency

$$\eta = \frac{P_{out}}{P_p} \quad (4.133)$$

which approaches the differential efficiency  $\eta_D$  if the laser is pumped many times over threshold, i.e.  $r = 2g_0/2l \rightarrow \infty$

$$\eta_D = \frac{\partial P_{out}}{\partial P_p} = \eta(r \rightarrow \infty) \quad (4.134)$$

$$= \frac{T}{2l_{int} + T} P_{sat} \frac{2^*}{A_{eff} h f_P} \sigma \tau_L \quad (4.135)$$

$$= \frac{T}{2l_{int} + T} \cdot \frac{h f_L}{h f_P}. \quad (4.136)$$

Thus the efficiency of a laser is fundamentally limited by the ratio of output coupling to total losses and the quantum defect in pumping. Therefore, one would expect that the optimum output coupling is achieved with the largest output coupler, however, this is not true as we considered the case of operating many times above threshold.

## 4.6 Q-Switching

The energy stored in the laser medium can be released suddenly by increasing the Q-value of the cavity so that the laser reaches threshold. This can be done actively, for example by quickly moving one of the resonator mirrors in place or passively by placing a saturable absorber in the resonator [5, 16]. Hellwarth was first to suggest this method only one year after the invention of the laser. As a rough orientation for a solid-state laser, the following relation for the relevant time scales is generally valid

$$\tau_L \gg T_R \gg \tau_p. \quad (4.137)$$

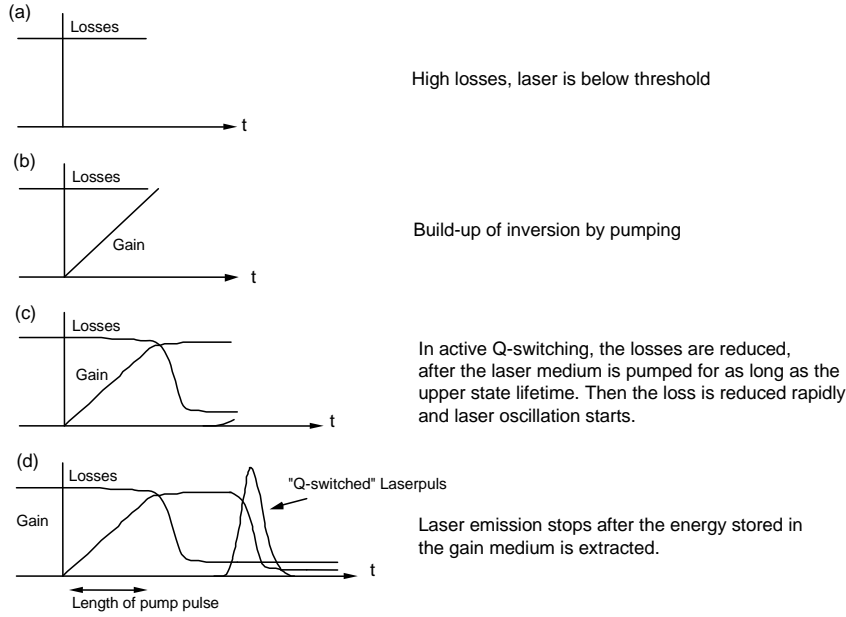


Figure 4.11: Gain and loss dynamics of a Q-switched laser.

Fig. 4.11 shows the principle dynamics of a Q-switched laser. The laser is pumped by a pump pulse with a length on the order of the upper-state lifetime, while the intracavity losses are kept high enough, so that the laser can not reach threshold. Therefore, the laser medium acts as an energy storage. The energy only relaxes by spontaneous and nonradiative transitions. Then suddenly the intracavity loss is reduced, for example by a rotating cavity mirror or by sudden saturation of the intracavity losses. The laser is pumped way above threshold and the light field builds up exponentially with the net gain until the pulse energy comes close to the saturation energy of the gain medium. The gain saturates and is extracted, so that the laser is shut off by the pulse itself.

A typical Q-switched pulse is asymmetric: The rise time is proportional to the net gain after the Q-value of the cavity is switches to a high value. The light intensity growths proportional to  $2g_0/T_R$ . When the gain is depleted, the fall time mostly depends on the cavity decay time  $\tau_p$ . For short Q-switched pulses a short cavity length, high gain and a large change in the cavity Q is necessary. If the Q-switching is not fast, the pulse width may be

limited by the speed of the switch. Typical switching times for electro-optical and acousto-optical active switches are 10 ns and 50 ns, respectively

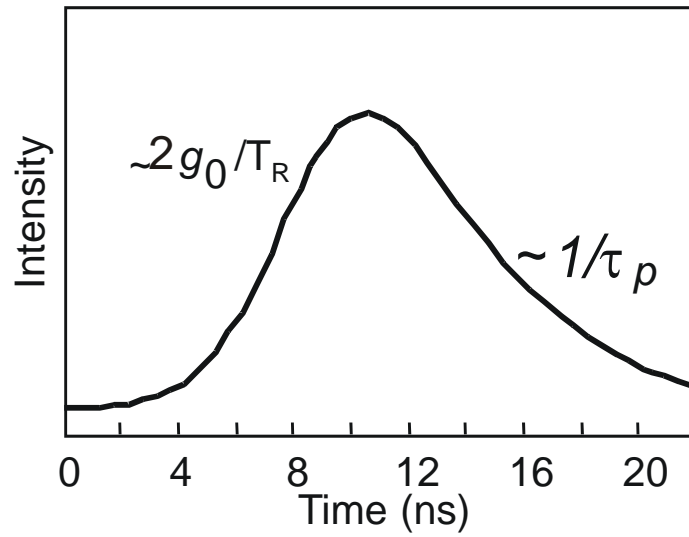


Figure 4.12: Asymmetric actively Q-switched pulse.

For example, with a diode-pumped Nd:YAG microchip laser [10] using an electro-optical switch based on  $LiTaO_3$  Q-switched pulses as short as 270 ps at repetition rates of 5 kHz, peak powers of 25 kW at an average power of 34 mW, and pulse energy of  $6.8 \mu\text{J}$  have been generated (Figure ??).

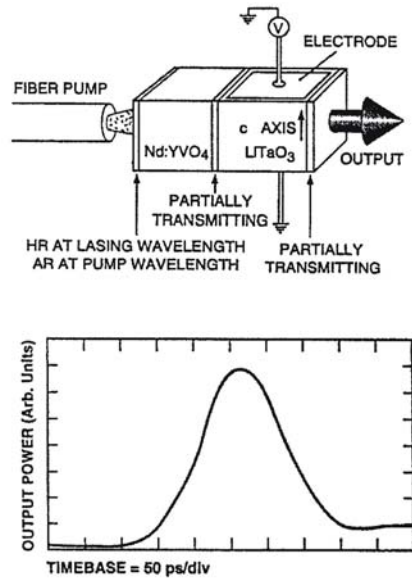


Figure 4.13: Q-switched microchip laser using an electro-optic switch. The pulse is measured with a sampling scope [12]

Similar results were achieved with Nd:YLF [11] and the corresponding setup is shown in Fig. 4.14.

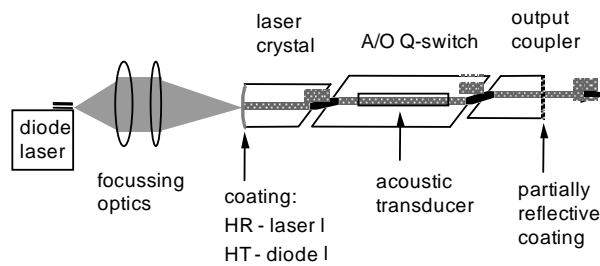


Figure 4.14: Set-up of an actively Q-switched laser.

### 4.6.1 Single-Frequency Q-Switched Pulses

Q-switched lasers only deliver stable output if they oscillate single frequency. Usually this is not automatically achieved. One method to achieve this is by seeding with a single-frequency laser during Q-switched operation, so that there is already a population in one of the longitudinal modes before the pulse is building up. This mode will extract all the energy before the other modes can do, see Figure 4.15

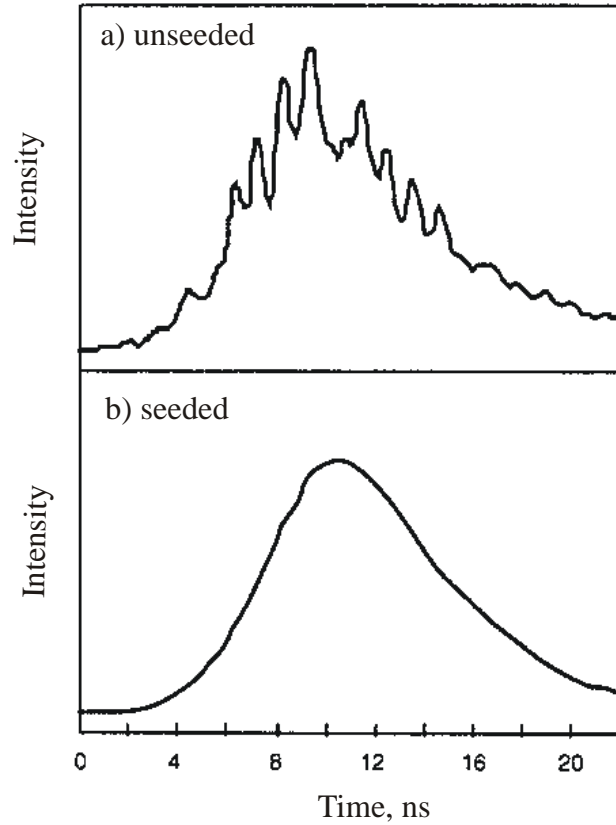


Figure 4.15: Output intensity of a Q-switched laser without a) and with seeding b).

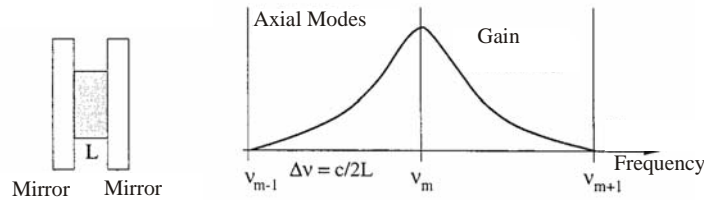


Figure 4.16: In a microchip laser the resonator can be so short, that there is only one longitudinal mode within the gain bandwidth.

Another possibility to achieve single-mode output is either using an etalon in the cavity or making the cavity so short, that only one longitudinal mode is within the gain bandwidth (Figure 4.16). This is usually only the case if the cavity length is on the order of a few millimeters or below. The microchip laser [10][15][14] can be combined with an electro-optic modulator to achieve very compact high peak power lasers with sub-nanosecond pulsewidth (Figure ??).



### 4.6.2 Active Q-Switching

We want to get some insight into the pulse built-up and decay of the actively Q-switched pulse. We consider the ideal situation, where the loss of the laser cavity can be instantaneously switched from a high value to a low value, i.e. the quality factor is switched from a low value to a high value, respectively (Figure: 4.17)

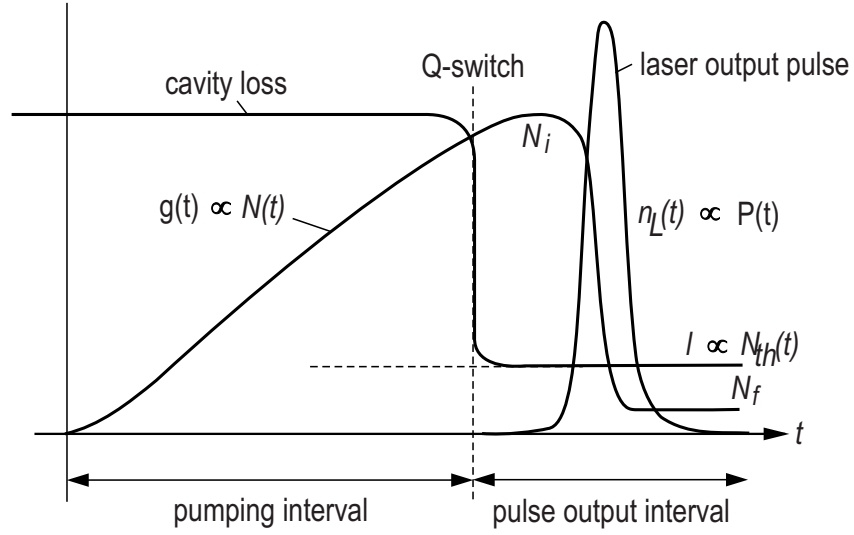


Figure 4.17: Active Q-Switching dynamics assuming an instantaneous switching [16].

#### Pumping Interval:

During pumping with a constant pump rate  $R_p$ , proportional to the small signal gain  $g_0$ , the inversion is built up. Since there is no field present, the gain follows the simple equation:

$$\frac{d}{dt}g = -\frac{g - g_0}{\tau_L}, \quad (4.138)$$

or

$$g(t) = g_0(1 - e^{-t/\tau_L}), \quad (4.139)$$

**Pulse Built-up-Phase:**

Assuming an instantaneous switching of the cavity losses we look for an approximate solution to the rate equations starting of with the initial gain or inversion  $g_i = hf_L N_{2i}/(2E_{sat}) = hf_L N_i/(2E_{sat})$ , we can safely leave the index away since there is only an upper state population. We further assume that during pulse built-up the stimulated emission rate is the dominate term changing the inversion. Then the rate equations simplify to

$$\frac{d}{dt}g = -\frac{gP}{E_{sat}} \quad (4.140)$$

$$\frac{d}{dt}P = \frac{2(g-l)}{T_R}P, \quad (4.141)$$

resulting in

$$\frac{dP}{dg} = \frac{2E_{sat}}{T_R} \left( \frac{l}{g} - 1 \right). \quad (4.142)$$

We use the following initial conditions for the intracavity power  $P(t=0) = 0$  and initial gain  $g(t=0) = g_i = r \cdot l$ . Note,  $r$  means how many times the laser is pumped above threshold after the Q-switch is operated and the intracavity losses have been reduced to  $l$ . Then 4.142 can be directly solved and we obtain

$$P(t) = \frac{2E_{sat}}{T_R} \left( g_i - g(t) + l \ln \frac{g(t)}{g_i} \right). \quad (4.143)$$

From this equation we can deduce the maximum power of the pulse, since the growth of the intracavity power will stop when the gain is reduced to the losses,  $g(t)=l$ , (Figure 4.17)

$$P_{\max} = \frac{2lE_{sat}}{T_R} (r - 1 - \ln r) \quad (4.144)$$

$$= \frac{E_{sat}}{\tau_p} (r - 1 - \ln r). \quad (4.145)$$

This is the first important quantity of the generated pulse and is shown normalized in Figure 4.18.

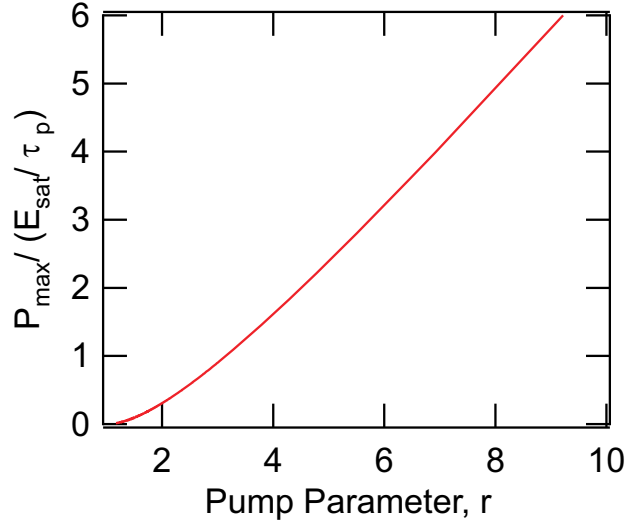


Figure 4.18: Peak power of emitted pulse as function of pump parameter.

Next, we can find the final gain  $g_f$ , that is reached once the pulse emission is completed, i.e. that is when the right side of (4.143) vanishes

$$\left( g_i - g_f + l \ln \left( \frac{g_f}{g_i} \right) \right) = 0 \quad (4.146)$$

Using the pump parameter  $r = g_i/l$ , this gives as an expression for the ratio between final and initial gain or between final and initial inversion

$$1 - \frac{g_f}{g_i} + \frac{1}{r} \ln \left( \frac{g_f}{g_i} \right) = 0, \quad (4.147)$$

$$1 - \frac{N_f}{N_i} + \frac{1}{r} \ln \left( \frac{N_f}{N_i} \right) = 0, \quad (4.148)$$

which depends only on the pump parameter. Assuming further, that there are no internal losses, then we can estimate the pulse energy generated by

$$E_P = (N_i - N_f) h f_L. \quad (4.149)$$

This is also equal to the output coupled pulse energy since no internal losses are assumed. Thus, if the final inversion gets small all the energy stored in

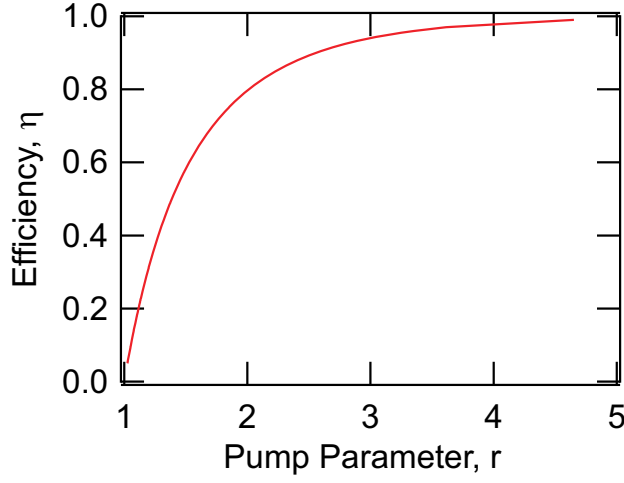


Figure 4.19: Energy extraction efficiency as a function of pump power.

the gain medium can be extracted. We define the energy extraction efficiency  $\eta$

$$\eta = \frac{N_i - N_f}{N_i}, \quad (4.150)$$

that tells us how much of the initially stored energy can be extracted using eq.(4.148)

$$\eta + \frac{1}{r} \ln(1 - \eta) = 0. \quad (4.151)$$

This efficiency is plotted in Figure 4.19.

Note, the energy extraction efficiency only depends on the pump parameter  $r$ . Now, the emitted pulse energy can be written as

$$E_P = \eta(r) N_i h f_L. \quad (4.152)$$

and we can estimate the pulse width of the emitted pulse by the ratio between pulse energy and peak power using (4.145) and (4.152)

$$\begin{aligned} \tau_{Pulse} &= \frac{E_P}{2lP_{peak}} = \tau_p \frac{\eta(r)}{(r - 1 - \ln r)} \frac{N_i h f_L}{2lE_{sat}} \\ &= \tau_p \frac{\eta(r)}{(r - 1 - \ln r)} \frac{g_i}{l} \\ &= \tau_p \frac{\eta(r) \cdot r}{(r - 1 - \ln r)}. \end{aligned} \quad (4.153)$$

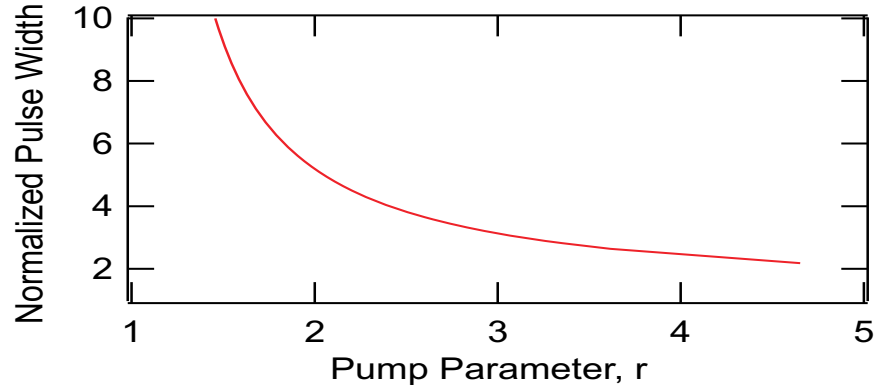


Figure 4.20: Normalized pulse width as a function of pump parameter.

The pulse width normalized to the cavity decay time  $\tau_p$  is shown in Figure 4.20.

### 4.6.3 Passive Q-Switching

In the case of passive Q-switching the intracavity loss modulation is performed by a saturable absorber, which introduces large losses for low intensities of light and small losses for high intensity.

Relaxation oscillations are due to a periodic exchange of energy stored in the laser medium by the inversion and the light field. Without the saturable absorber these oscillations are damped. If for some reason there is too much gain in the system, the light field can build up quickly. Especially for a low gain cross section the backaction of the growing laser field on the inversion is weak and it can grow further. This growth is favored in the presence of loss that saturates with the intensity of the light. The laser becomes unstable, the field intensity grows as long as the gain does not saturate below the net loss, see Fig.4.21.

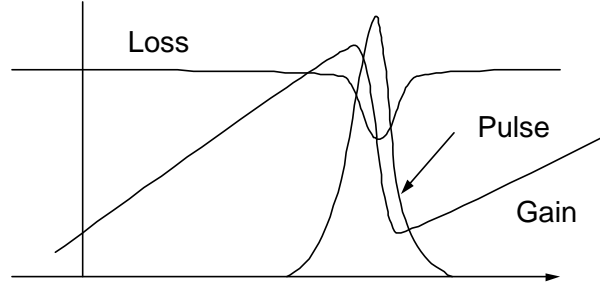


Figure 4.21: Gain and loss dynamics of a passively Q-switched laser

Now, we want to show that the saturable absorber leads to a destabilization of the relaxation oscillations resulting in the giant pulse laser.

We extend our laser model by a saturable absorber as shown in Fig. 4.22

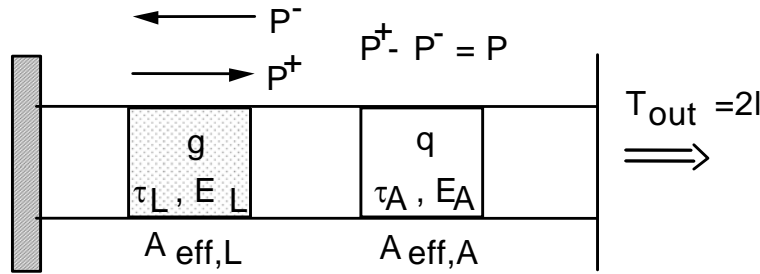


Figure 4.22: Simple laser model described by rate equations. We assume small output coupling so that the laser power within one roundtrip can be considered position independent. Neglecting standing wave effects in the cavity, the field density is related to twice the circulating power  $P^+$  or  $P^-$ .

### Rate equations for a passively Q-switched laser

We make the following assumptions: First, the transverse relaxation times of the equivalent two level models for the laser gain medium and for the saturable absorber are much faster than any other dynamics in our system, so that we can use rate equations to describe the laser dynamics. Second, we assume that the changes in the laser intensity, gain and saturable absorption

are small on a time scale on the order of the round-trip time  $T_R$  in the cavity, (i.e. less than 20%). Then, we can use the rate equations of the laser as derived above plus a corresponding equation for the saturable loss  $q$  similar to the equation for the gain.

$$T_R \frac{dP}{dt} = 2(g - l - q)P \quad (4.154)$$

$$T_R \frac{dg}{dt} = -\frac{g - g_0}{T_L} - \frac{gT_R P}{E_L} \quad (4.155)$$

$$T_R \frac{dq}{dt} = -\frac{q - q_0}{T_A} - \frac{qT_R P}{E_A} \quad (4.156)$$

where  $P$  denotes the laser power,  $g$  the amplitude gain per roundtrip,  $l$  the linear amplitude losses per roundtrip,  $g_0$  the small signal gain per roundtrip and  $q_0$  the unsaturated but saturable losses per roundtrip. The quantities  $T_L = \tau_L/T_R$  and  $T_A = \tau_A/T_R$  are the normalized upper-state lifetime of the gain medium and the absorber recovery time, normalized to the round-trip time of the cavity. The energies  $E_L = h\nu A_{eff,L}/2^*\sigma_L$  and  $E_A = h\nu A_{eff,A}/2^*\sigma_A$  are the saturation energies of the gain and the absorber, respectively. .

For solid state lasers with gain relaxation times on the order of  $\tau_L \approx 100 \mu s$  or more, and cavity round-trip times  $T_R \approx 10 \text{ ns}$ , we obtain  $T_L \approx 10^4$ . Furthermore, we assume absorbers with recovery times much shorter than the round-trip time of the cavity, i.e.  $\tau_A \approx 1 - 100 \text{ ps}$ , so that typically  $T_A \approx 10^{-4}$  to  $10^{-2}$ . This is achievable in semiconductors and can be engineered at will by low temperature growth of the semiconductor material [24, 34]. As long as the laser is running cw and single mode, the absorber will follow the instantaneous laser power. Then, the saturable absorption can be adiabatically eliminated, by using eq.(4.156)

$$q = \frac{q_0}{1 + P/P_A} \quad \text{with} \quad P_A = \frac{E_A}{\tau_A}, \quad (4.157)$$

and back substitution into eq.(4.154). Here,  $P_A$  is the saturation power of the absorber. At a certain amount of saturable absorption, the relaxation oscillations become unstable and Q-switching occurs. To find the stability criterion, we linearize the system

$$T_R \frac{dP}{dt} = 2(g - l - q(P))P \quad (4.158)$$

$$T_R \frac{dg}{dt} = -\frac{g - g_0}{T_L} - \frac{gT_R P}{E_L}. \quad (4.159)$$

### Stationary solution

As in the case for the cw-running laser the stationary operation point of the laser is determined by the point of zero net gain

$$\begin{aligned} g_s &= l + q_s \\ \frac{g_0}{1 + P_s/P_L} &= l + \frac{q_0}{1 + P_s/P_A}. \end{aligned} \quad (4.160)$$

The graphical solution of this equation is shown in Fig. 4.23

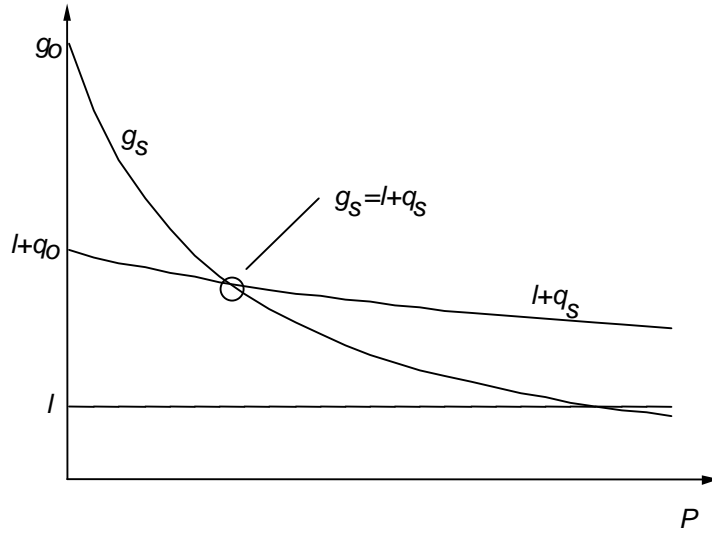


Figure 4.23: Graphical solution of the stationary operating point.

### Stability of stationary operating point or the condition for Q-switching

For the linearized system, the coefficient matrix corresponding to Eq.(4.121) changes only by the saturable absorber [27]:

$$T_R \frac{d}{dt} \begin{pmatrix} \Delta P_0 \\ \Delta g_0 \end{pmatrix} = A \begin{pmatrix} \Delta P_0 \\ \Delta g_0 \end{pmatrix}, \text{ with } A = \begin{pmatrix} -2 \frac{dq}{dP} \Big|_{cw} P_s & 2P_s \\ -\frac{g_s T_R}{E_L} & -\frac{T_R}{\tau_{stim}} \end{pmatrix} \quad (4.161)$$



The coefficient matrix  $A$  does have eigenvalues with negative real part, if and only if its trace is negative and the determinante is positive, which results in two conditions

$$-2P \frac{dq}{dP} \Big|_{cw} < \frac{r}{T_L} \quad \text{with} \quad r = 1 + \frac{P}{P_L} \quad \text{and} \quad P_L = \frac{E_L}{\tau_L}, \quad (4.162)$$

and

$$\frac{dq}{dP} \Big|_{cw} \frac{r}{T_L} + g_s \frac{1}{T_L P_L} > 0. \quad (4.163)$$

After cancelation of  $T_L$  we end up with

$$\left| \frac{dq}{dP} \Big|_{cw} \right| < \left| \frac{dg_s}{dP} \Big|_{cw} \right|. \quad (4.164)$$

For a laser which starts oscillating on its own, relation 4.164 is automatically fulfilled since the small signal gain is larger than the total losses, see Fig. 4.23. Inequality (4.162) has a simple physical explanation. The right hand side of (4.162) is the relaxation time of the gain towards equilibrium, at a given pump power and constant laser power. The left hand side is the decay time of a power fluctuation of the laser at fixed gain. If the gain can not react fast enough to fluctuations of the laser power, relaxation oscillations grow and result in passive Q-switching of the laser.

As can be seen from Eq.(4.160) and Eq.(4.162), we obtain

$$-2T_L P \frac{dq}{dP} \Big|_{cw} = 2T_L q_0 \frac{\frac{P}{\chi P_L}}{\left(1 + \frac{P}{\chi P_L}\right)^2} \Big|_{cw} < r \quad \text{with} \quad \chi = \frac{P_A}{P_L}, \quad (4.165)$$

where  $\chi$  is an effective "stiffness" of the absorber against cw saturation. The stability relation (4.165) is visualized in Fig. 4.24.

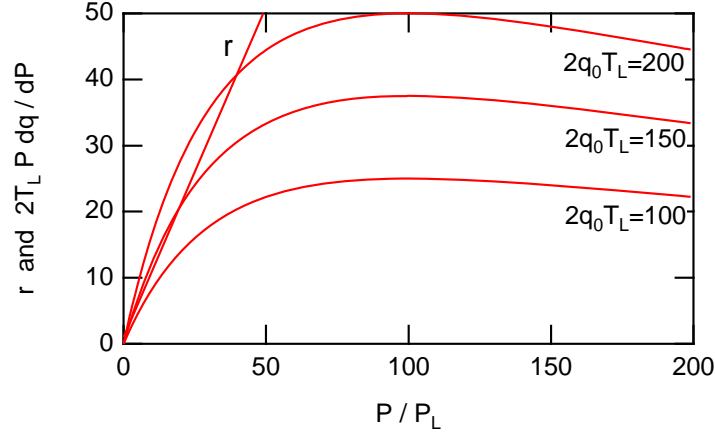


Figure 4.24: Graphical representation of cw-Q-switching stability relation for different products  $2q_0 T_L$ . The cw-stiffness used for the the plots is  $\chi = 100$ .

The tendency for a laser to Q-switch increases with the product  $q_0 T_L$  and decreases if the saturable absorber is hard to saturate, i.e.  $\chi \gg 1$ . As can be inferred from Fig. 4.24 and eq.(4.165), the laser can never Q-switch, i.e. the left side of eq.(4.165) is always smaller than the right side, if the quantity

$$MDF = \frac{2q_0 T_L}{\chi} < 1 \quad (4.166)$$

is less than 1. The abbreviation MDF stands for mode locking driving force, despite the fact that the expression (4.166) governs the Q-switching instability. We will see, in the next section, the connection of this parameter with mode locking. For solid-state lasers with long upper state life times, already very small amounts of saturable absorption, even a fraction of a percent, may lead to a large enough mode locking driving force to drive the laser into Q-switching. Figure 4.25 shows the regions in the  $\chi - P/P_L$  - plane where Q-switching can occur for fixed MDF according to relation (4.165). The area above the corresponding MDF-value is the Q-switching region. For  $MDF < 1$ , cw-Q-switching can not occur. Thus, if a cw-Q-switched laser has to be designed, one has to choose an absorber with a  $MDF > 1$ . The further the operation point is located in the cw-Q-switching domain the more pronounced the cw-Q-switching will be. To understand the nature of the instability we look at the eigen solution and eigenvalues of the linearized

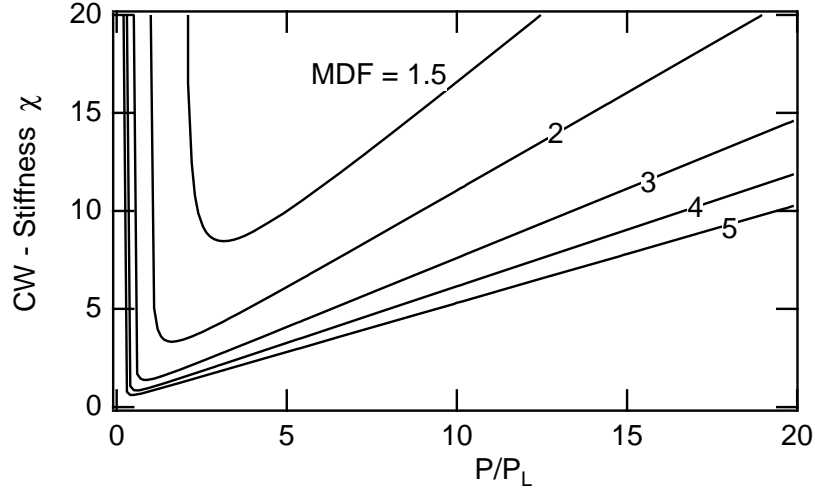


Figure 4.25: For a given value of the MDF, cw-Q-switching occurs in the area above the corresponding curve. For a MDF-value less than 1 cw-Qswitching can not occur.

equations of motion 4.161

$$\frac{d}{dt} \begin{pmatrix} \Delta P_0(t) \\ \Delta g_0(t) \end{pmatrix} = s \begin{pmatrix} \Delta P_0(t) \\ \Delta g_0(t) \end{pmatrix} \quad (4.167)$$

which results in the eigenvalues

$$sT_R = \frac{A_{11} + A_{22}}{2} \pm j \sqrt{A_{11}A_{22} - A_{12}A_{21} - \left( \frac{A_{11} + A_{22}}{2} \right)^2}. \quad (4.168)$$

With the matrix elements according to eq.(4.161) we get

$$s = \frac{-\frac{2}{T_R} \frac{dq}{dP} \Big|_{cw} P_s - \frac{1}{\tau_{stim}}}{2} \pm j\omega_Q \quad (4.169)$$

$$\omega_Q = \sqrt{-\frac{2}{T_R} \frac{dq}{dP} \Big|_{cw} P_s \frac{r}{\tau_L} + \frac{r-1}{\tau_p \tau_L} - \left( \frac{-\frac{2}{T_R} \frac{dq}{dP} \Big|_{cw} P_s - \frac{1}{\tau_{stim}}}{2} \right)^2} \quad (4.170)$$

where the pump parameter is now defined as the ratio between small signal gain the total losses in steady state, i.e.  $r = g_0/(l + q_s)$ . This somewhat

lengthy expression clearly shows, that when the system becomes unstable,  $-2 \frac{dq}{dP}|_{cw} P_s > \frac{T_R}{\tau_{stim}}$ , with  $\tau_L \gg \tau_p$ , there is a growing oscillation with frequency

$$\omega_Q \approx \sqrt{\frac{r-1}{\tau_p \tau_L}} \approx \sqrt{\frac{1}{\tau_p \tau_{stim}}}. \quad (4.171)$$

That is, passive Q-switching can be understood as a destabilization of the relaxation oscillations of the laser. If the system is only slightly in the instable regime, the frequency of the Q-switching oscillation is close to the relaxation oscillation frequency. If we define the growth rate  $\gamma_Q$ , introduced by the saturable absorber as a parameter, the eigen values can be written as

$$s = \frac{1}{2} \left( \gamma_Q - \frac{1}{\tau_{stim}} \right) \pm j \sqrt{\gamma_Q \frac{r}{\tau_L} + \frac{r-1}{\tau_p \tau_L} - \left( \frac{\gamma_Q - \frac{1}{\tau_{stim}}}{2} \right)^2}. \quad (4.172)$$

Figure 4.26 shows the root locus plot for a system with and without a saturable absorber. The saturable absorber destabilizes the relaxation oscillations. The type of bifurcation is called a Hopf bifurcation and results in an oscillation.

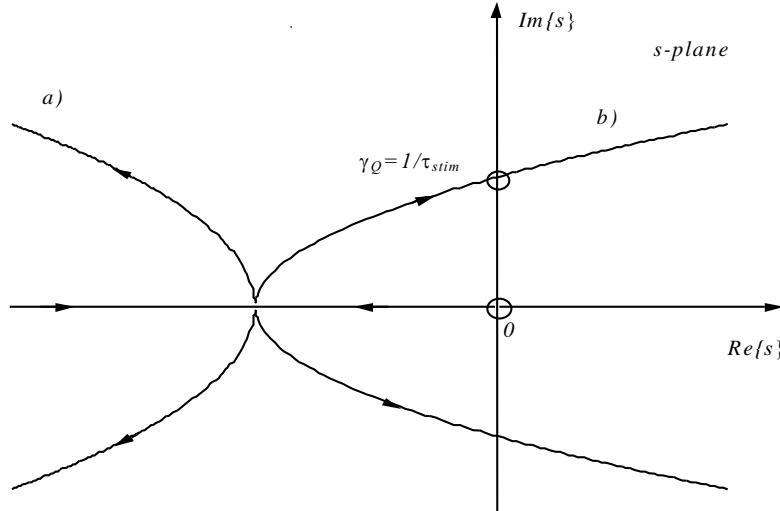


Figure 4.26: Root locus plot for the linearized rate equations. a) Without saturable absorber as a function of the pump parameter  $r$ ; b) With saturable absorber as a function of  $\gamma_Q$ .

As an example, we consider a laser with the following parameters:  $\tau_L = 250\mu s$ ,  $T_R = 4ns$ ,  $2l_0 = 0.1$ ,  $2q_0 = 0.005$ ,  $2g_0 = 2$ ,  $P_L/P_A = 100$ . The rate equations are solved numerically and shown in Figures 4.27 and 4.28.

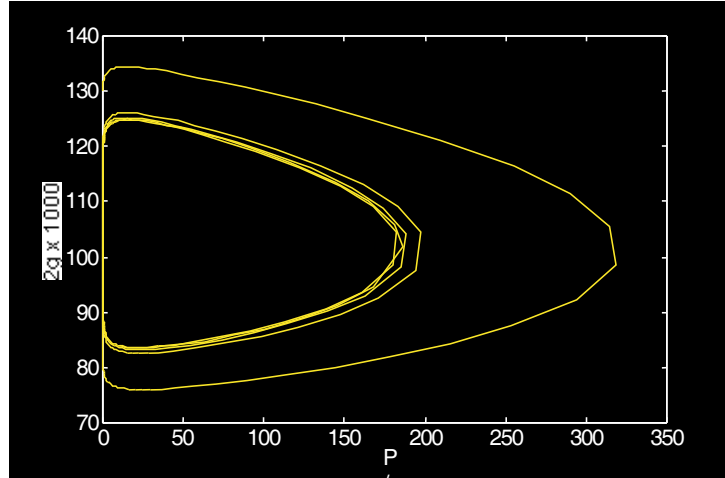


Figure 4.27: Phase space plot of the rate equations. It takes several oscillations, until the steady state limit cycle is reached.

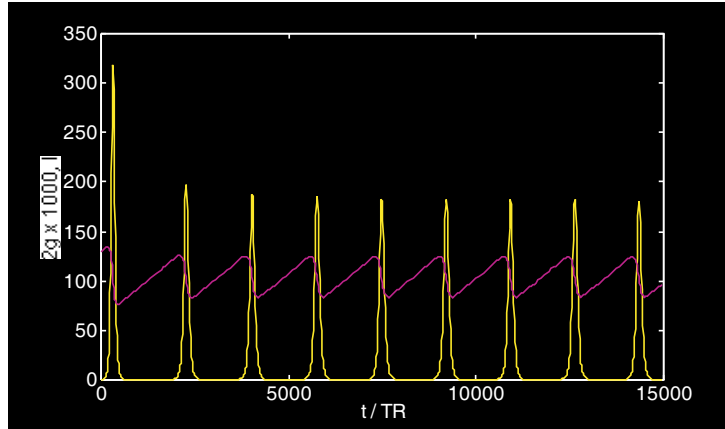


Figure 4.28: Solution for gain and output power as a function of time.

## 4.7 Example: Single Mode CW-Q-Switched Microchip Lasers

Q-switched microchip lasers are compact and simple solid-state lasers, which can provide a high peak power with a diffraction limited output beam. Due to the extremely short cavity length, typically less than 1 mm, single-frequency Q-switched operation with pulse widths well below a ns can be achieved. Pulse durations of 337 ps and 218 ps have been demonstrated with a passively Q-switched microchip laser consisting of a Nd:YAG crystal bonded to a thin piece of  $\text{Cr}^{4+}$ :YAG [12, 13]. Semiconductor saturable absorbers were used to passively Q-switch a monolithic Nd:YAG laser producing 100 ns pulses [42].

### 4.7.1 Set-up of the Passively Q-Switched Microchip Laser

Figure 4.29(a) shows the experimental set-up of the passively Q-switched microchip laser and Fig. 4.29(b) the structure of the semiconductor saturable absorber [16, 17]. The saturable absorber structure is a so called anti-resonant Fabry-Perot saturable absorber (A-FPSA), because in a microchip laser the beam size is fixed by the thermal lens that builds up in the laser crystal, when pumped with the diode laser. Thus, one can use the top reflector of the A-FPSA to scale the effective saturation intensity of the absorber with respect to the intracavity power. The 200 or 220  $\mu\text{m}$  thick Nd:YVO<sub>4</sub> or Nd:LaSc<sub>3</sub>(BO<sub>3</sub>)<sub>4</sub>, (Nd:LSB) laser crystal [43] is sandwiched between a 10% output coupler and the A-FPSA. The latter is coated for high reflection at the pump wavelength of 808 nm and a predesigned reflectivity at the laser wavelength of 1.062  $\mu\text{m}$ , respectively. The laser crystals are pumped by a semiconductor diode laser at 808 nm through a dichroic beamsplitter, that transmits the pump light and reflects the output beam at 1.064  $\mu\text{m}$  for the Nd:YVO<sub>4</sub> or 1.062  $\mu\text{m}$  for the Nd:LSB laser. To obtain short Q-switched pulses, the cavity has to be as short as possible. The highly doped laser crystals with a short absorption length of only about 100  $\mu\text{m}$  lead to a short but still efficient microchip laser [17]. The saturable absorber consists of a dielectric top mirror and 18 pairs of GaAs/InGaAs Multiple Quantum Wells (MQWs) grown on a GaAs/AlAs Bragg-mirror. The total optical thickness of the absorber is on the order of 1  $\mu\text{m}$ . Therefore, the increase of the cavity

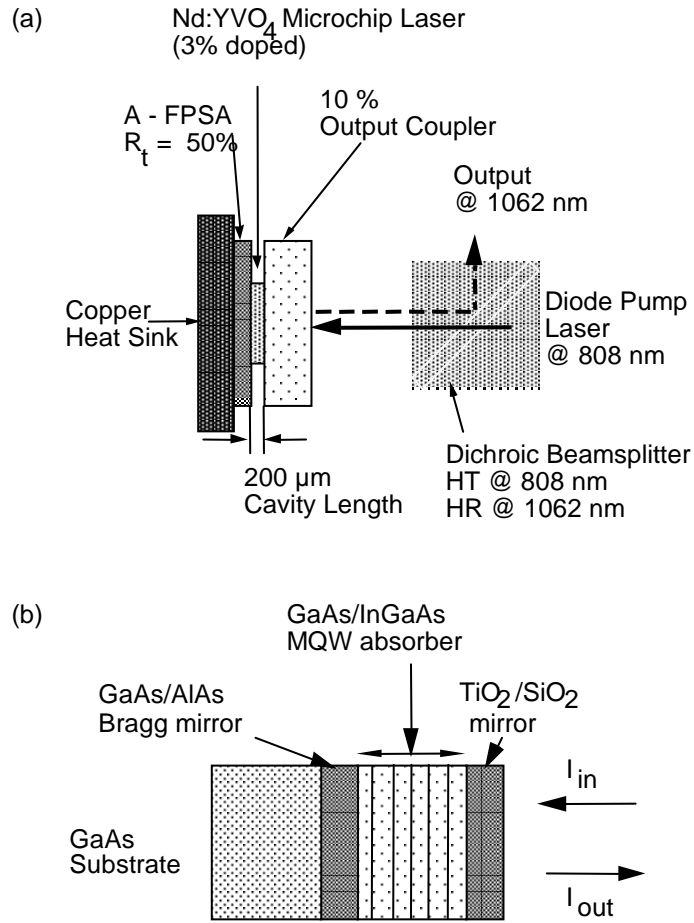


Figure 4.29: (a) Experimental set-up of the cw-passively Q-switched Nd:YVO<sub>4</sub> microchip-laser. (b) Structure of the anti-resonant Fabry-Perot semiconductor saturable absorber [41].

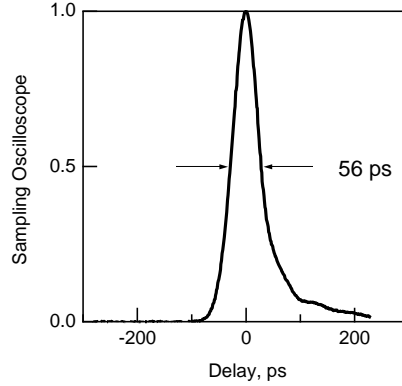


Figure 4.30: Single-Mode Q-switched pulse achieved with Nd:YVO<sub>4</sub> microchip laser.

length due to the absorber is negligible. For more details see [16, 17]. Pulses as short as 56 ps, Fig. (4.30), have been achieved with Nd:LSB-crystals.

#### 4.7.2 Dynamics of a Q-Switched Microchip Laser

The passively Q-switched microchip laser, shown in Fig. 4.29(a), is perfectly modeled by the rate equations (4.154) to (4.156). To understand the basic dependence of the cw-Q-switching dynamics on the absorber parameters, we performed numerical simulations of the Nd:LSB microchip laser, as shown in Fig. 4.29. The parameter set used is given in Table 4.2. For these parameters, we obtain according to eq.(4.160) a mode locking driving force of  $MDF = 685$ . This laser operates clearly in the cw-Q-switching regime as soon as the laser is pumped above threshold. Note, the Q-switching condition (4.166) has only limited validity for the microchip laser considered here, because, the cavity length is much shorter than the absorber recovery time. Thus the adiabatic elimination of the absorber dynamics is actually no longer justified. Figures 4.31 and 4.32 show the numerical solution of the set of rate equations (4.154) to (4.156) on a microsecond timescale and a picosecond timescale close to one of the pulse emission events.

No analytic solution to the set of rate equations is known. Therefore, optimization of Q-switched lasers has a long history [8, 9], which in general results in complex design criteria [9], if the most general solution to the rate



parameter	value
$2 g_0$	0.7
$2 q_0$	0.03
$2 l$	0.14
$T_R$	2.7 ps
$\tau_L$	87 $\mu$ s
$\tau_A$	24 ps
$E_L$	20 $\mu$ J
$E_A$	7.7 nJ

Table 4.2: Parameter set used for the simulation of the dynamics of the Q-switched microchip laser.

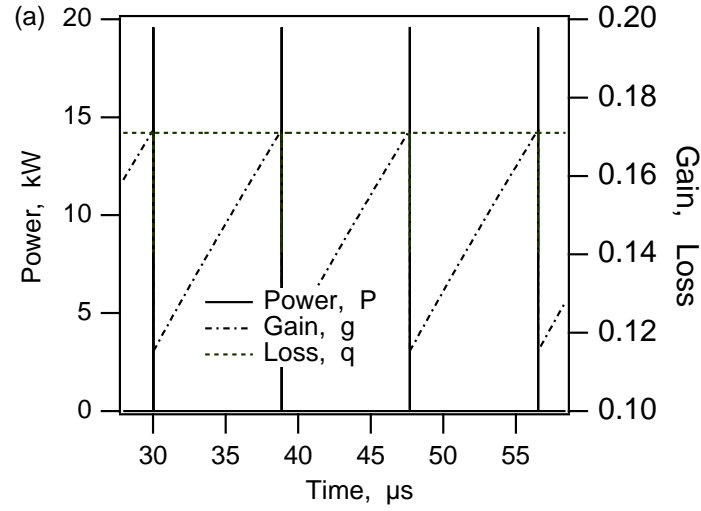


Figure 4.31: Dynamics of the Q-switched microchip laser by numerical solution of the rate equations on a microsecond timescale.

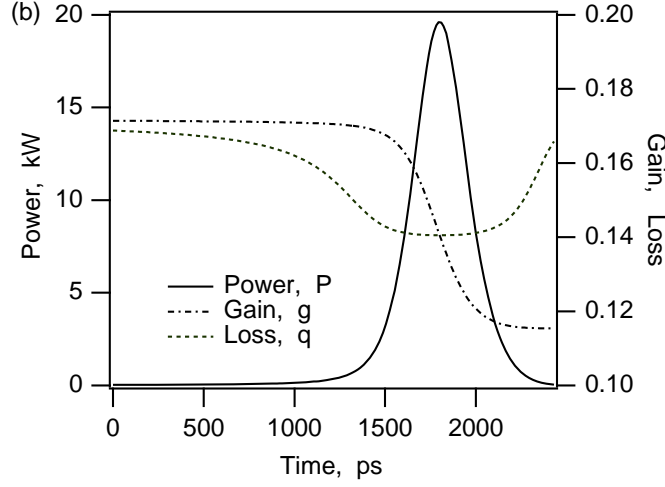


Figure 4.32: Dynamics of the Q-switched microchip laser by numerical solution of the rate equations on a picosecond timescale.

equations is considered. However, a careful look at the simulation results leads to a set of very simple design criteria, as we show in the following. As seen from Fig. 4.31, the pulse repetition time  $T_{rep}$  is many orders of magnitude longer than the width of a Q-switched pulse. Thus, between two pulse emissions, the gain increases due to pumping until the laser reaches threshold. This is described by eq.(4.155), where the stimulated emission term can be neglected. Therefore, the pulse repetition rate is determined by the relation that the gain has to be pumped to threshold again  $g_{th} = l + q_0$ , if it is saturated to the value  $g_f$  after pulse emission. In good approximation,  $g_f = l - q_0$ , as long as it is a positive quantity. If  $T_{rep} < \tau_L$ , one can linearize the exponential and we obtain

$$g_{th} - g_f = g_0 \frac{T_{rep}}{\tau_L} \quad (4.173)$$

$$T_{rep} = \tau_L \frac{g_{th} - g_f}{g_0} = \tau_L \frac{2q_0}{g_0}. \quad (4.174)$$

Figure 4.32 shows that the power increases because the absorber saturates faster than the gain. To obtain a fast raise of the pulse, we assume an absorber which saturates much easier than the gain, i.e.  $E_A \ll E_L$ , and the

recovery times of gain and absorption shall be much longer than the pulse width  $\tau_{pulse}$ ,  $\tau_A \gg \tau_{pulse}$ . Since, we assume a slow gain and a slow absorber, we can neglect the relaxation terms in eqs.(4.155) and (4.156) during growth and decay of the pulse. Then the equations for gain and loss as a function of the unknown Q-switched pulse shape  $f_Q(t)$

$$P(t) = E_P f_Q(t) \quad (4.175)$$

can be solved. The pulse shape  $f_Q(t)$  is again normalized, such that its integral over time is one and  $E_P$  is, therefore, the pulse energy. Analogous to the derivation for the Q-switched mode locking threshold in eqs.(4.189) and (4.190), we obtain

$$q(t) = q_0 \exp \left[ -\frac{E_P}{E_A} \int_{-\infty}^t f_Q(t') dt' \right], \quad (4.176)$$

$$g(t) = g_{th} \exp \left[ -\frac{E_P}{E_L} \int_{-\infty}^t f_Q(t') dt' \right]. \quad (4.177)$$

Substitution of these expressions into the eq.(4.154) for the laser power, and integration over the pulse width, determines the extracted pulse energy. The result is a balance between the total losses and the gain.

$$l + q_P(E_P) = g_P(E_P) \quad (4.178)$$

with

$$q_P(E_P) = q_0 \frac{1 - \exp \left[ -\frac{E_P}{E_A} \right]}{\frac{E_P}{E_A}}, \quad (4.179)$$

$$g_P(E_P) = g_{th} \frac{1 - \exp \left[ -\frac{E_P}{E_L} \right]}{\frac{E_P}{E_L}}. \quad (4.180)$$

Because, we assumed that the absorber is completely saturated, we can set  $q_P(E_P) \approx 0$ . Figure 4.33 shows the solution of eq.(4.178), which is the pulse energy as a function of the ratio between saturable and nonsaturable losses  $s = q_0/l$ . Also approximate solutions for small and large  $s$  are shown as the dashed curves. Thus, the larger the ratio between saturable and nonsaturable losses is, the larger is the intracavity pulse energy, which is not

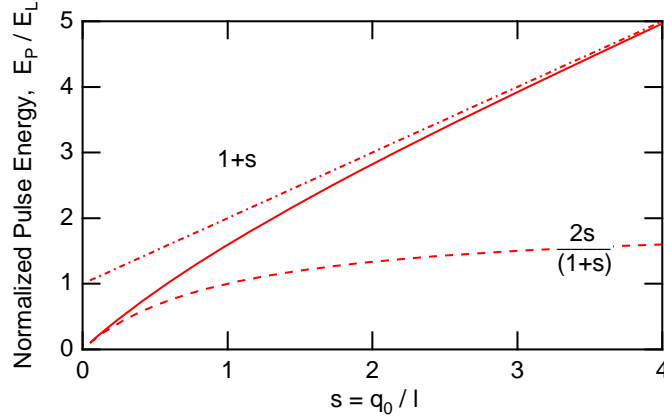


Figure 4.33: (—) Intracavity pulse energy as a function of the ratio between saturable and nonsaturable losses  $s$ . (---) Approximations for small and large values for  $s$ .

surprising. Note, the extracted pulse energy is proportional to the output coupling, which is  $2l$  if no other losses are present. If we assume,  $s \ll 1$ , then, we can use approximately the low energy approximation

$$E_P = 2E_L \frac{q_0}{l + q_0}. \quad (4.181)$$

The externally emitted pulse energy is then given by

$$E_P^{ex} = 2lE_P = E_L \frac{4lq_0}{l + q_0}. \quad (4.182)$$

Thus, the total extracted pulse energy is completely symmetric in the saturable and non saturable losses. For a given amount of saturable absorption, the extracted pulse energy is maximum for an output coupling as large as possible. Of course threshold must still be reached, i.e.  $l + q_0 < g_0$ . Thus, in the following, we assume  $l > q_0$  as in Fig. 4.32. The absorber is immediately bleached, after the laser reaches threshold. The light field growth and extracts some energy stored in the gain medium, until the gain is saturated to the low loss value  $l$ . Then the light field decays again, because the gain is below the loss. During decay the field can saturate the gain by a similar amount as during build-up, as long as the saturable losses are smaller than

the constant output coupler losses  $l$ , which we shall assume in the following. Then the pulse shape is almost symmetric as can be seen from Fig. 4.32(b) and is well approximated by a secant hyperbolicus square for reasons that will become obvious in a moment. Thus, we assume

$$f_Q(t) = \frac{1}{2\tau_P} \text{sech}^2\left(\frac{t}{\tau_P}\right). \quad (4.183)$$

With the assumption of an explicit pulse form, we can compute the pulse width by substitution of this ansatz into eq.(4.154) and using (4.176), (4.177)

$$-\frac{T_R}{\tau_P} \tanh\left(\frac{t}{\tau_P}\right) = g_{th} \exp\left[-\frac{E_P}{2E_L} \left(1 + \tanh\left(\frac{t}{\tau_P}\right)\right)\right] - l. \quad (4.184)$$

Again, we neglect the saturated absorption. If we expand this equation up to first order in  $E_P/E_L$  and compare coefficients, we find from the constant term the energy (4.182), and from the tanh-term we obtain the following simple expression for the pulse width

$$\tau_P = \frac{T_R}{q_0}. \quad (4.185)$$

For the FWHM pulse width of the resulting  $\text{sech}^2$ -pulse we obtain

$$\tau_{P,FWHM} = 1.75 \frac{T_R}{q_0}. \quad (4.186)$$

Thus, for optimum operation of a Q-switched microchip laser, with respect to minimum pulse width and maximum extracted energy in the limits considered here, we obtain a very simple design criterium. If we have a maximum small signal round-trip gain  $g_0$ , we should design an absorber with  $q_0$  somewhat smaller than  $g_0/2$  and an output coupler with  $q_0 < l < g_0 - q_0$ , so that the laser still fullfills the cw-Q-switching condition. It is this simple optimization, that allowed us to reach the shortest pulses ever generated from a cw-Q-switched solid-state laser. Note, for a maximum saturable absorption of  $2 q_0 = 13\%$ , a cavity roundtrip time of  $T_R = 2.6$  ps for the Nd:YVO<sub>4</sub> laser, one expects from (4.186) a pulse width of about  $\tau_P = 70$  ps, which is close to what we observed in the experiment above. We achieved pulses between 56 and 90 ps [17]. The typical extracted pulse energies were on the order of  $E_P = 0.1 - 0.2$   $\mu$ J for pulses of about 60 ps [17]. Using a saturation energy of

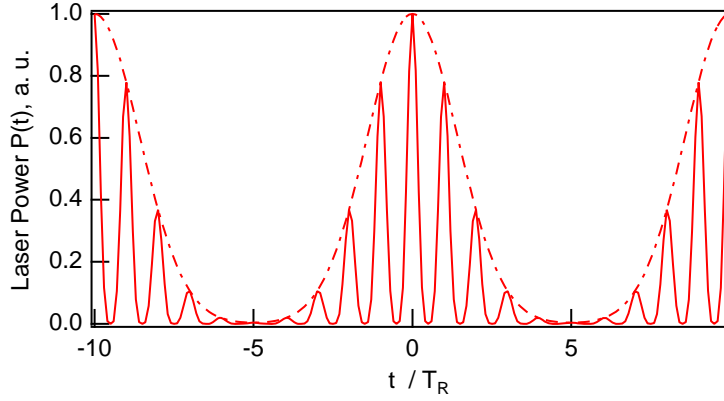


Figure 4.34: Laser output power as a function of time, when operating in the Q-switched mode-locked regime.

about  $E_L = 30 \mu\text{J}$  and an output coupler loss of  $2l = 0.1$ , we expect, according to (4.182), a maximum extracted pulse energy of  $E_P^{ex} = 2 \mu\text{J}$ . Thus, we have a deviation of one order of magnitude, which clearly indicates that the absorber still introduces too much of nonsaturable intracavity losses. Lowering of these losses should lead to  $\mu\text{J} - 50 \text{ ps}$  pulses from this type of a very simple and cheap laser, when compared with any other pulse generation technique.

## 4.8 Q-Switched Mode Locking

To understand the regime of Q-switched mode locking, we reconsider the rate equations (4.154) to (4.156). Fig. 4.34 shows, that we can describe the laser power on two time scales. One is on the order of the Q-switching envelope and occurs on multiple round-trips in the laser cavity,  $T = mT_R$ . Therefore, it is on the order of microseconds. The other time scale  $t$  is a short time scale on the order of the pulse width, i.e. picoseconds. Assuming a normalized pulse shape  $f_n(t)$  for the  $n$ -th pulse such that

$$\int_{-T_R/2}^{T_R/2} f_n(t - nT_R) dt = 1, \quad (4.187)$$

we can make the following ansatz for the laser power

$$P(T, t) = E_P(T) \sum_{n=-\infty}^{\infty} f_n(t - nT_R). \quad (4.188)$$

Here,  $E_P(T = mT_R)$  is the pulse energy of the  $m$ -th pulse, which only changes appreciably over many round-trips in the cavity. The shape of the  $m$ -th pulse,  $f_m(t)$ , is not yet of further interest. For simplicity, we assume that the mode-locked pulses are much shorter than the recovery time of the absorber. In this case, the relaxation term of the absorber in Eq.(4.157) can be neglected during the duration of the mode-locked pulses. Since the absorber recovery time is assumed to be much shorter than the cavity round-trip time, the absorber is unsaturated before the arrival of a pulse. Thus, for the saturation of the absorber during one pulse, we obtain

$$q(T = mT_R, t) = q_0 \exp \left[ -\frac{E_P(T)}{E_A} \int_{-T_R/2}^t f_m(t') dt' \right]. \quad (4.189)$$

Then, the loss in pulse energy per roundtrip can be written as

$$q_P(T) = \int_{-T_R/2}^{T_R/2} f_m(t) q(T = mT_R, t) dt = q_0 \frac{1 - \exp \left[ -\frac{E_P(T)}{E_A} \right]}{\frac{E_P(T)}{E_A}}. \quad (4.190)$$

Eq. (4.190) shows that the saturable absorber saturates with the pulse energy and not with the average intensity of the laser, as in the case of cw-Q-switching (4.157). Therefore, the absorber is much more strongly bleached at the same average power. After averaging Eqs.(4.154) and (4.155) over one round-trip, we obtain the following two equations for the dynamics of the pulse energy and the gain on a coarse grained time scale  $T$ :

$$T_R \frac{dE_P}{dT} = 2(g - l - q_P(E_P))E_P, \quad (4.191)$$

$$T_R \frac{dg}{dT} = -\frac{g - g_0}{T_L} - \frac{gE_P}{E_L}. \quad (4.192)$$

This averaging is allowed, because the saturation of the gain medium within one pulse is negligible, due to the small interaction cross section of the solid-state laser material. Comparing Eqs.(4.154), (4.155) and (4.157) with (4.189), (4.191) and (4.192), it becomes obvious that the stability criterion

(4.158) also applies to Q-switched mode locking if we replace the formula for cw-saturation of the absorber (4.157) by the formula for pulsed saturation (4.190). Then, stability against Q-switched mode locking requires

$$-2E_P \frac{dq_P}{dE_P} \Big|_{cw-mod} < \frac{r}{T_L} \Big|_{cw-mod}, \quad (4.193)$$

with

$$-2E_P \frac{dq_P}{dE_P} \Big|_{cw-mod} = 2q_0 \frac{1 - \exp \left[ -\frac{E_P}{E_A} \right] \left( 1 + \frac{E_P}{E_A} \right)}{\frac{E_P}{E_A}}. \quad (4.194)$$

When expressed in terms of the average power  $P = E_P/T_R$ , similar to Eq.(4.165), we obtain

$$-2T_L E_P \frac{dq_P}{dE_P} \Big|_{cw-mod} = 2T_L q_0 \frac{1 - \exp \left[ -\frac{P}{\chi_P P_L} \right] \left( 1 + \frac{P}{\chi_P P_L} \right)}{\frac{P}{\chi_P P_L}}, \quad (4.195)$$

where  $\chi_P = \chi T_A$  describes an effective stiffness of the absorber compared with the gain when the laser is cw-mode-locked at the same average power as the cw laser. Thus, similar to the case of cw-Q-switching and mode locking it is useful to introduce the driving force for Q-switched mode locking

$$QMDF = \frac{2q_0 T_L}{\chi_P}. \quad (4.196)$$

Figure 4.35 shows the relation (4.193) for different absorber strength. In going from Fig. 4.24 to Fig. 4.35, we used  $T_A = 0.1$ . We see, that the short normalized recovery time essentially leads to a scaling of the abscissa, when going from Fig. 4.24 to Fig. 4.35 while keeping all other parameters constant. Comparing Eqs.(4.166) with (4.196), it follows that, in the case of cw-mode locking, the absorber is more strongly saturated by a factor of  $1/T_A$ , which can easily be as large as 1000. Therefore, the Q-switched mode locking driving force is much larger than the mode locking driving force, MDF. Accordingly, the tendency for Q-switched mode locking is significantly higher than for cw Q-switching. However, now, it is much easier to saturate the absorber with an average power well below the damage threshold of the absorber (Fig. 4.35). Therefore, one is able to leave the regime of Q-switched mode locking at a large enough intracavity power.



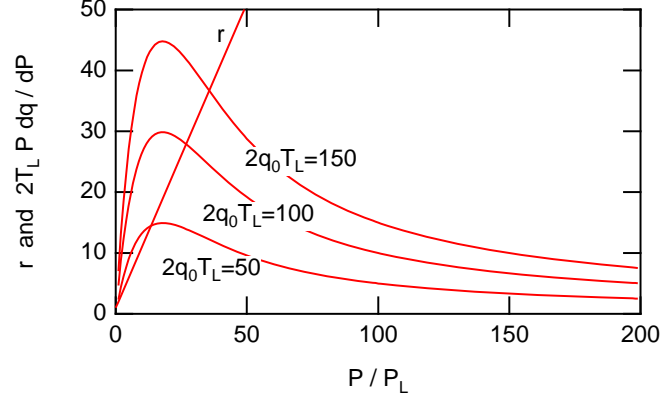


Figure 4.35: Visualization of the stability relations for Q-switched mode locking for different products  $2q_0 T_L$ . The assumed stiffness for pulsed operation is  $\chi_P = 10$ , which corresponds to  $T_A = 0.1$ . The functional form of the relations for cw Q-switching and Q-switched mode locking is very similar. The change in the stiffness, when going from cw to pulsed saturation, thus essentially rescales the x-axis. For low-temperature grown absorbers,  $T_A$  can be as small as  $10^{-6}$

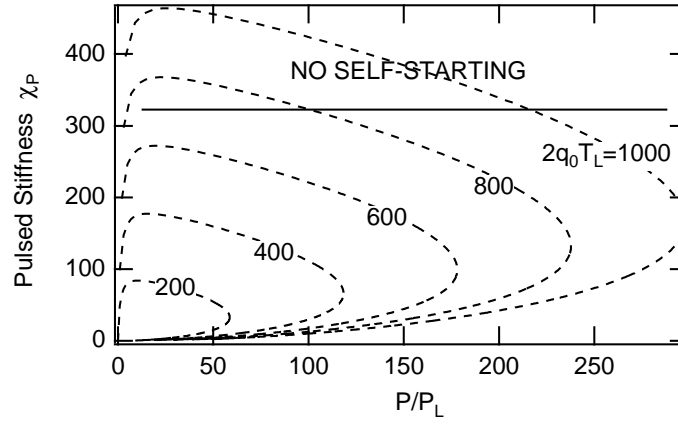


Figure 4.36: Self-Starting of mode locking and stability against Q-switched mode locking

We summarize our results for Q-switched mode locking in Fig. 4.36. It shows the stability boundary for Q-switched mode locking according to eq.(4.193), for different strengths of the saturable absorber, i.e. different values  $2q_0T_L$ . One may also derive minimum critical mode locking driving force for self-starting modelocking of the laser  $MDF_c$  due to various processes in the laser [28][29][31][32]. Or, with the definition of the pulsed stiffness, we obtain

$$\chi_{p,c} \leq \frac{2q_0T_L}{MDF_c} T_A. \quad (4.197)$$

Thus, for a self-starting laser which shows pure cw-mode locking, we have to design the absorber such that its MDF is greater than this critical value. Or expressed differently, the pulsed stiffness has to be smaller than the critical value  $\chi_{p,c}$ , at a fixed value for the absorber strength  $q_0$ . There is always a trade-off: On one hand, the mode locking driving force has to be large enough for self-starting. On the other hand the saturable absorption has to be small enough, so that the laser can be operated in a parameter regime where it is stable against Q-switching mode locking, see Fig. (4.36).

## 4.9 Summary

Starting from a simple two level laser and absorber model, we characterized the dynamics of solid-state lasers mode-locked and Q-switched by a saturable absorber. The unique properties of solid-state laser materials, i.e. their long upper-state life time and their small cross sections for stimulated emission, allow for a separation of the laser dynamics on at least two time scales. One process is the energy build-up and decay, which occurs typically on a time scale of the upper state lifetime or cavity decay time of the laser. The other process is the pulse shaping, which occurs within several roundtrips in the cavity. Separating these processes, we can distinguish between the different laser dynamics called cw-Q-switching, Q-switched mode locking and cw-mode locking. We found the stability boundaries of the different regimes, which give us guidelines for the design of absorbers for a given solid state laser to favour one of these regimes. Semiconductor absorbers are a good choice for saturable absorbers to modelock lasers, since the carrier lifetime can be engineered by low temperature growth [24]. When the pulses become short enough, the laser pulse saturates the absorber much more efficiently, which stabilizes the laser against undesired Q-switched mode locking. It has

been demonstrated experimentally, that this technique can control the laser dynamics of a large variety of solid-state lasers, such as Nd:YAG, Nd:YLF, Nd:YV0<sub>4</sub>, [22] in the picosecond regime.

With semiconductor devices and soliton formation due to negative GVD and SPM, we can use similar semiconductor absorbers to modelock the lasers in the femtosecond regime [39]. The stability criteria derived here can be applied to both picosecond and femtosecond lasers. However, the characteristics of the absorber dynamics may change drastically when going from picosecond to femtosecond pulses [40]. Especially, the saturation energy may depend not only on excitation wavelength, but also on the pulsewidth. In addition there may be additional loss mechanisms for the pulse, for example due to soliton formation there are additional filter losses of the pulse which couple to the energy of the pulse via the area theorem. This has to be taken into account, before applying the theory to fs-laser systems, which will be discussed in more detail later.

# Bibliography

- [1] I. I. Rabi: "Space Quantization in a Gyating Magnetic Field,". Phys. Rev. **51**, 652-654 (1937).
- [2] L. Allen and J. H. Eberly: Optical Resonance and Two-Level Atoms, Dover (1987).
- [3] B. R. Mollow, "Power Spectrum of Light Scattered by Two-Level Systems," Phys. Rev **188**, 1969-1975 (1969).
- [4] P. Meystre, M. Sargent III: Elements of Quantum Optics, Springer Verlag (1990).
- [5] R. W. Hellwarth, Eds., Advances in Quantum Electronics, Columbia Press, New York (1961).
- [6] A. E. Siegman, "Lasers," University Science Books, Mill Valley, California (1986).
- [7] O. Svelto, "Principles of Lasers," Plenum Press, NY 1998.
- [8] W. G. Wagner and B. A. Lengyel "Evolution of the Giant Pulse in a Laser," J. Appl. Opt. **34**, 2040 – 2046 (1963).
- [9] J. J. Degnan, "Theory of the Optimally Coupled Q-switched Laser," IEEE J. Quantum Electron. **QE-25**, 214 – 220 (1989). and "Optimization of Passively Q-switched Lasers," IEEE J. Quantum Electron. **QE-31**, 1890 – 1901 (1995).
- [10] J. J. Zayhowski, C. D. III, Optics Lett. 17, 1201 (1992)
- [11] 5. H. Plaessmann, K. S. Yamada, C. E. Rich, W. M. Grossman, Applied Optics 32, 6618 (1993)

- [12] J. J. Zayhowski, C. Dill, "Diode-pumped passively Q-switched picosecond microchip lasers," *Opt. Lett.* **19**, pp. 1427 – 1429 (1994).
- [13] J. J. Zayhowski, J. Ochoa, C. Dill, "UV generation with passively Q-switched picosecond microchip lasers," *Conference on Lasers and Electro Optics*, (Baltimore, USA) 1995, paper CTuM2 p. 139.
- [14] P. Wang, S.-H. Zhou, K. K. Lee, Y. C. Chen, "Picosecond laser pulse generation in a monolithic self-Q-switched solid-state laser," *Opt. Com* **114**, pp. 439 – 441 (1995).
- [15] J. J. Zayhowski, "Limits imposed by spatial hole burning on the single-mode operation of standing-wave laser cavities," *Opt. Lett.* **15**, 431 – 433 (1990).
- [16] B. Braun, F. X. Kärtner, U. Keller, J.-P. Meyn and G. Huber, "Passively Q-switched 180 ps Nd:LaSc<sub>3</sub>(BO<sub>3</sub>)<sub>4</sub> microchip laser," *Opt. Lett.* **21**, pp. 405 – 407 (1996).
- [17] B. Braun, F. X. Kärtner, G. Zhang, M. Moser and U. Keller, "56 ps Passively Q-switched diode-pumped microchip laser," *Opt. Lett.* **22**, 381-383, 1997.
- [18] O. Forster, "Analysis I, Differential- und Integralrechnung einer Veränderlichen," Vieweg, Braunschweig (1983).
- [19] E. P. Ippen, "Principles of passive mode locking," *Appl. Phys.* **B 58**, pp. 159 – 170 (1994).
- [20] A. Penzkofer, "Passive Q-switching and mode-locking for the generation of nanosecond to femtosecond Pulses," *Appl. Phys.* **B 46**, pp. 43 – 60 (1988).
- [21] U. Keller, D. A. B. Miller, G. D. Boyd, T. H. Chiu, J. F. Ferguson, M. T. Asom, "Solid-state low-loss intracavity saturable absorber for Nd:YLF lasers: an antiresonant semiconductor Fabry-Perot saturable absorber," *Opt. Lett.* **17**, pp. 505 – 507 (1992).
- [22] U. Keller, "Ultrafast all-solid-state laser technology," *Appl. Phys.* **B 58**, pp. 347-363 (1994).

- [23] J. P. Meyn, "Neodym-Lanthan-Scandium-Borat: Ein neues Material für miniaturisierte Festkörperlaser," PhD Thesis, Universität Hamburg.
- [24] G. L. Witt, R. Calawa, U. Mishra, E. Weber, Eds., "Low Temperature (LT) GaAs and Related Materials," **241** Pittsburgh, (1992).
- [25] H. Haken, "Synergetics: An Introduction," Springer Verlag, Berlin (1983).
- [26] A. Yariv, "Quantum Electronics", Wiley Interscience (1975).
- [27] H. A. Haus, "Parameter ranges for cw passive modelocking," IEEE J. Quantum Electron., QE-**12**, pp. 169 – 176 (1976).
- [28] E. P. Ippen, L. Y. Liu, H. A. Haus, "Self-starting condition for additive-pulse modelocked lasers," Opt. Lett. **15**, pp. 183 – 18 (1990).
- [29] F. Krausz, T. Brabec, C. Spielmann, "Self-starting passive modelocking," Opt. Lett. **16**, pp. 235 – 237 (1991).
- [30] H. A. Haus, E. P. Ippen, "Self-starting of passively mode-locked lasers," Opt. Lett. **16**, pp. 1331 – 1333 (1991).
- [31] J. Herrmann, "Starting dynamic, self-starting condition and modelocking threshold in passive, coupled-cavity or Kerr-lens mode-locked solid-state lasers," Opt. Com. **98**, pp. 111 – 116 (1993).
- [32] C. J. Chen, P. K. A. Wai and C. R. Menyuk, "Self-starting of passively modelocked lasers with fast saturable absorbers," Opt. Lett. **20**, pp. 350 – 352 (1995).
- [33] R. W. Boyd, "Nonlinear Optics," Academic Press, New York, (1992).
- [34] L. R. Brovelli, U. Keller, T. H. Chiu, "Design and Operation of Antiresonant Fabry-Perot Saturable Semiconductor Absorbers for Mode-Locked Solid-State Lasers," J. Opt. Soc. of Am. B **12**, pp. 311 – 322 (1995).
- [35] K. Smith, E. J. Greer, R. Wyatt, P. Wheatley, N. J. Doran, "Totally integrated erbium fiber soliton laser pumped by laser diode," Electr. Lett. **27**, pp. 244 – 245 (1990).

- [36] U. Keller, T. K. Woodward, D. L. Sivco, A. Y. Cho, "Coupled-Cavity Resonant Passive Modelocked Nd:Yttrium Lithium Fluoride Laser," *Opt. Lett.* **16** pp. 390 – 392 (1991).
- [37] U. Keller, T. H. Chiu, "Resonant passive modelocked Nd:YLF laser," *IEEE J. Quantum Electron.* **QE-28**, pp. 1710 – 1721 (1992).
- [38] G. P. Agrawal, N. A. Olsson, "Self-Phase Modulation and Spectral Broadening of Optical Pulses in Semiconductor Laser Amplifiers," *IEEE J. Quantum Electron.* **25**, pp. 2297 - 2306 (1989).
- [39] D. Kopf, K. J. Weingarten, L. Brovelli, M. Kamp, U. Keller, "Diode-pumped 100-fs passively mode-locked Cr:LiSAF using an A-FPSA," *Opt. Lett.* **19**, pp. (1994).
- [40] W. H. Knox, D. S. Chemla G. Livescu, J. E. Cunningham, and J. E. Henry, "Femtosecond Carrier Thermalization in Dense Fermi Seas," *Phys. Rev. Lett.* **61**, 1290 – 1293 (1988).
- [41] B. Braun, U. Keller, "Single frequency Q-switched ring laser with an antiresonant Fabry-Perot saturable absorber," *Opt. Lett.* **20**, pp. 1020 – 1022 (1995).
- [42] S. A. Kutovoi, V. V. Laptev, S. Y. Matsnev, "Lanthanum scandoborate as a new highly efficient active medium of solid state lasers," *Sov. J. Quantum Electr.* **21**, pp. 131 – 132 (1991).
- [43] B. Beier, J.-P. Meyn, R. Knappe, K.-J. Boller, G. Huber, R. Wallenstein, *Appl. Phys. B* **58**, 381 – (1994).

# Chapter 5

## Active Mode Locking

For simplicity, we assume, that the laser operates in the transverse fundamental modes and, therefore, we only have to treat the longitudinal modes of the laser similar to a simple plane parallel Fabry-Perot resonator (Figure: 5.1). We consider one polarization of the field only, however, as we will say later for some mode-locked laser polarization dynamics will become important.

The task of mode-locking is to get as many of the longitudinal modes lasing in a phase synchronous fashion, such that the superposition of all modes represents a pulse with a spatial extent much shorter than the cavity. The pulse will then propagate at the group velocity corresponding to the center frequency of the pulse.

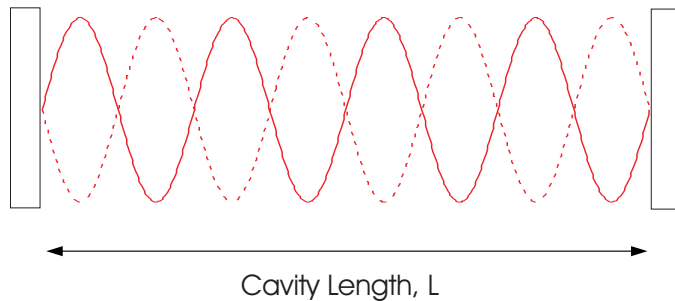


Figure 5.1: Fabry-Perot resonator



## 5.1 The Master Equation of Mode Locking

Lets consider for the moment the cold cavity (i.e. there is only a simple linear medium in the cavity no lasing). The most general solution for the intracavity field is a superpositon of left- and rightward running waves

$$E^{(left)}(z, t) = Re \left\{ \sum_{n=0}^{\infty} \hat{E}_n e^{j(\Omega_n t + K_n z)} \right\}, \quad (5.1)$$

and

$$E^{(right)}(z, t) = Re \left\{ \sum_{n=0}^{\infty} \hat{E}_n e^{j(\Omega_n t - K_n z)} \right\}. \quad (5.2)$$

The possible values for the wavenumbers are  $K_n = n\pi/L$ , resulting from the boundary conditions on metallic mirrors or periodicity after one roundtrip in the cavity. If the mirrors are perfectly reflecting, the leftward and rightward moving waves Eqs.(5.1) and (5.2) contain the same information and it is sufficient to treat only one of them. Usually one of the cavity mirrors is not perfectly reflecting in order to couple out light, however, this can be considered a perturbation to the ideal mode structure.

We consider the modes in Eq.(5.2) as a continuum and replace the sum by an integral

$$E^{(right)}(z, t) = \frac{1}{2\pi} Re \left\{ \int_{K=0}^{\infty} \hat{E}(K) e^{j(\Omega(K)t - Kz)} dK \right\} \quad (5.3)$$

with

$$\hat{E}(K_m) = \hat{E}_m 2L. \quad (5.4)$$

Eq.(5.3) is similar to the pulse propagation discussed in chapter 2 and describes the pulse propagation in the resonator. However, here it is rather an initial value problem, rather than a boundary value problem. Note, the wavenumbers of the modes are fixed, not the frequencies. To emphasize this even more, we introduce a new time variable  $T = t$  and a local time frame  $t' = t - z/v_{g,0}$ , instead of the propagation distance  $z$ , where  $v_{g,0}$  is the group velocity at the central wave number  $K_{n_0}$  of the pulse

$$v_{g,0} = \left. \frac{\partial \omega}{\partial k} \right|_{k=0} = \left. \left( \frac{\partial k}{\partial \omega} \right)^{-1} \right|_{\omega=0}. \quad (5.5)$$

For introduction of a slowly varying envelope, we shift the frequency and wavenumber by the center frequency  $\omega_0 = \Omega_{n_0}$  and center wave number  $k_0 = K_{n_0}$

$$k = K - K_{n_0}, \quad (5.6)$$

$$\omega(k) = \Omega(K_{n_0} + k) - \Omega_{n_0}, \quad (5.7)$$

$$\hat{E}(k) = \hat{E}(K_{n_0} + k), \quad (5.8)$$

The temporal evolution of the pulse is then determined by

$$E^{(right)}(z, t) = \frac{1}{2\pi} \text{Re} \left\{ \int_{-K_{n_0} \rightarrow -\infty}^{\infty} \hat{E}(k) e^{j(\omega(k)t - kz)} dk \right\} e^{j(\omega_0 t - k_0 z)}. \quad (5.9)$$

Analogous to chapter 2, we define a slowly varying field envelope, that is already normalized to the total power flow in the beam

$$A(z, t) = \sqrt{\frac{A_{eff}}{2Z_0}} \frac{1}{2\pi} \int_{-\infty}^{\infty} \hat{E}(k) e^{j(\omega(k)t - kz)} dk. \quad (5.10)$$

With the retarded time  $t'$  and time  $T$ , we obtain analogous to Eq. (??).

$$A(T, t') = \sqrt{\frac{A_{eff}}{2Z_0}} \frac{1}{2\pi} \int_{-\infty}^{\infty} \hat{E}(k) e^{j((\omega(k) - v_{g,0}k)T + kv_{g,0}t')} dk. \quad (5.11)$$

which can be written as

$$T_R \frac{\partial A(T, t')}{\partial T} \Big|_{(GDD)} = j \sum_{n=2}^{\infty} D_n \left( -j \frac{\partial}{\partial t'} \right)^n A(T, t'), \quad (5.12)$$

with the dispersion coefficients per resonator round-trip  $T_R = \frac{2L}{v_{g,0}}$

$$D_n = \frac{2L}{n! v_{g,0}^{n+1}} \frac{\partial^{n-1} v_g(k)}{\partial k^{n-1}} \Big|_{k=0}. \quad (5.13)$$

The dispersion coefficients (5.13) look somewhat suspicious, however, it is not difficult to show, that they are equivalent to derivatives of the roundtrip phase  $\phi_R(\Omega) = \frac{\Omega}{c} n(\Omega) 2L$  in the resonator at the center frequency

$$D_n = -\frac{1}{n!} \frac{\partial^n \phi_R^{(n)}(\Omega)}{\partial \Omega^n} \Big|_{\Omega=\omega_0}, \quad (5.14)$$

Sofar, only the lossless resonator is treated. The gain and loss can be modelled by adding a term like

$$T_R \frac{\partial A(T, t')}{\partial T} \Big|_{(loss)} = -lA(T, t') \quad (5.15)$$

where  $l$  is the amplitude loss per round-trip. In an analogous manner we can write for the gain

$$T_R \frac{\partial A(T, t')}{\partial T} \Big|_{(gain)} = \left( g(T) + D_g \frac{\partial^2}{\partial t'^2} \right) A(T, t'), \quad (5.16)$$

where  $g(T)$  is the gain and  $D_g$  is the curvature of the gain at the maximum of the Lorentzian lineshape.

$$D_g = \frac{g(T)}{\Omega_g^2} \quad (5.17)$$

$D_g$  is the gain dispersion.  $g(T)$  is an average gain, which can be computed from the rate equation valid for each unit cell in the resonator. The distributed gain obeys the equation

$$\frac{\partial g(z, t)}{\partial t} = -\frac{g - g_0}{\tau_L} - g \frac{|A(z, t)|^2}{E_L}, \quad (5.18)$$

where  $E_L$  is the saturation energy  $E_L = \frac{h\nu_L}{2\sigma_L} A_{eff}$ ,  $\tau_L$  the upper state lifetime and  $\sigma_L$  the gain cross section. For typical solid-state lasers, the intracavity pulse energy is much smaller than the saturation energy. Therefore, the gain changes within one roundtrip are small. Furthermore, we assume that the gain saturates spatially homogeneous,  $g(z, t') = g(t')$ . Then, the equation for the average gain  $g(T)$  can be found by averaging (5.18) over one round-trip and we obtain

$$\frac{\partial g(T)}{\partial T} = -\frac{g - g_0}{\tau_L} - g \frac{W(T)}{E_L T_R}, \quad (5.19)$$

where  $W(T)$  is the intracavity pulse energy at time  $t = T$

$$W(T) = \int_{t'=-T_R/2}^{T_R/2} |A(T, t')|^2 dt' \approx \int_{-\infty}^{\infty} |A(T, t')|^2 dt'. \quad (5.20)$$

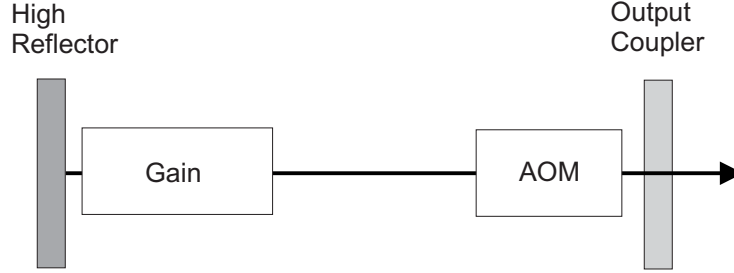


Figure 5.2: Actively modelocked laser with an amplitude modulator (Acousto-Optic-Modulator).

Taking all effects into account, the linear ones: loss, dispersion, gain and gain dispersion, as well as the nonlinear ones like saturable absorption and self-phase modulation, we end up with the master equation of modelocking

$$\begin{aligned}
 T_R \frac{\partial A(T, t')}{\partial T} &= -lA(T, t') + j \sum_{n=2}^{\infty} D_n \left( j \frac{\partial}{\partial t'} \right)^n A(T, t') \\
 &+ g(T) \left( 1 + \frac{1}{\Omega_g^2} \frac{\partial^2}{\partial t'^2} \right) A(T, t') \\
 &- q(T, t') A(T, t') - j\delta |A(T, t')|^2 A(T, t').
 \end{aligned} \tag{5.21}$$

To keep notation simple, we replace  $t'$  by  $t$  again. This equation was first derived by Haus [4] under the assumption of small changes in pulse shape per round-trip and per element passed within one round-trip.

## 5.2 Active Mode Locking by Loss Modulation

Active mode locking was first investigated in 1970 by Kuizenga and Siegman using a gaussian pulse analyses, which we want to delegate to the exercises [3]. Later in 1975 Haus [4] introduced the master equation approach (5.21). We follow the approach of Haus, because it also shows the stability of the solution.

We introduce a loss modulator into the cavity, for example an acousto-optic modulator, which periodically varies the intracavity loss according to

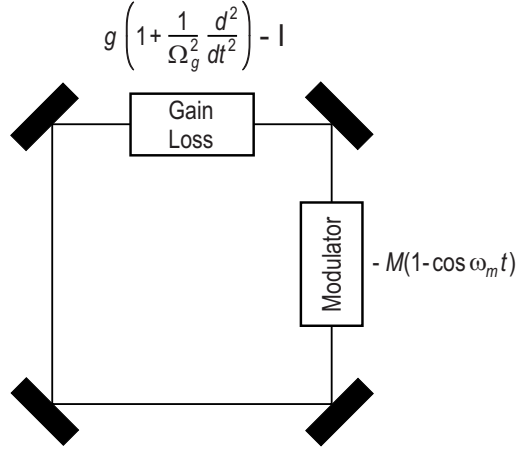


Figure 5.3: Schematic representation of the master equation for an actively mode-locked laser.

$q(t) = M(1 - \cos(\omega_M t))$ . The modulation frequency has to be very precisely tuned to the resonator round-trip time,  $\omega_M = 2\pi/T_R$ , see Fig.5.2. The modelocking process is then described by the master equation

$$T_R \frac{\partial A}{\partial T} = \left[ g(T) + D_g \frac{\partial^2}{\partial t^2} - l - M(1 - \cos(\omega_M t)) \right] A. \quad (5.22)$$

neglecting GDD and SPM. The equation can be interpreted as the total pulse shaping due to gain, loss and modulator, see Fig.5.3.

If we fix the gain in Eq. (5.22) at its stationary value, what ever it might be, Eq.(5.22) is a linear p.d.e, which can be solved by separation of variables. The pulses, we expect, will have a width much shorter than the round-trip time  $T_R$ . They will be located in the minimum of the loss modulation where the cosine-function can be approximated by a parabola and we obtain

$$T_R \frac{\partial A}{\partial T} = \left[ g - l + D_g \frac{\partial^2}{\partial t^2} - M_s t^2 \right] A. \quad (5.23)$$

$M_s$  is the modulation strength, and corresponds to the curvature of the loss modulation in the time domain at the minimum loss point

$$D_g = \frac{g}{\Omega_g^2}, \quad (5.24)$$

$$M_s = \frac{M\omega_M^2}{2}. \quad (5.25)$$

The differential operator on the right side of (5.23) corresponds to the Schrödinger-Operator of the harmonic oscillator problem. Therefore, the eigen functions of this operator are the Hermite-Gaussians

$$A_n(T, t) = A_n(t)e^{\lambda_n T/T_R}, \quad (5.26)$$

$$A_n(t) = \sqrt{\frac{W_n}{2^n \sqrt{\pi} n! \tau_a}} H_n(t/\tau_a) e^{-\frac{t^2}{2\tau_a^2}}, \quad (5.27)$$

where  $\tau_a$  defines the width of the Gaussian. The width is given by the fourth root of the ratio between gain dispersion and modulator strength

$$\tau_a = \sqrt[4]{D_g/M_s}. \quad (5.28)$$

Note, from Eq. (5.26) we can follow, that the gain per round-trip of each eigenmode is given by  $\lambda_n$  (or in general the real part of  $\lambda_n$ ), which are given by

$$\lambda_n = g_n - l - 2M_s\tau_a^2(n + \frac{1}{2}). \quad (5.29)$$

The corresponding saturated gain for each eigen solution is given by

$$g_n = \frac{1}{1 + \frac{W_n}{P_L T_R}}, \quad (5.30)$$

where  $W_n$  is the energy of the corresponding solution and  $P_L = E_L/\tau_L$  the saturation power of the gain. Eq. (5.29) shows that for given  $g$  the eigen solution with  $n = 0$ , the ground mode, has the largest gain per roundtrip. Thus, if there is initially a field distribution which is a superposition of all eigen solutions, the ground mode will grow fastest and will saturate the gain to a value

$$g_s = l + M_s\tau_a^2. \quad (5.31)$$

such that  $\lambda_0 = 0$  and consequently all other modes will decay since  $\lambda_n < 0$  for  $n \geq 1$ . This also proves the stability of the ground mode solution [4]. Thus active modelocking without detuning between resonator round-trip time and modulator period leads to Gaussian steady state pulses with a FWHM pulse width

$$\Delta t_{FWHM} = 2 \ln 2 \tau_a = 1.66 \tau_a. \quad (5.32)$$

The spectrum of the Gaussian pulse is given by

$$\tilde{A}_0(\omega) = \int_{-\infty}^{\infty} A_0(t) e^{i\omega t} dt \quad (5.33)$$

$$= \sqrt{\sqrt{\pi} W_n \tau_a} e^{-\frac{(\omega \tau_a)^2}{2}}, \quad (5.34)$$

and its FWHM is

$$\Delta f_{FWHM} = \frac{1.66}{2\pi \tau_a}. \quad (5.35)$$

Therefore, the time-bandwidth product of the Gaussian is

$$\Delta t_{FWHM} \cdot \Delta f_{FWHM} = 0.44. \quad (5.36)$$

The stationary pulse shape of the modelocked laser is due to the parabolic loss modulation (pulse shortening) in the time domain and the parabolic filtering (pulse stretching) due to the gain in the frequency domain, see Figs. 5.4 and 5.5. The stationary pulse is achieved when both effects balance. Since external modulation is limited to electronic speed and the pulse width does only scale with the inverse square root of the gain bandwidth actively modelocking typically only results in pulse width in the range of 10-100ps.

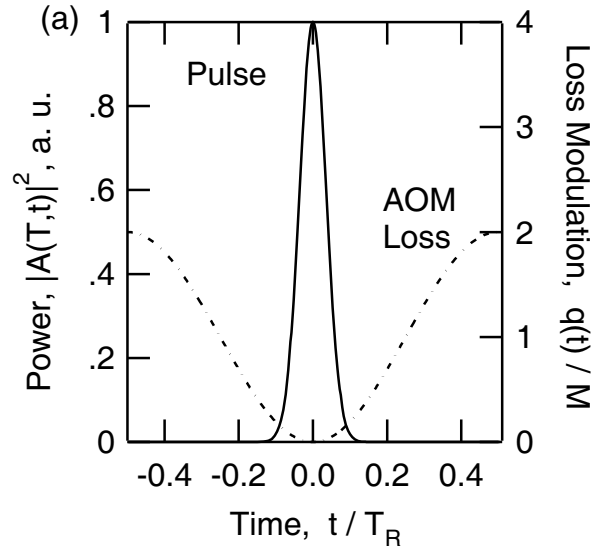


Figure 5.4: (a) Loss modulation gives pulse shortening in each roundtrip

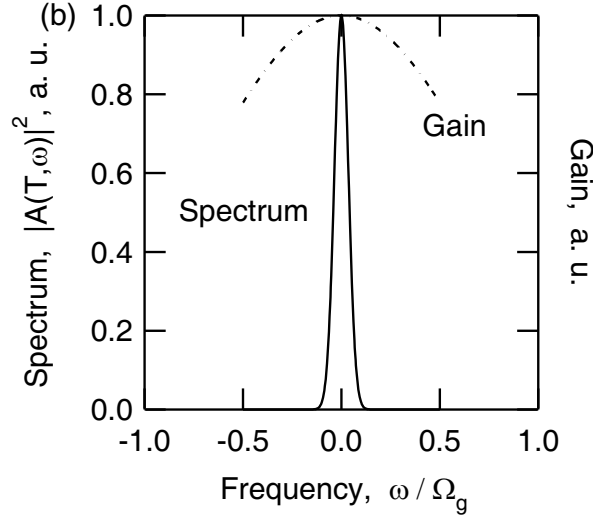


Figure 5.5: (b) the finite gain bandwidth gives pulse broadening in each roundtrip. For a certain pulse width there is balance between the two processes.

For example: Nd:YAG;  $2l = 2g = 10\%$ ,  $\Omega_g = \pi \Delta f_{FWHM} = 0.65$  THz,  $M = 0.2$ ,  $f_m = 100$  MHz,  $D_g = 0.24$  ps<sup>2</sup>,  $M_s = 4 \cdot 10^{16} s^{-1}$ ,  $\tau_p \approx 99$  ps.

With the pulse width (5.28), Eq.(5.31) can be rewritten in several ways

$$g_s = l + M_s \tau_a^2 = l + \frac{D_g}{\tau_a^2} = l + \frac{1}{2} M_s \tau_a^2 + \frac{1}{2} \frac{D_g}{\tau_a^2}, \quad (5.37)$$

which means that in steady state the saturated gain is lifted above the loss level  $l$ , so that many modes in the laser are maintained above threshold. There is additional gain necessary to overcome the loss of the modulator due to the finite temporal width of the pulse and the gain filter due to the finite bandwidth of the pulse. Usually

$$\frac{g_s - l}{l} = \frac{M_s \tau_a^2}{l} \ll 1, \quad (5.38)$$

since the pulses are much shorter than the round-trip time and the stationary pulse energy can therefore be computed from

$$g_s = \frac{g_0}{1 + \frac{W_s}{P_L T_R}} = l. \quad (5.39)$$



Figure 5.6: Modelocking in the frequency domain: The modulator transvers energy from each mode to its neighboring mode, thereby redistributing energy from the center to the wings of the spectrum. This process seeds and injection locks neighboring modes.

The name modelocking originates from studying this pulse formation process in the frequency domain. Note, the term

$$-M [1 - \cos(\omega_M t)] A$$

does generate sidebands on each cavity mode present according to

$$\begin{aligned} & -M [1 - \cos(\omega_M t)] \exp(j\omega_{n_0} t) \\ = & -M \left[ \exp(j\omega_{n_0} t) - \frac{1}{2} \exp(j(\omega_{n_0} t - \omega_M t)) - \frac{1}{2} \exp(j(\omega_{n_0} t + \omega_M t)) \right] \\ = & M \left[ -\exp(j\omega_{n_0} t) + \frac{1}{2} \exp(j\omega_{n_0-1} t) + \frac{1}{2} \exp(j\omega_{n_0+1} t) \right] \end{aligned}$$

if the modulation frequency is the same as the cavity round-trip frequency. The sidebands generated from each running mode is injected into the neighboring modes which leads to synchronisation and locking of neighboring modes, i.e. mode-locking, see Fig.5.6

### 5.3 Active Mode-Locking by Phase Modulation

Side bands can also be generated by a phase modulator instead of an amplitude modulator. However, the generated sidebands are out of phase with

the carrier, which leads to a chirp on the steady state pulse. We can again use the master equation to study this type of modelocking. All that changes is that the modulation becomes imaginary, i.e. we have to replace  $M$  by  $jM$  in Eq.(5.22)

$$T_R \frac{\partial A}{\partial T} = \left[ g(T) + D_g \frac{\partial^2}{\partial t^2} - l - jM (1 - \cos(\omega_M t)) \right] A. \quad (5.40)$$

The imaginary unit can be pulled through much of the calculation and we arrive at the same Hermite Gaussian eigen solutions (5.26,5.27), however, the parameter  $\tau_a$  becomes  $\tau'_a$  and is now complex and not quite the pulse width

$$\tau'_a = \sqrt[4]{-j} \sqrt[4]{D_g/M_s}. \quad (5.41)$$

The ground mode or stationary solution is given by

$$A_0(t) = \sqrt{\frac{W_s}{2^n \sqrt{\pi} n! \tau'_a}} e^{-\frac{t^2}{2\tau_a^2} \frac{1}{\sqrt{2}}(1+j)}, \quad (5.42)$$

with  $\tau_a = \sqrt[4]{D_g/M_s}$  as before. We end up with chirped pulses. How does the pulse shortening actually work, because the modulator just puts a chirp on the pulse, it does actually not shorten it? One can easily show, that if a Gaussian pulse with chirp parameter  $\beta$

$$A_0(t) \sim e^{-\frac{t^2}{2\tau_a^2} \frac{1}{\sqrt{2}}(1+j\beta)}, \quad (5.43)$$

has a chirp  $\beta > 1$ , subsequent filtering is actually shortening the pulse.

## 5.4 Active Mode Locking with Additional SPM

Due to the strong focussing of the pulse in the gain medium also additional self-phase modulation can become important. Lets consider the case of an actively mode-locked laser with additional SPM, see Fig. 5.7. One can write down the corresponding master equation

$$T_R \frac{\partial A}{\partial T} = \left[ g(T) + D_g \frac{\partial^2}{\partial t^2} - l - M_s t^2 - j\delta |A|^2 \right] A. \quad (5.44)$$

Unfortunately, there is no analytic solution to this equation. But it is not difficult to guess what will happen in this case. As long as the SPM is not

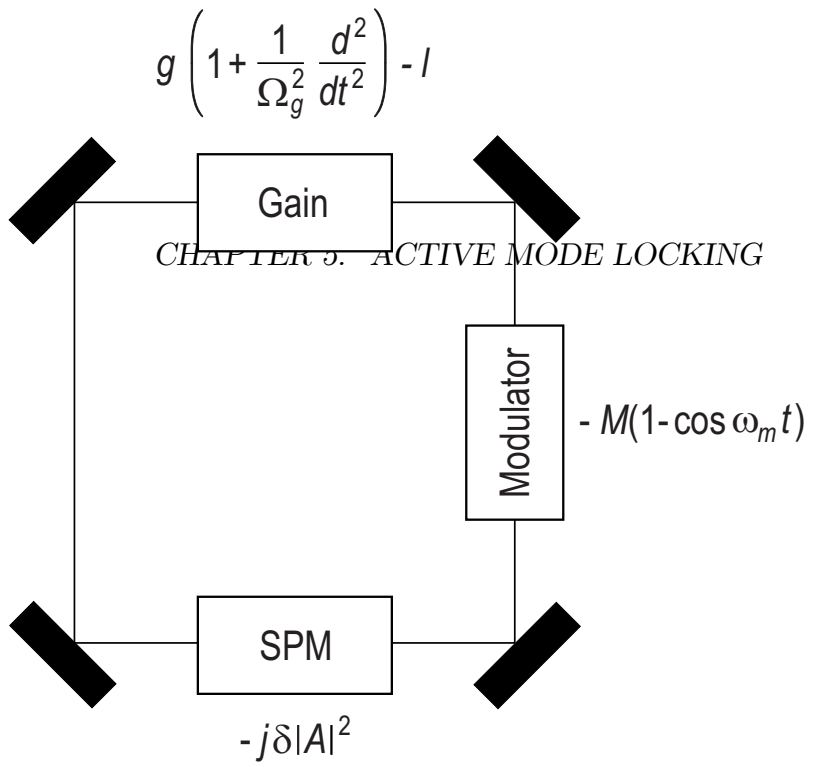


Figure 5.7: Active mode-locking with SPM

excessive, the pulses will experience additional self-phase modulation, which creates a chirp on the pulse. Thus one can make an ansatz with a chirped Gaussian similar to (5.43) for the steady state solution of the master equation (5.44)

$$A_0(t) = A e^{-\frac{t^2}{2\tau_a^2}(1+j\beta)+j\Psi T/T_R} \quad (5.45)$$

Note, we allow for an additional phase shift per roundtrip  $\Psi$ , because the added SPM does not leave the phase invariant after one round-trip. This is still a steady state solution for the intensity envelope. Substitution into the master equation using the intermediate result

$$\frac{\partial^2}{\partial t^2} A_0(t) = \left\{ \frac{t^2}{\tau_a^4} (1+j\beta)^2 - \frac{1}{\tau_a^2} (1+j\beta) \right\} A_0(t). \quad (5.46)$$

leads to

$$\begin{aligned} j\Psi A_0(t) = & \left\{ g - l + D_g \left[ \frac{t^2}{\tau_a^4} (1+j\beta)^2 - \frac{1}{\tau_a^2} (1+j\beta) \right] \right. \\ & \left. - M_s t^2 - j\delta |A|^2 e^{-\frac{t^2}{\tau_a^2}} \right\} A_0(t). \end{aligned} \quad (5.47)$$

To find an approximate solution we expand the Gaussian in the bracket, which is a consequence of the SPM to first order in the exponent.

$$j\Psi = g - l + D_g \left[ \frac{t^2}{\tau_a^4} (1 + j\beta)^2 - \frac{1}{\tau_a^2} (1 + j\beta) \right] - M_s t^2 - j\delta |A|^2 \left( 1 - \frac{t^2}{\tau_a^2} \right). \quad (5.48)$$

This has to be fulfilled for all times, so we can compare coefficients in front of the constant terms and the quadratic terms, which leads to two complex conditions. This leads to four equations for the unknown pulsewidth  $\tau_a$ , chirp  $\beta$ , round-trip phase  $\Psi$  and the necessary excess gain  $g - l$ . With the nonlinear peak phase shift due to SPM,  $\phi_0 = \delta |A|^2$ . Real and Imaginary parts of the quadratic terms lead to

$$0 = \frac{D_g}{\tau_a^4} (1 - \beta^2) - M_s, \quad (5.49)$$

$$0 = 2\beta \frac{D_g}{\tau_a^4} + \frac{\phi_0}{\tau_a^2}, \quad (5.50)$$

and the constant terms give the excess gain and the additional round-trip phase.

$$g - l = \frac{D_g}{\tau_a^2}, \quad (5.51)$$

$$\Psi = D_g \left[ -\frac{1}{\tau_a^2} \beta \right] - \phi_0. \quad (5.52)$$

The first two equations directly give the chirp and pulse width.

$$\beta = -\frac{\phi_0 \tau_a^2}{2D_g} \quad (5.53)$$

$$\tau_a^4 = \frac{D_g}{M_s + \frac{\phi_0^2}{4D_g}}. \quad (5.54)$$

However, one has to note, that this simple analysis does not give any hint on the stability of these approximate solution. Indeed computer simulations show, that after an additional pulse shorting of about a factor of 2 by SPM beyond the pulse width already achieved by pure active mode-locking on its own, the SPM drives the pulses unstable [5]. This is one of the reasons, why very broadband laser media, like Ti:sapphire, can not simply generate

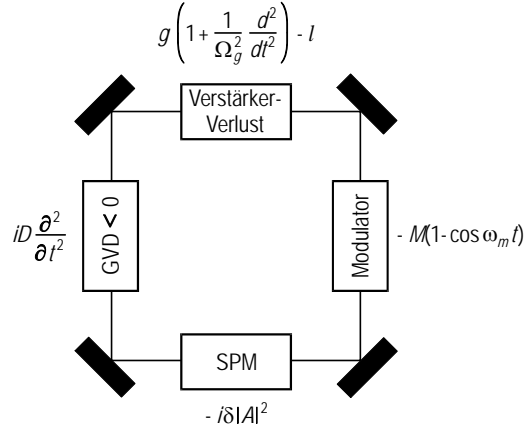


Figure 5.8: Active mode-locking with additional soliton formation

femtosecond pulses via active modelocking. The SPM occurring in the gain medium for very short pulses drives the modelocking unstable. Additional stabilization measures have to be adopted. For example the addition of negative group delay dispersion might lead to stable soliton formation in the presence of the active modelocker.

## 5.5 Active Mode Locking with Soliton Formation

Experimental results with fiber lasers [8, 9, 11] and solid state lasers [10] indicated that soliton shaping in the negative GDD regime leads to pulse stabilization and considerable pulse shorting. With sufficient negative dispersion and self-phase modulation in the system and picosecond or even femtosecond pulses, it is possible that the pulse shaping due to GDD and SPM is much stronger than due to modulation and gain filtering, see Fig. 5.8. The resulting master equation for this case is

$$T_R \frac{\partial A}{\partial T} = \left[ g + (D_g - j |D|) \frac{\partial^2}{\partial t^2} - l - M (1 - \cos(\omega_M t)) - j \delta |A|^2 \right] A. \quad (5.55)$$

For the case, that soliton formation takes over, the steady state solution a soliton plus a continuum contribution

$$A(T, t) = (a(x)e^{jpt} + a_c(T, t)) e^{-j\theta} \quad (5.56)$$

with

$$a(x) = A \operatorname{sech}(x), \quad \text{and} \quad x = \frac{1}{\tau}(t + 2D \int_0^T p(T') dT' - t_0) \quad (5.57)$$

where  $a_c$  is the continuum contribution. The phase is determined by

$$\theta(T) = \theta_0(T) - \frac{D}{T_R} \int_0^T \left( \frac{1}{\tau(T')^2} - p(T')^2 \right) dT', \quad (5.58)$$

whereby we always assume that the relation between the soliton energy and soliton width is maintained (3.9)

$$\frac{|D|}{\tau(T)^2} = \frac{\delta A(T)^2}{2}. \quad (5.59)$$

We also allow for a continuous change in the soliton amplitude  $A$  or energy  $W = 2A^2\tau$  and the soliton variables phase  $\theta_0$ , carrier frequency  $p$  and timing  $t_0$ .  $\phi_0$  is the soliton phase shift per roundtrip

$$\phi_0 = \frac{|D|}{\tau^2}. \quad (5.60)$$

However, we assume that the changes in carrier frequency, timing and phase stay small. Introducing (5.56) into (5.55) we obtain according to the soliton perturbation theory developed in chapter 3.5

$$\begin{aligned} & T_R \left[ \frac{\partial a_c}{\partial T} + \frac{\partial W}{\partial T} \mathbf{f}_w + \frac{\partial \Delta \theta}{\partial T} \mathbf{f}_\theta + \frac{\partial \Delta p}{\partial T} \mathbf{f}_p + \frac{\partial \Delta t}{\partial T} \mathbf{f}_t \right] \\ &= \phi_0 \mathbf{L}(\mathbf{a}_c + \Delta p \mathbf{f}_p) + \mathbf{R}(\mathbf{a} + \Delta p \mathbf{f}_p + \mathbf{a}_c) \\ & \quad - M \omega_M \sin(\omega_M \tau x) \Delta t \mathbf{a}(x) \end{aligned} \quad (5.61)$$

The last term arises because the active modelocker breaks the time invariance of the system and leads to a restoring force pushing the soliton back to its equilibrium position.  $\mathbf{L}$ ,  $\mathbf{R}$  are the operators of the linearized NSE and of the active mode locking scheme, respectively

$$\mathbf{R} = g \left( 1 + \frac{1}{\Omega_g^2 \tau^2} \frac{\partial^2}{\partial x^2} \right) - l - M (1 - \cos(\omega_M \tau x)), \quad (5.62)$$

The vectors  $\mathbf{f}_w$ ,  $\mathbf{f}_\theta$ ,  $\mathbf{f}_p$  and  $\mathbf{f}_t$  describe the change in the soliton when the soliton energy, phase, carrier frequency and timing varies.

### 5.5.1 Stability Condition

We want to show, that a stable soliton can exist in the presence of the modelocker and gain dispersion if the ratio between the negative GDD and gain dispersion is sufficiently large. From (5.61) we obtain the equations of motion for the soliton parameters and the continuum by carrying out the scalar product with the corresponding adjoint functions. Specifically, for the soliton energy we get

$$\begin{aligned} T_R \frac{\partial W}{\partial T} &= 2 \left( g - l - \frac{g}{3\Omega_g^2 \tau^2} - \frac{\pi^2}{24} M \omega_M^2 \tau^2 \right) W \\ &+ < \mathbf{f}_w^{(+)} | \mathbf{R} \mathbf{a}_c > . \end{aligned} \quad (5.63)$$

We see that gain saturation does not lead to a coupling between the soliton and the continuum to first order in the perturbation, because they are orthogonal to each other in the sense of the scalar product (3.37). This also means that to first order the total field energy is contained in the soliton.

Thus to zero order the stationary soliton energy  $W_0 = 2A_0^2 \tau$  is determined by the condition that the saturated gain is equal to the total loss due to the linear loss  $l$ , gain filtering and modulator loss

$$g - l = \frac{\pi^2}{24} M \omega_M^2 \tau^2 + \frac{g}{3\Omega_g^2 \tau^2} \quad (5.64)$$

with the saturated gain

$$g = \frac{g_0}{1 + W_0/E_L}. \quad (5.65)$$

Linearization around this stationary value gives for the soliton perturbations

$$\begin{aligned}
T_R \frac{\partial \Delta W}{\partial T} &= 2 \left( - \frac{g}{(1 + W_0/E_L)} \left( \frac{W_0}{E_L} + \frac{1}{3\Omega_g^2 \tau^2} \right) \right. \\
&\quad \left. + \frac{\pi^2}{12} M \omega_M^2 \tau^2 \right) \Delta W + \langle \mathbf{f}_w^{(+)} | \mathbf{R} \mathbf{a}_c \rangle
\end{aligned} \tag{5.66}$$

$$T_R \frac{\partial \Delta \theta}{\partial T} = \langle \mathbf{f}_\theta^{(+)} | \mathbf{R} \mathbf{a}_c \rangle \tag{5.67}$$

$$T_R \frac{\partial \Delta p}{\partial T} = - \frac{4g}{3\Omega_g^2 \tau^2} \Delta p + \langle \mathbf{f}_p^{(+)} | \mathbf{R} \mathbf{a}_c \rangle \tag{5.68}$$

$$\begin{aligned}
T_R \frac{\partial \Delta t}{\partial T} &= - \frac{\pi^2}{6} M \omega_M^2 \tau^2 \Delta t + 2|D| \Delta p \\
&\quad + \langle \mathbf{f}_t^{(+)} | \mathbf{R} \mathbf{a}_c \rangle
\end{aligned} \tag{5.69}$$

and for the continuum we obtain

$$\begin{aligned}
T_R \frac{\partial g(k)}{\partial T} &= j\Phi_0(k^2 + 1)g(k) + \langle \mathbf{f}_k^{(+)} | \mathbf{R} \mathbf{a}_c \rangle \\
&\quad + \langle \mathbf{f}_k^{(+)} | \mathbf{R} (\mathbf{a}_0(x) + \Delta w \mathbf{f}_w + \Delta p \mathbf{f}_p) \rangle \\
&\quad - \langle \mathbf{f}_k^{(+)} | M \omega_M \sin(\omega_M \tau x) \mathbf{a}_0(x) \rangle . \Delta t
\end{aligned} \tag{5.70}$$

Thus the action of the active modelocker and gain dispersion has several effects. First, the modelocker leads to a restoring force in the timing of the soliton (5.69). Second, the gain dispersion and the active modelocker lead to coupling between the perturbed soliton and the continuum which results in a steady excitation of the continuum.

However, as we will see later, the pulse width of the soliton, which can be stabilized by the modelocker, is not too far from the Gaussian pulse width by only active mode locking. Then relation

$$\omega_M \tau \ll 1 \ll \Omega_g \tau \tag{5.71}$$

is fulfilled. The weak gain dispersion and the weak active modelocker only couples the soliton to the continuum, but to first order the continuum does not couple back to the soliton. Neglecting higher order terms in the matrix elements of eq.(5.70) [6] results in a decoupling of the soliton perturbations from the continuum in (5.66) to (5.70). For a laser far above threshold, i.e.



$W_0/E_L \gg 1$ , gain saturation always stabilizes the amplitude perturbation and eqs.(5.67) to (5.69) indicate for phase, frequency and timing fluctuations. This is in contrast to the situation in a soliton storage ring where the laser amplifier compensating for the loss in the ring is below threshold [14].

By inverse Fourier transformation of (5.70) and weak coupling, we obtain for the associated function of the continuum

$$\begin{aligned} T_R \frac{\partial G}{\partial T} = & \left[ g - l + j\Phi_0 + \frac{g}{\Omega_g^2} (1 - jD_n) \frac{\partial^2}{\partial t^2} \right. \\ & \left. - M(1 - \cos(\omega_M t)) \right] G + \mathcal{F}^{-1} \left\{ \langle \mathbf{f}_k^{(+)} | \mathbf{R} \mathbf{a}_0(x) \rangle \right. \\ & \left. - \langle \mathbf{f}_k^{(+)} | M \omega_M \sin(\omega_M \tau x) \mathbf{a}_0(x) \rangle \Delta t \right\} \end{aligned} \quad (5.72)$$

where  $D_n$  is the dispersion normalized to the gain dispersion

$$D_n = |D| \Omega_g^2 / g. \quad (5.73)$$

Note, that the homogeneous part of the equation of motion for the continuum, which governs the decay of the continuum, is the same as the homogeneous part of the equation for the noise in a soliton storage ring at the position where no soliton or bit is present [14]. Thus the decay of the continuum is not affected by the nonlinearity, but there is a continuous excitation of the continuum by the soliton when the perturbing elements are passed by the soliton. Thus under the above approximations the question of stability of the soliton solution is completely governed by the stability of the continuum (5.72). As we can see from (5.72) the evolution of the continuum obeys the active mode locking equation with GVD but with a value for the gain determined by (5.64). In the parabolic approximation of the cosine, we obtain again the Hermite Gaussians as the eigensolutions for the evolution operator but the width of these eigensolutions is now given by

$$\tau_c = \tau_a \sqrt[4]{(1 - jD_n)} \quad (5.74)$$

and the associated eigenvalues are

$$\lambda_m = j\Phi_0 + g - l - M \omega_M^2 \tau_a^2 \sqrt{(1 - jD_n)} \left(m + \frac{1}{2}\right). \quad (5.75)$$

The gain is clamped to the steady state value given by condition (5.64) and we obtain

$$\lambda_m = +j\Phi_0 + \frac{1}{3}\sqrt{D_g M_s} \left[ \left(\frac{\tau_a}{\tau}\right)^2 + \frac{\pi^2}{4} \left(\frac{\tau_a}{\tau}\right)^{-2} - 6\sqrt{(1-jD_n)}\left(m + \frac{1}{2}\right) \right]. \quad (5.76)$$

Stability is achieved when all continuum modes see a net loss per roundtrip,  $Re\{\lambda_m\} < 0$  for  $m \geq 0$ , i.e. we get from (5.76)

$$\left(\frac{\tau_a}{\tau}\right)^2 + \frac{\pi^2}{4} \left(\frac{\tau}{\tau_a}\right)^2 < 3Re\{\sqrt{(1-jD_n)}\}. \quad (5.77)$$

Relation (5.77) establishes a quadratic inequality for the pulse width reduction ratio  $\xi = (\tau_a/\tau)^2$ , which is a measure for the pulse width reduction due to soliton formation

$$\xi^2 - 3Re\{\sqrt{(1-jD_n)}\}\xi + \frac{\pi^2}{4} < 0. \quad (5.78)$$

As has to be expected, this inequality can only be satisfied if we have a minimum amount of negative normalized dispersion so that a soliton can be formed at all

$$D_{n,crit} = 0.652. \quad (5.79)$$

Therefore our perturbation ansatz gives only meaningful results beyond this critical amount of negative dispersion. Since  $\xi$  compares the width of a Gaussian with that of a secant hyperbolic it is more relevant to compare the full width half maximum of the intensity profiles of the corresponding pulses which is given by

$$R = \frac{1.66}{1.76} \sqrt{\xi}. \quad (5.80)$$

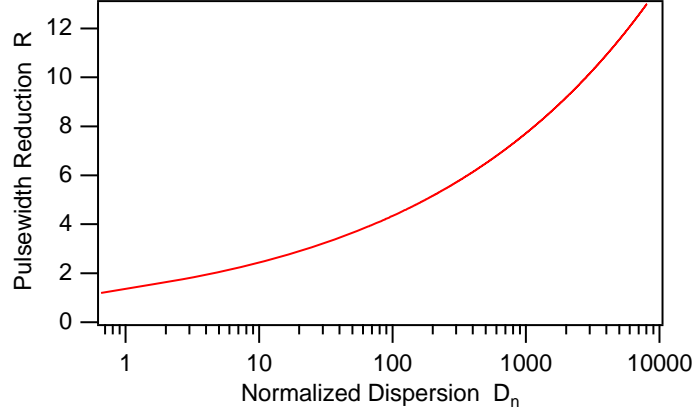


Figure 5.9: Pulsewidth reduction as a function of normalized dispersion. Below  $D_{n,crit} = 0.652$  no stable soliton can be formed.

Figure 5.9 shows the maximum pulse width reduction  $R$  allowed by the stability criterion (5.78) as a function of the normalized dispersion. The critical value for the pulse width reduction is  $R_{crit} \approx 1.2$ . For large normalized dispersion Fig. 1 shows that the soliton can be kept stable at a pulse width reduced by up to a factor of 5 when the normalized dispersion can reach a value of 200. Even at a moderate negative dispersion of  $D_n = 5$ , we can achieve a pulsewidth reduction by a factor of 2. For large normalized dispersion the stability criterion (5.78) approaches asymptotically the behavior

$$\xi < \sqrt{\frac{9D_n}{2}} \quad \text{or} \quad R < \frac{1.66}{1.76} \sqrt[4]{\frac{9D_n}{2}}. \quad (5.81)$$

Thus, the possible pulse-width reduction scales with the fourth root of the normalized dispersion indicating the need of an excessive amount of dispersion necessary to maintain a stable soliton while suppressing the continuum. The physical reason for this is that gain filtering and the active modelocker continuously shed energy from the soliton into the continuum. For the soliton the action of GVD and SPM is always in balance and maintains the pulse shape. However, as can be seen from (5.72), the continuum, which can be viewed as a weak background pulse, does not experience SPM once it is generated and therefore gets spread by GVD. This is also the reason why the eigenstates of the continuum consist of long chirped pulses that scale

also with the fourth root of the dispersion (5.74). Then, the long continuum pulses suffer a much higher loss in the active modulator in contrast to the short soliton which suffers reduced gain when passing the gain medium due to its broader spectrum. The soliton is stable as long as the continuum sees less roundtrip gain than the soliton.

In principle by introducing a large amount of negative dispersion the theory would predict arbitrarily short pulses. However, the master equation (5.55) only describes the laser system properly when the nonlinear changes of the pulse per pass are small. This gives an upper limit to the nonlinear phase shift  $\Phi_0$  that the soliton can undergo during one roundtrip. A conservative estimation of this upper limit is given with  $\Phi_0 = 0.1$ . Then the action of the individual operators in (5.55) can still be considered as continuous. Even if one considers larger values for the maximum phase shift allowed, since in fiber lasers the action of GVD and SPM occurs simultaneously and therefore eq.(5.55) may describe the laser properly even for large nonlinear phase shifts per roundtrip, one will run into intrinsic soliton and sideband instabilities for  $\Phi_0$  approaching  $2\pi$  [29, 30]. Under the condition of a limited phase shift per roundtrip we obtain

$$\tau^2 = \frac{|D|}{\Phi_0}. \quad (5.82)$$

Thus from (5.32), the definition of  $\xi$ , (5.81) and (5.82) we obtain for the maximum possible reduction in pulsewidth

$$R_{max} = \frac{1.66}{1.76} \sqrt[12]{\frac{(9\Phi_0/2)^2}{D_g M_s}} \quad (5.83)$$

and therefore for the minimum pulsewidth

$$\tau_{min} = \sqrt[6]{\frac{2D_g^2}{9\Phi_0 M_s}}. \quad (5.84)$$

The necessary amount of normalized negative GVD is then given by

$$D_n = \frac{2}{9} \sqrt[3]{\frac{(9\Phi_0/2)^2}{D_g M_s}}. \quad (5.85)$$

Eqs.(5.83) to (5.85) constitute the main results of this paper, because they allow us to compute the possible pulse width reduction and the necessary

gain material	$\frac{\Omega_g}{2\pi (THz)}$	M	$\frac{\omega_M}{2\pi (MHz)}$	$\frac{D_g}{(ps^2)}$	$M_s \cdot (ps^2)$	$\frac{\tau_{a,FWHM}}{(ps)}$
Nd:YAG	0.06	0.2	250	0.7	$2.5 \cdot 10^{-7}$	68
Nd:glass	4	0.2	250	$158 \cdot 10^{-6}$	$2.5 \cdot 10^{-7}$	8.35
Cr:LiSAF	32	0.2	250	$2.4 \cdot 10^{-6}$	$2.5 \cdot 10^{-7}$	3
Ti:sapphire	43	0.01	100	$1.4 \cdot 10^{-6}$	$2 \cdot 10^{-9}$	8.5

gain material	$R_{max}$	$\frac{\tau_{min,FWHM}}{(ps)}$	$D_n$	$\frac{\tau_{trans}}{T_R}$	
Nd:YAG	3	22.7	23.4	702	
Nd:glass	6	1.4	385	11,538	
Cr:LiSAF	8.6	0.35	1563	46,600	
Ti:sapphire	13.5	0.63	9367	281,000	

Table 5.1: Maximum pulsewidth reduction and necessary normalized GVD for different laser systems. In all cases we used for the saturated gain  $g = 0.1$  and the soliton phase shift per roundtrip  $\Phi_0 = 0.1$ . For the broadband gain materials the last column indicates rather long transient times which calls for regenerative mode locking.

negative GVD for a given laser system. Table (5.1) shows the evaluation of these formulas for several gain media and typical laser parameters.

Table 5.1 shows that soliton formation in actively mode-locked lasers may lead to considerable pulse shortening, up to a factor of 10 in Ti:sapphire. Due to the 12th root in (5.83) the shortening depends mostly on the bandwidth of the gain material which can change by several orders of magnitude for the different laser materials. The amount of negative dispersion for achieving this additional pulse shortening is in a range which can be achieved by gratings, Gires-Tournois interferometers, or prisms.

Of course, in the experiment one has to stay away from these limits to suppress the continuum sufficiently. However, as numerical simulations show, the transition from stable to instable behaviour is remarkably sharp. The reason for this can be understood from the structure of the eigenvalues for the continuum (5.76). The time scale for the decay of transients is given by the inverse of the real part of the fundamental continuum mode which diverges at the transition to instability. Nevertheless, a good estimate for this transient time is given by the leading term of the real part of (5.76)

$$\frac{\tau_{trans}}{T_R} = \frac{1}{Re\{\lambda_0\}} \approx \frac{3}{\sqrt{D_g M_s R^2}} \quad (5.86)$$

This transient time is also shown in Table (5.1) for different laser systems. Thus these transients decay, if not too close to the instability border, on time scales from approximately 1,000 up to some 100,000 roundtrips, depending strongly on the gain bandwidth and modulation strength. Consequently, to first order the eigenvalues of the continuum modes, which are excited by the right hand side of (5.72), are purely imaginary and independent of the mode number, i.e.  $\lambda_n \approx j\Phi_0$ . Therefore, as long as the continuum is stable, the solution to (5.72) is given by

$$\begin{aligned} G(x) &= \frac{-j}{\Phi_0} \mathcal{F}^{-1} \left\{ < \mathbf{f}_k^{(+)} | \mathbf{R} \mathbf{a}_0(x) > \right. \\ &\quad \left. - M_s \tau^2 < \mathbf{f}_k^{(+)} | x \mathbf{a}_0(x) > \frac{\Delta t}{\tau} \right\}. \end{aligned} \quad (5.87)$$

Thus, in steady state the continuum is on the order of

$$|G(x)| \approx \frac{A_0}{\Phi_0} \frac{D_g}{\tau^2} = \frac{A_0}{D_n}. \quad (5.88)$$

which demonstrates again the spreading of the continuum by the dispersion. Equation (5.88) shows that the nonlinear phase shift of the solitary pulse per round trip has to be chosen as large as possible. This also maximizes the normalized dispersion, so that the radiation shed from the soliton into the continuum changes the phase rapidly enough such that the continuum in steady state stays small. Note that the size of the generated continuum according to (5.88) is rather independent of the real part of the lowest eigenvalue of the continuum mode. Therefore, the border to instability is very sharply defined. However, the time scale of the transients at the transition to instability can become arbitrarily long. Therefore, numerical simulations are only trustworthy if the time scales for transients in the system are known from theoretical considerations as those derived above in (5.86). The simulation time for a given laser should be at least of the order of 10 times  $\tau_{trans}$  or even longer, if operated close to the instability point, as we will see in the next section.

### 5.5.2 Numerical simulations

Table 5.1 shows that soliton formation in actively mode-locked lasers may lead to considerable pulse shortening, up to a factor of 10 in Ti:sapphire. We want to illustrate that at the example of a Nd:YAG laser, which is chosen due to its moderate gain bandwidth, and therefore, its large gain dispersion. This will limit the pulsewidth reduction possible to about 3, but the decay time of the continuum (5.86) (see also Table 5.1) is then in a range of 700 roundtrips so that the steady state of the mode-locked laser can be reached with moderate computer time, while the approximations involved are still satisfied. The system parameters used for the simulation are shown in table 5.2. For the simulation of eq.(5.55) we use the standard split-step Fourier transform method. Here the discrete action of SPM and GDD per roundtrip is included by choosing the integration step size for the  $T$  integration to be the roundtrip time  $T_R$ . We used a discretisation of 1024 points over the bandwidth of  $1THz$ , which corresponds to a resolution in the time domain of  $1ps$ . The following figures, show only one tenth of the simulated window in time and frequency.

Figure 5.10 shows the result of the simulation starting with a 68-ps-long Gaussian pulse with a pulse energy of  $W = 40$  nJ for  $D_n = 24$ , i.e.  $D = -17$  ps<sup>2</sup>. For the given SPM coefficient this should lead to stable pulse shortening by a factor of  $R = 2.8$ . Thus after at least a few thousand roundtrips the

parameter	value
$l$	0.1
$g_0$	1
$P_L$	1W
$\Omega_g$	$2\pi \cdot 60GHz$
$\omega_M$	$2\pi \cdot 0.25GHz$
$T_{in}$	$\lambda_{in}$

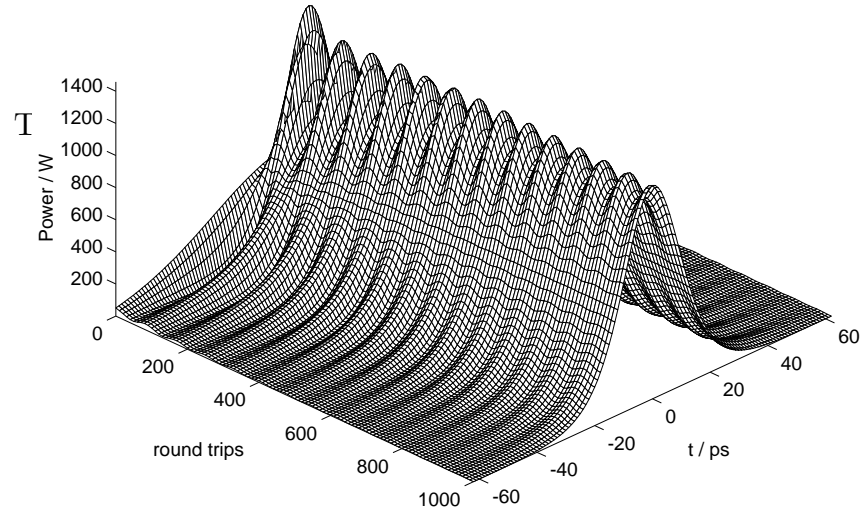


Figure 5.10: Time evolution of the pulse intensity in a Nd:YAG laser for the parameters in Table 5.2,  $D = -17ps^2$ , for the first 1,000 roundtrips in the laser cavity, starting with a 68ps long Gaussian pulse.



laser should be in steady state again with a FWHM pulsewidth of 24 ps. Fig. 5.10 shows the pulse evolution over the first thousand round-trips, i.e.  $4\mu\text{s}$  real time. The long Gaussian pulse at the start contains an appreciable amount of continuum. The continuum part of the solution does not experience the nonlinear phase shift due to SPM in contrast to the soliton. Thus the soliton interferes with the continuum periodically with the soliton period of  $T_{\text{soliton}}/T_R = 2\pi/\phi_0 = 20\pi$ . This is the reason for the oscillations of the pulse amplitude seen in Fig. 5.10 which vanish with the decay of the continuum. Note also that the solitary pulse is rapidly formed, due to the large nonlinear phase shift per roundtrip. Figure 5.11 shows the simulation in time and frequency domain over 10,000 roundtrips. The laser reaches steady state after about 4,000 roundtrips which corresponds to  $6 \times \tau_{\text{trans}}$  and the final pulsewidth is 24 ps in exact agreement with the predictions of the analytic formulas derived above.

Lower normalized dispersion of  $D_n = 15$  or  $D = -10 \text{ ps}^2$  only allows for a reduction in pulsewidth by  $R = 2.68$ . However, using the same amount of SPM as before we leave the range of stable soliton generation.

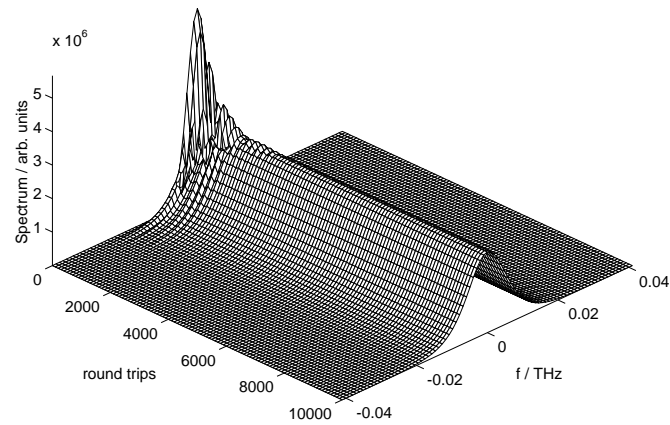


Figure 5.11: Time evolution of the intensity (a) and spectrum (b) for the same parameters as Fig. 2 over 10,000 roundtrips. The laser reaches steady state after about 4,000 roundtrips.

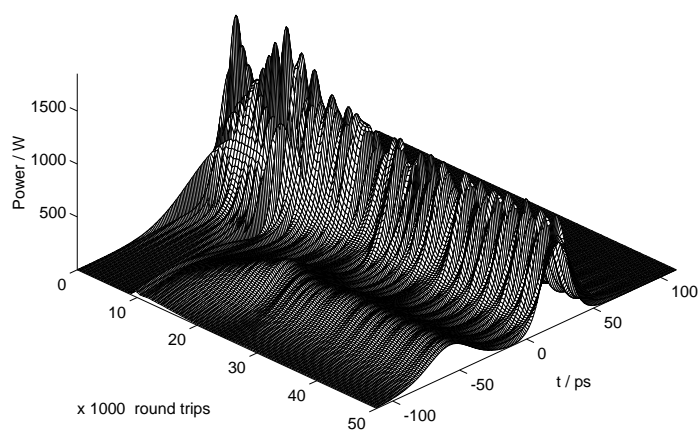
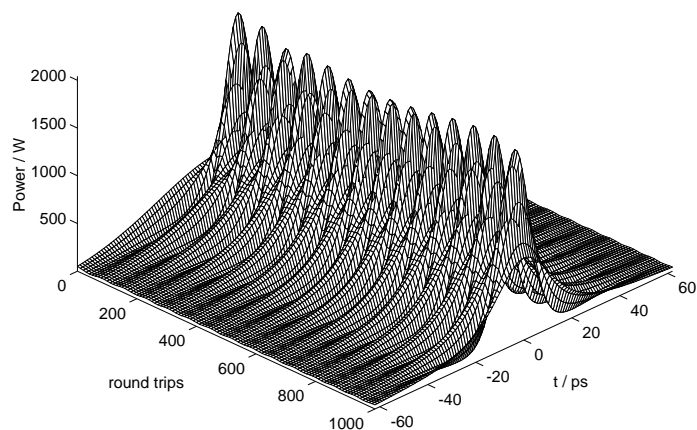


Figure 5.12: (a) Time evolution of the intensity in a Nd:YAG laser for the parameters in Table 5.2 over the first 1,000 round-trips. The amount of negative dispersion is reduced to  $D = -10ps^2$ , starting again from a 68ps long pulse. The continuum in this case does not decay as in Fig. 5.2 and 5.3 due to the insufficient dispersion. (b) Same simulation over 50,000 round-trips.

Figure 5.12(a) shows similar to Fig. 5.10 the first 1,000 roundtrips in that case. Again the solitary pulse is rapidly formed out of the long Gaussian initial pulse. But in contrast to the situation in Fig. 5.10, the continuum does not any longer decay on this time scale. The dispersion is too low to spread the continuum rapidly enough. The continuum then accumulates over many roundtrips as can be seen from Fig. 5.12(b). After about 10,000 roundtrips the continuum has grown so much that it extracts an appreciable amount of energy from the soliton. But surprisingly the continuum modes stop growing after about 30,000 roundtrips and a new quasi stationary state is reached.

### 5.5.3 Experimental Verification

The theory above explains very well the ps Ti:sapphire experiments [10] in the regime where the pulses are stabilized by the active modelocker alone. Gires-Tournois interferometers were used to obtain large amounts of negative GDD to operate the laser in the stable soliton regime derived above. Here we want to discuss in more detail the experimental results obtained recently with a regeneratively, actively mode-locked Nd:glass laser [7], resulting in 310 fs. If SPM and GVD could be neglected, the weak modelocker would produce Gaussian pulses with a FWHM of  $\tau_{a,FWHM} = 10$  ps. However, the strong SPM prevents stable pulse formation. The negative dispersion available in the experiment is too low to achieve stable soliton formation, because the pulse width of the soliton at this power level is given by  $\tau = 4|D|/(\delta W) = 464$  fs, for the example discussed. The normalized dispersion is not large enough to allow for such a large pulse width reduction. Providing enough negative dispersion results in a 310 fs perfectly sech-shaped soliton-like pulse as shown in Fig. 5.13. A numerical simulation of this case would need millions of roundtrips through the cavity until a stationary state is reached. That means milliseconds of real time, but would necessitate days of computer time. Also the transition to instable behaviour has been observed, which is the characteristic occurrence of a short solitary fs-pulse together with a long ps-pulse due to the instable continuum as we have found in the numerical simulation for the case of a Nd:YAG laser (see Fig. 5.12(b)). Figure 5.14 shows the signal of a fast detector diode on the sampling oscilloscope. The detector has an overall bandwidth of  $25\text{GHz}$  and therefore can not resolve the fs-pulse, but can resolve the width of the following roughly  $100\text{ps}$  long pulse.

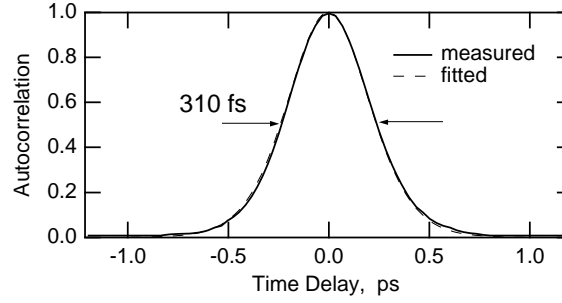


Figure 5.13: Autocorrelation of the actively mode-locked pulse (solid line) and corresponding  $\text{sech}^2$  fit (dashed line) with additional soliton formation.

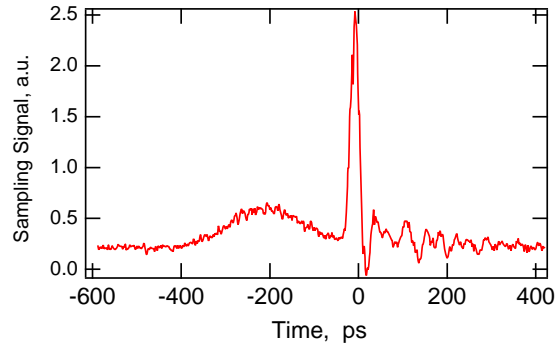


Figure 5.14: Sampling signal of fast detector when the mode-locked laser operates at the transition to instability. The short fs pulse can not be resolved by the detector and therefore results in a sharp spike corresponding to the detector response time. In advance of the fs-pulse travels a roughly 100ps long pulse.

## 5.6 Active Modelocking with Detuning

So far, we only considered the case of perfect synchronism between the round-trip of the pulse in the cavity and the external modulator. Technically, such perfect synchronism is not easy to achieve. One way would be to do regenerative mode locking, i.e. a part of the output signal of the modelocked laser is detected, the beatnote at the round-trip frequency is filtered out from the detector, and sent to an amplifier, which drives the modulator. This procedure enforces synchronism if the cavity length undergoes fluctuations due to acoustic vibrations and thermal expansion.

Nevertheless, it is interesting to know how sensitive the system is against detuning between the modulator and the resonator. It turns out that this is a physically and mathematically rich situation, which applies to many other phenomena occurring in externally driven systems, such as the transition from laminar to turbulent flow in hydrodynamics. This transition has puzzled physicists for more than a hundred years [15]. During the last 5 to 10 years, a scenario for the transition to turbulence has been put forward by Trefethen and others [16]. This model gives not only a quantitative description of the kind of instability that leads to a transition from laminar, i.e. highly ordered dynamics, to turbulent flow, i.e. chaotic motion, but also an intuitive physical picture why turbulence is occurring. Such a picture is the basis for many laser instabilities especially in synchronized laser systems. According to this theory, turbulence is due to strong transient growth of deviations from a stable stationary point of the system together with a nonlinear feedback mechanism. The nonlinear feedback mechanism couples part of the amplified perturbation back into the initial perturbation. Therefore, the perturbation experiences strong growth repeatedly. Once the transient growth is large enough, a slight perturbation from the stable stationary point renders the system into turbulence. Small perturbations are always present in real systems in the form of system intrinsic noise or environmental noise and, in computer simulations, due to the finite precision. The predictions of the linearized stability analysis become meaningless in such cases. The detuned actively modelocked laser is an excellent example of such a system, which in addition can be studied analytically. The detuned case has been only studied experimentally [17][18] or numerically [19] so far. Here, we consider an analytical approach. Note, that this type of instability can not be detected by a linear stability analysis which is widely used in laser theories and which we use in this course very often to prove stable pulse formation.

One has to be aware that such situations may arise, where the results of a linearized stability analysis have only very limited validity.

The equation of motion for the pulse envelope in an actively modelocked laser with detuning can be written as

$$T_M \frac{\partial A(T, t)}{\partial T} = \left[ g(T) - l + D_f \frac{\partial^2}{\partial t^2} - M(1 - \cos(\omega_M t)) + T_d \frac{\partial}{\partial t} \right] A(T, t). \quad (5.89)$$

Here,  $A(T, t)$  is the pulse envelope as before. There is the time  $T$  which is coarse grained on the time scale of the resonator round-trip time  $T_R$  and the time  $t$ , which resolves the resulting pulse shape. The saturated gain is denoted by  $g(T)$  and left dynamical, because we no longer assume that the gain and field dynamics reaches a steady state eventually. The curvature of the intracavity losses in the frequency domain, which limit the bandwidth of the laser, is given by  $D_f$  and left fixed for simplicity.  $M$  is the depth of the loss modulation introduced by the modulator with angular frequency  $\omega_M = 2\pi/T_M$ , where  $T_M$  is the modulator period. Note that Eq.(5.89) describes the change in the pulse between one period of modulation. The detuning between resonator round-trip time and the modulator period is  $T_d = T_M - T_R$ . This detuning means that the pulse hits the modulator with some temporal off-set after one round-trip, which can be described by adding the term  $T_d \frac{\partial}{\partial t} A$  in the master equation. The saturated gain  $g$  obeys a separate ordinary differential equation

$$\frac{\partial g(T)}{\partial T} = -\frac{g(T) - g_0}{\tau_L} - g \frac{W(T)}{P_L}. \quad (5.90)$$

As before,  $g_0$  is the small signal gain due to the pumping,  $P_L$  the saturation power of the gain medium,  $\tau_L$  the gain relaxation time and  $W(T) = \int |A(T, t)|^2 dt$  the total field energy stored in the cavity at time  $T$ .

As before, we expect pulses with a pulse width much shorter than the round-trip time in the cavity and we assume that they still will be placed in time near the position where the modulator introduces low loss (Figure 5.15), so that we can still approximate the cosine by a parabola

$$T_M \frac{\partial A}{\partial T} = \left[ g - l + D_f \frac{\partial^2}{\partial t^2} - M_s t^2 + T_d \frac{\partial}{\partial t} \right] A. \quad (5.91)$$

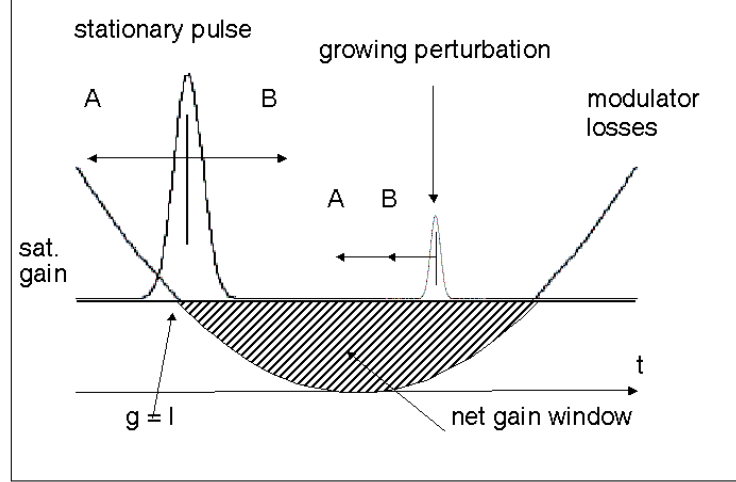


Figure 5.15: Drifting pulse dynamics in a detuned actively modelocked laser for the situation, where the modulator period is larger than the cavity round-trip time. The displacement A is caused by the mismatch between the cavity round-trip time and the modulator period. The displacement B is due to unequal losses experienced by the front and the back of the pulse in the modulator. The gain saturates to a level where a possible stationary pulse experiences no net gain or loss, which opens up a net gain window following the pulse. Perturbations within that window get amplified while drifting towards the stationary pulse.

Here,  $M_s = M\omega_M^2/2$  is the curvature of the loss modulation at the point of minimum loss as before. The time  $t$  is now allowed to range from  $-\infty$  to  $+\infty$ , since the modulator losses make sure that only during the physically allowed range  $-T_R/2 \ll t \ll T_R/2$  radiation can build up.

In the case of vanishing detuning, i.e.  $T_d = 0$ , the differential operator on the right side of (5.91), which generates the dynamics and is usually called a evolution operator  $\hat{L}$ , corresponds to the Schrödinger operator of the harmonic oscillator. Therefore, it is useful to introduce the creation and annihilation operators

$$\hat{a} = \frac{1}{\sqrt{2}} \left( \frac{\tau_a \partial}{\partial t} + \frac{t}{\tau_a} \right), \quad \hat{a}^\dagger = \frac{1}{\sqrt{2}} \left( -\frac{\tau_a \partial}{\partial t} + \frac{t}{\tau_a} \right), \quad (5.92)$$



with  $\tau_a = \sqrt[4]{D_f/M_s}$ . The evolution operator  $\hat{L}$  is then given by

$$\hat{L} = g - l - 2\sqrt{D_f M_s} \left( \hat{a}^\dagger \hat{a} + \frac{1}{2} \right) \quad (5.93)$$

and the evolution equation (5.91) can be written as

$$T_M \frac{\partial A}{\partial T} = \hat{L} A. \quad (5.94)$$

Consequently, the eigensolutions of this evolution operator are the Hermite-Gaussians, which we used already before

$$A_n(T, t) = u_n(t) e^{\lambda_n T / T_M} \quad (5.95)$$

$$u_n(t) = \sqrt{\frac{W_n}{2^n \sqrt{\pi} n! \tau_a}} H_n(t/\tau_a) e^{-\frac{t^2}{2\tau_a^2}} \quad (5.96)$$

and  $\tau_a$  is the pulsewidth of the Gaussian. (see Figure 5.16a)

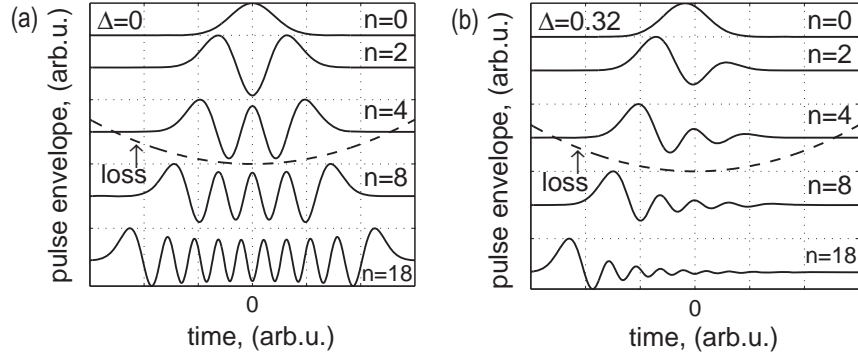


Figure 5.16: Lower order eigenmodes of the linearized system for zero detuning,  $\Delta = 0$ , (a) and for a detuning,  $\Delta = 0.32$ , in (b).

The eigenmodes are orthogonal to each other because the evolution operator is hermitian in this case.

The round-trip gain of the eigenmode  $u_n(t)$  is given by its eigenvalue (or in general by the real part of the eigenvalue) which is given by  $\lambda_n = g_n - l - 2\sqrt{D_f M_s}(n + 0.5)$  where  $g_n = g_0 \left(1 + \frac{W_n}{P_L T_R}\right)^{-1}$ , with  $W_n = \int |u_n(t)|^2 dt$ .

The eigenvalues prove that, for a given pulse energy, the mode with  $n = 0$ , which we call the ground mode, experiences the largest gain. Consequently, the ground mode will saturate the gain to a value such that  $\lambda_0 = 0$  in steady state and all other modes experience net loss,  $\lambda_n < 0$  for  $n > 0$ , as discussed before. This is a stable situation as can be shown rigorously by a linearized stability analysis [?]. Thus active modelocking with perfect synchronization produces Gaussian pulses with a  $1/e$ -half width of the intensity profile given by  $\tau_a$ .

In the case of non zero detuning  $T_d$ , the situation becomes more complex. The evolution operator, (5.93), changes to

$$\hat{L}_D = g - l - 2\sqrt{D_f M_s} \left[ (\hat{a}^\dagger - \Delta) (\hat{a} + \Delta) + \left(\frac{1}{2} + \Delta^2\right) \right] \quad (5.97)$$

with the normalized detuning

$$\Delta = \frac{1}{2\sqrt{2D_f M_s}} \frac{T_d}{\tau_a}. \quad (5.98)$$

Introducing the shifted creation and annihilation operators,  $\hat{b}^\dagger = \hat{a}^\dagger + \Delta$  and  $\hat{b} = \hat{a} + \Delta$ , respectively, we obtain

$$\hat{L}_D = \Delta g - 2\sqrt{D_f M_s} (\hat{b}^\dagger \hat{b} - 2\Delta \hat{b}) \quad (5.99)$$

with the excess gain

$$\Delta g = g - l - 2\sqrt{D_f M_s} \left(\frac{1}{2} + \Delta^2\right) \quad (5.100)$$

due to the detuning. Note, that the resulting evolution operator is not any longer hermitian and even not normal, i.e.  $[A, A^\dagger] \neq 0$ , which causes the eigenmodes to become nonnormal [21]. Nevertheless, it is an easy exercise to compute the eigenvectors and eigenvalues of the new evolution operator in terms of the eigenstates of  $\hat{b}^\dagger \hat{b}$ ,  $|l\rangle$ , which are the Hermite Gaussians centered around  $\Delta$ . The eigenvectors  $|\varphi_n\rangle$  to  $\hat{L}_D$  are found by the ansatz

$$|\varphi_n\rangle = \sum_{l=0}^n c_l^n |l\rangle, \text{ with } c_{l+1}^n = \frac{n-l}{2\Delta\sqrt{l+1}} c_l^n. \quad (5.101)$$

The new eigenvalues are  $\lambda_n = g_n - l - 2\sqrt{D_f M_s}(\Delta^2 + n + 0.5)$ . By inspection, it is again easy to see, that the new eigenstates form a complete basis in

$L_2(\mathbb{R})$ . However, the eigenvectors are no longer orthogonal to each other. The eigensolutions as a function of time are given as a product of a Hermite Polynomial and a shifted Gaussian  $u_n(t) = \langle t | \varphi_n \rangle \sim H_n(t/\tau_a) \exp \left[ -\frac{(t-\sqrt{2}\Delta\tau_a)^2}{2\tau_a^2} \right]$ . Again, a linearized stability analysis shows that the ground mode, i.e.  $|\varphi_0\rangle$ , a Gaussian, is a stable stationary solution. Surprisingly, the linearized analysis predicts stability of the ground mode for all values of the detuning in the parabolic modulation and gain approximation. This result is even independent from the dynamics of the gain, i.e. the upper state lifetime of the active medium, as long as there is enough gain to support the pulse. Only the position of the maximum of the ground mode,  $\sqrt{2}\Delta \cdot \tau_a$ , depends on the normalized detuning.

Figure 5.15 summarizes the results obtained so far. In the case of detuning, the center of the stationary Gaussian pulse is shifted away from the position of minimum loss of the modulator. Since the net gain and loss within one round-trip in the laser cavity has to be zero for a stationary pulse, there is a long net gain window following the pulse in the case of detuning due to the necessary excess gain. Figure 2 shows a few of the resulting lowest order eigenfunctions for the case of a normalized detuning  $\Delta = 0$  in (a) and  $\Delta = 0.32$  in (b). These eigenfunctions are not orthogonal as a result of the nonnormal evolution operator

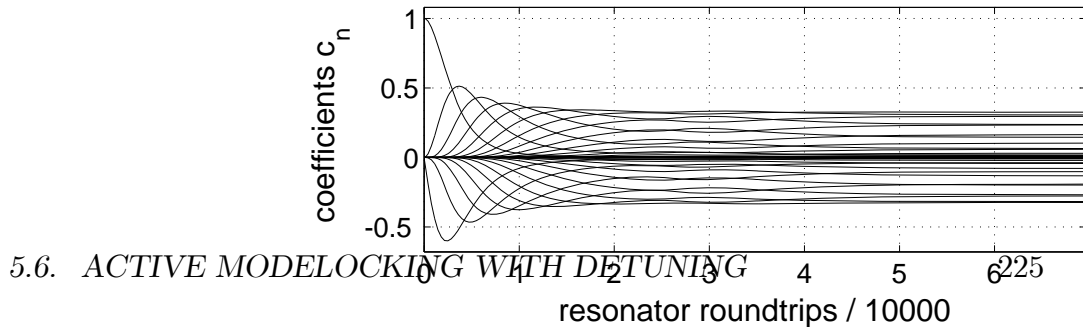
### 5.6.1 Dynamics of the Detuned Actively Mode-locked Laser

To get insight into the dynamics of the system, we look at computer simulations for a Nd:YLF Laser with the parameters shown in Table 5.3 Figures

$E_L = 366 \mu J$	$g_0 = 0.79$
$\tau_L = 450 \mu s$	$M_s = 2.467 \cdot 10^{17} s^{-2}$
$\Omega_g = 1.12 THz$	$D_g = 2 \cdot 10^{-26} s^2$
$T_R = 4 ns$	$\tau_a = 17 ps$
$l = 0.025$	$\lambda_0 = 1.047 \mu m$
$M = 0.2$	

Table 5.3: Data used in the simulations of a Nd:YLF laser.

5.17 show the temporal evolution of the coefficient  $c_n$ , when the master equa-



tion is decomposed into Hermite Gaussians centered at  $t=0$  according to Eq.(5.96).

$$A(T, t) = \sum_{n=0}^{\infty} c_n(T) u_n(t)$$

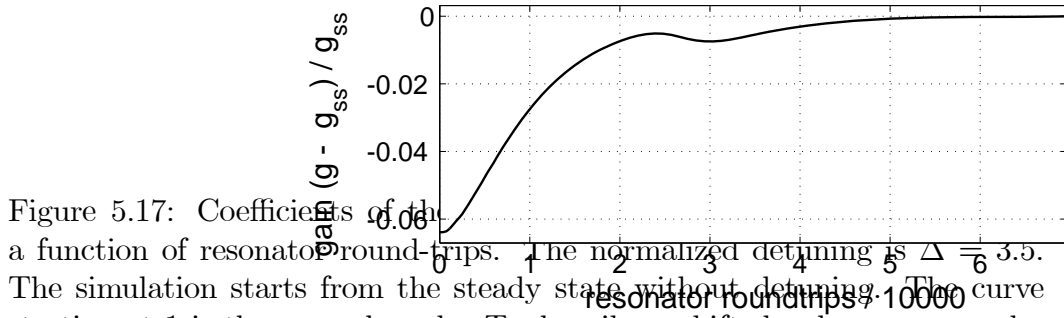
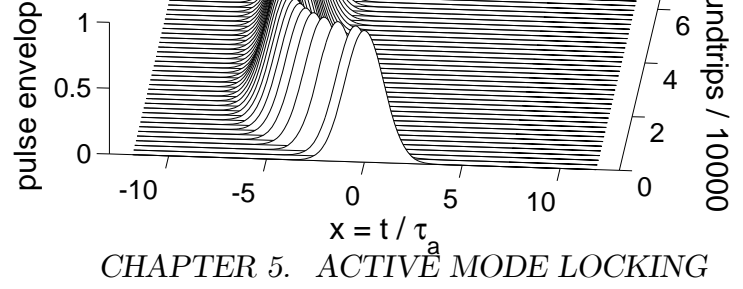


Figure 5.17: Coefficients of the pulse envelope as a function of resonator roundtrips. The normalized detuning is  $\Delta = 3.5$ . The simulation starts from the steady state without detuning. The curve starting at 1 is the ground mode. To describe a shifted pulse, many modes are necessary.

Figure 5.18 and 5.19 shows the deviation from the steady state gain and the pulse envelope in the time domain for a normalized detuning of  $\Delta = 3.5$ .

Figure 5.18: Gain as a function of the number of roundtrips. It changes to a higher level.



226

## CHAPTER 5. ACTIVE MODE LOCKING

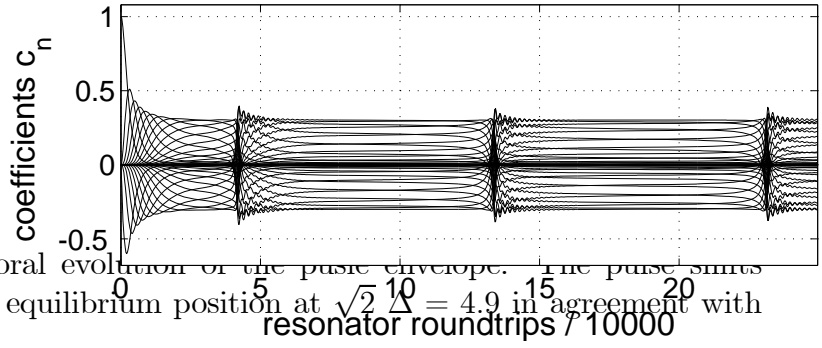


Figure 5.19: Temporal evolution of the pulse envelope. The pulse shifts slowly into the new equilibrium position at  $\sqrt{2} \Delta = 4.9$  in agreement with the simulation.

Figures 5.20 to 5.22 show the same quantities for a slightly higher normalized detuning of  $\Delta = 4$ .

Figure 5.20: Temporal evolution of the coefficients in a Hermite-Gaussian Basis at a normalized detuning of  $\Delta = 4$ . Almost periodically short interrupting events of the otherwise regular motion can be easily recognized (Intermittent Behavior). Over an extended period time between such events the laser approaches almost a steady state.

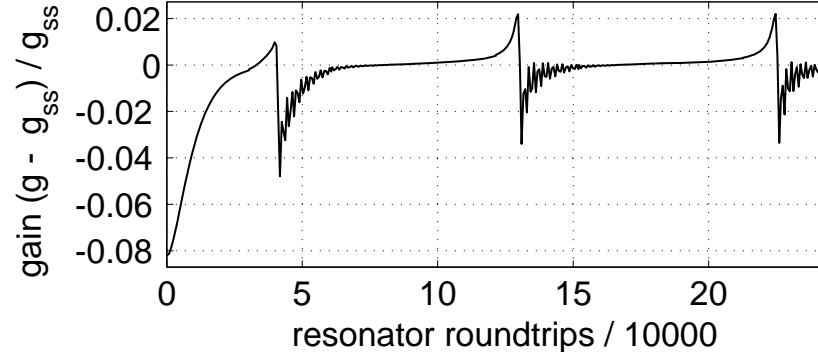
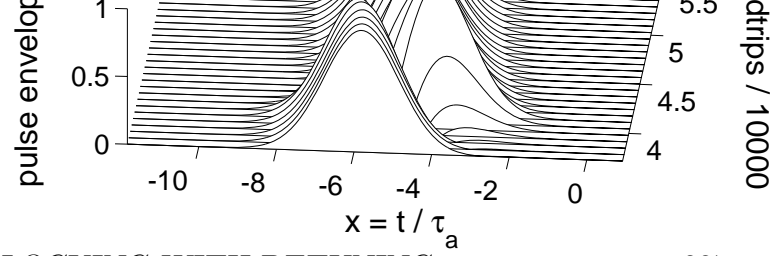


Figure 5.22: Time evolution of pulse envelope.

Figure 5.21: Temporal evolution of deviation from quasi steady state gain.

The pictures clearly show that the system does not approach a steady state anymore, but rather stays turbulent, i.e. the dynamics is chaotic.

### 5.6.2 Nonnormal Systems and Transient Gain

To get insight into the dynamics of a nonnormal time evolution, we consider the following two-dimensional nonnormal system

$$\frac{du}{dt} = Au, \quad u(0) = u_0, \quad u(t) = e^{At}u_0 \quad (5.102)$$

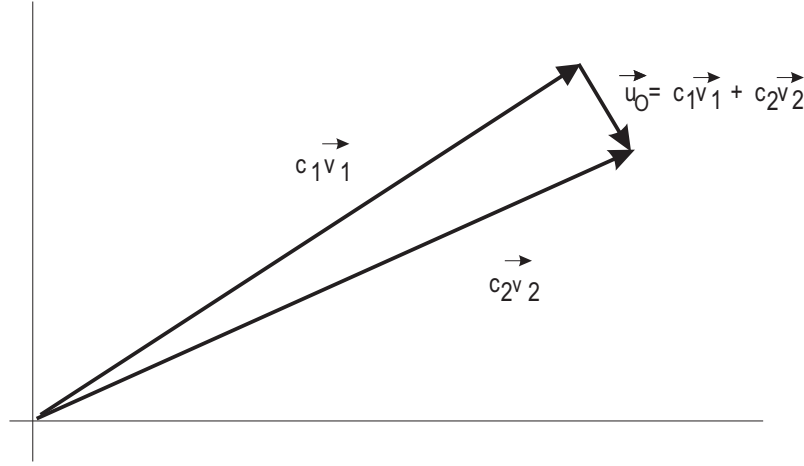


Figure 5.23: Decomposition of an initial perturbation in the eigen basis.

with

$$A = \begin{pmatrix} -\frac{1}{2} & \frac{a}{2} \\ 0 & -1 \end{pmatrix} \Rightarrow A^\dagger = \begin{pmatrix} -\frac{1}{2} & 0 \\ \frac{a}{2} & -1 \end{pmatrix}, \quad [A, A^\dagger] = \frac{a}{4} \begin{pmatrix} a & 1 \\ 1 & a \end{pmatrix} \neq 0. \quad (5.103)$$

The parameter  $a$  scales the strength of the nonnormality, similar to the detuning  $\Delta$  in the case of a modelocked laser or the Reynolds number in hydrodynamics, where the linearized Navier-Stokes Equations constitute a nonnormal system.

The eigenvalues and vectors of the linear system are

$$\lambda_1 = -\frac{1}{2}, \quad v_1 = \begin{pmatrix} 1 \\ 0 \end{pmatrix}, \quad \lambda_2 = -1, \quad v_2 = \frac{1}{\sqrt{1+a^2}} \begin{pmatrix} a \\ -1 \end{pmatrix} \quad (5.104)$$

The eigenvectors build a complete system and every initial vector can be decomposed in this basis. However, for large  $a$ , the two eigenvectors become more and more parallel, so that a decomposition of a small initial vector almost orthogonal to the basis vectors needs large components (Figure 5.23)

The solution is

$$u(t) = e^{At} u_0 = c_1 e^{-t/2} \vec{v}_1 + c_2 e^{-t} \vec{v}_2.$$

Since the eigenvalues are negative, both contributions decay, and the system is stable. However, one eigen component decays twice as fast than

the other one. Of importance to us is the transient gain that the system is showing due to the fact of near parallel eigen vectors. Both coefficients  $c_1$  and  $c_2$  are large. When one of the components decays, the other one is still there and the resulting vector

$$u(t \rightarrow 2) \approx c_1 e^{-1} \vec{v}_1.$$

can be much larger than the initial perturbation during this transient phase. This is transient gain. It can become arbitrarily large for large  $a$ .

### 5.6.3 The Nonnormal Behavior of the Detuned Laser

The nonnormality of the operator,  $[\hat{L}_D, \hat{L}_D^\dagger] \sim \Delta$ , increases with detuning. Figure 5.24 shows the normalized scalar products between the eigenmodes for different values of the detuning

$$C(m, n) = \left| \frac{\langle \varphi_m | \varphi_n \rangle}{\sqrt{\langle \varphi_m | \varphi_m \rangle \langle \varphi_n | \varphi_n \rangle}} \right|. \quad (5.105)$$

The eigenmodes are orthogonal for zero detuning. The orthogonality vanishes with increased detuning. The recursion relation (5.101) tells us that the overlap of the new eigenmodes with the ground mode increases for increasing detuning. This corresponds to the parallelization of the eigenmodes of the linearized problem which leads to large transient gain,  $\|e^{\hat{L}_D t}\|$ , in a nonnormal situation [16]. Figure 5.24d shows the transient gain for an initial perturbation from the stationary ground mode calculated by numerical simulations of the linearized system using an expansion of the linearized system in terms of Fock states to the operator  $\hat{b}$ . A normalized detuning of  $\Delta = 3$  already leads to transient gains for perturbations of the order of  $10^6$  within 20,000 round-trips which lead to an enormous sensitivity of the system against perturbations. An analytical solution of the linearized system neglecting the gain saturation shows that the transient gain scales with the detuning according to  $\exp(2\Delta^2)$ . This strong super exponential growth with increasing detuning determines the dynamics completely.



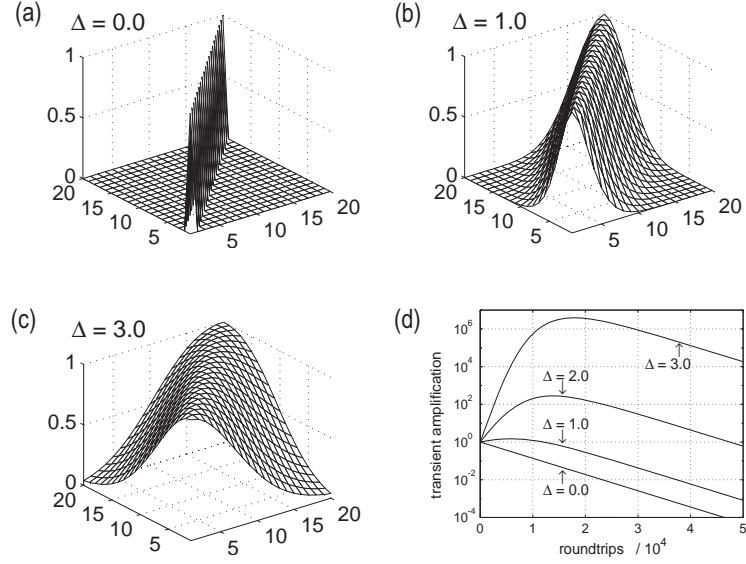


Figure 5.24: Scalar products of eigenvectors as a function of the eigenvector index for the cases  $\Delta = 0$  shown in (a),  $\Delta = 1$  in (b) and  $\Delta = 3$  in (c). (d) shows the transient gain as a function of time for these detunings computed and for  $\Delta = 2$ , from the linearized system dynamics.

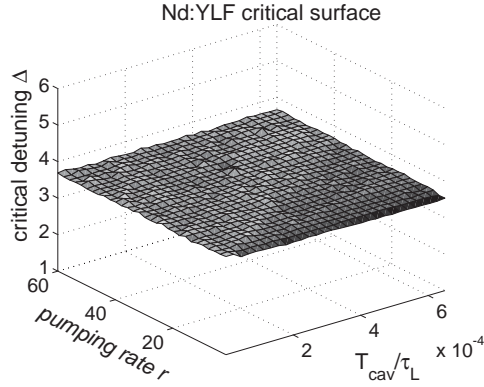


Figure 5.25: Critical detuning obtained from numerical simulations as a function of the normalized pumping rate and cavity decay time divided by the upper-state lifetime. The critical detuning is almost independent of all laser parameters shown. The mean critical detuning is  $\Delta \approx 3.65$ .

Figure 5.25 shows the surface of the transition to turbulence in the parameter space of a Nd:YLF laser, i.e. critical detuning  $\Delta$ , the pumping rate  $r = g_0/l$  and the ratio between the cavity decay time  $T_{cav} = T_R/l$  and the upper state lifetime  $\tau_L$ . In this model, we did not include the spontaneous emission.

The transition to turbulence always occurs at a normalized detuning of about  $\Delta \approx 3.7$  which gives a transient gain  $\exp(2\Delta^2) = 10^{12}$ . This means that already uncertainties of the numerical integration algorithm are amplified to a perturbation as large as the stationary state itself. To prove that the system dynamics becomes really chaotic, one has to compute the Liapunov coefficient [22]. The Liapunov coefficient describes how fast the phase space trajectories separate from each other, if they start in close proximity. It is formally defined in the following way. Two trajectories  $y(t)$  and  $z(t)$  start in close vicinity at  $t = t_0$

$$\|y(t_0) - z(t_0)\| = \varepsilon = 10^{-4}. \quad (5.106)$$

Then, the system is run for a certain time  $\Delta t$  and the logarithmic growth rate, i.e. Liapunov coefficient, of the distance between both trajectories is evaluated using

$$\lambda_0 = \ln \left( \frac{\|y(t_0 + \Delta t) - z(t_0 + \Delta t)\|}{\varepsilon} \right) \quad (5.107)$$

For the next iteration the trajectory  $z(t)$  is rescaled along the distance between  $y(t_0 + \Delta t)$  and  $z(t_0 + \Delta t)$  according to

$$z(t_1) = y(t_0 + \Delta t) + \varepsilon \frac{y(t_0 + \Delta t) - z(t_0 + \Delta t)}{\|y(t_0 + \Delta t) - z(t_0 + \Delta t)\|}. \quad (5.108)$$

The new points of the trajectories  $z(t_1 + \Delta t)$  and  $y(t_1 + \Delta t) = y(t_0 + 2\Delta t)$  are calculated and a new estimate for the Liapunov coefficient  $\lambda_1$  is calculated using Eq.(5.107) with new indices. This procedure is continued and the Liapunov coefficient is defined as the average of all the approximations over a long enough iteration, so that its changes are below a certain error bound from iteration to iteration.

$$\lambda = \frac{1}{N} \sum_{n=0}^N \lambda_n \quad (5.109)$$

Figure 5.26 shows the Liapunov coefficient of the Nd:YLF laser discussed above, as a function of the normlized detuning. When the Liapunov coefficient becomes positive, i.e. the system becomes exponentially sensitive to

small changes in the initial conditions, the system is called chaotic. The graph clearly indicates that the dynamics is chaotic above a critical detuning of about  $\Delta_c \approx 3.7$ .

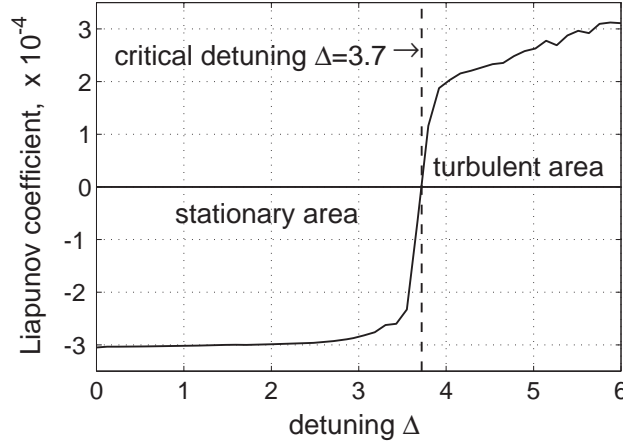


Figure 5.26: Liapunov coefficient over normalized detuning.

In the turbulent regime, the system does not reach a steady state, because it is nonperiodically interrupted by a new pulse created out of the net gain window, see Figure 5.15, following the pulse for positive detuning. This pulse saturates the gain and the nearly formed steady state pulse is destroyed and finally replaced by a new one. The gain saturation provides the nonlinear feedback mechanism, which strongly perturbs the system again, once a strong perturbation grows up due to the transient linear amplification mechanism.

The critical detuning becomes smaller if additional noise sources, such as the spontaneous emission noise of the laser amplifier and technical noise sources are taken into account. However, due to the super exponential growth, the critical detuning will not depend strongly on the strength of the noise sources. If the spontaneous emission noise is included in the simulation, we obtain the same shape for the critical detuning as in Fig. 5.25, however the critical detuning is lowered to about  $\Delta_c \approx 2$ . Note that this critical detuning is very insensitive to any other changes in the parameters of the system. Therefore, one can expect that actively mode-locked lasers without regenerative feedback run unstable at a real detuning, see (5.98) given by

$$T_d = 4\sqrt{2D_f M_s \tau_a} \quad (5.110)$$

For the above Nd:YLF laser, using the values in Table 5.3 results in a relative precision of the modulation frequency of

$$\frac{T_d}{T_R} = 1.7 \cdot 10^{-6}.$$

The derived value for the frequency stability can easily be achieved and maintained with modern microwave synthesizers. However, this requires that the cavity length of Nd:YLF laser is also stable to this limit. Note that the thermal expansion coefficient for steel is  $1.6 \cdot 10^{-5}/K$ .

## 5.7 Summary

The main result of this section is, that pure active mode locking with an amplitude modulator leads to Gaussian pulses. The width is inverse proportional to the square root of the gain bandwidth. Mode locking can also be achieved by a phase modulator which leads to chirped Gaussian pulses. A soliton much shorter than the Gaussian pulse due to pure active mode locking can be stabilized by an active modelocker. This finding also has an important consequence for passive mode locking. It implies that a slow saturable absorber, i.e. an absorber with a recovery time much longer than the width of the soliton, is enough to stabilize the pulse, i.e. to modelock the laser. Finally, we looked into the sensitivity of active mode locking on synchronism between the cavity roundtrip frequency and the modulation frequency. This dynamics is characterized by a transition to chaos which is governed by a universal detuning parameter, which is typically on the order of  $10^{-6}$ .



# Bibliography

- [1] H. A. Haus, "Short Pulse Generation", in Compact Sources of Ultrashort Pulses, ed. by I. N. Duling III, Cambridge University Press (1995).
- [2] D. J. Kuizenga and A. E. Siegman, "FM and AM Mode Locking of the Homogeneous Laser - Part I: Theory," IEEE J. of Quantum Electron. **QE-6**, pp. 694 – 708 (1970).
- [3] D. J. Kuizenga and A. E. Siegman, "FM and AM modelocking of the homogeneous laser - part I: theory," IEEE J. Qunat. Electron. **6**, pp. 694 – 701 (1970).
- [4] H. A. Haus, "A Theory of Forced Mode Locking", IEEE Journal of Quantum Electronics **QE-11**, pp. 323 - 330 (1975).
- [5] H. A. Haus and Y. Silberberg, "Laser modelocking with addition of nonlinear index", IEEE Journal of Quantum Electronics **QE-22**, pp. 325 - 331 (1986).
- [6] F. X. Kärtner, D. Kopf, U. Keller, "Solitary pulse stabilization and shortening in actively mode-locked lasers," J. Opt. Soc. of Am. **B12**, pp. 486 – 496 (1995).
- [7] D. Kopf, F. X. Kärtner, K. J. Weingarten, U. Keller, "Pulse shortening in a Nd:glass laser by gain reshaping and soliton formation, Opt. Lett. **19**, 2146 – 2248 (1994).
- [8] J.D. Kafka and T. Baer, "Mode-locked erbium-doped fiber laser with soliton pulse shaping", Opt. Lett. **14**, pp. 1269 – 1271 (1989).
- [9] K. Smith, R. P. Davey, B. P. Nelson and E.J. Greer, "Fiber and Solid-State Lasers", (Digest No. 120), London, UK, 19 May 1992, P.1/1-4.

- [10] J.D. Kafka, M. L. Watts and J.W.J. Pieterse, "Picosecond and femtosecond pulse generation in a regeneratively mode-locked Ti:Sapphire laser", IEEE J. Quantum Electron. **QE-28**, pp. 2151 – 2162 (1992).
- [11] F. Fontana, N. Ridi, M. Romagnoli, P. Franco, "Fully integrated 30 ps modelocked fiber laser electronically tunable over 1530 - 1560 nm", Opt. Comm. **107**, pp. 240 – 244 (1994).
- [12] D. J. Jones, H. A. Haus and E. P. Ippen, "Solitons in an Actively Mod-locked Fiber Laser," to appear in Opt. Lett.
- [13] U. Keller, T. H. Chiu and J. F. Ferguson, "Self-starting femtosecond mode-locked Nd:glass laser using intracavity saturable absorber,"- Opt. Lett. **18**, pp. 1077 - 1079 (1993).
- [14] H. A. Haus and A. Mecozzi, "Long-term storage of a bit stream of solitons", Opt. Lett. **21**, 1500 – 1502 (1992).
- [15] Lord Kelvin, Philos. Mag. **24**, 188 (1887); A. Sommerfeld, Int. Mathem. Kongr. Rom 1908, Vol. III, S. 116; W. M. F. Orr, Proc. Irish Acad. **27**, (1907).
- [16] L. Trefethen, A. Trefethen, S. C. Reddy u. T. Driscoll, Science **261**, 578 (1993); S. C. Reddy, D. Henningson, J. Fluid Mech. **252**, 209 (1993); Phys. Fluids **6**, 1396 (1994); S. Reddy et al., SIAM J. Appl. Math. **53**; 15 (1993); T. Gebhardt and S. Grossmann, Phys. Rev. E **50**, 3705 (1994).
- [17] H. J. Eichler, Opt. Comm. **56**, 351 (1986). H. J. Eichler, I. G. Koltchanov and B. Liu, Appl. Phys. B **61**, 81 (1995).
- [18] U. Morgner and F. Mitschke, Phys. Rev.A**54**, 3149 (1997).
- [19] H. J. Eichler, I. G. Koltchanov and B. Liu, Appl. Phys. B **61**, 81 - 88 (1995).
- [20] H. A. Haus, D. J. Jones, E. P. Ippen and W. S. Wong, Journal of Light-wave Technology, 14, 622 (1996).
- [21] G. Bachman and L. Narici, "Functional Analysis", New York, Academic Press (1966).
- [22] A. Wolf, J. B. Swift, H. L. Swinney and J. A. Vastano, Physica D **16**, 285 (1985).

## Chapter 6

# Passive Modelocking

As we have seen in chapter 5 the pulse width in an actively modelocked laser is inverse proportional to the fourth root of the curvature in the loss modulation. In active modelocking one is limited to the speed of electronic signal generators. Therefore, this curvature can never be very strong. However, if the pulse can modulate the absorption on its own, the curvature of the absorption modulation can become large, or in other words the net gain window generated by the pulse can be as short as the pulse itself. In this case, the net gain window shortens with the pulse. Therefore, passively modelocked lasers can generate much shorter pulses than actively modelocked lasers.

However, a suitable saturable absorber is required for passive modelocking. Depending on the ratio between saturable absorber recovery time and final pulse width, one may distinguish between the regimes of operation shown in Figure 6.1, which depicts the final steady state pulse formation process. In a solid state laser with intracavity pulse energies much lower than the saturation energy of the gain medium, gain saturation can be neglected. Then a fast saturable absorber must be present that opens and closes the net gain window generated by the pulse immediately before and after the pulse. This modelocking principle is called fast saturable absorber modelocking, see Figure 6.1 a).

In semiconductor and dye lasers usually the intracavity pulse energy exceeds the saturation energy of the gain medium and so the the gain medium undergoes saturation. A short net gain window can still be created, almost independent of the recovery time of the gain, if a similar but unpumped medium is introduced into the cavity acting as an absorber with a somewhat lower saturation energy than the gain medium. For example, this can be



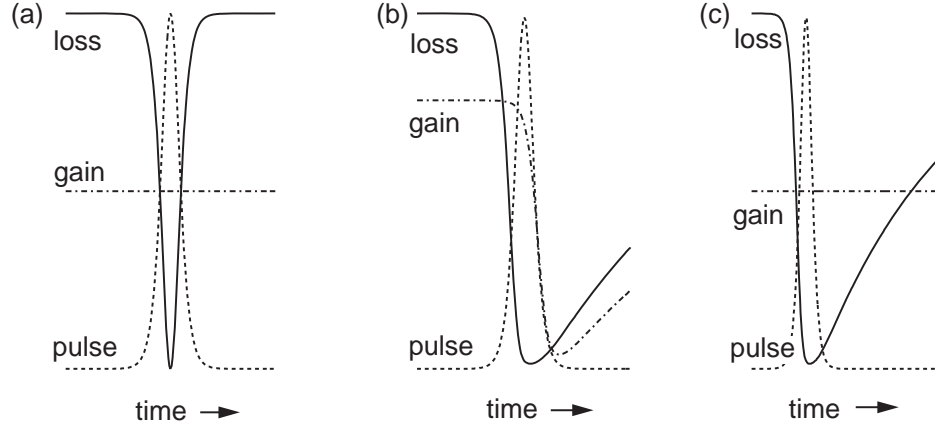


Figure 6.1: Pulse-shaping and stabilization mechanisms owing to gain and loss dynamics in passively mode-locked lasers: (a) using only a fast saturable absorber; (b) using a combination of gain and loss saturation; (c) using a saturable absorber with a finite relaxation time and soliton formation.

arranged for by stronger focusing in the absorber medium than in the gain medium. Then the absorber bleaches first and opens a net gain window, that is closed by the pulse itself by bleaching the gain somewhat later, see Figure 6.1 b). This principle of modelocking is called slow-saturable absorber modelocking.

When modelocking of picosecond and femtosecond lasers with semiconductor saturable absorbers has been developed it became obvious that even with rather slow absorbers, showing recovery times of a few picoseconds, one was able to generate sub-picosecond pulses resulting in a significant net gain window after the pulse, see Figure 6.1 c). From our investigation of active modelocking in the presence of soliton formation, we can expect that such a situation may still be stable up to a certain limit in the presence of strong soliton formation. This is the case and this modelocking regime is called soliton modelocking, since solitary pulse formation due to SPM and GDD shapes the pulse to a stable sech-shape despite the open net gain window following the pulse.

## 6.1 Slow Saturable Absorber Mode Locking

Due to the small cross section for stimulated emission in solid state lasers, typical intracavity pulse energies are much smaller than the saturation energy of the gain. Therefore, we neglected the effect of gain saturation due to one pulse so far, the gain only saturates with the average power. However, there are gain media which have large gain cross sections like semiconductors and dyes, see Table 4.1, and typical intracavity pulse energies may become large enough to saturate the gain considerably in a single pass. In fact, it is this effect, which made the mode-locked dye laser so successful. The model for the slow saturable absorber mode locking has to take into account the change of gain in the passage of one pulse [1, 2]. In the following, we consider a modelocked laser, that experiences in one round-trip a saturable gain and a slow saturable absorber. In the dye laser, both media are dyes with different saturation intensities or with different focusing into the dye jets so that gain and loss may show different saturation energies. The relaxation equation of the gain, in the limit of a pulse short compared with its relaxation time, can be approximated by

$$\frac{dg}{dt} = -g \frac{|A(t)|^2}{E_L} \quad (6.1)$$

The coefficient  $E_L$  is the saturation energy of the gain. Integration of the equation shows, that the gain saturates with the pulse energy  $E(t)$

$$E(t) = \int_{-T_{R/2}}^t dt |A(t)|^2 \quad (6.2)$$

when passing the gain

$$g(t) = g_i \exp[-E(t)/E_L] \quad (6.3)$$

where  $g_i$  is the initial small signal gain just before the arrival of the pulse. A similar equation holds for the loss of the saturable absorber whose response (loss) is represented by  $q(t)$

$$q(t) = q_0 \exp[-E(t)/E_A] \quad (6.4)$$

where  $E_A$  is the saturation energy of the saturable absorber. If the background loss is denoted by  $l$ , the master equation of mode-locking becomes

$$T_R \frac{\partial}{\partial T} A = [g_i (\exp(-E(t)/E_L)) A - lA - q_0 \exp(-E(t)/E_A)] A + \frac{1}{\Omega_f^2} \frac{\partial^2}{\partial t^2} A \quad (6.5)$$

Here, we have replaced the filtering action of the gain  $D_g = \frac{1}{\Omega_f^2}$  as produced by a separate fixed filter. An analytic solution to this integro-differential equation can be obtained with one approximation: the exponentials are expanded to second order. This is legitimate if the population depletions of the gain and saturable absorber media are not excessive. Consider one of these expansions:

$$q_0 \exp(-E(t)/E_A) \approx q_0 \left[ 1 - (E(t)/E_A) + \frac{1}{2} (E(t)/E_A)^2 \right]. \quad (6.6)$$

We only consider the saturable gain and loss and the finite gain bandwidth. Then the master equation is given by

$$T_R \frac{\partial A(T, t)}{\partial T} = \left[ g(t) - q(t) - l + D_f \frac{\partial^2}{\partial t^2} \right] A(T, t). \quad (6.7)$$

The filter dispersion,  $D_f = 1/\Omega_f^2$ , effectively models the finite bandwidth of the laser, that might not be only due to the finite gain bandwidth, but includes all bandwidth limiting effects in a parabolic approximation. Suppose the pulse is a symmetric function of time. Then the first power of the integral gives an antisymmetric function of time, its square is symmetric. An antisymmetric function acting on the pulse  $A(t)$  causes a displacement. Hence, the steady state solution does not yield zero for the change per pass, the derivative  $\frac{1}{T_R} \frac{\partial A}{\partial T}$  must be equated to a time shift  $\Delta t$  of the pulse. When this is done one can confirm easily that  $A(t) = A_o \operatorname{sech}(t/\tau)$  is a solution of (6.6) with constraints on its coefficients. Thus we, are looking for a "steady state" solution  $A(t, T) = A_o \operatorname{sech}(\frac{t}{\tau} + \alpha \frac{T}{T_R})$ . Note, that  $\alpha$  is the fraction of the pulsewidth, the pulse is shifted in each round-trip due to the shaping by loss and gain. The constraints on its coefficients can be easily found using

the following relations for the sech-pulse

$$E(t) = \int_{-T_R/2}^t dt |A(t)|^2 = \frac{W}{2} \left( 1 + \tanh\left(\frac{t}{\tau} + \alpha \frac{T}{T_R}\right) \right) \quad (6.8)$$

$$E(t)^2 = \left( \frac{W}{2} \right)^2 \left( 2 + 2 \tanh\left(\frac{t}{\tau} + \alpha \frac{T}{T_R}\right) - \operatorname{sech}^2\left(\frac{t}{\tau} + \alpha \frac{T}{T_R}\right) \right) \quad (6.9)$$

$$T_R \frac{\partial}{\partial T} A(t, T) = -\alpha \tanh\left(\frac{t}{\tau} + \alpha \frac{T}{T_R}\right) A(t, T) \quad (6.10)$$

$$\frac{1}{\Omega_f^2} \frac{\partial^2}{\partial t^2} A(t, T) = \frac{1}{\Omega_f^2 \tau^2} \left( 1 - 2 \operatorname{sech}^2\left(\frac{t}{\tau} + \alpha \frac{T}{T_R}\right) \right) A(t, T), \quad (6.11)$$

substituting them into the master equation (6.5) and collecting the coefficients in front of the different temporal functions. The constant term gives the necessary small signal gain

$$g_i \left[ 1 - \frac{W}{2E_L} + \left( \frac{W}{2E_L} \right)^2 \right] = l + q_0 \left[ 1 - \frac{W}{2E_A} + \left( \frac{W}{2E_A} \right)^2 \right] - \frac{1}{\Omega_f^2 \tau^2}. \quad (6.12)$$

The constant in front of the odd  $\tanh$ -function delivers the timing shift per round-trip

$$\alpha = \frac{\Delta t}{\tau} = g_i \left[ \frac{W}{2E_L} - \left( \frac{W}{2E_L} \right)^2 \right] - q_0 \left[ \frac{W}{2E_A} - \left( \frac{W}{2E_A} \right)^2 \right]. \quad (6.13)$$

And finally the constant in front of the  $\operatorname{sech}^2$ -function determines the pulsewidth

$$\frac{1}{\tau^2} = \frac{\Omega_f^2 W^2}{8} \left( \frac{q_0}{E_A^2} - \frac{g_i}{E_L^2} \right) \quad (6.14)$$

These equations have important implications. Consider first the equation for the inverse pulsewidth, (6.14). In order to get a real solution, the right hand side has to be positive. This implies that  $q_0/E_A^2 > g_i/E_L^2$ . The saturable absorber must saturate more easily, and, therefore more strongly, than the gain medium in order to open a net window of gain (Figure 6.2).

This was accomplished in a dye laser system by stronger focusing into the saturable absorber-dye jet (Reducing the saturation energy for the saturable absorber) than into the gain-dye jet (which was inverted, i.e. optically

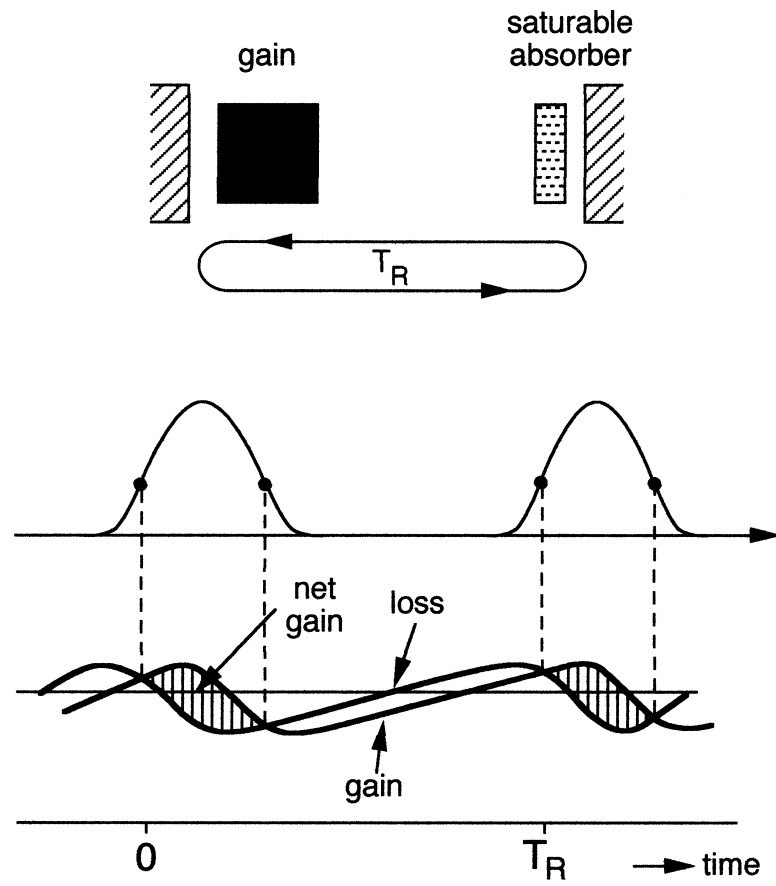


Figure 6.2: Dynamics of a laser mode-locked with a slow saturable absorber.

pumped). Equation (6.12) makes a statement about the net gain before passage of the pulse. The net gain before passage of the pulse is

$$\begin{aligned} g_i - q_0 - l = & -\frac{1}{\Omega_f^2 \tau^2} + g_i \left[ \frac{W}{2E_L} - \left( \frac{W}{2E_L} \right)^2 \right] \\ & - q_0 \left[ \frac{W}{2E_A} - \left( \frac{W}{2E_A} \right)^2 \right]. \end{aligned} \quad (6.15)$$

Using condition (6.14) this can be expressed as

$$g_i - q_0 - l = g_i \left[ \frac{W}{2E_L} \right] - q_0 \left[ \frac{W}{2E_A} \right] + \frac{1}{\Omega_f^2 \tau^2}. \quad (6.16)$$

This gain is negative since the effect of the saturable absorber is larger than that of the gain. Since the pulse has the same exponential tail after passage as before, one concludes that the net gain after passage of the pulse is the same as before passage and thus also negative. The pulse is stable against noise build-up both in its front and its back. This principle works if the ratio between the saturation energies for the saturable absorber and gain  $\chi_P = E_A/E_P$  is very small. Then the shortest pulsewidth achievable with a given system is

$$\tau = \frac{2\sqrt{2}}{\sqrt{q_0}\Omega_f} \frac{E_A}{W} > \frac{\sqrt{2}}{\sqrt{q_0}\Omega_f}. \quad (6.17)$$

The greater sign comes from the fact that our theory is based on the expansion of the exponentials, which is only true for  $\frac{W}{2E_A} < 1$ . Note that the modelocking principle of the dye laser is a very fascinating one due to the fact that actually none of the elements in the system are fast. It is the interplay between two media that opens a short window in time on the scale of femtoseconds. The media themselves just have to be fast enough to recover completely between one round trip, i.e. on a nanosecond timescale.

Over the last fifteen years, the dye laser has been largely replaced by solid state lasers, which offer even more bandwidth than dyes and are on top of that much easier to handle because they do not show degradation over time. With it came the need for a different mode locking principle, since the saturation energy of these broadband solid-state laser media are much higher than the typical intracavity pulse energies. The absorber has to open and close the net gain window.

## 6.2 Fast Saturable Absorber Mode Locking

The dynamics of a laser modelocked with a fast saturable absorber is again covered by the master equation (5.21) [3]. Now, the losses  $q$  react instantly on the intensity or power  $P(t) = |A(t)|^2$  of the field

$$q(A) = \frac{q_0}{1 + \frac{|A|^2}{P_A}}, \quad (6.18)$$

where  $P_A$  is the saturation power of the absorber. There is no analytic solution of the master equation (5.21) with the absorber response (6.18). Therefore, we make expansions on the absorber response to get analytic insight. If the absorber is not saturated, we can expand the response (6.18) for small intensities

$$q(A) = q_0 - \gamma|A|^2, \quad (6.19)$$

with the saturable absorber modulation coefficient  $\gamma = q_0/P_A$ . The constant nonsaturated loss  $q_0$  can be absorbed in the losses  $l_0 = l + q_0$ . The resulting master equation is, see also Fig. 6.3

$$T_R \frac{\partial A(T, t)}{\partial T} = \left[ g - l_0 + D_f \frac{\partial^2}{\partial t^2} + \gamma|A|^2 + jD_2 \frac{\partial^2}{\partial t^2} - j\delta|A|^2 \right] A(T, t). \quad (6.20)$$

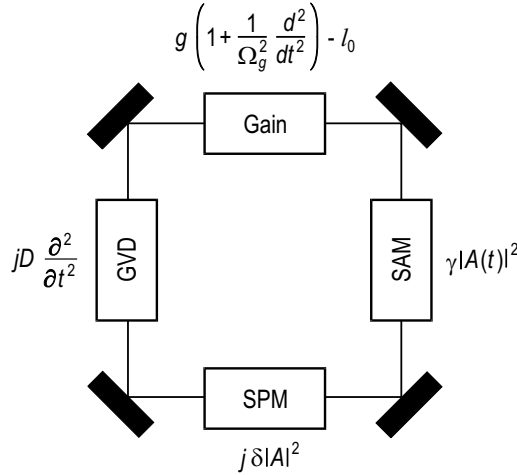


Figure 6.3: Schematic representation of the master equation for a passively modelocked laser with a fast saturable absorber.

Eq. (6.20) is a generalized Ginzburg-Landau equation well known from superconductivity with a rather complex solution manifold.

### 6.2.1 Without GDD and SPM

We consider first the situation without SPM and GDD, i.e.  $D_2 = \delta = 0$

$$T_R \frac{\partial A(T, t)}{\partial T} = \left[ g - l_0 + D_f \frac{\partial^2}{\partial t^2} + \gamma |A|^2 \right] A(T, t). \quad (6.21)$$

Up to the imaginary unit, this equation is still very similar to the NSE. To find the final pulse shape and width, we look for the stationary solution

$$T_R \frac{\partial A_s(T, t)}{\partial T} = 0.$$

Since the equation is similar to the NSE, we try the following ansatz

$$A_s(T, t) = A_s(t) = A_0 \operatorname{sech} \left( \frac{t}{\tau} \right). \quad (6.22)$$

Note, there is

$$\frac{d}{dx} \operatorname{sech} x = -\tanh x \operatorname{sech} x, \quad (6.23)$$

$$\begin{aligned} \frac{d^2}{dx^2} \operatorname{sech} x &= \tanh^2 x \operatorname{sech} x - \operatorname{sech}^3 x, \\ &= (\operatorname{sech} x - 2 \operatorname{sech}^3 x). \end{aligned} \quad (6.24)$$

Substitution of the ansatz (6.22) into the master equation (6.21), assuming steady state, results in

$$\begin{aligned} 0 &= \left[ (g - l_0) + \frac{D_f}{\tau^2} \left[ 1 - 2 \operatorname{sech}^2 \left( \frac{t}{\tau} \right) \right] \right. \\ &\quad \left. + \gamma |A_0|^2 \operatorname{sech}^2 \left( \frac{t}{\tau} \right) \right] \cdot A_0 \operatorname{sech} \left( \frac{t}{\tau} \right). \end{aligned} \quad (6.25)$$

Comparison of the coefficients with the  $\operatorname{sech}$ - and  $\operatorname{sech}^3$ -expressions results in the conditions for the pulse peak intensity and pulse width  $\tau$  and for the saturated gain

$$\frac{D_f}{\tau^2} = \frac{1}{2} \gamma |A_0|^2, \quad (6.26)$$

$$g = l_0 - \frac{D_f}{\tau^2}. \quad (6.27)$$



From Eq.(6.26) and with the pulse energy of a sech pulse, see Eq.(3.8),  $W = 2|A_0|^2\tau$ ,

$$\tau = \frac{4D_f}{\gamma W}. \quad (6.28)$$

Eq. (6.28) is rather similar to the soliton width with the exception that the conservative pulse shaping effects GDD and SPM are replaced by gain dispersion and saturable absorption. The soliton phase shift per roundtrip is replaced by the difference between the saturated gain and loss in Eq.(6.28). It is interesting to have a closer look on how the difference between gain and loss  $\frac{D_f}{\tau^2}$  per round-trip comes about. From the master equation (6.21) we can derive an equation of motion for the pulse energy according to

$$T_R \frac{\partial W(T)}{\partial T} = T_R \frac{\partial}{\partial T} \int_{-\infty}^{\infty} |A(T, t)|^2 dt \quad (6.29)$$

$$= T_R \int_{-\infty}^{\infty} \left[ A(T, t)^* \frac{\partial}{\partial T} A(T, t) + c.c. \right] dt \quad (6.30)$$

$$= 2G(g_s, W)W, \quad (6.31)$$

where  $G$  is the net energy gain per roundtrip, which vanishes when steady state is reached [3]. Substitution of the master equation into (6.30) with

$$\int_{-\infty}^{\infty} (\text{sech}^2 x) dx = 2, \quad (6.32)$$

$$\int_{-\infty}^{\infty} (\text{sech}^4 x) dx = \frac{4}{3}, \quad (6.33)$$

$$- \int_{-\infty}^{\infty} \text{sech} x \frac{d^2}{dx^2} (\text{sech} x) dx = \int_{-\infty}^{\infty} \left( \frac{d}{dx} \text{sech} x \right)^2 dx = \frac{2}{3}. \quad (6.34)$$

results in

$$G(g_s, W) = g_s - l_0 - \frac{D_f}{3\tau^2} + \frac{2}{3}\gamma|A_0|^2 \quad (6.35)$$

$$= g_s - l_0 + \frac{1}{2}\gamma|A_0|^2 = g_s - l_0 + \frac{D_f}{\tau^2} = 0 \quad (6.36)$$

with the saturated gain

$$g_s(W) = \frac{g_0}{1 + \frac{W}{P_L T_R}} \quad (6.37)$$

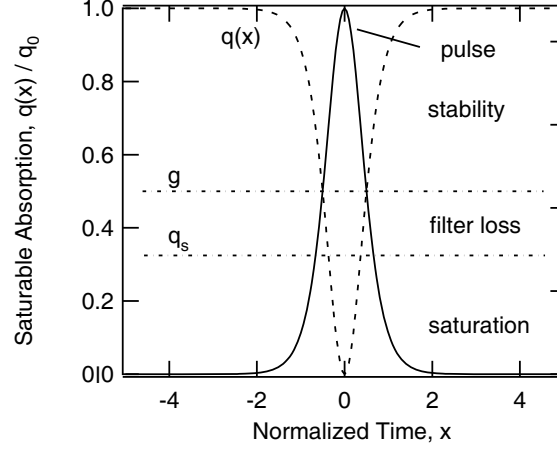


Figure 6.4: Gain and loss in a passively modelocked laser using a fast saturable absorber on a normalized time scale  $x = t/\tau$ . The absorber is assumed to saturate linearly with intensity according to  $q(A) = q_0 \left(1 - \frac{|A|^2}{A_0^2}\right)$ .

Equation (6.36) together with (6.28) determines the pulse energy

$$\begin{aligned} g_s(W) &= \frac{g_0}{1 + \frac{W}{P_L T_R}} = l_0 - \frac{D_f}{\tau^2} \\ &= l_0 - \frac{(\gamma W)^2}{16 D_g} \end{aligned} \quad (6.38)$$

Figure 6.4 shows the time dependent variation of gain and loss in a laser modelocked with a fast saturable absorber on a normalized time scale. Here, we assumed that the absorber saturates linearly with intensity up to a maximum value  $q_0 = \gamma A_0^2$ . If this maximum saturable absorption is completely exploited see Figure 6.5. The minimum pulse width achievable with a given saturable absorption  $q_0$  results from Eq.(6.26)

$$\frac{D_f}{\tau^2} = \frac{q_0}{2}, \quad (6.39)$$

to be

$$\tau = \sqrt{\frac{2}{q_0}} \frac{1}{\Omega_f}. \quad (6.40)$$

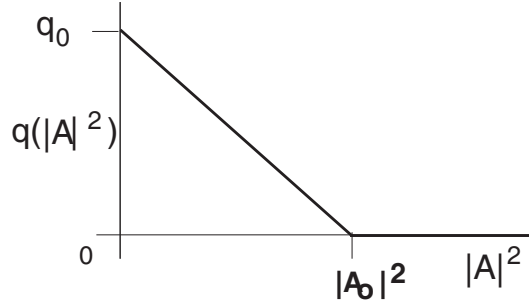


Figure 6.5: Saturation characteristic of an ideal saturable absorber

Note that in contrast to active modelocking, now the achievable pulse width is scaling with the inverse gain bandwidth, which gives much shorter pulses. Figure 6.4 can be interpreted as follows: In steady state, the saturated gain is below loss, by about one half of the exploited saturable loss before and after the pulse. This means, that there is net loss outside the pulse, which keeps the pulse stable against growth of instabilities at the leading and trailing edge of the pulse. If there is stable mode-locked operation, there must be always net loss far away from the pulse, otherwise, a continuous wave signal running at the peak of the gain would experience more gain than the pulse and would break through. From Eq.(6.35) follows, that one third of the exploited saturable loss is used up during saturation of the absorber and actually only one sixth is used to overcome the filter losses due to the finite gain bandwidth. Note, there is a limit to the minimum pulse width, which comes about, because the saturated gain (6.27) is  $g_s = l + \frac{1}{2}q_0$  and, therefore, from Eq.(6.40), if we assume that the finite bandwidth of the laser is set by the gain, i.e.  $D_f = D_g = \frac{g}{\Omega_g^2}$  we obtain for  $q_0 \gg l$

$$\tau_{\min} = \frac{1}{\Omega_g} \quad (6.41)$$

for the linearly saturating absorber model. This corresponds to mode locking over the full bandwidth of the gain medium, since for a sech-shaped pulse, the time-bandwidth product is 0.315, and therefore,

$$\Delta f_{FWHM} = \frac{0.315}{1.76 \cdot \tau_{\min}} = \frac{\Omega_g}{1.76 \cdot \pi}. \quad (6.42)$$

As an example, for Ti:sapphire this corresponds to  $\Omega_g = 270$  THz,  $\tau_{\min} = 3.7$  fs,  $\tau_{FWHM} = 6.5$  fs.

### 6.2.2 With GDD and SPM

After understanding what happens without GDD and SPM, we look at the solutions of the full master equation (6.20) with GDD and SPM. It turns out, that there exist steady state solutions, which are chirped hyperbolic secant functions [4]

$$A_s(T, t) = A_0 \left( \operatorname{sech} \left( \frac{t}{\tau} \right) \right)^{(1+j\beta)} e^{j\psi T/T_R}, \quad (6.43)$$

$$= A_0 \operatorname{sech} \left( \frac{t}{\tau} \right) \exp \left[ j\beta \ln \operatorname{sech} \left( \frac{t}{\tau} \right) + j\psi T/T_R \right]. \quad (6.44)$$

Where  $\psi$  is the round-trip phase shift of the pulse, which we have to allow for. Only the intensity of the pulse becomes stationary. There is still a phase-shift per round-trip due to the difference between the group and phase velocity (these effects have been already transformed away) and the nonlinear effects. As in the last section, we can substitute this ansatz into the master equation and compare coefficients. Using the following relations

$$\frac{d}{dx} (f(x)^b) = b f(x)^{b-1} \frac{d}{dx} f(x) \quad (6.45)$$

$$\frac{d}{dx} (\operatorname{sech} x)^{(1+j\beta)} = -(1+j\beta) \tanh x (\operatorname{sech} x)^{(1+j\beta)}, \quad (6.46)$$

$$\frac{d^2}{dx^2} (\operatorname{sech} x)^{(1+j\beta)} = ((1+j\beta)^2 - (2+3j\beta-\beta^2) \operatorname{sech}^2 x) \quad (6.47)$$

$$(\operatorname{sech} x)^{(1+j\beta)}. \quad (6.48)$$

in the master equation and comparing the coefficients to the same functions leads to two complex equations

$$\frac{1}{\tau^2} (D_f + jD_2) (2 + 3j\beta - \beta^2) = (\gamma - j\delta) |A_0|^2, \quad (6.49)$$

$$l_0 - \frac{(1+j\beta)^2}{\tau^2} (D_f + jD_2) = g - j\psi. \quad (6.50)$$

These equations are extensions to Eqs.(6.26) and (6.27) and are equivalent to four real equations for the phase-shift per round-trip  $\psi$ , the pulse width

$\tau$ , the chirp  $\beta$  and the peak power  $|A_0|^2$  or pulse energy. The imaginary part of Eq.(6.50) determines the phase-shift only, which is most often not of importance. The real part of Eq.(6.50) gives the saturated gain

$$g = l_0 - \frac{1 - \beta^2}{\tau^2} D_f + \frac{2\beta D_2}{\tau^2}. \quad (6.51)$$

The real part and imaginary part of Eq.(6.49) give

$$\frac{1}{\tau^2} [D_f (2 - \beta^2) - 3\beta D_2] = \gamma |A_0|^2, \quad (6.52)$$

$$\frac{1}{\tau^2} [D_2 (2 - \beta^2) + 3\beta D_f] = -\delta |A_0|^2. \quad (6.53)$$

We introduce the normalized dispersion,  $D_n = D_2/D_f$ , and the pulse width of the system without GDD and SPM, i.e. the width of the purely saturable absorber modelocked system,  $\tau_0 = 4D_f/(\gamma W)$ . Dividing Eq.(6.53) by (6.52) and introducing the normalized nonlinearity  $\delta_n = \delta/\gamma$ , we obtain a quadratic equation for the chirp,

$$\frac{D_n (2 - \beta^2) + 3\beta}{(2 - \beta^2) - 3\beta D_n} = -\delta_n,$$

or after some reordering

$$\frac{3\beta}{2 - \beta^2} = \frac{\delta_n + D_n}{-1 + \delta_n D_n} \equiv \frac{1}{\chi}. \quad (6.54)$$

Note that  $\chi$  depends only on the system parameters. Therefore, the chirp is given by

$$\beta = -\frac{3}{2}\chi \pm \sqrt{\left(\frac{3}{2}\chi\right)^2 + 2}. \quad (6.55)$$

Knowing the chirp, we obtain from Eq.(6.52) the pulsewidth

$$\tau = \frac{\tau_0}{2} (2 - \beta^2 - 3\beta D_n), \quad (6.56)$$

which, with Eq.(6.54), can also be written as

$$\tau = \frac{3\tau_0}{2} \beta (\chi - D_n) \quad (6.57)$$

In order to be physically meaningful the pulse width has to be a positive number, i.e. the product  $\beta(\chi - D_n)$  has always to be greater than 0, which determines the root in Eq.(6.55)

$$\beta = \begin{cases} -\frac{3}{2}\chi + \sqrt{\left(\frac{3}{2}\chi\right)^2 + 2}, & \text{for } \chi > D_n \\ -\frac{3}{2}\chi - \sqrt{\left(\frac{3}{2}\chi\right)^2 + 2}, & \text{for } \chi < D_n \end{cases}. \quad (6.58)$$

Figure 6.6(a,b and d) shows the resulting chirp, pulse width and nonlinear round-trip phase shift with regard to the system parameters [4][5]. A necessary but not sufficient criterion for the stability of the pulses is, that there must be net loss leading and following the pulse. From Eq.(6.51), we obtain

$$g_s - l_0 = -\frac{1 - \beta^2}{\tau^2} D_f + \frac{2\beta D_2}{\tau^2} < 0. \quad (6.59)$$

If we define the stability parameter  $S$

$$S = 1 - \beta^2 - 2\beta D_n > 0, \quad (6.60)$$

$S$  has to be greater than zero, as shown in Figure 6.6 (d).

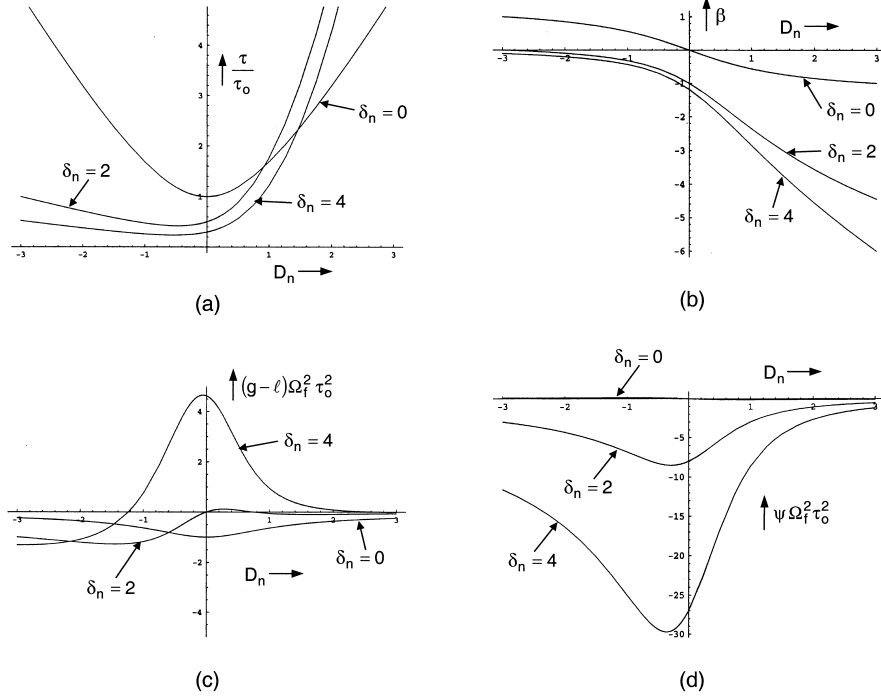


Figure 6.6: (a) Pulsewidth, (b) Chirp parameter, (c) Net gain following the pulse, which is related to stability. (d) Phase shift per pass. [4]

Figure 6.6 (a-d) indicate that there are essentially three operating regimes. First, without GDD and SPM, the pulses are always stable. Second, if there is strong soliton-like pulse shaping, i.e.  $\delta_n \gg 1$  and  $-D_n \gg 1$  the chirp is always much smaller than for positive dispersion and the pulses are soliton-like. At last, the pulses are even chirp free, if the condition  $\delta_n = -D_n$  is fulfilled. Then the solution is

$$A_s(T, t) = A_0 \left( \text{sech} \left( \frac{t}{\tau} \right) \right) e^{j\psi T/T_R}, \text{ for } \delta_n = -D_n. \quad (6.61)$$

Note, for this discussion we always assumed a positive SPM-coefficient. In this regime we also obtain the shortest pulses directly from the system, which can be a factor 2-3 shorter than by pure saturable absorber modelocking. Note that Figure 6.6 indicates even arbitrarily shorter pulses if the nonlinear index, i.e.  $\delta_n$  is further increased. However, this is only an artifact of

the linear approximation of the saturable absorber, which can now become arbitrarily large, compare (6.18) and (6.19). As we have found from the analysis of the fast saturable absorber model, Figure 6.4, only one sixth of the saturable absorption is used for overcoming the gain filtering. This is so, because the saturable absorber has to shape and stabilize the pulse against breakthrough of cw-radiation. With SPM and GDD this is relaxed. The pulse shaping can be done by SPM and GDD alone, i.e. soliton formation and the absorber only has to stabilize the pulse. But then all of the saturable absorption can be used up for stability, i.e. six times as much, which allows for additional pulse shortening by a factor of about  $\sqrt{6} = 2.5$  in a parabolic filter situation. Note, that for an experimentalist a factor of three is a large number. This tells us that the 6.5 fs limit for Ti:sapphire derived above from the saturable absorber model can be reduced to 2.6 fs including GDD and SPM, which is about one optical cycle of 2.7 fs at a center wavelength of 800nm. At that point, all the approximations we have made so far break down. If the amount of negative dispersion is reduced too much, i.e. pulses become too short, the absorber cannot keep them stable anymore.

If there is strong positive dispersion, the pulses again become stable and long, but highly chirped. The pulse can then be compressed externally, however not completely to their transform limit, because these are nonlinearly chirped pulses, see Eq.(6.43).

In the case of strong solitonlike pulse shaping, the absorber doesn't have to be really fast, because the pulse is shaped by GDD and SPM and the absorber has only to stabilize the soliton against the continuum. This regime has been called Soliton mode locking.

## 6.3 Soliton Mode Locking

If strong soliton formation is present in the system, the saturable absorber doesn't have to be fast [6][7][8], see Figure 6.7. The master equation describing the mode locking process is given by

$$T_R \frac{\partial A(T, t)}{\partial T} = \left[ g - l + (D_f + jD) \frac{\partial^2}{\partial t^2} - j\delta |A(T, t)|^2 - q(T, t) \right] A(T, t). \quad (6.62)$$



The saturable absorber obeys a separate differential equation that describes the absorber response to the pulse in each round trip

$$\frac{\partial q(T, t)}{\partial t} = -\frac{q - q_0}{\tau_A} - \frac{|A(T, t)|^2}{E_A}. \quad (6.63)$$

Where  $\tau_A$  is the absorber recovery time and  $E_A$  the saturation energy. If the soliton shaping effects are much larger than the pulse

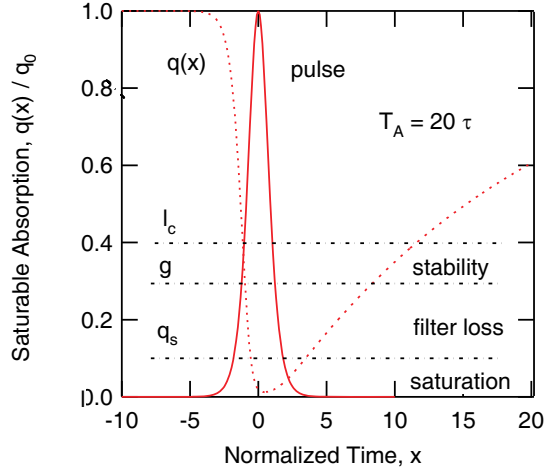


Figure 6.7: Response of a slow saturable absorber to a soliton-like pulse. The pulse experiences loss during saturation of the absorber and filter losses. The saturated gain is equal to these losses. The loss experienced by the continuum,  $l_c$  must be higher than the losses of the soliton to keep the soliton stable.

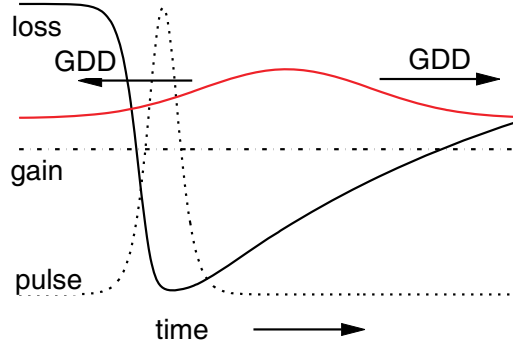


Figure 6.8: The continuum, that might grow in the open net gain window following the pulse is spread by dispersion into the regions of high absorption.

shaping due to the filter and the saturable absorber, the steady state pulse will be a soliton and continuum contribution similar to the case of active mode locking with strong soliton formation as discussed in section 5.5

$$A(T, t) = \left( A \operatorname{sech}\left(\frac{t}{\tau}\right) + a_c(T, t) \right) e^{-j\phi_0 \frac{T}{T_R}} \quad (6.64)$$

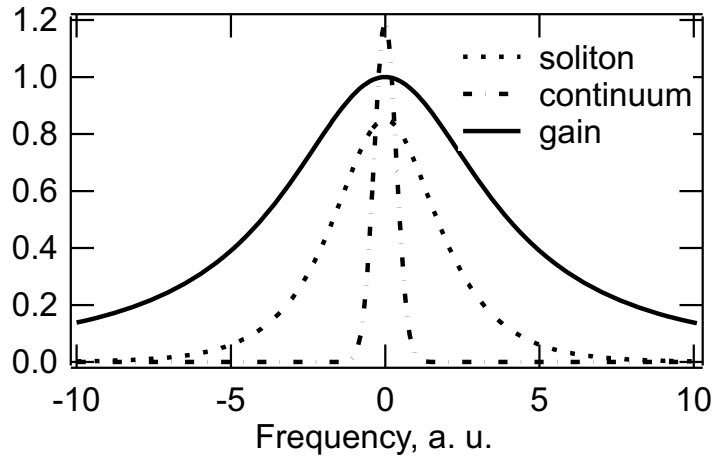


Figure 6.9: Normalized gain, soliton and continuum. The continuum is a long pulse exploiting the peak of the gain

The continuum can be viewed as a long pulse competing with the soliton for the available gain. In the frequency domain, see Figure 6.9, the soliton has a broad spectrum compared to the continuum. Therefore, the continuum experiences the peak of the gain, whereas the soliton spectrum on average experiences less gain. This advantage in gain of the continuum has to be compensated for in the time domain by the saturable absorber response, see Figure 6.8. Whereas for the soliton, there is a balance of the nonlinearity and the dispersion, this is not so for the continuum. Therefore, the continuum is spread by the dispersion into the regions of high absorption. This mechanism has to clean up the gain window following the soliton and caused by the slow recovery of the absorber. As in the case of active modelocking, once the soliton is too short, i.e. a too long net-gain window arises, the loss of the continuum may be lower than the loss of the soliton, see Figure 6.7 and the continuum may break through and destroy the single pulse soliton solution. As a rule of thumb the absorber recovery time can be about 10 times longer than the soliton width. This modelocking principle is especially important for modelocking of lasers with semiconductor saturable absorbers, which show typical absorber recovery times that may range from 100fs-100 ps. Pulses as short as 13fs have been generated with semiconductor saturable absorbers [11]. Figure 6.10 shows the measured spectra from a Ti:sapphire laser modelocked with a saturable absorber for different values for the intracavity dispersion. Lowering the dispersion, increases the bandwidth of the soliton and therefore its loss, while lowering at the same time the loss for the continuum. At some value of the dispersion the laser has to become unstable by break through of the continuum. In the example shown, this occurs at a dispersion value of about  $D = -500fs^2$ . The continuum break-through is clearly visible by the additional spectral components showing up at the center of the spectrum. Reducing the dispersion even further might lead again to more stable but complicated spectra related to the formation of higher order solitons. Note the spectra shown are time averaged spectra.

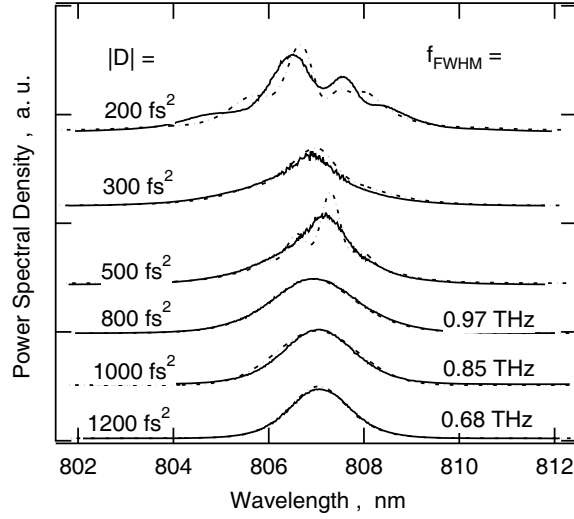


Figure 6.10: Measured (—) and simulated (---) spectra from a semiconductor saturable absorber modelocked Ti:sapphire laser for various values of the net intracavity dispersion.

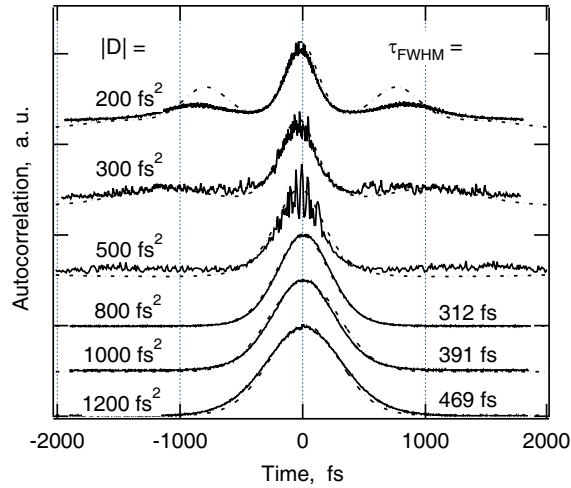


Figure 6.11: Measured (—) and simulated (---) autocorrelations corresponding to the spectra shown in Figure 6.10.

The continuum leads to a background pedestal in the intensity autocor-

relation of the emitted pulse, see Figure 6.11. The details of the spectra and autocorrelation may strongly depend on the detailed absorber response.

## 6.4 Dispersion Managed Soliton Formation

The nonlinear Schrödinger equation describes pulse propagation in a medium with continuously distributed dispersion and self-phase-modulation. For lasers generating pulses as short as 10 fs and below, it was first pointed out by Spielmann et al. that large changes in the pulse occur within one roundtrip and that the ordering of the pulse-shaping elements within the cavity has a major effect on the pulse formation [9]. The discrete action of linear dispersion in the arms of the laser resonator and the discrete, but simultaneous, action of positive SPM and positive GDD in the laser crystal cannot any longer be neglected. The importance of strong dispersion variations for the laser dynamics was first discovered in a fiber laser and called stretched pulse modelocking [11]. The positive dispersion in the Er-doped fiber section of a fiber ring laser was balanced by a negative dispersive passive fiber. The pulse circulating in the ring was stretched and compressed by as much as a factor of 20 in one roundtrip. One consequence of this behavior was a dramatic decrease of the nonlinearity and thus increased stability against the SPM induced instabilities. The sidebands, due to periodic perturbations of the soliton, as discussed in section 3.6, are no longer observed (see Fig. 6.12).

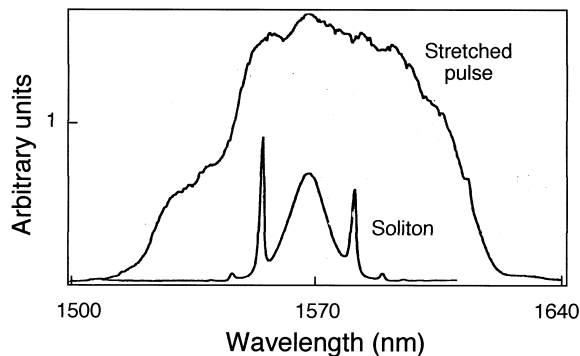


Figure 6.12: Spectra of mode-locked Er-doped fiber lasers operating in the conventional soliton regime, i.e. net negative dispersion and in the stretched pulse mode of operation at almost zero average dispersion [11].

The energy of the output pulses could be increased 100 fold. The minimum pulsewidth was 63 fs, with a bandwidth much broader than the erbium gain bandwidth [12]. Figure 6.12 also shows the spectral enhancement of the fiber laser in the dispersion managed regime. The generation of ultrashort pulses from solid state lasers like Ti:sapphire has progressed over the past decade and led to the generation of pulses as short as 5 fs directly from the laser. At such short pulse lengths the pulse is stretched up to a factor of ten when propagating through the laser crystal creating a dispersion managed soliton [10]. The spectra generated with these lasers are not of simple shape for many reasons. Here, we want to consider the impact on the spectral shape and laser dynamics due to dispersion managed soliton formation.

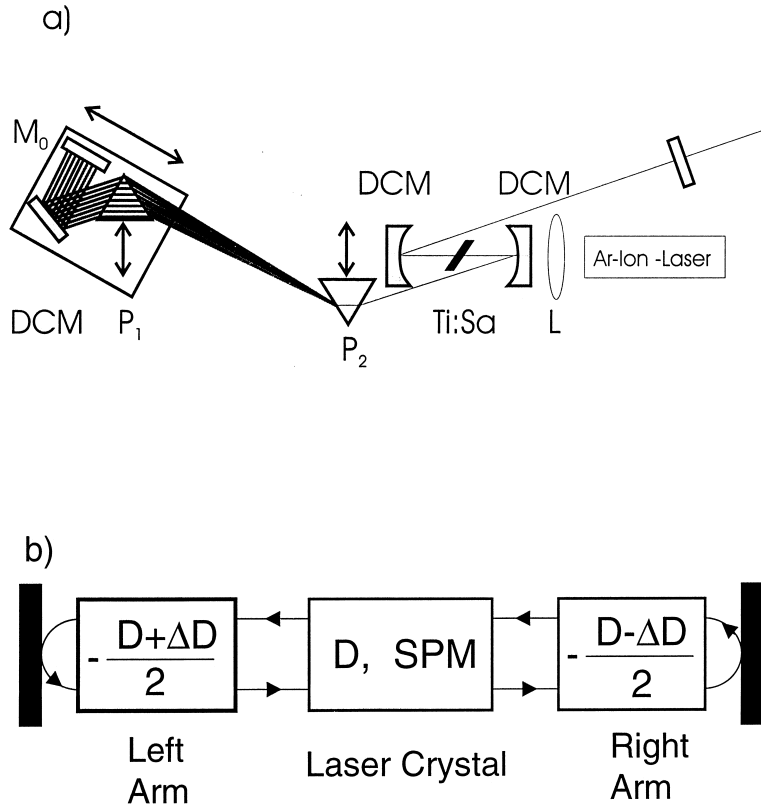


Figure 6.13: (a) Schematic of a Kerr-lens mode-locked Ti:sapphire laser: P's, prisms; L, lens; DCM's, double-chirped mirror; TiSa, Ti:sapphire. (b) Correspondence with dispersion-managed fiber transmission.

A mode-locked laser producing ultrashort pulses consists at least of a gain medium (Ti:sapphire crystal) and dispersion balancing components (mirrors, prism pairs), see Fig. 6.13 a. The system can be decomposed into the resonator arms and the crystal, see Fig. 6.13 b. To achieve ultrashort pulses, the dispersion-balancing components should produce near-zero net dispersion while the dispersion element(s) individually produce significant group delay over the broad bandwidth of the laser pulse. This fact suggests an analogy with dispersion-managed pulse propagation along a dispersion-managed fiber transmission link [14]. A system with sufficient variation of dispersion can support solitary waves. One can show that the Kerr nonlinearity produces a self-consistent nonlinear scattering potential that permits formation of a periodic solution with a simple phase factor in a system with zero net dispersion. The pulses are analogous to solitons in that they are self-consistent solutions of the Hamiltonian (lossless) problem as the conventional solitons discussed above. But they are not secant hyperbolic in shape. Figure 6.15 shows a numerical simulation of a self-consistent solution of the Hamiltonian pulse-propagation problem in a linear medium of negative dispersion and subsequent propagation in a nonlinear medium of positive dispersion and positive self-phase modulation, following the equation

$$\frac{\partial}{\partial z}A(z, t) = jD(z)\frac{\partial^2}{\partial t^2}A(z, t) - j\delta(z)|A|^2A(z, t) \quad (6.65)$$

In Fig. 6.15 the steady state intensity profiles are shown at the center of the negative dispersion segment over 1000 roundtrips. It is clear that the solution repeats itself from period to period, i.e. there is a new solitary wave that solves the piecewise nonlinear Schroedinger equation 6.65, dispersion managed soliton. In contrast to the conventional soliton the dispersion managed soliton of equation 6.65 (with no SAM and no filtering) resemble Gaussian pulses down to about  $-10$  dB from the peak, but then show rather complicated structure, see Fig. 6.15. The dispersion map  $D(z)$  used is shown as an inset in Figure 6.14. One can additionally include saturable gain, Lorentzian gain filtering, and a fast saturable absorber. Figure 6.14 shows the behavior in one period (one round trip through the resonator) including these effects. The response of the absorber is  $q(A) = q_o/(1 + |A|^2/P_A)$ , with  $q_o = 0.01/\text{mm}$  and  $P_A = 1$  MW. The bandwidth-limited gain is modeled by the Lorentzian profile with gain bandwidth  $2\pi \times 43$  THz. The filtering and saturable absorption reduce the spectral and temporal side lobes of the Hamiltonian problem. As can be inferred from Fig. 6.14, the steady state pulse formation can be

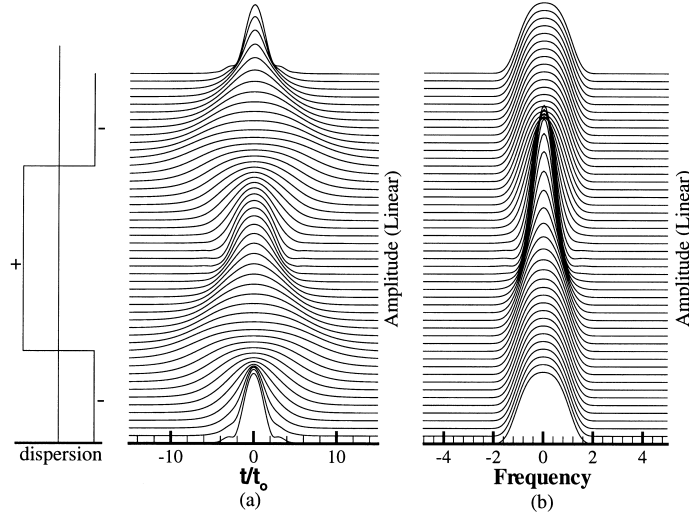


Figure 6.14: Pulse shaping in one round trip. The negative segment has no nonlinearity.

understood in the following way. By symmetry the pulses are chirp free in the middle of the dispersion cells. A chirp free pulse starting in the center of the gain crystal, i.e. nonlinear segment is spectrally broadened by the SPM and disperses in time due to the GVD, which generates a rather linear chirp over the pulse. After the pulse is leaving the crystal it experiences negative GVD during propagation through the left or right resonator arm, which is compressing the positively chirped pulse to its transform limit at the end of the arm, where an output coupler can be placed. Back propagation towards the crystal imposes a negative chirp, generating the time reversed solution of the nonlinear Schrödinger equation (6.65). Therefore, subsequent propagation in the nonlinear crystal is compressing the pulse spectrally and temporally to its initial shape in the center of the crystal. The spectrum is narrower in the crystal than in the negative-dispersion sections, because it is negatively prechirped before it enters the SPM section and spectral spreading occurs again only after the pulse has been compressed. This result further explains that in a laser with a linear cavity, for which the negative dispersion is located in only one arm of the laser resonator (i.e. in the prism pair and no use of chirped mirrors) the spectrum is widest in the arm that contains the negative dispersion. In a laser with a linear cavity, for which the negative



dispersion is equally distributed in both arms of the cavity, the pulse runs through the dispersion map twice per roundtrip. The pulse is short at each end of the cavity and, most importantly, the pulses are identical in each pass through the crystal, which exploits the saturable absorber action (Kerr-Lens Modelocking in this case, as will be discussed in the next chapter) twice per roundtrip, in contrast to an asymmetric dispersion distribution in the resonator arms. Thus a symmetric dispersion distribution leads to an effective saturable absorption that is twice as strong as an asymmetric dispersion distribution resulting in substantially shorter pulses. Furthermore, the dispersion swing between the negative and positive dispersion sections is only half, which allows for shorter dispersion-managed solitons operating at the same average power level.

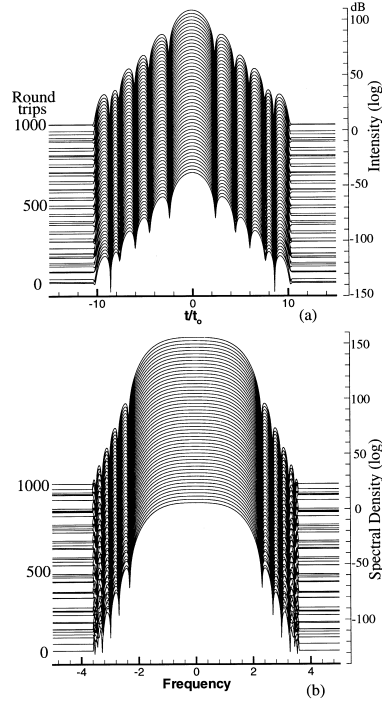


Figure 6.15: Simulation of the Hamiltonian problem. Intensity profiles at the center of the negatively dispersive segment are shown for successive roundtrips. The total extent in 1000 roundtrips.  $D = D^{(\pm)} = \pm 60 \text{ fs}^2/\text{mm}$ , segment of crystal length  $L = 2 \text{ mm}$ ,  $\tau_{\text{FWHM}} = 5.5 \text{ fs}$ ,  $\delta = 0$  for  $D < 0$ ,  $\delta = 1 \text{ (MW mm)}^{-1}$  for  $D > 0$ . [10]

To further illustrate the efficiency of the dispersion managed soliton formation, we present a series of simulations that start with a linear segment of negative dispersion and a nonlinear segment of positive dispersion of the same magnitude, saturable absorber action, and filtering.

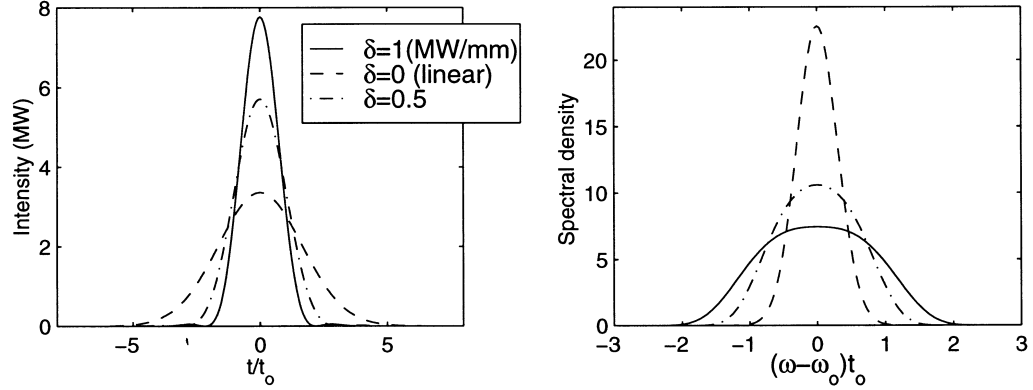


Figure 6.16: Sequence of pulse profiles in the center of the negatively dispersive segment for three magnitudes of SPM.  $t_o = 3$  fs, with solid curves (5.5 fs) for  $\delta = 1$  (MW mm) $^{-1}$ , dashed-dotted curve (7 fs) for  $\delta = 0.5$  (MW mm) $^{-1}$ , and dashed curves for no SPM of  $\delta = 0$ . The dispersion map is of Fig. 6.14. The output coupler loss is 3%.[10]

The dashed curve in Figure 6.16 shows the pulse shape for gain, loss, saturable absorption and gain filtering only. We obtained the other traces by increasing the SPM while keeping the energy fixed through adjustment of the gain. As one can see, increasing the SPM permits shorter pulses. The shortest pulse can be approximately three times shorter than the pulse without SPM. The parameters chosen for the simulations are listed in the figure caption. In this respect, the behavior is similar to the fast saturable absorber case with conventional soliton formation as discussed in the last section.

A major difference in the dispersion managed soliton case is illustrated in Fig. 6.17. The figure shows the parameter ranges for a dispersion-managed soliton system (no gain, no loss, no filtering) that is unbalanced such as to result in the net dispersion that serves as the abscissa of the figure. Each curve gives the locus of energy versus net cavity dispersion for a stretching ratio  $S = LD/\tau_{FWHM}^2$  (or pulse width with fixed crystal length  $L$ ). One can see that for pulse width longer than 8 fs with crystal length  $L = 2$  mm, no solution of finite energy exists in the dispersion managed system for zero or positive net dispersion. Pulses of durations longer than 8 fs require net negative dispersion. Hence one can reach the ultrashort dispersion managed

soliton operation at zero net dispersion only by first providing the system with negative dispersion. At the same energy, one can form a shorter pulse by reducing the net dispersion, provided that the 8 fs threshold has been passed. For a fixed dispersion swing  $\pm D$ , the stretching increases quadratically with the spectral width or the inverse pulse width. Long pulses with no stretching have a sech shape. For stretching ratios of 3-10 the pulses are Gaussian shaped. For even larger stretching ratios the pulse spectra become increasingly more flat topped, as shown in Fig. 6.16.

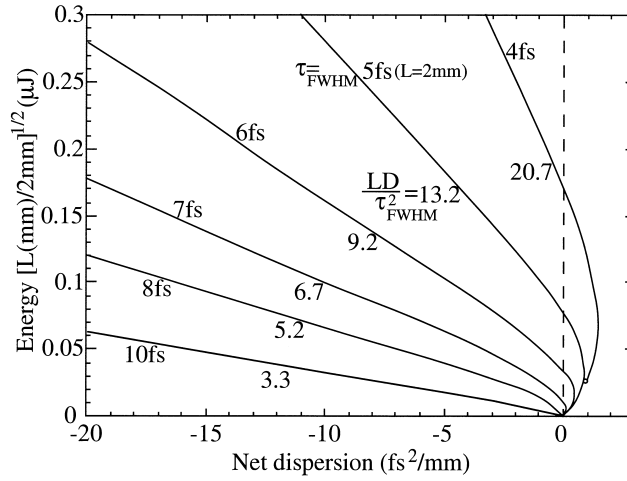


Figure 6.17: Energy of the pulse in the lossless dispersion-managed system with stretching  $S = LD/\tau_{\text{FWHM}}^2$  or for a fixed crystal length  $L$  and pulsewidth as parameters;  $D = 60 \text{ fs}^2/\text{mm}$  for Ti:sapphire at 800 nm [10].

To gain insight into the laser dynamics and later on in their noise and tuning behavior, it is advantageous to formulate also a master equation approach for the dispersion managed soliton case [16]. Care has to be taken of the fact that the Kerr-phase shift is produced by a pulse of varying amplitude and width as it circulates around the ring. The Kerr-phase shift for a pulse of constant width,  $\delta|a|^2$  had to be replaced by a phase profile that mimics the average shape of the pulse, weighted by its intensity. Therefore, the SPM action is replaced by

$$\delta|A|^2 = \delta_o|A_o|^2 \left( 1 - \mu \frac{t^2}{\tau^2} \right) \quad (6.66)$$

where  $A_o$  is the pulse amplitude at the position of minimum width. The Kerr-phase profile is expanded to second order in  $t$ . The coefficient  $\delta_o$  and  $\mu$  are evaluated variationally. The saturable absorber action is similarly expanded. Finally, the net intracavity dispersion acting on average on the pulse is replaced by the effective dispersion  $D_{\text{net}}$  in the resonator within one roundtrip. The master equation becomes

$$T_R \frac{\partial}{\partial T} A = (g - l)A + \left( \frac{1}{\Omega_f^2} + jD_{\text{net}} \right) \frac{\partial^2}{\partial t^2} A + (\gamma_o - j\delta_o) |A_o|^2 \left( 1 - \mu \frac{t^2}{\tau^2} \right) A \quad (6.67)$$

This equation has Gaussian-pulse solutions. The master equation (6.67) is a patchwork, it is not an ordinary differential equation. The coefficients in the equation depend on the pulse solution and eventually have to be found iteratively. Nevertheless, the equation accounts for the pulse shaping in the system in an analytic fashion. It will allow us to extend the conventional soliton perturbation theory to the case of dispersion managed solitons.

There is one more interesting property of the stretched pulse operation that needs to be emphasized. Dispersion managed solitons may form even when the net dispersion as seen by a linearly propagating pulse is zero or slightly positive. This is a surprising result which was discovered in the study of dispersion managed soliton propagation [14]. It turns out that the stretched pulse changes its spectrum during propagation through the two segments of fiber with opposite dispersion or in the case of a Ti:Sapphire laser in the nonlinear crystal. The spectrum in the segment with normal (positive) dispersion is narrower, than in the segment of anomalous (negative) dispersion, see Figure 6.14. The pulse sees an effective net negative dispersion, provided that the positive  $D_{\text{net}}$  is not too large. In (6.67) the  $D_{\text{net}}$  is to be replaced by  $D_{\text{eff}}$  which can be computed variationally. Thus, dispersion managed soliton-like solutions can exist even when  $D_{\text{net}}$  is zero. However, they exist only if the stretching factor is large, see Figure 6.17.

A remarkable property of the dispersion managed solitons is that they do not radiate (generate continuum) even though they propagate in a medium with abrupt dispersion changes. This can be understood by the fact, that the dispersion managed soliton is a solution of the underlying dynamics incorporating already the periodic dispersion variations including the Kerr-effect.

This is in contrast to the soliton in a continuously distributed dispersive environment, where periodic variations in dispersion and nonlinearity leads to radiation.



# Bibliography

- [1] G.H.C. New: "Pulse evolution in mode-locked quasicontinuous lasers," IEEE J. Quantum Electron. **10**, 115-124 (1974)
- [2] H. A. Haus, "Theory of Mode Locking with a Slow Saturable Absorber," IEEE J. Quantum Electron. **11**, pp. 736 – 746 (1975).
- [3] H. A. Haus, "Theory of modelocking with a fast saturable absorber," J. Appl. Phys. **46**, pp. 3049 – 3058 (1975).
- [4] H. A. Haus, J. G. Fujimoto, E. P. Ippen, "Structures for additive pulse modelocking," J. Opt. Soc. of Am. **B 8**, pp. 2068 – 2076 (1991).
- [5] E. P. Ippen, "Principles of passive mode locking," Appl. Phys. **B 58**, pp. 159 – 170 (1994).
- [6] F. X. Kärtner and U. Keller, "Stabilization of soliton-like pulses with a slow saturable absorber," Opt. Lett. **20**, 16 – 19 (1995).
- [7] F.X. Kärtner, I.D. Jung, U. Keller: TITLE, "Soliton Modelocking with Saturable Absorbers," Special Issue on Ultrafast Electronics, Photonics and Optoelectronics, IEEE J. Sel. Top. Quantum Electron. **2**, 540-556 (1996)
- [8] I. D. Jung, F. X. Kärtner, L. R. Brovelli, M. Kamp, U. Keller, "Experimental verification of soliton modelocking using only a slow saturable absorber," Opt. Lett. **20**, pp. 1892 – 1894 (1995).
- [9] C. Spielmann, P.F. Curley, T. Brabec, F. Krausz: Ultrabroad-band femtosecond lasers, IEEE J. Quantum Electron. **30**, 1100-1114 (1994).



- [10] Y. Chen, F. X. Kärtner, U. Morgner, S. H. Cho, H. A. Haus, J. G. Fujimoto, and E. P. Ippen, "Dispersion managed mode-locking," *J. Opt. Soc. Am. B* **16**, 1999-2004, 1999.
- [11] K. Tamura, E.P. Ippen, H.A. Haus, L.E. Nelson: 77-fs pulse generation from a stretched-pulse mode-locked all-fiber ring laser, *Opt. Lett.* **18**, 1080-1082 (1993)
- [12] K. Tamura, E.P. Ippen, H.A. Haus: Pulse dynamics in stretched-pulse lasers, *Appl. Phys. Lett.* **67**, 158-160 (1995)
- [13] F.X. Kärtner, J. A. d. Au, U. Keller, "Mode-Locking with Slow and Fast Saturable Absorbers-What's the Difference,". *Sel. Top. Quantum Electron.* **4**, 159 (1998)
- [14] J.H.B. Nijhof, N.J. Doran, W. Forysiak, F.M. Knox: Stable soliton-like propagation in dispersion-managed system with net anomalous, zero, and normal dispersion, *Electron. Lett.* **33**, 1726-1727 (1997)
- [15] Y. Chen, H.A. Haus: Dispersion-managed solitons in the net positive dispersion regime, *J. Opt. Soc. Am. B* **16**, 24-30 (1999)
- [16] H.A. Haus, K. Tamura, L.E. Nelson, E.P. Ippen, "Stretched-pulse additive pulse modelocking in fiber ring lasers: theory and experiment," *IEEE J. Quantum Electron.* **31**, 591-598 (1995)
- [17] I. D. Jung, F. X. Kärtner, N. Matuschek, D. H. Sutter, F. Morier-Genoud, Z. Shi, V. Scheuer, M. Tilsch, T. Tschudi, U. Keller, "Semiconductor saturable absorber mirrors supporting sub-10 fs pulses," *Appl. Phys. B* **65**, pp. 137-150 (1997).

# Chapter 7

## Kerr-Lens and Additive Pulse Mode Locking

There are many ways to generate saturable absorber action. One can use real saturable absorbers, such as semiconductors or dyes and solid-state laser media. One can also exploit artificial saturable absorbers. The two most prominent artificial saturable absorber modelocking techniques are called Kerr-Lens Mode Locking (KLM) and Additive Pulse Mode Locking (APM). APM is sometimes also called Coupled-Cavity Mode Locking (CCM). KLM was invented in the early 90's [1][2][3][4][5][6][7], but was already predicted to occur much earlier [8][9][10].

### 7.1 Kerr-Lens Mode Locking (KLM)

The general principle behind Kerr-Lens Mode Locking is sketched in Fig. 7.1. A pulse that builds up in a laser cavity containing a gain medium and a Kerr medium experiences not only self-phase modulation but also self focussing, that is nonlinear lensing of the laser beam, due to the nonlinear refractive index of the Kerr medium. A spatio-temporal laser pulse propagating through the Kerr medium has a time dependent mode size as higher intensities acquire stronger focussing. If a hard aperture is placed at the right position in the cavity, it strips of the wings of the pulse, leading to a shortening of the pulse. Such combined mechanism has the same effect as a saturable absorber. If the electronic Kerr effect with response time of a few femtoseconds or less is used, a fast saturable absorber has been created. Instead of a sep-

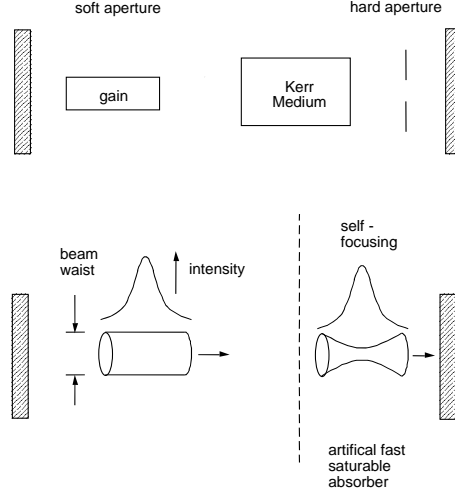


Figure 7.1: Principle mechanism of KLM. The hard aperture can be also replaced by the soft aperture due to the spatial variation of the gain in the laser crystal.

arate Kerr medium and a hard aperture, the gain medium can act both as a Kerr medium and as a soft aperture (i.e. increased gain instead of saturable absorption). The sensitivity of the laser mode size on additional nonlinear lensing is drastically enhanced if the cavity is operated close to the stability boundary of the cavity. Therefore, it is of prime importance to understand the stability ranges of laser resonators. Laser resonators are best understood in terms of paraxial optics [11][12][14][13][15].

### 7.1.1 Review of Paraxial Optics and Laser Resonator Design

The solutions to the paraxial wave equation, which keep their form during propagation, are the Hermite-Gaussian beams. Since we consider only the fundamental transverse modes, we are dealing with the Gaussian beam

$$U(r, z) = \frac{U_o}{q(z)} \exp \left[ -jk \frac{r^2}{2q(z)} \right], \quad (7.1)$$

with the complex q-parameter  $q = z + jb$  or its inverse

$$\frac{1}{q(z)} = \frac{1}{R(z)} - j \frac{\lambda}{\pi w^2(z)}. \quad (7.2)$$

The Gaussian beam intensity  $I(z, r) = |U(r, z)|^2$  expressed in terms of the power  $P$  carried by the beam is given by

$$I(r, z) = \frac{2P}{\pi w^2(z)} \exp \left[ -\frac{2r^2}{w^2(z)} \right]. \quad (7.3)$$

The use of the q-parameter simplifies the description of Gaussian beam propagation. In free space propagation from  $z_1$  to  $z_2$ , the variation of the beam parameter  $q$  is simply governed by

$$q_2 = q_1 + z_2 - z_1, \quad (7.4)$$

where  $q_2$  and  $q_1$  are the beam parameters at  $z_1$  and  $z_2$ . If the beam waist, at which the beam has a minimum spot size  $w_0$  and a planar wavefront ( $R = \infty$ ), is located at  $z = 0$ , the variations of the beam spot size and the radius of curvature are explicitly expressed as

$$w(z) = w_o \left[ 1 + \left( \frac{\lambda z}{\pi w_o^2} \right)^2 \right]^{1/2}, \quad (7.5)$$

and

$$R(z) = z \left[ 1 + \left( \frac{\pi w_o^2}{\lambda z} \right)^2 \right]. \quad (7.6)$$

The angular divergence of the beam is inversely proportional to the beam waist. In the far field, the half angle divergence is given by,

$$\theta = \frac{\lambda}{\pi w_o}, \quad (7.7)$$

as illustrated in Figure 7.2.

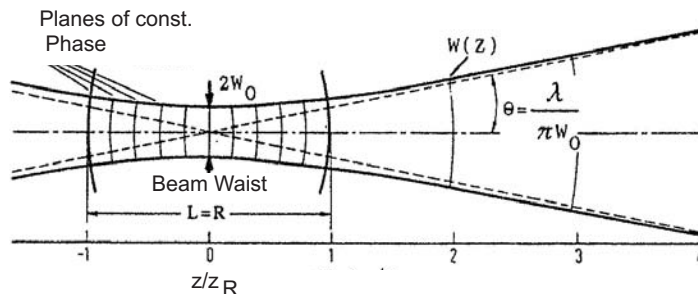


Figure 7.2: Gaussian beam and its characteristics.

Due to diffraction, the smaller the spot size at the beam waist, the larger the divergence. The Rayleigh range is defined as the distance from the waist over which the beam area doubles and can be expressed as

$$z_R = \frac{\pi w_o^2}{\lambda}. \quad (7.8)$$

The confocal parameter of the Gaussian beam is defined as twice the Rayleigh range

$$b = 2z_R = \frac{2\pi w_o^2}{\lambda}, \quad (7.9)$$

and corresponds to the length over which the beam is focused. The propagation of Hermite-Gaussian beams through paraxial optical systems can be efficiently evaluated using the ABCD-law [11]

$$q_2 = \frac{Aq_1 + B}{Cq_1 + D} \quad (7.10)$$

where  $q_1$  and  $q_2$  are the beam parameters at the input and the output planes of the optical system or component. The ABCD matrices of some optical elements are summarized in Table 7.1. If a Gaussian beam with a waist  $w_{01}$  is focused by a thin lens a distance  $z_1$  away from the waist, there will be a

new focus at a distance

$$z_2 = f + \frac{(z_1 - f)f^2}{(z_1 - f)^2 + \left(\frac{\pi w_{01}^2}{\lambda}\right)^2}, \quad (7.11)$$

and a waist  $w_{02}$

$$\frac{1}{w_{02}^2} = \frac{1}{w_{01}^2} \left(1 - \frac{z_1}{f}\right)^2 + \frac{1}{f^2} \left(\frac{\pi w_{01}}{\lambda}\right)^2 \quad (7.12)$$

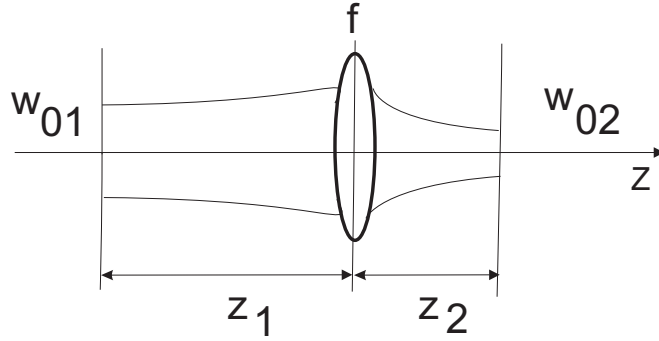


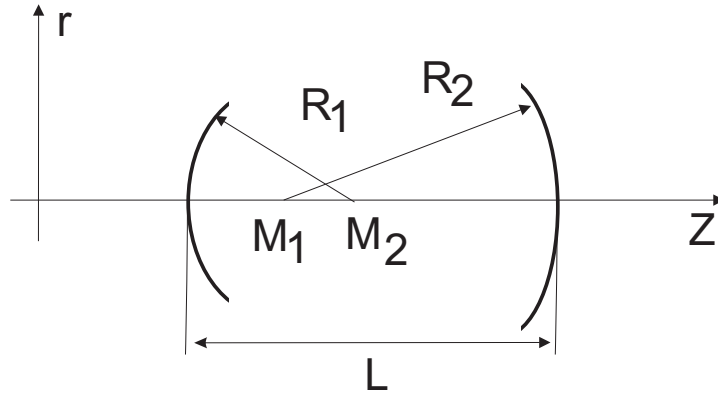
Figure 7.3: Focusing of a Gaussian beam by a lens.

### 7.1.2 Two-Mirror Resonators

We consider the two mirror resonator shown in Figure 7.4.

Optical Element	ABCD-Matrix
Free Space Distance $L$	$\begin{pmatrix} 1 & L \\ 0 & 1 \end{pmatrix}$
Thin Lens with focal length $f$	$\begin{pmatrix} 1 & 0 \\ -1/f & 1 \end{pmatrix}$
Mirror under Angle $\theta$ to Axis and Radius $R$ Sagittal Plane	$\begin{pmatrix} 1 & 0 \\ \frac{-2\cos\theta}{R} & 1 \end{pmatrix}$
Mirror under Angle $\theta$ to Axis and Radius $R$ Tangential Plane	$\begin{pmatrix} 1 & 0 \\ \frac{-2}{R\cos\theta} & 1 \end{pmatrix}$
Brewster Plate under Angle $\theta$ to Axis and Thickness $d$ , Sagittal Plane	$\begin{pmatrix} 1 & \frac{d}{n} \\ 0 & 1 \end{pmatrix}$
Brewster Plate under Angle $\theta$ to Axis and Thickness $d$ , Tangential Plane	$\begin{pmatrix} 1 & \frac{d}{n^3} \\ 0 & 1 \end{pmatrix}$

Table 7.1: ABCD matrices for commonly used optical elements.

Figure 7.4: Two-Mirror Resonator with curved mirrors with radii of curvature  $R_1$  and  $R_2$ .

The resonator can be unfolded for an ABCD-matrix analysis, see Figure 7.5.

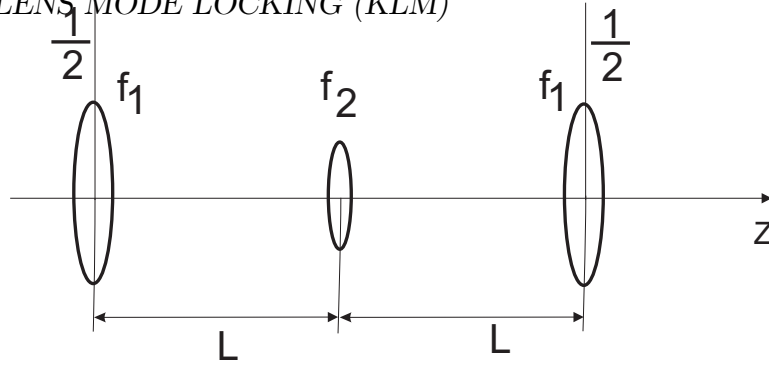


Figure 7.5: Two-mirror resonator unfolded. Note, only one half of the focusing strength of mirror 1 belongs to a fundamental period describing one resonator roundtrip.

The product of ABCD matrices describing one roundtrip according to Figure 7.5 are then given by

$$M = \begin{pmatrix} 1 & 0 \\ \frac{-1}{2f_1} & 1 \end{pmatrix} \begin{pmatrix} 1 & L \\ 0 & 1 \end{pmatrix} \begin{pmatrix} 1 & 0 \\ \frac{-1}{f_2} & 1 \end{pmatrix} \begin{pmatrix} 1 & L \\ 0 & 1 \end{pmatrix} \begin{pmatrix} 1 & 0 \\ \frac{-1}{2f_1} & 1 \end{pmatrix} \quad (7.13)$$

where  $f_1 = R_1/2$ , and  $f_2 = R_2/2$ . To carry out this product and to formulate the cavity stability criteria, it is convenient to use the cavity parameters  $g_i = 1 - L/R_i$ ,  $i = 1, 2$ . The resulting cavity roundtrip ABCD-matrix can be written in the form

$$M = \begin{pmatrix} (2g_1g_2 - 1) & 2g_2L \\ 2g_1(g_1g_2 - 1)/L & (2g_1g_2 - 1) \end{pmatrix} = \begin{pmatrix} A & B \\ C & D \end{pmatrix}. \quad (7.14)$$

### Resonator Stability

The ABCD matrices describe the dynamics of rays propagating inside the resonator. An optical ray is characterized by the vector  $\mathbf{r} = \begin{pmatrix} r \\ r' \end{pmatrix}$ , where  $r$  is the distance from the optical axis and  $r'$  the slope of the ray to the optical axis. The resonator is stable if no ray escapes after many round-trips, which is the case when the eigenvalues of the matrix  $M$  are less than or equal to one. Since we have a lossless resonator, i.e.  $\det|M| = 1$ , the product of the eigenvalues has to be 1 and, therefore, the stable resonator corresponds to the case of a complex conjugate pair of eigenvalues with a magnitude of 1.



The eigenvalue equation to  $M$  is given by

$$\det |M - \lambda \cdot 1| = \det \begin{vmatrix} (2g_1g_2 - 1) - \lambda & 2g_2L \\ 2g_1(g_1g_2 - 1)/L & (2g_1g_2 - 1) - \lambda \end{vmatrix} = 0, \quad (7.15)$$

$$\lambda^2 - 2(2g_1g_2 - 1)\lambda + 1 = 0. \quad (7.16)$$

The eigenvalues are

$$\lambda_{1/2} = (2g_1g_2 - 1) \pm \sqrt{(2g_1g_2 - 1)^2 - 1}, \quad (7.17)$$

$$= \begin{cases} \exp(\pm\theta), \cosh \theta = 2g_1g_2 - 1, & \text{for } |2g_1g_2 - 1| > 1 \\ \exp(\pm j\psi), \cos \psi = 2g_1g_2 - 1, & \text{for } |2g_1g_2 - 1| \leq 1 \end{cases}. \quad (7.18)$$

The case of a complex conjugate pair with a unit magnitude corresponds to a stable resonator. Therefore, the stability criterion for a stable two mirror resonator is

$$|2g_1g_2 - 1| \leq 1. \quad (7.19)$$

The stable and unstable parameter ranges are given by

$$\text{stable} : 0 \leq g_1 \cdot g_2 = S \leq 1 \quad (7.20)$$

$$\text{unstable} : g_1g_2 \leq 0; \text{ or } g_1g_2 \geq 1. \quad (7.21)$$

where  $S = g_1 \cdot g_2$ , is the stability parameter of the cavity. The stability criterion can be easily interpreted geometrically. Of importance are the distances between the mirror mid-points  $M_i$  and cavity end points, i.e.  $g_i = (R_i - L)/R_i = -S_i/R_i$ , as shown in Figure 7.6.

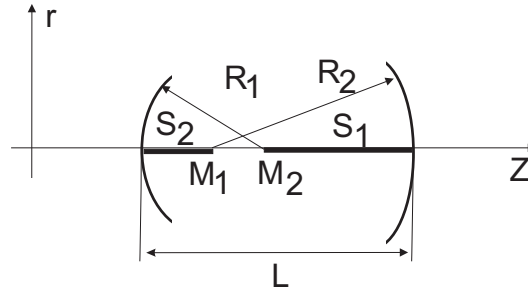


Figure 7.6: The stability criterion involves distances between the mirror mid-points  $M_i$  and cavity end points. i.e.  $g_i = (R_i - L)/R_i = -S_i/R_i$ .

The following rules for a stable resonator can be derived from Figure 7.6 using the stability criterion expressed in terms of the distances  $S_i$ . Note, that the distances and radii can be positive and negative

$$\text{stable : } 0 \leq \frac{S_1 S_2}{R_1 R_2} \leq 1. \quad (7.22)$$

The rules are:

- A resonator is stable, if the mirror radii, laid out along the optical axis, overlap.
- A resonator is unstable, if the radii do not overlap or one lies within the other.

Figure 7.7 shows stable and unstable resonator configurations.

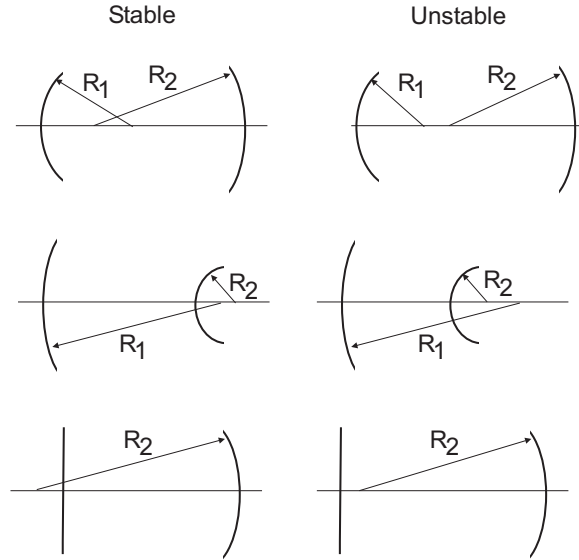


Figure 7.7: Illustration of stable and unstable resonator configurations.

For a two-mirror resonator with concave mirrors and  $R_1 \leq R_2$ , we obtain the general stability diagram as shown in Figure 7.8. There are two ranges for the mirror distance  $L$ , within which the cavity is stable,  $0 \leq L \leq R_1$  and

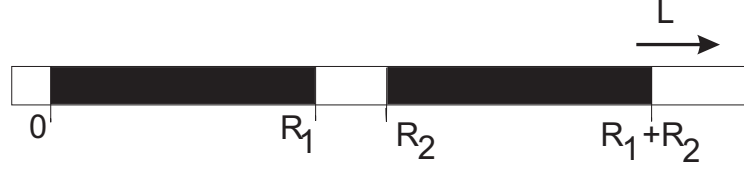


Figure 7.8: Stable regions (black) for the two-mirror resonator.

$R_2 \leq L \leq R_1 + R_2$ . It is interesting to investigate the spot size at the mirrors and the minimum spot size in the cavity as a function of the mirror distance  $L$ .

### Resonator Mode Characteristics

The stable modes of the resonator reproduce themselves after one round-trip, i.e. from Eq.(7.10) we find

$$q_1 = \frac{Aq_1 + B}{Cq_1 + D} \quad (7.23)$$

The inverse  $q$ -parameter, which is directly related to the phase front curvature and the spot size of the beam, is determined by

$$\left(\frac{1}{q}\right)^2 + \frac{A-D}{B} \left(\frac{1}{q}\right) + \frac{1-AD}{B^2} = 0. \quad (7.24)$$

The solution is

$$\left(\frac{1}{q}\right)_{1/2} = -\frac{A-D}{2B} \pm \frac{j}{2|B|} \sqrt{(A+D)^2 - 1} \quad (7.25)$$

If we apply this formula to (7.15), we find the spot size on mirror 1

$$\left(\frac{1}{q}\right)_{1/2} = -\frac{j}{2|B|} \sqrt{(A+D)^2 - 1} = -j \frac{\lambda}{\pi w_1^2}. \quad (7.26)$$

or

$$w_1^4 = \left(\frac{2\lambda L}{\pi}\right)^2 \frac{g_2}{g_1} \frac{1}{1 - g_1 g_2} \quad (7.27)$$

$$= \left(\frac{\lambda R_1}{\pi}\right)^2 \frac{R_2 - L}{R_1 - L} \left(\frac{L}{R_1 + R_2 - L}\right). \quad (7.28)$$

By symmetry, we find the spot size on mirror 3 via switching index 1 and 2:

$$w_2^4 = \left( \frac{2\lambda L}{\pi} \right)^2 \frac{g_1}{g_2} \frac{1}{1 - g_1 g_2} \quad (7.29)$$

$$= \left( \frac{\lambda R_2}{\pi} \right)^2 \frac{R_1 - L}{R_2 - L} \left( \frac{L}{R_1 + R_2 - L} \right). \quad (7.30)$$

The intracavity focus can be found by transforming the focused Gaussian beam with the propagation matrix

$$\begin{pmatrix} 1 & z_1 \\ 0 & 1 \end{pmatrix} \begin{pmatrix} 1 & 0 \\ 0 & 1 \end{pmatrix}$$

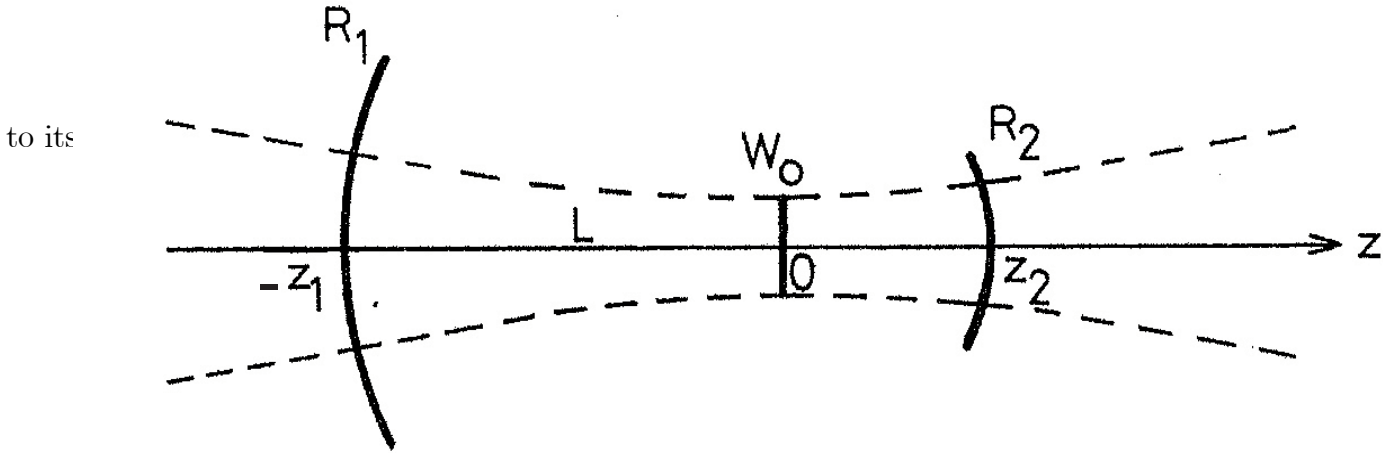


Figure 7.9: Two-mirror resonator

A short calculation results in

$$z_1 = L \frac{g_2 (g_1 - 1)}{2g_1 g_2 - g_1 - g_2} \quad (7.32)$$

$$= \frac{L(L - R_2)}{2L - R_1 - R_2}, \quad (7.33)$$

and, again, by symmetry

$$z_2 = L \frac{g_1 (g_2 - 1)}{2g_1 g_2 - g_1 - g_2} \quad (7.34)$$

$$= \frac{L(L - R_1)}{2L - R_1 - R_2} = L - z_1. \quad (7.35)$$

The spot size in the intracavity focus is

$$w_o^4 = \left( \frac{\lambda L}{\pi} \right)^2 \frac{g_1 g_2 (1 - g_1 g_2)}{(2g_1 g_2 - g_1 - g_2)^2} \quad (7.36)$$

$$= \left( \frac{\lambda}{\pi} \right)^2 \frac{L(R_1 - L)(R_2 - L)(R_1 + R_2 - L)}{(R_1 + R_2 - 2L)^2}. \quad (7.37)$$

All these quantities for the two-mirror resonator are shown in Figure 7.11. Note, that all resonators and the Gaussian beam are related to the confocal resonator as shown in Figure 7.10.

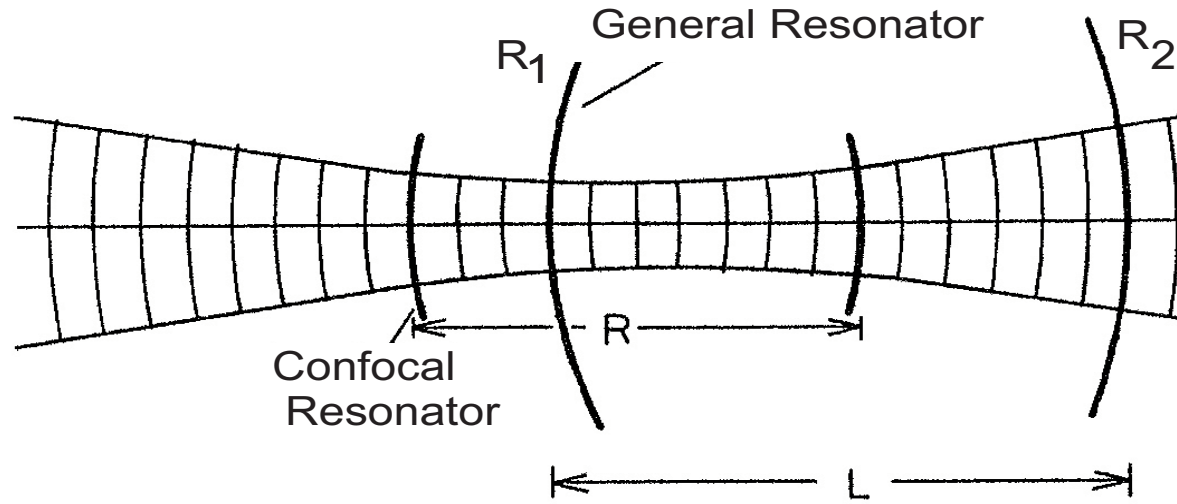


Figure 7.10: Two-mirror resonator and its relationship with the confocal resonator.

### 7.1. KERR-LENS MO.

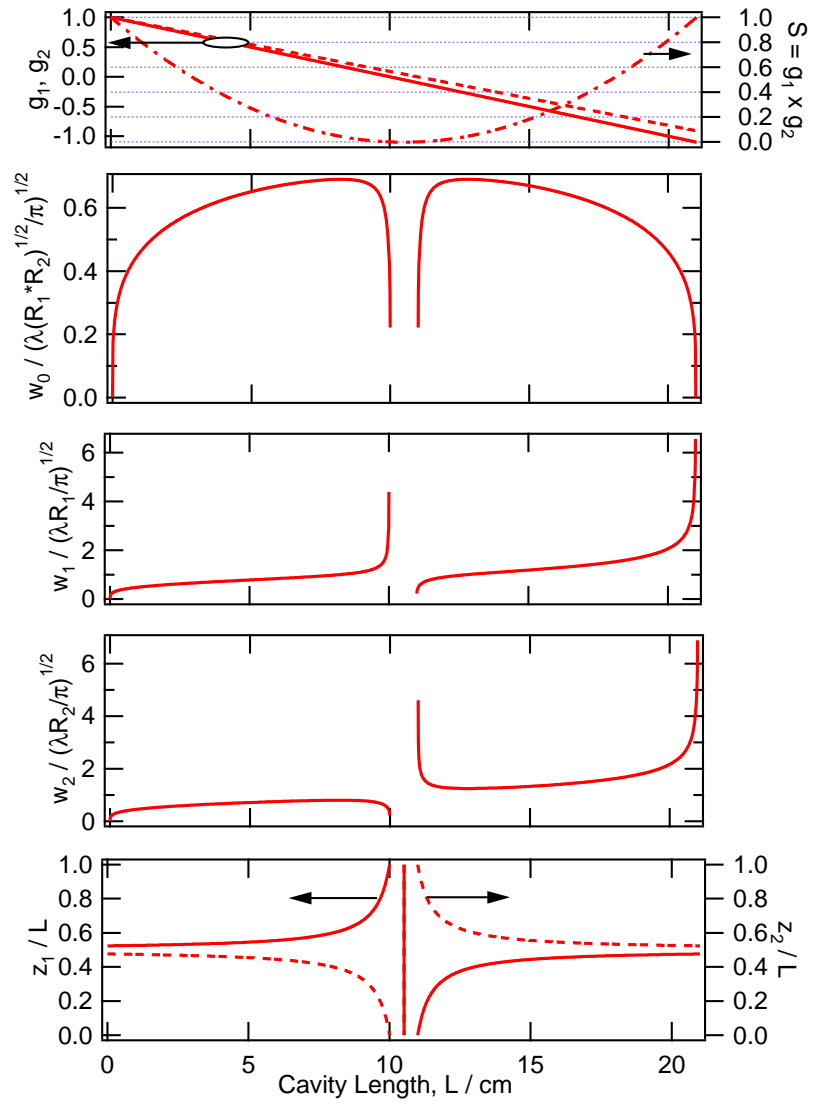


Figure 7.11: From top to bottom: Cavity parameters,  $g_1$ ,  $g_2$ ,  $S$ ,  $w_0$ ,  $w_1$ ,  $w_2$ ,  $z_1$  and  $z_2$  for the two-mirror resonator with  $R_1 = 10$  cm and  $R_2 = 11$  cm.

### 7.1.3 Four-Mirror Resonators

More complex resonators, like the four-mirror resonator depicted in Figure 7.12 a) can be transformed to an equivalent two-mirror resonator as shown in Figure 7.4 b) and c)

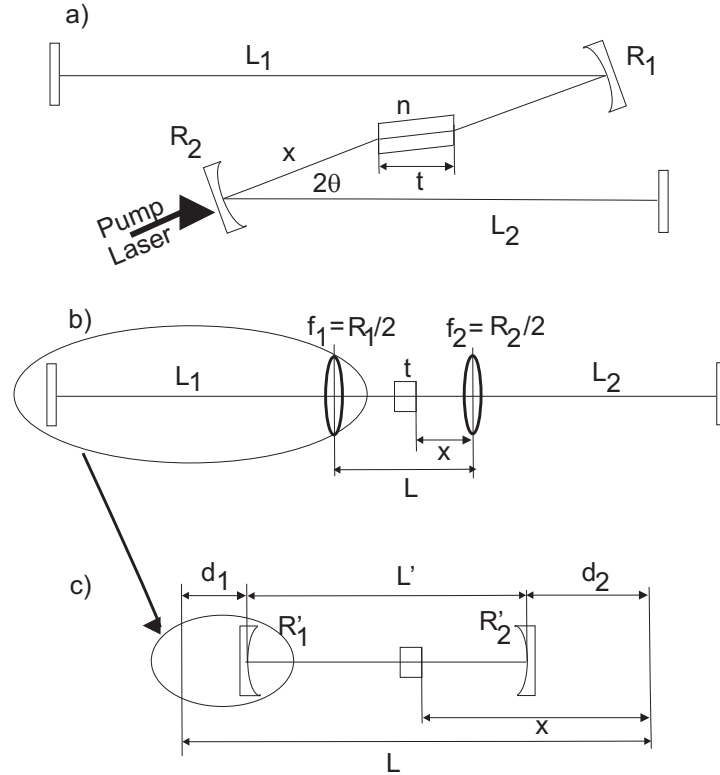


Figure 7.12: a) Four-mirror resonator with gain medium of refractive index  $n$ , and thickness  $t$ . Folding angles have to be adjusted for astigmatism compensation. b) Equivalent lens cavity. Note that the new focal length do not yet account for the different equivalent radii of curvature due to nonnormal incidence on the mirrors. c) Equivalent two-mirror cavity with imaged end mirrors.

Each of the resonator arms (end mirror,  $L_1$ ,  $R_1$ ) or (end mirror,  $L_2$ ,  $R_2$ ) is equivalent to a new mirror with a new radius of curvature  $R'_{1/2}$  positioned a distance  $d_{1/2}$  away from the old reference plane [12]. This follows simply from the fact that each symmetric optical system is equivalent to a lens positioned

at a distance  $d$  from the old reference plane

$$\begin{aligned} M &= \begin{pmatrix} A & B \\ C & A \end{pmatrix} = \begin{pmatrix} 1 & d \\ 0 & 1 \end{pmatrix} \begin{pmatrix} 1 & 0 \\ -\frac{1}{f} & 1 \end{pmatrix} \begin{pmatrix} 1 & d \\ 0 & 1 \end{pmatrix} \\ &= \begin{pmatrix} 1 - \frac{d}{f} & d\left(2 - \frac{d}{f}\right) \\ -\frac{1}{f} & 1 - \frac{d}{f} \end{pmatrix} \end{aligned} \quad (7.38)$$

with

$$\begin{aligned} d &= \frac{A-1}{C} \\ -\frac{1}{f} &= C \end{aligned} \quad (7.39)$$

The matrix of the resonator arm 1 is given by

$$M = \begin{pmatrix} 1 & 0 \\ -\frac{2}{R_1} & 1 \end{pmatrix} \begin{pmatrix} 1 & 2L_1 \\ 0 & 1 \end{pmatrix} \begin{pmatrix} 1 & 0 \\ -\frac{2}{R_1} & 1 \end{pmatrix} = \begin{pmatrix} 1 - \frac{4L_1}{R_1} & 2L_1 \\ -\frac{4}{R_1}\left(1 - \frac{2L_1}{R_1}\right) & 1 - \frac{4L_1}{R_1} \end{pmatrix} \quad (7.40)$$

from which we obtain

$$d_1 = -\frac{R_1}{2} \frac{1}{1 - R_1/(2L_1)}, \quad (7.41)$$

$$R'_1 = -\left(\frac{R_1}{2}\right)^2 \frac{1}{L_1[1 - R_1/(2L_1)]}. \quad (7.42)$$

For arm lengths  $L_{1/2}$  much larger than the radius of curvature, the new radius of curvature is roughly by a factor of  $\frac{R_1}{4L_1}$  smaller. Typical values are  $R_1 = 10$  cm and  $L_1 = 50$  cm. Then the new radius of curvature is  $R'_1 = 5$  mm. The analogous equations apply to the other resonator arm

$$d_2 = -\frac{R_2}{2} \frac{1}{1 - R_2/(2L_2)}, \quad (7.43)$$

$$R'_2 = -\left(\frac{R_2}{2}\right)^2 \frac{1}{L_2[1 - R_2/(2L_2)]}. \quad (7.44)$$

Note that the new mirror radii are negative for  $R_i/L_i < 1$ . The new distance  $L'$  between the equivalent mirrors is then also negative over the region where the resonator is stable, see Fig.7.8. We obtain

$$L' = L + d_1 + d_2 = L - \frac{R_1 + R_2}{2} - \delta \quad (7.45)$$



$$\delta = \frac{R_1}{2} \left[ \frac{1}{1 - R_1/(2L_1)} - 1 \right] + \frac{R_2}{2} \left[ \frac{1}{1 - R_2/(2L_2)} - 1 \right] \quad (7.46)$$

$$= -(R'_1 + R'_2) \quad (7.47)$$

or

$$L = \frac{R_1 + R_2}{2} - (R'_1 + R'_2) + L' \quad (7.48)$$

From the discussion in section 7.1.2, we see that the stability ranges cover at most a distance  $\delta$ . Figure 7.13 shows the resonator characteristics as a function of the cavity length  $L$  for the following parameters  $R_1 = R_2 = 10$  cm and  $L_1 = 100$  cm and  $L_2 = 75$  cm, which lead to

$$\begin{aligned} d_1 &= -5.26 \text{ cm} \\ R'_1 &= -0.26 \text{ cm} \end{aligned} \quad (7.49)$$

$$\begin{aligned} d_2 &= -5.36 \text{ cm} \\ R'_2 &= -0.36 \text{ cm} \end{aligned} \quad (7.50)$$

$$L' = L - 10.62 \text{ cm} \quad (7.51)$$

Note, that the formulas (7.27) to (7.37) can be used with all quantities replaced by the corresponding primed quantities in Eq.(7.49) - (7.51). The result is shown in Fig. 7.13. The transformation from  $L$  to  $L'$  transforms the stability ranges according to Fig. 7.14. The confocal parameter of the laser mode is approximately equal to the stability range.

### Astigmatism Compensation

So far, we have considered the curved mirrors under normal incidence. In a real cavity this is not the case and one has to analyze the cavity performance for the tangential and sagittal beam separately. The gain medium, usually a thin plate with a refractive index  $n$  and a thickness  $t$ , generates astigmatism. Astigmatism means that the beam foci for sagittal and tangential plane are not at the same position. Also, the stability regions of the cavity are different for the different planes and the output beam is elliptical. This is so, because a beam entering a plate under an angle refracts differently in both planes, as described by different ABCD matrices for tangential and sagittal plane, see Table 7.1. Fortunately, one can balance the astigmatism of the beam due to

### 7.1. KERR-LENS MOI

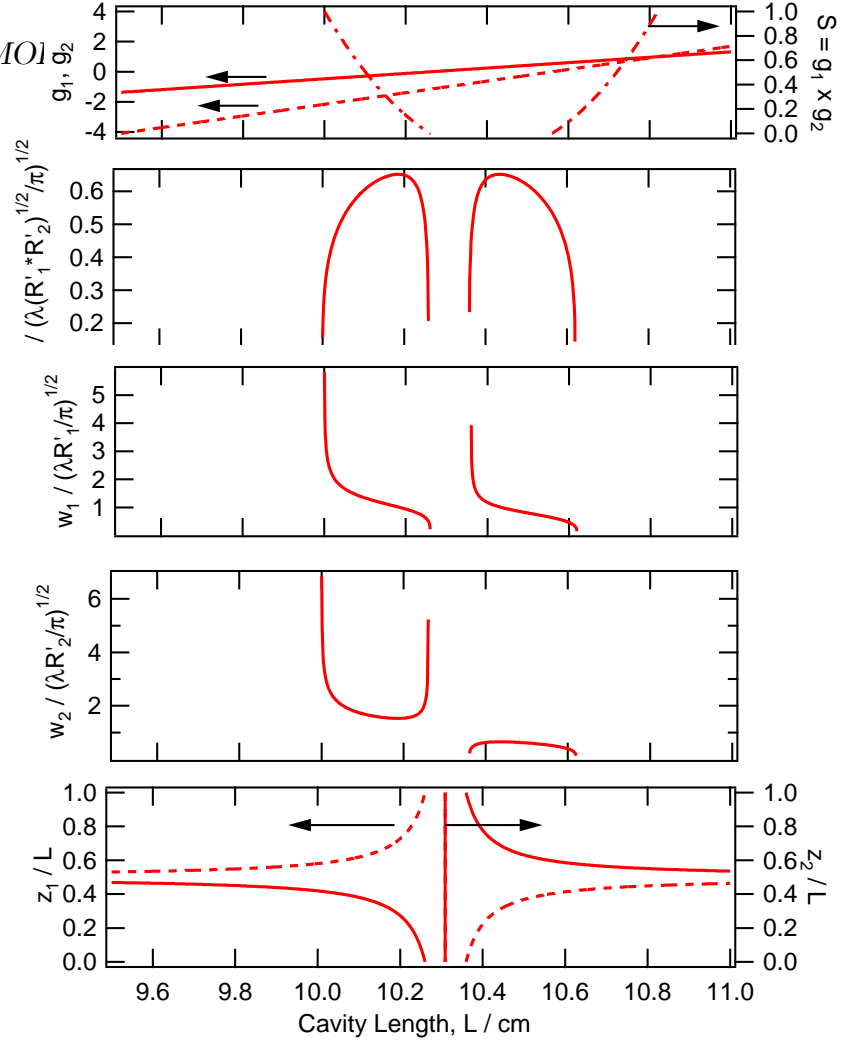


Figure 7.13: From top to bottom: Cavity parameters,  $g_1, g_2, S, w_0, w_1, w_2, z_1$  and  $z_2$  for the four-mirror resonator with  $R_1 = R_2 = 10$  cm,  $L_1 = 100$  cm and  $L_2 = 75$  cm.

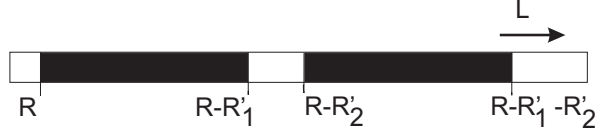


Figure 7.14: Transformed stability range for the four mirror resonator with  $R = (R_1 + R_2)/2$ .

the plate by the astigmatism introduced by the curved mirrors at a specific incidence angle  $\theta$  on the mirrors [12]. The focal length of the curved mirrors under an angle are given by

$$\begin{aligned} f_s &= f / \cos \theta \\ f_t &= f \cdot \cos \theta \end{aligned} \quad (7.52)$$

The propagation distance in a plate with thickness  $t$  under Brewster's angle is given by  $t\sqrt{n^2 + 1}/n$ . Thus, the equivalent traversing distances in the sagittal and the tangential planes are (Table 7.1),

$$\begin{aligned} d_s &= t\sqrt{n^2 + 1}/n^2 \\ d_f &= t\sqrt{n^2 + 1}/n^4 \end{aligned} \quad (7.53)$$

The different distances have to compensate for the different focal lengths in the sagittal and tangential planes. Assuming two identical mirrors  $R = R_1 = R_2$ , leads to the condition

$$d_s - 2f_s = d_t - 2f_t. \quad (7.54)$$

With  $f = R/2$  we find

$$R \sin \theta \tan \theta = Nt, \text{ where } N = \sqrt{n^2 + 1} \frac{n^2 - 1}{n^4} \quad (7.55)$$

Note, that  $t$  is the thickness of the plate as opposed to the path length of the beam in the plate. The equation gives a quadratic equation for  $\cos \theta$

$$\cos^2 \theta + \frac{Nt}{R} \cos \theta - 1 = 0 \quad (7.56)$$

$$\cos \theta_{1/2} = -\frac{Nt}{2R} \pm \sqrt{1 + \left(\frac{Nt}{2R}\right)^2} \quad (7.57)$$

Since the angle is positive, the only solution is

$$\theta = \arccos \left[ \sqrt{1 + \left(\frac{Nt}{2R}\right)^2} - \frac{Nt}{2R} \right]. \quad (7.58)$$

This concludes the design and analysis of the linear resonator.

### 7.1.4 The Kerr Lensing Effects

At high intensities, the refractive index in the gain medium becomes intensity dependent

$$n = n_0 + n_2 I. \quad (7.59)$$

The Gaussian intensity profile of the beam creates an intensity dependent index profile

$$I(r) = \frac{2P}{\pi w^2} \exp \left[ -2\left(\frac{r}{w}\right)^2 \right]. \quad (7.60)$$

In the center of the beam the index can be approximated by a parabola

$$n(r) = n'_0 \left( 1 - \frac{1}{2} \gamma^2 r^2 \right), \text{ where} \quad (7.61)$$

$$n'_0 = n_0 + n_2 \frac{2P}{\pi w^2}, \quad \gamma = \frac{1}{w^2} \sqrt{\frac{8n_2 P}{n'_0 \pi}}. \quad (7.62)$$

A thin slice of a parabolic index medium is equivalent to a thin lens. If the parabolic index medium has a thickness  $t$ , then the ABCD matrix describing the ray propagation through the medium at normal incidence is [16]

$$M_K = \begin{pmatrix} \cos \gamma t & \frac{1}{n'_0 \gamma} \sin \gamma t \\ -n'_0 \gamma \sin \gamma t & \cos \gamma t \end{pmatrix}. \quad (7.63)$$

Note that, for small  $t$ , we recover the thin lens formula ( $t \rightarrow 0$ , but  $n'_0 \gamma^2 t = 1/f = \text{const.}$ ). If the Kerr medium is placed under Brewster's angle, we again have to differentiate between the sagittal and tangential planes. For the

sagittal plane, the beam size entering the medium remains the same, but for the tangential plane, it opens up by a factor  $n'_0$

$$\begin{aligned} w_s &= w \\ w_t &= w \cdot n'_0 \end{aligned} \quad (7.64)$$

The spotsize propotional to  $w^2$  has to be replaced by  $w^2 = w_s w_t$ . Therefore, under Brewster angle incidence, the two planes start to interact during propagation as the gamma parameters are coupled together by

$$\gamma_s = \frac{1}{w_s w_t} \sqrt{\frac{8n_2 P}{n'_0 \pi}} \quad (7.65)$$

$$\gamma_t = \frac{1}{w_s w_t} \sqrt{\frac{8n_2 P}{n'_0 \pi}} \quad (7.66)$$

Without proof (see [12]), we obtain the matrices listed in Table 7.2. For low

Optical Element	ABCD-Matrix
Kerr Medium Normal Incidence	$M_K = \begin{pmatrix} \cos \gamma t & \frac{1}{n'_0 \gamma} \sin \gamma t \\ -n'_0 \gamma \sin \gamma t & \cos \gamma t \end{pmatrix}$
Kerr Medium Sagittal Plane	$M_{Ks} = \begin{pmatrix} \cos \gamma_s t & \frac{1}{n'_0 \gamma_s} \sin \gamma_s t \\ -n'_0 \gamma_s \sin \gamma_s t & \cos \gamma_s t \end{pmatrix}$
Kerr Medium Tangential Plane	$M_{Kt} = \begin{pmatrix} \cos \gamma_t t & \frac{1}{n'^3_0 \gamma_t} \sin \gamma_t t \\ -n'^3_0 \gamma_t \sin \gamma_t t & \cos \gamma_t t \end{pmatrix}$

Table 7.2: ABCD matrices for Kerr media, modelled with a parabolic index profile  $n(r) = n'_0 \left(1 - \frac{1}{2} \gamma^2 r^2\right)$ .

peak power  $P$ , the Kerr lensing effect can be neglected and the matrices in Table 7.2 converge towards those for linear propagation. When the laser is mode-locked, the peak power  $P$  rises by many orders of magnitude, roughly the ratio of cavity round-trip time to the final pulse width, assuming a constant pulse energy. For a 100 MHz, 10 fs laser, this is a factor of  $10^6$ . With the help of the matrix formulation of the Kerr effect, one can iteratively find the steady state beam waists in the laser. Starting with the values for the linear cavity, one can obtain a new resonator mode, which gives improved

values for the beam waists by calculating a new cavity round-trip propagation matrix based on a given peak power  $P$ . This scheme can be iterated until there is only a negligible change from iteration to iteration. Using such a simulation, one can find the change in beam waist at a certain position in the resonator between cw-operation and mode-locked operation, which can be expressed in terms of the delta parameter

$$\delta_{s,t} = \frac{1}{p} \frac{w_{s,t}(P, z) - w_{s,t}(P = 0, z)}{w_{s,t}(P = 0, z)} \quad (7.67)$$

where  $p$  is the ratio between the peak power and the critical power for self-focusing

$$p = P/P_{crit}, \text{ with } P_{crit} = \lambda_L^2 / (2\pi n_2 n_0^2). \quad (7.68)$$

To gain insight into the sensitivity of a certain cavity configuration for KLM, it is interesting to compute the normalized beam size variations  $\delta_{s,t}$  as a function of the most critical cavity parameters. For the four-mirror cavity, the natural parameters to choose are the distance between the crystal and the pump mirror position,  $x$ , and the mirror distance  $L$ , see Figure 7.12. Figure 7.15 shows such a plot for the following cavity parameters  $R_1 = R_2 = 10$  cm,  $L_1 = 104$  cm,  $L_2 = 86$  cm,  $t = 2$  mm,  $n = 1.76$  and  $P = 200$  kW.

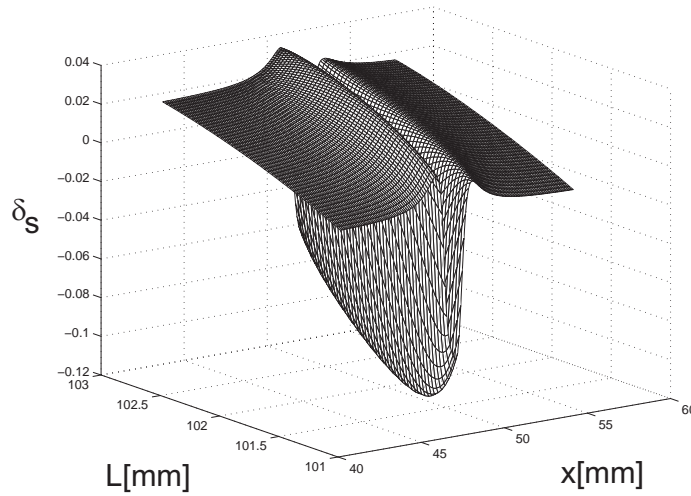


Figure 7.15: Beam narrowing ratio  $\delta_s$ , for cavity parameters  $R_1 = R_2 = 10$  cm,  $L_1 = 104$  cm,  $L_2 = 86$  cm,  $t = 2$  mm,  $n = 1.76$  and  $P = 200$  kW (Courtesy of Onur Kuzucu).

The Kerr lensing effect can be exploited in different ways to achieve mode locking.

### Soft-Aperture KLM

In the case of soft-aperture KLM, the cavity is tuned in such a way that the Kerr lensing effect leads to a shrinkage of the laser mode when mode-locked. The non-saturated gain in a laser depends on the overlap of the pump mode and the laser mode. From the rate equations for the radial photon distribution  $N(r)$  and the inversion  $N_P(r)$  of a laser, which are proportional to the intensities of the pump beam and the laser beam, we obtain a gain, that is proportional to the product of  $N(r)$  and  $N_P(r)$ . If we assume that the focus of the laser mode and the pump mode are at the same position and neglect the variation of both beams as a function of distance, we obtain

$$\begin{aligned} g &\sim \int_0^\infty N(r) * N_P(r) r dr \\ &\sim \int_0^\infty \frac{2P_P}{\pi w_P^2} \exp\left[-\frac{2r^2}{w_P^2}\right] \frac{2}{\pi w_L^2} \exp\left[-\frac{2r^2}{w_L^2}\right] r dr \end{aligned}$$

With the beam cross sections of the pump and the laser beam in the gain medium,  $A_P = \pi w_P^2$  and  $A_L = \pi w_L^2$ , we obtain

$$g \sim \frac{1}{A_P + A_L}.$$

If the pump beam is much more strongly focused in the gain medium than the laser beam, a shrinkage of the laser mode cross section in the gain medium leads to an increased gain. When the laser operates in steady state, the change in saturated gain would have to be used for the investigation. However, the general argument carries through even for this case. Figure 7.16 shows the variation of the laser mode size in and close to the crystal in a soft-aperture KLM laser due to self-focusing.

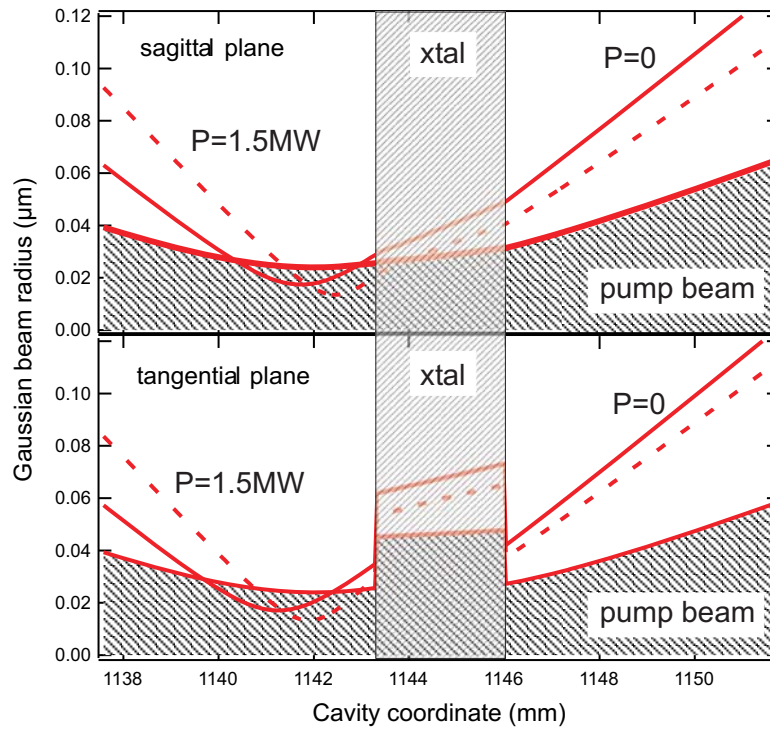


Figure 7.16: Variation of laser mode size in and close to the crystal in a soft aperture KLM laser due to self-focussing.

### Hard-Aperture KLM

In a hard-aperture KLM-Laser, one of the resonator arms contains (usually close to the end mirrors) an aperture such that it cuts the beam slightly. When Kerr lensing occurs and leads to a shrinkage of the beam at this position, the losses of the beam are reduced. Note, that depending on whether the aperture is positioned in the long or short arm of the resonator, the operating point of the cavity at which Kerr lensing favours or opposes mode-locking may be quite different (see Figure 7.13).



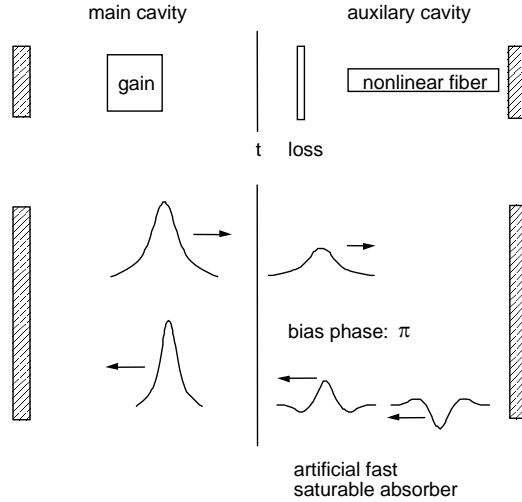


Figure 7.17: Principle mechanism of APM.

## 7.2 Additive Pulse Mode Locking

Like Kerr-Lens Mode Locking also Additive Pulse Mode Locking (APM) is an artificial saturable absorber effect [17][18][19][20][21][22]. Figure 7.17 shows the general principle at work. A small fraction of the light emitted from the main laser cavity is injected externally into a nonlinear fiber. In the fiber strong SPM occurs and introduces a significant phase shift between the peak and the wings of the pulse. In the case shown the phase shift is  $\pi$

A part of the modified and heavily distorted pulse is reinjected into the cavity in an interferometrically stable way, such that the injected pulse interferes constructively with the next cavity pulse in the center and destructively in the wings. This superposition leads to a shorter intracavity pulse and the pulse shaping generated by this process is identical to the one obtained from a fast saturable absorber. Again, an artificial saturable absorber action is generated.

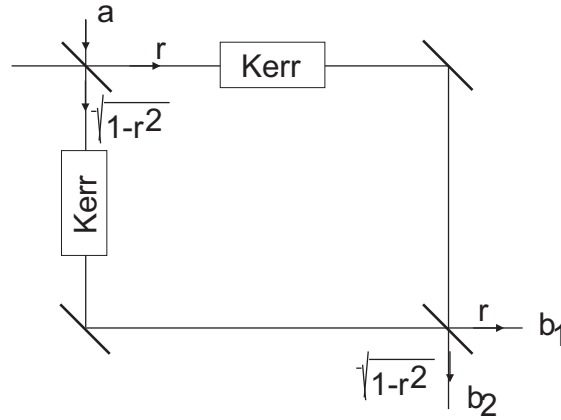


Figure 7.18: Schematic of nonlinear Mach-Zehnder interferometer.

Figure 7.18 shows a simple nonlinear interferometer. In practice, such an interferometer can be realized in a self-stabilized way by the use of both polarizations in an isotropic Kerr medium with polarizer and analyzer as shown in Figure 7.19.

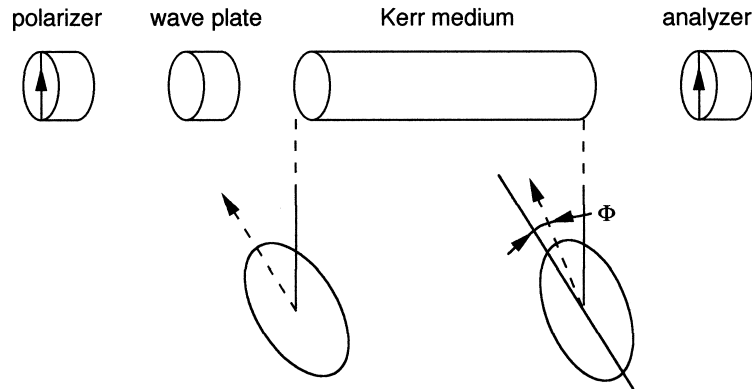


Figure 7.19: Nonlinear Mach-Zehnder interferometer using nonlinear polarization rotation in a fiber [25].

The Kerr effect rotates the polarization ellipse and thus transforms phase modulation into amplitude modulation. The operation is in one-to-one correspondence with that of the nonlinear Mach-Zehnder interferometer of Fig.

7.18. The system of Figure 7.18 can be analyzed rather simply and thus it is worthwhile to look at the derivation and the implicit assumptions. The couplers are described by the scattering matrices

$$S = \begin{bmatrix} r & j\sqrt{1-r^2} \\ j\sqrt{1-r^2} & r \end{bmatrix}. \quad (7.69)$$

The outputs of the interferometer are then

$$b_1 = [r^2 e^{-j\phi_1} - (1-r^2)e^{-j\phi_2}] a, \quad (7.70)$$

$$b_2 = j2r\sqrt{1-r^2} \exp\left[-j\frac{\phi_1 + \phi_2}{2}\right] \cos\left[\frac{\phi_2 - \phi_1}{2}\right] a, \quad (7.71)$$

$\phi_1$  and  $\phi_2$  are the phase shifts in the two arms composed of both linear "bias" contributions  $\phi_{bi}$  and the Kerr phase shifts  $\phi_{Ki}$

$$\phi_i = \phi_{bi} + \phi_{Ki}, \quad (i = 1, 2), \quad (7.72)$$

$$\phi_{Ki} = \kappa_i |a|^2, \quad (i = 1, 2). \quad (7.73)$$

The power in output port two is related to the linear and nonlinear losses

$$\begin{aligned} |b_2|^2 &= 2r^2 (1-r^2) (1 + \cos[\phi_2 - \phi_1]) |a|^2 \\ &= 2r^2 (1-r^2) \{ (1 + \cos[\phi_{b2} - \phi_{b1}]) - \\ &\quad - \sin[\phi_{b2} - \phi_{b1}] (\phi_{K2} - \phi_{K1}) \} |a|^2, \end{aligned} \quad (7.74)$$

where we linearized the cosine and assumed that the Kerr phase shifts are small. Depending on the bias phase  $\phi_b = \phi_{b2} - \phi_{b1}$ , the amplitude loss is

$$l = r^2 (1-r^2) (1 + \cos \phi_b) |a|^2, \quad (7.75)$$

and the  $\gamma$ -parameter of the equivalent fast saturable absorber is

$$\gamma = (\kappa_2 - \kappa_1) r^2 (1-r^2) \sin \phi_b. \quad (7.76)$$

If the interferometer forms part of a resonant system, the frequency of the system is affected by the phase shift of the interferometer and in turn affects the phase.

When the resonant frequencies of the linear system ( $\gamma = \delta = 0$ ) without the interferometer should remain the resonant frequencies with the interferometer, the net phase shift of the interferometer has to be chosen to be zero. Since a small loss has been assumed and hence  $r^2 \gg 1-r^2$

$$\text{Im} [r^2 e^{-j\phi_{b1}} - (1-r^2) e^{-j\phi_{b2}}] = \text{Im} [r^2(1-j\phi_{b1}) - (1-r^2) e^{-j\phi_{b2}}] = 0 \quad (7.77)$$

or

$$\phi_{b1} = \frac{(1 - r^2)}{r^2} \sin \phi_{b2}. \quad (7.78)$$

and  $\cos \phi_{b1} = 1$ . With this adjustment and  $\phi = \phi_{b2}$ , the response of the interferometer becomes

$$\begin{aligned} b_1 \approx & a + \Delta a = a - (1 - r^2) (1 + \cos \phi) a \\ & + (1 - r^2) (\phi_{K2} - \phi_{K1}) \sin \phi a \\ & - j r^2 \phi_{K1} + j (1 - r^2) \phi_{K2} \cos \phi a. \end{aligned} \quad (7.79)$$

This gives for the parameters of the master equation  $l$ ,  $\gamma$  and  $\delta$

$$l = (1 - r^2) (1 + \cos \phi), \quad (7.80)$$

$$\gamma = (\kappa_2 - \kappa_1) (1 - r^2) \sin \phi, \quad (7.81)$$

$$\delta = \kappa_1 r^2 - \kappa_2 (1 - r^2) \cos \phi. \quad (7.82)$$

Due to the special choice of the bias phase there is no contribution of the nonlinear interferometer to the linear phase. This agrees with expressions (7.75) and (7.76). The Kerr coefficients are

$$\kappa_1 = r^2 \left( \frac{2\pi}{\lambda} \right) \frac{n_2}{A_{eff}} L_{Kerr}, \quad (7.83)$$

$$\kappa_2 = (1 - r^2) \left( \frac{2\pi}{\lambda} \right) \frac{n_2}{A_{eff}} L_{Kerr}. \quad (7.84)$$

Here,  $\lambda$  is the free space wavelength of the optical field,  $A_{eff}$  is the effective area of the mode,  $n_2$  the intensity dependent refractive index, and  $L_{Kerr}$  is the length of the Kerr medium. Figure 7.20 is the saturable absorber coefficient  $\gamma$  normalized to the loss and Kerr effect (note that  $\gamma$  goes to zero when the loss goes to zero) as a function of  $r^2$ .

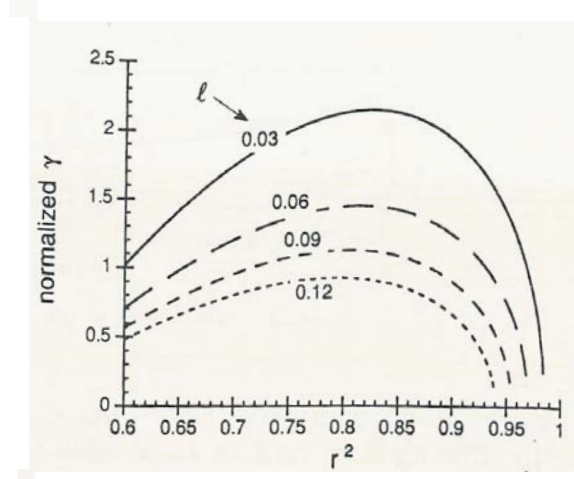


Figure 7.20: Normalized saturable absorber coefficient  $\gamma / \left[ \left( \frac{2\pi}{\lambda} \right) \frac{n_2}{A_{eff}} L_{Kerr} l \right]$  as a function of  $r^2$  with loss  $l$  as parameter [25].

Large saturable absorber coefficients can be achieved at moderate loss values.

# Bibliography

- [1] D. E. Spence, P. N. Kean, W. Sibbett, "60-fsec pulse generation from a self-mode-locked Ti:Sapphire laser", *Opt. Lett.* **16**, pp. 42 – 44 (1991)
- [2] U. Keller, G. W 'tHooft, W. H. Knox, J. E. Cunningham, "Femtosecond Pulses from a Continuously Self-Starting Passively Mode-Locked Ti:Sapphire Laser," *Opt. Lett.* **16**, pp.1022 – 1024 (1991).
- [3] D. K. Negus, L. Spinelli, N. Goldblatt, G. Feugnet, "Sub-100 femtosecond pulse generation by Kerr lens modelocking in Ti:Sapphire," in *Advanced Solid-State Lasers*, G. Dube, L. Chase, Eds. (Optical Society of America, Washington, D.C., 1991), **10**, pp.120 – 124.
- [4] F. Salin, J. Squier and M. Piche, "Mode locking of  $\text{Ti:Al}_2\text{O}_3$  lasers and self-focusing: a Gaussian approximation," *Opt. Lett.* **16**, pp. 1674 – 1676 (1991).
- [5] M. Piche, F. Salin, "Self-mode locking of solid-state lasers without apertures", *Opt. Lett.* **18**, pp. 1041 – 1043 (1993).
- [6] G. Cerullo, S. De Silvestri, V. Magni, L. Pallaro, "Resonators for Kerr-lens mode-locked femtosecond Ti:sapphire lasers", *Opt. Lett.* **19**, pp. 807 – 809 (1994).
- [7] G. Cerullo, S. De Silvestri, V. Magni, "Self-starting Kerr Lens Mode-Locking of a Ti:Sapphire Laser", *Opt. Lett.* **19**, pp. 1040 – 1042 (1994).
- [8] L. Dahlström, "Passive modelocking and Q-switching of high power lasers by means of the optical Kerr effect," *Opt. Comm.* **5**, pp. 157 – 162 (1972).

- [9] E. G. Lariontsev and V. N. Serkin, "Possibility of using self-focusing for increasing contrast and narrowing of ultrashort light pulses," *Sov. J. Quant. Electron.* **5**, pp. 769 – 800 (1975).
- [10] K. Sala, M. C. Richardson, N. R. Isenor, "Passive modelocking of Lasers with the optical Kerr effect modulator," *IEEE J. Quant. Electron.* **QE-13**, pp. 915 – 924 (1977).
- [11] H. Kogelnik and T. Li, "Laser Beams and Resonators," *Appl. Opt.* **5**, pp. 1550 – 1566 (1966).
- [12] H. Kogelnik, E. P. Ippen, A. Dienes and C. V. Shank, "Astigmatically Compensated Cavities for CW Dye Lasers," *IEEE J. Quantum Electron.* **QE-8**, pp. 373 – 379 (1972).
- [13] O. Svelto, "Principles of Lasers," 3rd Edition, Plenum Press, New York and London, (1989).
- [14] H. A. Haus, "Fields and Waves in Optoelectronics", Prentice Hall 1984.
- [15] F. K. Kneubühl and M. W. Sigrist, "Laser," 3rd Edition, Teubner Verlag, Stuttgart (1991).
- [16] A. E. Siegman, "Lasers," University Science Books, Mill Valley, California (1986).
- [17] K. J. Blow and D. Wood, "Modelocked lasers with nonlinear external cavities," *J. Opt. Soc. Am. B* **5**, pp. 629 – 632 (1988).
- [18] K. J. Blow and B. P. Nelson, "Improved mode locking of an F-center laser with a nonlinear nonsoliton external cavity," *Opt. Lett.* **13**, pp. 1026 – 1028 (1988).
- [19] P. N. Kean, X. Zhu, D. W. Crust, R. S. Grant, N. Langford and W. Sibbett, "Enhanced mode locking of color-center lasers," *Opt. Lett.* **14**, pp. 39 – 41 (1989).
- [20] J. Mark, L. Y. Liu, K. L. Hall, H. A. Haus and E. P. Ippen, "Femtosecond pulse generation in a laser with a nonlinear external resonator," *Opt. Lett.* **14**, pp. 48 – 50 (1989).

- [21] E. P. Ippen, H. A. Haus and L. Y. Liu, "Additive pulse mode locking," *J. Opt. Soc. Am. B* **6**, pp. 1736 – 1745 (1989).
- [22] J. Goodberlet, J. Jacobson and J. G. Fujimoto, P. A. Schultz and T. Y. Fan, "Self-starting additive-pulse mode-locked diode-pumped Nd:YAG laser", *Opt. Lett.* **15**, pp. 504 –506 (1990).
- [23] F. X. Kärtner, L. R. Brovelli, D. Kopf, M. Kamp, I. Calasso and U. Keller: "Control of Solid-State Laser Dynamics by Semiconductor Devices, *Optical Engineering*, **34**, pp. 2024 – 2036, (1995).
- [24] K. Tamura, "Additive-pulse limiting", *Opt. Lett.* **19**, pp. 31 – 33 (1994).
- [25] H. A. Haus, J. G. Fujimoto and E. P. Ippen, "Analytic Theory of Additive Pulse and Kerr Lens Mode Locking," *IEEE J. Quantum Electron.* **28**, pp. 2086 – 2095 (1992).
- [26] H. A. Haus, J. G. Fujimoto and E. P. Ippen, "Structures of Additive Pulse Mode Locking," *J. Opt. Soc. Am.* **8**, pp. 2068 – 2076 (1991).





## Chapter 8

# Semiconductor Saturable Absorbers

Sofar we only considered artificial saturable absorbers, but there is of course the possibility to use real absorbers for modelocking. A prominent candidate for a saturable absorber is semiconductor material, which was pioneered by Islam, Knox and Keller [1][2][3]. The great advantage of using semiconductor materials is that the wavelength range over which these absorbers operate can be chosen by material composition and bandstructure engineering, if semiconductor heterostructures are used (see Figure 8.1). Even though, the basic physics of carrier dynamics in these structures is to a large extent well understood [4], the actual development of semiconductor saturable absorbers for mode locking is still very much ongoing.

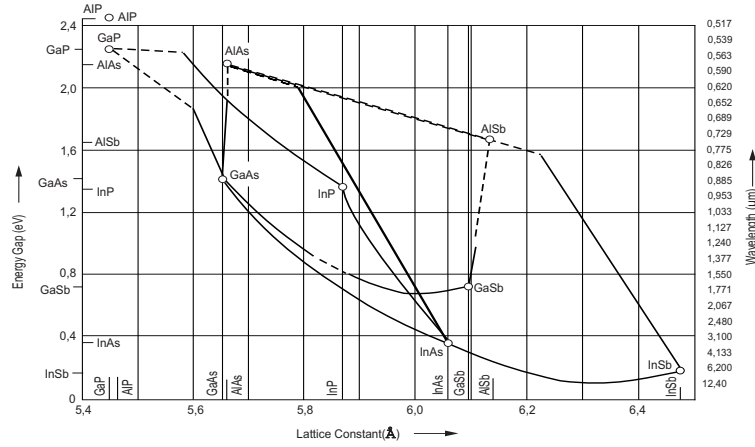


Figure 8.1: Energy Gap, corresponding wavelength and lattice constant for various compound semiconductors. The dashed lines indicate indirect transitions.

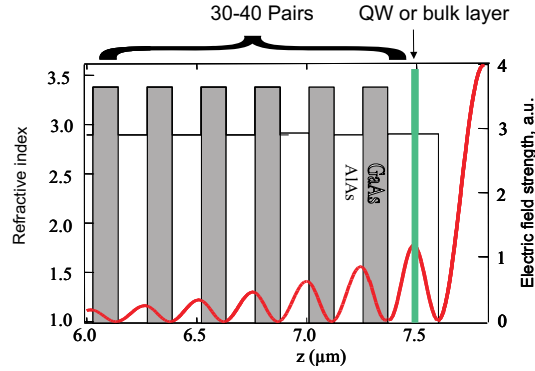


Figure 8.2: Typical semiconductor saturable absorber structure. A semiconductor heterostructure (here AlAs/GaAs) is grown on a GaAs-Wafer (20-40 pairs). The layer thicknesses are chosen to be quarter wave at the center wavelength at which the laser operates. This structure acts as a quarter-wave Bragg mirror. On top of the Bragg mirror, a half-wave thick layer of the low index material (here AlAs) is grown, which has a field maximum in its center. At the field maximum, either a bulk layer of GaAlAs or a single- or multiple Quantum Well (MQW) structure is embedded, which acts as a saturable absorber for the operating wavelength of the laser.

A typical semiconductor saturable absorber structure is shown in Figure 8.2. A semiconductor heterostructure (here AlAs/GaAs) is grown on a GaAs-Wafer (20-40 pairs). The layer thicknesses are chosen to be quarter wave at the center wavelength at which the laser operates. These structures act as quarter-wave Bragg mirror. On top of the Bragg mirror, a half-wave thick layer of the low index material (here AlAs) is grown, which has a field-maximum in its center. At the field maximum, either a bulk layer of a compound semiconductor or a single-or multiple Quantum Well (MQW) structure is embedded, which acts as a saturable absorber for the operating wavelength of the laser. The absorber mirror serves as one of the endmirrors in the laser (see Figure 8.3).

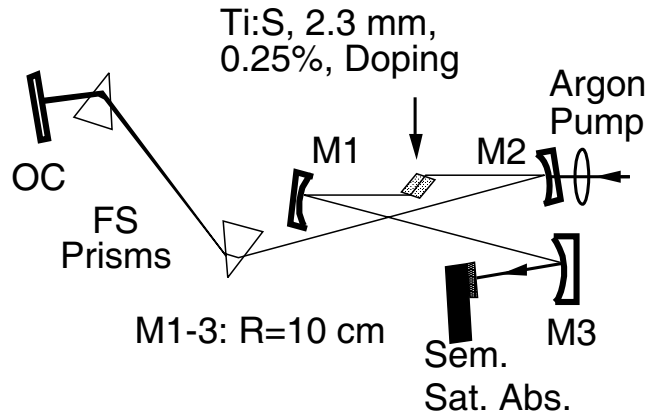


Figure 8.3: The semiconductor saturable absorber, mounted on a heat sink, is used as one of the cavity end mirrors. A curved mirror determines the spot-size of the laser beam on the saturable absorber and, therefore, scales the energy fluence on the absorber at a given intracavity energy.

## 8.1 Carrier Dynamics and Saturation Properties

There is a rich ultrafast carrier dynamics in these materials, which can be favorably exploited for saturable absorber design. The carrier dynamics in bulk semiconductors occurs on three major time scales (see Figure 8.4 [5]). When electron-hole pairs are generated, this excitation can be considered

as an equivalent two-level system if the interaction between the carriers is neglected, which is a very rough assumption.

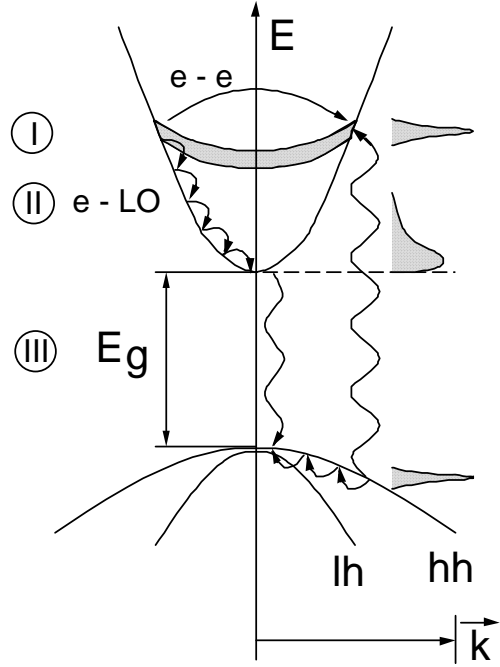


Figure 8.4: Carrier dynamics in a bulk semiconductor material. Three time scales can be distinguished. I. Coherent carrier dynamics, which at room temperature may last between 10-50 fs depending on excitation density. II. Thermalization between the carriers due to carrier-carrier scattering and cooling to the lattice temperature by LO-Phonon emission. III. Carrier-trapping or recombination [5].

There is a coherent regime (I) with a duration of 10-50 fs depending on conditions and material. Then in phase (II), carrier-carrier scattering sets in and leads to destruction of coherence and thermalization of the electron and hole gas at a high temperature due to the excitation of the carriers high in the conduction or valence band. This usually happens on a 60 - 100 fs time scale. On a 300fs - 1ps time scale, the hot carrier gas interacts with the lattice mainly by emitting LO-phonons (37 meV in GaAs). The carrier gas cools down to lattice temperature. After the thermalization and cooling processes, the carriers are at the bottom of the conduction and valence band,

respectively. The carriers vanish (III) either by getting trapped in impurity states, which can happen on a 100 fs - 100 ps time scale, or recombine over recombination centers or by radiation on a nanosecond time-scale. Carrier-lifetimes in III-VI semiconductors can reach several tens of nanoseconds and in indirect semiconductors like silicon or germanium lifetimes can be in the millisecond range. The carrier lifetime can be engineered over a large range of values from 100 fs - 30ns, depending on the growth conditions and purity of the material. Special low-temperature growth that leads to the formation or trapping and recombination centers as well as ion-bombardment can result in very short lifetimes [9]. Figure 8.5 shows a typical pump probe response of a semiconductor saturable absorber when excited with a 100 fs long pulse. The typical bi-temporal behavior stems from the fast thermalization (spectral hole-burning)[7] and carrier cooling and the slow trapping and recombination processes.

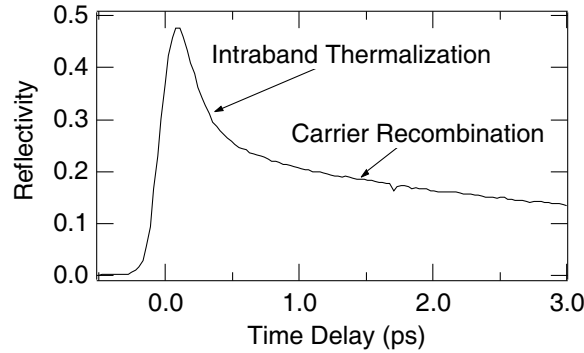


Figure 8.5: Pump probe response of a semiconductor saturable absorber mirror with a multiple-quantum well InGaAs saturable absorber grown at low temperature [3].

With the formula for the saturation intensity of a two-level system Eq. (4.70), we can estimate a typical value for the saturation fluence  $F_A$  (saturation energy density) of a semiconductor absorber for interband transitions. The saturation fluence  $F_A$ , also related to the absorption cross-section  $\sigma_A$ , is

then given by

$$F_A = \frac{\hbar f}{\sigma_A} = I_A \tau_A = \frac{\hbar^2}{2T_2 Z_F |\vec{M}|^2} \quad (8.1)$$

$$= \frac{\hbar^2 n_0}{2T_2 Z_{F0} |\vec{M}|^2} \quad (8.2)$$

The value for the dipole moment for interband transitions in III-V semiconductors is about  $d = 0.5$  nm with little variation for the different materials. Together with a dephasing time on the order of  $T_2 = 20$  fs and a linear refractive index  $n_0 = 3$ , we obtain

$$F_A = \frac{\hbar^2 n_0}{2T_2 Z_{F0} |\vec{M}|^2} = 35 \frac{\mu J}{cm^2} \quad (8.3)$$

Figure 8.6 shows the saturation fluence measurement and pump probe trace with 10 fs excitation pulses at 800 nm on a broadband GaAs semiconductor saturable absorber based on a metal mirror shown in Figure 8.7 [11]. The pump probe trace shows a 50 fs thermalization time and long time bleaching of the absorption recovering on a 50 ps time scale due to trapping and recombination.

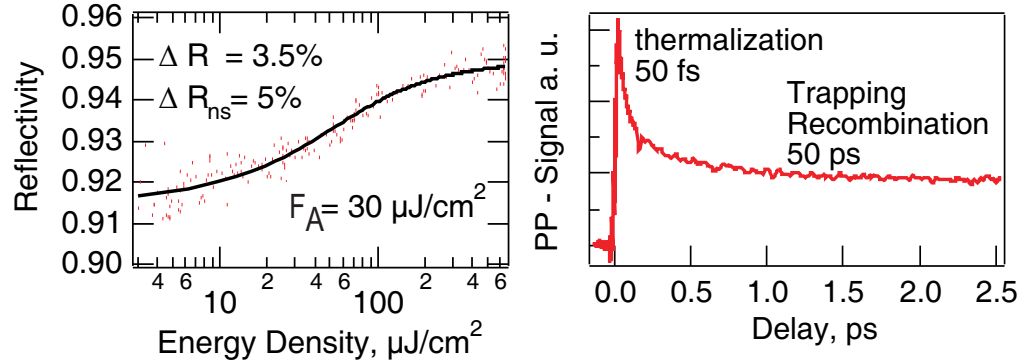


Figure 8.6: Saturation fluence and pump probe measurements with 10 fs pulses on a broadband metal mirror based GaAs saturable absorber. The dots are measured values and the solid line is the fit to a two-level saturation characteristic [11].

A typical value for the fluence at which damage is observed on an absorber is on the order of a few  $\text{mJ}/\text{cm}^2$ . Saturating an absorber by a factor of 10 without damaging it is still possible. The damage threshold is strongly dependent on the growth, design, fabrication and mounting (heat sinking) of the absorber.

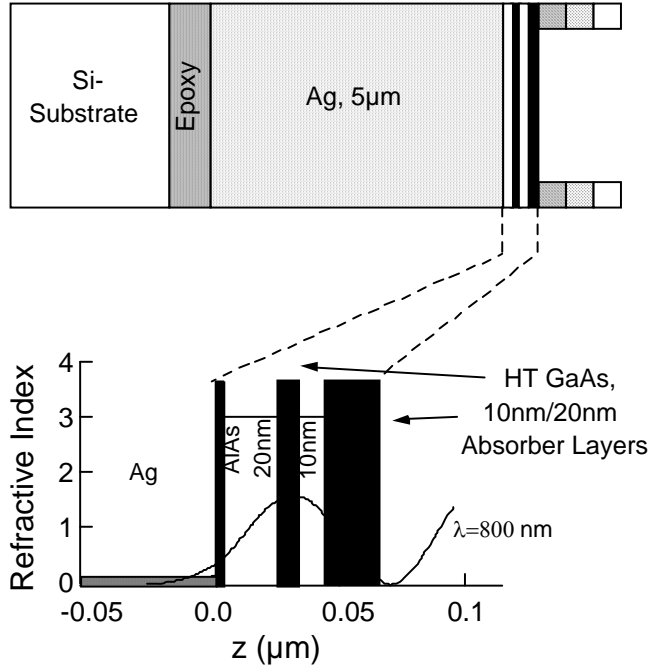


Figure 8.7: GaAs saturable absorber grown on a GaAs wafer and transferred onto a metal mirror by post growth processing [10].

## 8.2 High Fluence Effects

To avoid Q-switched mode-locking caused by a semiconductor saturable absorber, the absorber very often is operated far above the saturation fluence or enters this regime during Q-switched operation. Therefore it is also important to understand the nonlinear optical processes occurring at high excitation levels [13]. Figure 8.8 shows differential pump probe measurements on a semiconductor saturable absorber mirror similar to Figure 8.2 but adapted to the  $1.55 \mu\text{m}$  range for the development of pulsed laser sources for optical



communication. The structure is a GaAs/AlAs-Bragg-mirror with an InP half-wave layer and an embedded InGaAsP quantum well absorber with a band edge at  $1.530 \mu\text{m}$ . The mirror is matched to air with an  $\text{Al}_2\text{O}_3$  single-layer Ar-coating. At low fluence ( $5.6 \mu\text{J}$ ) the bleaching dynamics of the QWs are dominant. At higher fluences, two-photon absorption (TPA) and free carrier absorption (FCA) in the InP half-wave layer develop and eventually dominate [13].

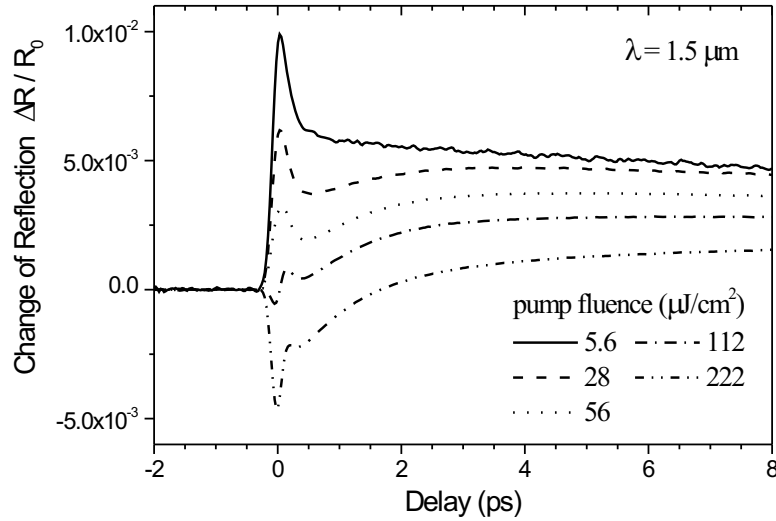


Figure 8.8: Differential reflectivity measurements of a semiconductor saturable absorber mirror (GaAs/AlAs-Bragg-mirror and InP half-wave layer with embedded InGaAsP quantum well absorber for the  $1.55 \mu\text{m}$  range. The mirror is matched to air with an  $\text{Al}_2\text{O}_3$  single-layer ar-coating). At low fluence the bleaching dynamics of the QWs are dominant. At higher fluences, TPA and FCA develop and eventually dominate [13].

The assumption that TPA and FCA are responsible for this behaviour has been verified experimentally. Figure 8.9 shows differential reflectivity measurements under high fluence excitation at  $1.56 \mu\text{m}$  for a saturable absorber mirror structure in which absorption bleaching is negligible (solid curve). The quantum well was placed close to a null of the field. A strong TPA peak is followed by induced FCA with a single  $\sim 5\text{ps}$  decay for FCA. Both of these dynamics do not significantly depend on the wavelength of the excitation, as long as the excitation remains below the band gap. The  $\sim 5\text{ps}$  decay is

attributed to carrier diffusion across the InP half-wave layer [13]. The dashed curve shows the differential absorption of a  $\sim 350 \mu\text{m}$  thick InP substrate in which a standing-wave pattern is not formed and the  $\sim 5\text{ps}$  decay is absent. The inset in Figure 8.9 shows the power dependence of TPA and FCA. As expected, TPA and FCA vary linearly and quadratically, respectively, with pump power. The pump-induced absorption of the probe (TPA) is linearly dependent on the pump power. Since FCA is produced by carriers that are generated by the pump alone via TPA, FCA scales with the square of the pump power.

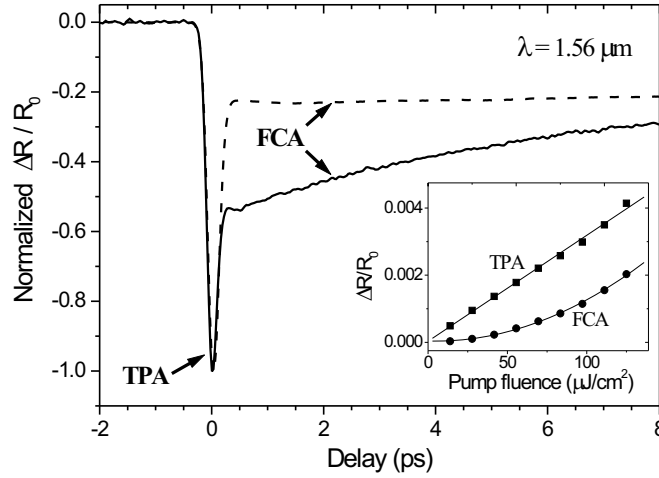


Figure 8.9: Differential reflectivity measurements under high fluence excitation at  $1.56 \mu\text{m}$  for a saturable absorber mirror structure in which absorption bleaching is negligible (solid curve). The  $\sim 5 \text{ ps}$  decay for FCA is attributed to carrier diffusion across the InP half-wave layer. The dashed curve shows the differential absorption of a  $\sim 350 \mu\text{m}$  thick InP substrate in which a standing-wave pattern is not formed. (Inset) Linear and quadratic fluence dependence of the TPA and FCA components, respectively.

These high fluence effects lead to strong modifications of the saturation characteristics of a saturable absorber. The importance of the high fluence effects was first recognized in resonant absorbers (see Figure 8.10). The field inside the absorber is enhanced by adding a top reflector and a proper spacer layer. This leads to an effective lower saturation fluence when viewed with

respect to the intracavity fluence or intensity. Therefore, high fluence effects are already reached at low intracavity intensities (see Figure 8.9).

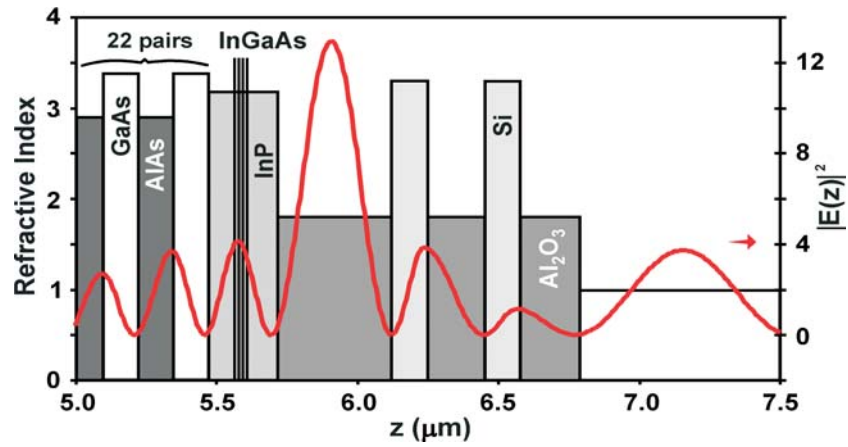


Figure 8.10: A top reflector is added to the semiconductor saturable absorber such that the field in the quantum well is resonantly enhanced by about a factor of 10 in comparison to the non resonant case.

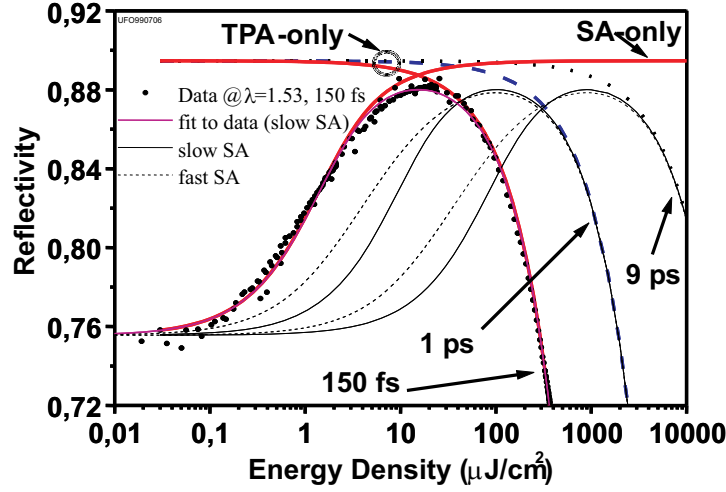


Figure 8.11: Saturation fluence measurement (dots) of the resonant absorber shown in Figure 8.10 with 150 fs pulses at  $1.53 \mu\text{m}$ . Fits are shown using a fast or slow saturable absorber and TPA. Also the scaled saturation characteristics of the absorber are shown when used in a laser with longer pulse durations.

The roll-over of the saturation characteristics has positive and negative consequences for mode locking. First, if the roll-over can be reached with the available intracavity pulse energy, Q-switching can be suppressed. Second if the roll-over occurs too early, the pulses break up into multiple pulses to optimize the net gain for the overall pulse stream.

### 8.3 Break-up into Multiple Pulses

In the treatment of mode locking with fast and slow saturable absorbers we only concentrated on stability against energy fluctuations (Q-switched mode locking) and against break through of cw-radiation or continuum. Another often observed instability is the break-up into multiple pulses. The existence of such a mechanism is obvious if soliton pulse shaping processes are present. If we assume that the pulse is completely shaped by the soliton-like pulse shaping processes, the FWHM pulse width is given by

$$\tau_{FWHM} = 1.76 \frac{4|D_2|}{\delta W}. \quad (8.4)$$

where  $W$  denotes the pulse energy.  $D_2$  the negative dispersion and  $\delta$  the self-phase modulation coefficient. With increasing pulse energy, of course the absorber becomes more strongly saturated, which leads to shorter pulses according to the saturable absorber and the soliton formula. At a certain point, the absorber will saturate and can not provide any further pulse stabilization. However, the Kerr nonlinearity may not yet saturate and, therefore, the soliton formula dictates an ever decreasing pulse width for increasing pulse energy. Such a process continues, until either the continuum breaks through, because the soliton loss becomes larger than the continuum loss, or the pulse breaks up into two pulses. The pulses will have reduced energy per pulse and each one will be longer and experiences a reduced loss due to the finite gain bandwidth. Due to the reduced pulse energy, each of the pulses will suffer increased losses in the absorber, since it is not any longer as strongly saturated as before. However, once the absorber is already over saturated by the single pulse solution, it will also be strongly saturated for the double-pulse solution. The filter loss due to the finite gain bandwidth is heavily reduced for the double-pulse solution. As a result, the pulse will break up into double-pulses. To find the transition point where the break-up into multiple pulses occurs, we write down the round-trip loss due to the gain and filter losses and the saturable absorber according to 6.35

$$l_m = \frac{D_f}{3\tau_m^2} + q_s(W_m), \quad (8.5)$$

where,  $q_s(W_m)$  is the saturation loss experienced by the pulse when it propagates through the saturable absorber. This saturation loss is given by

$$q_s(W) = \frac{1}{W} \int_{-\infty}^{+\infty} q(T, t) |A_s(t)|^2 dt. \quad (8.6)$$

This expression can be easily evaluated for the case of a sech-shaped steady state pulse in the fast saturable absorber model with

$$q_{fast}(t) = \frac{q_0}{1 + \frac{|A(t)|^2}{P_A}}, \quad \text{where} \quad P_A = \frac{E_A}{\tau_A}. \quad (8.7)$$

and the slow saturable absorber model, where the relaxation term can be neglected because of  $\tau_A \gg \tau$ .

$$q_{slow}(t) = q_0 \exp \left[ -\frac{1}{E_A} \int_{-\infty}^t |A_s(t')|^2 dt' \right]. \quad (8.8)$$

For the slow absorber 8.8 the absorber losses (8.6) can be evaluated independent of pulse shape to be

$$q_{s,slow}(W) = q_0 \frac{1 - \exp\left[-\frac{W}{E_A}\right]}{\frac{W}{E_A}}. \quad (8.9)$$

Thus for a slow absorber the losses depend only on pulse energy. In contrast, for a fast absorber, the pulse shape must be taken into account and, for a sech-shaped pulse, one obtains [14]

$$q_{s,fast}(W) = q_0 \sqrt{\frac{1}{\alpha(1+\alpha)}} \tanh^{-1} \left[ \sqrt{\frac{\alpha}{1+\alpha}} \right], \text{ with } \alpha = \frac{W}{2P_A\tau}, \quad (8.10)$$

and the pulse energy of one pulse of the multiple pulse solution. The energy is determined from the total gain loss balance

$$\frac{g_0}{1 + \frac{mW_m}{P_L T_R}} = l + l_m. \quad (8.11)$$

Most often, the saturable absorber losses are much smaller than the losses due to the output coupler. In that case the total losses are fixed independent of the absorber saturation and the filter losses. Then the average power does not depend on the number of pulses in the cavity. If this is the case, one pulse of the double pulse solution has about half of the energy of the single pulse solution, and, therefore, the width of the double pulse is twice as large as that of the single pulse according to (8.4). Then the filter and absorber losses for the single and double pulse solution are given by

$$l_1 = \frac{D_f}{3\tau_1^2} + q_s(W_1), \quad (8.12)$$

$$l_2 = \frac{D_f}{12\tau_1^2} + q_s\left(\frac{W_1}{2}\right). \quad (8.13)$$

The single pulse solution is stable against break-up into double pulses as long as

$$l_1 \leq l_2 \quad (8.14)$$

is fulfilled. This is the case, if the difference in the filter losses between the single and double pulse solution is smaller than the difference in the saturable absorber losses

$$\frac{D_f}{4\tau_1^2} < \Delta q_s(W) = q_s\left(\frac{W}{2}\right) - q_s(W). \quad (8.15)$$

Figure 8.12 shows the difference in the saturable absorption for a single pulse and a double pulse solution as a function of the ratio between the single pulse peak power and saturation power for a fast absorber and as a function of the ratio between the single pulse energy and saturation energy for a slow absorber. Thus, for both cases the optimum saturation ratio, at which the largest discrimination between single and double pulses occurs and, therefore, the shortest pulse before break-up into multiple pulses occurs, is about 3. Note, that to arrive at this absolute number, we assumed that the amount of saturable absorption is negligible in comparison with the other intracavity losses, so that the saturated gain level and the gain and filter dispersion are fixed.

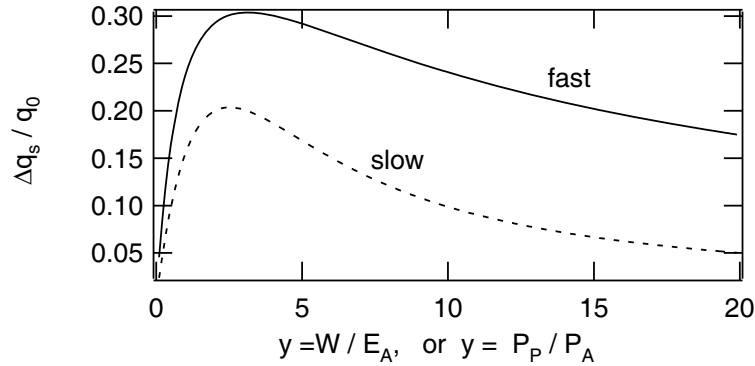


Figure 8.12: Difference in loss experienced by a sech-shaped pulse in a slow (- -) and a fast (—) saturable absorber for a given pulse energy or peak power, respectively.

At this optimum operation point, the discrimination against multiple break-up of a fast absorber is about 50% larger than the value of the slow absorber. Since the minimum pulsewidth scales with the square root of  $\Delta q_s(W)$ , see Eq. (8.15), the minimum pulsewidth of the slow absorber is only about 22% longer than with an equally strong fast saturable absorber. Figure 8.12 also predicts that a laser modelocked by a fast saturable absorber is much more stable against multiple pulse break-up than a slow saturable absorber if it is oversaturated. This is due to the fact that a fast saturable absorber saturates with the peak power of the pulse in comparison with a slow saturable absorber, which saturates with the pulse energy. When the pulse breaks up into a pulse twice as long with half energy in each, the peak power of the

individual pulses changes by a factor of four. Therefore, the discrimination between long and short pulses is larger in the case of a fast saturable absorber, especially for strong saturation. Note that Fig. 8.12 is based on the simple saturation formulas for fast and slow saturable absorbers Eqs. (8.9) and (8.10). We compare these predictions with numerical simulations and experimental observations made with a Nd:glass laser [15][16].

The Nd:glass laser described in ref. [15] was modelocked by a saturable absorber which showed a fast recovery time of  $\tau_A = 200$  fs, a modulation depth of  $q_0 = 0.005$  and a saturation energy of  $E_A = 17$  nJ. The other laser parameters can be found in [16]. Without the solitonlike pulse formation (GDD and SPM is switched off), the laser is predicted to produce about 200 fs short pulses with a single pulse per round-trip, very similar to what was discussed in the fast saturable absorber mode locking in Chapter 6. The dynamics becomes very much different if the negative GDD and positive SPM are included in the simulation, (see Figure 8.13)

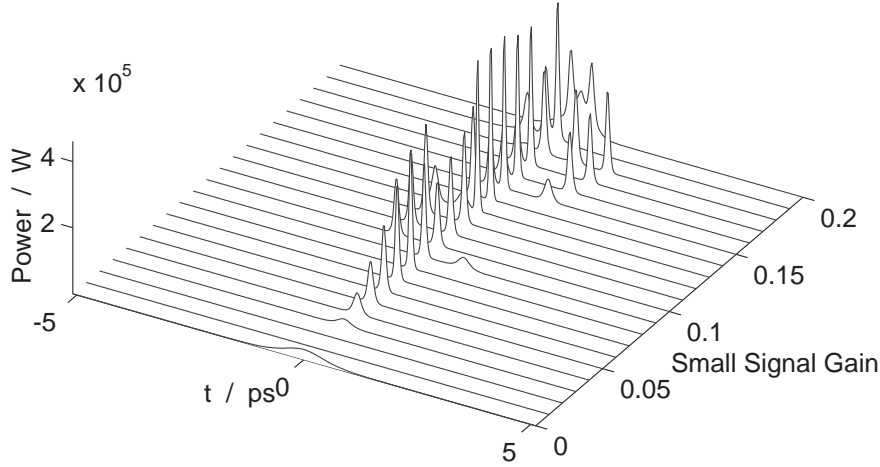


Figure 8.13: Each trace shows the pulse intensity profile obtained after 20,000 cavity round-trips in a diode-pumped Nd:glass laser according to [15]. When the laser reaches the double-pulse regime the multiple pulses are in constant motion with respect to each other. The resulting pulse train is no longer stationary.



With increasing small signal gain, i. e. increasing pulse energy, the soliton shortens to 80 fs due to the solitonlike pulse shaping, (Figure 8.13).

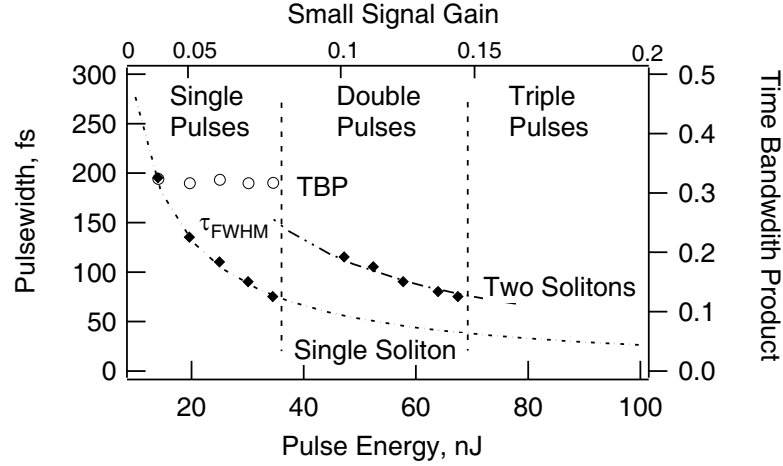


Figure 8.14: Steady state pulse width ( $\bullet$ ) and time-bandwidth product ( $\circ$ ) for a Nd:glass laser modelocked by a saturable absorber with a 200 fs recovery time with GDD and SPM included, shown as a function of the intracavity pulse energy. The time-bandwidth product is only meaningful in the single pulse regime, where it is shown. The pulses are almost transform limited sech-pulses. The pulse width in the multiple pulse regime is only unique in the parameter region where multiple pulses of similar height and width are achieved. The pulses break up into multiple pulses when the absorber is about three times saturated.

The pulse width follows nicely the soliton relation (8.4), (dash-dotted line). The pulses become shorter, by about a factor of 2.5, than without GDD and SPM before the pulse breaks up into longer double-pulses. The pulse break-up into double-pulses occurs when the absorber is about two times saturated, close to the point where the shortest pulse can be expected according to the discussion above. Figure 8.13 shows, that the break-up point for the double pulses is also very close to the instability for continuum break-through. Indeed the first pulse train after break-up at a small signal gain of  $g_0 = 0.09$  shows the coexistence of a longer and a shorter pulse, which indicates continuum break-through. But the following five traces are double pulses of equal height and energy. For even stronger saturation of the

absorber the double-pulses break-up into triple pulses and so on. Then the dynamics becomes even more complex. This behavior has been observed in detail in a Nd:glass laser [15], (see Figure 8.15), as well as in Cr4+:YAG lasers [17]. The simulations just discussed match the parameters of the Nd:glass experiments.

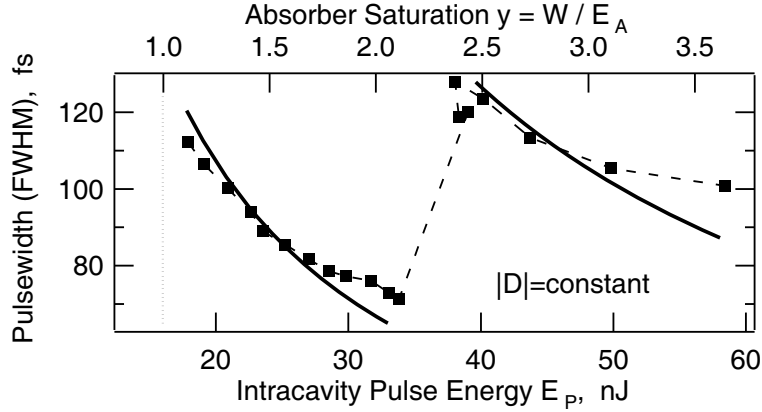


Figure 8.15: Pulsewidth in a Nd:glass laser [15] as a function of intracavity stored energy, i.e. pulse energy for a single pulse per round-trip. Dots measured values and solid line fits for a single and double-pulse solitonlike pulse stream.

Figure 8.15 clearly shows the scaling of the observed pulse width according to the soliton formula until the pulses break up at a saturation ratio of about 2. Notice, that the absorber recovery time of 200 fs is not much shorter than the pulse width achieved. Nevertheless, the optimum saturation ratio is close to the expected one of about 3. The break-up into pure double and triple pulses can be observed more clearly if the absorber recovery time is chosen to be shorter, so that continuum break-through is avoided. Figure 8.16 shows the final simulation results obtained after 20,000 round-trips in the cavity, if we reduce the absorber recovery time from 200 fs to 100 fs, again for different small signal gain, e.g. intracavity power levels and pulse energies. Now, we observe a clean break-up of the single-pulse solution into double-pulses and at even higher intracavity power levels the break-up into triple pulses without continuum generation in between. Note that the spacing between the pulses is very much different from what has been observed for the 200 fs response time. This spacing will depend on the details of the absorber and may also

be influenced by the dynamic gain saturation even if it is only a very small effect in this case [17].

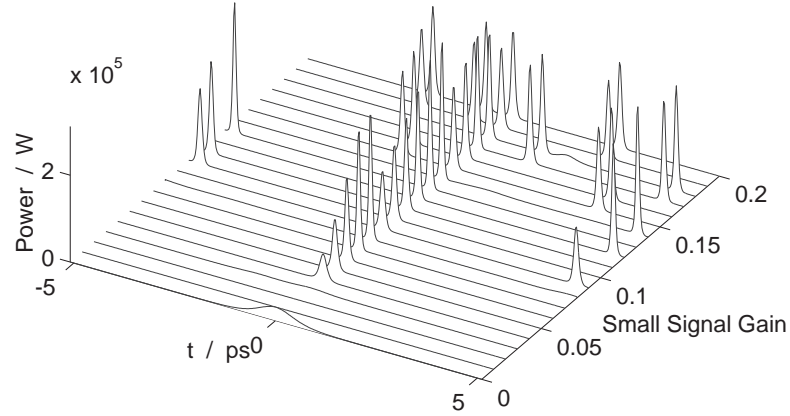


Figure 8.16: Each trace shows the pulse intensity profile obtained after 20,000 cavity round-trips for an absorber with a response time  $\tau_A = 100$  fs for different values of the small-signal gain. The simulations are always started with a 1 ps initial pulse shown as the first trace. Note that only the single pulse solutions are stationary.

## 8.4 Summary

Real absorbers do have the advantage of providing direct amplitude modulation and do not exploit additional cavities or operation of the resonator close to its stability boundary to achieve effective phase to amplitude conversion. Especially in compact resonator designs, as necessary for high-repetition rate lasers in the GHz range, semiconductor saturable absorbers with their low saturation energies and compactness offer unique solutions to this important technological challenge.

# Bibliography

- [1] M. N. Islam, E. R. Sunderman, C. E. Soccolich, I. Bar-Joseph, N. Sauer, T. Y. Chang, and B. I. Miller: "Color Center Lasers Passively Mode Locked by Quantum Wells," *IEEE J. Quantum Electronics*. **25**, 2454-2463 (1989).
- [2] S. Tsuda, W. H. Knox, E. A. de Souza, W. Y. Jan, and J. E. Cunningham, "Mode-Locking Ultrafast Solid-State Lasers with Saturable-Bragg Reflectors," *IEEE J. Sel. Top. Quantum Electronics* **2**, 454-464 (1996).
- [3] U. Keller, "Semiconductor nonlinearities for solid-state laser modelocking and Q-switching," in *Semiconductors and Semimetals*, Vol. **59A**, edited by A. Kost and E. Garmire, Academic Press, Boston 1999.
- [4] J. Shah, "Ultrafast Spectroscopy of Semiconductors and Semiconductor Nanostructures," *Series in Solid-State Sciences* **115**, Springer Verlag, Berlin (1996).
- [5] E. O. Goebel, "Ultrafast Spectroscopy of Semiconductors," in *Advances in Solid State Physics* **30**, pp. 269 – 294 (1990).
- [6] W. H. Knox, R. L. Fork, M. C. Downer, D. A. B. Miller, D. S. Chemla and C. V. Shank, "Femtosecond Excitation of Nonthermal Carrier Populations in GaAs Quantum Wells," *Phys. Rev. Lett.* **54**, pp. 1306 – 1309 (1985).
- [7] J. L. Oudar, D. Hulin, A. Migus, A. Antonetti, F. Alexandre, "Subpicosecond Spectral Hole Burning Due to Nonthermalized Photoexcited Carriers in GaAs," *Phys. Rev. Lett.* **55**, pp. 2074 – 2076 (1985).
- [8] W. H. Knox, C. Hirleimann, D. A. B. Miller, J. Shah, D. S. Chemla and C. V. Shank, "Femtosecond Dynamics of Resonantly Excited Excitons in

- Room-Temperature GaAs Quantum Wells," *Phys. Rev. Lett.* **56**, 1191 – 1193 (1986).
- [9] G. L. Witt, R. Calawa, U. Mishra, E. Weber, Eds., "Low Temperature (LT) GaAs and Related Materials," **241**, Pittsburgh, (1992).
- [10] R. Fluck, I. D. Jung, G. Zhang, F. X. Kärtner, and U. Keller, "Broad-band saturable absorber for 10 fs pulse generation," *Opt. Lett.* **21**, 743-745 (1996).
- [11] I. D. Jung, F. X. Kärtner, N. Matuschek, D. H. Sutter, F. Morier-Genoud, Z. Shi, V. Scheuer, M. Tilsch, T. Tschudi, U. Keller, "Semiconductor saturable absorber mirrors supporting sub-10 fs pulses," *Appl. Phys. B* **65**, pp. 137-150 (1997).
- [12] E. R. Thoen, E. M. Koontz, M. Joschko, P. Langlois, T. R. Schibli, F. X. Kärtner, E. P. Ippen, and L. A. Kolodziejski, "Two-photon absorption in semiconductor saturable absorber mirrors," *Appl. Phys. Lett.* **74**, 3927-3929, (1999).
- [13] P. Langlois, M. Joschko, E. R. Thoen, E. M. Koontz, F. X. Kärtner, E. P. Ippen, and L. A. Kolodziejski, "High fluence ultrafast dynamics of semiconductor saturable absorber mirrors," *Appl. Phys. Lett.* **75**, 3841-3843, (1999).
- [14] T. R. Schibli, E. R. Thoen, F. X. Kaertner, E. P. Ippen, "Suppression of Q-switched mode-locking and break-up into multiple pulses by inverse saturable absorption," *App. Phys. B* **70**, 41-49 (2000).
- [15] J. Aus der Au, D. Kopf, F. Morier-Genoud, M. Moser and U. Keller, "60-fs pulses from a diode-pumped Nd:glass laser," *Opt. Lett.* **22**, 207-309 (1997).
- [16] F.X. Kärtner, J. A. d. Au, U. Keller, "Mode-Locking with Slow and Fast Saturable Absorbers-What's the Difference," *Sel. Top. Quantum Electron.* **4**, 159 (1998).
- [17] B. C. Collings, K. Bergman, W. H. Knox, "Truely fundamental solitons in a passively mode-locked short cavity Cr<sup>4+</sup>:YAG laser.," *Opt. Lett.*, **22**, 1098-1100 (1997).

# Chapter 9

## Pulse Characterization

Characterization of ultrashort laser pulses with pulse widths greater than 20 ps can be directly performed electronically using high speed photo detectors and sampling scopes. Photo detectors with bandwidth of 100 GHz are available. For shorter pulses usually some type of autocorrelation or cross-correlation in the optical domain using nonlinear optical effects has to be performed, i.e. the pulse itself has to be used to measure its width, because there are no other controllable events available on such short time scales.

### 9.1 Intensity Autocorrelation

Pulse duration measurements using second-harmonic intensity autocorrelation is a standard method for pulse characterisation. Figure 9.1 shows the setup for a background free intensity autocorrelation. The input pulse is split in two, and one of the pulses is delayed by  $\tau$ . The two pulses are focussed into a nonlinear optical crystal in a non-collinear fashion. The nonlinear optical crystal is designed for efficient second harmonic generation over the full bandwidth of the pulse, i.e. it has a large second order nonlinear optical susceptibility and is phase matched for the specific wavelength range. We do not consider the  $z$ -dependence of the electric field and phase-matching effects. To simplify notation, we omit normalization factors. The induced nonlinear polarization is expressed as a convolution of two interfering electric-fields  $E_1(t)$ ,  $E_2(t)$  with the nonlinear response function of the medium, the

second order nonlinear susceptibility  $\chi^{(2)}$ .

$$P^{(2)}(t) \propto \iint_{-\infty}^{\infty} \chi^{(2)}(t - t_1, t - t_2) \cdot E_1(t_1) \cdot E_2(t_2) dt_1 dt_2$$

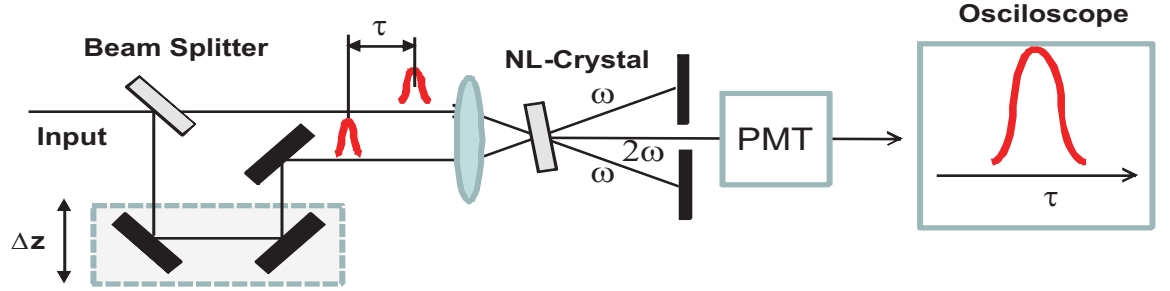


Figure 9.1: Setup for a background free intensity autocorrelation. To avoid dispersion and pulse distortions in the autocorrelator reflective optics and a thin crystal has to be used for measuring very short, typically sub-100 fs pulses.

We assume the material response is instantaneous and replace  $\chi^{(2)}(t - t_1, t - t_2)$  by a Dirac delta-function  $\chi^{(2)} \cdot \delta(t - t_1) \cdot \delta(t - t_2)$  which leads to

$$P^{(2)}(t) \propto E_1(t) \cdot E_2(t) \quad (9.1)$$

Due to momentum conservation, see Figure 9.1, we may separate the product  $E(t) \cdot E(t - \tau)$  geometrically and suppress a possible background coming from simple SHG of the individual pulses alone. The signal is zero if the pulses don't overlap.

$$P^{(2)}(t) \propto E(t) \cdot E(t - \tau). \quad (9.2)$$

$I(x)$ $x = t/T$	$\frac{\tau_p}{\tau_A}$	$\frac{\tau_p}{T}$
1. Rectangle: $I(x) = \begin{cases} 1, &  x  \leq 1/2 \\ 0, &  x  > 1/2 \end{cases}$	1	1
2. Parabola: $I(x) = \begin{cases} 1 - x^2, &  x  \leq 1/2 \\ 0, &  x  > 1/2 \end{cases}$	0.8716	$\sqrt{2}$
3. Sinc <sup>2</sup> $I(x) = \text{Sinc}^2(x)$	0.7511	2.7833
4. Gaussian $I(x) = e^{-x^2}$	0.7071	$2\sqrt{\ln 2}$
5. Triangle $I(x) = \begin{cases} 1 -  x , &  x  \leq 1 \\ 0, &  x  > 1 \end{cases}$	0.6922	1
6. Sech <sup>2</sup> $I(x) = \text{Sech}^2(x)$	0.6482	1.7627
7. Lorentzian $I(x) = \frac{1}{1+x^2}$	0.5	2
8. Onesided Exponential $I(x) = \begin{cases} e^{-x}, & x \geq 0 \\ 0, & x < 0 \end{cases}$	0.5	$\ln 2$
9. Twosided Exponential $I(x) = e^{-2 x }$	0.4130	$\ln 2$

Table 10.1: Pulse shapes and its deconvolution factors relating FWHM,  $\tau_p$ , of the pulse to FWHM,  $\tau_A$ , of the intensity autocorrelationfunction.

The electric field of the second harmonic radiation is directly proportional to the polarization, assuming a nondepleted fundamental radiation and the use of thin crystals. Due to momentum conservation, see Figure 9.1, we find

$$I_{AC}(\tau) \propto \int_{-\infty}^{\infty} |A(t)A(t-\tau)|^2 dt. \quad (9.3)$$

$$\propto \int_{-\infty}^{\infty} I(t)I(t-\tau) dt, \quad (9.4)$$



with the complex envelope  $A(t)$  and intensity  $I(t) = |A(t)|^2$  of the input pulse. The photo detector integrates because its response is usually much slower than the pulsewidth. Note, that the intensity autocorrelation is symmetric by construction

$$I_{AC}(\tau) = I_{AC}(-\tau). \quad (9.5)$$

It is obvious from Eq.(9.3) that the intensity autocorrelation does not contain full information about the electric field of the pulse, since the phase of the pulse in the time domain is completely lost. However, if the pulse shape is known the pulse width can be extracted by deconvolution of the correlation function. Table 10.1 gives the deconvolution factors for some often used pulse shapes.

## 9.2 Interferometric Autocorrelation (IAC)

A pulse characterization method, that also reveals the phase of the pulse is the interferometric autocorrelation introduced by J. C. Diels [2], (Figure 9.2 a). The input beam is again split into two and one of them is delayed. However, now the two pulses are sent colinearly into the nonlinear crystal. Only the SHG component is detected after the filter.

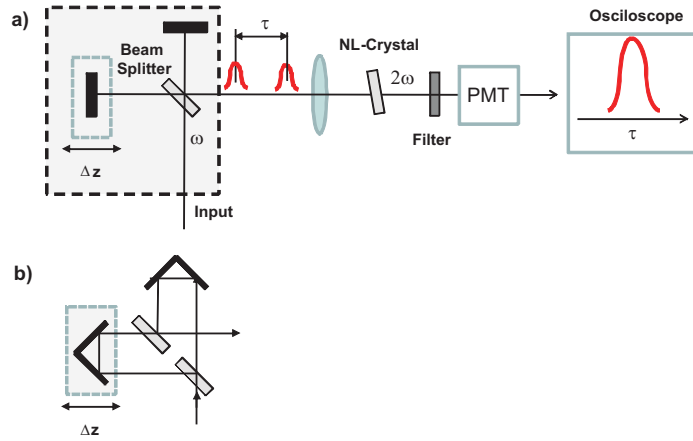


Figure 9.2: (a) Setup for an interferometric autocorrelation. (b) Delay stage, so that both beams are reflected from the same air/medium interface imposing the same phase shifts on both pulses.

The total field  $E(t, \tau)$  after the Michelson-Interferometer is given by the two identical pulses delayed by  $\tau$  with respect to each other

$$E(t, \tau) = E(t + \tau) + E(t) \quad (9.6)$$

$$= A(t + \tau)e^{j\omega_c(t+\tau)}e^{j\phi_{CE}} + A(t)e^{j\omega_c t}e^{j\phi_{CE}}. \quad (9.7)$$

$A(t)$  is the complex amplitude, the term  $e^{j\omega_c t}$  describes the oscillation with the carrier frequency  $\omega_c$  and  $\phi_{CE}$  is the carrier-envelope phase. Eq. (9.1) writes

$$P^{(2)}(t, \tau) \propto (A(t + \tau)e^{j\omega_c(t+\tau)}e^{j\phi_{CE}} + A(t)e^{j\omega_c t}e^{j\phi_{CE}})^2 \quad (9.8)$$

This is only ideally the case if the paths for both beams are identical. If for example dielectric or metal beamsplitters are used, there are different reflections involved in the Michelson-Interferometer shown in Fig. 9.2 (a) leading to a differential phase shift between the two pulses. This can be avoided by an exactly symmetric delay stage as shown in Fig. 9.2 (b).

Again, the radiated second harmonic electric field is proportional to the polarization

$$E(t, \tau) \propto (A(t + \tau)e^{j\omega_c(t+\tau)}e^{j\phi_{CE}} + A(t)e^{j\omega_c t}e^{j\phi_{CE}})^2. \quad (9.9)$$

The photo-detector (or photomultiplier) integrates over the envelope of each individual pulse

$$\begin{aligned} I(\tau) &\propto \int_{-\infty}^{\infty} \left| (A(t + \tau)e^{j\omega_c(t+\tau)} + A(t)e^{j\omega_c t})^2 \right|^2 dt. \\ &\propto \int_{-\infty}^{\infty} \left| A^2(t + \tau)e^{j2\omega_c(t+\tau)} \right. \\ &\quad \left. + 2A(t + \tau)A(t)e^{j\omega_c(t+\tau)}e^{j\omega_c t} \right. \\ &\quad \left. + A^2(t)e^{j2\omega_c t} \right|^2 dt. \end{aligned} \quad (9.10)$$

Evaluation of the absolute square leads to the following expression

$$\begin{aligned} I(\tau) &\propto \int_{-\infty}^{\infty} \left[ |A(t + \tau)|^4 + 4|A(t + \tau)|^2|A(t)|^2 + |A(t)|^4 \right. \\ &\quad \left. + 2A(t + \tau)|A(t)|^2A^*(t)e^{j\omega_c \tau} + \text{c.c.} \right. \\ &\quad \left. + 2A(t)|A(t + \tau)|^2A^*(t + \tau)e^{-j\omega_c \tau} + \text{c.c.} \right. \\ &\quad \left. + A^2(t + \tau)(A^*(t))^2e^{j2\omega_c \tau} + \text{c.c.} \right] dt. \end{aligned} \quad (9.11)$$

The carrier-envelope phase  $\phi_{CE}$  drops out since it is identical to both pulses. The interferometric autocorrelation function is composed of the following terms

$$I(\tau) = I_{back} + I_{int}(\tau) + I_{\omega}(\tau) + I_{2\omega}(\tau) . \quad (9.12)$$

Background signal  $I_{back}$ :

$$I_{back} = \int_{-\infty}^{\infty} (|A(t+\tau)|^4 + |A(t)|^4) dt = 2 \int_{-\infty}^{\infty} I^2(t) dt \quad (9.13)$$

Intensity autocorrelation  $I_{int}(\tau)$ :

$$I_{int}(\tau) = 4 \int_{-\infty}^{\infty} |A(t+\tau)|^2 |A(t)|^2 dt = 4 \int_{-\infty}^{\infty} I(t+\tau) \cdot I(t) dt \quad (9.14)$$

Coherence term oscillating with  $\omega_c$ :  $I_{\omega}(\tau)$ :

$$I_{\omega}(\tau) = 4 \int_{-\infty}^{\infty} \text{Re} \left[ \left( I(t) + I(t+\tau) \right) A^*(t) A(t+\tau) e^{j\omega\tau} \right] dt \quad (9.15)$$

Coherence term oscillating with  $2\omega_c$ :  $I_{2\omega}(\tau)$ :

$$I_{2\omega}(\tau) = 2 \int_{-\infty}^{\infty} \text{Re} \left[ A^2(t) (A^*(t+\tau))^2 e^{j2\omega\tau} \right] dt \quad (9.16)$$

Eq. (9.12) is often normalized relative to the background intensity  $I_{back}$  resulting in the interferometric autocorrelation trace

$$I_{IAC}(\tau) = 1 + \frac{I_{int}(\tau)}{I_{back}} + \frac{I_{\omega}(\tau)}{I_{back}} + \frac{I_{2\omega}(\tau)}{I_{back}}. \quad (9.17)$$

Eq. (9.17) is the final equation for the normalized interferometric autocorrelation. The term  $I_{int}(\tau)$  is the intensity autocorrelation, measured by non-colinear second harmonic generation as discussed before. Therefore, the averaged interferometric autocorrelation results in the intensity autocorrelation sitting on a background of 1.

Fig. 9.3 shows a calculated and measured IAC for a sech-shaped pulse. As with the intensity autocorrelation, by construction the interferometric autocorrelation has to be also symmetric:

$$I_{IAC}(\tau) = I_{IAC}(-\tau) \quad (9.18)$$

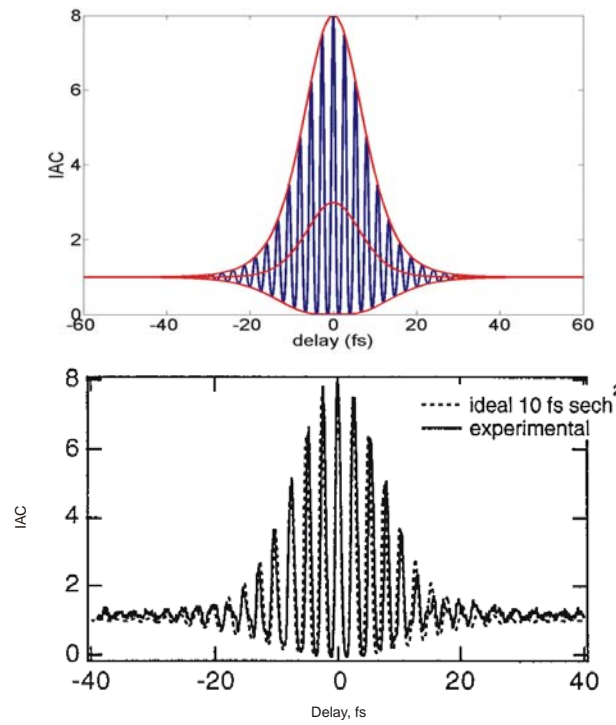


Figure 9.3: Computed and measured interferometric autocorrelation traces for a 10 fs long sech-shaped pulse.

This is only true if the beam path between the two replicas in the setup are completely identical, i.e. there is not even a phase shift between the two pulses. A phase shift would lead to a shift in the fringe pattern, which shows up very strongly in few-cycle long pulses. To avoid such a symmetry breaking, one has to arrange the delay line as shown in Figure 9.2 b so that each pulse travels through the same amount of substrate material and undergoes the same reflections and transmissions.

At  $\tau = 0$ , all integrals are identical

$$\begin{aligned}
 I_{back} &\equiv 2 \int |A(t)|^4 dt \\
 I_{int}(\tau = 0) &\equiv 2 \int |A^2(t)|^2 dt = 4 \int |A(t)|^4 dt = 2I_{back} \\
 I_{\omega}(\tau = 0) &\equiv 2 \int |A(t)|^2 A(t) A^*(t) dt = 8 \int |A(t)|^4 dt = 4I_{back} \\
 I_{2\omega}(\tau = 0) &\equiv 2 \int A^2(t) (A^2(t))^* dt = 2 \int |A(t)|^4 dt = I_{back}
 \end{aligned} \tag{9.19}$$

Then, we obtain for the interferometric autocorrelation at zero time delay

$$\begin{aligned}
 I_{IAC}(\tau)|_{\max} &= I_{IAC}(0) = 8 \\
 I_{IAC}(\tau \rightarrow \pm\infty) &= 1 \\
 I_{IAC}(\tau)|_{\min} &\rightarrow 0
 \end{aligned} \tag{9.20}$$

This is the important 1:8 ratio between the wings and the pick of the IAC, which is a good guide for proper alignment of an interferometric autocorrelator. For a chirped pulse the envelope is not any longer real. A chirp in the pulse results in nodes in the IAC. Figure 9.4 shows the IAC of a chirped sech-pulse

$$A(t) = \left( \operatorname{sech} \left( \frac{t}{\tau_p} \right) \right)^{(1+j\beta)}$$

for different chirps.

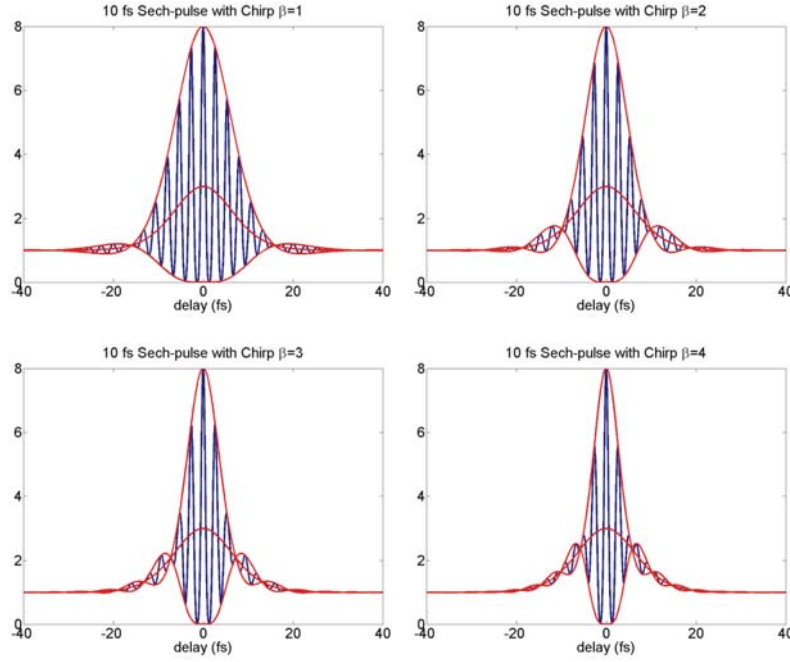


Figure 9.4: Influence of increasing chirp on the IAC.

### 9.2.1 Interferometric Autocorrelation of an Unchirped Sech-Pulse

Envelope of an unchirped sech-pulse

$$A(t) = \text{sech}(t/\tau_p) \quad (9.21)$$

Interferometric autocorrelation of a sech-pulse

$$I_{IAC}(\tau) = 1 + \{2 + \cos(2\omega_c\tau)\} \frac{3 \left( \left( \frac{\tau}{\tau_p} \right) \cosh \left( \frac{\tau}{\tau_p} \right) - \sinh \left( \frac{\tau}{\tau_p} \right) \right)}{\sinh^3 \left( \frac{\tau}{\tau_p} \right)} \quad (9.22)$$

$$+ \frac{3 \left( \sinh \left( \frac{2\tau}{\tau_p} \right) - \left( \frac{2\tau}{\tau_p} \right) \right)}{\sinh^3 \left( \frac{\tau}{\tau_p} \right)} \cos(\omega_c\tau)$$

### 9.2.2 Interferometric Autocorrelation of a Chirped Gaussian Pulse

Complex envelope of a Gaussian pulse

$$A(t) = \exp \left[ -\frac{1}{2} \left( \frac{t}{\tau_p} \right)^2 (1 + j\beta) \right]. \quad (9.23)$$

Interferometric autocorrelation of a Gaussian pulse

$$\begin{aligned} I_{IAC}(\tau) = & 1 + \left\{ 2 + e^{-\frac{\beta^2}{2} \left( \frac{\tau}{\tau_p} \right)^2} \cos(2\omega_c \tau) \right\} e^{-\frac{1}{2} \left( \frac{\tau}{\tau_p} \right)^2} \\ & + 4e^{-\frac{3+\beta^2}{8} \left( \frac{\tau}{\tau_p} \right)^2} \cos \left( \frac{\beta}{4} \left( \frac{\tau}{\tau_p} \right)^2 \right) \cos(\omega_c \tau). \end{aligned} \quad (9.24)$$

### 9.2.3 Second Order Dispersion

It is fairly simple to compute in the Fourier domain what happens in the presence of dispersion.

$$E(t) = A(t)e^{j\omega_c t} \xrightarrow{F} \tilde{E}(\omega) \quad (9.25)$$

After propagation through a dispersive medium we obtain in the Fourier domain.

$$\tilde{E}'(\omega) = \tilde{E}(\omega)e^{-i\Phi(\omega)}$$

and

$$E'(t) = A'(t)e^{j\omega_c t}$$

Figure 9.5 shows the pulse amplitude before and after propagation through a medium with second order dispersion. The pulse broadens due to the dispersion. If the dispersion is further increased the broadening increases and the interferometric autocorrelation traces shown in Figure 9.5 develop a characteristic pedestal due to the term  $I_{int}$ . The width of the interferometrically sensitive part remains the same and is more related to the coherence time in the pulse, that is proportional to the inverse spectral width and does not change.

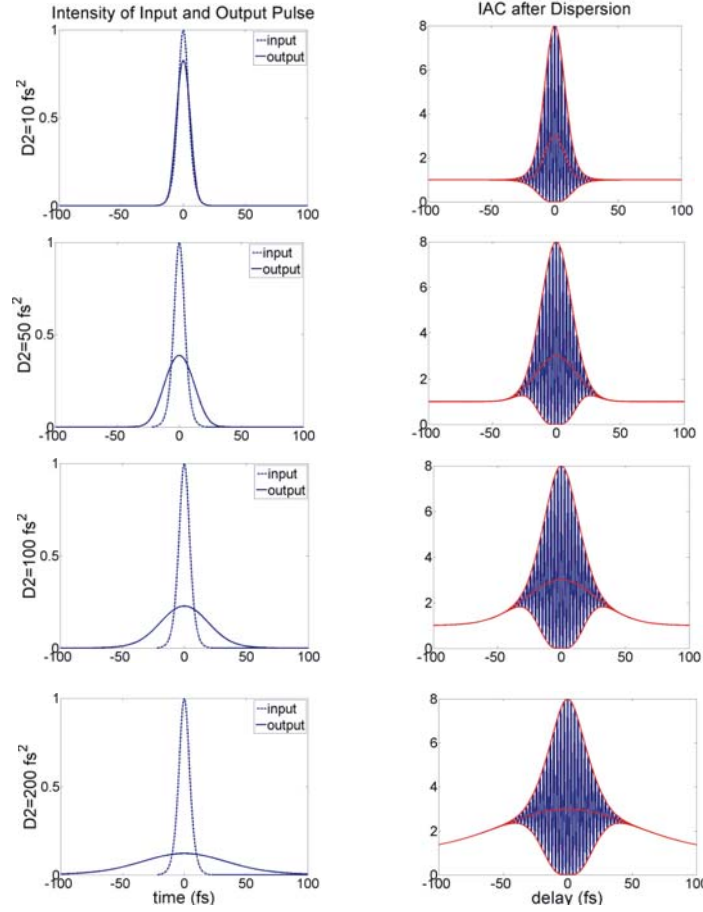


Figure 9.5: Effect of different amounts of second order dispersion on a transform limited 10 fs Sech-pulse.

### 9.2.4 Third Order Dispersion

We expect, that third order dispersion affects the pulse significantly for

$$\frac{D_3}{\tau^3} > 1$$

which is for a 10fs sech-pulse  $D_3 > \left(\frac{10 \text{ fs}}{1.76}\right)^3 \sim 183 \text{ fs}^3$ . Figure 9.6 and 9.7 show the impact on pulse shape and interferometric autocorrelation. The odd dispersion term generates asymmetry in the pulse. The interferometric autocorrelation develops characteristic nodes in the wings.



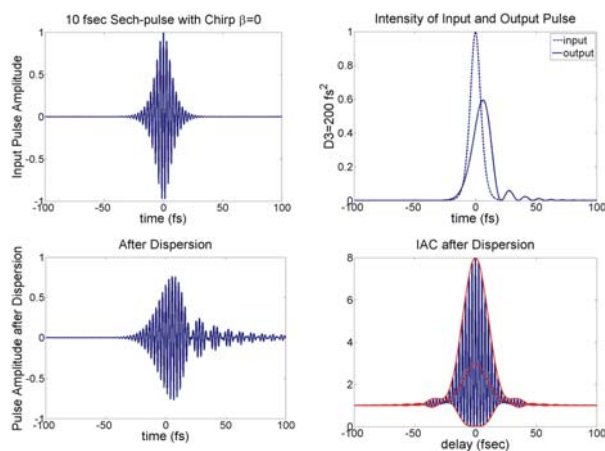


Figure 9.6: Impact of  $200 \text{ fs}^3$  third order dispersion on a 10 fs pulse at a center wavelength of 800 nm and its interferometric autocorrelation.

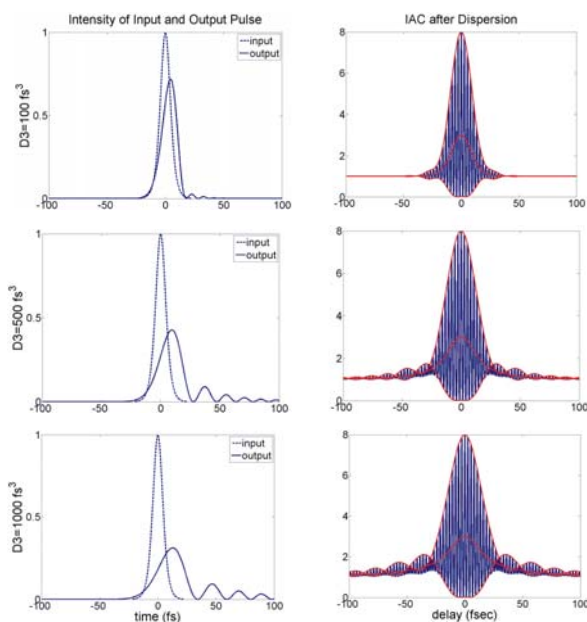


Figure 9.7: Changes due to increasing third order Dispersion from 100-1000  $\text{fs}^3$  on a 10 fs pulse at a center wavelength of 800 nm.

### 9.2.5 Self-Phase Modulation

Self-phase modulation without compensation by proper negative dispersion generates a phase over the pulse in the time domain. This phase is invisible in the intensity autocorrelation, however it shows up clearly in the IAC, see Figure 9.8 for a Gaussian pulse with a peak nonlinear phase shift  $\phi_0 = \delta A_0^2 = 2$  and Figure 9.8 for a nonlinear phase shift  $\phi_0 = 3$ .

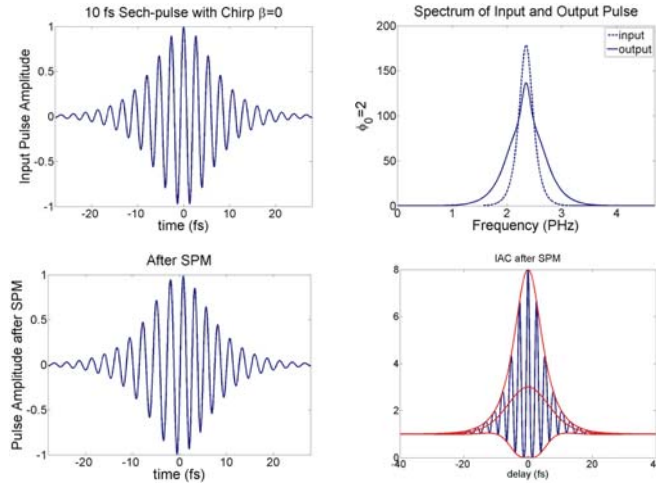


Figure 9.8: Change in pulse shape and interferometric autocorrelation in a 10 fs pulse at 800 nm subject to pure self-phase modulation leading to a nonlinear phase shift of  $\phi_0 = 2$ .

From the experience gained by looking at the above IAC-traces for pulses undergoing second and third order dispersions as well as self-phase modulation we conclude that it is in general impossible to predict purely by looking at the IAC what phase perturbations a pulse might have. Therefore, it was always a wish to reconstruct uniquely the electrical field with respect to amplitude and phase from the measured data. In fact one can show rigorously, that amplitude and phase of a pulse can be derived uniquely from the IAC and the measured spectrum up to a time reversal ambiguity [1]. Furthermore, it has been shown that a cross-correlation of the pulse with a replica chirped in a known medium and the pulse spectrum is enough to reconstruct the pulse [3]. Since the spectrum of the pulse is already given only the phase has to be determined. If a certain phase is assumed, the electric field and

the measured cross-correlation or IAC can be computed. Minimization of the error between the measured cross-correlation or IAC will give the desired spectral phase. This procedure has been dubbed PICASO (Phase and Intensity from Cross Correlation and Spectrum Only).

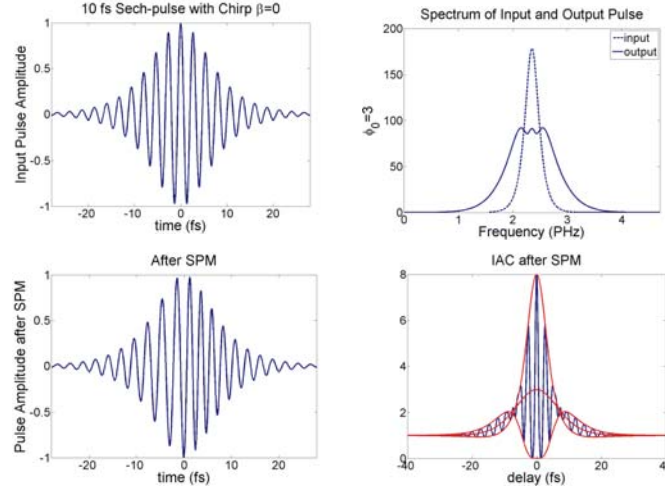


Figure 9.9: Change in pulse shape and interferometric autocorrelation in a 10 fs pulse at 800 nm subject to pure self-phase modulation leading to a nonlinear phase shift of  $\phi_0 = 3$ .

Note, also instead of measuring the autocorrelation and interferometric autocorrelation with SHG one can also use two-photon absorption or higher order absorption in a semiconductor material (Laser or LED) [4].

However today, the two widely used pulse characterization techniques are Frequency Resolved Optical Gating (FROG) and Spectral Phase Interferometry for Direct Electric Field Reconstruction (SPIDER)

### 9.3 Frequency Resolved Optical Gating (FROG)

We follow closely the book of Rick Trebino, who invented FROG. In frequency resolved optical gating, the pulse to be characterized is gated by another ultrashort pulse [5]. The gating is no simple linear sampling technique, but the pulses are crossed in a medium with an instantaneous nonlinearity ( $\chi^{(2)}$  or  $\chi^{(3)}$ ) in the same way as in an autocorrelation measurement (Figures 9.1

and 9.10). The FROG-signal is a convolution of the unknown electric-field  $E(t)$  with the gating-field  $g(t)$  (often a copy of the unknown pulse itself). However, after the interaction of the pulse to be measured and the gate pulse, the emitted nonlinear optical radiation is not put into a simple photo detector, but is instead spectrally resolved detected. The general form of the frequency-resolved intensity, or Spectrogram  $S_F(\tau, \omega)$  is given by

$$S_F(\tau, \omega) \propto \left| \int_{-\infty}^{\infty} E(t) \cdot g(t - \tau) e^{-j\omega t} dt \right|^2. \quad (9.26)$$

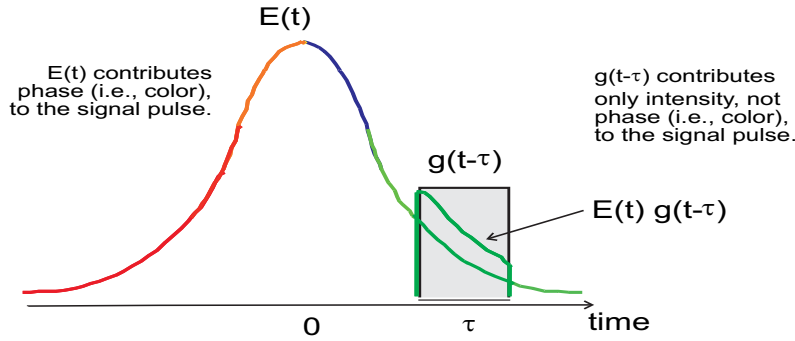


Figure 9.10: The spectrogram of a waveform  $E(t)$  tells the intensity and frequency in a given time interval [5].

Representations of signals, or waveforms in general, by time-frequency distributions has a long history. Most notably musical scores are a temporal sequence of tones giving its frequency and volume, see Fig. 9.11.

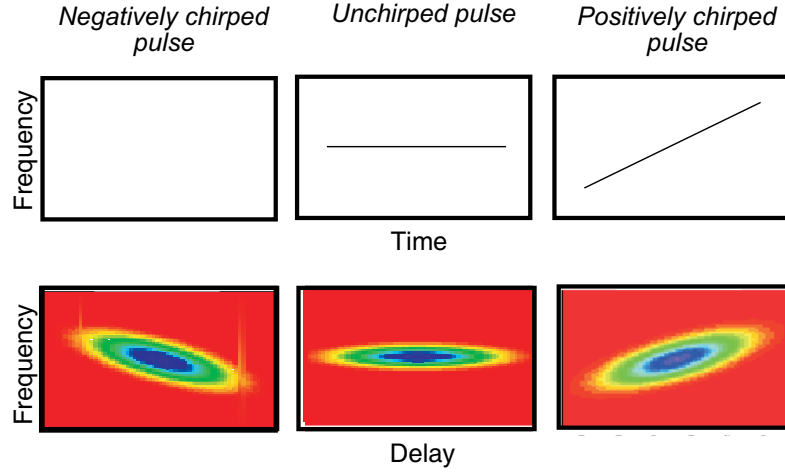


Figure 9.12: Like a musical score, the spectrogram visually displays the frequency vs. time [5].

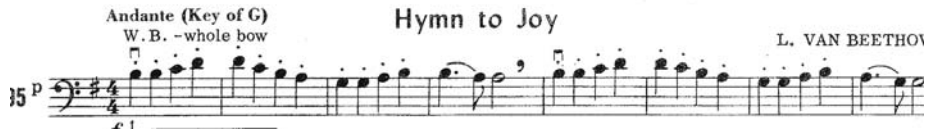


Figure 9.11: A musical score is a time-frequency representation of the signal to be played.

Time-frequency representations are well known in the radar community, signal processing and quantum mechanics [9] (Spectrogram, Wigner-Distribution, Husimi-Distribution, ...), Figure 9.12 shows the spectrogram of differently chirped pulses. Like a musical score, (see Fig. 9.11) the spectrogram visually displays the frequency vs. time.

Note, that the gate pulse in the FROG measurement technique does not to be very short. In fact if we have

$$g(t) \equiv \delta(t) \quad (9.27)$$

then

$$S_F(\tau, \omega) = |E(\tau)|^2 \quad (9.28)$$

and the phase information is completely lost. There is no need for short gate pulses. A gate length of the order of the pulse length is sufficient. It temporally resolves the slow components and spectrally the fast components.

### 9.3.1 Polarization Gate FROG

Figure 9.13 shows the setup [6][7]. FROG is based on the generation of a well defined gate pulse, eventually not yet known. This can be achieved by using the pulse to be measured and an ultrafast nonlinear interaction. For example the electronic Kerr effect can be used to induce an ultrafast polarization modulation, that can gate the pulse with a copy of the same pulse.

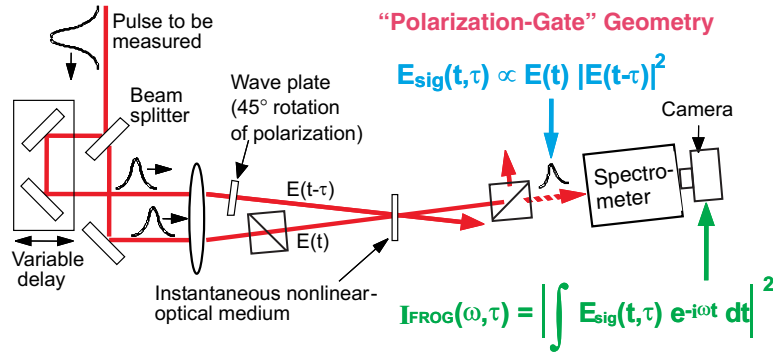


Figure 9.13: Polarization Gate FROG setup. The instantaneous Kerr-effect is used to rotate the polarization of the signal pulse  $E(t)$  during the presence of the gate pulse  $E(t - \tau)$  proportional to the intensity of the gate pulse [5].

The signal analyzed in the FROG trace is, see Figure 9.14,

$$E_{\text{sig}}(t, \tau) = E(t) |E(t - \tau)|^2 \quad (9.29)$$

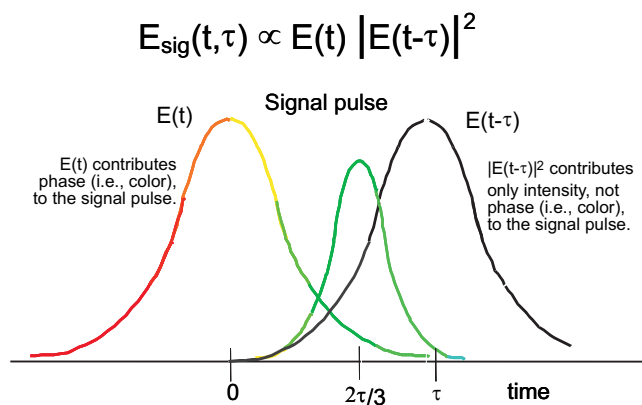


Figure 9.14: The signal pulse reflects the color of the gated pulse at the time  $2\tau/3$  [5]

The FROG traces generated from a PG-FROG for chirped pulses is identical to Fig. 9.12. Figure 9.15 shows FROG traces of more complicated pulses

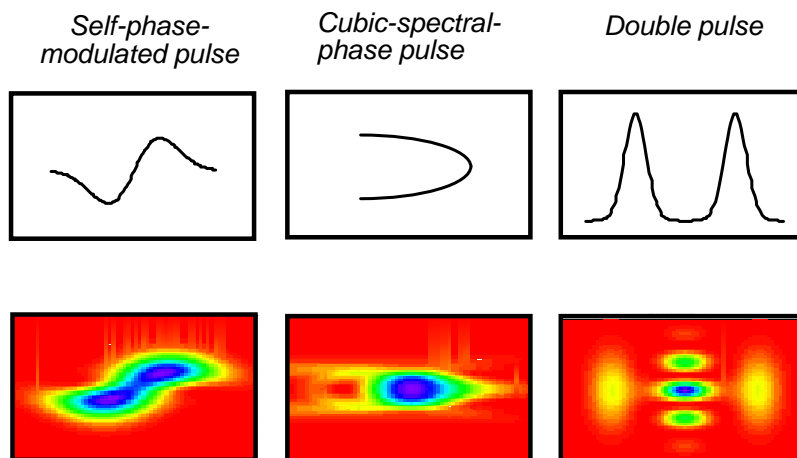


Figure 9.15: FROG traces of more complicated pulses.

### 9.3.2 FROG Inversion Algorithm

Spectrogram inversion algorithms need to know the gate function  $g(t - \tau)$ , which in the given case is related to the yet unknown pulse. So how do we get from the FROG trace to the pulse shape with respect to amplitude and phase? If there is such an algorithm, which produces solutions, the question of uniqueness of this solution arises. To get insight into these issues, we realize, that the FROG trace can be written as

$$I_{FROG}(\tau, \omega) \propto \left| \int_{-\infty}^{\infty} E_{sig}(t, \tau) e^{-j\omega t} dt \right|^2 \quad (9.30)$$

Writing the signal field as a Fourier transform in the time variable, i.e.

$$E_{sig}(t, \tau) = \int_{-\infty}^{\infty} \hat{E}_{sig}(t, \Omega) e^{-j\Omega \tau} d\Omega \quad (9.31)$$

yields

$$I_{FROG}(\tau, \omega) \propto \left| \int_{-\infty}^{\infty} \int_{-\infty}^{\infty} \hat{E}_{sig}(t, \Omega) e^{-j\omega t - j\Omega \tau} dt d\Omega \right|^2. \quad (9.32)$$

This equation shows that the FROG-trace is the magnitude square of a two-dimensional Fourier transform related to the signal field  $E_{sig}(t, \Omega)$ . The inversion of Eq.(9.32) is known as the 2D-phase retrieval problem. Fortunately algorithms for this inversion exist [8] and it is known that the magnitude (or magnitude square) of a 2D-Fourier transform (FT) essentially uniquely determines also its phase, if additional conditions, such as finite support or the relationship (9.29) is given. Essentially unique means, that there are ambiguities but they are not dense in the function space of possible 2D-transforms, i.e. they have probability zero to occur.

Furthermore, the unknown pulse  $E(t)$  can be easily obtained from the modified signal field  $\hat{E}_{sig}(t, \Omega)$  because

$$\hat{E}_{sig}(t, \Omega) = \int_{-\infty}^{\infty} E_{sig}(t, \tau) e^{j\Omega \tau} d\tau \quad (9.33)$$

$$= \int_{-\infty}^{\infty} E(t) g(t - \tau) e^{-j\Omega \tau} d\tau \quad (9.34)$$

$$= E(t) G^*(\Omega) e^{-j\Omega t} \quad (9.35)$$

with

$$G(\Omega) = \int_{-\infty}^{\infty} g(\tau) e^{-j\Omega \tau} d\tau. \quad (9.36)$$



Thus there is

$$E(t) \propto \hat{E}_{sig}(t, 0). \quad (9.37)$$

The only condition is that the gate function should be chosen such that  $G(\Omega) \neq 0$ . This is very powerful.

### Fourier Transform Algorithm

The Fourier transform algorithm also commonly used in other phase retrieval problems is schematically shown in Fig. 9.16

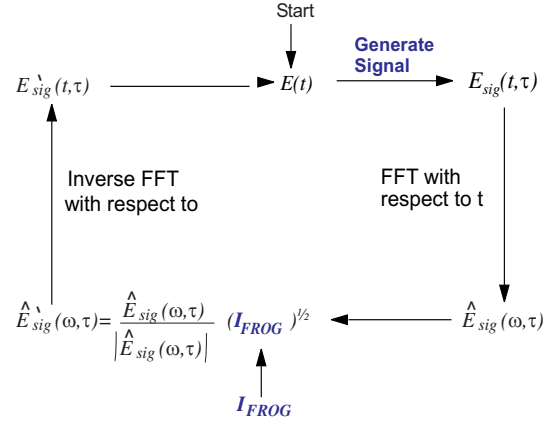


Figure 9.16: Fourier transform algorithm for FROG trace inversion. The blue operations indicate the constraints due to the gating technique used and the FROG data [5]

### Generalized Projections

The signal field  $E_{sig}(t, \tau)$  has to fulfill two constraints, which define sets see Fig. 9.17. The intersection between both sets results in yields  $E(t)$ . Moving to the closest point in one constraint set and then the other yields convergence to the solution, if the two sets are convex. Unfortunately, the FROG constraints are not convex. Nevertheless the algorithm works surprisingly well. For more information consult with reference [5].

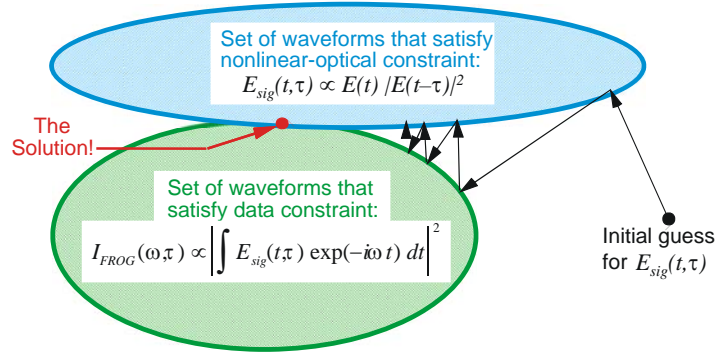


Figure 9.17: Generalized Projections applied to FROG [5].

### 9.3.3 Second Harmonic FROG

So far we only discussed PG-FROG. However, if we choose a  $\chi^{(2)}$  nonlinearity, e.g. SHG, and set the gating-field equal to a copy of the pulse  $g(t) \equiv E(t)$ , we are measuring in eq.(9.26) the spectrally resolved autocorrelation signal. The marginals of the measured FROG-trace do have the following properties

$$\int_{-\infty}^{\infty} S_F(\tau, \omega) d\omega \propto \int_{-\infty}^{\infty} |E(t)|^2 \cdot |g(t - \tau)|^2 dt. \quad (9.38)$$

$$\int_{-\infty}^{\infty} S_F(\tau, \omega) d\tau \propto \left| \int_{-\infty}^{\infty} \hat{E}(\omega) \cdot \hat{G}(\omega - \omega') d\omega' \right|^2. \quad (9.39)$$

For the case, where  $g(t) \equiv E(t)$ , we obtain

$$\int_{-\infty}^{\infty} S_F(\tau, \omega) d\omega \propto I_{AC}(\tau). \quad (9.40)$$

$$\int_{-\infty}^{\infty} S_F(\tau, \omega) d\tau \propto \left| \hat{E}_{2\omega}(\omega) \right|^2. \quad (9.41)$$

The setup to measure the Frog-trace is identical with the setup to measure the intensity autocorrelation function (Figure 9.1) only the photodetector for the second harmonic is replaced by a spectrometer (Figure 9.18).

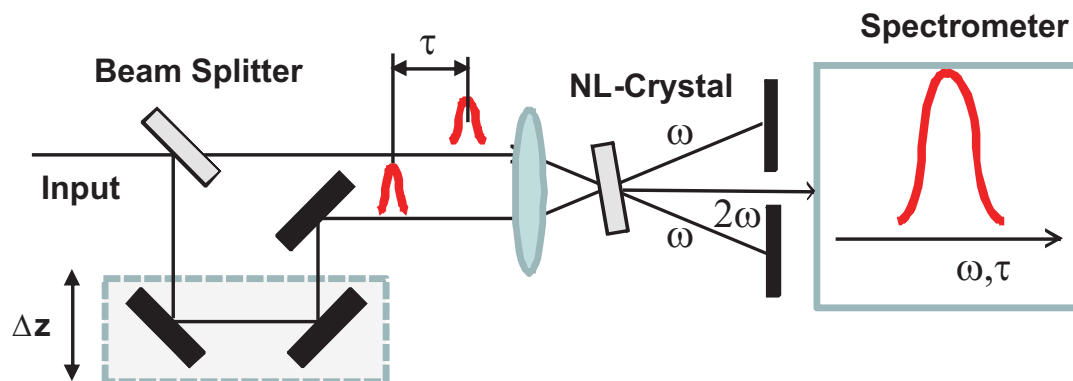


Figure 9.18: SHG-FROG setup.

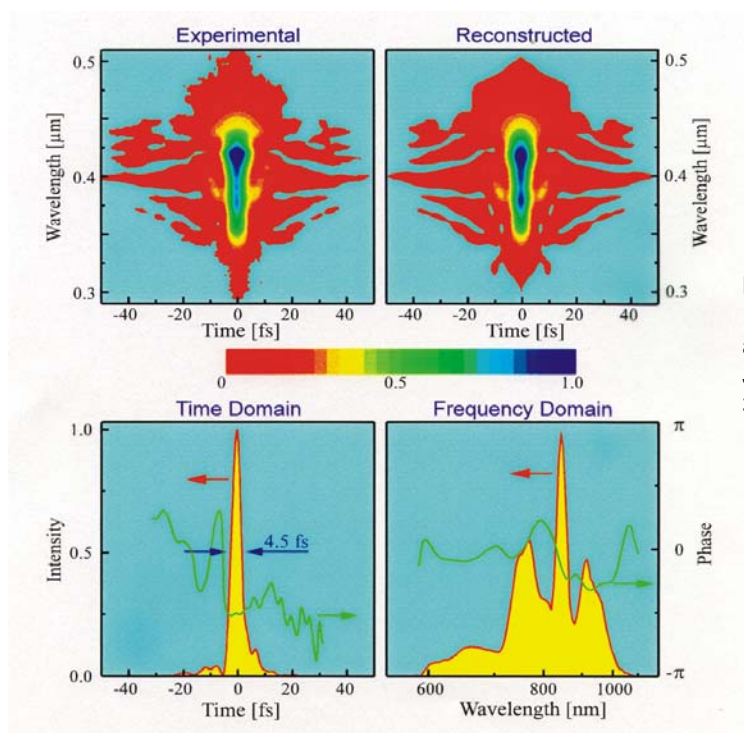


Figure 9.19: FROG measurement of a 4.5 fs laser pulse.

Since the intensity autocorrelation function and the integrated spectrum

can be measured simultaneously, this gives redundancy to check the correctness of all measurements via the marginals (9.38, 9.39). Figure 9.19 shows the SHG-FROG trace of the shortest pulses measured sofar with FROG.

### 9.3.4 FROG Geometries

The Frog-signal  $E_{sig}$  can also be generated by a nonlinear interaction different from SHG or PG, see table 9.20[5].

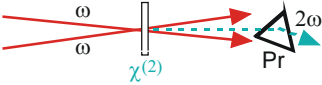
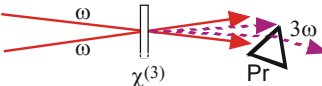
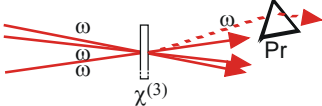
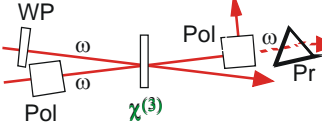
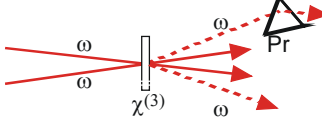
		<b>FROG geometries: Pros and Cons</b>				
			<b>Sensitivity</b>	<b>Ambiguities</b>		
Second-harmonic generation	<b>SHG</b>		.001 nJ	Direction of time; Rel. phase of multiple pulses	most sensitive; most accurate	
Third-harmonic generation	<b>THG</b>		1 nJ	Relative phase of multiple pulses	tightly focused beams	
Transient-grating	<b>TG</b>		10 nJ	None	useful for UV & transient-grating experiments	
Polarization-gate	<b>PG</b>		100 nJ	None	simple, intuitive, best scheme for amplified pulses	
Self-diffraction	<b>SD</b>		1000 nJ	None	useful for UV	

Figure 9.20: FROG geometries and their pros and cons.

## 9.4 Spectral Interferometry and SPIDER

Spectral Phase Interferometry for Direct Electric-Field Reconstruction (SPIDER) avoids iterative reconstruction of the phase profile. Iterative Fourier transform algorithms do have the disadvantage of sometimes being rather time consuming, preventing real-time pulse characterization. In addition, for "pathological" pulse forms, reconstruction is difficult or even impossible. It is mathematically not proven that the retrieval algorithms are unambiguous especially in the presence of noise.

Spectral shearing interferometry provides an elegant method to overcome these disadvantages. This technique has been first introduced by C. Iaconis and I.A. Walmsley in 1999 [11] and called spectral phase interferometry for direct electric-field reconstruction – SPIDER. Before we discuss SPIDER let's look at spectral interferometry in general

### 9.4.1 Spectral Interferometry

The spectrum of a pulse can easily be measured with a spectrometer. The pulse would be completely known, if we could determine the phase across the spectrum. To determine this unknown phase spectral interferometry for pulse measurement has been proposed early on by Froehly and others [12]. If we would have a well referenced pulse with field  $E_R(t)$ , superimpose the unknown electric field  $E_S(t)$  delayed with the reference pulse and interfere them in a spectrometer, see Figure 9.21, we obtain for the spectrometer output

$$E_I(t) = E_R(t) + E_S(t - \tau) \quad (9.42)$$

$$\hat{S}(\omega) = \left| \int_{-\infty}^{+\infty} E_I(t) e^{-j\omega t} dt \right|^2 = \left| \hat{E}_R(\omega) + \hat{E}_S(\omega) e^{-j\omega\tau} \right|^2 \quad (9.43)$$

$$= \hat{S}_{DC}(\omega) + \hat{S}^{(-)}(\omega) e^{j\omega\tau} + \hat{S}^{(+)}(\omega) e^{-j\omega\tau} \quad (9.44)$$

with

$$\hat{S}^{(+)}(\omega) = \hat{E}_R^*(\omega) \hat{E}_S(\omega) \quad (9.45)$$

$$\hat{S}^{(-)}(\omega) = \hat{S}^{(+)*}(\omega) \quad (9.46)$$

Where (+) and (-) indicate as before, well separated positive and negative "frequency" signals, where "frequency" is now related to  $\tau$  rather than  $\omega$ .

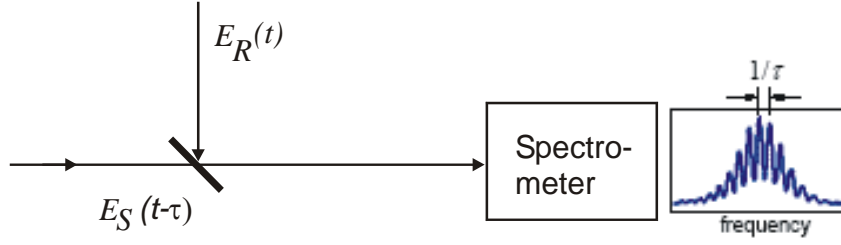


Figure 9.21: Spectral Interferometry of a signal pulse with a reference pulse.

If  $\tau$  is chosen large enough, the inverse Fourier transformed spectrum  $S(t) = F^{-1}\{\hat{S}(\omega)\}$  results in well separated signals, see Figure 9.22.

$$S(t) = S_{DC}(t) + S^{(-)}(t + \tau) + \hat{S}^{(+)}(t - \tau) \quad (9.47)$$

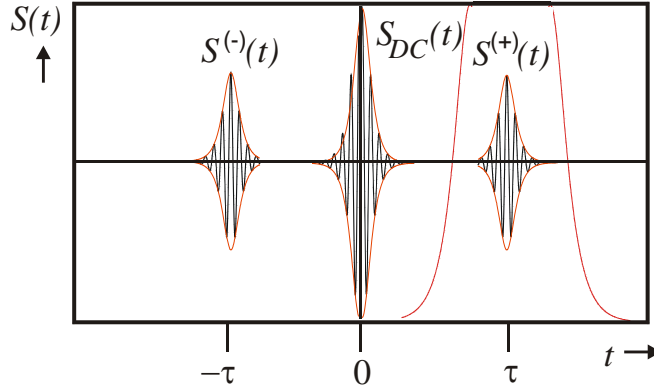


Figure 9.22: Decomposition of SPIDER signal.

We can isolate either the positive or negative frequency term with a filter in the time domain. Back transformation of the corresponding term to the frequency domain and computation of the spectral phase of one of the terms results in the spectral phase of the signal up to the known phase of the reference pulse and a linear phase contribution from the delay.

$$\Phi^{(+)}(\omega) = \arg\{\hat{S}^{(+)}(\omega)e^{j\omega\tau}\} = \varphi_S(\omega) - \varphi_R(\omega) + \omega\tau \quad (9.48)$$

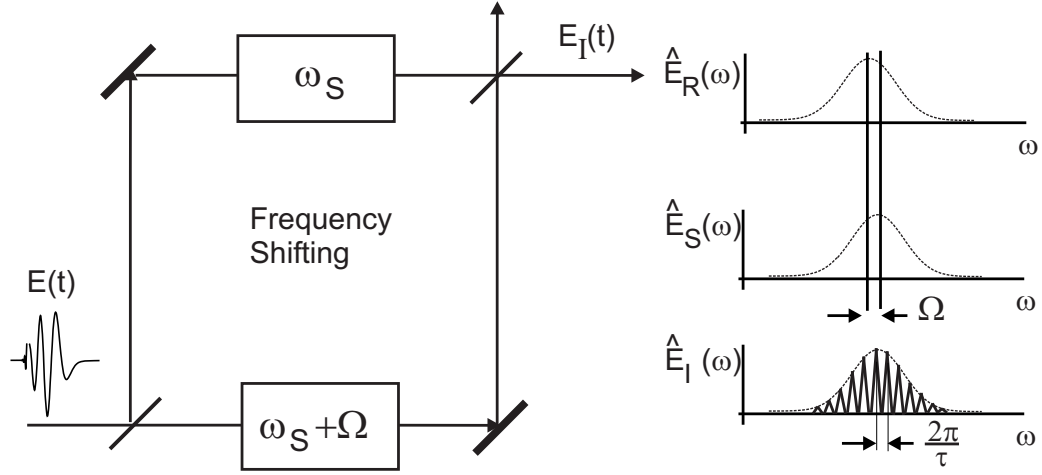


Figure 9.23: The principle of operation of SPIDER.

### 9.4.2 SPIDER

What can we do if we don't have a well characterized reference pulse? C. Iaconis and I.A. Walmsley [11] came up with the idea of generating two up-converted spectra slightly shifted in frequency and to investigate the spectral interference of these two copies, see Figure 9.23. We use

$$E_R(t) = E(t)e^{j\omega_s t} \quad (9.49)$$

$$E_S(t) = E(t - \tau)e^{j(\omega_s + \Omega)t} \quad (9.50)$$

$$E_I(t) = E_R(t) + E_S(t) \quad (9.51)$$

where  $\omega_s$  and  $\omega_s + \Omega$  are the two frequencies used for upconversion and  $\Omega$  is called the spectral shear between the two pulses.  $E(t)$  is the unknown electric field with spectrum

$$\hat{E}(\omega) = \left| \hat{E}(\omega) \right| e^{j\varphi(\omega)} \quad (9.52)$$

Spectral interferometry using these specially constructed signal and reference pulses results in

$$\hat{S}(\omega) = \left| \int_{-\infty}^{+\infty} E_I(t) e^{-j\omega t} dt \right|^2 = \hat{S}_{DC}(\omega) + \hat{S}^{(-)}(\omega) e^{j\omega\tau} + \hat{S}^{(+)}(\omega) e^{-j\omega\tau} \quad (9.53)$$

$$\hat{S}^{(+)}(\omega) = \hat{E}_R^*(\omega) \hat{E}_S(\omega) = \hat{E}^*(\omega - \omega_s) \hat{E}(\omega - \omega_s - \Omega) \quad (9.54)$$

$$\hat{S}^{(-)}(\omega) = \hat{S}^{(+)*}(\omega) \quad (9.55)$$

The phase  $\psi(\omega) = \arg[\hat{S}^{(+)}(\omega)e^{-j\omega\tau}]$  derived from the isolated positive spectral component is

$$\psi(\omega) = \varphi(\omega - \omega_s - \Omega) - \varphi(\omega - \omega_s) - \omega\tau. \quad (9.56)$$

The linear phase  $\omega\tau$  can be subtracted off after independent determination of the time delay  $\tau$ . It is obvious that the spectral shear  $\Omega$  has to be small compared to the spectral bandwidth  $\Delta\omega$  of the pulse, see Fig. 9.23. Then the phase difference in Eq.(9.56) is proportional to the group delay in the pulse, i.e.

$$-\Omega \frac{d\varphi}{d\omega} = \psi(\omega), \quad (9.57)$$

or

$$\varphi(\omega) = -\frac{1}{\Omega} \int_0^\omega \psi(\omega') d\omega'. \quad (9.58)$$

Note, an error  $\Delta\tau$  in the calibration of the time delay  $\tau$  results in an error in the chirp of the pulse

$$\Delta\varphi(\omega) = -\frac{\omega^2}{2\Omega} \Delta\tau. \quad (9.59)$$

Thus it is important to chose a spectral shear  $\Omega$  that is not too small. How small does it need to be? We essentially sample the phase with a sample spacing  $\Omega$ . The Nyquist theorem states that we can uniquely resolve a pulse in the time domain if it is only nonzero over a length  $[-T, T]$ , where  $T = \pi/\Omega$ . On the other side the shear  $\Omega$  has to be large enough so that the fringes in the spectrum can be resolved with the available spectrometer.

### SPIDER Setup

We follow the work of Gallmann et al. [?] that can be used for characterization of pulses only a few optical cycles in duration. The setup is shown in Figure 9.24.



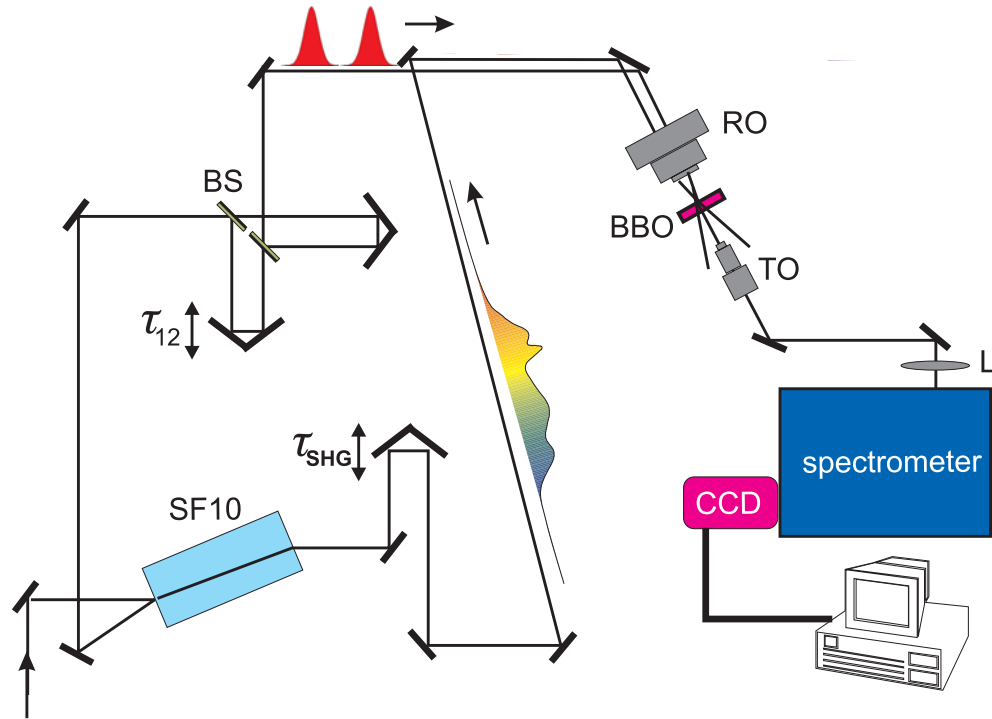


Figure 9.24: SPIDER setup; SF10: 65 mm glass block ( $\text{GDD}/z \approx 160 \text{ fs}^2/\text{mm}$ ), BS: metallic beam splitters ( $\approx 200 \mu\text{m}$ , Cr–Ni coating 100 nm),  $\tau$ : adjustable delay between the unchirped replica,  $\tau_{SHG}$ : delay between unchirped pulses and strongly chirp pulse, RO: reflective objective (Ealing–Coherent, x35, NA=0.5,  $f=5.4 \text{ mm}$ ), TO: refractive objective, L: lens, spectrometer: Lot-Oriel MS260i, grating: 400 l/mm, Blaze-angle 350 nm, CCD: Andor DU420 CCI 010, 1024 x 255 pixels,  $26 \mu\text{m}/\text{pixel}$  [13].

### Generation of two replica without additional chirp:

A Michelson-type interferometer generates two unchirped replicas. The beam-splitters BS have to be broadband, not to distort the pulses. The delay  $\tau$  between the two replica has to be properly chosen, i.e. in the setup shown it was about 400-500 fs corresponding to 120-150  $\mu\text{m}$  distance in space.

**Spectral shearing:**

The spectrally sheared copies of the pulse are generated by sum-frequency generation (SFG) with quasi-monochromatic beams at frequencies  $\omega_s$  and  $\omega_s + \Omega$ . These quasi monochromatic signals are generated by strong chirping of a third replica (cf. Fig. 9.24) of the signal pulse that propagates through a strongly dispersive glass slab. For the current setup we estimate for the broadening of a Gaussian pulse due to the glass dispersion from 5 fs to approximately 6 ps. Such a stretching of more than a factor of thousand assures that SFG occurs within an optical bandwidth less than 1 nm, a quasi-monochromatic signal. Adjustment of the temporal overlap  $\tau_{SHG}$  with the two unchirped replica is possible by a second delay line. The stretched pulse can be computed by propagation of the signal pulse  $E(t)$  through the strongly dispersive medium with transfer characteristic

$$H_{glass}(\omega) = e^{-jD_{glass}(\omega-\omega_c)^2/2} \quad (9.60)$$

neglecting linear group delay and higher order dispersion terms. We obtain for the analytic part of the electric field of the stretched pulse leaving the glass block by convolution with the transfer characteristic

$$\begin{aligned} E_{stretch}(t) &= \int_{-\infty}^{+\infty} \hat{E}(\omega) e^{-jD_{glass}(\omega-\omega_c)^2/2} e^{j\omega t} d\omega = \\ &= e^{jt^2/(2D_{glass})} e^{j\omega_c t} \int_{-\infty}^{+\infty} \hat{E}(\omega) e^{-jD_{glass}((\omega-\omega_c)-t/D_{glass})^2/2} d\omega \end{aligned} \quad (9.61)$$

If the spectrum of the pulse is smooth enough, the stationary phase method can be applied for evaluation of the integral and we obtain

$$E_{stretch}(t) \propto e^{j\omega_c(t+t^2/(2D_{glass}))} \hat{E}(\omega = \omega_c + t/D_{glass}) \quad (9.63)$$

Thus the field strength at the position where the instantaneous frequency is

$$\omega_{inst} = \frac{d}{dt} \omega_c(t + t^2/(2D_{glass})) = \omega_c + t/D_{glass} \quad (9.64)$$

is given by the spectral amplitude at that frequency,  $\hat{E}(\omega = \omega_c + t/D_{glass})$ . For large stretching, i.e.

$$|\tau_p/D_{glass}| \ll |\Omega| \quad (9.65)$$

the up-conversion can be assumed to be quasi monochromatic.

**SFG:**

A BBO crystal (wedged 10–50  $\mu\text{m}$ ) is used for type I phase-matched SFG. Type II phase-matching would allow for higher acceptance bandwidths. The pulses are focused into the BBO-crystal by a reflective objective composed of curved mirrors. The signal is collimated by another objective. Due to SFG with the chirped pulse the spectral shear is related to the delay between both pulses,  $\tau$ , determined by Eq.(9.64) to be

$$\Omega = -\tau/D_{glass}. \quad (9.66)$$

Note, that conditions (9.65) and (9.66) are consistent with the fact that the delay between the two pulses should be much larger than the pulse width  $\tau_p$  which also enables the separation of the spectra in Fig.9.22 to determine the spectral phase using the Fourier transform method. For characterization of sub-10fs pulses a crystal thickness around 30  $\mu\text{m}$  is a good compromise. Efficiency is still high enough for common cooled CCD-cameras, dispersion is already sufficiently low and the phase matching bandwidth large enough.

**Signal detection and phase reconstruction:**

An additional lens focuses the SPIDER signal into a spectrometer with a CCD camera at the exit plane. Data registration and analysis is performed with a computer. The initial search for a SPIDER signal is performed by chopping and Lock-In detection. The chopper wheel is placed in a way that the unchirped pulses are modulated by the external part of the wheel and the chirped pulse by the inner part of the wheel. Outer and inner part have different slit frequencies. A SPIDER signal is then modulated by the difference (and sum) frequency which is discriminated by the Lock-In amplifier. Once a signal is measured, further optimization can be obtained by improving the spatial and temporal overlap of the beams in the BBO-crystal.

One of the advantages of SPIDER is that only the missing phase information is extracted from the measured data. Due to the limited phase-matching bandwidth of the nonlinear crystal and the spectral response of grating and CCD, the fundamental spectrum is not imaged in its original form but rather with reduced intensity in the spectral wings. But as long as the interference fringes are visible any damping in the spectral wings and deformation of the spectrum does not impact the phase reconstruction process the SPIDER

technique delivers the correct information. The SPIDER trace is then generated by detecting the spectral interference of the pulses

$$E_R(t) = E(t)\hat{E}(\omega_s)e^{j\omega_s t} \quad (9.67)$$

$$E_S(t) = E(t - \tau)\hat{E}(\omega_s + \Omega)e^{j(\omega_s + \Omega)t} \quad (9.68)$$

$$E_I(t) = E_R(t) + E_S(t) \quad (9.69)$$

The positive and negative frequency components of the SPIDER trace are then according to Eqs.(9.55)

$$\hat{S}^{(+)}(\omega) = \hat{E}_R^*(\omega)\hat{E}_S(\omega) \quad (9.70)$$

$$= \hat{E}^*(\omega - \omega_s)\hat{E}(\omega - \omega_s - \Omega)\hat{E}^*(\omega_s)\hat{E}(\omega_s - \Omega)$$

$$\hat{S}^{(-)}(\omega) = \hat{S}^{(+)*}(\omega) \quad (9.71)$$

and the phase  $\psi(\omega) = \arg[\hat{S}^{(+)}(\omega)e^{-j\omega\tau}]$  derived from the isolated positive spectral component subtraction already the linear phase offset is

$$\psi(\omega) = \varphi(\omega - \omega_s - \Omega) - \varphi(\omega - \omega_s) + \varphi(\omega_s - \Omega) - \varphi(\omega_s). \quad (9.72)$$

Thus up to an additional constant it delivers the group delay within the pulse to be characterized. A constant group delay is of no physical significance.

### SPIDER-Calibration

This is the most critical part of the SPIDER measurement. There are three quantities to be determined with high accuracy and reproducibility:

- delay  $\tau$
- shift  $\omega_s$
- shear  $\Omega$

#### Delay $\tau$ :

The delay  $\tau$  is the temporal shift between the unchirped pulses. It appears as a frequency dependent phase term in the SPIDER phase, Eqs. (9.56) and leads to an error in the pulse chirp if not properly subtracted out, see Eq.(9.59).

A determination of  $\tau$  should preferentially be done with the pulses detected by the spectrometer but without the spectral shear so that the observed fringes are all exactly spaced by  $1/\tau$ . Such an interferogram may

be obtained by blocking the chirped pulse and overlapping of the individual SHG signals from the two unchirped pulses. A Fourier transform of the interferogram delivers the desired delay  $\tau$ . In practice, this technique might be difficult to use. Experiment and simulation show that already minor changes of  $\tau$  ( $\pm 1$  fs) significantly alter the reconstructed pulse duration ( $\approx \pm 1 - 10\%$ ).

Another way for determination of  $\tau$  is the following. As already mentioned,  $\tau$  is accessible by a differentiation of the SPIDER phase with respect to  $\omega$ . The delay  $\tau$  therefore represents a constant GDD. An improper determination of  $\tau$  is thus equivalent to a false GDD measurement. The real physical GDD of the pulse can be minimized by a simultaneous IAC measurement. Maximum signal level, respectively shortest IAC trace means an average GDD of zero. The pulse duration is then only limited by higher order dispersion not depending on  $\tau$ . After the IAC measurement, the delay  $\tau$  is chosen such that the SPIDER measurement provides the shortest pulse duration. This is justified because through the IAC we know that the pulse duration is only limited by higher order dispersion and not by the  $\text{GDD} \propto \tau$ . The disadvantage of this method is that an additional IAC setup is needed.

#### Shift $\omega_s$ :

The SFG process shifts the original spectrum by a frequency  $\omega_s \approx 300$  THz towards higher frequencies equivalent to about 450 nm when Ti:sapphire pulses are characterized. If the SPIDER setup is well adjusted, the square of the SPIDER interferogram measured by the CCD is similar to the fundamental spectrum. A determination of the shift can be done by correlating both spectra with each other. Determination of  $\omega_s$  only influences the frequency too which we assign a given phase value, which is not as critical.

#### Shear $\Omega$ :

The spectral shear is uncritical and can be estimated by the glass dispersion and the delay  $\tau$ .

### **9.4.3 Characterization of Sub-Two-Cycle Ti:sapphire Laser Pulses**

The setup and the data registration and processing can be optimized such that the SPIDER interferogram and the reconstructed phase, GDD and intensity envelope are displayed on a screen with update rates in the range of 0.5-1s.

Real-time SPIDER measurements enabled the optimization of external

dispersion compensation leading to 4.8 fs pulses directly from a laser [13], see Figure 9.25.

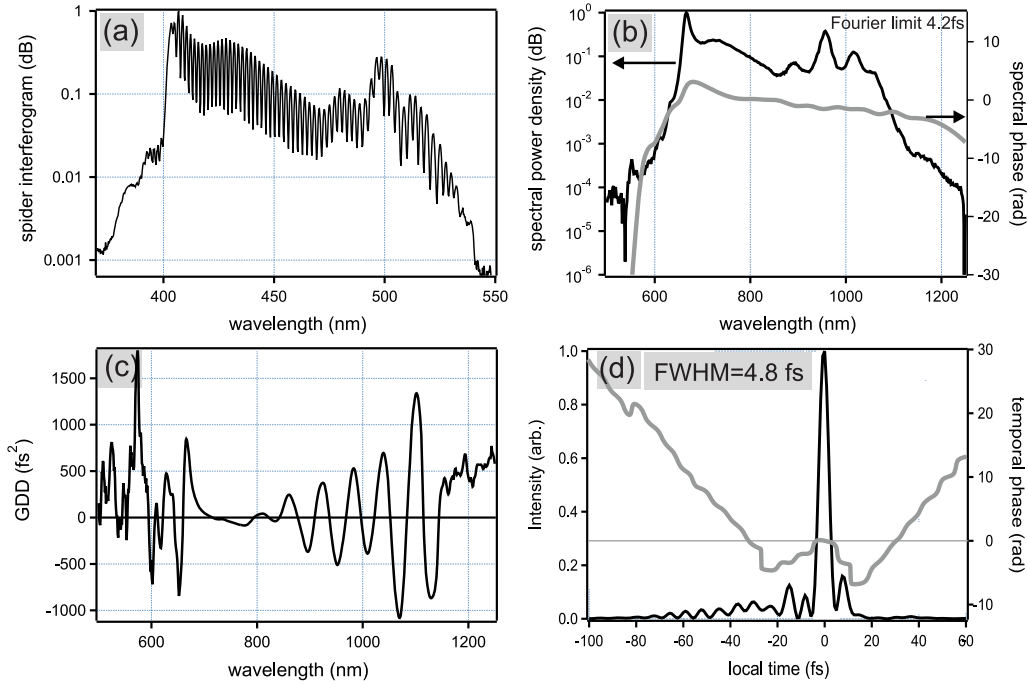


Figure 9.25: SPIDER measurement of a 4.8 fs Ti:sapphire laser pulse. (a) SPIDER interferogram on a logarithmic scale. (b) Spectral power density and spectral phase of the pulse. (c) Calculated GDD of the pulse. (d) Intensity envelope and temporal phase curve [13].

Figure 9.25(a) shows the SPIDER interferogram as detected by the CCD camera. The interferogram is modulated up to 90%, the resolutions limit in the displayed graphic can not resolve this. The large number of interference fringes assures reliable phase calculation. Figure (b) displays the laser spectrum registered by the optical spectrum analyzer on a logarithmic scale. The calculated spectral phase curve is added in this plot. The small slope of the phase curve corresponds to a constant GD which is an unimportant time shift. Fig. 9.25 (c) depicts the GDD obtained from the phase by two derivatives with respect to the angular frequency  $\omega$ . The last Figure (d) shows the

intensity envelope with a FWHM pulse duration of 4.8 fs together with the temporal phase curve.

#### 9.4.4 Pros and Cons of SPIDER

Advantages	Disadvantages
direct analytical phase extraction	complex experimental setup
no moving mirrors or other components	precise delay calibration necessary
possible real-time characterization	"compact" spectrum necessary
	(no zero-intensity intervals)
simple 1-D data acquisition	need for expensive CCD-camera
minor dependence on spectral response	
of nonlinear crystal and spectrometer	

### 9.5 Two-Dimensional Spectral Shearing Interferometry

As in SPIDER, also in two-dimensional spectral shearing interferometry (2DSI) one does upconvert two frequency components at  $\omega$  and  $\omega - \Omega$  of the pulse to a joint frequency, which then depends on the relative phase of the two components  $\phi(\omega) - \phi(\omega - \Omega)$ . In 2DSI, two chirped (quasi-CW) pulse copies are mixed with the short pulse to be measured in a type II phase matched BBO crystal, see Fig. 9.26. [14]. As we will see, this technique does not suffer from the calibration sensitivities of SPIDER nor the bandwidth limitations of FROG or interferometric autocorrelation (IAC). The advantage of type II upconversion with BBO is that the phase matching bandwidth is large in one axis (well over an octave) and small in the other, a perfect match for single-cycle pulse characterization. Furthermore, self-referenced frequency shifting roughly halves the relative bandwidth of the final signal allowing the measurement of pulses spanning 2 octaves from 650 nm to 2600 nm.

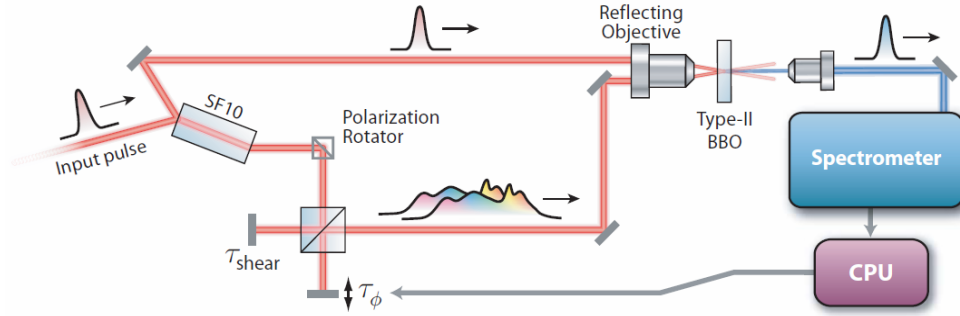


Figure 9.26: Setup for two-dimensional spectral shearing interferometry.

The two up-converted pulses are sheared spectrally, but are collinear forming a single pulse in time. The phase of one of the up-converted pulses is scanned over several cycles by vibrating the corresponding mirror in the interferometer over a few microns. The spectrum of the up-converted signal is recorded as a function of phase delay and wavelength, yielding a 2-D intensity function, see Fig. 9.27 (a) for a 5fs pulse and (b) for the same pulse propagated through 1 mm of fused quartz.

Since only the relative fringe phase matters, the delay scan does not need to be calibrated in any way, the only required calibration is for the shear a relatively insensitive parameter as discussed already before. The intensity of the upconverted signal is

$$I(\omega, \tau_{cw}) = |A(\omega)|^2 + |A(\omega - \Omega)|^2 + |A(\omega)|^2 + 2A(\omega)A(\omega - \Omega) \cos[\omega_{cw}\tau_{cw} + \phi(\omega) - \phi(\omega - \Omega)],$$

where

$$\phi(\omega) - \phi(\omega - \Omega) = \tau_{cw} \Omega + O[\Omega^2].$$

Fig. 9.27 (c) and (d), shows the spectrum of the pulse along with the extracted spectral group delays. The chirp introduced by the glass plate is reflected in the measurement with high precision demonstrating the high quality of pulse reconstruction achieved with this method. Fig. 9.28 shows the directly measured interferometric autocorrelation trace of a 5 fs pulse together with the computed trace using the reconstructed electric field of the pulse measured with 2DSI. The two traces agree very well with each other.



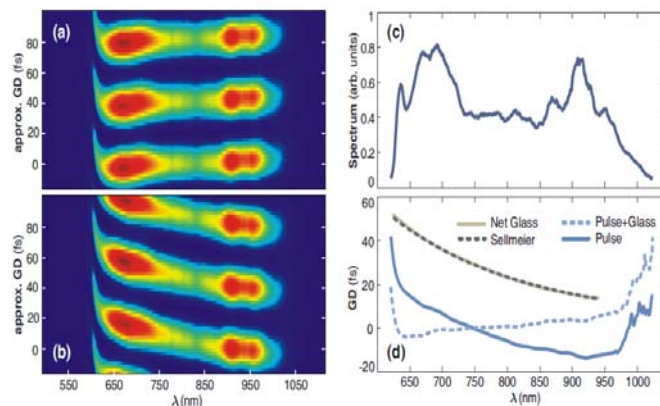


Figure 9.27: Raw 2DSI data from (a) a 5 fs laser pulse and (b) a pulse dispersed by 1 mm of fused silica. The spectrum is shown in (c) with the extracted group delay (GD) curves shown in (d) alongside the measured and Sellmeier-derived glass group delay.

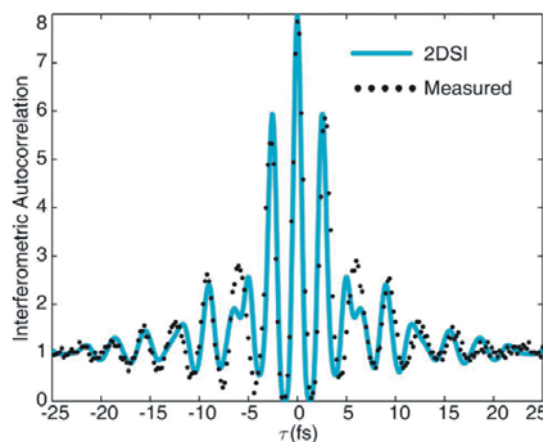


Figure 9.28: Calculated interferometric autocorrelation trace from the reconstructed electric field using 2DSI and directly measured interferometric autocorrelation of a 5 fs pulse.

# Bibliography

- [1] K. Naganuma, K. Mogi, H. Yamada, "General method for ultrashort light pulse chirp measurement," IEEE J. of Quant. Elec. **25**, 1225 - 1233 (1989).
- [2] J. C. Diels, J. J. Fontaine, and F. Simoni, "Phase Sensitive Measurement of Femtosecond Laser Pulses From a Ring Cavity," in Proceedings of the International Conf. on Lasers. 1983, STS Press: McLean, VA, p. 348-355. J. C. Diels et al., "Control and measurement of Ultrashort Pulse Shapes (in Amplitude and Phase) with Femtosecond Accuracy," Applied Optics **24**, 1270-82 (1985).
- [3] J.W. Nicholson, J. Jasapara, W. Rudolph, F.G. Ometto and A.J. Taylor, "Full-field characterization of femtosecond pulses by spectrum and cross-correlation measurements, "Opt. Lett. **24**, 1774 (1999).
- [4] D. T. Reid, et al., Opt. Lett. **22**, 233-235 (1997).
- [5] R. Trebino, "Frequency-Resolved Optical Gating: the Measurement of Ultrashort Laser Pulses," Kluwer Academic Press, Boston, (2000).
- [6] Trebino, et al., Rev. Sci. Instr., 68, 3277 (1997).
- [7] Kane and Trebino, Opt. Lett., 18, 823 (1993).
- [8] Stark, Image Recovery, Academic Press, 1987.
- [9] L. Cohen, "Time-frequency distributions-a review, " Proceedings of the IEEE, **77**, 941 - 981 (1989).

- [10] L. Gallmann, D. H. Sutter, N. Matuschek, G. Steinmeyer and U. Keller, "Characterization of sub-6fs optical pulses with spectral phase interferometry for direct electric-field reconstruction," *Opt. Lett.* **24**, 1314 (1999).
- [11] C. Iaconis and I. A. Walmsley, Self-Referencing Spectral Interferometry for Measuring Ultrashort Optical Pulses, *IEEE J. of Quant. Elec.* **35**, 501 (1999).
- [12] C. Froehly, A. Lacourt, J. C. Vienot, "Notions de reponse impulsionnelle et de fonction de tranfert temporelles des pupilles optiques, justifications experimentales et applications," *Nouv. Rev. Optique* 4, **18** (1973).
- [13] Richard Ell, "Sub-Two Cycle Ti:sapphire Laser and Phase Sensitive Nonlinear Optics," PhD-Thesis, University of Karlsruhe (TH), (2003).
- [14] J.R. Birge, R. Ell, and F. X. Kärtner, "Two-dimensional spectral shearing interferometry for few-cycle pulse characterization," *Optics Letters* **31**, 2063 (2006).

## Chapter 10

# Femtosecond Laser Frequency Combs

So far we only considered the deterministic steady state pulse formation in ultrashort pulse laser systems due to the most important pulse shaping mechanisms prevailing in today's femtosecond lasers. Due to the recent interest in using modelocked lasers for frequency metrology and high-resolution laser spectroscopy as well as phase sensitive nonlinear optics the noise and tuning properties of mode combs emitted by modelocked lasers is of much current interest. Soliton-perturbation theory is well suited to successfully predict the noise behavior of many solid-state and fiber laser systems [1] as well as changes in group- and phase velocity in modelocked lasers due to intracavity nonlinear effects [5]. We start off by reconsidering the derivation of the master equation for describing the pulse shaping effects in a mode-locked laser. We assume that in steady-state the laser generates at some position  $z = 0$  (for example at the point of the output coupler) inside the laser a sequence of pulses with the envelope  $a(T = mT_R, t)$ . These envelopes are the solutions of the corresponding master equation, where the dynamics per roundtrip is described on a slow time scale  $T = mT_R$ . Then the pulse train emitted from the laser including the carrier is

$$A(t) = \sum_{m=-\infty}^{+\infty} a(T = mT_R, t) e^{j\left[\omega_c\left(t - \frac{1}{v_p}2mL\right)\right]} \quad (10.1)$$

$$= \sum_{m=-\infty}^{+\infty} a(T = mT_R, t) e^{j\left[\omega_c\left(t - mT_R + \left(\frac{1}{v_g} - \frac{1}{v_p}\right)2mL\right)\right]} \quad (10.2)$$

with repetition rate  $f_R = 1/T_R = v_g/2L$  and center frequency  $\omega_c$ . Both the repetition rate and the carrier frequency are in general subject to slow drifts due to mirror vibrations, changes in intracavity pulse energy that might be further converted into phase and group velocity changes. Note, the center frequency and repetition rate are only defined for times long compared to the roundtrip time in the laser. Usually, they only change on a time scale three orders of magnitude slower than the expectation value of the repetition rate.

## 10.1 The Mode Comb

Lets suppose the pulse envelope, repetition rate, and center frequency have approached there stationary values and any perturbations and noise are absent. Then the corresponding time domain signal is sketched in Figure 10.1.

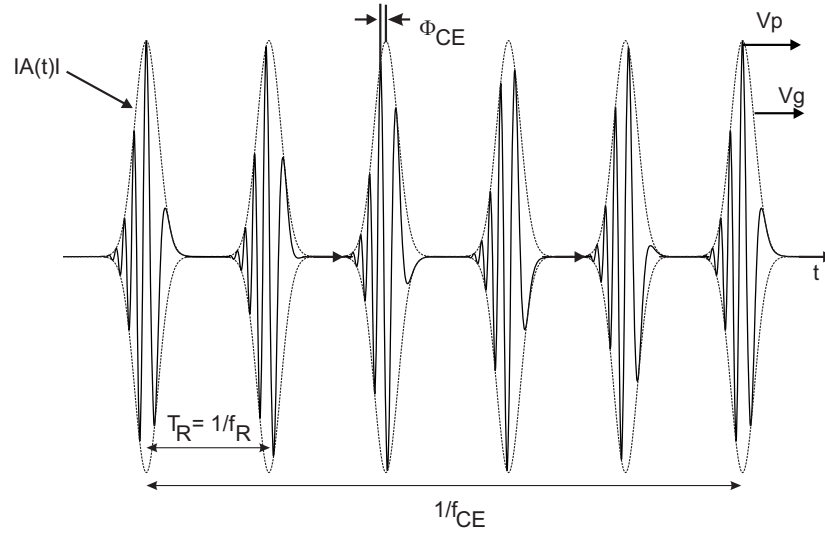


Figure 10.1: Pulse train emitted from a noise free mode-locked laser. The pulses can have chirp. The intensity envelope repeats itself with repetition rate  $f_R$ . The electric field is only periodic with the rate  $f_{CE}$  if it is related to the repetition rate by a rational number.

The pulse  $a(T = mT_R, t)$  is the steady state solution of the master equation describing the laser system, as studied in chapter 6. Let's assume that the steady state solution is a soliton

$$a(t, T) = a_s(t) e^{-j\phi_0 \frac{T}{T_R}} \quad (10.3)$$

with

$$a_s(t) = A_0 \operatorname{sech}\left(\frac{t - t_0}{\tau}\right) \quad (10.4)$$

and the soliton phase shift

$$\phi_0 = \frac{1}{2} \delta A_0^2 = \frac{|D|}{\tau^2} \quad (10.5)$$

Thus, there is a carrier envelope phase shift  $\Delta\phi_{CE}$  from pulse to pulse due to dispersion and self-phase modulation is given by

$$\begin{aligned} \Delta\phi_{CE, dispSPM} &= \omega_c \left( \frac{1}{v_g} - \frac{1}{v_p} \right) \Big|_{\omega_c} 2L - \phi_0 + \operatorname{mod}(2\pi) \\ &= \omega_c T_R \left( 1 - \frac{v_g}{v_p} \right) - \phi_0 + \operatorname{mod}(2\pi) \end{aligned} \quad (10.6)$$

The full expression for the laser electric field Eq.(10.2) is then, where we keep the carrier-envelop phase shift  $\Delta\phi_{CE}$  at the moment open to eventually acquired additional contributions from other nonlinear processes and not just the contribution due to dispersion and self-phase modulation

$$A(t) = \sum_{m=-\infty}^{+\infty} a_s(t - mT_R) e^{j[\omega_c(t - mT_R) + m\Delta\phi_{CE}]} \quad (10.7)$$

The Fourier transform of the unperturbed pulse train is

$$\begin{aligned} \hat{A}(\omega) &= \hat{a}_s(\omega - \omega_c) \sum_{m=-\infty}^{+\infty} e^{j(\Delta\phi_{CE} - \omega T_R)m} \\ &= \hat{a}_s(\omega - \omega_c) \sum_{m=-\infty}^{+\infty} e^{jmT_R \left( \frac{\Delta\phi_{CE}}{T_R} - \omega \right)} \\ &= \hat{a}_s(\omega - \omega_c) \frac{2\pi}{T_R} \sum_{n=-\infty}^{+\infty} \delta \left( \omega - \left( \frac{\Delta\phi_{CE}}{T_R} + n\omega_R \right) \right). \end{aligned} \quad (10.8)$$

which is shown in Figure 10.2. Note, that here we used the identity for a  $\delta$ -comb in time and frequency domain

$$\sum_{m=-\infty}^{+\infty} e^{jm2\pi x} = \sum_{n=-\infty}^{+\infty} \delta(x - 2\pi n). \quad (10.9)$$

Each comb line is shifted by the carrier-envelope offset frequency  $f_{CE} = \frac{\Delta\phi_{CE}}{2\pi T_R}$  from the origin

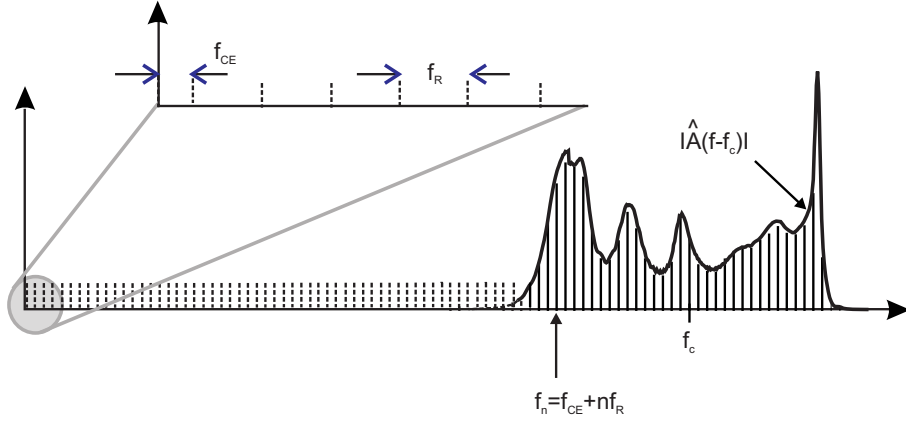


Figure 10.2: Optical mode comb of a mode-locked laser output.

To obtain self-consistent equations for variations in repetition rate and center frequency and the other pulse parameters due to intracavity power fluctuations and noise, we employ soliton-perturbation theory. This is for example justified for the case of fast saturable absorber modelocking in the negative dispersion region, where the steady state pulse is close to a soliton as discussed in chapter 6, especially, when the ratio of gain filtering to dispersion is equal to the ratio of SAM action to self-phase modulation, see Eq. (6.61). Then the steady state solution of the master equation is a soliton-like pulse, stabilized by the irreversible dynamics and subject to additional perturbations due to the environment and noise

$$\begin{aligned} T_R \frac{\partial}{\partial T} a &= jD \frac{\partial^2}{\partial t^2} a - j\delta |a|^2 a \\ &+ (g - l)a + D_f \frac{\partial^2}{\partial t^2} a + \gamma |a|^2 a + L_{\text{pert}} \end{aligned} \quad (10.10)$$

Due to the irreversible processes and the perturbations, the solution to (10.10) is a soliton like pulse with perturbations in amplitude, phase, frequency and timing plus some continuum

$$a(t, T) = [a_s(t, T) + a_c(T, t)] e^{-j\phi_o T/T_R} e^{j\Delta p(T)t} e^{-j\Delta\theta} \quad (10.11)$$

with pulse energy  $w_0 = 2A_o^2\tau$ .

The perturbations cause fluctuations in amplitude, phase, center frequency and timing of the soliton and generate background radiation, i.e. continuum

$$\begin{aligned} \Delta A(T, t) = & \Delta w(T) f_w(t) + \Delta\theta(T) f_\theta(t) + \Delta p(T) f_p(t) \\ & + \Delta t(T) f_t(t) + a_c(T, t). \end{aligned} \quad (10.12)$$

where, we rewrote the amplitude perturbation as an energy perturbation. Note, that the  $f_i$  correspond to the first component of the vector in Eqs.(3.23) - (3.26). The dynamics of the pulse parameters due to the perturbed Nonlinear Schrödinger Equation (10.10) can be projected out from the perturbation using the adjoint basis  $\bar{f}_i^*$  corresponding to the first component of the vector in Eqs.(3.45) - (3.48) and the new orthogonality relation, see Chapter 3.5.

$$\text{Re} \left\{ \int_{-\infty}^{+\infty} \bar{f}_i^*(t) f_j(t) dt \right\} = \delta_{i,j}. \quad (10.13)$$

We obtain

$$\frac{\partial}{\partial T} \Delta w = -\frac{1}{\tau_w} \Delta w + \frac{1}{T_R} \text{Re} \left\{ \int_{-\infty}^{+\infty} \bar{f}_w^*(t) L_{\text{pert}}(T, t) dt \right\} \quad (10.14)$$

$$\frac{\partial}{\partial T} \Delta\theta(T) = \frac{2\phi_o}{T_R} \frac{\Delta w}{w_o} + \frac{1}{T_R} \text{Re} \left\{ \int_{-\infty}^{+\infty} \bar{f}_\theta^*(t) L_{\text{pert}}(T, t) dt \right\} \quad (10.15)$$

$$\frac{\partial}{\partial T} \Delta p(T) = -\frac{1}{\tau_p} \Delta p + \frac{1}{T_R} \text{Re} \left\{ \int_{-\infty}^{+\infty} \bar{f}_p^*(t) L_{\text{pert}}(T, t) dt \right\} \quad (10.16)$$

$$\frac{\partial}{\partial T} \Delta t = \frac{-2|D|}{T_R} \Delta p + \frac{1}{T_R} \text{Re} \left\{ \int_{-\infty}^{+\infty} \bar{f}_t^*(t) L_{\text{pert}}(T, t) dt \right\} \quad (10.17)$$

Note, that the irreversible dynamics does couple back the generated continuum to the soliton parameters. Here, we assume that this coupling is small



and neglect it in the following, see [1]. Due to gain saturation, gain filtering and saturable absorber action, the pulse energy and center frequency fluctuations are damped with normalized decay constants

$$\frac{1}{\tau_w} = (2g_d - 2\gamma A_o^2), \quad (10.18)$$

$$\frac{1}{\tau_p} = \frac{4}{3} \frac{g_s}{\Omega_g^2 \tau^2} \frac{1}{T_R}. \quad (10.19)$$

These perturbation equations and time constants can be derived similar to the case of active modelocking with soliton formation as treated in section 5.5, one only needs to replace the active modelocker by the saturable absorber. Here,  $g_s$  is the saturated gain and  $g_d$  is related to the differential gain by

$$g_s = \frac{g_o}{1 + \frac{w_o}{P_L T_R}} \quad (10.20)$$

$$g_d = \frac{dg_s}{dw_o} \cdot w_o \quad (10.21)$$

Note, in this model we assumed that the gain instantaneously follows the intracavity average power or pulse energy, which is not true in general. However, it is straight forward to include the relaxation of the gain by adding a dynamical gain model to the perturbation equations. For simplicity we shall neglect this here. Since the system is autonomous, there is no retiming and rephasing in the free running system.

## 10.2 Group- and Phase Velocity of Solitons

The Kerr-effect leads to a change of phase velocity of the pulse, resulting in the self-phase shift of the soliton,  $\phi_o$ , per round-trip. A change in group velocity does not appear explicitly in the solution of the NLSE. However, there should be an additional term added in the NLSE that also stems from the Kerr-effect and is called self-steepening. Here, we treat it as perturbation to the NLSE, (10.10)

$$L_{\text{pert}} = -\frac{\delta}{\omega_c} \frac{\partial}{\partial t} (|a(T, t)|^2 a(T, t)). \quad (10.22)$$

Usually the impact of this term on the pulse shape is small on the order of

$$\frac{1}{\omega_c \tau} = \frac{T_0}{2\pi \tau},$$

and, therefore, is only important for few-cycle pulses. However, it turns out that this term alters the group velocity of the soliton like pulse as much or as it turns out even twice as much as the nonlinear phase shift changes the phase velocity of the soliton-like pulse. We take this term into account in the form of a perturbation. This perturbation term is odd and real and therefore only leads to a timing shift in the soliton-like pulse, when substituted into Eq.(10.10).

$$T_R \frac{\partial \Delta t(T)}{\partial T} \Big|_{sst} = -\frac{\delta}{\omega_c} A_0^3 \operatorname{Re} \left\{ \int_{-\infty}^{+\infty} \bar{f}_t^*(t) \frac{\partial}{\partial t} \left( \sec h^3 \left( \frac{t}{\tau} \right) \right) dt \right\} \quad (10.23)$$

$$= \frac{\delta}{\omega_c} A_0^2 = \frac{2\phi_0}{\omega_c}. \quad (10.24)$$

This timing shift or group delay per round-trip, together with the nonlinear phase shift of the soliton leads to a phase change between carrier and envelope per roundtrip due to the Kerr effect in total given by

$$\Delta \phi_{CE,Kerr} = -\phi_0 + \omega_c T_R \frac{\partial}{\partial T} \Delta t(T) \Big|_{selfsteep} = -\frac{1}{2} \delta A_0^2 + \delta A_0^2 = \frac{1}{2} \delta A_0^2. \quad (10.25)$$

The compound effect of this phase delay per round-trip in the carrier versus envelope leads to a carrier-envelope frequency

$$f_{CE,Kerr} = \frac{\Delta \phi_{CE,Kerr}}{2\pi} f_R = \frac{\phi_0}{2\pi} f_R. \quad (10.26)$$

The group delay also changes the optical cavity length of the laser and therefore alters the repetition rate according to

$$\Delta f_R = -f_R^2 \Delta t(T) \Big|_{selfsteep} = -2\phi_0 \frac{f_R}{\omega_c} f_R = -\frac{2}{m_0} f_{CE}, \quad (10.27)$$

where  $m_0$  is the mode number of the carrier wave. Eq.(10.8), together with the linear and nonlinear contributions to the carrier-envelope frequency according to Eqs.(10.6), (10.26) and (10.27) determine the location of the m-th

line of the optical comb  $f_m = f_{CE} + mf_R$  with the total carrier-envelope frequency

$$\begin{aligned} f_{CE} &= \frac{\Delta\phi_{CE,disp} + \Delta\phi_{CE,Kerr}}{2\pi} f_R \\ &= \omega_c \left(1 - \frac{v_g}{v_p}\right) + \frac{\phi_0}{2\pi} f_R + \text{mod}(f_R) \end{aligned} \quad (10.28)$$

The shift in  $f_{CE}$  due to an intracavity pulse energy modulation and a change in cavity length is then

$$\Delta f_m = \Delta f_{CE,Kerr} + m\Delta f_R = f_{CE} \left(1 - \frac{2m}{m_0}\right) \frac{\Delta w}{w_0} - mf_R \frac{\Delta L}{L_0}. \quad (10.29)$$

Specifically, Eq. (10.29) predicts, that the mode with number  $m = m_0/2$ , i.e. the mode at half the center frequency, does not change its frequency as a function of intracavity pulse energy. Of course, one has to remember, that this model is so far based on self-phase modulation and self-steepening as the cause of a power dependent carrier-envelope offset frequency. There may be other mechanisms that cause a power dependent carrier envelope offset frequency. One such effect is the group delay caused by the laser gain medium another one is the carrier-envelope phase change due to a change in carrier frequency, which gives most likely a very strong additional dependence on pump power. Nevertheless, the formula (10.29) can be used for the control of the optical frequency comb of a femtosecond laser by controlling the cavity length and the intracavity pulse energy, via the pump power.

### 10.3 Femtosecond Laser Frequency Combs

Nevertheless, the formula (10.29) can be used for the control of the optical frequency comb of a femtosecond laser by controlling the cavity length and the intracavity pulse energy, via the pump power. According to Fig. 10.2 every line of the optical comb determined by

$$f_m = f_{CE} + mf_R. \quad (10.30)$$

Note, if the femtosecond laser emits a spectrum covering more than one octave, then one can frequency double part of the comb at low frequencies and beat it with the corresponding high frequency part of the comb on a

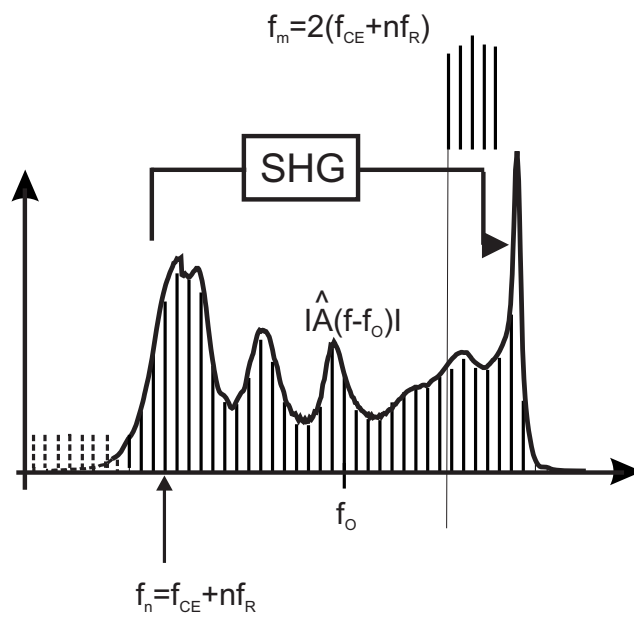


Figure 10.3:  $f$ -to- $2f$  interferometry to determine the carrier-envelope offset frequency.

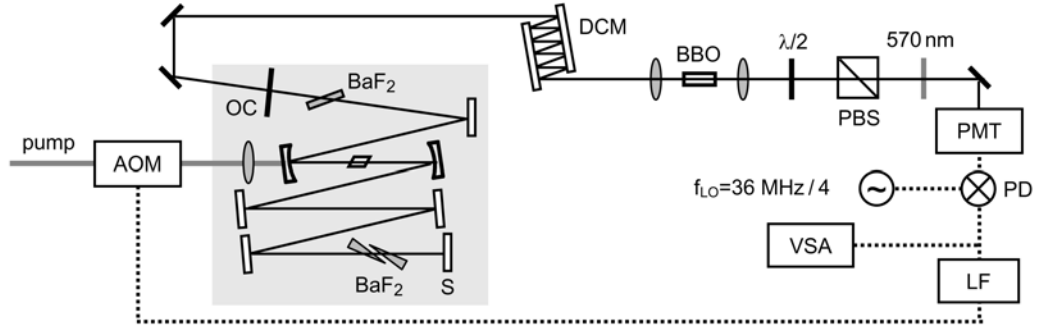


Figure 10.4: Carrier-envelope phase stabilized 200 MHz octave-spanning Ti:sapphire laser. The femtosecond laser itself is located inside the grey area. AOM, acousto-optical modulator; S, silver end mirror; OC, output coupling mirror; PBS, polarizing beam splitter cube; PMT, photomultiplier tube; PD, digital phase detector; LF, loop filter; VSA, vector signal analyzer. The carrier-envelope frequency is phase locked to 36 MHz.

photo detector, see Fig. 10.3. The result is a photodetector beat signal that consists of discrete lines at the beat frequencies

$$f_k = kf_R \pm f_{CE} \quad (10.31)$$

This method for determining the carrier-envelope offset frequency is called f-to-2f interferometry. The carrier-envelope offset frequency can be extracted with filters and synchronized to a local oscillator or to a fraction of the repetition rate of the laser, for example  $f_R/4$ .

Figure 10.4 shows the setup of an octave spanning 200 MHz Ti:sapphire laser where the carrier envelope offset frequency  $f_{CE}$  is locked to a local oscillator at 36 MHz using the f-to-2f self-referencing method [6]

The spectral output of this laser is shown in Figure 10.5. The spectral components at 1140 nm are properly delayed in a chirped mirror delay line against the spectral components at 570 nm. The 1140 nm range is frequency doubled in a 1 mm BBO-crystal and the frequency doubled light together with the fundamental at 570 nm is projected into the same polarization via a polarizing beam splitter. The signal is then filtered through a 10 nm wide filter and detected with a photomultiplier tube (PMT). A typical signal from the PMT is shown in Figure 10.6. Phase locking is achieved by a phase-locked loop (PLL)

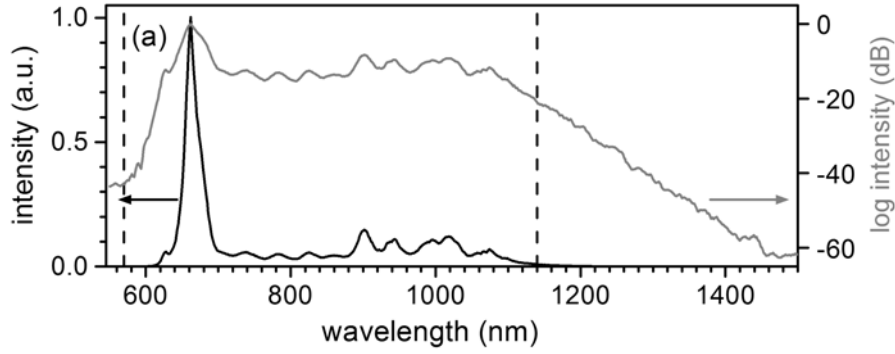


Figure 10.5: Output spectrum of the Ti:sapphire laser on a linear (black curve) and on a logarithmic scale (grey curve). The wavelengths 570 and 1140 nm used for self-referencing are indicated by two dashed lines.

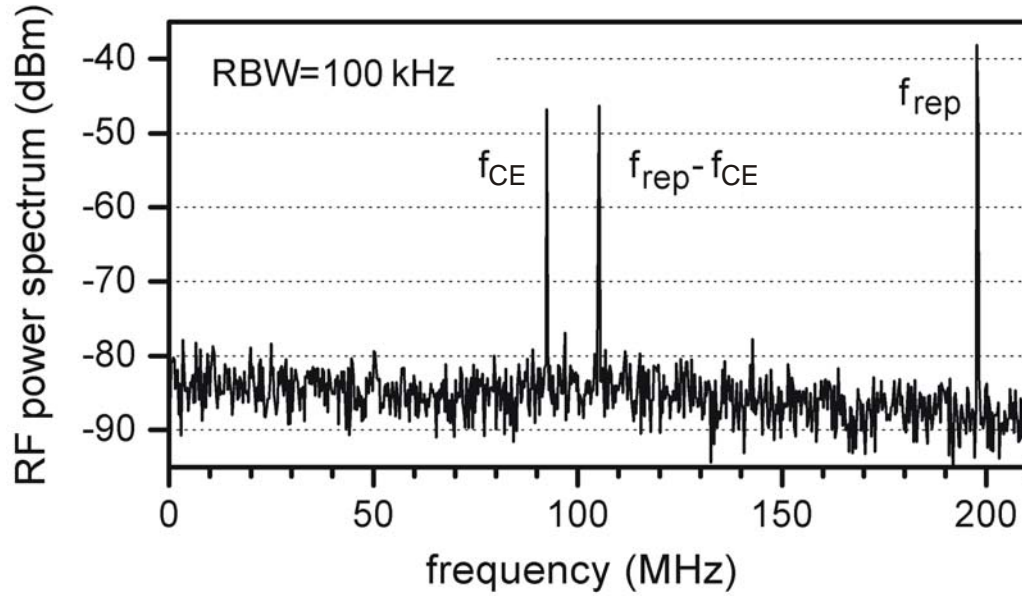


Figure 10.6: Radio-frequency power spectrum measured with a 100 kHz resolution bandwidth (RBW). The peak at the carrier-envelope frequency offset frequency exhibits a signal-to-noise ratio of  $\sim 35$  dB.

by feeding the error signal from a phase detector (mixer or digital phase detector) to an AOM placed in the pump beam (see Fig. 10.4) which modulates the pump power, which in turn changes the intracavity pulse energy, and thus changes the carrier-envelope frequency via Eq.(10.29). A bandpass filter is used to select the carrier-envelope beat signal at 170 MHz. This signal is amplified, in the case here, divided by 16 in frequency, and compared with a reference frequency  $f_{LO}$  supplied by a signal generator (Agilent 33250A) with the phase detector. The division of the carrier-envelope beat signal by 16 is to enhance the locking range of the PLL. The phase detector acts as a frequency discriminator when the loop is open, the output is thus the difference frequency between the carrier-envelope frequency and the designated locking frequency. The output signal is amplified in the loop filter, which in our case is a proportional and integral controller, and fed back to the AOM, closing the loop. The output of the phase detector is proportional to the remaining jitter between the carrier-envelope phase evolution and the local oscillator reduced by the division ratio 16. The power spectral density (PSD) of the carrier-envelope phase fluctuations are measured with a low frequency spectrum analyzer, in this case a vector signal analyzer (VSA) at the output of the phase detector. After proper rescaling by the division factor the phase error PSD is shown in Fig. 10.7. The measurement was taken in steps with an equal amount of points per decade. The PSD of the carrier-envelope phase fluctuations can be integrated to obtain the total phase error. In the range above 1 MHz (see Fig. 10.7), the accuracy of this measurement is limited by the noise floor of the vector signal analyzer. Here, an integrated carrier-envelope phase jitter of about 0.1 radian over the measured frequency range is obtained. The major contribution to the phase noise comes from low frequency fluctuations around 10-50 kHz, where the gain of the loop is not yet high enough. If in addition to the carrier-envelope frequency also the repetition rate of the laser is locked to a frequency standard, such as for example a Cesium clock, the femtosecond laser frequency comb in the optical domain is completely determined with microwave precision and can be used for optical frequency measurements [6].

## 10.4 Noise in Mode-Locked Lasers

Within the soliton perturbation theory framework the response of the laser to noise can be easily included. All we need to do is assume know an additional

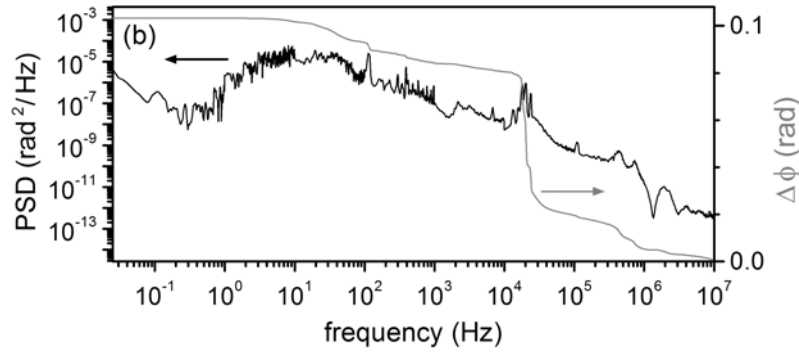


Figure 10.7: Carrier-envelope phase noise power spectral density (left) and integrated phase jitter (right) resulting in only 45 as accumulated carrier-envelope timing jitter.

perturbation in the master equation (10.10) that describes the stochastic impact of the noise sources in our system. In fact, there are many noise sources, most importantly noise of the pump laser, acoustics, i.e. mirror vibrations, air currents, if the laser is not properly covered and so on. However, even if one eliminates all these technical noise sources by careful design and control there is a fundamental noise source left over that ensures that quantum mechanical uncertainty relations are not violated, see [1]. Without going to much into detail these fundamental noise sources are due to the losses and the gain compensating the losses in the laser, which necessitates the introduction of fluctuations (noise) into the system via the dissipation-fluctuation theorem, which has a quantum mechanical analogon. From such considerations follows that the amplifier causes spontaneous emission noise due to the amplifying medium described by a saturated gain  $g_s$ . This leads to additive white noise in the perturbed master equation (10.10) with  $L_{\text{pert}} = \xi(t, T)$ , where  $\xi$  is a white Gaussian noise source with autocorrelation function

$$\langle \xi(t', T') \xi(t, T) \rangle = T_R^2 P_n \delta(t - t') \delta(T - T') \quad (10.32)$$

where the spontaneous emission noise energy  $P_n \cdot T_R$  with

$$P_n = \Theta \frac{2g_s}{T_R} \hbar \omega_c = \Theta \frac{\hbar \omega_c}{\tau_{ph}} \quad (10.33)$$

is added to the pulse within each roundtrip in the laser. Note, the factor  $\Theta > 1$  is called excess noise factor and describes how much worth the noise



performance of a real amplifier is in contrast to an ideal amplifier with gain  $g_s$ . The factor of 2 in eq.(10.33) comes from the fact that both gain and loss, which are equal for a steady state laser cause equal amounts of loss, because both result from coupling of the field to a reservoir. In the case of the gain, this is the amplifier medium in the case of loss this is the coupling of the resonator modes to the outside world, for example via the output coupler.  $\tau_{ph} = \frac{2g_s}{T_R} \sim \frac{2l}{T_R}$  is the cavity decay time or photon lifetime in the cavity. Note, that the noise is approximated by white noise, i.e. uncorrelated noise on both time scales  $t, T$ . The noise between different round-trips is certainly uncorrelated. However, white noise on the fast time scale  $t$ , assumes a flat gain, which is an approximation. By projecting out the equations of motion for the pulse parameters in the presence of this noise according to (10.12)–(10.17), we obtain the additional noise sources which are driving the energy, center frequency, timing and phase fluctuations in the mode-locked laser

$$\frac{\partial}{\partial T} \Delta w = -\frac{1}{\tau_w} \Delta w + S_w(T), \quad (10.34)$$

$$\frac{\partial}{\partial T} \Delta \theta(T) = \frac{2\phi_o}{T_R} \frac{\Delta w}{w_o} + S_\theta(T), \quad (10.35)$$

$$\frac{\partial}{\partial T} \Delta p(T) = -\frac{1}{\tau_p} \Delta p + S_p(T), \quad (10.36)$$

$$\frac{\partial}{\partial T} \Delta t = \frac{-2|D|}{T_R} \Delta p + S_t(T), \quad (10.37)$$

with

$$S_w(T) = \frac{1}{T_R} \text{Re} \left\{ \int_{-\infty}^{+\infty} \bar{f}_w^*(t) \xi(T, t) dt \right\}, \quad (10.38)$$

$$S_\theta(T) = \frac{1}{T_R} \text{Re} \left\{ \int_{-\infty}^{+\infty} \bar{f}_\theta^*(t) \xi(T, t) dt \right\}, \quad (10.39)$$

$$S_p(T) = \frac{1}{T_R} \text{Re} \left\{ \int_{-\infty}^{+\infty} \bar{f}_p^*(t) \xi(T, t) dt \right\}, \quad (10.40)$$

$$S_t(T) = \frac{1}{T_R} \text{Re} \left\{ \int_{-\infty}^{+\infty} \bar{f}_t^*(t) \xi(T, t) dt \right\}. \quad (10.41)$$

The new reduced noise sources obey the correlation functions

$$\langle S_w(T')S_w(T) \rangle = \frac{P_n}{4w_0}\delta(T - T'), \quad (10.42)$$

$$\langle S_\theta(T')S_\theta(T) \rangle = \frac{4}{3} \left(1 + \frac{\pi^2}{12}\right) \frac{P_n}{w_o}\delta(T - T'), \quad (10.43)$$

$$\langle S_p(T')S_p(T) \rangle = \frac{4}{3} \frac{P_n}{w_o}\delta(T - T'), \quad (10.44)$$

$$\langle S_t(T')S_t(T) \rangle = \frac{\pi^2}{3} \frac{P_n}{w_o}\delta(T - T'), \quad (10.45)$$

$$\langle S_i(T')S_j(T) \rangle = 0 \text{ for } i \neq j. \quad (10.46)$$

The power spectra of amplitude, phase, frequency and timing fluctuations are defined via the Fourier transforms of the autocorrelation functions

$$|\Delta\hat{w}(\Omega)|^2 = \int_{-\infty}^{+\infty} \langle \Delta\hat{w}(T + \tau)\Delta\hat{w}(T) \rangle e^{-j\Omega\tau} d\tau, \text{ etc.} \quad (10.47)$$

After a short calculation, the power spectra due to amplifier noise are

$$\left| \frac{\Delta\hat{w}(\Omega)}{w_o} \right|^2 = \frac{4}{1/\tau_w^2 + \Omega^2} \frac{P_n}{w_o}, \quad (10.48)$$

$$|\Delta\hat{\theta}(\Omega)|^2 = \frac{1}{\Omega^2} \left[ \frac{4}{3} \left(1 + \frac{\pi^2}{12}\right) \frac{P_n}{w_o} + \frac{16}{(1/\tau_p^2 + \Omega^2)} \frac{\phi_o^2}{T_R^2} \frac{P_n}{w_o} \right], \quad (10.49)$$

$$|\Delta\hat{p}(\Omega)\tau|^2 = \frac{1}{1/\tau_p^2 + \Omega^2} \frac{4}{3} \frac{P_n}{w_o}, \quad (10.50)$$

$$\left| \frac{\Delta\hat{t}(\Omega)}{\tau} \right|^2 = \frac{1}{\Omega^2} \left[ \frac{\pi^2}{3} \frac{P_n}{w_o} + \frac{1}{(1/\tau_p^2 + \Omega^2)} \frac{4}{3} \frac{|D|^2}{T_R^2 \tau^4} \frac{P_n}{w_o} \right]. \quad (10.51)$$

These equations indicate, that energy and center frequency fluctuations become stationary with mean square fluctuations

$$\left\langle \left( \frac{\Delta w}{w_o} \right)^2 \right\rangle = 2 \frac{P_n \tau_w}{w_o} \quad (10.52)$$

$$\langle (\Delta p \tau)^2 \rangle = \frac{2}{3} \frac{P_n \tau_p}{w_o} \quad (10.53)$$

whereas the phase and timing undergo a random walk with variances

$$\begin{aligned} \sigma_\theta^2(T) &= \langle (\Delta\theta(T) - \Delta\theta(0))^2 \rangle = \frac{4}{3} \left( 1 + \frac{\pi^2}{12} \right) \frac{P_n}{w_o} |T| \\ &\quad + 16 \frac{\phi_o^2}{T_R^2} \frac{P_n}{w_o} \tau_w^3 \left( \exp \left[ -\frac{|T|}{\tau_w} \right] - 1 + \frac{|T|}{\tau_w} \right) \end{aligned} \quad (10.54)$$

$$\begin{aligned} \sigma_t^2(T) &= \left\langle \left( \frac{\Delta t(T) - \Delta t(0)}{\tau} \right)^2 \right\rangle = \frac{\pi^2}{3} \frac{P_n}{w_o} |T| \\ &\quad + \frac{4}{3} \frac{|D|^2}{T_R^2 \tau^4} \frac{P_n}{w_o} \tau_p^3 \left( \exp \left[ -\frac{|T|}{\tau_p} \right] - 1 + \frac{|T|}{\tau_p} \right) \end{aligned} \quad (10.55)$$

The phase noise causes the fundamental finite width of every line of the mode-locked comb in the optical domain. The timing jitter leads to a finite linewidth of the detected microwave signal, which is equivalent to the lasers fundamental fluctuations in repetition rate. In the strict sense, phase and timing in a free running mode-locked laser (or autonomous oscillator) are not anymore stationary processes. Nevertheless, since we know these are Gaussian distributed variables, we can compute the amplitude spectra of phasors undergoing phase diffusion processes rather easily. The phase difference  $\varphi = \Delta\theta(T) - \Delta\theta(0)$  is a Gaussian distributed variable with variance  $\sigma$  and probability distribution

$$p(\varphi) = \frac{1}{\sqrt{2\pi\sigma}} e^{-\frac{\varphi^2}{2\sigma}}, \text{ with } \sigma = \langle \varphi^2 \rangle. \quad (10.56)$$

Therefore, the expectation value of a phasor with phase  $\varphi$  is

$$\begin{aligned} \langle e^{j\varphi} \rangle &= \frac{1}{\sqrt{2\pi\sigma}} \int_{-\infty}^{+\infty} e^{-\frac{\varphi^2}{2\sigma}} e^{j\varphi} d\varphi \\ &= e^{-\frac{1}{2}\sigma}. \end{aligned} \quad (10.57)$$

### 10.4.1 The Optical Spectrum

In the presence of noise the laser output changes from eq.(10.7) to a random process. For simplicity, we treat here only the impact of the ever increasing timing and phase fluctuations of the field, which explains the finite linewidth

of the optical and microwave spectrum of the femtosecond laser frequency combs in the optical and microwave domain. It is straight forward, but lengthy, to include also amplitude and carrier-frequency fluctuations. Neglecting the background continuum as well as amplitude fluctuations and carrier frequency fluctuations, we obtain:

$$A(t) = \sum_{m=-\infty}^{+\infty} A_0 \text{sech} \left( \frac{t - mT_R - \Delta t(mT_R)}{\tau} \right) e^{j\Delta\phi_{CE} \cdot m} e^{j\omega_c t} e^{-j\Delta\theta(mT_R)} \quad (10.58)$$

We assume a stationary process, so that the optical power spectrum can be computed from averages of the signal truncated in time according to

$$S_{AA}(\omega) = \lim_{T=2NT_R \rightarrow \infty} \frac{1}{T} \langle \hat{A}_T^*(\omega) \hat{A}_T(\omega) \rangle, \quad (10.59)$$

with the spectra related to a finite time interval

$$\begin{aligned} \hat{A}_T(\omega) = \int_{-T}^T A(t) e^{-j\omega t} dt &= \hat{a}_0(\omega - \omega_c) \sum_{m=-N}^N e^{jmT_R \left( \frac{\Delta\phi_{CE}}{T_R} - \omega \right)} \\ &\quad e^{-j[(\omega - \omega_c)\Delta t(mT_R) + \Delta\theta(mT_R)]} \end{aligned} \quad (10.60)$$

where  $\hat{a}_0(\omega)$  is the Fourier transform of the pulse shape. If  $A(t)$  would be an electronic signal, Eq.(10.59) is exactly what a modern digital microwave spectrum analyzer measures and computes. In this case

$$\hat{a}_0(\omega) = \int_{-\infty}^{\infty} A_0 \text{sech} \left( \frac{t}{\tau} \right) e^{-j\omega t} dt = A_0 \pi \tau \text{sech} \left( \frac{\pi}{2} \omega \tau \right) \quad (10.61)$$

With (10.59) the optical spectrum of the laser is given by

$$\begin{aligned} S_{AA}(\omega) &= \lim_{N \rightarrow \infty} |\hat{a}_s(\omega - \omega_c)|^2 \frac{1}{2NT_R} \sum_{m'=-N}^N \sum_{m=-N}^M e^{jT_R \left( \frac{\phi_{CE}}{T_R} - \omega \right) (m-m')} \\ &\quad \langle e^{+j[(\omega - \omega_c)(\Delta t(mT_R) - \Delta t(m'T_R)) - (\theta(mT_R) - \theta(m'T_R))]} \rangle \end{aligned} \quad (10.62)$$

Note, that the difference between the phases and the timing only depends on the difference  $k = m - m'$ . In the current model phase and timing fluctuations

are uncorrelated. Therefore, for  $N \rightarrow \infty$  we obtain

$$S_{AA}(\omega) = |\hat{a}_s(\omega - \omega_c)|^2 \frac{1}{T_R} \sum_{k=-\infty}^{\infty} e^{jT_R \left( \frac{\Delta\phi_{CE}}{T_R} - \omega \right) k} \langle e^{+j[2\pi(\omega - \omega_0)(\Delta t((m+k)T_R) - \Delta t(mT_R))]} \rangle \langle e^{-j(\Delta\theta((m+k)T_R) - \Delta\theta(mT_R))} \rangle. \quad (10.63)$$

The expectation values are exactly of the type calculated in (10.57), which leads to

$$S_{AA}(\omega) = \frac{|\hat{a}_s(\omega - \omega_c)|^2}{T_R} \sum_{k=-\infty}^{\infty} e^{jT_R \left( \frac{\phi_{CE}}{T_R} - \omega \right) k} e^{-\frac{1}{2}\sigma_\theta(kT_R)} e^{-\frac{1}{2}[(\omega - \omega_c)\tau]^2 \sigma_t(kT_R)} \quad (10.64)$$

Most often we are interested in the noise very close to the lines at frequency offsets much smaller than the inverse energy and frequency relaxation times  $\tau_w$  and  $\tau_p$ . This is determined by the long term behavior of the variances, which grow linearly in  $|T|$

$$\sigma_\theta(T) = \frac{4}{3} \left( 1 + \frac{\pi^2}{12} + 16 \frac{\tau_w^2}{T_R^2} \phi_o^2 \right) \frac{P_n}{w_o} |T| = 2\Delta\omega_\phi |T|, \quad (10.65)$$

$$\sigma_t(T) = \frac{1}{3} \left( \pi^2 + \frac{\tau_p^2}{T_R^2} \left( \frac{D}{\tau^2} \right)^2 \right) \frac{P_n}{w_o} |T| = 2\Delta\omega_t |T|. \quad (10.66)$$

with the rates

$$\Delta\omega_\phi = \frac{2}{3} \left( 1 + \frac{\pi^2}{12} + 16 \frac{\tau_w^2}{T_R^2} \phi_o^2 \right) \frac{P_n}{w_o}, \quad (10.67)$$

$$\Delta\omega_t = \frac{1}{6} \left( \pi^2 + \frac{\tau_p^2}{T_R^2} \left( \frac{D}{\tau^2} \right)^2 \right) \frac{P_n}{w_o}. \quad (10.68)$$

From the Poisson formula

$$\sum_{k=-\infty}^{+\infty} h[k] e^{-jkx} = \sum_{n=-\infty}^{+\infty} G(x + 2n\pi) \quad (10.69)$$

where

$$G(x) = \int_{-\infty}^{+\infty} h[k] e^{-jkx} dk, \quad (10.70)$$

and Eqs.(10.64) to (10.68) we finally arrive at the optical line spectrum of the mode-locked laser

$$S_{AA}(\omega) = \frac{|\hat{a}_0(\omega - \omega_c)|^2}{T_R^2} \sum_{n=-\infty}^{+\infty} \frac{2\Delta\omega_n}{(\omega - \omega_n)^2 + \Delta\omega_n^2} \quad (10.71)$$

which are Lorentzian lines at the mode comb positions

$$\omega_n = n\omega_R + \frac{\Delta\phi_{CE}}{T_R}, \quad (10.72)$$

with a half width at half maximum of

$$\Delta\omega_n = \Delta\omega_\phi + [\tau(\omega_n - \omega_c)]^2 \Delta\omega_t. \quad (10.73)$$

Estimating the number of modes M included in the comb by

$$M = \frac{T_R}{\tau}, \quad (10.74)$$

we see that the contribution of the timing fluctuations to the linewidth of the comb lines in the center of the comb is negligible. Thus the linewidth of the comb in the center is given by 10.67

$$\Delta\omega_\phi = \frac{2}{3} \left( 1 + \frac{\pi^2}{12} + 16 \frac{\tau_w^2}{T_R^2} \phi_o^2 \right) \frac{\Theta 2g_s}{N_0 T_R} \quad (10.75)$$

$$= \frac{2}{3} \left( 1 + \frac{\pi^2}{12} + 16 \frac{\tau_w^2}{T_R^2} \phi_o^2 \right) \frac{\Theta}{N_0 \tau_{ph}} \quad (10.76)$$

where  $N_0 = \frac{w_o}{\hbar\omega_c}$  is the number of photons in the cavity and  $\tau_{ph} = T_R/(2l)$  is the photon lifetime in the cavity. Note that this result for the mode-locked laser is closely related to the Schawlow-Towns linewidth of a continuous wave laser which is  $\Delta f_\phi = \frac{\Theta}{2\pi N_0 \tau_{ph}}$ . For a solid-state laser at around  $1\mu m$  wavelength with a typical intracavity pulse energy of 50 nJ corresponding to  $N_0 = 2.5 \cdot 10^{11}$  photons and 100 MHz repetition rate with a 10% output coupler and an excess noise figure of  $\Theta = 2$ , we obtain  $\Delta f_\phi \sim \frac{\Theta}{3\pi N_0 \tau_{ph}} = 8\mu Hz$  without the amplitude to phase conversion term depending on the nonlinear phase shift  $\phi_o$ . These intrinsic linewidths are due to fluctuations happening on a time scale faster than the round-trip time and, therefore, can not be compensated by external servo control mechanisms. For sub-10 fs lasers, the

spectra fill up the full gain bandwidth and the KLM is rather strong, so that the amplitude and center frequency relaxation times are on the order of 10-100 cavity roundtrips. In very short pulse Ti:sapphire lasers nonlinear phase shifts are on the order of 1 rad per roundtrip. Then most of the fluctuations are due to amplitude fluctuations converted into phase jitter. This contributions can increase the linewidth by a factor of 100-10000, which may bring the linewidth to the mHz and Hz level.

### 10.4.2 The Microwave Spectrum

Not only the optical spectrum is of interest also the spectrum of the photo detected output of the laser is of interest. Simple photo detection can convert the low jitter optical pulse stream into a comb of extremely low phase noise microwave signals. The photo detector current is proportional to the output power of the laser. Neglecting amplitude fluctuations, we find from Eq.(10.58)

$$I(t) = \eta \frac{e}{\hbar\omega_c} |A(T, t)|^2 = \eta \frac{e}{\hbar\omega_c\tau} \times \sum_{m=-\infty}^{+\infty} \frac{w_0}{2} \text{sech}^2 \left( \frac{t - mT_R - \Delta t(mT_R)}{\tau} \right), \quad (10.77)$$

where  $\eta$  is the quantum efficiency. We obtain for the Fourier transform of the photo current

$$\hat{I}_T(\omega) = \eta \frac{ew_0}{\hbar\omega_0\tau} |a_0|^2(\omega) \sum_{m=-N}^{+N} e^{-j\omega(mT_R + \Delta t(mT_R))}, \quad (10.78)$$

$$|a_0|^2(\omega) = \int_{-\infty}^{\infty} \frac{1}{2} \text{sech}^2(x) e^{-j\omega\tau x} dx \quad (10.79)$$

$$= \frac{\pi\omega\tau}{\sinh(\frac{\pi}{2}\omega\tau)}, \quad (10.80)$$

and its power spectrum according to Eq.(10.59)

$$\begin{aligned} S_{II}(\omega) &= \frac{(\eta e N_0)^2}{T_R} | |a_0|^2(\omega) |^2 \sum_{k=-\infty}^{+\infty} e^{-j\omega k T_R} \langle e^{-j\omega(\Delta t(kT_R) - \Delta t(0))} \rangle, \\ &= \frac{(\eta e N_0)^2}{T_R} | |a_0|^2(\omega) |^2 \sum_{k=-\infty}^{+\infty} e^{-j\omega k T_R} e^{-\frac{1}{2}[(\omega\tau)^2 \sigma_t(kT_R)]} \end{aligned} \quad (10.81)$$

Using the Poisson formula again results in

$$S_{II}(\omega) = \frac{(\eta e N_0)^2}{T_R^2} ||a_0|^2(\omega)|^2 \sum_{n=-\infty}^{+\infty} \frac{2\Delta\omega_{I,n}}{(\omega - n\omega_R)^2 + \Delta\omega_{I,n}^2} \quad (10.82)$$

with the linewidth  $\Delta\omega_{I,n}$  of the  $n$ -th harmonic

$$\begin{aligned} \Delta\omega_{I,n} &= \left(2\pi n \frac{\tau}{T_R}\right)^2 \Delta\omega_t \\ &= \left(\frac{2\pi n}{M}\right)^2 \Delta\omega_t. \end{aligned} \quad (10.83)$$

The fundamental line ( $n = 1$ ) of the microwave spectrum has a width which is  $M^2$ —times smaller than the optical linewidth. For a 10-fs laser with 100 MHz repetition rate, the number of modes  $M$  is about a million.

### 10.4.3 Example: Er-fiber laser:

Figure 10.8 shows the schematic of a recently constructed soliton Er-fiber laser. The noise behavior of such a laser has been discussed in [2][3][4].

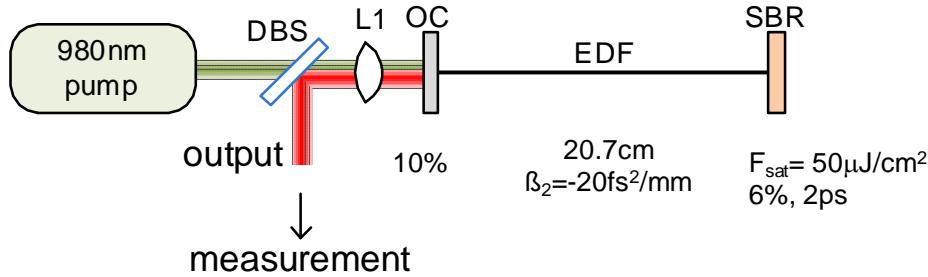


Figure 10.8: Schematic of soliton fiber laser modelocked with a semiconductor saturable Bragg reflector (SBR).

The timing jitter of the soliton laser shown in Figure 10.8 is computed in Table 10.1.

The soliton perturbation theory used should describe this type of laser very well, so it is interesting to see how well the theory describes the measurement. In reality, these quantum limited (ASE) and rather small optical and



Gain Half-Width Half Maximum	$\Omega_g = 2\pi \cdot \frac{0.3\mu\text{m}/\text{fs}}{(1.\mu\text{m})^2} 0.01\mu\text{m} = 19\text{THz}$
Saturated gain	$g_s = 0.13$
Pulse width	$\tau_{FWHM} = 180\text{fs}, \tau = \tau_{FWHM}/1.76 = 100\text{fs}$
Pulse repetition time	$T_R = 2\text{ns}$
Decay time for center freq. fluctuations	$\frac{1}{\tau_p} = \frac{4}{3} \frac{g_s}{\Omega_g^2 \tau^2 T_R} = \frac{0.05}{T_R}$
Intracavity power	$P = 120\text{mW}$
Intra cavity pulse energy / photon number	$w_o = 240\text{pJ}, \quad N_0 = 0.2 \cdot 10^{10}$
Noise power spectral density	$P_n = \Theta \frac{2g_s}{T_R} \hbar\omega_o$
Amplifier excess noise factor	$\Theta = 2$
ASE noise	$\frac{P_n}{w_o} = \Theta \frac{2g_s}{T_R N_0} = 0.13\text{Hz}$
Dispersion	$-8240\text{fs}^2$
Frequency-to-timing conv.	$\frac{4}{\pi^2} \frac{4 D ^2}{\tau^4} \frac{\tau_p^2}{T_R^2} = \left(\frac{2}{\pi} \cdot 1.6 \cdot 20\right)^2 = (20)^2$
Timing jitter density	$\left \frac{\Delta\hat{i}(\Omega)}{\tau}\right ^2 = \frac{1}{\Omega^2} \frac{\pi^2}{3} \frac{P_n}{w_o} \left(1 + \frac{4}{\pi^2} \frac{4 D ^2}{\tau^4} \frac{1}{(T_R^2/\tau_p^2 + T_R^2\Omega^2)}\right)$
Timing jitter $[f_{\min}, f_{\max}]$ for $f_{\min} \ll 1/\tau_p$ , $f_{\min} = 10\text{kHz}$ ,	$\Delta t = \tau \sqrt{\frac{1}{12 \cdot f_{\min}} \frac{P_n}{w_o} \left(1 + \frac{4}{\pi^2} \frac{4 D ^2}{\tau^4} \frac{\tau_p^2}{T_R^2}\right)} = 2\text{fs}$

Table 10.1: Parameters for the soliton laser of Figure 10.8.

microwave linewidths are difficult to observe, because they are most often swamped by technical noise such as fluctuations in pump power, which may cause gain fluctuations, or mirror vibrations, air-density fluctuations or thermal drifts, which directly cause changes in the lasers repetition rate. Figure 10.9 shows the single-sideband phase noise spectrum  $L(f)$  of the  $N=4$  harmonic of the fundamental repetition rate, i.e 1.963 GHz, in the photo current spectrum 10.82.

The phase of the  $N=4$ nd harmonic of the photocurrent 10.77 is directly related to the timing jitter by

$$\Delta\varphi(T) = 2\pi N f_R \Delta t(T) \quad (10.84)$$

The single-sideband phase noise is the power spectral density of these phase fluctuations defined in the same way as the power spectral density of the

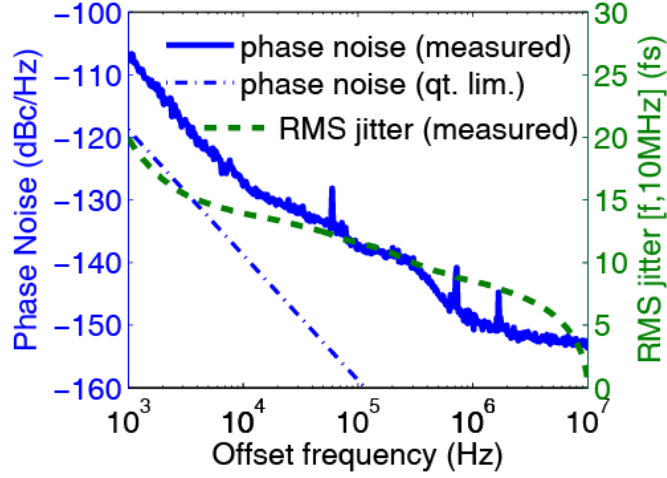


Figure 10.9: Timing jitter measurement of the output from the stretched pulse modelocked laser measured with a HP 5052 signal analyzer.

photocurrent itself, i.e.

$$L(f) = S_{\Delta\varphi\Delta\varphi}(\omega) \quad (10.85)$$

The phase fluctuations in a certain frequency interval can then be easily evaluated by

$$\Delta\varphi^2 = 2 \int_{f_{\min}}^{f_{\max}} L(f) df. \quad (10.86)$$

And the timing jitter is then

$$\Delta t = \frac{1}{2\pi N f_R} \sqrt{2 \int_{f_{\min}}^{f_{\max}} L(f) df}. \quad (10.87)$$

For the measurements shown in Figure 10.9 we obtain for the integrated timing jitter from 10kHz to 20 MHz of 12 fs. This is somewhat larger than the value calculated in table 10.1 of 2 fs. The discrepancy may have many reasons. The most obvious one is the resolution limit of the measurement instrument itself, which is on the order of 10 fs.



# Bibliography

- [1] H.A. Haus and A. Mecozzi: Noise of mode-locked lasers, *IEEE J. Quantum Electron.* **29**, 983-996 (1993).
- [2] S. Namiki and H. A. Haus: "Observation of nearly quantum-limited timing jitter in a P-APM all fiber ring laser", *J. of the Opt. Soc. of Am. B.*, **13**, 2817-2823 (1996).
- [3] S. Namiki and H. A. Haus: "Noise of the stretched pulse fiber ring laser: Part I—Theory", *IEEE J. of Quantum Electronics*, **33**, 640-659 (1997).
- [4] Ch. Xu, S. Namiki, H. A. Haus: "Noise in the Stretched Pulse Fiber Laser: Part II – Experiments", *IEEE J. of Quantum Electronics*, **33**, 660-668 (1997).
- [5] H.A. Haus and E.P. Ippen: Group velocity of solitons, *Opt. Lett.* **26**, 1654-1656 (2001)
- [6] D. J. Jones, S. A. Diddams, J. K. Ranka, R. S. Windeler, J. L. Hall, and S. T. Cundiff, *Science* **288**, 635 (2000).
- [7] H. Byun, D. Pudo, J. Chen, E. P. Ippen and F. X. Kärtner, „High repetition rate, 491 MHz, femtosecond fiber laser with low timing jitter,” *Optics Letters* **33**:(1)9, pp.2221-2223 (2008).



# Chapter 11

## Ultrafast Measurement Techniques

Since the invention of picosecond lasers in the 1960's different time resolved spectroscopic techniques have been developed to understand ultrafast processes that happen on timescales faster than even the most advanced streak cameras available. Also, today streak cameras reach sub-picosecond resolution.

### 11.1 Pump Probe Measurements

The simplest ultrafast measurement technique is called pump-probe measurement. It enables to measure the time dependence of an optical property in a sample with a weak probe pulse after initial excitation by strong optical pump pulse. For example:

- Change of absorption due to redistribution of populations in an atomic, molecular or solid-state systems caused by relaxation processes or reaction dynamics characterized by a time constant equal to  $T_1$ , the energy or population relaxation for the case of a two-level system.
- Refractive index changes
- Dichroism or birefringence changes, for example due to reorientation of molecules in the sample.
- Monitoring of fluorescence yield from certain states after excitation

- Coherent vibrations either of isolated molecules or of crystalline lattices
- Structural information concerning atomic-level order in crystalline samples may be probed

### 11.1.1 Non-Colinear Degenerate Pump-Probe Measurement:

Figure 11.1 shows a non-colinear degenerate pump-probe measurement setup. Degenerate means that both the pump and probe wavelength are the same. To suppress background light and low frequency noise of the probe beam the pump beam is chopped. Typical chopper frequencies of regular mechanical choppers are  $f_{ch} = 100\text{Hz} - 2\text{kHz}$ . Mechanical choppers up to 20kHz have been built. With acousto-optic modulators or electro-optic modulators chopper frequencies up to several hundred MHz are possible.

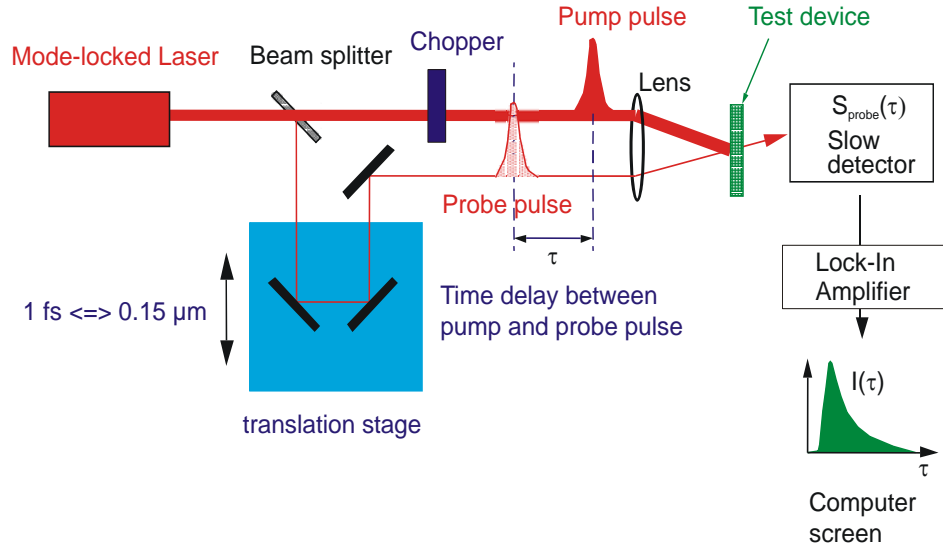


Figure 11.1: Non-colinear pump-probe setup with co-polarized pump-probe beams.

We denote  $S_{\text{pump}}(T) = S_0(T) + n(T)$  as the probe pulse energy, where

$S_0(T) = P_0 m(T)$  is the average pump pulse energy modulated by the chopper signal  $m(T)$  and  $n(T)$  may be some external noise at frequencies different from the signal  $m(T)$ .  $S_{in}(\tau)$  shall be the probe pulse energy sent towards the device under test and  $S_{probe}(T, \tau)$  the probe pulse energy transmitted through the device under test after a delay  $\tau$  with respect to the pump pulse. If the transmission of probe light is nonlinear, then the detected signal transmitted through the test device can be written as

$$\begin{aligned} S_{probe}(T, \tau) &= \tilde{T}(S_{pump}(T)) S_{in}(\tau) \\ &= \tilde{T}_0 S_{in}(\tau) + \frac{d\tilde{T}(\tau)}{dP} P_0 m(T) S_{in}(\tau) + \frac{d\tilde{T}}{dP} n(T) S_{in}(\tau) \end{aligned} \quad (11.1)$$

where  $\tilde{T}_0$  is the transmission without pump pulse,  $P_0$  is the pump pulse energy and  $m(T)$  the chopper modulation function. Lock-in detection means that there is a matched detection, which has a receiver signal

$$\begin{aligned} I(\tau) &= \int_{-T_M/2}^{+T_M/2} S_{probe}(T, \tau) \cdot m(T) dT \\ &= \left[ \tilde{T}_0 \int_{-T_M/2}^{+T_M/2} m(t) dt + \frac{d\tilde{T}(\tau)}{dP} P_0 \int_{-T_M/2}^{+T_M/2} m^2(t) dt \right. \\ &\quad \left. + \frac{d\tilde{T}}{dP} \int_{-T_M/2}^{+T_M/2} m(t) n(t) dt \right] S_{in}(\tau). \end{aligned} \quad (11.2)$$

The modulation function  $m(t)$  is chosen average free, for example a sinusoidal or rectangular waveform. If the modulation frequency is chosen high enough such that there is no spectral overlap between the modulation function and the low frequency noise  $n(t)$ , then the result is

$$I(\tau) = \frac{dT(\tau)}{dP} P_0 \int_{-T_M/2}^{+T_M/2} m^2(T) dT.$$

Or the time resolved differential transmission change is given by

$$\frac{dT(\tau)}{dP} = I(\tau) / \left( P_0 \int_{-T_M/2}^{+T_M/2} m^2(T) dT \right). \quad (11.3)$$

There are two effects that may generate redirection of pump light into the probe light and cause, what is called, a coherent artifact. The first one is



technical in nature. Due to surface roughness of the device under test pump light maybe scattered into the direction of the probe beam and reaches the detector. Second, because of the degeneracy of the pump and probe beam, they interfere in the medium and produce an absorption or index modulation in addition to the transmission change by the pump. Pump light can scatter off this grating and reaches the detector. We will discuss this phenomenon later when studying four-wave-mixing. In the context of degenerate pump probe this is called coherent artifact and a detailed discussion can be found in [1]. This can be suppressed to a large extent by choosing orthogonal pump and probe polarizations, if the transmission change is not polarization sensitive.

### **11.1.2 Colinear Pump-Probe Measurement:**

Sometimes pump and probe pulses have to be collinear, for example when pump probe measurements of waveguide devices have to be performed. Then pump and probe pulses, which might both be at the same center wavelength have to be made separable. This can be achieved by using orthogonal pump and probe polarization as shown in Figure 11.2 or by chopping pump and probe at different frequencies and detecting at the difference frequency, see Figure 11.3.

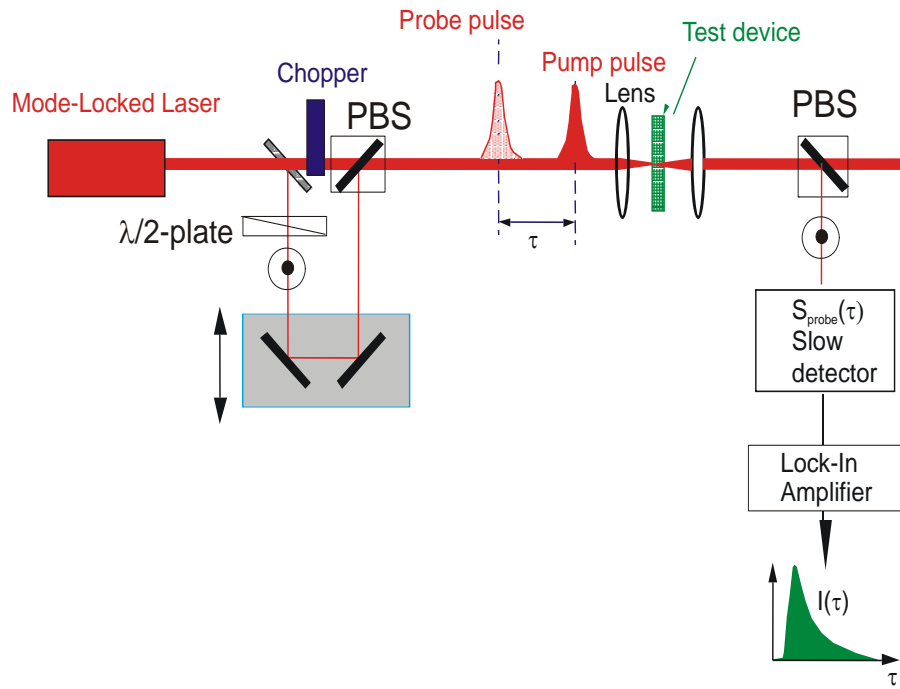


Figure 11.2: Colinear pump-probe with orthogonally polarized pump and probe beams.

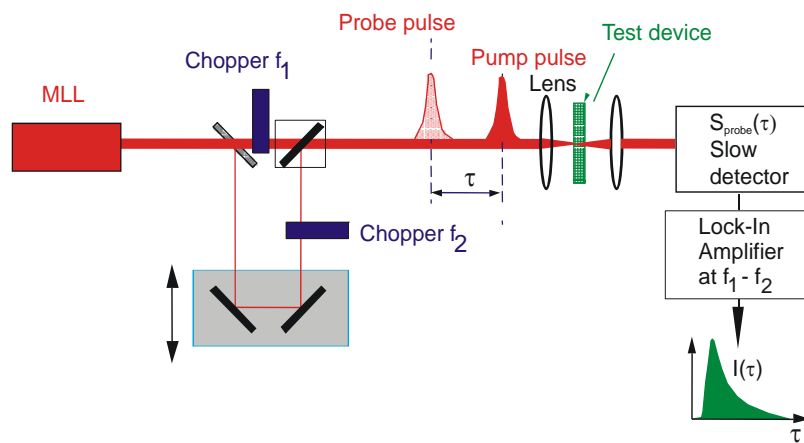


Figure 11.3: Colinear pump probe with chopping of pump and probe and lock-in detection at the difference frequency

### 11.1.3 Heterodyne Pump Probe

The lock-in detection is greatly improved if the difference frequency at which the detection occurs can be chosen higher and the signal can be filtered much better using a heterodyne receiver [2]. This is shown in Figure 11.4, where AOM's are used to diffract of a probe and reference pulse shifted by 39 and 40 MHz, respectively. The pump beam is chopped at 1kHz. After the test device the probe and reference pulse are overlaid with each other by delaying the reference pulse in a Michelson-Interferometer. The beat note between the probe and reference pulse at 1MHz is downconverted to baseband with a heterodyne receiver.

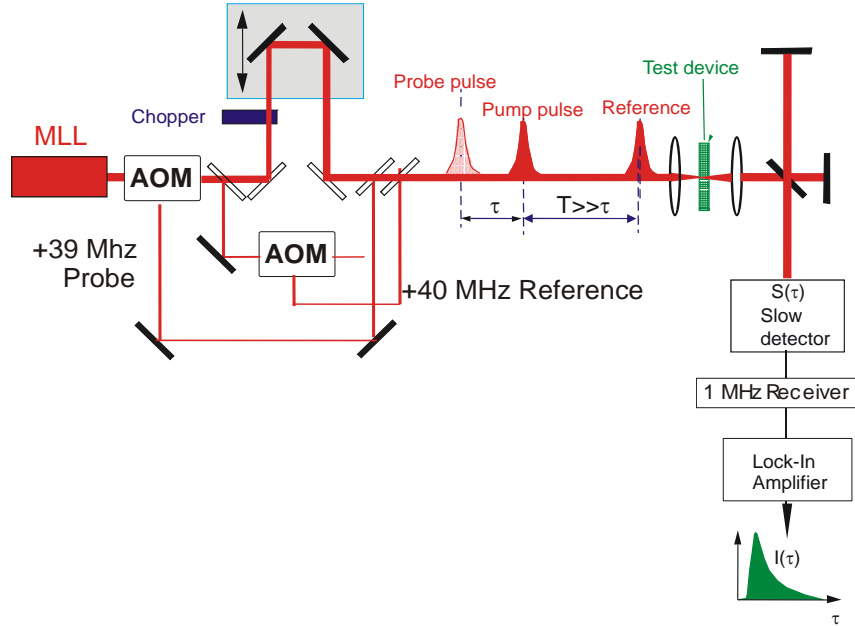


Figure 11.4: Colinear pump probe measurement with parallel polarization and large difference frequency.

If a AM or FM receiver is used and the interferometers generating the reference and probe pulse are interferometrically stable, both amplitude and phase nonlinearities can be detected with high signal to noise ratio [3][4].

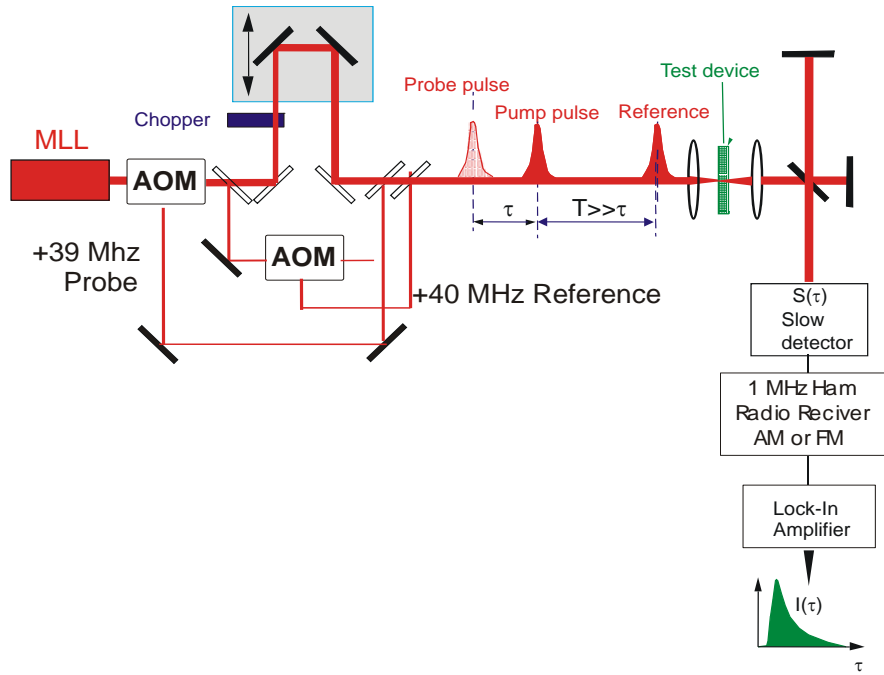


Figure 11.5: Heterodyne pump probe using AM and FM receiver to detect amplitude and phase nonlinearities.

## 11.2 Four-Wave Mixing

A more advanced ultrafast spectroscopy technique than pump-probe is four-wave mixing (FWM). It enables to investigate not only energy relaxation processes, as is the case in pump-probe measurements, but also dephasing processes in homogenous as well as inhomogeneously broadened materials. The typical set-up is shown in Fig. 11.6

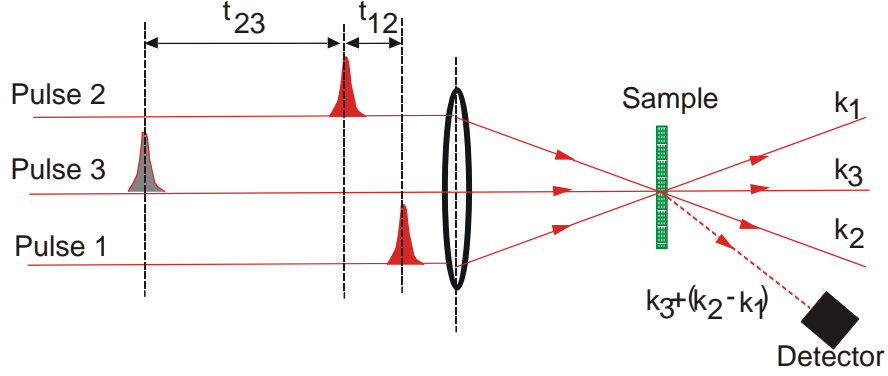


Figure 11.6: Typical Four-Wave-Mixing (FWM) beam geometry.

Lets assume these pulses interact resonantly with a two-level system modelled by the Bloch Equations derived in chapter 4.1.

$$\left(\Delta - \frac{1}{c_0^2} \frac{\partial^2}{\partial t^2}\right) \vec{E}(z, t) = \mu_0 \frac{\partial^2}{\partial t^2} \vec{P}(z, t), \quad (11.4)$$

$$\vec{P}(z, t) = -2N\vec{M}^* \underline{d}(z, t) \quad (11.5)$$

$$\dot{\underline{d}}(z, t) = -\left(\frac{1}{T_2} - j\omega_{eg}\right)\underline{d} + \frac{1}{2j\hbar} \vec{M} \vec{E}^{(+)} w, \quad (11.6)$$

$$\dot{w}(z, t) = -\frac{w - w_0}{T_1} + \frac{1}{j\hbar} (\vec{M}^* \vec{E}^{(-)} \underline{d} - \vec{M} \vec{E}^{(+)} \underline{d}^*) \quad (11.7)$$

The two-level system, located at  $z = 0$ , will be in the ground state, i.e.  $\underline{d}(t = 0) = 0$  and  $w(t = 0) = -1$ , before arrival of the first pulse. That is, no polarization is yet present. Lets assume the pulse interacting with the two-level system are weak and we can apply perturbation theory. Then the arrival of the first pulse, which shall be described as a  $\delta$ -impulse, with the complex field

$$\vec{E}(\vec{x}, t) = \vec{E}_0^{(+)} \delta(t) e^{j(\omega_{eg}t - j\vec{k}_1 \vec{x})} \quad (11.8)$$

will generate a polarization wave according to the Bloch-equations

$$\underline{d}(\vec{x}, t) = -\frac{\vec{M} \vec{E}_0^{(+)}}{2j\hbar} e^{j(\omega_{eg} - 1/T_2)t} e^{-j\vec{k}_1 \vec{x}} \delta(z), \quad (11.9)$$

which will decay with time. Once a polarization is created the second pulse

will change the population and induce a weak population grating

$$\Delta w(\vec{x}, t) = \frac{|\vec{M}\vec{E}_0^{(+)}|^2}{\hbar^2} e^{-t_{12}/T_2} e^{-j(\vec{k}_1 - \vec{k}_2)\vec{x}} e^{-(t-t_2)/T_1} \delta(z) + c.c., \quad (11.10)$$

When the third pulse comes, it will scatter off from this population grating, i.e. it will induce a polarization, that radiates a wave into the direction  $\vec{k}_3 + \vec{k}_2 - \vec{k}_1$  according to

$$d(\vec{x}, t) = \frac{\vec{M}\vec{E}_0^{(+)}}{2j\hbar} \frac{|\vec{M}\vec{E}_0^{(+)}|^2}{\hbar^2} e^{-t_{12}/T_2} e^{-t_{32}/T_1} e^{-j(\vec{k}_3 + \vec{k}_2 - \vec{k}_1)\vec{x}} \delta(z) \quad (11.11)$$

Thus the signal detected in this direction, see Fig. 11.6, which is proportional to the square of the radiating dipole layer

$$S(t) \sim |d(\vec{x}, t)|^2 \sim e^{-2t_{12}/T_2} e^{-2t_{32}/T_1} \quad (11.12)$$

will decay on two time scales. If the time delay between pulses 1 and 2,  $t_{12}$ , is only varied it will decay with the dephasing time  $T_2/2$ . If the time delay between pulses 2 and 3 is varied,  $t_{32}$ , the signal strength will decay with the energy relaxation time  $T_1/2$ . In that way both relaxation rates can be extracted for a given transition.

### 11.3 Electro-Optic Sampling:

Electro-Optic Sampling was invented in the early 1980's by Valdmanis and Mourou [5]. It is based on polarization rotation of a short laser pulse when propagating in a medium showing a linear electro-optic effect. The polarization rotation is due to an applied electric field, i.e. the optical pulse samples the instantaneous electric field, see Fig.11.7

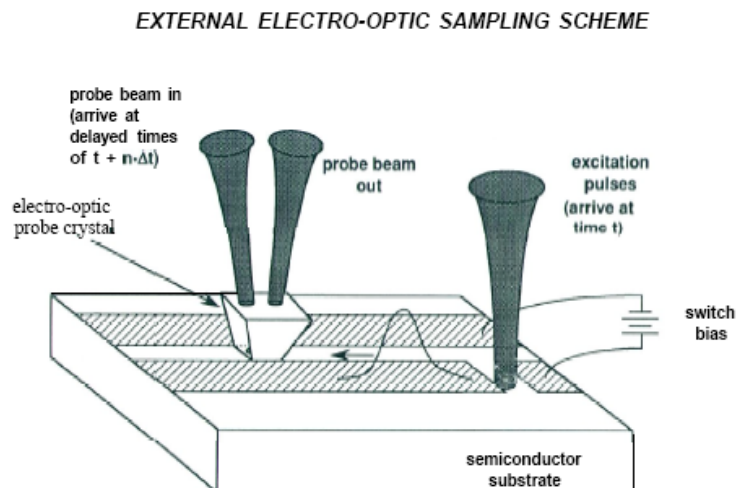


Figure 11.7: Electro-optic sampling scheme according to J. Whitaker, Univ. of Michigan, Ann Arbor.

In Fig. 11.7 a electric transient is generated with a photo-conductive switch activated by a femtosecond laser pulse. A delayed pulse samples the transient electronic pulse with an electro-optic probe as shown in Fig. 11.8.

*Electro-Optic Probe*

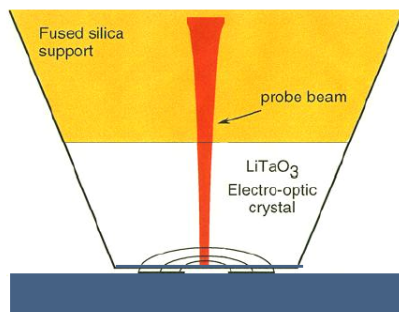


Figure 11.8: LiTaO<sub>3</sub>–Electro-Optic Probe according to J. Whitaker, Univ. Michigan.

Fig. 11.9 shows an overall version of an electro-optic sampling system according to J. Whitaker, Univ. of Michigan [7]

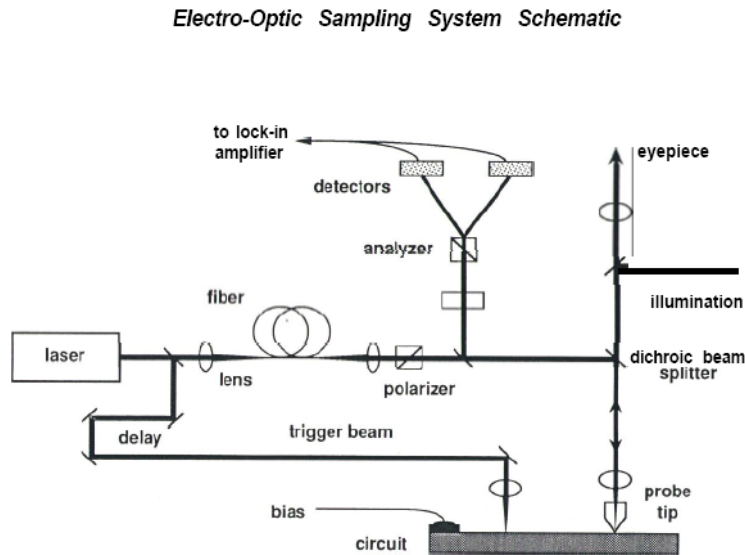


Figure 11.9: Electro-Optic Sampling System according to J. Whitaker, Univ. Michigan.

For further reading see references [9][6].

## 11.4 THz Spectroscopy and Imaging

This technique was pioneered by Ch. Fattinger and D. Grischkowsky [8]. Photo-conductive switches activated by sub-100 fs pulses or optical rectification with sub-100 fs pulses leads to the generation of THz electro-magnetic impulses, that can be received with similar photo-conductive receivers or by electro-optic sampling [9][10].



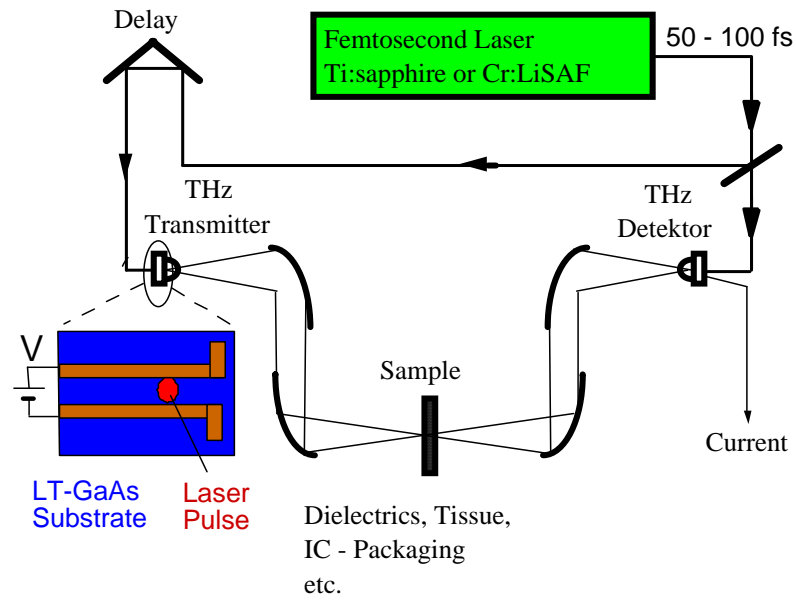


Figure 11.10: THz Time Domain Spectroscopy according to [9]

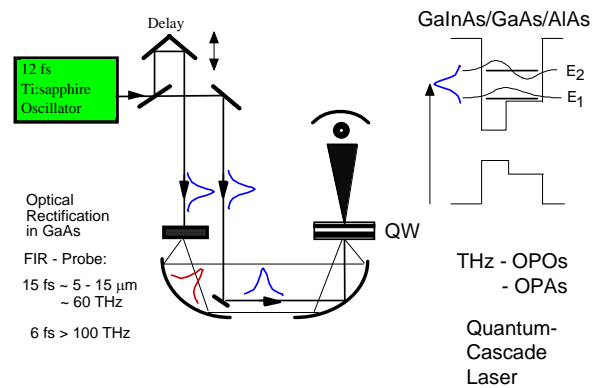


Figure 11.11: THz Time Domain Spectroscopy using optical rectification in GaAs [10].

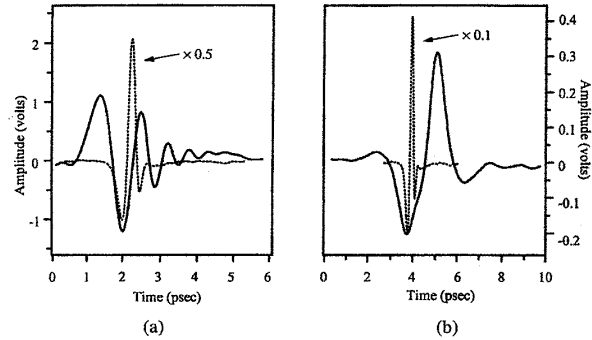


Figure 11.12: Terahertz waveforms modified by passage through (a) a 10mm block of stycast and (b) a chinese fortune cookie. The dashed lines show the shape of the input waveform multiplied by 0.5 in (a) and by 0.1 in 9b). In \*a( the transmitted plse exhibits a strong "chirp" due to frequency-dependent index, while in (b), pulse broadening indicates preferential absorption of high frequencies [9].

Figure 11.12 shows typical generated THz waveforms and distortions due to propagation through materials.



# Bibliography

- [1] A. M. Weiner, "Ultrafast Optics, Chapter 9" Wiley Series in Pure and Applied Optics (2009).
- [2] K. L. Hall, G. Lenz, E. P. Ippen, and G. Raybon, "Heterodyne pump-probe technique for time-domain studies of optical nonlinearities in waveguides," *Opt. Lett.* **17**, p.874-876, (1992).
- [3] K. L. Hall, A. M. Darwish, E. P. Ippen, U. Koren and G. Raybon, "Femtosecond index nonlinearities in InGaAsP optical amplifiers," *App. Phys. Lett.* **62**, p.1320-1322, (1993).
- [4] K. L. Hall, G. Lenz, A. M. Darwish, E. P. Ippen, "Subpicosecond gain and index nonlinearities in InGaAsP diode lasers," *Opt. Comm.* **111**, p.589-612 (1994).
- [5] J. A. Valdmanis, G. Mourou, and C. W. Gabel, "Picosecond electro-optic sampling system," *Appl. Phys. Lett.* **41**, p. 211-212 (1982).
- [6] B. H. Kolner and D. M. Bloom, "Electrooptic Sampling in GaAs Integrated Circuits," *IEEE J. Quantum Elect.* **22**, 79-93 (1986).
- [7] S. Gupta, M. Y. Frankel, J. A. Valdmanis, J. F. Whitaker, G. A. Mourou, F. W. Smith and A. R. Calaw , "Subpicosecond carrier lifetime in GaAs grown by molecular beam epitaxy at low temperatures," *App. Phys. Lett.* **59**, pp. 3276-3278 91991)
- [8] Ch. Fattinger, D. Grischkowsky, "Terahertz beams," *Appl. Phys. Lett.* **54**, pp.490-492 (1989)
- [9] D. M. Mittleman, R. H. Jacobsen, and M. Nuss, "T-Ray Imaging," *IEEE JSTQE* **2**, 679-698 (1996)

- [10] A. Bonvalet, J. Nagle, V. Berger, A. Migus, JL Martin, and M. Joffre, "Ultrafast Dynamic Control of Spin and Charge Density Oscillations in a GaAs Quantum Well," *Phys. Rev. Lett.* **76**, 4392 (1996).

# Chapter 12

## Short Pulse Amplification

The first part of this chapter follows to a large extent the presentation [1]. So far only generation of short pulses directly from laser oscillators was considered, which typically leads to low energy pulses with energy values ranging from few pJ to at most few  $\mu\text{J}$  in long cavity lasers operating at large average power levels.

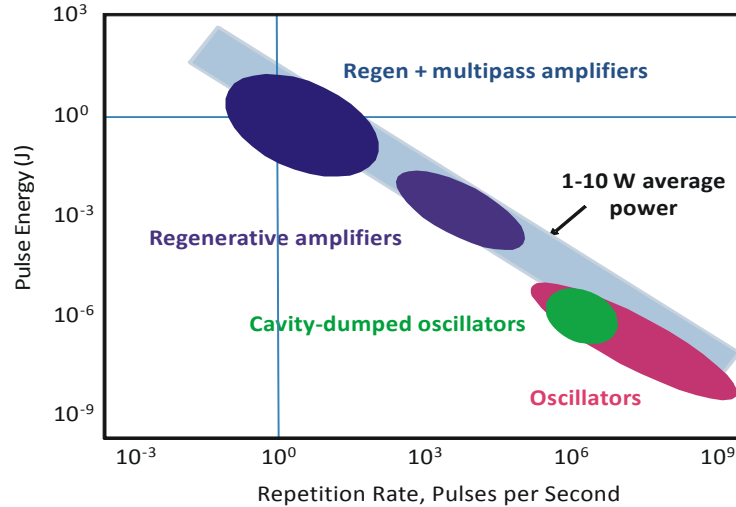


Figure 12.1: Schemes for generating high energy laser pulses.

Many applications require higher energy pulses. Today laser pulses with up to Joule and in rare cases to the kJ and MJ energy level are generated. In

the following, we want to understand how this can be accomplished. Figure 12.1 shows the different schemes to generate laser pulses with high pulse energy. Today, the average power level of ultrashort pulsed laser sources is in the range of 1-10 W and scaling to the 100 W and kW average power level is pursued and rapidly progressing.

## 12.1 Cavity Dumping

One way to generate higher energy pulses than available directly from an oscillator is to realize that the pulse energy inside an oscillator is actually higher than outside, if the laser operates with a low output coupling ratio to achieve lasing at all. Thus by simply opening the cavity, i.e. lowering the Q-factor of the cavity rapidly, which is opposite to Q-switching, the intracavity pulse energy can be dumped to the outside and used for experiments, see Fig. 12.2

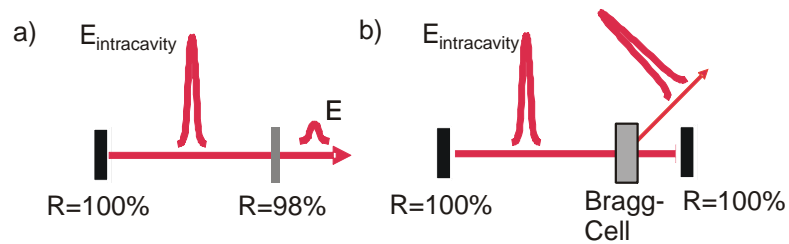


Figure 12.2: a) Laser with low output coupling. Intracavity pulse energy is 50-times higher than output coupled energy. b) Laser with Bragg cell for cavity dumping of the high energy intracavity laser pulse.[1]

A Bragg cell is an acousto-optic modulator, where a microwave pulse with a given carrier-frequency imprints an index grating in the material that acts as a Bragg reflector for the optical pulse. Another way to implement fast optical switching for cavity dumping is by using a Pockels cell, see Fig, 12.3.

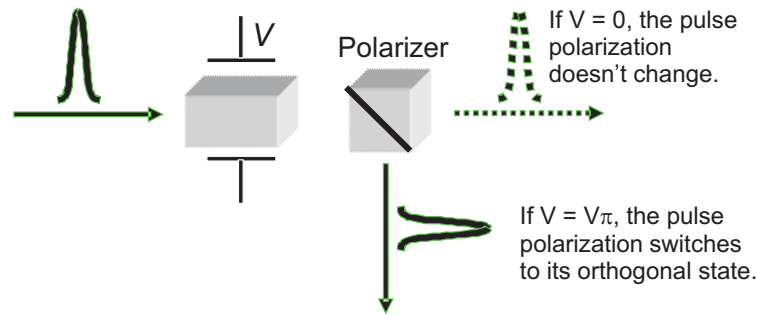


Figure 12.3: Abruptly switching a Pockels cell from zero voltage to a high voltage,  $V_\pi$ , results in a switching of the polarization from one state to its orthogonal state and therefore redirecting the path of the beam via a polarizer.[1]

The Pockels effect is the linear electro-optic effect, where an applied voltage, either orthogonal to the pulse propagation or longitudinal results in a change of refractive index in the medium. If the input polarization is properly chosen an applied voltage,  $V_\pi$ , of a certain magnitude may induce a differential phase shift of  $\pi$  resulting in a switching between orthogonal polarization states, which redirects the beam at a polarizer. Typical rise and fall times of Pockels cells are several nanoseconds and typical voltages  $V_\pi$  are on the order of kV for few millimeter diameter crystals. After the dumping of the pulse, the switch returns into the initial position and the laser field builds up again from whatever is left in the cavity – typically only 80-90% of the intracavity energy is dumped. In this way 10-50 times higher energy pulses at 10-50 times lower repetition rate can be generated.

## 12.2 Laser Amplifiers

A much more scalable way towards higher energy laser pulses is of course continuous amplification of a single pulse selected from a pulse train emitted from an oscillator or a cavity dumped oscillator to higher energy levels by propagating the laser pulse through an inverted laser medium. Here, it is of great advantage that the laser medium can store energy over a period of time equal to the upper state lifetime. Thus it is possible to optically pump the laser medium with a very high energy pump pulse, that is shorter than



the upper state life time of the laser amplifier transition. Then the medium is inverted and stores the energy of the pump pulse, see Fig. 12.4. The seed pulse to be amplified should arrive at the laser medium in a time much shorter than the upper state lifetime, propagate through the laser medium, gets amplified and hopefully is able to extract as much energy as stored in the medium minus the quantum defect in the laser emission. Since upper state lifetimes of typical solid-state laser media are in the range of  $\mu s - ms$  high energy pulses generated from Q-switched solid-state lasers, which typically have 10-100 ns duration can be used as pump pulses.

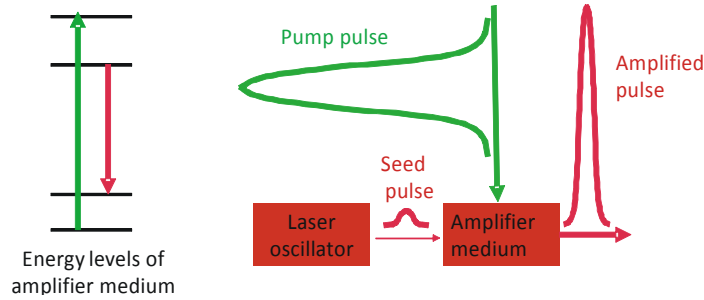


Figure 12.4: Laser amplifier: Pump pulse should be shorter than upper state lifetime. Signal pulse arrives at medium after pumping and well within the upper state lifetime to extract the energy stored in the medium, before it is lost due to energy relaxation.[1]

If the repetition rate of the pulses to be amplified is higher than the inverse upper state lifetime, the amplifier medium can also be pumped continuously without losing efficiency.

### 12.2.1 Frantz-Nodvick Equation

From the treatment of laser matter interaction and laser oscillation in chapter 4, we found that the power gain,  $2g$ , of a light beam with intensity  $I(z)$ , propagating through an inverted medium is proportional to the inversion,  $w(z)$  or in an ideal four level laser amplifier medium to the upper state population, and the interaction cross section  $\sigma$  of the amplifier transition

$$2g(z) = \sigma w(z). \quad (12.1)$$

The initial inversion or small signal gain is related to the absorbed pump fluence  $F'_{pump}$  per unit length, see Fig. 12.5.

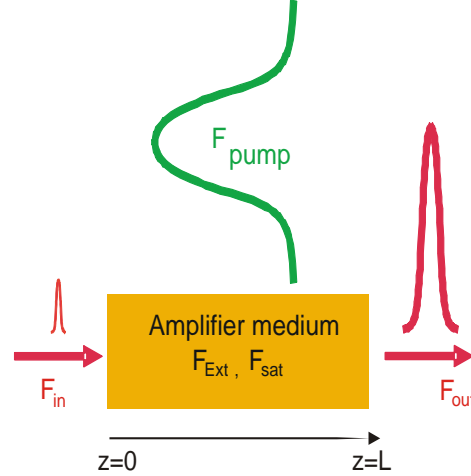


Figure 12.5: Pumping, seeding and amplification in a laser amplifier.[1]

Assuming a pump quantum efficiency  $\eta_{pump}$  for the transfer of pump photons into inverted transistions the small signal gain is given by,

$$2g_0(z) = \sigma w_0(z) = \sigma \frac{F'_{pump}}{hf_p} \eta_{pump} \quad (12.2)$$

$$= \frac{F'_{pump}}{F_{sat}} \frac{hf_L}{hf_p} \eta_{pump}, \quad (12.3)$$

where  $F_{sat} = \frac{hf_L}{\sigma}$ , is the saturation fluence of the amplifier and  $\int_0^L F'_{pump}(z)dz = F_{pump}$  is the integrated pump fluence pumping the amplifier. A light beam with intensity  $I(z)$  propagating in an amplifying medium with gain  $g(z)$  along the z-direction obeys the equations of motion

$$\frac{dI(z,t)}{dz} = 2g(z,t) I(z,t), \quad (12.4)$$

$$\frac{dg(z,t)}{dt} = -\frac{g(z,t)}{\tau_L} - \frac{gI(z,t)}{F_{sat}}. \quad (12.5)$$

In each slice of the medium with lenght  $dz$ , there is an inversion and therefore a gain  $g(z,t)$ . Typically, amplifier media with a long upperstate lifetime are

chosen, such that the light pulse propagates through the gain medium in a time much shorter than the upper state lifetime. Therefore, the relaxation of the of the gain medium during the amplification process can be neglected. Immediately before the arrival of the pulse to be amplified the medium is pumped with a short and intense optical or electrical pulse that brings the medium into the upper amplifier state resulting in a maximum initial gain  $g_0(z)$  of the amplifier medium. Neglecting gain relaxation during the pulse propagation and introducing the fluence or energy flux

$$F(z) = \int_{-\infty}^{+\infty} I(z, t) dt. \quad (12.6)$$

Neglecting gain relaxation, the equation for the gain in each length element  $dz$  along the propagation direction, Eq.(12.5), can be integrated

$$g(z, t) = g_0(z) \exp \left[ -\frac{1}{F_{sat}} \int_{-\infty}^t I(z, t') dt' \right]. \quad (12.7)$$

Substitution of this result into Eq.(12.4) gives

$$\frac{dI(z, t)}{dz} = 2g_0(z) \exp \left[ -\frac{1}{F_{sat}} \int_{-\infty}^t I(z, t') dt' \right] I(z, t). \quad (12.8)$$

This equation can be converted into an equation for the fluence by integration over time  $t$ , over the pulse length

$$\frac{dF(z)}{dz} = 2g_0(z) \exp \left[ -\frac{1}{F_{sat}} \int_{-\infty}^t I(z, t') dt' \right] \Big|_{t=-\infty}^{t=\infty}, \quad (12.9)$$

$$= 2g_0(z) \left( \exp \left[ -\frac{F(z)}{F_{sat}} \right] - 1 \right) F_{sat} \quad (12.10)$$

This equation can be solved by separation of variables

$$\begin{aligned} \frac{dF}{\exp \left[ -\frac{F}{F_{sat}} \right] - 1} &= 2g_0(z) dz, \\ \frac{dF}{1 - \exp \left[ \frac{F}{F_{sat}} \right]} \exp \left[ \frac{F}{F_{sat}} \right] \frac{1}{F_{sat}} &= 2g_0(z) dz, \\ \ln \left[ \exp \left[ \frac{F}{F_{sat}} \right] - 1 \right] \Big|_{F=F_{in}}^{F=F_{out}} &= 2 \int_0^L g_0(z) dz, \end{aligned} \quad (12.11)$$

and finally gives the Frantz-Nodvick equation

$$\frac{\exp\left[\frac{F_{out}}{F_{sat}}\right] - 1}{\exp\left[\frac{F_{in}}{F_{sat}}\right] - 1} = G_0 = \exp\left[2 \int_0^L g_0(z) dz\right] \quad (12.12)$$

where  $G_0$  is the input to output small signal gain of the amplifier, which can be also expressed in terms of the total extractable energy fluence

$$F_{ext} = F_{pump} \frac{f_L}{f_p} \eta_{pump}. \quad (12.13)$$

according to Eq.(12.3)

$$\frac{\exp\left[\frac{F_{out}}{F_{sat}}\right] - 1}{\exp\left[\frac{F_{in}}{F_{sat}}\right] - 1} = \exp\left[\frac{F_{ext}}{F_{sat}}\right]. \quad (12.14)$$

The Frantz-Nodvick equation takes a more transparent form when introducing the normalized fluences  $f = F/F_{sat}$  for input, output and extractable fluence. This equation shows the important relationship between energy gain achievable in an amplifier and extraction efficiency. This becomes more obvious when computing the actual gain achieved in the overall amplifier

$$\begin{aligned} G &= \frac{f_{out}}{f_{in}} = \frac{1}{f_{in}} \ln [1 + (e^{f_{in}} - 1) e^{f_{ext}}] = \frac{1}{f_{in}} \ln [1 + (e^{f_{in}} - 1) G_0] \\ &\approx \frac{1}{f_{in}} \ln [1 + f_{in} e^{f_{ext}}] \approx \begin{cases} e^{f_{ext}} = G_0, & \text{for } f_{in} e^{f_{ext}} \ll 1 \\ \frac{f_{ext}}{f_{in}}, & \text{for } f_{in} e^{f_{ext}} \gg 1 \end{cases}. \end{aligned} \quad (12.15)$$

This equation simply states, that as long as the input energy, seed energy, is so low that the amplifier does not saturate, the gain is the maximum total small signal gain of the amplifier. As soon as the output energy approaches saturation energy, the gain saturates and in the limit of total saturation the maximum gain is the ratio of the maximum extractable energy to input energy. The extraction efficiency showing how much of the extractable energy got actually extracted from the amplifier is

$$\begin{aligned} \eta_{eff} &= \frac{f_{out}}{f_{ext}} = \frac{1}{f_{ext}} \ln [1 + (e^{f_{in}} - 1) e^{f_{ext}}] = \frac{1}{\ln G_0} \ln [1 + (e^{f_{in}} - 1) G_0] \\ &\approx \frac{1}{f_{ext}} \ln [1 + f_{in} e^{f_{ext}}] \begin{cases} \frac{f_{in}}{f_{ext}} e^{f_{ext}} = \frac{f_{in}}{f_{ext}} G_0, & \text{for } f_{in} e^{f_{ext}} \ll 1 \\ 1, & \text{for } f_{in} e^{f_{ext}} \gg 1 \end{cases} \end{aligned} \quad (12.16)$$

This shows that one can not use the maximum gain and simultaneously extract the maximum energy. As an example, Figure 12.6 shows the gain and extraction efficiency for an amplifier with a small signal gain of 3. In this case, for an input energy equal to the saturation energy one can extract 80% of the extractable energy with a gain of about 2.2, roughly doubling the input energy.

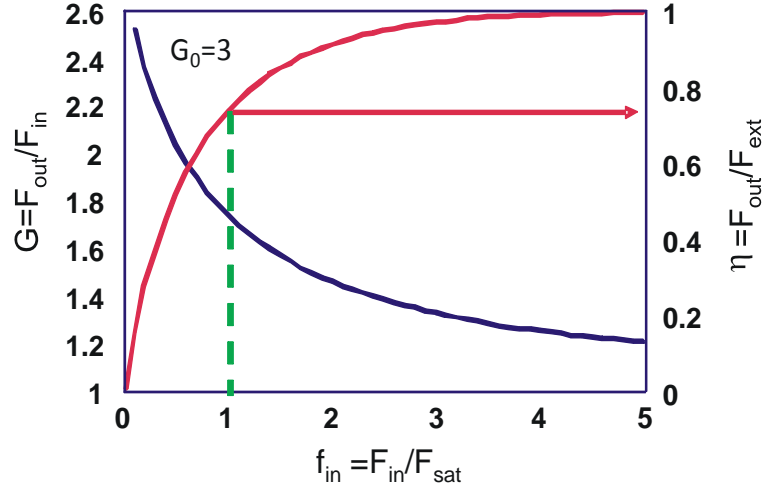
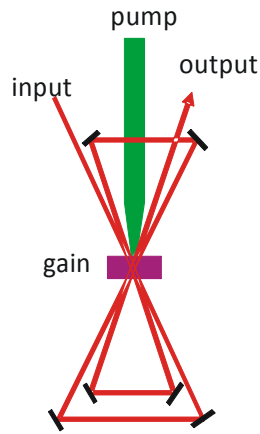


Figure 12.6: Gain and extraction efficiency of an amplifier for a small signal gain of  $G_0 = 3$ . [1]

Thus in a low gain amplifier one can only efficiently extract energy by seeding already with the a pulse fluence equal to the saturation fluence. This often needs amplification by many passes through the gain material in order to reach saturation energy. This multipass arrangement can be achieved in various ways. Figure 12.7 shows the two standard arrangements: a) multipass amplifier and b) regenerative amplifier. In case a) the beam path is arranged geometrically to pass the pumped gain region many times in such a way that there is good overlap of all beams in the gain medium for efficient gain extraction. Thermal distortions of the crystal and unsymmetric thermal lenses in the crystal may lead to a distortions in the laser beam. Therefore, for up to few mJ pulse energy most often the configuration b) is preferred. There a pulse from the pulse train coming in from an oscillator is selected and kept in the laser cavity for a certain number of round-trips until it is amplified to

large enough pulse energy extracting most of the available energy stored in the crystal. Then the pulse is switched out and the energy in the gain medium is replenished by receiving the next pump pulse, which prepares the system for the next amplification cycle. Typical repetition rates for this process are 1-500 kHz repetition rate. Depending on the upper state lifetime of the gain medium, the regenerative amplifier maybe pumped with a continuous wave (cw) operating pump laser.

a) Multi-pass amplifier



b) Regenerative amplifier

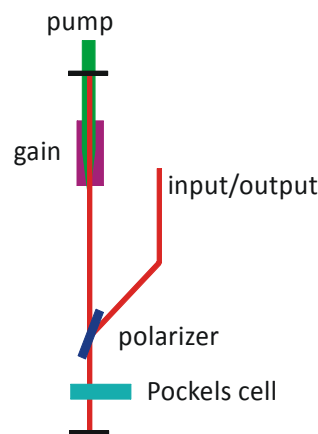


Figure 12.7: Multiple pass arrangements: a) Multi-pass amplifier, by re-directing the beam through the pumped crystal several times. b) Multi-pass amplification by switching a laser pulse in and out of a laser cavity after the pulse has propagated through the crystal a given number of time.[1]

### 12.2.2 Regenerative Amplifiers

Figure 12.8 shows two different configurations for regenerative amplifiers. Configuration (a) shows a regular

V-cavity Ti:sapphire laser with a Pockels cell placed in one arm, which will flip the polarization in a double pass when activated. The polarization of the input and intracavity beam is controlled by thinfilm polarizers (TFPs). In configuration (b) the spotsizes in the crystal is enlarged by the concave mirror M1 to enable higher output pulse energies.

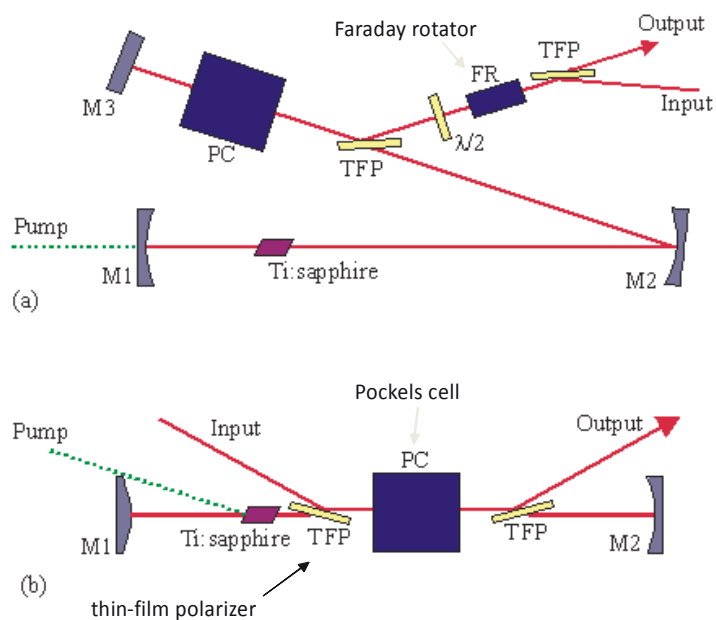


Figure 12.8: Different configurations for regenerative amplifiers. [1]

### 12.2.3 Multipass Amplifier

Figure 12.7 a) showed a multi-pass amplifier with only a few passes through the crystal. The configuration shown in Figure 12.9 shows a slightly missaligned ring cavity such that the beam passes many times on slightly different passes through the crystal. The pulse is selected from a pulse stream by a pockels cell.

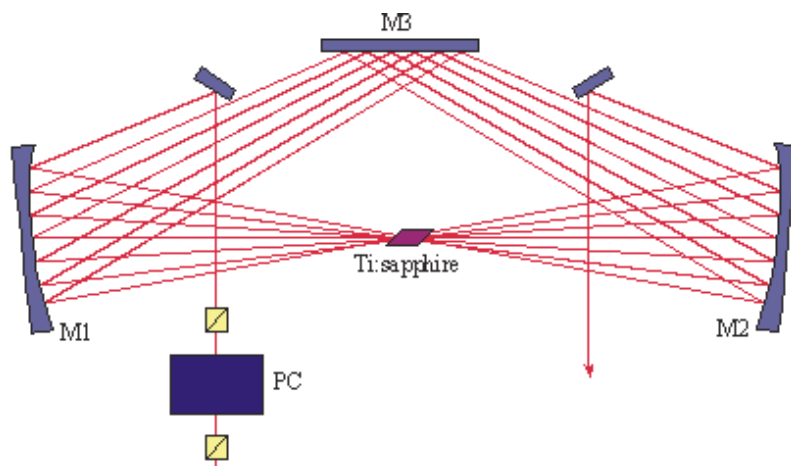


Figure 12.9: Multipass amplifier with many passes folded up many times in a cavity with slightly missaligned mirrors. [1]

## 12.3 Chirped Pulse Amplification

The extraction of pulse energy from the crystal in the form of pico and femtosecond pulses is rapidly limited by the nonlinearities of the amplifier crystal occurring due to the high peak power of short amplified pulses. Most notably self-focusing that occurs for peak power greater than the critical power for self-focusing or small scale self-focusing [ref]. It was recognized by Strickland and Mourou [2] that one can use chirping of the pulses and compression after the amplification to dramatically overcome those limitations and increase the peak powers and withit peak intensities achievable by the stretching ratio which can be as large as  $10^4 - 10^5$ , see Fig. 12.10.



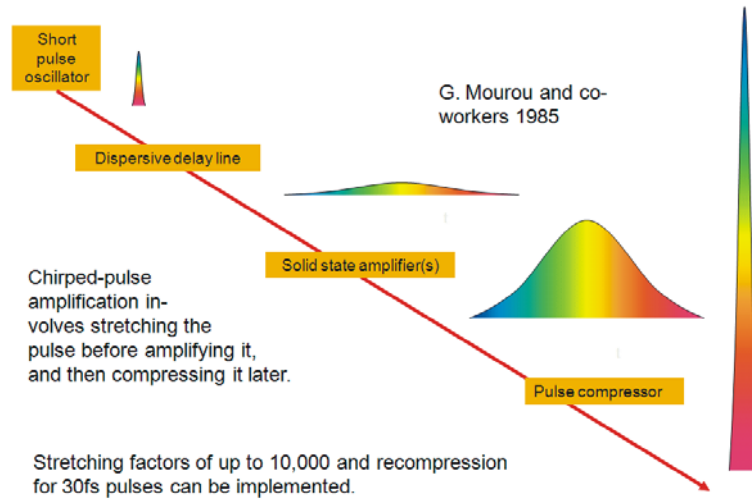


Figure 12.10: Principle of chirped pulse amplification. [1]

The amplifiers used can be only a regenerative amplifier or a regenerative amplifier followed by one or two stages of multipass amplification.

## 12.4 Stretchers and Compressors

Large stretching of pulses requires physically a large group delay between different spectral components. For femtosecond laser pulses with 10-50 fs duration stretching to almost 1 ns duration is typically achieved with grating pairs. The spatial dispersion of the different colors and with it the path length of the different colors can be further enlarged with an objective. In the design of these stretchers, one can start from the zero dispersion stretcher using the standard 4-f imaging system shown in Fig. 12.11 for the case that  $d = f$ . If  $d \neq f$  the dispersion is not any longer zero and can reach stretching ratios as large as  $10^4$ .

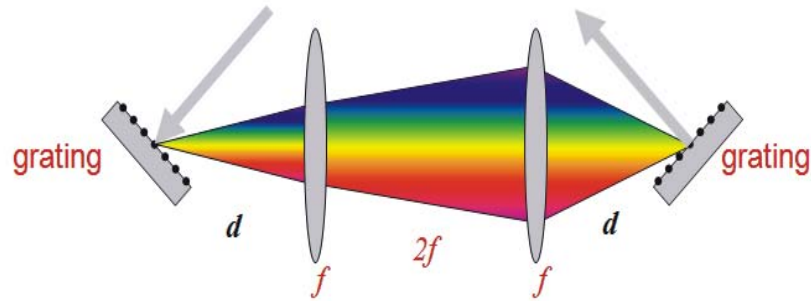


Figure 12.11: Principle arrangement of a grating based stretcher. [1]

To accommodate large beam diameters, avoiding the chromatic aberrations of lenses and utilizing only one grating such stretchers use reflective optics and are arranged in a back-folded geometry, see Fig. 12.12 as demonstrated by Lawrence Livermore National Laboratories, realizing a stretching ratio of 30,000.

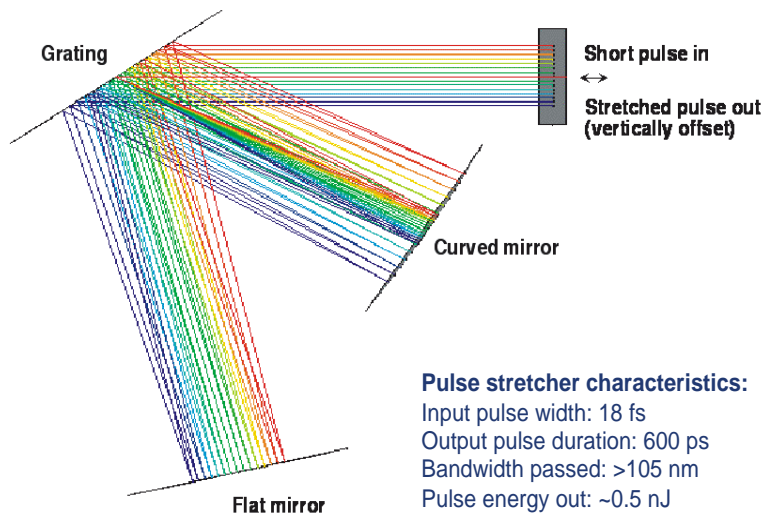


Figure 12.12: Backfolded stretcher designed by Lawrence Livermore National Laboratories. [1]

Software for the design of stretchers and compressors has been developed by Craig Siders and can be found under <http://dom.creol.ucf.edu/>. Figure 12.13 shows the typical fluences achievable from different laser materials due to the saturation fluence, doping of the material and the damage threshold of the material for various pulse lengths. Compression of the pulses enables to generate femtosecond pulses at these high energy fluences. Large cross section laser crystals of high optical quality are necessary to generate multiple 10 J pulses from Ti:sapphire lasers enabling Petawatt lasers.

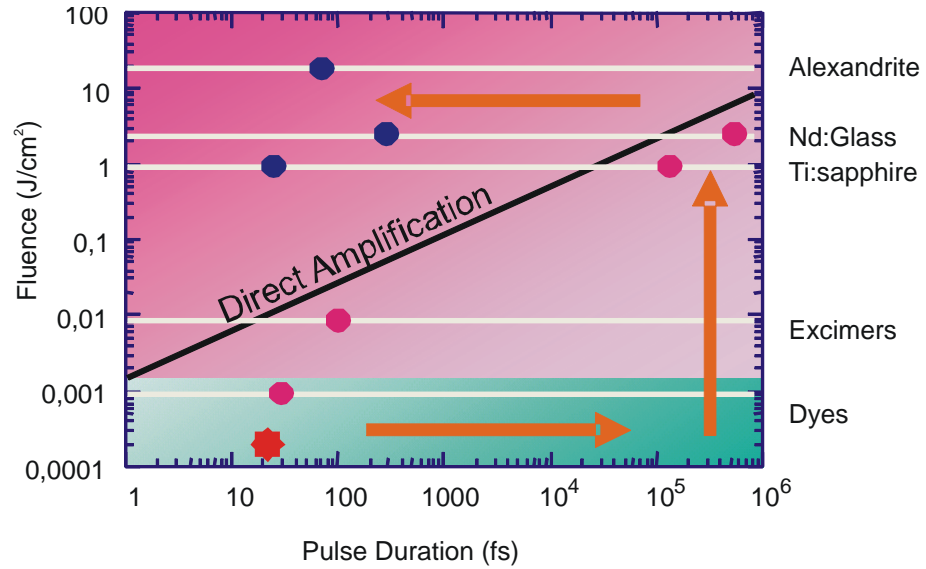


Figure 12.13: Achievable fluences using chirped pulse amplification for various stretching ratios. Compression of the pulses enables femtosecond pulses. [1]

Figure 12.14 shows the necessary beam diameters for a Ti:sapphire amplifier to extract various pulse energies. Note, the saturation fluence for Ti:sapphire is  $F_{sat} = hf_L/\sigma = 0.82 \text{ J/cm}^2$ . Therefore, the saturation energy of a beam with diameter 1mm is about 6 mJ.

Pump power 100 W	Rep rate		
	1 kHz	10 kHz	100 kHz
Extracted energy	20 mJ	1.8 mJ	0.2 mJ
Average Power	20 W	18 W	20 W
Beam diameter	3 mm	1 mm	250 $\mu\text{m}$

Figure 12.14: Beam diameter for Ti:sapphire amplifiers pumped by 100W of average power with a typical efficiency of 20% for various repetition rates and therefore extracted pulse energies after [1]

## 12.5 Gain Narrowing

For large amplification factors gain narrowing seriously restricts the achievable amplifier bandwidth. The impact of this effect on a 10 fs pulse in a Ti:sapphire amplifier is shown in Figure 12.15. Despite the large gain bandwidth of Ti:sapphire supporting 10 fs pulses and below from oscillators, amplifiers are typically limited to 20-30 fs pulses depending on amplification factor.

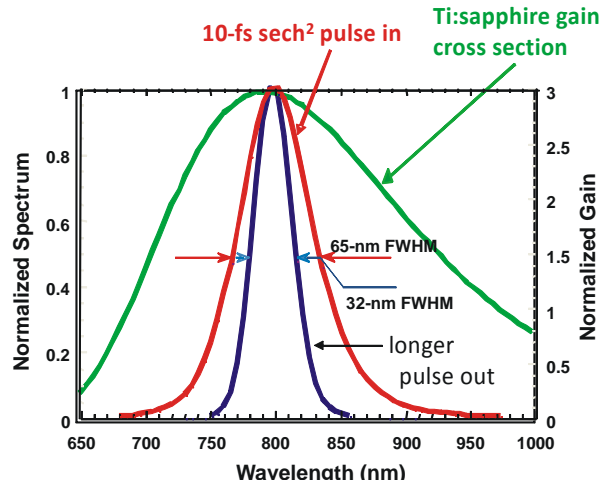


Figure 12.15: Influence of gain narrowing in a Ti:sapphire amplifier on a 10 fs seed pulse [1]

In fiber amplifiers, gain narrowing can be compensated by additional nonlinear spectral broadening. In bulk amplifiers gain narrowing has been partially compensated by intracavity filters, that are flattening the overall gain profile, see Fig. 12.16. Using dielectric filters for gain flattening sub-10 fs pulses from Ti:sapphire amplifiers have been demonstrated recently.

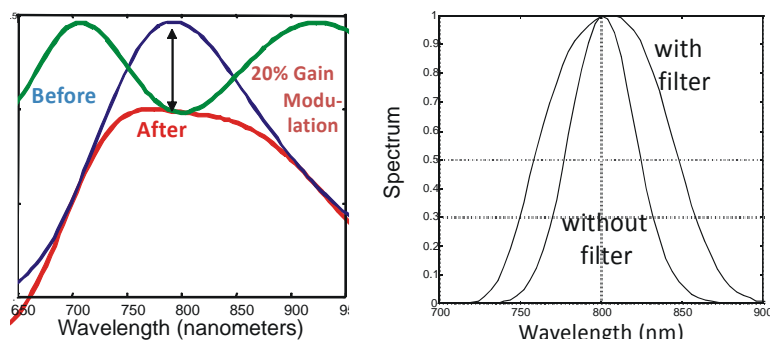


Figure 12.16: Gain flattening by intracavity filter. [1]

## 12.6 Pulse Contrast

Amplified laser pulses often have pure contrast both on a short and long time scale. Fig. 12.17 shows the pulse power as a function of time of a typical amplified pulse. There are pre pulses on the time scale of the repetition rate of the oscillator due to the limited contrast of the pockels cell during switching. This can be improved by using several pockels cells in sequence. Then there may be a back ground due to ASE, which eventually needs to be cleaned up between amplifier stages. Finally there can be a limited contrast due to the residual spectral phase, i.e. higher order dispersion. This background is a very serious problem for high intensity laser pulses where laser matter interaction at  $10^{20} \text{ W/cm}^2$  may be pursued. Even a background of  $10^{-8}$  is high enough to preionize material before the main laser pulse arrives at the target.

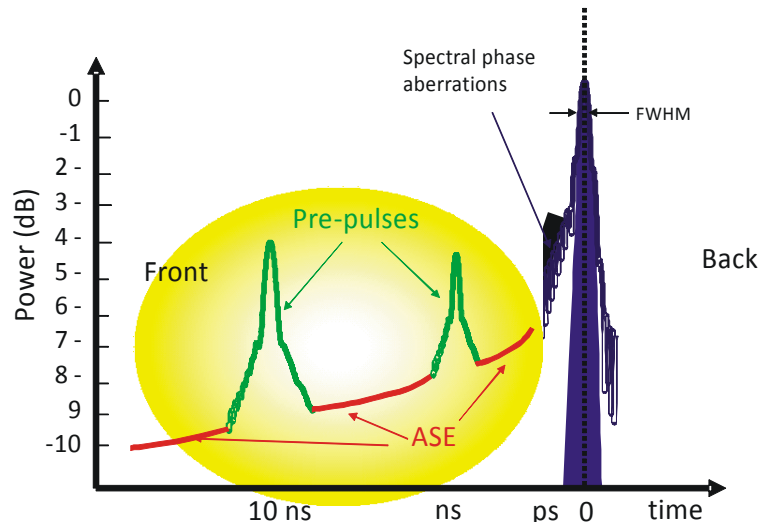


Figure 12.17: Contrast of amplified laser pulses. [1]

Figure 12.18 shows a typical third-order high resolution autocorrelation of an amplified laser pulse.

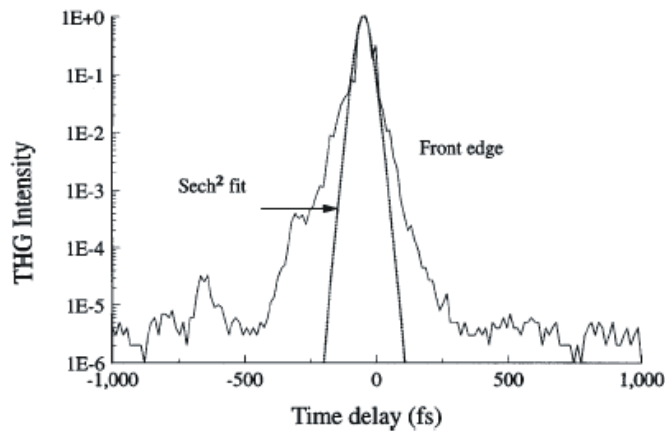


Figure 12.18: Typical high resolution autocorrelation of an amplified laser pulse. [1]

## 12.7 Scaling to Large Average Power by Cryogenic cooling

With increase of average power a thermal lens is building up in the laser crystal where the residual pump energy both due to the quantum defect and the imperfect energy extraction is dissipated into heat. This is problematic both in oscillators and amplifiers. In fiber lasers the thermal lensing is unproblematic since the mode is usually guided by a much stronger refractive index profile. Up to a certain extent this thermal lens can also be compensated in bulk lasers by including it in the resonator design or beam path design. But at a certain power level this is no longer possible. One way out of this dilemma is by cryogenic cooling of the crystal, see Fig. 12.19.

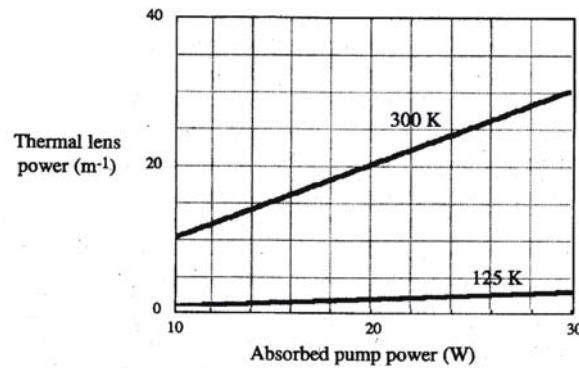


Figure 12.19: Reduction in thermal lensing due to cooling of a Ti:sapphire crystal.

It turns out, that it is a general feature of dielectric materials. Fig. 12.20 shows the thermal properties of YAG on which many very efficient picosecond laser materials such as Nd:YAG and Yb:YAG are based. The thermal lensing for a given heat load to the crystal is proportional to the ratio between the temperature coefficient of the refractive index or thermal expansion coefficient and the thermal conductivity. These ratios change by a factor of 30 when the crystal is cooled from 300 K to 100 K, which can be achieved using liquid nitrogen cooling.

## 12.7. SCALING TO LARGE AVERAGE POWER BY CRYOGENIC COOLING 421

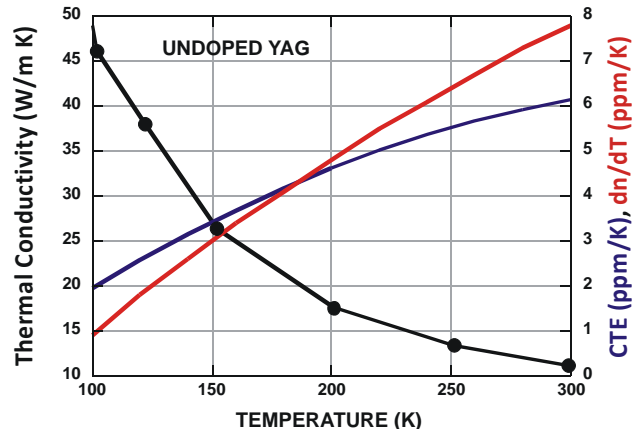


Figure 12.20: Thermal properties of undoped YAG as a function of temperature. [3]

Figure 12.21 shows a cryogenically cooled Yb:YAG power amplifier producing 287 W of 5.5-ps pulses with an excellent beam quality [4].

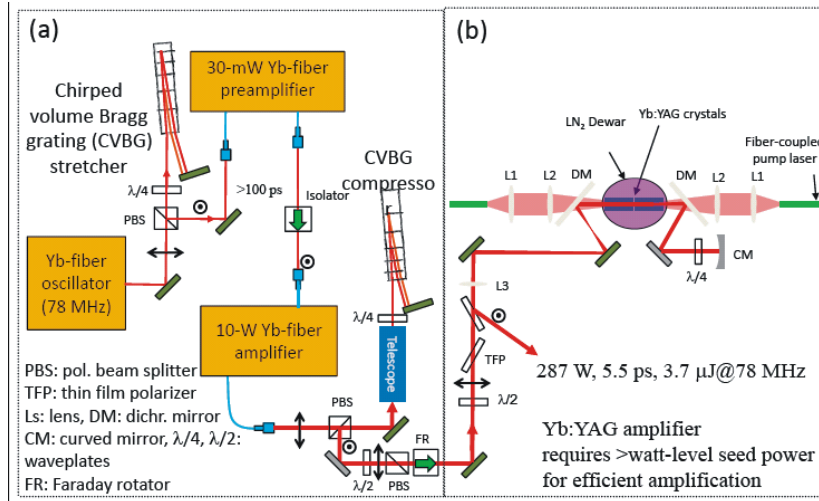


Figure 12.21: (a) Fiber CPA chain generating a 6W picosecond seed source for seeding of a 300W cryogenically cooled Yb:YAG power amplifier producing 287 W, average power 5.5-ps pulses.



## 12.8 Optical Parametric Amplifiers and Oscillators

Advances in laser technology together with the discovery of high quality nonlinear optical crystals have lead to the introduction of ultrafast optical parametric amplifiers as practical sources for femtosecond pulses tunable across the visible, near and far infrared spectral ranges. Here, we give a brief overview on ultrafast optical parametric amplifiers (OPA), giving the basic design principles for different frequency ranges and in addition presenting some advanced designs for the generation of ultrabroadband, few-optical-cycle pulses. Finally, we also briefly discuss the possibility of applying parametric amplification schemes to large-scale, high energy systems using optical parametric chirped pulse amplification (OPCPA). This chapter follows closely the review paper of Cerullo et al. [5].

### 12.8.1 Optical Parametric Generation (OPG)

The principle of OPG is quite simple: In a suitable nonlinear crystal, a high frequency and high intensity beam, called the pump beam, at frequency  $\omega_p$ , amplifies a lower frequency, lower intensity beam, called the signal beam, at frequency  $\omega_s$ ; in addition a third beam, called the idler beam, at frequency  $\omega_i$  is generated[6]. In the OPG process, the signal and idler beams play an interchangeable role. For simplicity, we assume in the following, that the signal is at higher frequency, i.e.  $\omega_s > \omega_i$ . The nomenclature is again taken from microwave engineering, where parametric amplifiers have been greatly used at highest frequencies until the arrival of High Electron Mobility Transistors (HEMTs) and GaAs-FET technology in the 80s. Parametric interaction often occurs in lossless media and then energy conservation has to be maintained, which enforces

$$\hbar\omega_p = \hbar\omega_s + \hbar\omega_i. \quad (12.17)$$

That is, a pump photon can be converted into a signal and an idler photon under energy conservation. As we will see from the propagation equation later, for the conversion to be efficient also momentum conservation has to be fulfilled, i.e. the process should be phase matched

$$\hbar\vec{k}_p = \hbar\vec{k}_s + \hbar\vec{k}_i. \quad (12.18)$$

Thus for a given pump frequency the signal and idler frequency can range from  $\omega_p/2 < \omega_s < \omega_p$  and the corresponding idler ranges from  $\omega_p/2 > \omega_i > 0$ , see Fig. 12.22. The case where signal and idler are both  $\omega_p/2$  is called degenerate parametric amplification, which is a delicate process especially if both the signal and idler beam occupy the same mode, i.e. they can not be distinguished and are identical. This case will not be considered here.

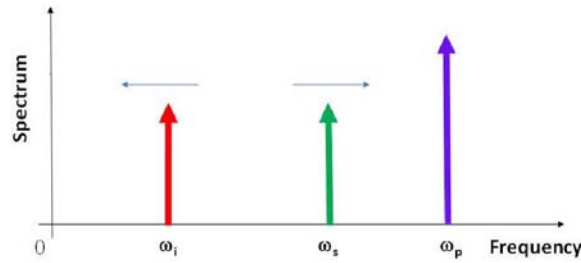


Figure 12.22: Optical parametric generation

Optical parametric generation in short crystals – necessary for broadband operation – is only possible with high efficiency at high intensities, typically on the order of  $\text{GW}/\text{cm}^2$  or even tens of  $\text{GW}/\text{cm}^2$ . Such high intensities can easily be generated using pico- and femtosecond pulses at moderate pulse energies of a few  $\mu\text{J}$ .

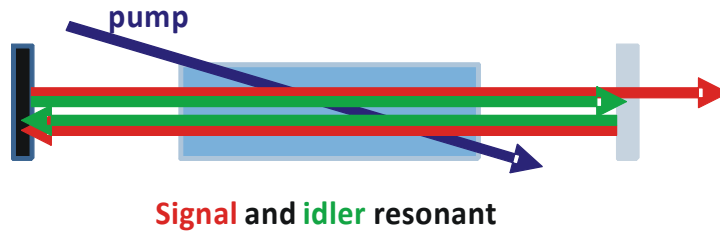


Figure 12.23: Schematic of a doubly resonant OPO. It is resonant for signal and idler. In addition the cavity length also has to match the pump repetition rate within a few micrometer, if the OPO is pulsed.

OPG can be exploited in two principle configurations. If the OPG crystal

is enclosed in a suitable optical cavity and the parametric gain exceeds the losses, the cavity starts oscillating like an ordinary laser and an optical parametric oscillator (OPO) is obtained. In this case either the signal and/or the idler can be resonant, see Fig.12.23. The second way consists in amplifying a weak signal beam, the so-called “seed” beam, thus obtaining an optical parametric amplifier (OPA). Like in a laser amplifier, amplification may occur in several stages. Both schemes are employed with ultrashort pulses, as well as in continuous wave (cw) and nanosecond pulse systems depending on the application. OPOs can be pumped by a small-scale femtosecond oscillator, and provide pulses at very high repetition rates, e.g. 100 MHz - 1 GHz. As with lasers, at average power levels of 1 W output energies of OPOs are low, typically a few nanojoules, and they require a cavity whose length is matched to the repetition rate of the pump laser within micrometers. Their tunability is limited by the bandwidth of the mirror coatings, so that several mirror sets may be required to span the whole tuning range. In contrast to OPOs, which may operate at moderate single pass gains, OPAs require high pump intensities, provided only by an amplified system, and operate at lower repetition rates ~typically from 1 to 100 kHz. on the other hand, they provide high output energies, broad frequency tunability and are simpler to operate, since they do not require any cavity length stabilization. Therefore, femtosecond OPOs and OPAs are complementary systems, used in different types of applications.

In the following, we will focus on femtosecond OPAs, which have reached a high level of stability and reliability. These systems are usually pumped by amplified Ti:sapphire lasers, providing pulses with millijoule-level energy depending on repetition rate and about 100 fs duration. Pumping can occur either at the fundamental wavelength (FW) at 800 nm or at the second harmonic (SH) at 400 nm of the laser beam. Femtosecond OPAs tunable from the ultraviolet (UV) to the mid-infrared (IR) have been demonstrated and produce pulse energies up to the 100  $\mu$ J level and higher if higher pump pulse energies are available. Typical overall efficiencies are on the order of 10%. In addition, femtosecond OPAs have the capability of generating pulses significantly shorter than the pump pulses, exploiting the large gain bandwidths available in the parametric interactions. They can therefore be used as effective pulse compressors. Recently ultrabroadband pulses with durations down to 5 fs in the visible and 10-15 fs in the near-IR have been demonstrated containing only a few optical cycles of the carrier frequency.

### 12.8.2 Nonlinear Optical Suszeptibilities

The total electric field propagating in the amplifier crystal can be described as a sum of pump, signal and idler field

$$\vec{E}(\vec{r}, t) = \sum_{\omega_a > 0} \sum_{i=1}^3 \frac{1}{2} \left\{ \hat{E}_i(\omega_a) e^{j(\omega_a t - \vec{k}_a \vec{r})} + c.c. \right\} \vec{e}_i. \quad (12.19)$$

where  $E_i(\omega_a)$  is the  $i$ -th cartesian component of the complex electric field vector with polarization  $\vec{e}_i$ . As usual the term  $c.c.$  (complex conjugate) contains the negative frequency components of the field  $E_i(-\omega_a) = E_i(\omega_a)^*$ . The nonlinear polarization is order with respect to powers of the electric field and since the polarization needs to be real it can also be sorted into positive and negative frequency components

$$\vec{P}(\vec{r}, t) = \sum_n \vec{P}^{(n)}(\vec{r}, t) \quad (12.20)$$

with

$$\vec{P}^{(n)}(\vec{r}, t) = \sum_{\omega_b > 0} \sum_{i=1}^3 \frac{1}{2} \left\{ P_i^{(n)}(\omega_b) e^{j(\omega_b t - \vec{k}'_b \vec{r})} + c.c. \right\} \vec{e}_i. \quad (12.21)$$

The  $i$ -th cartesian component of the  $n$ -th order nonlinear polarization with frequency  $\omega_b$  defines the  $n$ -th order nonlinear dielectric suszeptibility-Tensor via

$$P_i^{(n)}(\omega_b) = \frac{\varepsilon_0}{2^{m-1}} \sum_P \sum_{j \dots k} \chi_{ij \dots k}^{(n)}(\omega_b : \omega_1, \dots, \omega_n) E_j(\omega_1) \cdots E_k(\omega_n) \quad (12.22)$$

$$\omega_b = \sum_{i=1}^n \omega_i \text{ and } \mathbf{k}'_b = \sum_{i=1}^n \mathbf{k}_i. \quad (12.23)$$

Here, the summation  $P$  indicates summation over all permutations of  $\omega_1, \dots, \omega_n$ , leading to the same generated frequency  $\omega_b$  and  $m$  is the number of all fields with non vanishing frequency (no DC-fields). Here a few examples:

$$P_i^{(2)}(\omega_3) = \varepsilon_0 \sum_{jk} \chi_{ijk}^{(2)}(\omega_3 : \omega_1, \omega_2) \hat{E}_j(\omega_1) \hat{E}_k(\omega_2), \quad (12.24)$$

$$\omega_3 = \omega_1 + \omega_2 \text{ und } \mathbf{k}'_3 = \mathbf{k}_1 + \mathbf{k}_2. \quad (12.25)$$

( $\longrightarrow$  Sum Frequency Generation (SFG))

$$\hat{P}_i^{(2)}(\omega_3) = \varepsilon_0 \sum_{jk} \chi_{ijk}^{(2)}(\omega_3 : \omega_1, -\omega_2) \hat{E}_j(\omega_1) \hat{E}_k^*(\omega_2), \quad (12.26)$$

$$\omega_3 = \omega_1 - \omega_2 \text{ und } \mathbf{k}'_3 = \mathbf{k}_1 - \mathbf{k}_2. \quad (12.27)$$

( $\longrightarrow$  Difference Frequency Generation (DFG))

$$\hat{P}_i^{(2)}(\omega_2) = \varepsilon_0 \sum_{jk} \chi_{ijk}^{(2)}(\omega_2 : \omega_3, -\omega_1) \hat{E}_j(\omega_3) \hat{E}_k^*(\omega_1), \quad (12.28)$$

$$\omega_2 = \omega_3 - \omega_1 \text{ und } \mathbf{k}'_2 = \mathbf{k}_3 - \mathbf{k}_1. \quad (12.29)$$

( $\longrightarrow$  Parametric Generation (OPG))

$$\hat{P}_i^{(3)}(\omega_4) = \frac{6\varepsilon_0}{4} \sum_{jkl} \chi_{ijkl}^{(3)}(\omega_4 : \omega_1, \omega_2, -\omega_3) \hat{E}_j(\omega_1) \hat{E}_k(\omega_2) \hat{E}_l^*(\omega_3), \quad (12.30)$$

$$\omega_4 = \omega_1 + \omega_2 - \omega_3 \text{ und } \mathbf{k}'_4 = \mathbf{k}_1 + \mathbf{k}_2 - \mathbf{k}_3. \quad (12.31)$$

( $\longrightarrow$  Four Wave Mixing (FWM))

Note, that the susceptibilities are symmetric with respect to a permutation of the frequencies  $\{\omega_i\}$  together with the corresponding index, since it is arbitrary, which of the frequencies is denoted as  $\omega_1$ , e.g.

$$\chi_{ijk}^{(n)}(\omega : \omega_1, \omega_2, \dots) = \chi_{ikj}^{(n)}(\omega : \omega_2, \omega_1, \dots). \quad (12.32)$$

In the following, we consider only the case of OPG.

### 12.8.3 Continuous Wave OPA

Optical parametric amplification occurs due to the nonlinear interaction of the three waves: pump, signal and idler wave during propagation in the nonlinear medium. We can derive these three coupled equations by starting from the general wave equation (2.7), and adding to the linear polarization of the medium  $\vec{P}^{(l)}(\vec{r}, t)$  also the second order nonlinear contribution (12.28)

$$\left( \Delta - \frac{1}{c_0^2} \frac{\partial^2}{\partial t^2} \right) \vec{E} = \mu_0 \frac{\partial^2}{\partial t^2} \left( \vec{P}^{(l)}(\vec{r}, t) + \vec{P}^{(2)}(\vec{r}, t) \right). \quad (12.33)$$

The linear term will lead to a change in group and phase velocities of the

three waves described by the dispersion relation of the medium  $k(\omega)$ . Assuming that the three waves are different in frequency and propoagating along the  $z$ -direction, this equation can be separated in three equations for the amplitudes  $E_{p,s,i}(z)$  for each frequency component, where

$$\vec{E}_{p,s,i}(z, t) = \text{Re} \left\{ E_{p,s,i}(z) e^{j(\omega_{p,s,i}t - k_{p,s,i}z)} \vec{e}_{p,s,i} \right\}. \quad (12.34)$$

To do so, we also write the nonlinear polarization in its three contributions oscillating at different frequencies

$$\vec{P}_{p,s,i}^{(2)}(z, t) = \text{Re} \left\{ P_{p,s,i}^{(2)}(z) e^{j(\omega_{p,s,i}t - k'_{p,s,i}z)} \vec{e}_{p,s,i} \right\}. \quad (12.35)$$

and assuming the slowly-varying-envelope approximation  $d^2_{p,s,i}E(z)/dz^2 \ll 2k dE_{p,s,i}(z)/dz$ , we obtain

$$\frac{\partial E_{p,s,i}(z)}{\partial z} = -\frac{j c_0^2 \omega_{p,s,i}}{2n(\omega_{p,s,i})} P_{p,s,i}^{(2)}(z) e^{-j(k'_{p,s,i} - k_{p,s,i})z}. \quad (12.36)$$

Here,  $c_0$  is the speed of light in vacuum and  $n$  is the refractive index at the correponding frequency of the wave amplitude considered. Equation 12.36 shows that the nonlinear polarization acts as a source term changing the amplitude of the corresponding wave. Introducing the phase mismatch of the three waves

$$\Delta k = k(\omega_p) - k(\omega_s) - k(\omega_i). \quad (12.37)$$

and the effective nonlinearity and coupling coefficients

$$d_{eff} = \frac{1}{2} \chi_{ijk}^{(2)}(\omega_p : \omega_s, \omega_i), \quad \kappa_{p,s,i} = \omega_{p,s,i} d_{eff} / (n_{p,s,i} c_0). \quad (12.38)$$

we obtain

$$\frac{\partial E_p(z)}{\partial z} = -j \kappa_p E_s(z) E_i(z) e^{j \Delta k z}, \quad (12.39)$$

$$\frac{\partial E_s(z)}{\partial z} = -j \kappa_s E_p(z) E_i^*(z) e^{-j \Delta k z}, \quad (12.40)$$

$$\frac{\partial E_i(z)}{\partial z} = -j \kappa_i E_p(z) E_s^*(z) e^{-j \Delta k z}. \quad (12.41)$$

Using the intensity in each beam  $I_{p,s,i} = \frac{n_{p,s,i}}{2Z_{F0}} |E_{p,s,i}|^2$  and multiply each equation in (12.39) to (12.41) with  $n_{p,s,i} c_0 \varepsilon_0 E_{p,s,i}^*/2$ , and add the complex conjugate to it, one finds with

$$\left( \frac{1}{\omega_p} \right) \frac{dI_p}{dz} = \frac{j\varepsilon_0 d_{eff}}{2} E_p^* E_s E_i e^{-j\Delta k z} + c.c.,$$

and similarly for the other equations, the Manley-Rowe relation

$$-\frac{1}{\omega_p} \frac{dI_p}{dz} = \frac{1}{\omega_s} \frac{dI_s}{dz} = \frac{1}{\omega_i} \frac{dI_i}{dz}. \quad (12.42)$$

This equation, which involves the change in photon flux at pump, signal and idler, guarantees that for each pump photon a signal and idler photon is generated. Due to the scaling of photon energy with frequency the corresponding intensities and with them the power flow has to scale proportional to the frequencies. Note, this follows from energy conservation and the Maxwell equations, no quantum theory has been invoked.

### 12.8.4 Theory of Optical Parametric Amplification

Also, the parametric amplifier equations (12.39) to (12.41) can be solved exactly and the solutions can be expressed in terms of Jacobi-Elliptic functions, they do not give much insight at first. For the purpose here, we solve the parametric amplifier equations in the undepleted pump approximation, i.e. we assume the signal and idler fields are weak compared to the pump. Then the pump amplitude can be assumed as fixed,  $E_p = const.$ , unchanged by signal and idler

$$\frac{\partial E_s(z)}{\partial z} = -j\kappa_s E_p E_i^*(z) e^{-j\Delta k z}, \quad (12.43)$$

$$\frac{\partial E_i(z)}{\partial z} = -j\kappa_i E_p E_s^*(z) e^{-j\Delta k z}. \quad (12.44)$$

Solution of these equations for initial conditions of a small input signal field,  $E_s(z=0) = E_s(0)$ , and no idler,  $E_i(z=0) = 0$  can be attempted using the trial solutions  $E_s(z) \sim E_s(0) e^{gz-j\Delta k z/2}$  and  $E_i(z) \sim E_i(0) e^{gz-j\Delta k z/2}$ , where  $g$  is the parametric gain in amplitude that follows from the determinantal

condition. These equations look similar to coupled mode equations also not exactly. Using

$$\begin{vmatrix} g - j\frac{\Delta k}{2} & j\kappa_s E_p \\ j\kappa_i E_p^* & g + j\frac{\Delta k}{2} \end{vmatrix} = 0$$

or

$$g = \sqrt{\Gamma^2 - \left(\frac{\Delta k}{2}\right)^2}, \text{ with } \Gamma = \sqrt{\kappa_i \kappa_s |E_p|^2}. \quad (12.45)$$

Here,  $\Gamma$  is the maximum gain achieved under phase matching, i.e.  $\Delta k = 0$ , which can be also expressed in terms of the pump intensity

$$\Gamma^2 = \frac{\omega_s \omega_i}{n_s n_i c_0^2} d_{eff}^2 |E_p|^2 = \frac{2Z_{F0} \omega_s \omega_i}{n_p n_s n_i c_0^2} d_{eff}^2 |I_p|^2. \quad (12.46)$$

The general solutions to Eqs. (12.43) - (12.44) are

$$E_s(z) = \{E_s(0) \cosh gz + B \sinh gz\} e^{-j\Delta kz/2} \quad (12.47)$$

$$E_i(z) = \{E_i(0) \cosh gz + D \sinh gz\} e^{-j\Delta kz/2} \quad (12.48)$$

where the missing constants  $B$  and  $D$  have to be matched to fulfill Eqs. (12.43) - (12.44)

$$B = -j\frac{\Delta k}{2g} E_s(0) - j\frac{\kappa_1}{g} E_p E_i^*(0) \quad (12.49)$$

$$D = -j\frac{\Delta k}{2g} E_i(0) - j\frac{\kappa_2}{g} E_p^* E_s^*(0) \quad (12.50)$$

For the case of our initial conditions, vanishing idler input, we obtain finally for the intensities of signal and idler beam after a propagation distance  $L$

$$I_s(L) = I_s(0) \left[ 1 + \frac{\Gamma^2}{g^2} \sinh^2 gL \right], \quad (12.51)$$

$$I_i(L) = I_s(0) \frac{\omega_i}{\omega_s} \frac{\Gamma^2}{g^2} \sinh^2 gL. \quad (12.52)$$

For the case of perfect phase matching  $g = \Gamma$  and the case of large gain  $\Gamma L \gg 1$ , these equations simplify to



$$I_s(L) = \frac{1}{4} I_s(0) e^{2\Gamma L}, \quad (12.53)$$

$$I_i(L) = \frac{1}{4} I_s(0) \frac{\omega_i}{\omega_s} e^{2\Gamma L}. \quad (12.54)$$

The parametric gain is

$$G = \frac{I_s(L)}{I_s(0)} = \frac{1}{4} e^{2\Gamma L}, \quad (12.55)$$

growing exponentially with the crystal length  $L$  and gain  $\Gamma$ . Note, that the exponential growth of signal and idler waves along the crystal is qualitatively different from the quadratic growth occurring in other second order nonlinear phenomena, such as sum frequency generation or second harmonic generation. This difference can be understood intuitively in the following way: in a strong pump field, the presence of a seed photon at the signal wavelength stimulates the generation of an additional signal photon and of a photon at the idler wavelength. Likewise, due to the symmetry of signal and idler, the amplification of an idler photon stimulates the generation of a signal photon. Therefore, the generation of the signal field reinforces the generation of the idler field and vice versa, giving rise to a positive feedback that is responsible for the exponential growth of the waves. Equation (12.46) shows that the gain coefficient  $\Gamma$  depends on: (i) the pump intensity; (ii) the signal and idler wavelengths; (iii) the nonlinear coefficient  $d_{eff}$ ; and (iv) the refractive indexes at the three interacting wavelengths. To characterize a parametric interaction and compare different nonlinear materials, one defines the following figure of merit:

$$FOM = \frac{d_{eff}}{\sqrt{\lambda_s \lambda_i n_p n_s n_i}} \quad (12.56)$$

In the following we discuss some examples of parametric gain calculation relevant to ultrashort pulses, assuming perfect phase matching. Figure 12.24 shows a plot of the parametric gain in BBO, at the infrared pump wavelength  $\lambda_p = 0.8 \mu m$  and the signal wavelength  $\lambda_s = 1.2 \mu m$  as a function of pump intensity and for different crystal lengths. The gain scales as the exponential of the square root of the pump intensity:  $G \sim \exp(\alpha I_p)$ . At a pump intensity  $I_p = 25 \text{ GW/cm}^2$ , a gain  $G \simeq 6$  is calculated for a crystal length  $L = 1 \text{ mm}$ ; however, it rapidly increases to  $G > 10^6$  for  $L = 5 \text{ mm}$ . The same gain can be obtained with a 3 mm crystal increasing the pump intensity to  $75 \text{ GW/cm}^2$ .

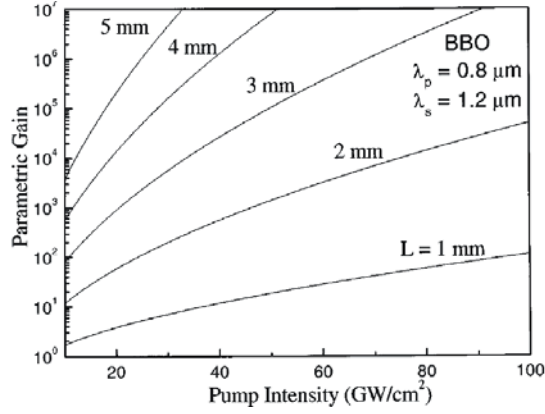


Figure 12.24: Parametric gain for an OPA at the pump wavelength  $\lambda_p = 0.8 \mu m$  and the signal wavelength  $\lambda_s = 1.2 \mu m$ , using type I phase matching in BBO ( $d_{eff} = 2 \text{ pm/V}$ ). [5]

The same plot for BBO at the visible pump wavelength  $\lambda_p = 0.4 \mu m$  and the signal wavelength  $\lambda_s = 0.6 \mu m$  is shown in Fig. 2.

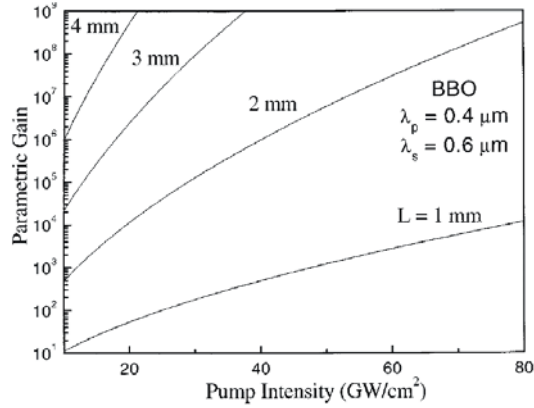


Figure 12.25: Parametric gain for an OPA at the pump wavelength  $\lambda_p = 0.4 \mu m$  and the signal wavelength  $\lambda_s = 0.6 \mu m$ , using type I phase matching in BBO ( $d_{eff} = 2 \text{ pm/V}$ ). [5]

In this case, at a pump intensity  $I_p = 25 \text{ GW/cm}^2$ , a gain  $G > 128$  is calculated for a crystal length  $L = 1 \text{ mm}$ , about a factor of 20 larger than

in the case of the infrared pump wavelength. The higher gain is due to the smaller values of  $\lambda_s$  and  $\lambda_i$ , which increases the figure of merit of the parametric interaction. Despite the improvement in figure of merit using a visible pump, the group velocity mismatch between the interacting pulses, as we will see later, prevents the use of long nonlinear crystals in this case. We now address the problem of phase matching.

### 12.8.5 Phase Matching

To achieve maximum gain, we must satisfy the phase matching condition,  $\Delta k = 0$ , which can be recast in the form

$$n_p = \frac{n_s \omega_s + n_i \omega_i}{\omega_p} \quad (12.57)$$

It is easy to show that this condition cannot be fulfilled in bulk isotropic materials in the normal dispersion region ( $n_i < n_s < n_p$ ). In some birefringent crystals, phase matching can be achieved by choosing for the higher frequency pump wave the polarization direction giving the lower refractive index. In the case, common in femtosecond OPAs, of negative uniaxial crystals ( $n_e < n_o$ ), the pump beam is polarized along the extraordinary direction, see Fig. 12.26

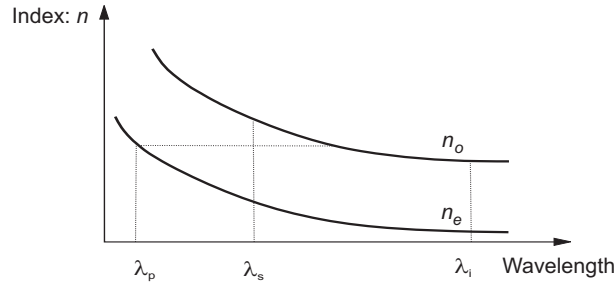


Figure 12.26: Type I noncritical phase matching.

If both signal and idler beams have the same ordinary polarization (perpendicular to that of the pump beam, this scheme is called type I phase matching (or  $o_s + o_i \rightarrow e_p$ ). If one of the two is polarized parallel to the pump beam, we talk about type II phase matching; in this case either the

signal ( $e_s + o_i \rightarrow e_p$ ) or the idler ( $o_s + e_i \rightarrow e_p$ ) can have the extraordinary polarization [7]. Both types of phase matching can be used and have their specific advantages according to the system under consideration. Usually the phase matching condition is achieved by adjusting the angle  $\theta$  between the wave vector of the propagating beams and the optical axis of the nonlinear crystal, angular phase matching, see Figure 12.27

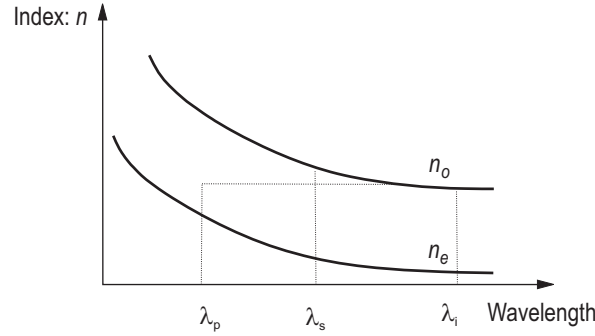


Figure 12.27: Type I critical phase matching by adjusting the angle  $\theta$  between wave vector of the propagating beam and the optical axis.

Alternatively, the refractive indices can be changed by adjusting the crystal temperature (temperature phase matching). As an example, we consider the case of a negative uniaxial crystal, for which type I phase matching is achieved when

$$n_{ep}(\theta)\omega_p = n_{os}\omega_s + n_{oi}\omega_i$$

$$\frac{1}{n_{ep}(\theta)^2} = \frac{\sin^2 \theta}{n_{ep}^2} + \frac{\cos^2 \theta}{n_{op}^2}$$

which leads to

$$\theta = \arcsin \left[ \frac{n_{ep}}{n_{ep}(\theta)} \sqrt{\frac{n_{op}^2 - n_{ep}^2(\theta)}{n_{op}^2 - n_{ep}^2}} \right].$$

Figures 12.28 and 12.29 show the phase matching angles as a function of wavelength for BBO types I and II OPAs at the pump wavelengths 0.8 and 0.4  $\mu\text{m}$ .

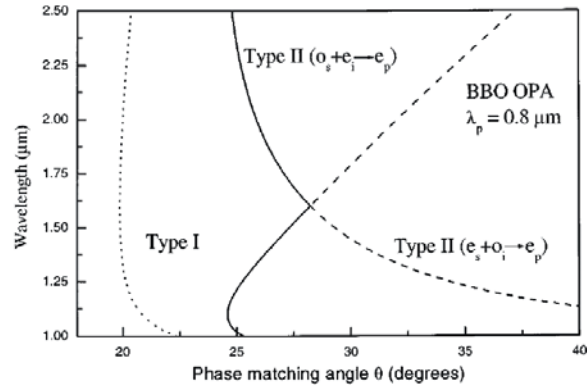


Figure 12.28: Angle tuning curves for a BBO OPA at the pump wavelength  $\lambda_p = 0.8 \mu\text{m}$  for type I phase matching (dotted line), type II ( $o_s + e_i \rightarrow e_p$ ) phase matching (solid line), and type II ( $e_s + o_i \rightarrow e_p$ ) phase matching (dashed line).

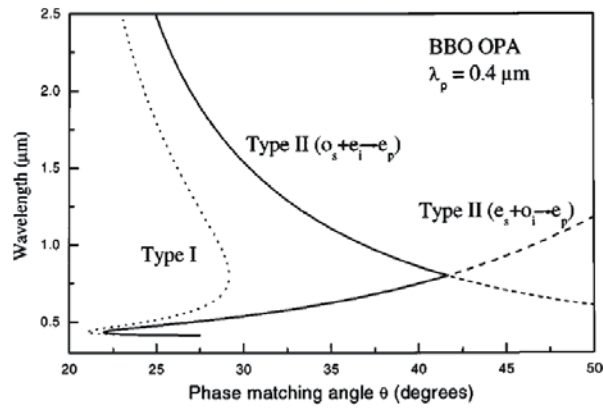


Figure 12.29: Angle tuning curves for a BBO OPA at the pump wavelength  $\lambda_p = 0.4 \mu\text{m}$  for type I phase matching (dotted line), type II ( $o_s + e_i \rightarrow e_p$ ) phase matching (solid line), and type II ( $e_s + o_i \rightarrow e_p$ ) phase matching (dashed line).

Note, that in general, the phase matching angle shows a less pronounced wavelength dependence for type I with respect to type II phase matching.

### 12.8.6 Quasi-Phase Matching

If in a given crystal, phase matching by using birefringents is not possible, one can eventually perform quasi-phase matching. [8], see Fig. 12.30. By periodic poling with a strong applied electric field, the nonlinear coefficient  $d_{eff}$  in a quasi phase matched material will be periodically modulated with a period  $2\ell_c = 2\pi/\Delta k$ .

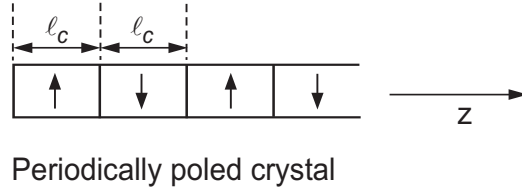


Figure 12.30: Variation of  $d_{eff}$  in a quasi phase matched material as a function of propagation distance.

The nonlinear coefficient can therefore be expanded into a Taylor series

$$d_{eff}(z) = \sum_{m=-\infty}^{+\infty} d_m e^{jm\kappa z}. \quad (12.58)$$

with  $\kappa = 2\pi/(2\ell_c) = \Delta k$ . It is obvious, that if this expression is substituted into equation (12.39), the term proportional to  $d_{-1}$  can facilitate phase matching.

### 12.8.7 Ultrashort Pulse Optical Parametric Amplification

So far we have studied the interaction of three monochromatic waves, i.e., cw beams. Now, we consider the case, relevant for femtosecond OPAs, where three pulses described by complex pulse envelopes

$$\vec{E}_{p,s,i}(z, t) = \text{Re} \left\{ E_{p,s,i}(z, t) e^{j(\omega_{p,s,i}t - k_{p,s,i}z)} \vec{e}_{p,s,i} \right\} \quad (12.59)$$

are considered. Each pulse envelope is now propagating at its group velocity and the equations for the pulse envelope change from the amplitude equations (12.39) - (12.41) to

$$\frac{\partial E_p}{\partial z} + \frac{1}{v_p} \frac{\partial E_p}{\partial t} = -j\kappa_p E_s E_i e^{j\Delta kz}, \quad (12.60)$$

$$\frac{\partial E_s}{\partial z} + \frac{1}{v_s} \frac{\partial E_s}{\partial t} = -j\kappa_s E_p E_i^* e^{-j\Delta kz}, \quad (12.61)$$

$$\frac{\partial E_i}{\partial z} + \frac{1}{v_i} \frac{\partial E_i}{\partial t} = -j\kappa_i E_p E_s^* e^{-j\Delta kz}, \quad (12.62)$$

where  $v_{p,s,i} = dk/d\omega|_{\omega_{p,s,i}}$  are the corresponding group velocities of pump, signal and idler. Note, it is straight forward to include other nonlinearities, that might become important, like self phase modulation or higher order dispersion terms. For numerical simulations, it is convenient to introduce the retarded time  $t' = t - z/v_p$ , to take out the trivial motion of the pump pulse, which leads to

$$\frac{\partial E_p}{\partial z} = -j\kappa_p E_s E_i e^{j\Delta kz}, \quad (12.63)$$

$$\frac{\partial E_s}{\partial z} + \left( \frac{1}{v_s} - \frac{1}{v_p} \right) \frac{\partial E_s}{\partial t} = -j\kappa_s E_p E_i^* e^{-j\Delta kz}, \quad (12.64)$$

$$\frac{\partial E_i}{\partial z} + \left( \frac{1}{v_i} - \frac{1}{v_p} \right) \frac{\partial E_i}{\partial t} = -j\kappa_i E_p E_s^* e^{-j\Delta kz}. \quad (12.65)$$

Despite the many simplifications, these equations capture the main issues of parametric amplification with ultrashort pulses, that are related to group velocity mismatch (GVM) between the interacting pulses. In particular, GVM between the pump and the amplified signal and idler pulses limits the interaction length over which parametric amplification takes place, while GVM between the signal and the idler beams limits the phase matching bandwidth. The useful interaction length for parametric interaction is quantified by the pulse splitting length, which is defined as the propagation length after which the signal (or the idler) pulse separates from the pump pulse in the absence of gain, and is expressed as

$$\ell_{jp} = \frac{\tau}{\delta_{jp}}, \text{ with } \delta_{jp} = \left( \frac{1}{v_j} - \frac{1}{v_p} \right), \quad (12.66)$$

where  $\tau$  is the pump pulse duration and  $\delta_{jp}$  is the GVM between pump and signal/idler. Note that the pulse splitting length becomes shorter for

decreasing pulse duration and for increasing GVM. GVM depends on the crystal type, pump wavelength, and type of phase matching. Figures 12.31 and 12.32 show examples of GVM curves for a BBO OPA pumped by 0.8 and 0.4  $\mu\text{m}$  pulses, respectively. Note that, due to greater dispersion values in the visible, GVM is in general larger in this wavelength range. For crystal lengths shorter than the pulse splitting length, GVM effects can be neglected, to a first approximation, and Eqs. (12.45) and (12.46), valid for cw beams, can be used for gain calculations. For crystals longer than or comparable to the pulse splitting length, GVM plays a crucial role and Eqs.(12.63) - (12.65) must be solved numerically to properly account for it.

There is a qualitatively significant difference between the cases in which  $\delta_{sp}$  and  $\delta_{ip}$  have the same or different signs.

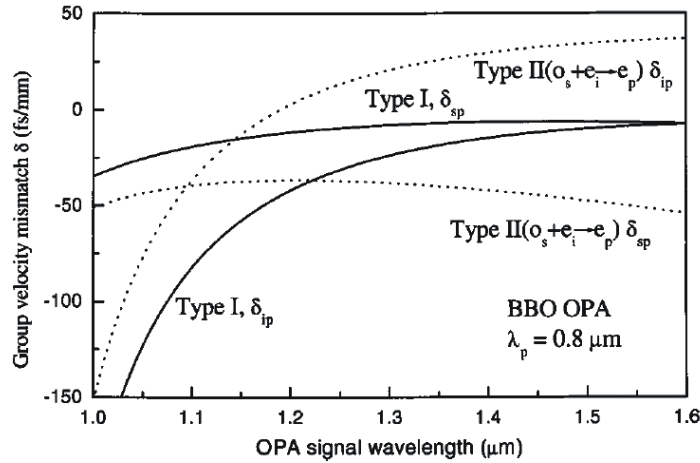


Figure 12.31: Pump-signal ( $\delta_{sp}$ ) and pump-idler ( $\delta_{ip}$ ) group velocity mismatch curves for a BBO OPA at the pump wavelength  $\lambda_p=0.8 \mu\text{m}$  for type I phase matching (solid line) and type II ( $o_s + e_i \rightarrow e_p$ ) phase matching (dashed line).



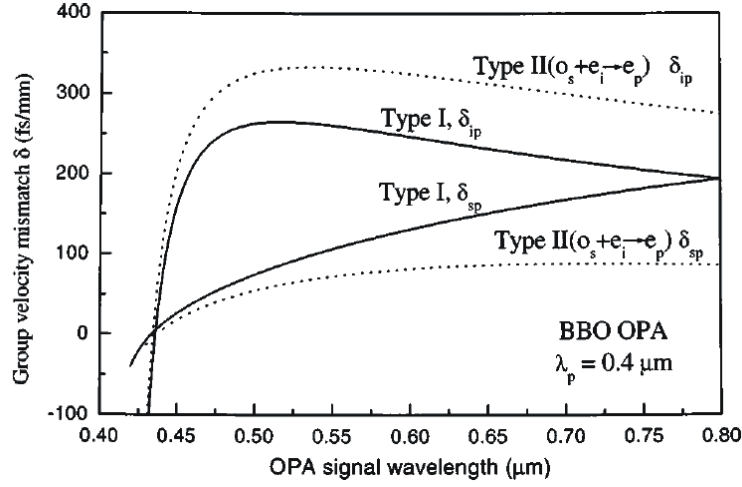


Figure 12.32: Pump-signal ( $\delta_{sp}$ ) and pump-idler ( $\delta_{ip}$ ) group velocity mismatch curves for a BBO OPA at the pump wavelength  $\lambda_p=0.4 \mu\text{m}$  for type I phase matching (solid line) and type II ( $o_s + e_i \rightarrow e_p$ ) phase matching (dashed line).

When  $\delta_{sp}\delta_{ip} > 0$ , both the signal and the idler pulses walk away from the pump in the same direction so that the gain rapidly decreases for propagation distances longer than the pulse splitting length and eventually saturates. On the other hand, when  $\delta_{sp}\delta_{ip} < 0$  signal and idler pulses move in opposite direction with respect to the pump; in this way the signal and idler pulses tend to stay localized under the pump pulse and the gain grows exponentially even for crystal lengths well in excess of the pulse splitting length. To try to rationalize this effect, we can consider the situation in which the signal pulse has moved slightly to the left and the idler pulse to the right of the pump pulse: during the parametric process, the signal pulse generates idler photons, which move to the right, i.e., towards the peak of the pump; on the other hand the idler pulse will generate signal photons which in turn move to the left, again towards the peak of the pump. This concentration of photons under the peak of the pump explains the exponential gain growth. In Fig. 12.33 we show an example of solution of Eqs. (12.63)-(12.65) for the case  $\delta_{sp}\delta_{ip} > 0$ ; we consider a type I BBO OPA pumped at  $0.4 \mu\text{m}$  with signal wavelength  $\lambda_s = 0.7 \mu\text{m}$ , with GVMs  $\delta_{sp}=167 \text{ fs/mm}$  and  $\delta_{ip}=220 \text{ fs/mm}$ . We see that, after an initial growth, the gain rapidly tends to saturate because both signal

and idler pulses temporally separate from the pump. Note that, because the trailing edge of the pulse resides for a longer time in the amplification region, there is a modest pulse shortening (20%–30%) and asymmetry.

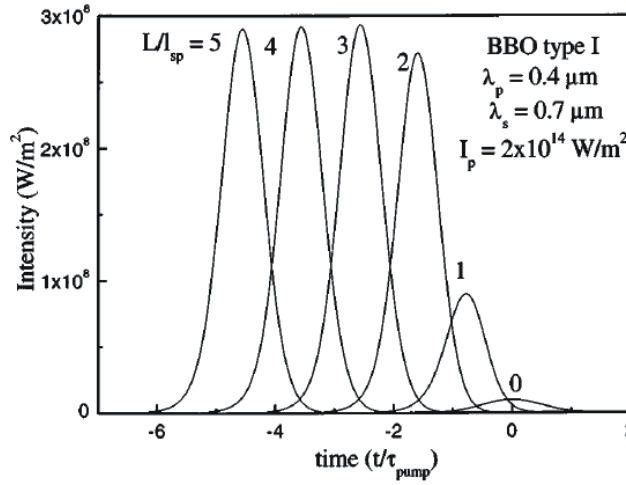


Figure 12.33: Signal pulse evolution for a BBO type I OPA with  $\lambda_p = 0.4 \mu\text{m}$ ,  $\lambda_s = 0.7 \mu\text{m}$ , for different lengths  $L$  of the nonlinear crystal. Pump intensity is  $20 \text{ GW/cm}^2$ . Time is normalized to the pump pulse duration and the crystal length to the pump-signal pulse splitting length.[5]

The case  $\delta_{sp}\delta_{ip} < 0$  is shown in Fig. 12.34; we consider a type II BBO OPA pumped at  $0.8 \mu\text{m}$  with signal wavelength  $\lambda_s = 0.8 \mu\text{m}$ , having group velocity mismatches  $\delta_{sp} = -47.5 \text{ fs/mm}$  and  $\delta_{ip} = 34.6 \text{ fs/mm}$ . Here we see that the signal growth stays exponential for propagation distances well exceeding the pulse splitting length and that the signal pulse tends to stay localized under the pump.

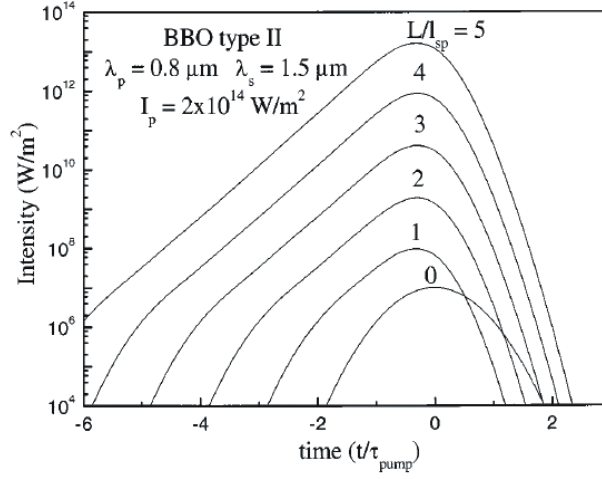


Figure 12.34: Signal pulse evolution for a BBO type II OPA with  $\lambda_p = 0.8 \mu\text{m}$ ,  $\lambda_s = 1.5 \mu\text{m}$ , for different lengths  $L$  of the nonlinear crystal. Pump intensity is  $20 \text{ GW/cm}^2$ . Time is normalized to the pump pulse duration and the crystal length to the pump-signal pulse splitting length.[5]

In the following, we will show that GVM between signal and idler pulses determines the phase matching bandwidth for the parametric amplification process. Let us assume that perfect phase matching is achieved for a given signal frequency  $\omega_s$  (and for the corresponding idler frequency  $\omega_i = \omega_p - \omega_s$ ). If the signal frequency increases to  $\omega_s + \Delta\omega$  energy conservation requires that the idler frequency decreases to  $\omega_i - \Delta\omega$ . The wave vector mismatch can then be approximated to the first order as

$$\Delta k = -\frac{dk_s}{d\omega} \Delta\omega + \frac{dk_i}{d\omega} \Delta\omega = \left( \frac{1}{v_i} - \frac{1}{v_s} \right) \Delta\omega, \quad (12.67)$$

Within the large-gain approximation, the full width at half maximum (FWHM) phase matching bandwidth can then be calculated as

$$\Delta f = -\frac{2\sqrt{\ln 2}}{\pi} \sqrt{\frac{\Gamma}{L}} \frac{1}{\left| \frac{1}{v_i} - \frac{1}{v_s} \right|}. \quad (12.68)$$

Large GVM between signal and idler waves dramatically decreases the phase matching bandwidth; large gain bandwidth can be expected when the OPA

approaches degeneracy, i.e.  $\omega_s = \omega_i$ , in type I phase matching or in the case of group velocity matching between signal and idler ( $v_s = v_i$ ). Obviously, in this case Eq. (e:opg.ubw) loses validity and the phase mismatch  $\Delta k$  must be expanded to the second order, giving

$$\Delta f = -\frac{2\sqrt[4]{\ln 2}}{\pi} \sqrt[4]{\frac{\Gamma}{L}} \frac{1}{\left| \frac{d^2 k_s}{d\omega^2} + \frac{d^2 k_i}{d\omega^2} \right|}. \quad (12.69)$$

Figures 12.35 and 12.36 show typical plots of phase matching bandwidths for BBO OPAs, pumped at 0.8 and 0.4  $\mu\text{m}$ , respectively. We see a remarkable difference between types I and II phase matching: for type II interaction, the bandwidth is smaller than in type I and stays more or less constant over the tuning range, while for type I interaction, as previously said, the bandwidth increases as the OPA approaches degeneracy. These features can be exploited for different applications: type I phase matching is used to achieve the shortest pulses, while type II phase matching allows to obtain relatively narrow bandwidths over broad tuning ranges, which are required for many spectroscopic investigations.

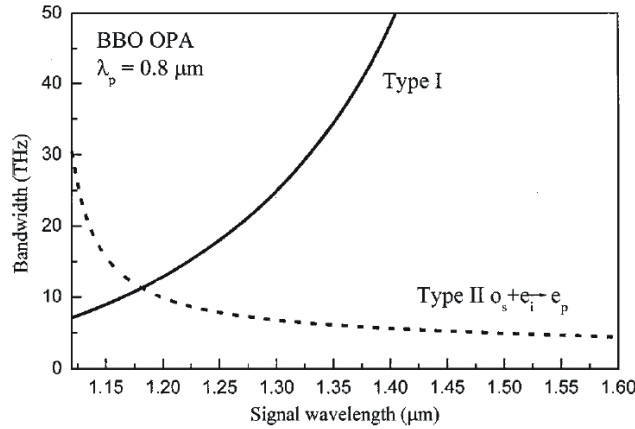


Figure 12.35: Phase matching bandwidth for a BBO OPA at the pump wavelength  $\lambda_p = 0.8 \mu\text{m}$  for type I phase matching (solid line) and type II  $o_s + e_i \rightarrow e_p$  phase matching (dashed line). Crystal length is 4 mm and pump intensity 50  $\text{GW}/\text{cm}^2$ .

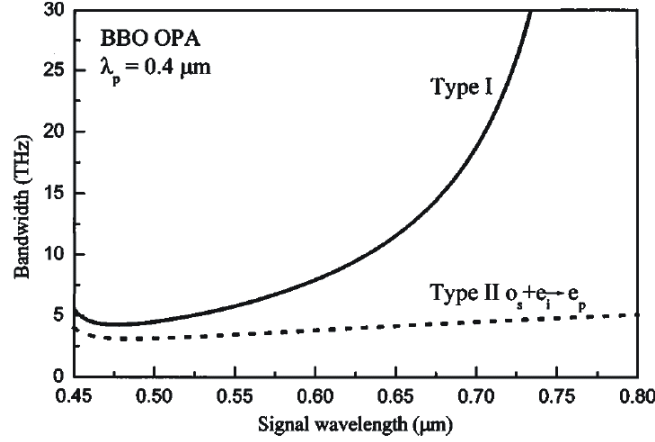


Figure 12.36: Phase matching bandwidth for a BBO OPA at the pump wavelength  $\lambda_p = 0.4 \mu\text{m}$  for type I phase matching (solid line) and type II  $o_s + e_i \rightarrow e_p$  phase matching (dashed line). Crystal length is 2 mm and pump intensity  $100 \text{ GW}/\text{cm}^2$ .

So far we have only considered a collinear interaction, in which, once the phase matching condition ( $\Delta k = 0$ ) is achieved, the group velocities of signal and idler, and thus the phase matching bandwidth, are set. Later, we will see that in a noncollinear interaction there is an additional degree of freedom, the pump-signal angle  $\alpha$ . Suitably selecting this angle, it is often possible to achieve simultaneously phase matching and group velocity matching between signal and idler, thus obtaining very broad gain bandwidths.

### 12.8.8 Optical Parametric Amplifier Designs

Before illustrating in detail some of the most common OPA designs, we will try to present a very general description of the operating principles of an OPA, according to the scheme shown in Fig. 12.37. Femtosecond OPAs are in general pumped by amplified Ti:sapphire lasers: standard systems typically run at 1 kHz repetition rate and generate pulses at the wavelength  $\lambda > 0.8 \mu\text{m}$ , with 0.5–1 mJ energy and duration ranging from 50 to 150 fs. Also higher repetition rates using lower pulse energies are possible. Pumping can take place at the FW or at the SH of the Ti:sapphire laser, i.e., 800 or 400 nm. Since the optical parametric amplification process consists of the

interaction of a weak signal beam with a strong pump beam, the first stage of any OPA system is the generation of the initial signal beam, the so-called seed beam. Since the seed beam is at a different frequency from the pump beam, a nonlinear optical process is required for its generation. Two different techniques have been used for the seed generation: parametric superfluorescence and white-light continuum generation. Parametric superfluorescence is high gain parametric amplification of the vacuum or quantum noise. In practice it is simply achieved by pumping a suitable nonlinear crystal, which is often of the same types as the ones used in the subsequent OPA stages; amplification will occur at those wavelengths for which the parametric interaction is phase matched. The advantage of parametric superfluorescence is the possibility of achieving large amplification and substantial seed pulse energies; its disadvantages are the inherent fluctuations of a process starting from quantum noise, and the poor spatial quality of the generated seed beam.

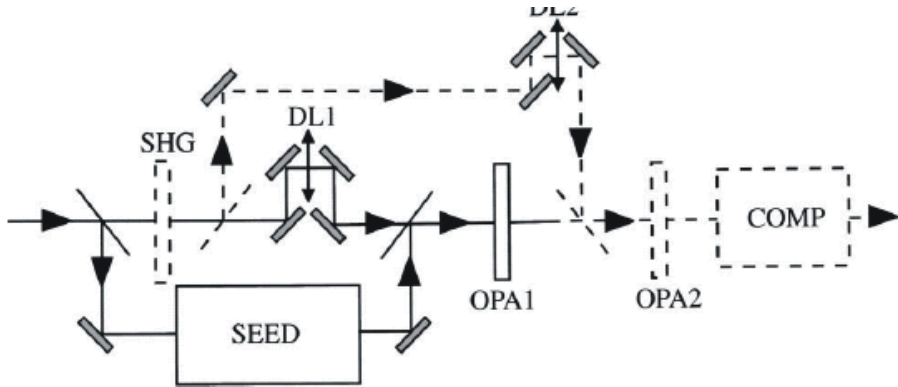


Figure 12.37: Scheme of an ultrafast optical parametric amplifier. SEED: seed generation stage; DL1, DL2: delay lines; OPA1, OPA2 parametric amplification stages; COMP: compressor.

It is essentially a noise burst. White light generation occurs when an intense ultrashort pulse is focused inside a transparent material, such as fused silica or sapphire: as a result of the interplay between self-focusing and self-phase modulation, a large spectral broadening takes place. Although the processes occurring during the generation of white-light continuum are still not fully understood, its properties are very good for generation of an OPA seed pulse. When focusing  $0.8 \mu\text{m}$ , 100 fs pulses into a sapphire plate, with

thickness ranging from 1 to 3 mm, the threshold for white-light generation is around 1  $\mu\text{J}$ . The exact value depends on the focusing conditions. The continuum spectrum extends throughout the visible down to 0.42  $\mu\text{m}$  and the near-IR up to 1.5  $\mu\text{m}$ , with an energy of approximately 10 pJ per nm of bandwidth. Under the correct conditions (i.e., a single self-focused filament) the white light has an excellent spatial quality, with a circular gaussian beam, and a very high pulse-to-pulse stability. When using materials with high thermal conductivity and low UV absorption such as sapphire, no long-term degradation of the material is experienced. Following generation of the seed pulse, the pump and seed pulses are combined in a suitable nonlinear crystal, in a first parametric amplification stage, preamplifier. To achieve temporal overlap, their relative timing must be adjusted by a delay line. Often the pump spot size in the nonlinear crystal is set by a telescope and is chosen to achieve the highest possible gain without causing optical damage of the crystal, or inducing third-order nonlinear effects (self-focusing, selfphase modulation, or white light generation) that would cause beam distortion or breakup. In case of parametric superfluorescence seed, the preamplifier is also used as a spatial filter, to improve the spatial coherence of the signal beam by amplifying only those spatial components of the superfluorescence that overlap the pump beam in the crystal. After the first amplification stage, the signal beam can be further amplified in a second stage, power amplifier. Usually this stage is driven into saturation, i.e., with significant pump depletion and conversion efficiency above 30%. In this regime, the amplified energy is less sensitive to seed fluctuations, and high pulse stability can be achieved. The purpose of using two amplification stages instead of one long crystal is twofold: (i) the GVM between pump and signal pulses in the first stage can be compensated by a delay line; and (ii) this scheme gives the flexibility of separately adjusting the pump intensity, and thus the parametric gain, in the two stages. After the power amplifier, signal and idler beams are separated from the pump and from each other using dichroic filters or mirrors. Finally, in case of broadband amplification, a pulse compressor is used to obtain transform-limited pulse duration. Figure 12.38 shows a specific design for a near IR-OPA.

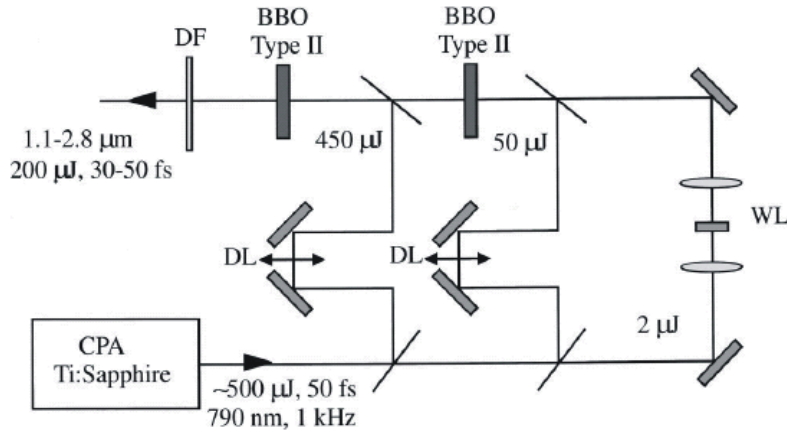


Figure 12.38: Scheme of a near-IR OPA DL: delay lines; WL: white light generation stage; DF: dichroic filter.

### 12.8.9 Noncollinear Optical Parametric Amplifier (NOPA)

Until recently the shortest pulses achieved from OPAs have been in the 30–50 fs range, limited either by the narrow phase matching bandwidths or by the long pump pulse duration. In the following we discuss a OPA scheme which overcome these difficulties and generate few-opticalcycle pulses with microjoule-level energy in the visible as well as in the infrared. In the visible, relatively long pump pulses ( $\sim 100$  fs) are used and the properties of non-collinear phase matching are exploited to achieve broadband amplification of the white-light seed; the amplified pulses are then compressed to sub-10 fs duration using suitable dispersive delay lines. In the infrared, ultrabroadband pulses can be generated using short (20–40 fs) pump pulses and exploiting nonlinear compression effects arising in the parametric amplification process at high conversion efficiencies.

In an OPA using a collinear interaction geometry, the propagation direction in the nonlinear crystal is selected to satisfy, for a given signal wavelength, the phase-matching condition  $\Delta k = 0$ . In this condition the signal and idler group velocities are fixed and so the phase matching bandwidth of the process, see Eq. (12.68). An additional degree of freedom can be introduced using a noncollinear geometry, such as that shown in Fig. 12.39 a): pump and signal wave vectors form an angle  $\alpha$  (independent of signal



wavelength) and the idler is emitted at an angle  $\Omega$  with respect to the signal.

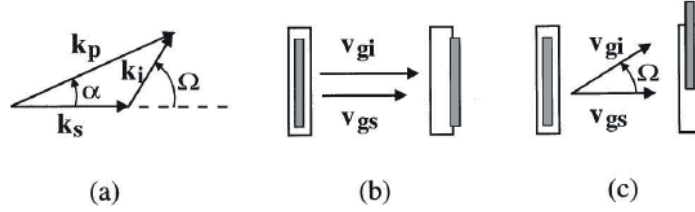


Figure 12.39: a) Schematic of a noncollinear interaction geometry; b) representation of signal and idler pulses in the case of collinear interaction; and c) same as b) for noncollinear interaction.

In this case the phase matching condition becomes a vector equation, which, projected on directions parallel and perpendicular to the signal wave vector, becomes

$$\Delta k_{par} = k_s \cos \alpha - k_s - k_i \cos \Omega = 0 \quad (12.70)$$

$$\Delta k_{perp} = k_s \sin \alpha - k_i \sin \Omega = 0 \quad (12.71)$$

Note, that the angle  $\Omega$  is not fixed, but depends on the signal wavelength. If the signal frequency increases by  $\Delta\omega$ , the idler frequency decreases by  $\Delta\omega$  and

the wave vector mismatches along the two directions can be approximated, to the first order, as

$$\Delta k_{par} = -\frac{dk_s}{d\omega_s} \Delta\omega + \frac{dk_i}{d\omega_i} \cos \Omega \Delta\omega - k_i \sin \Omega \frac{d\Omega}{d\omega_i} \Delta\omega = 0 \quad (12.72)$$

$$\Delta k_{perp} = \frac{dk_i}{d\omega_i} \sin \Omega \Delta\omega + k_i \cos \Omega \frac{d\Omega}{d\omega_i} \Delta\omega = 0 \quad (12.73)$$

To achieve broadband phase matching, both  $\Delta k_{par}$  and  $\Delta k_{perp}$  must vanish. Upon multiplying Eq. (12.72) by  $\cos(\Omega)$  and Eq. (12.73) by  $\sin(\Omega)$  and adding the results, we get

$$\frac{dk_i}{d\omega_i} - \cos \Omega \frac{dk_s}{d\omega_s} = 0 \quad (12.74)$$

which is equivalent to

$$v_i - v_s \cos \Omega = 0 \quad (12.75)$$

This equation shows that broadband phase matching can be achieved for a signal-idler angle  $\Omega$  such that the signal group velocity equals the projection of the idler group velocity along the signal direction. This effect is shown pictorially in Fig. 12.39 for a collinear geometry [Fig. 16b], signal and idler moving with different group velocities get quickly separated giving rise to pulse lengthening and bandwidth reduction, while in the noncollinear case [Fig. 16c] the two pulses manage to stay effectively overlapped. Note, that Eq. (12.75) can be satisfied only if  $v_i > v_s$ ; this is, however, always the case in the commonly used type I phase matching in negative uniaxial crystals, where both signal and idler see the ordinary refractive index. Equation (12.75) allows to determine the signal-idler angle  $\Omega$  required for broadband phase matching; from a practical point of view, it is more useful to know the pump-signal angle  $\alpha$ , which is given by

$$\alpha = \arcsin \left[ \frac{1 - \frac{v_s^2}{v_i^2}}{1 + 2v_s n_s \lambda_i / v_i n_i \lambda_s + (n_s \lambda_i / n_i \lambda_s)^2} \right] \quad (12.76)$$

As an example, in a type I BBO OPA pumped at  $\lambda_p = 0.4 \mu\text{m}$  for a signal wavelength  $\lambda_s = 0.6 \mu\text{m}$  broadband phase matching is achieved for  $\alpha = 53.7^\circ$ . To better illustrate the effect of noncollinear phase matching, in Fig. 12.40 we plot, for a type I BBO OPA pumped at  $0.4 \mu\text{m}$ , the phase matching angle  $\theta$  as a function of signal wavelength for different values of pump-signal angle  $\alpha$ . For a collinear configuration ( $\alpha = 0^\circ$ )  $\theta$  shows a strong dependence on the signal wavelength so that, for a fixed crystal orientation, phase matching can be achieved only over a narrow signal frequency range. By going to a noncollinear configuration and increasing  $\alpha$ , the wavelength dependence of  $\theta$  becomes progressively weaker until, for the optimum value  $\alpha = 3.7^\circ$ , a given crystal orientation ( $\theta \simeq 31.3^\circ$ ) allows to achieve simultaneously phase matching over an ultrabroad bandwidth, extending from  $0.5$  to  $0.75 \mu\text{m}$ . Note that, in this configuration, the symmetry between signal and idler is lost, because they propagate at different angles. This favorable property of the noncollinear geometry for broadband parametric amplification was first recognized by Gale et al.[9] and was exploited to build broadband OPOs generating pulses as short as 13 fs. Over the last decade, the same concept was extended by many research groups to OPAs seeded by the white-light continuum.

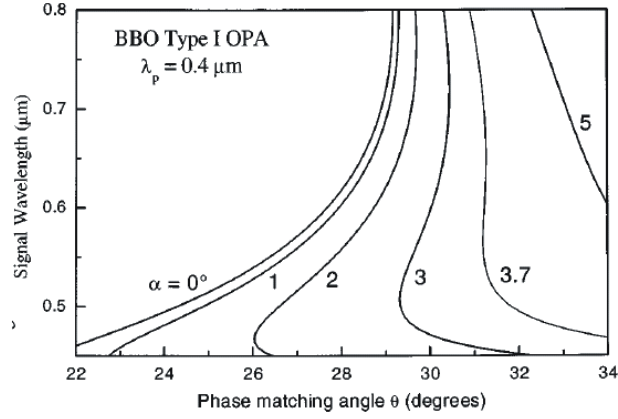


Figure 12.40: Phase-matching curves for a noncollinear type I BBO OPA pumped at  $\lambda_p = 0.4 \mu\text{m}$ , as a function of the pump-signal angle  $\alpha$ . [5]

A schematic of an experimental setup for an ultrabroadband noncollinear OPA (NOPA) is reported in Fig. 12.41

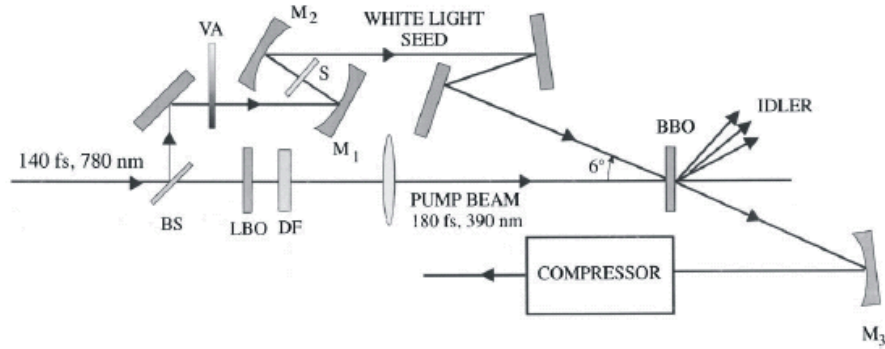


Figure 12.41: Scheme of a noncollinear visible OPA. BS: beam splitter; VA: variable attenuator; S: 1-mm-thick sapphire plate; DF: dichroic filter; M1, M2, M3, spherical mirrors. [5]

The system is pumped by an amplified Ti:sapphire laser, generating 140 fs pulses at  $0.78 \mu\text{m}$  and 1 kHz repetition rate with energy up to  $500 \mu\text{J}$ .

The pump pulses  $\sim 0.39 \mu\text{m}$  wavelength,  $10 \mu\text{J}$  energy,  $180 \text{ fs}$  duration are obtained by frequency doubling a fraction of the light in a 1-mm-thick lithium triborate crystal. The seed pulses are generated by focusing another small fraction of the FW beam, with energy of approximately  $2 \mu\text{J}$ , into a 1-mm-thick sapphire plate; by carefully controlling the energy incident on the plate (using a variable optical - density attenuator) and the position of the plate around the focus, a highly stable single-filament white-light continuum is generated. To avoid the introduction of additional chirp, reflective optics are employed to guide the white light to the amplification stage. Parametric gain is achieved in a 1-mm-thick BBO crystal, cut at  $53.2^\circ$ , using a singlepass configuration to increase the gain bandwidth. The chosen crystal length is close to the pulse-splitting length for signal and pump in the wavelength range of interest. The white light seed is imaged into the BBO crystal by spherical mirror M2, with a spot size nearly matching that of the pump beam. The amplified pulses have energy of approximately  $2 \mu\text{J}$ , peak-to-peak fluctuations of less than 7% and maintain a good TEM00 beam quality. Higher energies, up to  $10 \mu\text{J}$ , can be extracted by a second pass in the BBO crystal. After the gain stage the amplified pulses are collimated by the spherical mirror M3 and sent to the compressor. This design is quite similar to the OPAs reported in the last section, the main differences being the noncollinear geometry and the use of reflective optics to prevent pulse chirping.

The NOPA pulse bandwidth strongly depends on the system alignment and on the chirp of the white-light seed. A typical spectrum obtained under optimum alignment conditions is shown in Fig. 12.42 as a solid line: it extends over a FWHM bandwidth of  $180 \text{ THz}$  and is virtually not tunable, since it covers the maximum available gain bandwidth. Experimentally, this condition can be easily achieved by adjusting the pump-signal angle to match the apex angle of the strong parametric superfluorescence cone emitted by the BBO crystal when illuminated by the pump pulse. Narrower gain bandwidths, which may be required for some experiments, can be simply achieved by detuning the pump-seed angle from the optimum value and/or deliberately increasing the white light chirp: in this case, the NOPA can be tuned by slightly tilting the BBO crystal and/or varying the pump-seed delay. A typical sequence of amplified pulse spectra obtained under these conditions is shown in Fig. 12.42 as dashed lines.

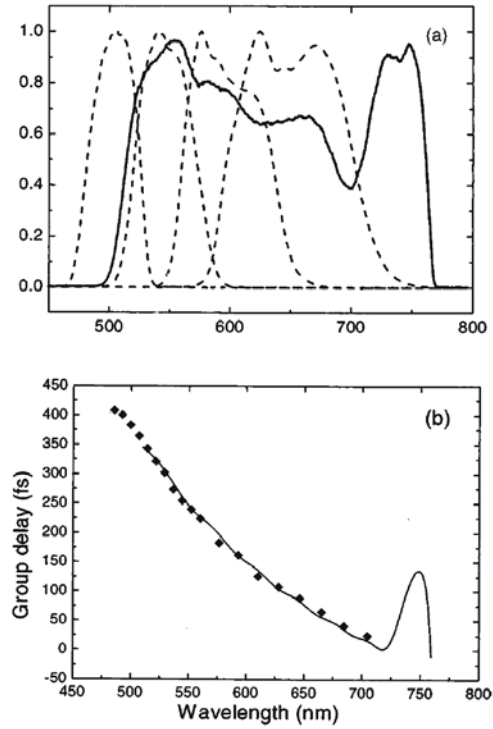


Figure 12.42: a) Solid line: NOPA spectrum under optimum alignment conditions; dashed line: sequence of spectra obtained by increasing the white light chirp; b) points: measured GD of the NOPA pulses; dashed line: GD after ten bounces on the ultrabroadband chirped mirrors.

The group delay (GD) versus frequency characteristics of the pulses generated was measured by upconversion and is shown in Fig. 12.42 (b). The measurement gives an overall GD of 400 fs between the red and the blue components of the spectrum; the main contributions to the dispersion are the sapphire plate, the BBO crystal, and the path  $\sim 3.5$  m in air. Accurately correcting the phase over such broad bandwidths poses a challenge on the compression system. The shortest pulses generated by the NOPA were obtained by a prism-chirped mirror combination and have a nearly transform-limited duration of 4.4 fs. Note the dramatic shortening of the pulsewidths with respect to the pump pulse duration, which is in the 100 fs range. As a matter of fact, using short pump pulses does not help in getting shorter pulses from the OPA, but on the contrary could be detrimental to the broad-

band amplification process, because of the reduced temporal overlap between the pump pulses and the chirped white-light seed. As an example for an all chirped mirror dispersion compensation, Fig. 12.42 (b) as a solid line the opposite of the GD generated by ten bounces on chirped mirrors which were custom designed to compensate for the NOPA dispersion: it can be seen that it matches the required GD very accurately over the wavelength range 0.51–0.71  $\mu\text{m}$ , with a root-mean-square deviation of only 1.8 fs.

For the pulses generated by the NOPA shown in Fig. 12.41 and compressed by the chirped mirror compressor, a full amplitude and phase characterization using the SPIDER technique resulted in the reconstructed pulse amplitude profile shown in Fig. 12.43.

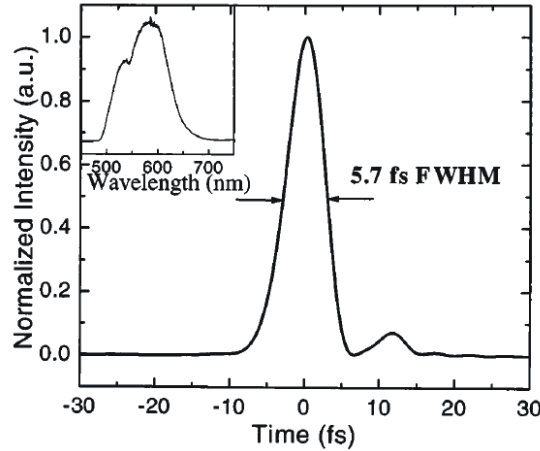


Figure 12.43: Reconstructed temporal intensity of the compressed NOPA pulse measured by the SPIDER technique. The inset shows the corresponding pulse spectrum.[5]

### 12.8.10 Optical Parametric Chirped Pulse Amplifiers OPCPA

Scaling to higher pulse energies and the use of high average power picosecond pump lasers can be achieved by applying chirped pulse amplification to the OPA concept. An example is given in Fig. 12.44.

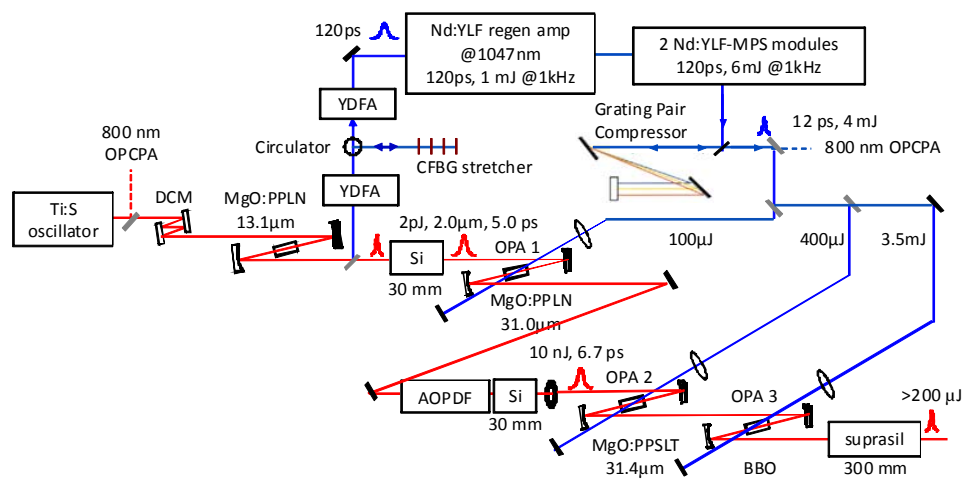


Figure 12.44: OPCPA system generating  $200\text{ }\mu\text{J}$ ,  $20\text{ fs}$  pulses at  $2\text{ }\mu\text{m}$ . It consists of a broadband Ti:sapphire laser. Seed pulses are generated via DFG in a quasi-phase matched MgO:PPLN. The 1060 nm portion of the Ti:sapphire spectrum is chirped in a fiber Bragg grating and seeds a Nd:YLF CPA generating 12-ps long 4 mJ pulses to pump a 3-stage OPCPA based on quasi-phase matched PPLN at  $2\text{ }\mu\text{m}$ . Pulse compression is achieved by a bulk suprasil and a AOPDF.

# Bibliography

- [1] Lecture on Ultrafast Amplifiers by Francois Salin, <http://www.physics.gatech.edu/gcuo/lectures/index.html>.
- [2] D. Strickland and G. Mourou, "Compression of amplified chirped optical pulses," *Optics Communications* **56**, pp 219-221 (1985).
- [3] D.J. Ripin, J.R. Ochoa, R.L. Aggarwal, and TY Fan, "165-W cryogenically cooled Yb:YAG laser," *Optics Letters* **29**, pp. 2154-56, (2004).
- [4] K. H. Hong, A. Siddiqui, J. Moses, J. Gopinath, J. Hybl, F. O. Ilday, T.Y. Fan and F. X. Kaertner, "Generation of 287-W, 5.5-ps pulses at 78-MHz repetition rate from a cryogenically-cooled Yb:YAG amplifier seeded by a fiber chirped-pulse amplification system," *Optics Letters* **33**, pp.2473-2475 (2008).
- [5] G. Cerullo and S. De Silvestri, "Ultrafast Optical Parametric Amplifiers," *Review of Scientific Instruments* **74**, pp. 1-17 (2003)
- [6] R. Boyd, *Nonlinear Optics* ~Academic, New York, 1992.
- [7] V. G. Dmitriev, G. G. Gurzadyan, and D. N. Nikogosyan, *Handbook of Nonlinear Optical Crystals*, Springer, Berlin (1991).
- [8] J. A. Armstrong, N. Bloembergen, J. Ducuing, P. S. Pershan, "Interactions between Light Waves in a Nonlinear Dielectric," *Phys. Rev.*, **127**, 6 (1962).
- [9] T. J. Driscoll, G. M. Gale, and F. Hache, *Opt. Commun.* 110, 638 (1994). G. M. Gale, M. Cavallari, T. J. Driscoll, and F. Hache, *Opt. Lett.* 20, 1562 (1995). G. M. Gale, M. Cavallari, and F. Hache, *J. Opt. Soc. Am. B* 15, 702 (1998). G. M. Gale, M. Cavallari, and F. Hache, *IEEE J. Sel. Top. Quantum Electron.* 4, 224 (1998).





## Chapter 13

# High Harmonic Generation

High harmonic generation (HHG) is a technique for producing spatially and temporally coherent extreme-ultraviolet (EUV) light, as well as light pulses as short as hundred attoseconds ( $1 \text{ attosecond} = 10^{-18} \text{ seconds}$ ). To support pulses at such short duration light with a frequency higher than the inverse pulse duration is required corresponding to EUV wavelength of tenth of nanometers and shorter. Construction of lasers at these wavelengths is challenging and other means of producing significant EUV radiation, such as synchrotrons and Free-Electron Lasers (FELs) are rather expensive. HHG has the potential for generating significant coherent EUV radiation, even in the form of ultrashort pulses with attosecond duration opening up the new field of ultrafast x-ray spectroscopy.

HHG occurs when an intense pulsed laser beam is focused into a (noble) gas jet or solid. The intensity of the laser light is chosen such that its electric field amplitude is comparable to the electric field in atoms. Such fields are able to detach electrons from atoms by tunnel ionization, as opposed to photo-ionization by a weak field with high enough photon energy. The detached electron is accelerated in the field and under certain conditions has significant probability to hit the ion left behind upon return. The "collision" results in the emission of high energy photons. This description is called three step model and depicted in Figure 13.1

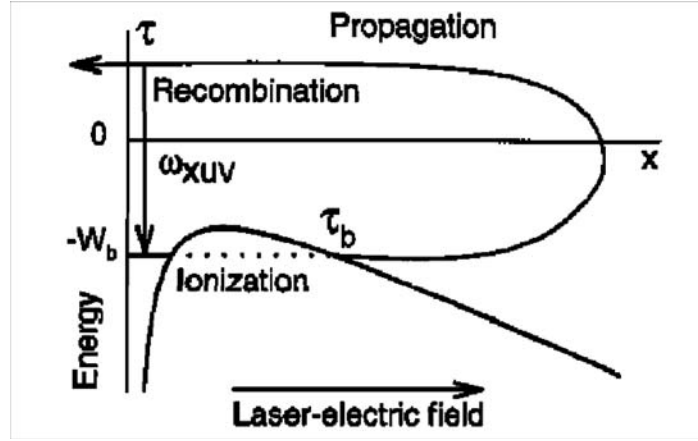


Figure 13.1: Three step model of High Order Harmonic Generation.

## 13.1 Atomic units

The dynamics of electrons in electric fields of atomic strength is most conveniently described in *atomic units*. Then typically atomic magnitudes are numbers of order one, which is very convenient. Atomic units are used in the vast majority of atomic physics literature, and in particular in the HHG literature.

In atomic units Planck's constant  $\hbar$ , the electron mass,  $m$ , and the electron charge,  $q$ , are set to one. Mass, charge and angular momentum are therefore measured relative to these magnitudes, and once three of them are given, the atomic unit for every other physical magnitude can be defined. In order to gain some intuition about atomic units, it is instructive to think about the Bohr hydrogen atom, with the electron moving around the proton in a circular orbit whose radius is the Bohr radius (see Fig. 13.2). Table 13.1 lists the definitions of some atomic units and conversion ratios to SI units:

For example, the hydrogen ionization energy is  $\frac{1}{2}\text{au}$ , and that of helium is about  $0.9\text{au}$ . Another example is the dielectric susceptibility of matter. Ignoring for the moment tensorial and non-instantaneous effects we can write for the polarization of a medium

$$P = \epsilon_0 (\chi^{(1)} E + \chi^{(2)} E^2 + \chi^{(3)} E^3 + \dots) \quad (13.1)$$

The nonlinear susceptibilities in SI units are of the order of  $10^{-12}$  for  $\chi^{(2)}$

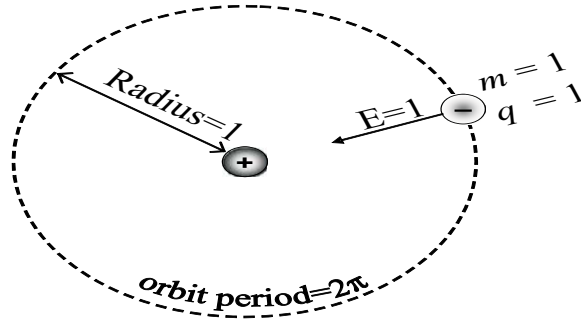


Figure 13.2: Definitions of atomic units through the Bohr model of the hydrogen atom.

and  $10^{-23}$  for  $\chi^{(3)}$ . When  $P$  and  $E$  are expressed in atomic units, all the  $\chi$ -s are of order one, because the electric field is then expressed in units of the electric field in an atom. We can argue that once the electric field reaches atomic fields, all harmonics of the fundamental laser wave will be observed, with intensities of similar orders of magnitude. Indeed HHG occurs only when such intensities are reached.

A typical field amplitude for HHG in helium is  $0.3 \text{ au} \approx 1.7 \times 10^9 \text{ V/cm}$ . The corresponding intensity is  $0.5 \cdot E^2 / 377 \Omega \approx 4 \times 10^{15} \text{ W/cm}^2$ . For a Ti:sapphire beam (800 nm wavelength) focused to a  $25 \mu\text{m}^2$  spot and for a pulse duration of 10 fs we find that the pulses should carry about 0.1 mJ of energy.

## 13.2 The three step model

HHG photon energies achieved today reach up to 1.3 keV, which is about 50 au. This high photon energy was achieved in helium. If we adopt the familiar picture (see Fig. 13.1), according to which a photon at certain energy is emitted when an electron “falls” from an excited state to the ground state, we see that the electron must “fall” from a very highly excited free state

Atomic unit of...	Definition	In SI units
Electric charge	The electron charge	$1.602 \times 10^{-19} \text{ C}$
Mass	The electron mass	$9.109 \times 10^{-31} \text{ kg}$
Length	The Bohr radius	$5.2917 \times 10^{-11} \text{ m}$
Time	$1/2\pi$ of the first Bohr orbit period	$24.189 \text{ asec}$
Energy	The potential energy of the electron in the first Bohr orbit	$27.21 \text{ eV} = 4.359 \times 10^{-18} \text{ J}$
Electric field	The electric field at the first Bohr orbit	$5.142 \times 10^{11} \text{ V/m}$

Table 13.1: Definitions of atomic units for some often used quantities and conversion to the SI system.

(50 times the binding energy). Since the potential is negative, high energy necessarily means high kinetic energy i. e. high velocity.

In order that a force of  $\sim 1 \text{ au}$  accelerates the electron to such high kinetic energy, it should travel a long distance away from the atom. According to the three step model, the electron is released from the atom by the laser field, accelerated in the free field away from the atom, then accelerated back towards the atom and collides with it. The energy lost in the collision shows up as a UV photon. The sequence of tunnel ionization, acceleration in the laser field and recollision is the called the three step model of HHG [2][3].

In order to estimate the energy acquired by the accelerating electron, we consider a free electron in a harmonic field of amplitude  $E$  and angular frequency  $\omega$ . The time-averaged kinetic energy equals

$$U_p = \left( \frac{qE}{2m\omega} \right)^2 = \left( \frac{E}{2\omega} \right)^2, \quad (13.2)$$

where the first expression is in general units ( $q$  is the electron charge) and the second one in atomic units. Note that this is a purely classical object since it does not involve  $\hbar$ .  $U_p$  is commonly referred to as the *ponderomotive energy*.

In order to achieve high ponderomotive energy,  $\omega$  must be a small number, that is, the optical frequency of the laser pulses must be much slower than atomic timescales.

### 13.2.1 Ionization

There are three regimes of ionization of an atom by an optical field. We consider here only fields of frequency  $\omega$  such that  $\omega < I_p$  ( $\hbar\omega < I_p$  in general units.  $I_p$  is the ionization potential of the atom). Therefore photoionization

1

T

$\gamma$

ic

b

in

re

r

e

-

s

1

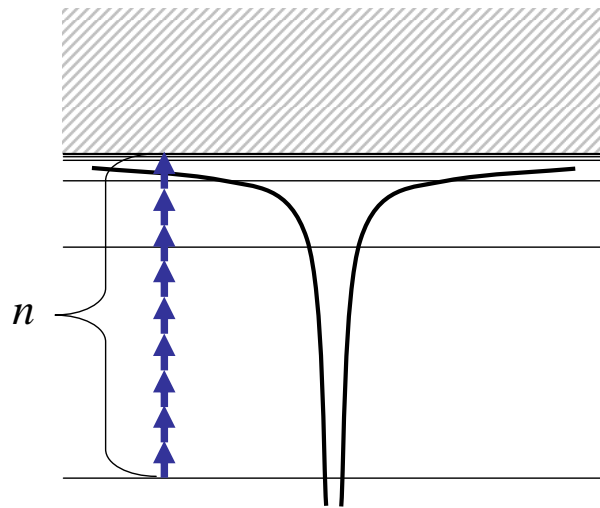


Figure 13.3: Ionization by  $n$  photons.

#### 2. Tunnelling regime.

Tunnelling is the dominant regime when  $U_p \gtrsim I_p$ , i.e.  $\gamma < 1$ , but  $E$  is small enough such that the barrier-suppression regime (the next one) is not yet reached, see Figure 13.4 and 13.5. The electron is released through tunnelling.

This regime is characterized by an exponential dependence of the ionization rate on the instantaneous electric field [4]:

$$w(E) \sim \exp \left( -\frac{2(2I_p)^{3/2}}{3E} \right), \quad (13.3)$$

where the ‘ $\sim$ ’ sign :

factor in  $E^n$ .

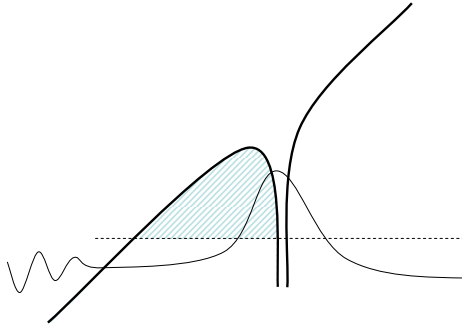


Figure 13.4: Ionization by tunnelling. The shaded area is the barrier, the classically forbidden region. The rate of tunnel ionization is exponential in the “area” under the barrier.

### 3. Barrier-suppression regime.

This regime is reached when the field is strong enough such that there is no energy barrier separating the electron from the free space (see Fig. 13.5). The barrier suppression regime is characterized by a nearly linear dependence of the ionization rate on the incident electric field.

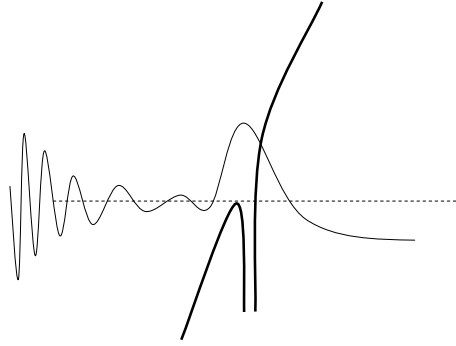


Figure 13.5: Ionization in the barrier-suppression regime.

When  $\omega \ll I_p$  the two last regimes are well described by the *quasi-static approximation*. The reason for this terminology is that the variation of the laser field is so slow that the instantaneous ionization rate coincides with a static one. Let then  $w(E)$  be the static ionization rate as function of the electric field. In the tunnelling and the barrier suppression regimes, with  $\omega \ll I_p$ , we therefore have

$$|a(t)|^2 = \exp \left( - \int_0^t w(E(t')) dt' \right), \quad (13.4)$$

where  $a(t)$  is the probability amplitude of finding the atom in the ground state. Note, that for  $\omega t \gg 1$  the ionization rate does not depend on  $\omega$ . This is in contrast with the multiphoton regime, where the rate exponentially decreases as  $\omega \rightarrow 0$ .

The static ionization rate  $w(E)$  is well described in the tunnelling regime by the Ammosov-Delone-Krainov formula [4]. For hydrogen and helium  $w(E)$  has been numerically calculated to high precision, and is shown in Fig. 13.6



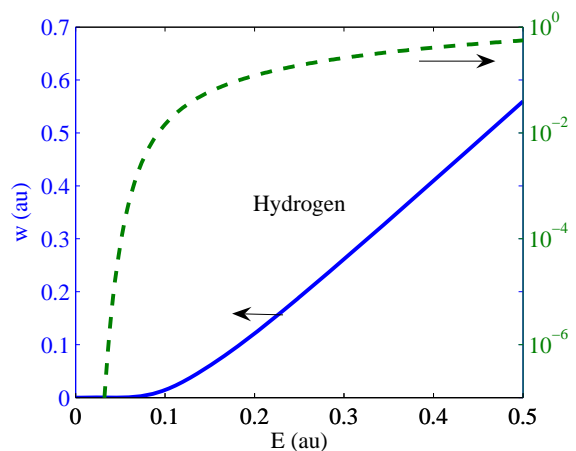


Figure 13.6: Static ionization rate for Hydrogen on a linear and logarithmic scale.

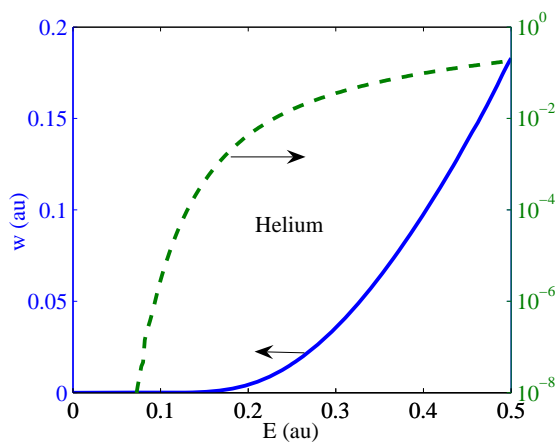


Figure 13.7: Static ionization rate for Helium on a linear and logarithmic scale..

### 13.2.2 Propagation

According to the correspondence principle, at high energies quantum mechanics should resemble classical mechanics. Indeed it turns out that the

propagation of the freed electron can be very well described classically. Since the Coulomb force exerted on the electron by the ion is negligible compared to the laser field during most of the electron excursion, the motion of the electron is well described by a free electron accelerated in the presence of the electric field of the laser pulse. Since we expect that the electrons do not reach relativistic speeds, we can neglect the Lorentz Force. It also turns out that the right after the tunneling, the velocity of the electron vanishes, i.e. the electron starts with zero velocity in the external field.

$$\ddot{x}(t) = E_0 \cos \omega t \quad (13.5)$$

$$\dot{x}(t) = \frac{E_0}{\omega} \sin \omega t - \frac{E_0}{\omega} \sin \omega t_0 \quad (13.6)$$

$$x(t) = -\frac{E_0}{\omega^2} \cos \omega t - (t - t_0) \frac{E_0}{\omega} \sin \omega t_0 + \frac{E_0}{\omega^2} \cos \omega t_0, \quad (13.7)$$

see Figure 13.8. Here,  $t_0$  is the time at which the electron was released from the atom. It is assumed that the electron is released with zero initial velocity. This assumption can be justified quantum mechanically. Since the electron is a quantum particle, it is released at all possible times  $t_0$  “together”. Each moment there is a probability amplitude to be released, depending (in the quasi-static approximation) on the electric field at that moment.

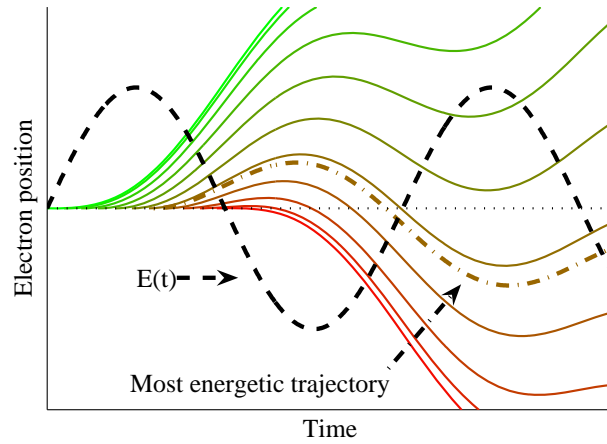


Figure 13.8: The position of the electron as function of time for different “ionization times”  $t_0$ . The “most energetic trajectory” refers to the solution where the electron encounters the nucleus with the maximal kinetic energy.

According to the three step model, the energy lost by the electron when it recollides with the nucleus is released as an HHG photon. We therefore wish to know how much kinetic energy the electron has when it returns. To this end we need to solve the Eq. (13.5) for  $x(t) = 0$  for some  $t$  and compute the kinetic energy  $\dot{x}^2(t)/2$  at that instant.

The solution cannot be expressed in terms of elementary functions. However, it can be easily found on a computer. It is easy to see that electrons re-encounter the nucleus only if they are released when the magnitude of the field is *decreasing* (see Fig. 13.8). The kinetic energy upon the first encounter of the electron with the nucleus is plotted in Fig. 13.9 as function of the ionization time  $t_0$ . It reaches a maximum for  $\omega t \approx 0.31$ , and the maximum approximately equals  $3.17U_p$ , which the ponderomotive energy  $U_p = \left(\frac{E}{2\omega}\right)^2$  of an electron in the laser field..

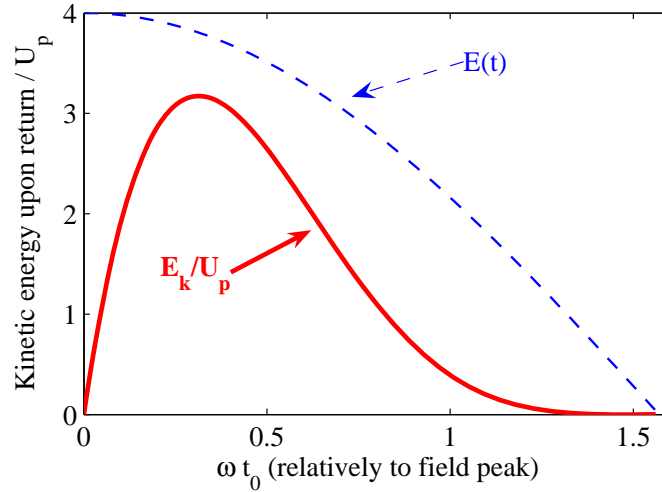


Figure 13.9: Kinetic energy upon return to the nucleus as function of the “ionization time”. The maximum is achieved about 0.31 radians after the peak of the electric field. For that case, the kinetic energy upon return reaches  $3.17U_p$ . The dashed curve is the electric field.

### 13.2.3 Recombination

A proper description of the recombination stage requires a quantum mechanical treatment of the rescattering problem and the emission of radiation. We

need to start from the Schroedinger equation of an electron bound to the atom, later partially tunneling ionized and accelerated. This is described by the Schroedinger equation of a single active electron in dipole approximation

$$i\frac{d}{dt}|\psi\rangle = H|\psi\rangle - E(t)x \quad (13.8)$$

with the atomic Hamiltonian

$$H = -\frac{1}{2}\nabla^2 + V(\vec{r}), \quad (13.9)$$

where,  $V(\vec{r})$  is the effective atomic potential confining the electron to the atom. Due to the interaction with the laser field we expect that the wavefunction of the electron, that is initially in the ground state  $|0\rangle$  with energy eigenvalue  $-I_P$ , where  $I_P$  is the ionization potential, evolves into a superposition state between the ground state with probability amplitude  $a(t)$  and a wavefunction describing the freed electron

$$|\psi(t)\rangle = a(t)|0\rangle + |\varphi(t)\rangle. \quad (13.10)$$

The freed electron together with the remaining ion forms a dipole and the expected value of the dipole moment is like for a two level system atom

$$\vec{d}(t) = \langle\psi(t)|\vec{x}|\psi(t)\rangle. \quad (13.11)$$

However, what acts as the source for electromagnetic radiation is not the dipole moment but rather the dipole acceleration. With the Ehrenfest Theorem in Quantum Mechanics, which is simply the Heisenberg equation of motion for the electrons kinetic momentum

$$\ddot{\vec{x}} = -\nabla V(\vec{r}) + E(t)\hat{x} \quad (13.12)$$

and neglecting the external field coming from the laser, since it doesn't contain Harmonics, the dipole acceleration contributing to HHG can be written as

$$\ddot{\vec{d}}_{HHG}(t) = -\langle \psi(t) | \nabla V(\vec{r}) | \psi(t) \rangle \quad (13.13)$$

$$= -|a(t)|^2 \langle 0 | \nabla V(\vec{r}) | 0 \rangle - a(t) \langle \varphi(t) | \nabla V(\vec{r}) | 0 \rangle \\ - a^*(t) \langle \psi(t) | \nabla V(\vec{r}) | 0 \rangle - \langle \varphi(t) | \nabla V(\vec{r}) | \varphi(t) \rangle. \quad (13.14)$$

$$\sim -a^*(t) \langle \varphi(t) | \nabla V(\vec{r}) | 0 \rangle - a(t) \langle 0 | \nabla V(\vec{r}) | \varphi(t) \rangle \quad (13.15)$$

$$= \ddot{\xi}(t) + \ddot{\xi}^*(t), \text{ with } \ddot{\xi}(t) = -a^*(t) \langle \varphi(t) | \nabla V(\vec{r}) | 0 \rangle \quad (13.16)$$

The first term vanishes, because of inversion symmetry of the atomic ground state and the last term is neglected, because it is expected to be small.

After some calculations, the result is [5]

$$\ddot{\xi}(t) = 2^{3/2} \pi (2I_P)^{1/4} e^{i\pi/4} \sum_n \frac{a(t_{nb}(t))a(t) \sqrt{w(E t_{nb}(t))}}{E(t_{nb}(t))(t - t_{nb}(t))^{3/2}} \vec{\alpha}_{rec} e^{-iS_n(t)}.$$

Here, the probability amplitudes of the ground state enter at the birthtime  $t_{nb}(t)$ , and  $t$ , if  $t$  is the recollision time of the trajectory. The recombination

matrix element  $\vec{\alpha}_{rec} = \langle k(t) | \nabla V(\vec{r}) | 0 \rangle$  and  $S_n(t) = \frac{1}{2} \int_{t_{nb}(t)}^t k(t')^2 dt' + I_P(t -$

$t_{nb}(t))$  is the classical action, the electron picks up during acceleration. The sum over  $n$  is the sum over all trajectories arriving at time  $t$ .

It is plausible that the energy released during recombination equals the kinetic energy the electron acquired plus the ionization potential, since the electron transitions from the continuum to a state with energy  $-I_p$ . In particular, we can expect the maximal energy released in the collision to be

$$\omega_{\text{hmax}} = I_p + 3.17U_p. \quad (13.17)$$

Figure 13.10 shows the Fourier transform of the calculated dipole acceleration for hydrogen excited by Ti:sapphire (800nm, corresponding to  $\omega = 0.057\text{au}$ ) pulses with an ideal sinusoidal single cycle pulse ( $E(t) = E_0 \sin \omega t$ ). The field amplitude used is shown near each spectrum. ( $\omega_{\text{hmax}} = I_p + 3.17U_p$  in atomic units). Remarkably Eq. (13.17), which is obtained from very simple considerations, gives the correct prediction for the cutoff of the spectrum. No harmonics above  $\omega_{\text{hmax}}$  are observed<sup>1</sup>, see Fig. 13.10. However, below the

<sup>1</sup>To be more precise, quantum mechanical analysis reveals that the cutoff formula  $\omega_{\text{hmax}} = 1.28I_p + 3.17U_p$ .

cutoff energy we observe oscillations in the high harmonic spectrum. This results from interference of contributions from the long and short trajectories, which contribute to the same frequency, energy, as can be seen from Fig. 13.8.

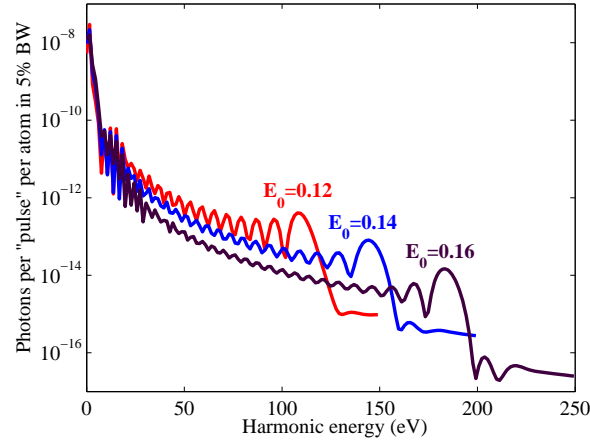


Figure 13.10: Simulated HHG spectra for hydrogen excited by Ti:sapphire (800nm, corresponding to  $\omega = 0.057\text{au}$ ) pulses with an ideal sinusoidal single cycle pulse ( $E(t) = E_0 \sin \omega t$ ). The field amplitude is denoted near each spectrum.

Figure 13.11 shows the kinetic energy normalized to the pondermotive potential that each trajectory contributes as a function of arrival time.

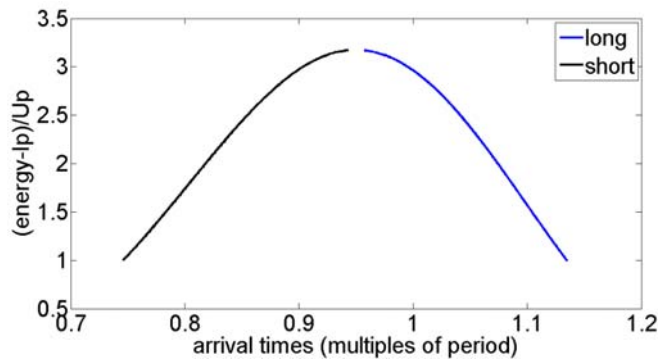


Figure 13.11: Kinetic Energy of long and short trajectories as a function of arrival time.

Figure 13.12 shows the Fourier transform of the calculated dipole acceleration for hydrogen excited by Ti:sapphire pulses with a secant hyperbolic pulses hape, 5fs FWHM duration and a maximal field amplitude of 0.12au. The spectrum is the cummulative effect of several cycles

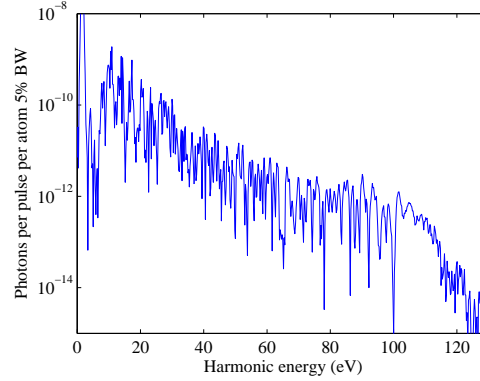


Figure 13.12: Simulated HHG spectra for hydrogen excited by Ti:sapphire (800nm, corresponding to  $\omega = 0.057\text{au}$ ) pulses with a secant hyperbolic pulse with 5fs FWHM duration and a maximal field amplitude of 0.12au.

The spectrum is the cummulative effect of several cycles, where in each half cycle a small fraction of the atoms are ionized, see Fig. fch13\_multicyclehhg

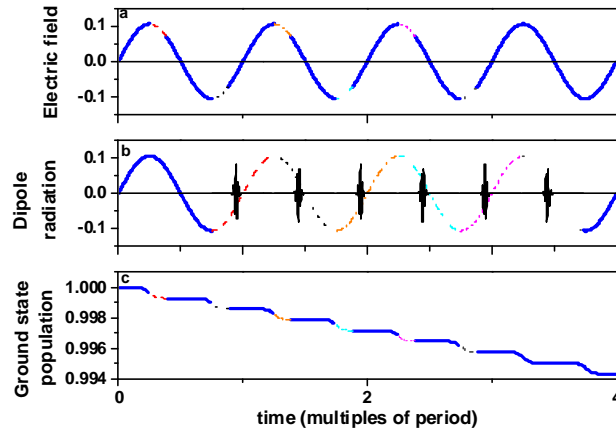


Figure 13.13: High harmonic generation dynamics in a multicycle pulse.

### 13.3 Attosecond pulses

The electron which acquires the largest amount of kinetic energy leaves the atom  $0.31\omega^{-1}$  after each peak of the field and hits the nucleus back at time  $4.4\omega^{-1}$  (about  $3/4$  of a cycle) after that peak (see Figs. 13.8, 13.14). Electrons that hit the nucleus later (short trajectories) or earlier (long trajectories) have less kinetic energy upon return. Thus the HHG radiation emitted by the recolliding electron has two contributions, one from the long and one from the short trajectories, both of which are down or up chirped (see Fig. 13.15).

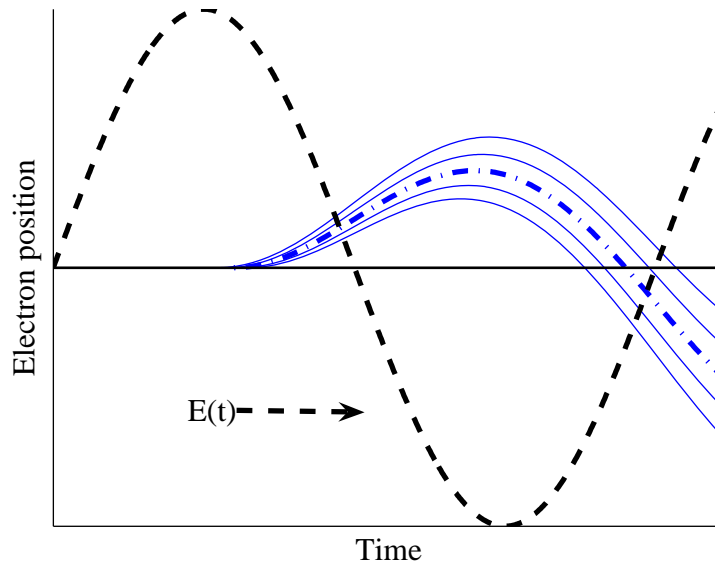


Figure 13.14: A single cycle, with a single recollision, leading to an isolated attosecond pulse. Most energetic trajectory (dash dotted line).



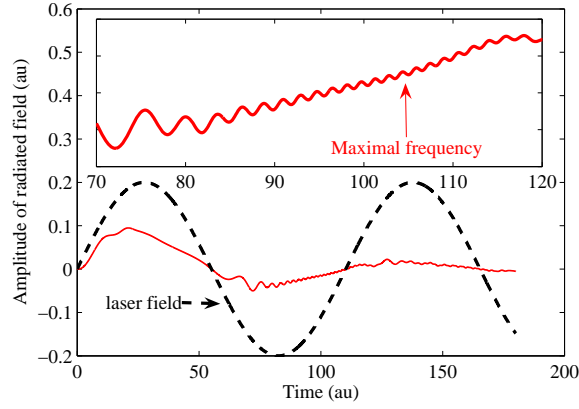


Figure 13.15: Neighborhood of the most energetic trajectory, which is responsible for the highest frequency radiation emitted.

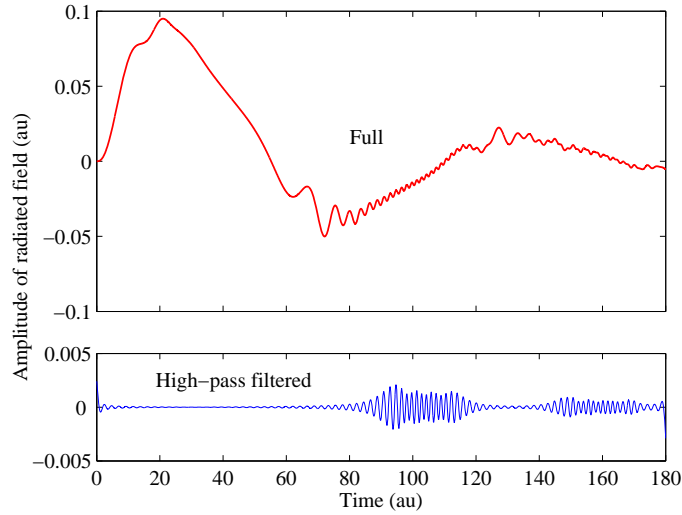


Figure 13.16: The same as Fig. 13.14a, before and after high-pass filtering.

There are several possibilities to select attosecond duration pulses, from this emission. First it was proposed to select isolated attosecond pulses, by using about two-cycle pulses and using high pass filtering of the emitted HHG

radiation to select the cut-off spectrum produced by the highest field cycle. Such a filtering is possible by using a multilayer MoSi-mirrors. Fig. 13.16 shows simulated electric field amplitude of the emitted HHG radiation before and after high-pass filtering. At the output of the filter we observe isolated pulses of several hundreds of attoseconds [7][9]. Other possibilities are to use polarization gating to achieve HHG in a single cycle from a few-cycle pulse and select the emission from the short or long trajectories and compression of these chirped emission using material dispersion in thin metal films [8]. The gating techniques have been further refined over the last years to a scheme called double-optical gating where both polarization and second harmonic field is used to further constrain HHG within a multicycle pulse.

### 13.3.1 The intensity challenge

HHG was discovered in 1987. Due to the progress in short pulse high energy Ti:sapphire lasers (30fs, 1mJ) it became possible to expose atoms to very high field strength before complete ionization and in 1997 EUV radiation down to 2.5 nm wavelength was demonstrated using HHG [6]. The shortest HHG wavelength demonstrated so far is 1nm (2005), however the efficiencies are very small at these short wavelengths.

### 13.3.2 The necessity of short drive pulses

Short pulses are a necessity for HHG in order to avoid depletion of the ground state during previous pulse maxima.

Fig. 13.17 shows the population of the ground state of Helium calculated with Eq. (13.4). When the pulses are not short enough (50fs in that particular example) most of the ground state is already depleted before the peak of the pulse is reached. Therefore the HHG radiation is released by electric fields of lower amplitude than the peak of the pulse, and most of the intensity of the pulse is "wasted".

The shorter the pulses become, the higher will be the ground state population when the atom experiences the peak of the electric field. Therefore short (few-cycle) pulses are a necessity for HHG, even when sufficient peak power is available.

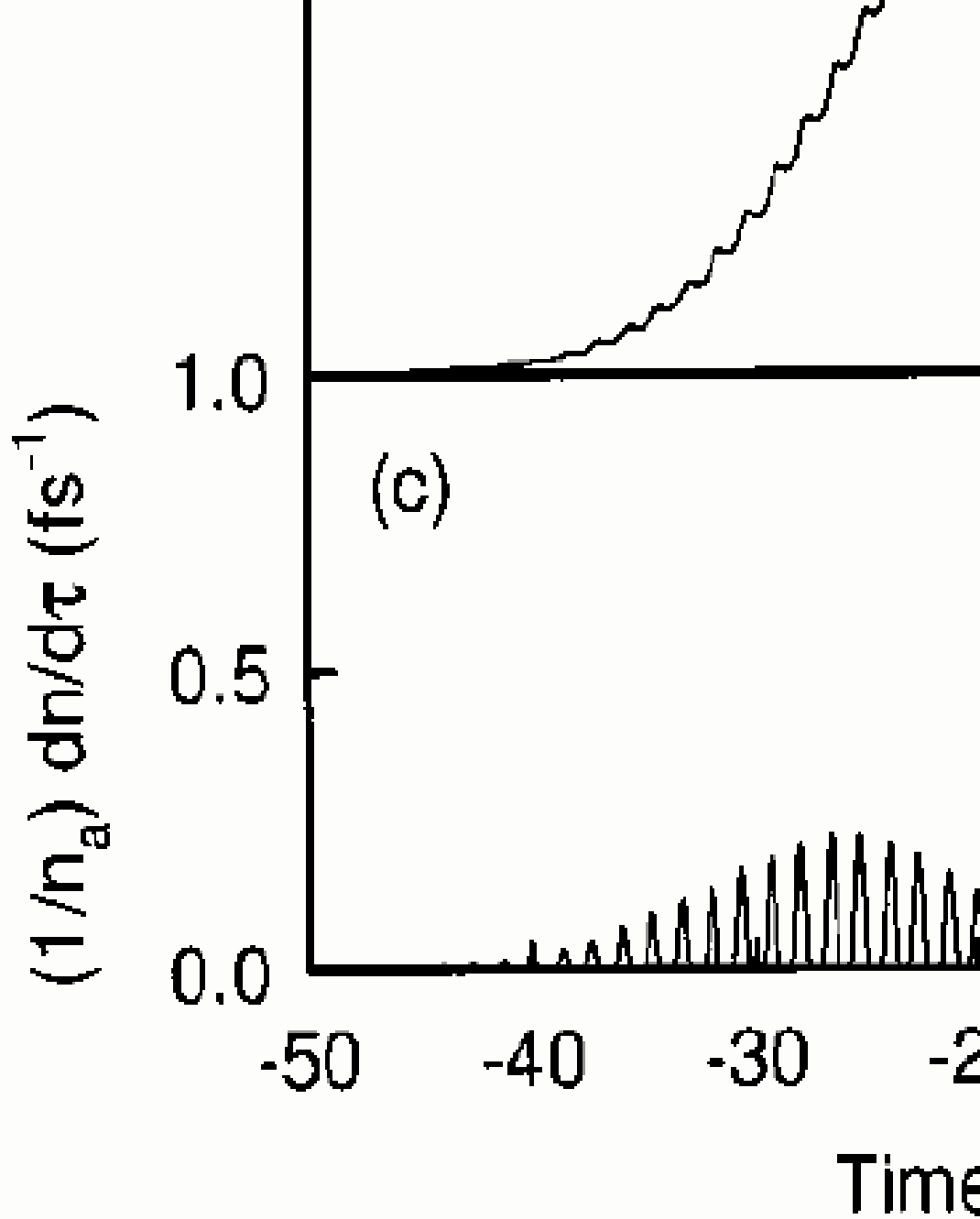


Figure 13.17: Ionization of helium in the presence of a linearly polarized electric field of a laser pulse with 800nm wavelength and a peak intensity  $4 \times 10^{15} \text{W/cm}^2$ : (a) electric field; (b) fraction of ionized electrons; (c) instantaneous ionization rate. The thin and the thick lines represent pulses of durations of 50fs and 5fs FWHM, respectively.[1]

Figure 13.18: Helium in the presence of a linearly polarized electric field of a laser pulse with 800nm wavelength and a peak intensity  $4 \times 10^{15} \text{W/cm}^2$ : (a) electric field; (b) fraction of ionized electrons; (c) instantaneous ionization rate. The thin and the heavy lines represent pulses of durations of 50fs and 5fs FWHM.

### 13.3.3 Quantum diffusion

The simple classical picture of the propagation stage gives the correct cutoff law. However quantum mechanically the electron propagates along many trajectories at the same time. In particular, there is an uncertainty in the lateral initial velocity of the electron, and it therefore has returning electron wave packet has components that miss the nucleus.

The above described behavior is called quantum diffusion: free electron wavepackets expand as they propagate, just like a light pulse in a dispersive medium. The electron wavepacket expands as  $\sqrt{\tau}$  ( $\tau$  is the time of propagation between ionization and recombination) in each spatial direction.

Therefore the amplitude in the center of the wavepacket decreases as  $\tau^{-3/2}$ . The amplitude of the emitted HHG electric field therefore scales like  $\tau^{-3/2}$ , and the intensity – like  $\tau^{-3}$ . The travel time is about an optical cycle.

The intensity of the HHG radiation therefore cubically decreases with increasing drive wavelength. However the spectral cutoff energy quadratically increases with it and the ionization of the atom can be reduced. The question what is the ideal drive wavelength to achieve maximum HHG for a desired wavelength range is not yet resolved.

### 13.3.4 Propagation effects – phase matching

In order to achieve efficient HHG, the contributions from single atoms emitting at different cycles and positions in the medium must interfere constructively with one another. Just like in second harmonic generation or optical parametric generation, phase matching is required. Phase matching is achieved, if the refractive index of the generated EUV radiation is equal to the index experienced by the driver laser pulse in the gas. The EUV radiation only weakly interacts with the gas and therefore propagates at the speed of light. However, the drive laser pulse experiences the dispersion from the gas, which increases the refractive index and the negative index of the free electrons generated (plasma). Choosing the proper ionization level and gas pressure is therefore important to achieve phase matching of the driver pulse and the generated EUV radiation.

Because of the phase mismatch and also because the spatial profile of the driver pulses, the pulse is distorted by the index profile of the free electrons, i.e. plasma defocusing of the laser beam occurs. Another limitation on the length comes from absorption: the longer the gas jet, the more it begins to absorb the HHG photons. These effects severely limit the HHG conversion efficiency.

# Bibliography

- [1] T. Brabec and F. Krausz, "Intense few-cycle laser fields: Frontiers of nonlinear optics," *Rev. Mod. Phys.* **72**, 545-591 (2000).
- [2] P. B. Corkum, "Plasma Perspective on Strong-Field Multiphoton Ionization," *Phys. Rev. Lett.* **71**, 1994-1997 (1993).
- [3] M. Lewenstein, Ph. Balcou, M. Yu. Ivanov, A. L'Huillier, and P. B. Corkum, "Theory of High Harmonic Generation by low-frequency laser fields," *Phys. Rev. A* **49**, 2117-2132 (1994).
- [4] M.V. Ammosov, N. B. Delone, and V. P. Krainov, *Sov. Phys. JETP* **64**, 1191 (1986).
- [5] A. Gordon and F. X. Kaertner, "Quantitative Modeling of Single Atom High Harmonic Generation," *PRL* **95**, 223901 (2005).
- [6] \bibitem{MurnaneScience98} A. Rundquist, C. G. Durfee, Z. H. Chang, C. Herne, S. Backus, M. M. Murnane, and H. C. Kapteyn, *Science* {\bf 280}, 1412 (1998).
- [7] M. Hentschel, R. Kienberger, C. Spielmann, G. A. Reider, N. Milosevic, T. Brabec, P. Corkum, U. Heinzmann, M. Drescher, and F. Krausz, "Attosecond metrology," *Nature*, vol. **414**, pp. 509-513, 2001.
- [8] G. Sansone, E. Benedetti, F. Calegari, C. Vozzi, L. Avaldi, R. Flammini, L. Poletto, P. Villoresi, C. Altucci, R. Velotta, S. Stagira, S. D. Silvestri, and M. Nisoli, "Isolated Single-Cycle Attosecond Pulses," *Science*, vol. **314**, pp. 443-446, 2006.

- [9] E. Goulielmakis, M. Schultze, M. Hofstetter, V. S. Yakovlev, J. Gagnon, M. Uiberacker, A. L. Aquila, E. M. Gullikson, D. T. Attwood, R. Kienberger, F. Krausz, and U. Kleineberg, "Single-Cycle Nonlinear Optics," *Science*, vol. **320**, pp. 1614 2008.